NEAR-WALL SIMILARITY IN THREE-DIMENSIONAL TURBULENT BOUNDARY LAYERS

by

Mark Harris Tennant

Dissertation submitted to the Graduate Faculty of the
Virginia Polytechnic Institute and State University
in partial fulfillment of the requirements for the degree of

DOCTOR OF PHILOSOPHY

in

Mechanical Engineering

APPROVED:

F. J. Pierce, Chairman

J. B. Jones

H. L. Moses

W. C. Thomas

C. B. Ling

November, 1977

Blacksburg, Virginia

ACKNOWLEDGEMENTS

I wish to express my sincerest appreciation to Dr. Felix J. Pierce, my major advisor, for his help, encouragement, and personal counsel. Because of him, my time spent here has been a valuable experience that has allowed me to learn, mature, and grow professionally.

I am indebted to Dr. J. B. Jones, Dr. W. C. Thomas, Dr. H. L. Moses, and Dr. C. B. Ling, who served on my advisory committee, for their helpful suggestions.

Mr. J. E. McAllister, Mr. J. A. Rule, and Mr. J. T. Walker deserve a great share of the recognition for this work owing to their contributions in both the experimental and computer simulation phases of this study. I thank them all.

To Jack Gray and all the shop personnel, my many thanks. Such a large experimental undertaking would have been impossible without their help.

My mother, Mrs. Evelyn H. Tennant and my brothers, Jeffery S. and Jonathan C. Tennant have given me constant encouragement and support. My many thanks to them.

Finally, no one has had a more positive influence on my life than my father, Paul S. Tennant. Though he did not live to see the completion of this work, his guidance was deeply felt throughout these last four years. To him I dedicate this manuscript and the effort spent in its completion.

TABLE OF CONTENTS

TABLE OF CONTENTS (Continued)

LIST OF FIGURES

LIST OF TABLES

NOMENCLATURE

C	additive similarity law constant in the logarithmic region
C_f	wall friction coefficient, $\frac{\tau_w}{\frac{\rho U^2}{2}}$
C_p	constant pressure specific heat
d	inside diameter of probe
d_m	diameter of floating element disk
d_p	distance between plates
D	outside diameter of probe
f	functional relation for near-wall similarity, $q^+=f(y^+)$
F	compressibility factor, $M_t r(\gamma'-1)/2$
h_1, h_2, h_3	form metrics
I_1	$\int_o^{y^+} f^2 dy^+$
I_2	$\int_o^{y^+} I_1/y^+ dy^+$
I_3	$f\int_o^{y^+} f dy^+ - I_1$
ℓ	mixing length
L	length scale
M	Mach number
M_t	Mach number, $q^*/\sqrt{\gamma' R_w T_w}$
p	pressure
$q_{equivalent}$	as defined by Eqs. 42, 44, 45, 47, 50, and 51
q_w	wall velocity component

q_{wake}	wake velocity component
q^+	nondimensionalized velocity in three-dimensional flow, $q_{equivalent}/q^*$
q^*	wall friction velocity in three-dimensional flow
q_ξ^*	freestream component of q^*
r	recovery factor
R_w	gas constant at wall
Re_{unit}	tunnel unit Reynolds number at entrance, U/ν
Re_x	Reynolds number, Ux/ν
Re_θ	Reynolds number, $\frac{U}{\nu}\int_o^\infty \frac{u}{U}(1-\frac{u}{U})\,dy$
S	$(1 + \alpha' y^+)^{\frac{1}{2}}$
S_o	$(1 + 0.1108\ \alpha')^{\frac{1}{2}}$
t	thickness of floating element lip
T	temperature, absolute
u	velocity component in freestream direction except for in wall shear stress direction [6] or in the x direction [56]
u^*	wall friction velocity, $\sqrt{\tau_w/\rho}$ except for in freestream direction [55], [6]
U	freestream velocity
u_0	developed velocity profile, $\int[1 + (\frac{dv}{du})^2]^{\frac{1}{2}}du$
U_0	tunnel reference velocity
v	velocity component in y direction
w	velocity component in z direction

w^* wall friction velocity in cross flow direction [55], [6]

x coordinate along the tunnel axis except for in wall shear stress direction [6] or in freestream direction [61]

y coordinate perpendicular to the wall

y^+ nondimensionalized distance from the wall, yq^*/ν

z coordinate normal to x

α pressure gradient parameter, $\frac{\nu}{\rho u^{*3}} \frac{dp}{dx}$

α' pressure gradient parameter, $\frac{\nu}{\rho u^{*3} h_1} \frac{\partial p}{\partial x}$

α_ℓ direction of laminar component of shear stress

α_0 angle between the freestream direction and a velocity vector

α_x pressure gradient parameter, $\frac{\nu}{\rho q^{*3}} \frac{\partial p}{\partial x}$

α_z pressure gradient parameter, $\frac{\nu}{\rho q^{*3}} \frac{\partial p}{\partial z}$

α_1 wall shear stress gradient parameter, $\frac{\nu}{u^{*2}} \frac{du^*}{dx}$

β angle between the wall shear stress vector and the tunnel axis

β_0 $-\tan^{-1} \delta_2/\delta_1$

β_t direction of the turbulent shear stress component

β_x wall shear stress gradient parameter, $\frac{\nu}{q^{*2}} \frac{\partial q^*}{\partial x}$

β_z wall shear stress angle gradient parameter, $\frac{\nu}{q^*} \frac{\partial \Phi_\tau}{\partial x}$

β_1	wall shear stress gradient parameter, $\frac{\nu}{u^{*2}} \frac{du^*}{dx}$
γ	angle between the limiting wall velocity vector and a velocity vector
γ'	specific heat ratio
δ	boundary layer thickness
δ_1	$\int_0^\infty (1 - u/U)\, dy$
δ_2	$-\int_0^\infty \frac{w}{U}\, dy$
$\varepsilon_1, \varepsilon_2, \varepsilon_3$	component of eddy viscosity
ζ	direction normal to freestream direction
θ	angle between pressure gradient and wall shear stress vectors
θ'	angle between freestream and wall shear stress directions
κ	von Karman's constant
μ	absolute viscosity
ν	kinematic viscosity
ξ	freestream direction coordinate
ρ	density
τ	shear stress
τ_{meter}	wall shear stress as measured by a floating element device
τ_t	turbulent shear stress
τ_w	wall shear stress

Φ	velocity vector direction [60]
Φ_τ	angular rotation of coordinate system [6]
Ψ	angular displacement of the total shear relative to the wall shear stress direction [60]

I. INTRODUCTION

It is important in the comprehension of this work that the reader be familiar with the fundamental concepts, significance, and problems surrounding near-wall similarity in three-dimensional turbulent boundary layers. These introductory remarks are offered as a preliminary guide to the engineer or scientist who may find the topic only vaguely familiar.

A. NEAR-WALL SIMILARITY

If it can be assumed that the flow close to a smooth wall can be determined completely by local conditions, a universal velocity distribution must be valid near the surface. Under such circumstances, the flow is said to exhibit near-wall similarity. The flow is similar in the sense that velocity profiles can be non-dimensionalized so that they collapse upon one another in a small region near the wall.

In the very near-wall region of a two-dimensional turbulent boundary layer, the viscous sublayer where viscous shear dominates, the velocity profile is linear and it can be shown that:

$$\frac{u}{u^*} = \frac{yu^*}{\nu} \tag{1}$$

where the nondimensionalizing parameter, u^*, is defined as $\sqrt{\tau_w/\rho}$, the friction velocity. A little further from the wall, but still within the lower ~15% of the boundary layer, is a region where the

flow is fully turbulent but still affected by the presence of the wall. There the nondimensionalized velocity profile is represented by a logarithmic function from where this region derives its name. This function can be shown to have the form:

$$\frac{u}{u^*} = \frac{1}{\kappa} \ln \frac{yu^*}{\nu} + \text{constant} \qquad (2)$$

where κ is called von Kármán's constant. Equation 2 is commonly referred to as the law of the wall.

The viscous sublayer together with this logarithmic region is sometimes called the extended near-wall or inner region. A mathematical expression such as that suggested by Spalding [1] that models the entire inner region can be called an extended law of the wall.

In two dimensions the similarity law for the logarithmic region can be derived a number of ways. By comparing the inner region parameters to those in the outer region, the remaining portion of the boundary layer, and by using dimensional analysis the logarithmic form can be demonstrated. Mixing length theory or eddy viscosity theory along with the assumption of constant shear stress also will predict the logarithmic behavior.

Experimentally, two-dimensional turbulent boundary layer studies have repeatedly confirmed the universal velocity distribution. Direct measurements of wall shear stress have verified the similarity law for the logarithmic region. The success and degree of applicability of this simple two-dimensional similarity law is quite remarkable.

As yet, no similarity law has been verified for use in three-dimensional turbulent boundary layers.

B. THREE-DIMENSIONAL TURBULENT BOUNDARY LAYERS

A basic characteristic of three-dimensional boundary layers is that, unlike the two-dimensional case, the velocity vector changes direction as the distance from the wall is varied. A velocity profile that exhibits such behavior is said to be skewed. The only exceptions are for plane of symmetry flows and axisymmetric flows without a circumferential flow component, neither of which are of interest to this study. Skewing of the velocity profile may be pressure driven or shear driven. Most attention has been given to pressure driven flows where the transverse pressure gradient imposed on the boundary layer by the freestream streamline curvature generates the cross flows (skewing). Shear driven flows are caused by the transverse shearing of the inner layers of the boundary layer such as caused by sidewise motion of the wall relative to the freestream.

Research emphasis has been placed on three-dimensional turbulent boundary layers that are thin or fairly thin as defined by Bradshaw [2]. These are boundary layers in which derivatives of the velocities and turbulent stresses are small in the freestream and cross flow directions when compared to derivatives normal to the wall. Types of three-dimensional turbulent boundary layers include:

1) complex flows in the corners between flat intersecting walls,

2) flows that are everywhere collateral and which derive their quasi-three-dimensional nature exclusively by simple convergence or divergence of the flow external to the layer,
3) plane of symmetry flows which are also collateral
4) flows dependent on only two space coordinates such as yawed infinite plates or wings,
5) full three-dimensional flows such as wings of finite span, wing-body junctions, free-jet flows over a flat wall impinging against a back wall, flow over fully three-dimensional bodies, flow in curved ducts, and turbomachinery cascades, and,
6) shear driven flows such as flow over rotating surfaces in compressors, turbines, and helicoptor blades.

Corner flows have weak secondary flows and, though of some importance, are difficult to study experimentally since the degree of skewing is limited. Flows that are everywhere collateral may be handled as quasi-two-dimensional and therefore are not of general interest to a study of three-dimensional flows. The last three kinds of three-dimensional flows are of general interest, and all but the first kind meet Bradshaw's requirements and can be classified as thin or fairly thin.

C. IMPORTANCE OF THREE-DIMENSIONAL NEAR-WALL SIMILARITY

The importance of near-wall similarity is derived primarily

from two considerations: (1) the need to determine wall shear stress in a convenient manner for design purposes and (2) the dependence of all flow prediction techniques on near-wall similarity either by requiring the closure models to return the similarity law for the logarithmic region or to use that law as a boundary condition.

Surface shear stress or skin friction can be an important component of drag. Surface shear is a result of the shearing actions over adjacent fluid layers near the surface, and is found by integrating the wall shear stress over the body surface. The other usual component of drag, pressure drag, is found by integrating the surface pressure acting on a body in the direction of flow.

Determination of the wall shear stress is therefore an important element in the determination of the drag on an object. Knowledge of the drag is essential for determining flow losses in machinery such as turbines, compressors, and fans or for determining performance of aircraft, projectiles, or the like. It is obvious that for the most part flow patterns for these cases, whether internal or external, are three-dimensional and turbulent.

Since direct measurement of wall shear is difficult, a significant contribution by Clauser [3] to the study of two-dimensional turbulent boundary layers was his finding that wall shear stress can be inferred from the velocity field using the similarity law for the logarithmic region. A three-dimensional similarity law might allow calculation of wall shear using velocity field information obtained analytically or experimentally much in the same manner.

Such a law might also make possible the use of indirect wall shear measurement techniques in three-dimensional flows such as the Preston tube, which is currently used in two-dimensional flows and depends on a priori knowledge of the form of the similarity law.

It can be therefore stated that establishment of near-wall similarity in three-dimensional turbulent boundary layers is of fundamental interest in itself. Additionally, a close examination of current prediction techniques for three-dimensional flows offers additional reasons for the importance of near-wall similarity studies.

Many three-dimensional prediction techniques depend to a greater or lesser extent on the assumed existence of near-wall similarity. Finite difference techniques have so far demonstrated their superiority over other prediction methods. Current closure methods in common use include mean field and transport equations closures.

Mean field closures, also referred to as zero-order models, use partial differential equations for the mean velocity field and mixing length or eddy viscosity models to directly model local turbulent shear stresses. For the most part the algebraic expressions developed for two-dimensional turbulent boundary layers are used without modification in three-dimensional turbulent boundary layers. These models usually have been formulated to return near-wall behavior compatible with classic two-dimensional near-wall similarity. For extension to three-dimensional flows, knowledge of

the nature of near-wall similarity is imperative.

Transport equation closures involve additional partial differential equations such as the turbulent kinetic energy equation or the diffusion equation to provide closure. Popular practice for proponents of these methods is to omit viscous shear terms in the motion equations and use a three-dimensional near-wall similarity law to provide the necessary boundary condition instead of the usual no-slip wall condition. Though clearly not a requirement of these models, practioners continue to use this matching technique because of the significant reductions in computational time that result, since near-wall regions require a denser grid spacing to accurately model the large gradients that occur there. By matching the velocity field to a near-wall similarity law, these numerous and time consuming calculations can be avoided.

D. THE PROBLEM

While the importance of near-wall similarity is evident, there is a problem. Unlike the two-dimensional case, no near-wall similarity law for three-dimensional turbulent boundary layers can be formulated from first principles. Mixing length or eddy viscosity models cannot resolve the problem. Dimensional analysis falters.

Most attempts at formulating a three-dimensional near-wall similarity law have relied heavily on modifications of the successful two-dimensional near-wall similarity law. Though some of these suggested three-dimensional near-wall similarity laws appear to

collapse some velocity profiles, none can be verified until it can be shown that the nondimensionalizing parameter, the friction velocity, is related to wall shear stress in three-dimensional flows in the same way as in the two-dimensional case. Since this has never been adequately demonstrated for any proposed three-dimensional near-wall similarity law, no such law has ever been shown to be valid.

It would appear that the only way available to establish the existence of near-wall similarity in a three-dimensional turbulent boundary layer or the form of any three-dimensional near-wall similarity law would be by physical experiment. Such an experiment must measure all local parameters including the velocity profile, the pressure gradient, and the wall shear stress including direct measurement of both its magnitude and direction. While experiments have been reported which have measured velocity and pressure field data, no direct measurement of both the magnitude and direction of wall shear stress in a three-dimensional turbulent boundary layer has been previously reported in the literature.

In 1972 Nash and Patel [4] wrote, "The applicability of the law of the wall in a three-dimensional boundary layer is of considerable importance in calculation procedures which use the differential equations since it is often used as the inner boundary condition. The exact form this law should take is likely to remain open to controversy until a satisfactory method is developed for the direct measurement of the direction and magnitude of the wall

shear stress in a three-dimensional flow."

In 1974 Chandrashekhar [5] stated, "The most important lacuna in three-dimensional turbulent boundary layer studies is a reliable technique by which both the magnitude and the direction of the wall shear stress vector can be measured. The technique is essential for gaining confidence in using the available methods for inferring wall shear stress from the mean flow velocity profile data. Thus independent direct measurements would go a long way in deciding upon the relative merits of the various methods available."

The insistence on direct measurements is essential since indirect measurement techniques such as wall pitot tubes, Stanton tubes, Preston tubes, heated elements and the like all derive their usefulness from a priori knowledge of the existence and form of near-wall similarity. The common practice of using these two-dimensionally calibrated instruments in three-dimensional flows is not valid since this assumes that the nature of two-dimensional and three-dimensional near-wall flow is the same without regard to the changing direction of the velocity vector in the three-dimensional flow. As van den Berg [6] has stated, "The measurement of the wall shear stress with a wall pitot is based on the assumption of the existence of a universal velocity distribution near the wall at a given wall shear stress." He further states, "Yet this procedure to find the wall shear stress can not be regarded as really satisfactory. The only correct way to establish the wall shear stress would be the direct measurement of the wall shear force, e.g. on

a floating element, but this appears to be very difficult."

E. SCOPE OF WORK

This study provides the first comprehensive data needed for the eventual evaluation of the validity and form of near-wall similarity in a three-dimensional turbulent boundary layer. An experimental investigation of an incompressible three-dimensional pressure driven flow around a circular cylinder protruding from a wall was completed. Measurements including velocity profile data, static pressure field data, and direct measurements of magnitude and direction of local wall shear stress using an omnidirectional floating element device will be presented. Comparisons will be shown between measured data and existing three-dimensional near-wall similarity models. With measurements of this type now possible, a wide variety of flow conditions and geometries can be studied which should eventually lead to a determination of the existence and (if confirmed) form and extent of near-wall similarity in three-dimensional turbulent boundary layers.

II. LITERATURE SURVEY

A. INTRODUCTION

A historical view of fluids mechanics research indicates that the study of turbulent three-dimensional boundary layers is relatively young. In 1904 Prandtl made his classic boundary layer approximations. A review paper of three-dimensional boundary layers by Cooke and Hall [7] in 1960 offered the observation that "Very little work on (three-dimensional) turbulent boundary layers has been done. What little there is relies rather heavily on two-dimensional work, especially for the empirical value of the skin friction." Twelve years later a review paper on three-dimensional turbulent boundary layers by Nash and Patel [4] opens with the statement that, "The subject of three-dimensional turbulent boundary layers, although of great practical importance, is still in its infancy." They further state that, "... advances in the art of calculating three-dimensional turbulent boundary layers have stemmed, almost entirely, from the application of techniques first established in two dimensions. Often the extension of these techniques to three dimensions is made in the absence of experimental verification of their continued validity."

The first experimental study of three-dimensional turbulent boundary layers was by Gruschwitz [8] in 1935. By 1960 there were still less than 20 experimental studies reported. Since the mid-sixties, the research pace has accelerated to about six studies

a year. Johnston [9] has counted approximately 80 investigations since the first one by Gruschwitz.

The direction of research should be noted. The central problem in calculating any turbulent flow is the mathematical modeling of the turbulent shear stresses. Analytical studies have concentrated on improving these closure techniques and upon improving numerical methods for solving the resulting set of equations. Experimental studies have for the most part sought to provide velocity field data for comparison with the numerical solutions. In the seventies, some studies have also included measurements of the turbulent shear stresses for comparison with numerical predictions.

Though the fundamental importance of near-wall similarity in three-dimensional turbulent boundary layers in inferring wall shear, in providing input for modeling near-wall turbulent stresses, and in reducing calculation times, is widely recognized, relatively little effort has been spent or headway achieved in addressing the fundamental questions surrounding the subject. As late as 1976, Johnston [9] in a review of three-dimensional experimental studies noted "the need for further development and testing of an improved three-dimensional law of the wall." Fundamental three-dimensional turbulent boundary layer studies cannot continue indefinitely while the foundation stone of near-wall similarity rests on uncertain footing.

The following literature review will seek to briefly disclose

the analytical basis for near-wall similarity in two-dimensional flows, since three-dimensional near-wall similarity laws rely heavily on the experience gained from the two-dimensional case. Models for three-dimensional near-wall similarity laws and their bases will also be discussed.

Owing to their essential role in verifying any analytical model for a three-dimensional law of the wall, experimental techniques in two and three dimensions for the determination of wall shear stress will also be discussed. Both direct and indirect techniques will be examined in order to demonstrate the inherent superiority of direct measurements as a verification technique. Error sources and their effect on three-dimensional measurements will be part of that examination.

B. TWO-DIMENSIONAL NEAR-WALL SIMILARITY

The current concept of a turbulent boundary layer on a smooth wall provides for an inner region which is directly affected by the presence of the wall and an outer region which is only indirectly affected by the wall through interactions with the inner region. The outer region is fully turbulent and governed by von Kármán's [10] velocity-defect law,

$$U - u = f(\tau_w, \rho, y, \delta) \tag{3}$$

The inner region, which comprises only approximately 15% of the whole boundary layer, may be further divided into three subregions

extending from the wall: 1) a thin region adjacent to the wall called the viscous sublayer where viscous shear dominates, 2) a very small region called the transition region where both viscous shear and turbulent shear are important, 3) and a fully turbulent region called the logarithmic region where turbulent shear dominates. Figure 1 shows these regions on a nondimensional plot of velocity versus the log of distance from the wall. The inner region is governed by the inner law suggested by Prandtl [11]:

$$u = f(\tau_w, \rho, \mu, y). \tag{4}$$

The entire inner region is sometimes referred to as the extended near-wall region and is of interest to this study. The nature of the functional relationship given in Eq. 4 changes from one sub-region to another.

In the viscous sublayer, only the viscous shear is important and since the region is very thin,

$$\mu \frac{du}{dy} = \tau \simeq \tau_w. \tag{5}$$

It follows that

$$u = \tau_w \, y/\mu. \tag{6}$$

It is convenient to define $u^* \equiv \sqrt{\tau_w/\rho}$, the wall friction velocity, in order to nondimensionalize Eq. 6 so that,

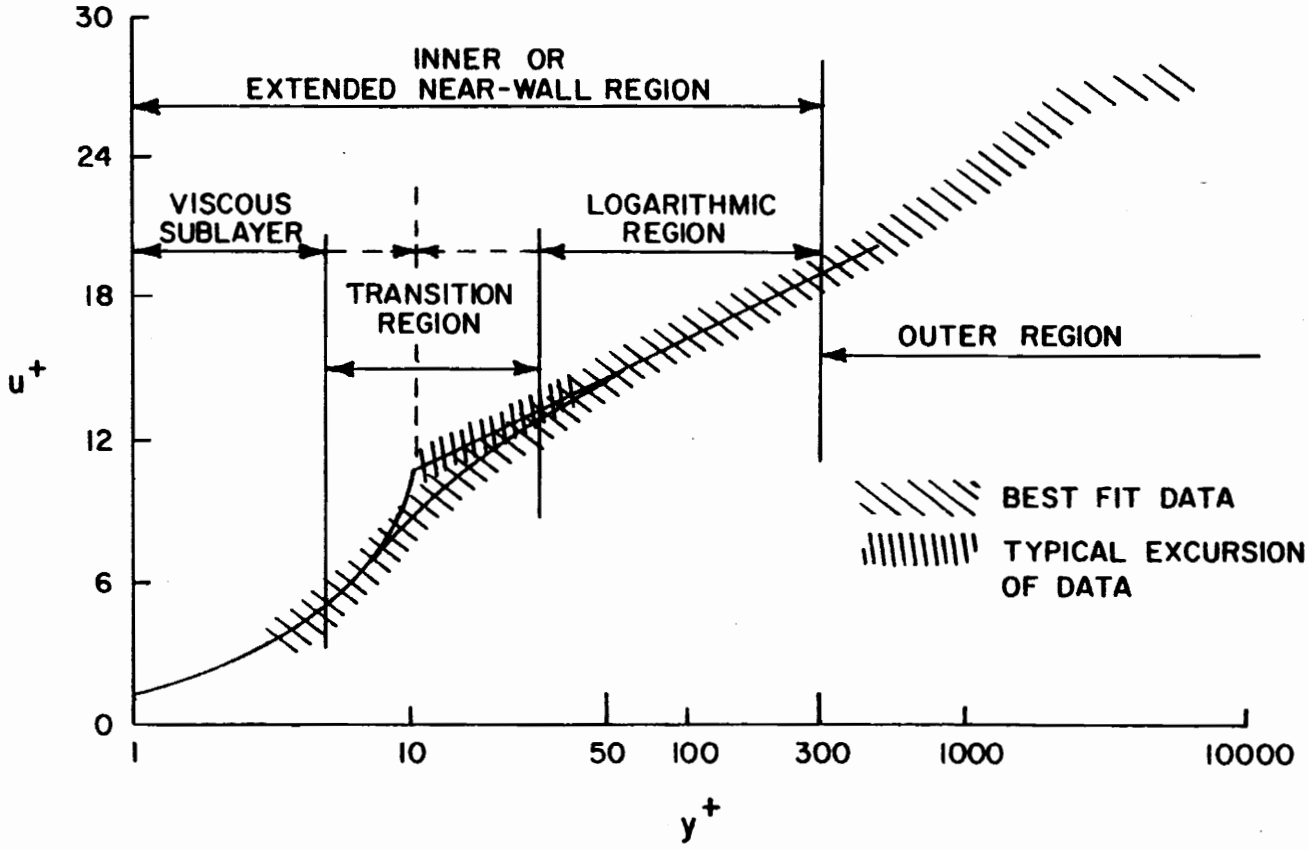

Figure 1. Near-Wall Similarity Regions

$$\frac{u}{u^*} = \frac{u^* y}{\nu} \quad . \tag{7}$$

If we define

$$u^+ = \frac{u}{u^*} \tag{8}$$

and

$$y^+ = \frac{u^* y}{\nu} \tag{8}$$

then for the viscous sublayer,

$$u^+ = y^+ . \tag{9}$$

There are a number of ways of deriving the relationship that holds in the logarithmic region. Hinze [12] provides possibly the best compilation of these derivations. For demonstration purposes Prandtl's mixing-length theory will be reviewed. Since the logarithmic region is fully turbulent,

$$\tau \simeq \rho \, \ell^2 \left|\frac{\partial u}{\partial y}\right| \frac{\partial u}{\partial y} \quad . \tag{10}$$

Prandtl made two important assumptions: 1) that the mixing length in this region is proportional to the distance from the wall, i.e.,

$$\ell = \kappa y \tag{11}$$

where κ is von Kármán's constant, and 2) that since this inner region is small,

$$\tau = \text{constant} = \tau_w. \tag{12}$$

It follows that

$$\tau_w = \rho \kappa^2 y^2 \left(\frac{du}{dy}\right)^2. \tag{13}$$

Introducing the wall friction velocity and separating the variables, one obtains

$$\frac{u^*}{\kappa} \frac{dy}{y} = du. \tag{14}$$

Now utilizing the definitions in Eqs. 8, Eq. 14 may be rewritten

$$\frac{1}{\kappa} \frac{dy^+}{y^+} = du^+. \tag{15}$$

Integration results in

$$u^+ = \frac{1}{\kappa} \ln y^+ + C \tag{16}$$

where κ, von Kármán's constant, and the constant C are experimentally determined. More about these constants will be discussed later.

Other methods of deriving this logarithmic expression include eddy viscosity theory [12], turbulent energy equation [13], and dimensional analysis [14,15]. Indeed it is from the dimensional analysis approach that the wall friction velocity is found to be a suitable nondimensionalized velocity characterizing the wall turbulence.

The relation for the transition region is assumed so that a smooth transition takes place between the viscous sublayer and the logarithmic region. Sometimes this relationship takes the form of

$$u^+ = A' \ln y^+ + B' \tag{17}$$

where A' and B' are constants different from $1/\kappa$ and C. This three-formula representation of the inner region may be set aside in favor of a single formula for the entire inner region.

Spalding [1] and later Kleinstein [16] independently developed a single formula for the inner region. Their expression is,

$$y^+ = u^+ + e^{-\kappa C}[e^{\kappa u^+} - 1 - \kappa u^+ - \frac{(\kappa u^+)^2}{2} - \frac{(\kappa u^+)^3}{6}]. \tag{18}$$

Development of this relation requires the assumption, as was made previously, of constant shear. This expression also satisfies the requirements that the eddy viscosity is proportional to the cube of the distance from the wall in the viscous sublayer as first noted by Reichardt [17], and that the eddy viscosity vary as the exponential of the distance from the wall as the similarity law in the logarithmic region requires. Elrod [18] in a later study concluded that the eddy viscosity varies more closely with the fourth power of the distance from the wall. Spalding altered his equation to satisfy that requirement by adding the term, $-\frac{(\kappa u^+)^4}{4!}$, to the bracketed expression in Eq. 18. This additional term does

little to alter the curve as is shown in Fig. 2.

Other empirical expressions have been developed by Rotta [19], Reichardt [17], Deissler [20], van Driest [21], and Mellor [22]; however, none of these results in the useful closed form expression of Spalding. More recently, Rasmussen [23] and Green [24] have developed single formula expressions, however they appear to offer little advantage over Spalding's form. Very recently Dean [25] has combined Spalding's inner law with a single polynomial for Coles' wake function [26] for the outer region as developed by Finley et al. [27] and later by Granville [28]. The result is a single formula for the whole turbulent boundary layer profile.

It would be useful at this point to discuss the effects of pressure gradient and inertial effects on the similarity law for the logarithmic region. Since only smooth walls will be studied, no roughness effects will be considered. Prandtl's constant shear assumption seems adequate for many flows even for moderate pressure gradients or moderately accelerating flows. For cases where these conditions do not exist, the shear stress distribution will vary throughout the boundary layer. At the wall, the turbulent shear, as well as the velocities parallel and normal to the wall go to zero. Therefore the momentum equation provides that the viscous shear stress gradient be balanced by the pressure gradient:

$$\frac{\partial}{\partial y}\left(\mu \frac{\partial u}{\partial y}\right) = \frac{dp}{dx} . \tag{19}$$

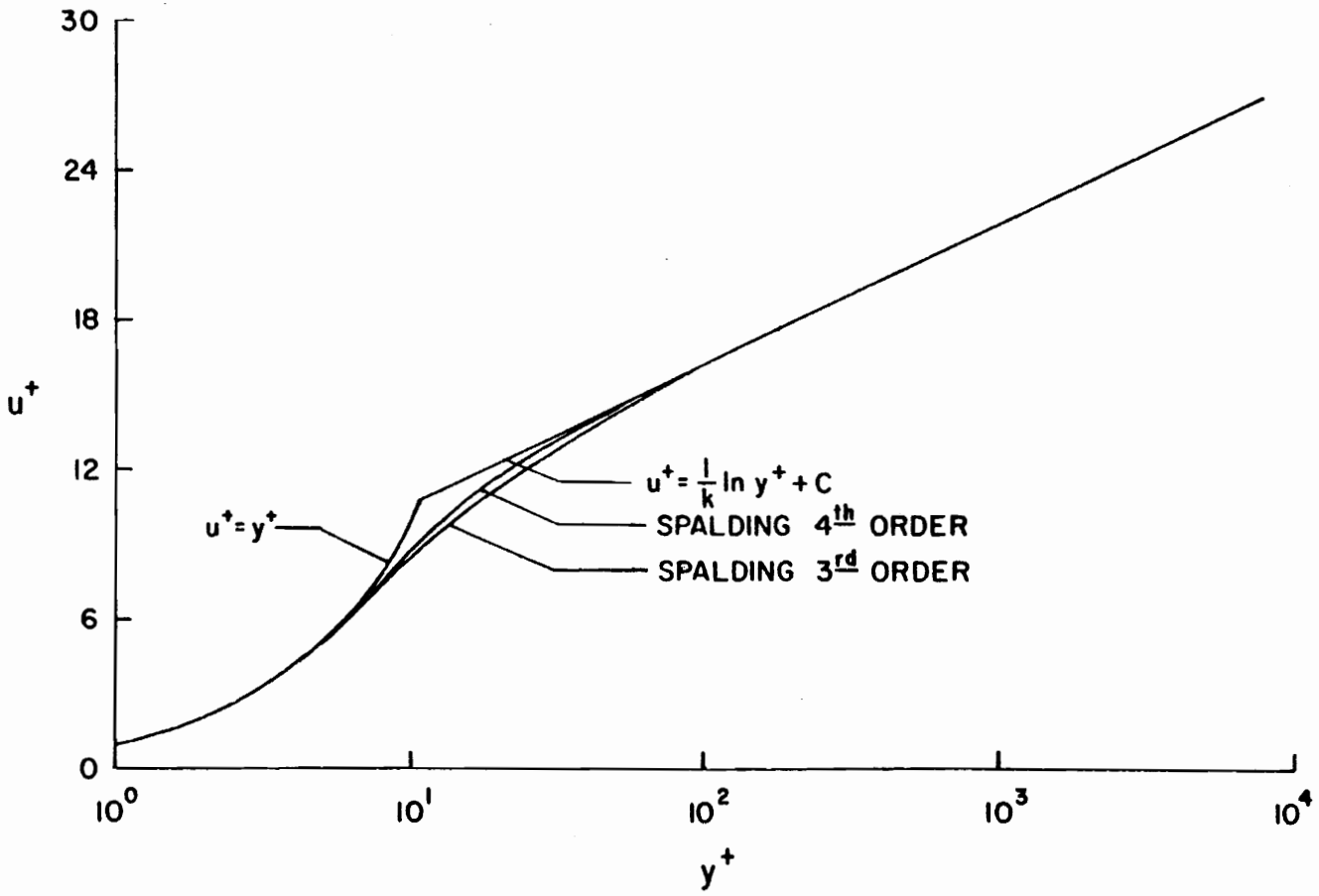

Figure 2. Comparison of Near-Wall Similarity Formulas

Noting that at the wall $\mu \frac{\partial u}{\partial y} = \tau_w$, one can write

$$\tau = \tau_w + \frac{dp}{dx} y + 0(y^3). \tag{20}$$

Ignoring the higher order terms caused by inertial effects for the moment, Eq. 20 may be rewritten in the form

$$\frac{\tau}{\tau_w} = 1 + \alpha\, y^+ \tag{21}$$

where

$$\alpha = \frac{\nu}{\rho u^{*3}} \frac{dp}{dx} .$$

Utilizing the mixing length assumption as before, Eqs. 10 and 11, it can be shown that,

$$\left(\frac{\tau}{\tau_w}\right)^{1/2} = \kappa y^+ \frac{du^+}{dy^+} . \tag{22}$$

By combining Eqs. 21 and 22 and integrating, it can be shown that

$$u^+ = \frac{1}{\kappa}\left[\ln y^+ + \kappa c + 2 \ln\left[\frac{2}{(1+\alpha y^+)^{1/2}+1}\right] + 2(1+\alpha y^+)^{1/2} - 2\right]. \tag{23}$$

This equation was originally derived by Townsend and for zero pressure gradient reduces to the near-wall similarity law for the logarithmic region. Van den Berg [6] points out that for $\alpha y^+ << 1$, Eq. 23 may be simplified to:

$$u^+ = \frac{1}{\kappa}\left[\ln y^+ + \kappa c + \frac{\alpha y^+}{2}\right]. \tag{24}$$

Variations of this analysis have been made by Patel [29], McDonald [30], Townsend [13], and Mellor [31].

The higher order terms in Eq. 20 that have thus far been ignored represent the influence of acceleration of the flow which results from the large velocity gradients near the wall. Van den Berg [6] estimates that in the logarithmic region, these terms are on the order of half as large as the pressure gradient effects.

Allowance for the inertial terms can be made by multiplying the pressure gradient term by a factor representing the contribution of the inertial terms in the region considered [32]. A constant shear gradient is assumed. Townsend [33] and van den Berg [6] suggest that since the shear gradient is essentially not constant, a more satisfying procedure would be to estimate the contribution of the inertial effects as a function of the wall shear stress gradient in the flow direction. If the shear stress varies little with distance from the wall, the velocity profile may be assumed to depend only on the shear stress at the wall. A first approximation of the inertial terms for a given wall shear gradient in the flow direction can therefore be calculated by employing the near-wall similarity law.

Following the derivation of van den Berg [6], we may write the near-wall similarity law in a more general form:

$$u^+ = f(y^+) \tag{25}$$

It follows that the velocity derivatives may be written as

$$\frac{\partial u}{\partial x} = \frac{du^*}{dx} \left[f + y^+ \frac{df}{dy^+} \right] \tag{26}$$

$$\frac{\partial u}{\partial y} = \frac{u^{*2}}{\nu} \frac{df}{dy^+} .$$

Continuity provides that

$$v = - \int_0^y \frac{du}{dx} \, dy = - \frac{du^*}{dx} \, yf . \tag{27}$$

By substituting these velocity gradients into the momentum equation and integrating, one finds that

$$\tau - \tau_w = y \frac{dp}{dx} + \rho \int_0^y \left(u \frac{\partial u}{\partial x} + v \frac{\partial u}{\partial y} \right) dy, \tag{28}$$

or in nondimensional form,

$$\frac{\tau}{\tau_w} = 1 + \alpha y^+ + \beta_1 I_1(y^+) \tag{29}$$

where

$$\beta_1 = \frac{\nu}{u^{*2}} \frac{du^*}{dx} ,$$

and

$$I_1 = \int_0^{y^+} f^2 \, dy^+ .$$

Applying mixing length theory as before, Eqs. 22 and 29 may be

combined to give

$$\frac{\partial u^+}{\partial y^+} = \frac{1}{\kappa y^+} (1 + \alpha y^+ + \beta_1 I_1)^{1/2}. \tag{30}$$

Assuming that αy^+ and $\beta_1 I_1$, are small, Eq. 30 may be approximated to ease integration as

$$\frac{\partial u^+}{\partial y^+} = \frac{1}{\kappa y^+} (1 + \frac{\alpha y^+}{2} + \frac{\beta_1 I_1}{2}). \tag{31}$$

Integrating gives

$$u^+ = \frac{1}{\kappa}[\ln y^+ + \kappa c + \frac{\alpha y^+}{2} + \frac{\beta_1 I_2}{2}] \tag{32}$$

where

$$I_2 = \int_0^{y^+} \frac{I_1}{y^+} \, dy^+.$$

To evaluate the integrals I_1 and I_2, van den Berg suggests the use of the similarity law for the logarithmic region giving

$$I_1 = \frac{y^+}{\kappa^2} [\ln y^+ + (\kappa c - 1)]^2 + \frac{y^+}{\kappa^2} + \text{constant}. \tag{33}$$

For large values of y^+, the last two terms become small and may be neglected. Substituting Eq. 33 into the expression of I_2 gives

$$I_2 = \frac{y^+}{\kappa^2} (\ln y^+)^2. \tag{34}$$

Substitution of I_1 and I_2 results in a near-wall similarity law including pressure and inertial effects of the form,

$$u^+ = \frac{1}{\kappa}\left[\ln y^+ + \kappa c + \frac{\alpha y^+}{2} + \frac{\beta_1 (\ln y^+)^2 y^+}{2\kappa^2}\right]. \qquad (35)$$

Once a two-dimensional similarity law is established, its usefulness is enhanced by the ability to infer wall shear from velocity profile data. As an example, the two-dimensional similarity law for the logarithmic region can be multiplied by u^*/U to give

$$\frac{u}{U} = \frac{u^*}{U}\left[\frac{1}{\kappa}\ln\left(\frac{y\,U\,u^*}{\nu\,U}\right) + c\right]. \qquad (36)$$

Defining a wall friction coefficient C_f as

$$C_f \equiv \frac{\tau_w}{\rho U^2/2},$$

Eq. 36 may be rewritten as

$$\frac{u}{U} = \sqrt{\frac{C_f}{2}}\left[\frac{1}{\kappa}\ln\left(\frac{y\,U}{\nu}\sqrt{\frac{C_f}{2}}\right) + c\right]. \qquad (37)$$

By plotting u/U versus $\ln \frac{yU}{\nu}$, this relation suggested by Clauser [3] yields a family of curves having as a parameter, constant values of skin friction coefficient. Such a plot is referred to as a Clauser chart.

Bradshaw [34] has suggested a somewhat simpler method. One suitable reference point in the logarithmic curve is chosen, and

plotted on a y versus u/U plot using U/u^* as the variable parameter. The resulting single curve can be plotted along with the velocity profile. By noting the intersection of the two curves, unique values of u/U and U/u^* can be obtained, thereby giving the wall shear stress. It appears that this method is somewhat less attractive than the Clauser charts since a very small part of the velocity profile is used to determine the wall shear. In short, that small portion of the velocity profile used is severely tested for its local accuracy.

An alternative to both the previous methods has been suggested by Kline and Schraub [35]. They noted that

$$u^+y^+ = uy/\nu. \tag{38}$$

Rewriting the similarity law in the logarithmic region explicitly in terms of y^+ gives

$$y^+ = e^{\kappa u^+} - \kappa c$$

or

$$0 = -y^+ + e^{\kappa u^+} - \kappa c. \tag{39}$$

Multiplying by u^+ gives

$$0 = \frac{-uy}{\nu} + u^+ e^{\kappa u^+} - \kappa c. \tag{40}$$

Since $\frac{uy}{\nu}$ is known throughout the boundary layer, usually at discrete y locations either by numerical calculation or by velocity profile

measurements, Eq. 40 is simply a transcendental equation that may be solved for u^* at each y location. This method can also be extended to Spalding's relation, Eq. 18. This method has the advantage in experimental studies of providing an individual value of wall shear stress for each velocity data point in the boundary layer. Hence, it follows that any desired portion of the velocity profile may be used to determine an approximation of the wall shear.

The preceding paragraph leads to an important observation commonly overlooked by the casual investigator. Simply stated, the value of wall shear inferred from a law of the wall is subject to variation depending on a number of variables. Included in these variables are: 1) the value of the constants κ and C used, 2) the choice of the law or laws used, 3) the portion of the inner region used to infer the wall shear, and 4) the accuracy of the velocity data itself.

Table 1 shows a listing of some of the law of the wall constants found in the literature and Fig. 3 shows how the similarity law in the logarithmic region is shifted for some of these constants. The area $50 \leq y^+ \leq 300$ is noted since this is the area in which the similarity law in the logarithmic region is usually assumed to be valid. From the scatter of the curves it should be obvious that choice of constants will affect the inferred wall shear stress. Cole's or Patel's constants are the most commonly accepted. Both are nearly equal and give nearly the same curves. It should be noted however that only Smith and Walker's constants were determined

Table 1. Law of the Wall Constants

$$u^+ = \frac{1}{\kappa} \ln y^+ + C$$

Investigator	κ	C
Coles (1968) [36]	0.41	5.0
Patel (1965) [37]	0.42	5.45
Clauser (1956) [15]	0.41	4.9
Smith and Walker (1956) [38]	0.46	7.15
Staff of N.P.L. (1958) [39]	0.47	5.9
Spalding (1961) [1]	0.40	5.5
Laufer (1950) [40]	0.33	5.5
Doench (1926) [41]	0.40	5.0
Townsend (1956) [33]	0.41	5.85
Klebanoff and Diehl (1951) [42]	0.40	4.2
Schultz-Grunow (1940) [43]	0.39	4.07
Coles (1956) [26]	0.40	5.1

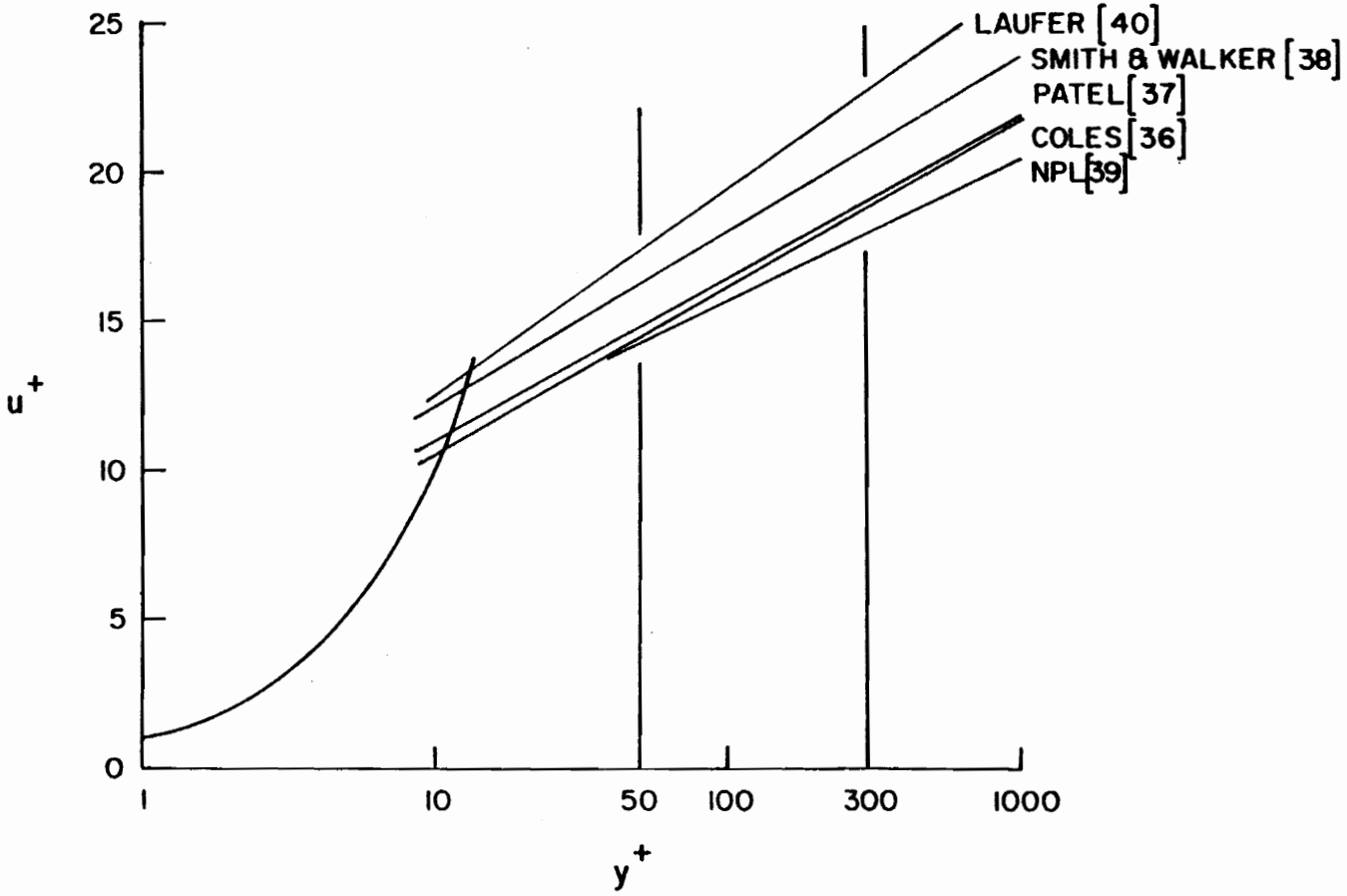

Figure 3. Effect of the Law of the Wall Constants

with direct measurement of wall shear stress.

To quantify the possible scatter in inferred wall shear stress, the following example is presented. Consider a boundary layer at $y^+ = 135$ where the mean velocity is 15.24 m/s (50 ft/sec) and the density is 1.1 kg/m^3 (0.069 lbm/ft^3), conditions that are similar to those for this experiment. If Patel's constants are considered as the reference, Laufer's constants result in a wall shear stress 29% low. Using the NPL constants, the inferred wall shear stress is 10% high. These are extremes, however the qualitative effect is amply demonstrated.

Figure 2 shows the two-formula law of the wall ($u^+ = y^+$ and the similarity law for the logarithmic region) as well as Spalding's 3rd and 4th order expressions using Patel's constants. The choice of a formula or formulas can be important especially if data in the transition region is used. It seems unlikely that there is not a smooth connection between the viscous sublayer and the logarithmic regions. Therefore either a three-formula law of the wall that includes an expression for the transition region or Spalding's formula would appear to more nearly model expected behavior. Spalding's single formula is easier to use than the three-formula law of the wall and is preferred. Spalding's fourth order formula appears to offer little variation, so Spalding's third order formula was used in this study.

Figure 1 shows how data normally falls on a law of the wall plot using Patel's constants. Two types of data are noted. The

first is called the 'best fit data' and is usually shown when an author wishes to demonstrate the success of the similarity law for the logarithmic region. Lindgren and Chao's [44] and Laufer's [45] fully developed pipe flow data usually are shown. The second type of data fits the logarithmic region in the region $50 \leq y^+ \leq 300$ but tends to show an upward excursion as the transition region is approached from the edge of the boundary layer. This data is typical of much data in the literature and coincidentally of this study. Coles [36] assumed these excursions were due to the uncertainty of data measured in such close proximity to the wall and therefore suggested that all data for $y^+ \leq 50$ by ignored. The more recent work of Pierce and Gold [46], however, indicates that these excursions cannot be easily dismissed and the reader is referred to their work for an excellent discussion of the matter.

C. THREE-DIMENSIONAL NEAR-WALL SIMILARITY

Most analytical approaches used in the study of three-dimensional turbulent boundary layers rely heavily on the experience gained in two-dimensional turbulent boundary layers. This section will outline briefly eleven proposed but unverified models for a suitable similarity model in three dimensions.

The first six models to be discussed have approaches centered on finding an equivalent velocity for a three-dimensional turbulent boundary layer which, when inserted into the two-dimensional near-wall similarity law, would collapse the velocity profiles, i.e.,

$$q^+ = \frac{q_{equivalent}}{q^*} = f\left(\frac{yq^*}{\nu}\right) = \frac{1}{\kappa} \ln \frac{yq^*}{\nu} + C. \qquad (41)$$

where $q^* = \sqrt{\tau_w/\rho}$ just as u^* was defined. At least for small deviations from two-dimensional flows, this seems to be a reasonable approach. The assertion by the investigators that $q^* = \sqrt{\tau_w/\rho}$ is without verification, and it should be noted that the parameter q^* might collapse the velocity profiles without being related to wall shear. It is noted once again that only direct measurement of wall shear stress can verify the relationship between wall shear stress and q^* because indirect wall shear stress measurement techniques depend on a priori knowledge of the existence and form of near-wall similarity.

For the reader's convenience, Fig. 4 shows a sketch of a three-dimensional turbulent boundary layer velocity profile skewed in one direction only and Fig. 5 shows a typical polar plot of such a velocity profile. Both notation and the coordinate system used in the first six models are also shown.

In 1956 Coles [26] suggested that the velocity vector, $\vec{q} = \vec{u} + \vec{w}$, could be expressed as the sum of a wall, $\vec{q}_w$, and a wake, $\vec{q}_{wake}$, component. He reasoned that: (1) near the wall the wake component would be small, (2) that the direction of the mean flow near the surface is also the direction of the wall shear, τ_w, as well as the direction of the wall velocity component, and (3) that the component of velocity in this direction, $\vec{q}_w$, may be described by the two-dimensional similarity laws. Coles' model results in

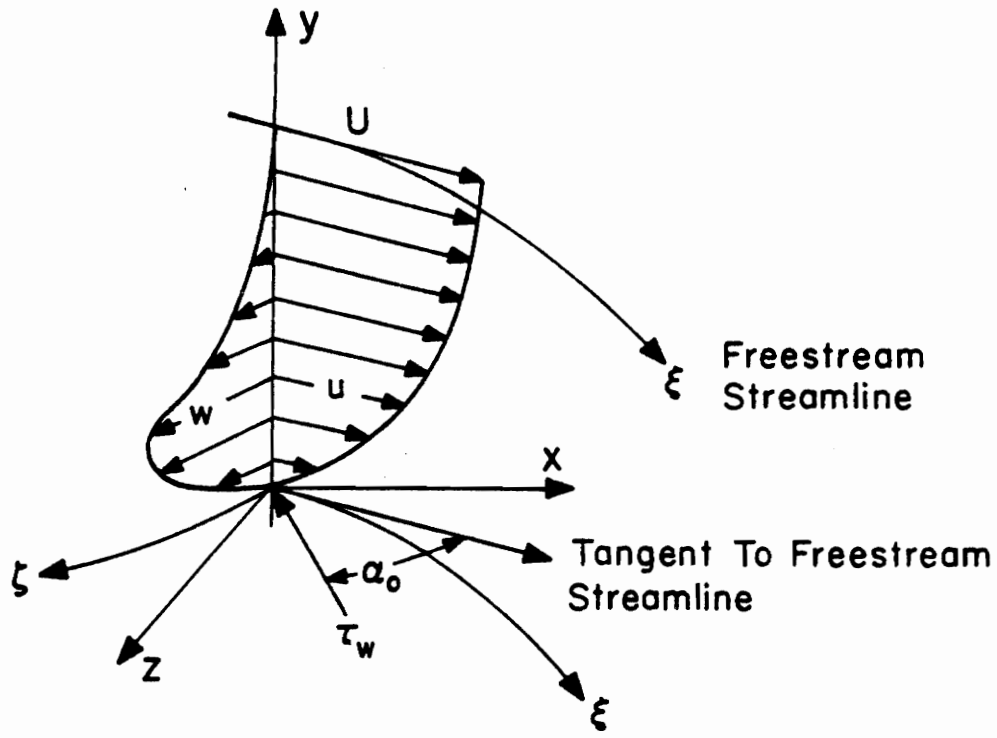

Figure 4. Typical Three-Dimensional Skewed Boundary Layer

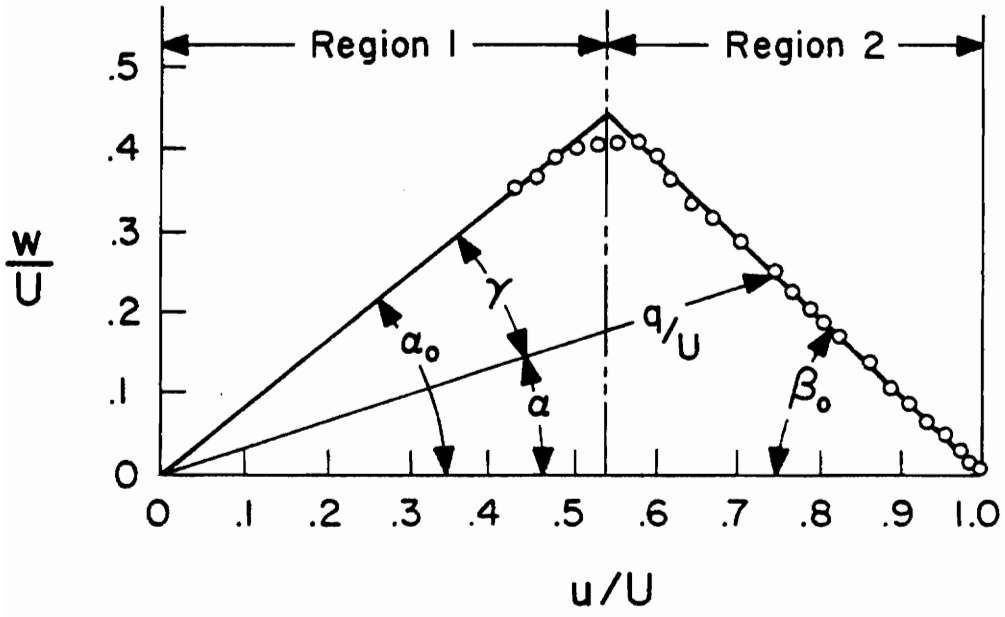

Figure 5. Polar Plot of Typical Three-Dimensional Skewed Boundary Layer.

$$q^+ = \frac{q_w}{q^*} \simeq \frac{q \cos \gamma}{q^*} \quad . \tag{42}$$

Coles used the data of Kuethe, McKee, and Curry [47] on a swept airfoil to test his model. Coles points out that large angles of skew were noted throughout the boundary layer, but that "sudden" changes in flow direction within the sublayer were assumed to be fictitious. The airfoil used was an elliptical planform with the major axis swept back at an angle of 25.0°. Though the velocity profiles seemed to be fairly well represented by Coles' theory, no direct or indirect measurements of wall shear stress were included.

Four years later, Johnston [48] introduced a second model. He noted the existence of an apparently collateral region very near the wall. He proposed that the angle which the velocity vector has with respect to the freestream approaches the angle α_0 in the collateral region, and that α_0 is the angle the wall shear vector has with respect to the freestream such that

$$\lim_{y \to 0} \frac{w}{u} = \tan \alpha_0 . \tag{43}$$

He proposed that the two-dimensional similarity law for the logarithmic region be used for local velocities in the direction of α_0, and expressed as u/cos α_0. He therefore defines his nondimensional velocity as,

$$q^+ = \frac{q_{equivalent}}{q^*} = \frac{u/\cos \alpha_0}{q^*} \quad . \tag{44}$$

When q is along α_0, u/cos α_0 is equal to the physically real q. When q is not along α_0, u/cos α_0 leads to physically unreal velocities. Johnston based his model on the experimental measurements of Kuethe, et al. [47] discussed previously, Gruschwitz [8] in a turning passage of a rectangular duct, and his own study over a flat wall bounding a two-dimensional air jet impinging against a perpendicular back wall. No direct or indirect wall shear measurements were noted.

Both Cole's and Johnston's models assume that the mean flow near the surface is in the same direction as the wall shear stress. The dangers in such an assumption should be recognized. In 1969, Rogers and Head [49] developed a precise velocity measurement system for three-dimensional boundary layers. Their measurements indicated that large changes of flow angle may occur all the way to the surface, i.e., that no region of collateral flow exists. In addition, Pierce and East [50] have demonstrated, by the use of a finite difference solution to a three-dimensional turbulent boundary where the viscous stresses were retained in the motion equations, that no near-wall collateral flow is predicted by analysis. Since only the viscous equations are being solved in the very near-wall region, the Reynolds stress model used is immaterial and the existence of a collateral region appears to be inconsistent with the governing equations. It is therefore especially important to note that when three-dimensional experimental measurements are made of the velocity profiles, typically to limits $y^+ > 10$, the direction of the velocity vector nearest to the wall is probably not the limiting wall streamline direction

or the direction of wall shear. It is unfortunate that the polar plot shown in Fig. 5 has gained such extensive use, since it tends to obscure small angle changes near the wall and suggests support of the false assumption of near-wall collateral flow.

It should be noted that only for profiles where the boundary layer is skewed in one direction does the triangular shape of the polar plot develop. For flows where there is recurvature of the freestream lines, such as in a S-shaped duct, bilateral skewing may occur. Figures 6 and 7 show a bilaterally skewed three-dimensional profile and a typical polar plot. Note that the polar plot no longer retains its triangular shape.

Returning to near-wall similarity models, in 1963 Hornung and Joubert [51] completed a study of flow around a circular cylinder with trailing edge standing on a plate. Their measurements seemed to confirm Johnston's polar plot; however they showed that in contradiction to Johnston's assumption, the peak did not necessarily lie within the viscous sublayer. Hornung and Joubert proposed without explanation that the freestream profile follows the two-dimensional similarity law for the logarithmic region, i.e.

$$q^+ = \frac{q_{equivalent}}{q^*} = \frac{u}{q^*} \,. \qquad (45)$$

They indicated that their model applied "up to the point where the boundary layer becomes yawed," usually to $y^+ < 150$. No direct or indirect measurements of wall shear were reported.

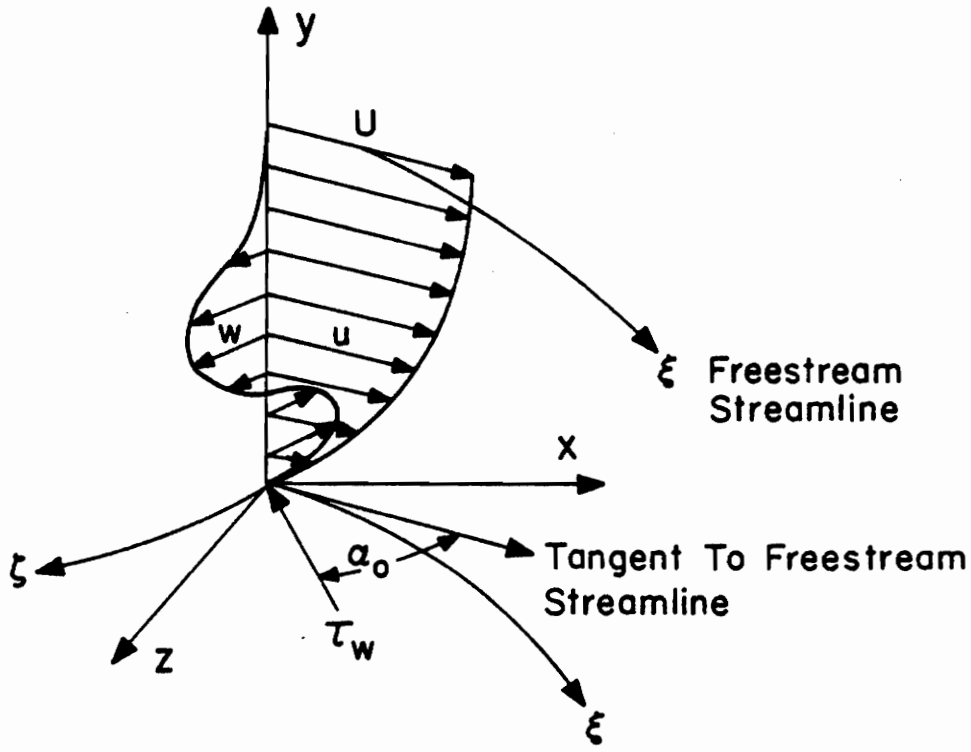

Figure 6. Bilaterally Skewed Three-Dimensional Boundary Layer

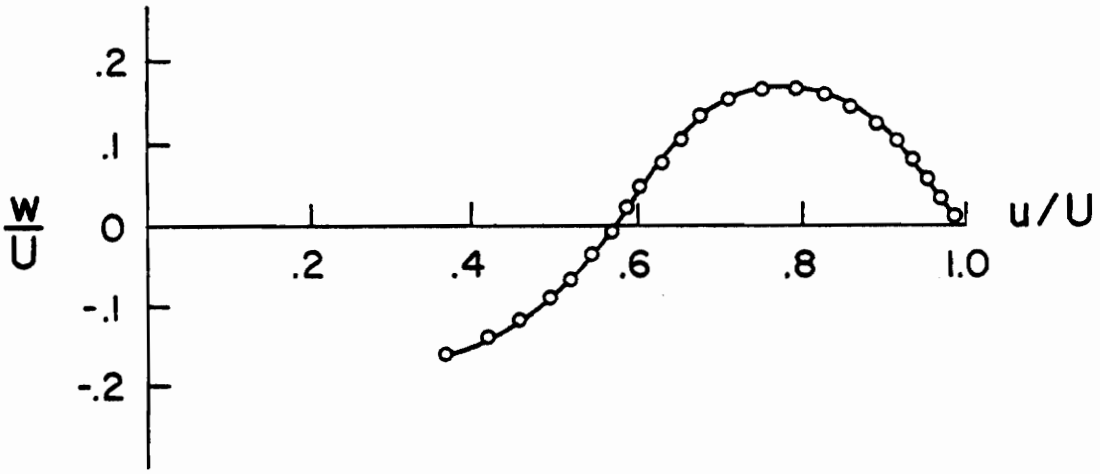

Figure 7. Polar Plot of Bilaterally Skewed Three-Dimensional Boundary Layer

A similar model of unknown origin was first reported by Pierce and Krommenhoek [52] in 1968. Without substantiation, the model assumes that

$$q^+ = \frac{u}{q^*_{\xi}} \tag{46}$$

where $q^*_{\xi xi}$ is the freestream component of q^* and equal to $q^*\sqrt{\cos\ \alpha}$. Therefore it may be written that

$$q^+ = \frac{q_{equivalent}}{q^*} = \frac{u/\sqrt{\cos\ \alpha_0}}{q^*} \tag{47}$$

In 1969 East and Hoxey [53] modified Johnston's model slightly. By applying the sine rule to Johnston's polar plot, they noted that

$$\sin(\alpha_0 + \beta_0) = (\kappa_1 q^*/U)\ \sin\ \beta_0 \tag{48}$$

where U is the freestream velocity and $\beta_0 = -\tan^{-1}\ \delta_2/\delta_1$. Solving for α_0 gives

$$\alpha_0 = \sin^{-1}[(\kappa_1 q^*/U)^{-1}\sin\ \beta_0] - \beta_0$$

where κ_1 is an empirical constant defined by the equation

$$\frac{\kappa_1\ u^*}{U} = \left(\frac{u}{U}\right)_{apex}.$$

Their experimental setup was similar to that of Hornung and Joubert,

and when their data was plotted in polar form they noted a "definite trend" of vague description. To reduce this trend they suggested that the angle α_0 be written as

$$\alpha_0 = \sin^{-1}[(\kappa_1 q^*/U_0)^{-1} \sin \beta_0] - \beta_0 \qquad (49)$$

where $\kappa_1 \simeq 19.45$ and U_0 is the "working section reference velocity." Under these conditions, East and Hoxey indicate that α_0 is actually no longer related to the polar plot. The equivalent velocity is written just as it was for Johnston's model,

$$q^+ = \frac{q_{equivalent}}{q^*} = \frac{q/\cos \alpha_0}{q^*} \qquad (50)$$

but with α_0 redefined as above. Unfortunately East and Hoxey never indicate a value for U_0, so for this study U_0 was simply set equal to 25.9 m/s (85.0 ft/sec). Both Preston tube and razor blade methods for indirectly measuring wall shear were used.

The last of these simple models was suggested by Prahlad [54] in 1968, and based on studies of flow around a circular cylinder and an inclined flat plate placed normal to the tunnel wall. Without explanation Prahlad assumes that the magnitude of the velocity without regard to direction could be used so that

$$q^+ = \frac{q_{equivalent}}{q^*} = \frac{q}{q^*} . \qquad (51)$$

Preston tubes were used to measure wall shear stress indirectly.

Prahlad noted that larger Preston tubes give smaller values of skin friction than smaller Preston tubes. He concludes that, "This deviation implies departures from wall similarity and consequent errors in the use of the Preston tube technique in these flows."

The last five models tend to become quite complicated. Each of these models will be discussed briefly in order of ascending difficulty. The complications encountered in these last models come about through consideration of some or all of the following: 1) pressure gradients, 2) wall shear gradients, 3) wall shear angle gradients, and 4) separate consideration of velocity components.

The model recommended by Chandrashekhar and Swamy [55] in 1976 is characterized by the separate consideration of the freestream and cross flow components of velocity. Examining the data of East and Hoxey cited earlier, Chandrashekhar and Swamy observed that logarithmic functions could be applied separately to the freestream and cross flow components of velocity such that

$$\frac{u}{u^*} = A' \log_{10} \frac{y\, u^*}{\nu} + B' \qquad (52)$$

where $A' = 5.4$ and $B' = 4.9$, and

$$\frac{w}{w^*} = D' \log_{10} \frac{y\, w^*}{\nu} + E' \qquad (53)$$

where $D' = 1.0$ and $E' = 11.8$.

The parameters u^* and w^* are the wall friction velocities in the

freestream and cross flow directions respectively. The value of the constants, A', B', D', and E'were determined from the East and Hoxey data. Wall shear was indirectly measured using both the Preston tube and razor blade techniques. Figure 8 is a plot of Eqs. 52 and 53.

Perry and Joubert [56] developed a model in 1965 using similarity arguments and treating the near-wall region as an equilibrium layer. Their model relates the mean velocity distribution with the pressure gradient vector and the wall shear vector. The theory was compared with the data of Hornung and Joubert cited earlier; however, the results were inconclusive due to a lack of sufficient data. No direct or indirect measurements of wall shear were incorporated. Since the details of the analysis by Perry and Joubert are quite lengthy, only a brief outline of the development of their model will follow.

Considering a prismatic element with sides dx, dy, and dz at a short distance y from the wall, a force balance on the element gives,

$$\frac{\partial p}{\partial x} + \frac{\partial \tau_{xy}}{\partial y} + \frac{\partial \tau_{xz}}{\partial z} = 0 \qquad (54)$$

$$\frac{\partial p}{\partial y} + \frac{\partial \tau_{yx}}{\partial x} + \frac{\partial \tau_{yz}}{\partial z} = 0$$

$$\frac{\partial p}{\partial z} + \frac{\partial \tau_{zx}}{\partial x} + \frac{\partial \tau_{yz}}{\partial y} = 0.$$

Using Townsend's equilibrium layer concept [13] led Perry and Joubert

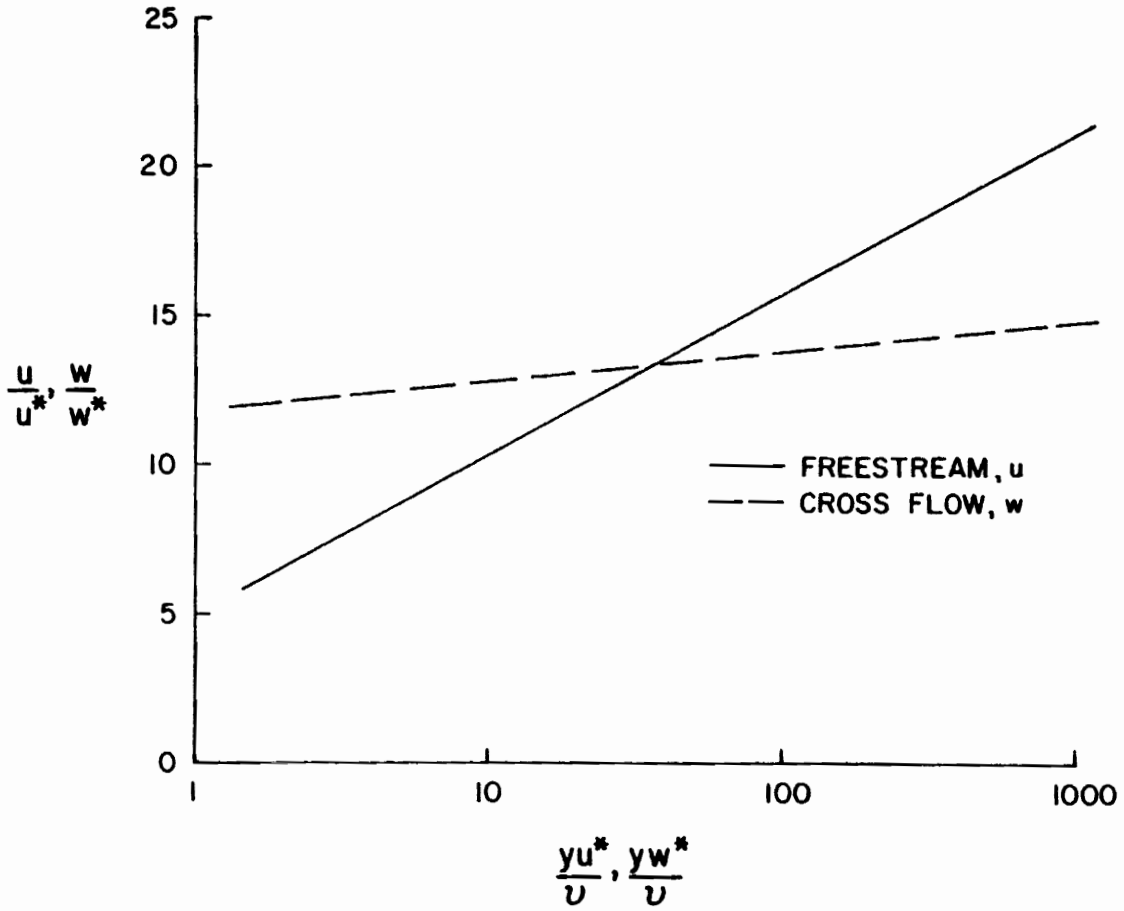

Figure 8. Three-Dimensional Near-Wall Similarity Model as Given by Chandrashekhar and Swamy [55]

to an eddy viscosity model by which the shear stresses and strain rates are related with

$$\tau_{xy} = \rho\ \varepsilon_1\ [\frac{\partial u}{\partial y} + \frac{\partial v}{\partial x}] \tag{55}$$

$$\tau_{xz} = \rho\ \varepsilon_2\ [\frac{\partial u}{\partial z} + \frac{\partial w}{\partial x}]$$

$$\tau_{yz} = \rho\ \varepsilon_3\ [\frac{\partial v}{\partial z} + \frac{\partial w}{\partial y}]$$

where ε_1, ε_2, and ε_3 are the three components of the eddy viscosity expression.

Close to the wall $\frac{\partial}{\partial x}$, $\frac{\partial}{\partial z} << \frac{\partial}{\partial y}$ for the velocity, hence

$$\tau_{xy} = \varepsilon_1\ \rho\ \frac{\partial u}{\partial y}$$

$$\tau_{xz} = 0$$

$$\tau_{yz} = \varepsilon_3\ \rho\ \frac{\partial w}{\partial y}$$

and Eq. 54 becomes

$$\frac{\partial p}{\partial x} = -\frac{\partial \tau_{xy}}{\partial y} \tag{57}$$

$$\frac{\partial p}{\partial y} = 0$$

$$\frac{\partial p}{\partial z} = -\frac{\partial \tau_{yz}}{\partial y}\ .$$

Integration of Eqs. 57 gives

$$\tau_{xy} = \tau_{xy_w} - y \frac{\partial p}{\partial x} \tag{58}$$

$$\tau_{yz} = \tau_{yz_w} - y \frac{\partial p}{\partial z}$$

where w denotes conditions at the wall. Perry and Joubert assumed that the eddy viscosity is isotropic and that the maximum shear stress acts in the same direction as the maximum strain rate. They suggest that

$$[\tau_{xy}^2 + \tau_{yz}^2]^{1/2} = \rho\varepsilon[(\frac{du}{dy})^2+(\frac{dw}{dy})^2]^{1/2}, \tag{59}$$

and by dimensional reasoning that

$$\varepsilon = \kappa\rho^{-1/2}[\tau_{xy}^2 + \tau_{yz}^2]^{1/4} y. \tag{60}$$

Substitution of Eqs. 58 and 60 into Eq. 59 gives, after simplification,

$$[\tau_w^2 - 2y\ \tau_w\ \rho\alpha\ \cos\ \theta + y^2\alpha^2]^{1/4} = \rho^{1/2}\kappa y[(\frac{du}{dy})^2+(\frac{dw}{dy})^2]^{1/2} \tag{61}$$

where

$$\tau_w = [\tau_{xy_w}^2 + \tau_{yz_w}^2]^{1/2}$$

$$\alpha = \frac{1}{\rho}\ [(\frac{\partial p}{\partial x})^2 + (\frac{\partial p}{\partial z})^2]^{1/2}$$

$$\tau_w \rho \cos \Theta = \tau_{xy_w} \left(\frac{\partial p}{\partial x}\right) + \tau_{yz_w} \left(\frac{\partial p}{\partial z}\right)$$

and Θ is the angle between the pressure gradient and wall shear vectors. Integration of Eq. 61 gives

$$\frac{u_0}{q^*} = \frac{\int [1 + (\frac{dv}{du})^2]^{1/2} \, du}{q^*} \tag{62}$$

$$= \frac{1}{\kappa} \int \frac{1}{y^+} \left[1 - 2 \cos \Theta \left(\frac{\alpha\nu}{q^{*3}}\right) y^+ + \left(\frac{\alpha\nu}{q^{*3}}\right)^2 y^{+2}\right]^{1/4} dy^+$$

where $q^* = \sqrt{\tau_w/\rho}$ and $y^+ = yq^*/\nu$. The integral on the left side of the equation represents the 'developed' velocity profile and is equal to the length of the arc on a polar plot. In the limit for small value of y^+ within the logarithmic region,

$$\frac{u_0}{q^*} = \frac{1}{\kappa} \ln y^+ + C,$$

so that Eq. 62 can be altered to read

$$\frac{u_0}{q^*} = \frac{1}{\kappa} \int_0^{y^+} \frac{1}{y^+} \left[1 - 2 \cos\Theta \left(\frac{\alpha\nu}{q^{*3}}\right) y + \left(\frac{\alpha\nu}{q^{*3}}\right)^2 y^{+2}\right]^{1/4} dy^+ + C. \tag{63}$$

Equation 63 is plotted in Fig. 9 for various values of Θ. The effect of the pressure gradient parameter, $\alpha\nu/q^{*3}$, is to cause the deviations

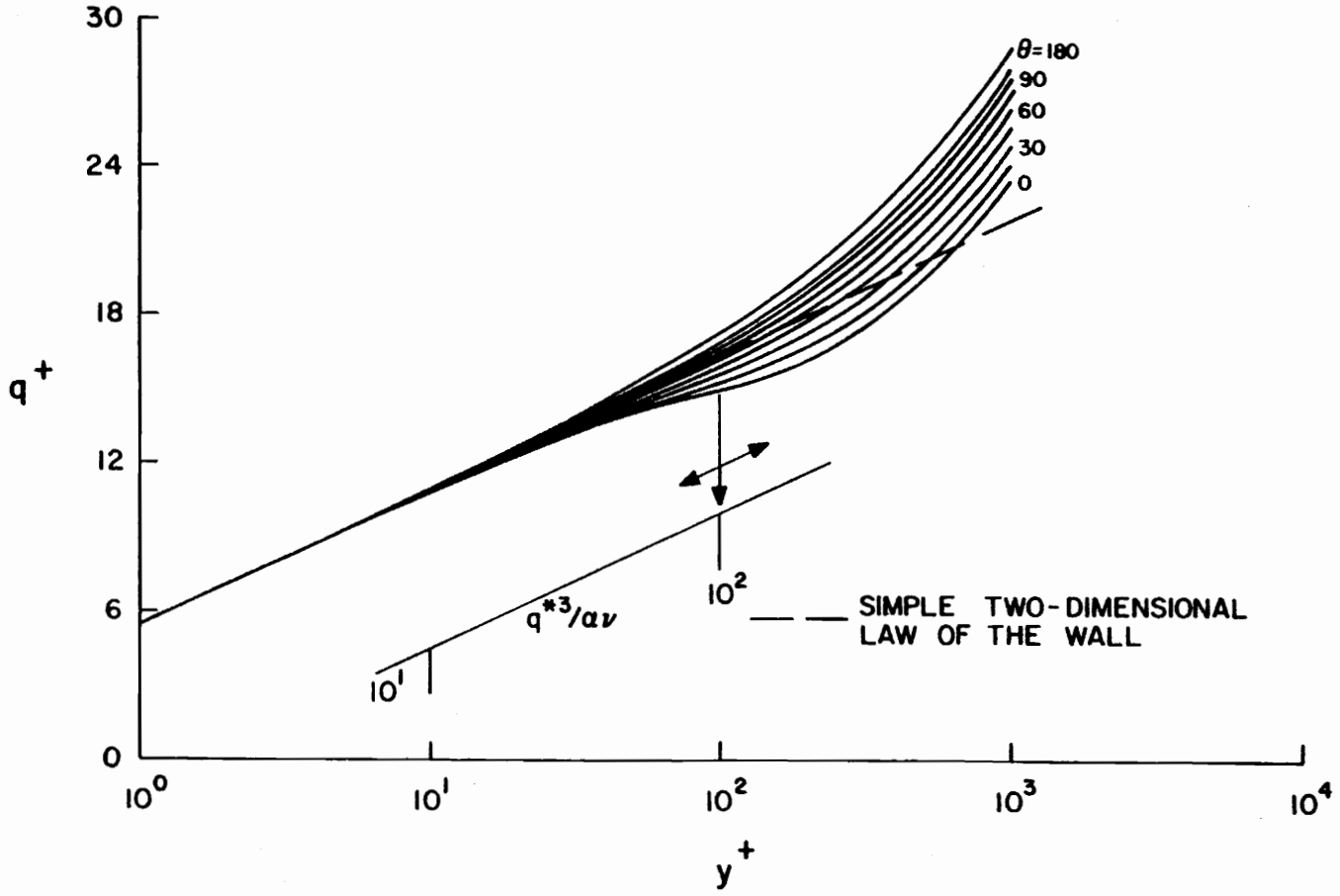

Figure 9. Three-Dimensional Near-Wall Similarity Model as Given by Perry and Joubert [56]

from the simple logarithmic line to shift bodily up and down along the line. A value of $\Theta = 0$ corresponds to the two-dimensional favorable pressure gradient case. A value of $\Theta = 180$ corresponds to the adverse pressure gradient case. It should be noted that Θ depends on a priori knowledge of the direction of wall shear.

Following the same general method as outlined for the two-dimensional case in Chapter II, van den Berg [6] developed a model in 1973 that includes both pressure gradient and inertial effects. His theory was compared with a limited number of measurements by van den Berg and Elsenaar [57] and Vermeulen [58]. Wall shear was indirectly measured by the Stanton tube and sublayer fence methods respectively. The van den Berg and Elsenaar experiment was carried out on a swept flat plate with an induced pressure distribution, while Vermeulen's experiment was in the boundary layer of a curved duct. Van den Berg emphasizes that his model is not valid for large pressure gradients or for large changes of shear stress from the wall value. In short, his model is not reported to be valid for large deviations from the two-dimensional similarity law.

Beginning as in the two-dimensional case, near-wall similarity in the near-wall region can be expressed by

$$q^+ = f(y^+)$$

Therefore one may choose to write that

$$u = u^* f(y^+) \quad \text{and} \quad w = w^* f(y^+) \tag{64}$$

where u^* and w^* are the components of the vector $q^* = \sqrt{\tau_w/\rho}$. Equation 64 may be substituted into the equations of motion, and the velocity v may be eliminated with the continuity equation. Van den Berg suggests that a simplification of the mathematics can be rendered if the x-z plane of the wall is rotated such that the x-axis is now in the direction of the wall shear stress. With the substitution and the transformation of coordinates complete (and therefore $w^* = 0$), the equations of motion would be written as

$$u \frac{\partial u}{\partial x} + v \frac{\partial u}{\partial y} + w \frac{\partial u}{\partial z} = q^* \frac{\partial u^*}{\partial x} f^2 + q^* \frac{\partial w^*}{\partial z} \frac{df}{dy^+} \int_0^{y^+} f dy^+ \tag{65}$$

$$u \frac{\partial w}{\partial x} + v \frac{\partial w}{\partial y} + w \frac{\partial w}{\partial z} = q^* \frac{\partial w}{\partial x} f^2.$$

Solving for the shear stress distribution gives

$$\frac{\tau_x}{\tau_w} = 1 + \frac{\nu}{\rho q^{*3}} \frac{\partial p}{\partial x} + \frac{\nu}{q^{*2}} \frac{\partial u^*}{\partial x} I_1(y^+) + \frac{\nu}{q^{*2}} \frac{\partial w^*}{\partial z} I_3(w^*) \tag{66}$$

$$\frac{\tau_z}{\tau_w} = \frac{\nu}{\rho q^{*3}} \frac{\partial p}{\partial z} y^+ + \frac{\nu}{q^{*2}} \frac{\partial w^*}{\partial z} I_1(y^+)$$

where

$$I_3 = \int_0^{y^+} [\frac{df}{dy^+} \int_0^{y^+} f \, dy^+] \, dy^+ = f \int_0^{y^+} f \, dy^+ - I_1$$

and

$$I_1 = \int_0^{y^+} f^2 \, dy^+.$$

The integrals I_1 and I_3 were obtained by numerical integration using data tabulated by Coles [59]. Since I_3 was found to be significantly smaller than I_1, it was omitted. Noting that for the coordinate system used,

$$\frac{\partial u^*}{\partial x} = \frac{\partial q^*}{\partial x} \quad \text{and} \quad \frac{\partial w^*}{\partial x} = q^* \frac{\partial \phi_\tau}{\partial x} \tag{67}$$

where ϕ_τ is the angle of rotation of the coordinate system, the shear stress distribution may be rewritten as

$$\frac{\tau_x}{\tau_w} = 1 + \alpha_x y^+ + \beta_x I_1(y^+) \tag{68}$$

$$\frac{\tau_z}{\tau_w} = \alpha_z y^+ + \beta_z I_1 (y^+)$$

where

$$\beta_x = \frac{\nu}{q^{*2}} \frac{\partial q^*}{\partial x}, \quad \beta_z = \frac{\nu}{q^*} \frac{\partial \phi_\tau}{\partial x},$$

$$\alpha_x = \frac{\nu}{\rho q^{*3}} \frac{\partial P}{\partial x}, \text{ and } \alpha_z \frac{\nu}{\rho q^{*3}} \frac{\partial P}{\partial z}.$$

Using mixing length relations and noting that $\tau_z << \tau_x$, van den Berg

writes

$$\frac{\partial u^+}{\partial y^+} = \frac{1}{\kappa y^+} \left(\frac{\tau_x}{\tau_w}\right)^{1/2} \tag{69}$$

$$\frac{\partial w^+}{\partial y^+} = \frac{1}{\kappa y^+} \left(\frac{\tau_z}{\tau_w}\right)^{1/2}.$$

Substitution of Eqs. 68 into Eqs. 69 and integration gives

$$u^+ = \frac{1}{\kappa} \left[\ln y^+ + \frac{1}{2} \alpha_x y^+ + \frac{1}{2} \beta_x + I_2(y^+)\right] + c \tag{70}$$

and

$$w^+ = \frac{1}{\kappa} \left[\alpha_z y^+ + \beta_z I_2(y^+) + B\right]$$

where

$$I_2 \simeq \frac{1}{\kappa^2} [\ln y^+]^2 y^+ \text{ and } B \simeq b \alpha_z$$

with $b \simeq 13$. Thus van den Berg's model reduces to

$$u^+ = \frac{1}{\kappa} \left[\ln y^+ + \frac{1}{2} \alpha_x y^+ + \frac{1}{2} \beta_x \frac{(\ln y^+)^2 y^+}{\kappa^2}\right] + c \tag{71}$$

and

$$w^+ = \frac{1}{\kappa} \left[\alpha_z (y^+ + b) + \beta_z \frac{(\ln y^+)^2 y^+}{\kappa^2}\right].$$

When only the pressure gradient effects are considered, van den Berg's model reduces to a model similar to that of Perry and

Joubert. Figure 10 shows the effect of various Θ-values, as defined in Perry and Joubert's analysis, on the u component of velocity. The qualitative results are similar to those of Perry and Joubert's. For this plot, all the inertial terms are set to zero. Figure 11 shows a similar plot on a linear scale for the w component of velocity. Finally Fig. 12 shows a typical similarity plot by van den Berg showing data comparison with the two-dimensional similarity law, van den Berg's model with inertial terms set to zero, and with the inertial terms included. It should be noted that the inclusion of the inertial terms requires a priori knowledge of the magnitude and direction of wall shear.

East [60] has developed a model for use with compressible flows. Eight differential equations are developed which must be solved simultaneously using a Runge-Kutta scheme. No experimental data were used for comparison, however, a simplified model for the incompressible case was developed. Basically, East attempts to take into account the rotation of the stress vector as it moves away from the surface. He makes the first order approximation that

$$|\tau| = |\tau_w| \text{ and } \psi = y\left(\frac{\partial \psi}{\partial y}\right)_w \tag{72}$$

where ψ is the angular displacement of the total shear relative to the wall shear stress direction. The total shear stress is composed of a laminar component, $\mu \frac{\partial q}{\partial y}$, in the direction α_ℓ and a turbulent component, τ_t, in the direction β_t. Through a shear stress polar diagram, East relates the stresses and angles by

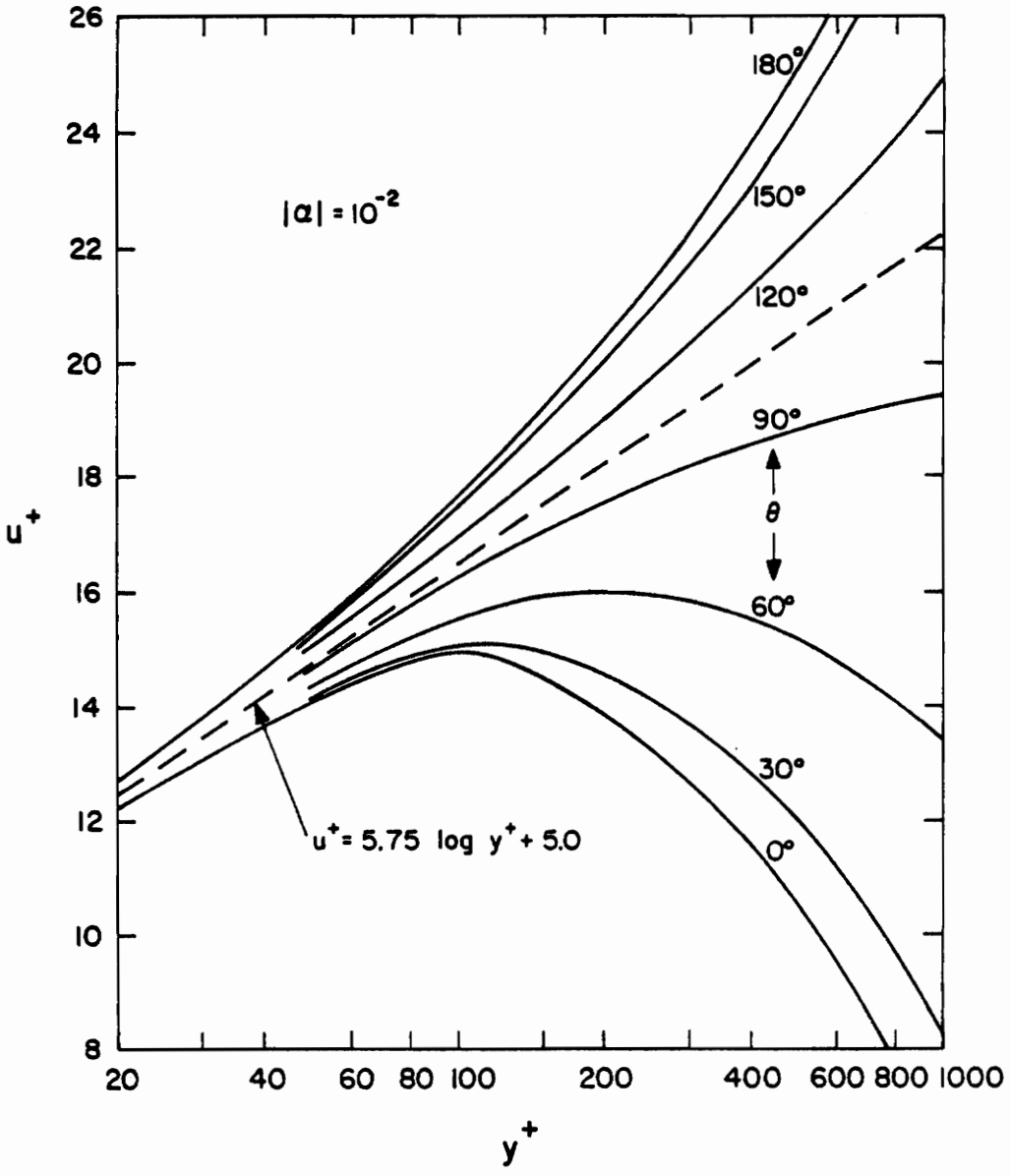

Figure 10. The Velocity in the Direction of the Wall Shear Stress at Various Θ and $|\alpha| = 10^{-2}$ as Given by van den Berg [6]

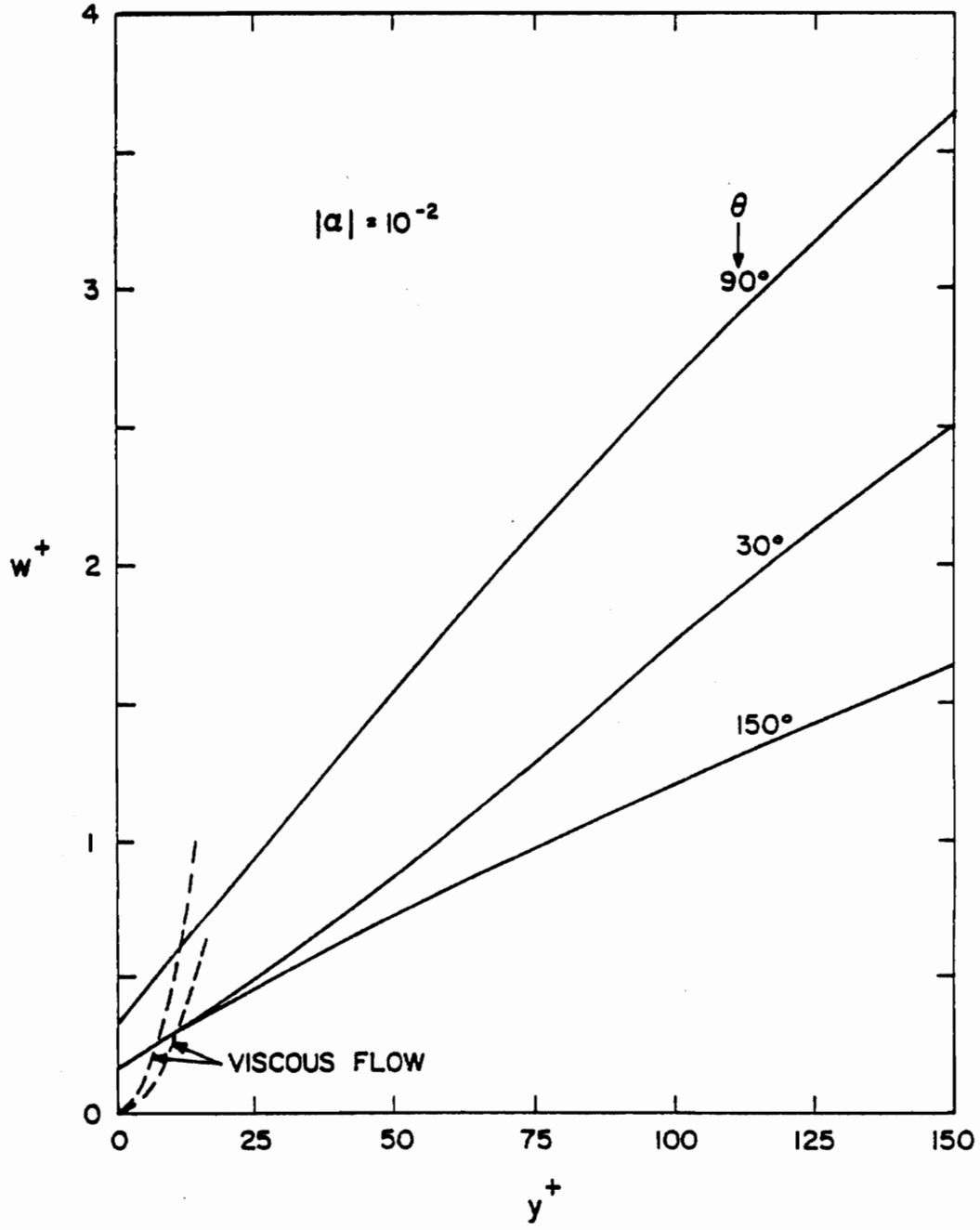

Figure 11. The Velocity Normal to the Wall Shear Stress at Various Θ and $|\alpha| = 10^{-2}$, $b = 13$, as Given by van den Berg [6]

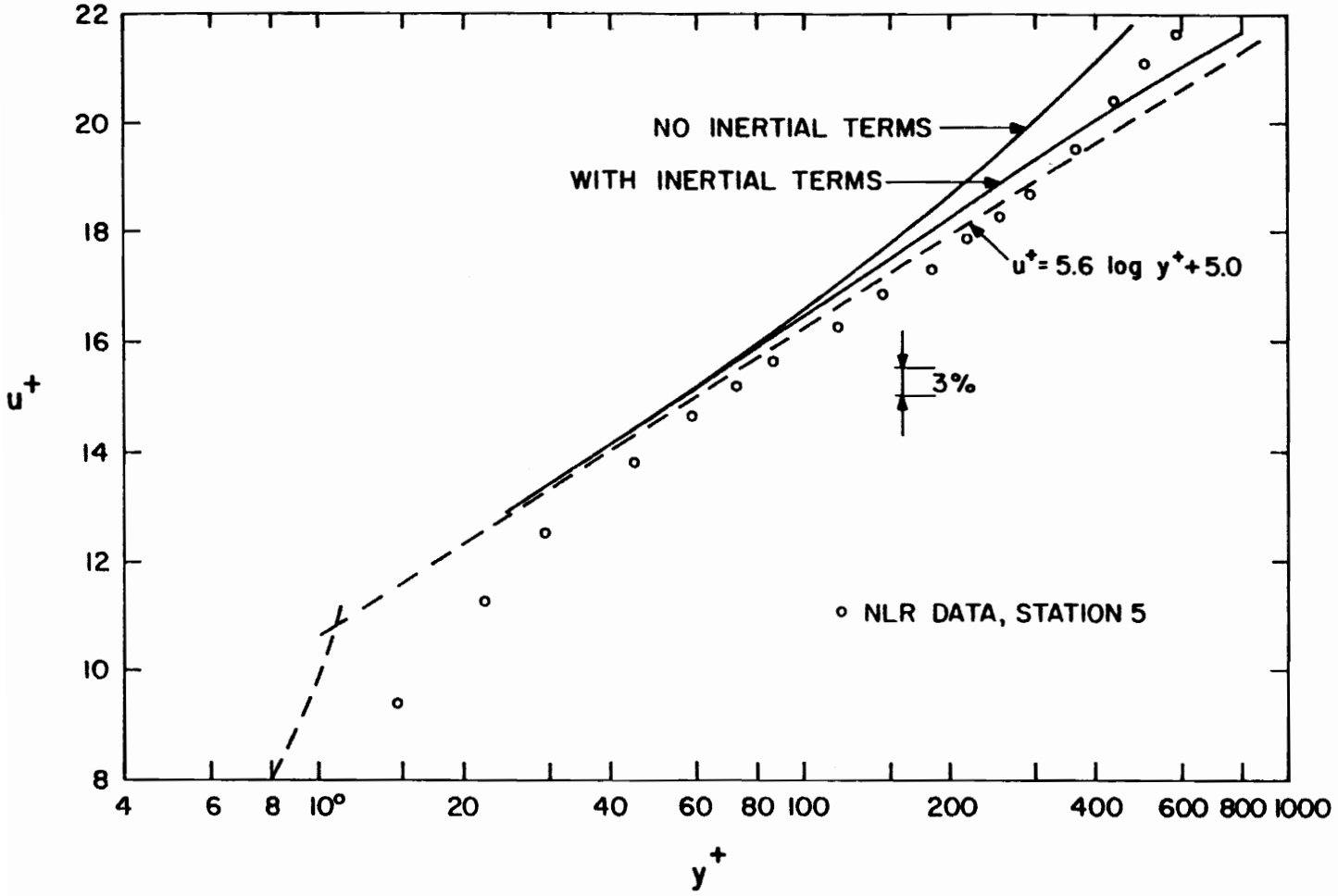

Figure 12. Comparison of van den Berg's Three-Dimensional Similarity Model [6] for small αy^+ with Experimental Data [57] . $\alpha_x = -3.0 \times 10^{-3}$, $\beta_x = -10.0 \times 10^{-6}$

$$\tau^2 = \mu^2\left(\frac{\partial q}{\partial y}\right)^2 + \tau_t^2 + 2\mu\left|\frac{\partial q}{\partial y}\right| \ |\tau_t| \ \cos(\alpha_\ell - \beta_t) \tag{73}$$

and

$$\frac{|\tau_t|}{\sin\ (\alpha_\ell - \ \psi)} = \frac{|\tau|}{\sin\ (\alpha_\ell - \beta_t)} \ . \tag{74}$$

Nondimensionalizing and rearranging of Eqs. 73 and 74 gives

$$\mu^+ \left|\frac{\partial q^+}{\partial y^+}\right| = \pm\ [1 - \tau^{+2} \sin^2(y^+(\frac{\partial \psi}{\partial y^+})_w(\alpha_\ell^+ - \beta_t^+))]^{1/2}$$

$$- \tau^+ \cos[y^+\ (\frac{\partial \psi}{\partial y^+})_w\ (\alpha_\ell^+ - \beta_t^+)] \tag{75}$$

where the negative root is taken if

$$\cos\ [y^+\ (\frac{\partial \psi}{\partial y^+})_w\ (\alpha_\ell^+ - 1)] < 0$$

and

$$\alpha^+ y^+ (\frac{\partial \psi}{\partial y^+})_w = \tan^{-1}\ \frac{\sin[y^+(\frac{\partial \psi}{\partial y^+})_w] - \tau^+ \sin[y^+ \beta_t^+ (\frac{\partial \psi}{\partial y^+})_w]}{\cos[y^+(\frac{\partial \psi}{\partial y^+})_w] - \tau^+ \cos[y^+ \beta_t^+ (\frac{\partial \psi}{\partial y^+})_w]} \ . \tag{76}$$

The nondimensionalized terms are defined by:

$$q^+ = \frac{q}{q^*},\ q^* = \sqrt{\tau_w/\rho_w}\ ,\ y^+ = yq^*/\nu_w \tag{77}$$

$$\mu^+ = \frac{\mu}{\mu_w}, \quad \tau^+ = \frac{\tau_t}{\tau_w}, \quad \alpha_\ell{}^+ = \frac{\alpha_\ell}{y^+(\frac{\partial\psi}{\partial y^+})_w}$$

$$\beta_t{}^+ = \frac{\beta_t}{y^+(\frac{\partial\psi}{\partial y^+})_w}, \text{ and } \psi^+ = \frac{\psi}{y^+(\frac{\partial\psi}{\partial y^+})_w} = 1.$$

Examination of a velocity gradient polar plot gives

$$\frac{\partial|q|}{\partial y} = \left|\frac{\partial q}{\partial y}\right| \cos(\alpha_\ell - \phi) \tag{78}$$

and

$$\frac{\partial\phi}{\partial y} = \frac{\left|\frac{\partial q}{\partial y}\right|}{|q|} \sin(\alpha_\ell - \phi) \tag{79}$$

where ϕ is the velocity vector direction. Written in nondimensionalized form, Eqs. 78 and 79 give:

$$\frac{\partial|q^*|}{\partial y^+} = \left|\frac{\partial q^+}{\partial y^+}\right| \cos[y^+(\frac{\partial\psi}{\partial y^+})_w(\alpha_\ell{}^+ - \phi^+)] \tag{80}$$

and

$$\frac{\partial[y^+(\frac{\partial\psi}{\partial y^+})_w\phi^+]}{\partial y^+} = \frac{\frac{\partial q^+}{\partial y^+}}{q^+} \sin[y^+(\frac{\partial\psi}{\partial y^+})_w(\alpha_\ell{}^+ - \phi^+)] \tag{81}$$

where

$$\phi^+ = \frac{\phi}{y^+(\frac{\partial\psi}{\partial y^+})_w}.$$

The temperature distribution is assumed to be given by the Crocco law,

$$C_p T + \frac{r\, q^2}{2} = \text{constant} = C_p T_w \tag{82}$$

where r is the recovery factor. The temperature distribution in nondimensional form is then written as,

$$T^+ = \frac{T}{T_w} = 1 - F^2\, q^{+2} \tag{83}$$

where F, the compressibility factor is defined as

$$F = M_t \sqrt{\frac{r(\gamma' - 1)}{2}}\ , \tag{84}$$

γ' is the ratio of the specific heats, and M_t, the Mach number, is defined as

$$M_t = \frac{q^*}{\sqrt{\gamma'\, R_w\, T_w}}\ . \tag{85}$$

With this temperature distribution, it can be shown that

$$\rho^+ = (1 - F^2\, q^{+2})^{-1} \tag{86}$$

and

$$\mu^+ = (1 - F^2\, q^{+2})^{n} \tag{87}$$

where $n \simeq .76$ at sea level.

East further modifies Bradshaw's Reynolds stress transport equations by including a fluctuating pressure term of the form

$$p' = C_1 \rho v |q| \tag{88}$$

where C_1 is assumed constant. In polar coordinates Bradshaw's equations become

$$0 = - \left|\frac{\partial q}{\partial y}\right| \sin(\alpha_\ell - \beta_t) + C_1 |q| \frac{\partial \beta_t}{\partial y} \tag{89}$$

and

$$0 = \frac{|\tau|}{\rho} \left|\frac{\partial q}{\partial y}\right| [\cos(\alpha_\ell - \beta_t) - C_1 \cos(\alpha_\ell - \phi)] \tag{90}$$

$$- \left(\frac{\tau}{\rho}\right)^{3/2} \frac{(1 - C_1)}{L} - \frac{C_1 |q|}{\rho} \frac{\partial \tau}{\partial y}$$

where L is the length scale. Written in nondimensional form Eqs. 89 and 90 become

$$\frac{\partial [y^+ (\frac{\partial \psi}{\partial y^+})_w \beta_t^+}{\partial y^+} = [\left|\frac{\partial q^+}{\partial y^+}\right| \sin(y^+ (\frac{\partial \psi}{\partial y^+})_w (\alpha_\ell^+ - \beta_t^+))]/C_1 |q^+| \tag{91}$$

and

$$\frac{\partial \tau^+}{\partial y^+} = [\tau^+ \left|\frac{\partial q^+}{\partial y^+}\right| [\cos(y^+ (\frac{\partial \psi}{\partial y^+})_w (\alpha_\ell^+ - \beta_t^+))$$

$$- C_1 \cos\left(y^+\left(\frac{\partial\psi}{\partial y^+}\right)_w (\alpha_\ell^+ - \phi^+)\right)] - \frac{\tau^{+3/2}(1 - C_1)}{\kappa\, y^+\sqrt{\rho^+}}]/C_1|q^+|. \qquad (92)$$

Equations 75, 76, 80, 81, 86, 87, 91, and 92 together form a closed set that describe conditions in the near-wall region in terms of the independent variables y^+, F, and $\left(\frac{\partial\psi}{\partial y^+}\right)_w$.

East looked at two cases: small cross flows and large cross flows. For the small cross flows case, Eqs. 80, 91, and 92 reduce to

$$\frac{\partial|q^*|}{\partial y^+} = \left|\frac{\partial q^*}{\partial y^+}\right| \qquad (93)$$

$$\left|\frac{\partial q^*}{\partial y^+}\right| = \frac{\tau_t^{+3/2}}{\kappa y^+\sqrt{\rho^+}} \qquad (94)$$

$$\frac{\partial(y^+\,\beta_t^+)}{\partial y^+} = \frac{1}{C_1|q^+|}\left|\frac{\partial q^+}{\partial y^+}\right| y^+(\alpha_\ell^+ - \beta_t^+) \qquad (95)$$

Since the laminar stress contribution is small in the overlap layer, East uses the approximations that $\tau_t^+ \simeq 1$ and $\beta_t^+ \simeq 1$. Combining Eqs. 94 and 86 then gives:

$$q^+ = \frac{1}{F}\sin[F(\frac{1}{\kappa}\ln y^+ + C)] \qquad (96)$$

The bracketed term is recognized as the logarithmic portion of the two-dimensional similarity law. Indeed in the limit for the case

of incompressible flows, Eq. 96 becomes the similarity law for the logarithmic region. East proposes that this bracketed term be replaced by the analytic expression of Green [24] to give:

$$q^+ = \frac{1}{F} \sin\{F[\frac{1}{2\kappa} \ln(y^{+2} \frac{\kappa}{D} + 1) - D_1(1 - \exp(-\frac{y^+}{D}))]\} \qquad (97)$$

where

$$D_1 = 9(1 + 45F^2).$$

This analytic expression extends the model to the wall, and is roughly equivalent to Spalding's extended law of the wall in two dimensions. In essence then, East's model indicates that for small cross flows, Prahlad's model holds true.

For large cross flows, no simple analytic form could be determined by East. An empirical fit for flow situations where $\alpha_\ell \leq \pi$ results in

$$q^+ = q_0{}^+[1 - 0.25(1 - \cos(y^+ (\frac{\partial \psi}{\partial y^+})_w))] \qquad (98)$$

where $q_0{}^+$ is the value of q^+ given in Eq. 97. Figure 13 shows a similarity plot for the incompressible flow case for various values of $(\frac{\partial \psi}{\partial y^+})_w$. Two points should be noted: 1) that no effect on the similarity law for the logarithmic region is seen until values of $y^+ > 200$ which is nearly outside the expected limit of the logarithmic region, and 2) that the gradient of the angle of rotation of the

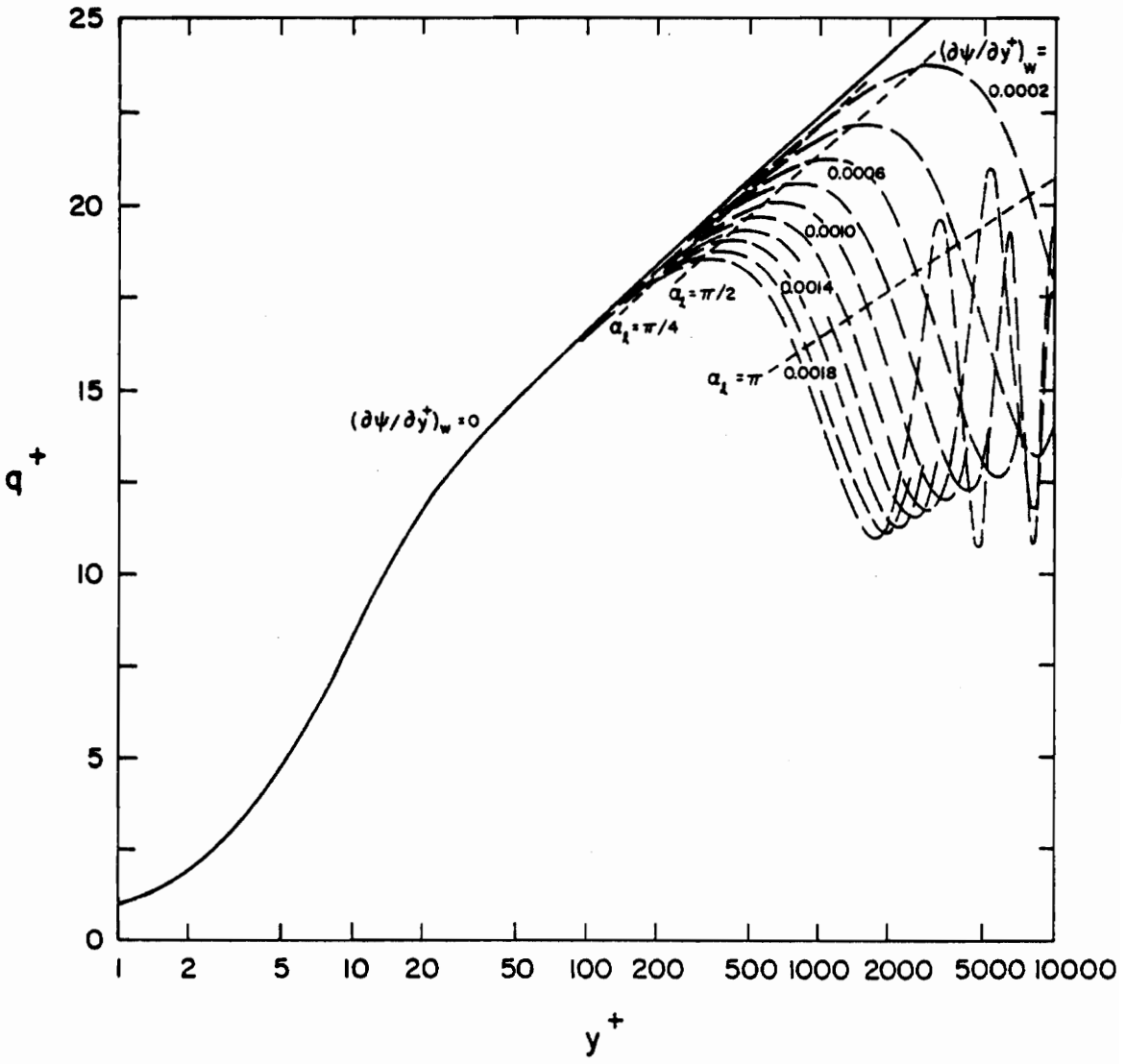

Figure 13. Three-Dimensional Near-Wall Similarity Model for Large Cross Flows as Given by East [60]

shear stress vector at the wall is a most difficult parameter to measure.

Finally, the eleventh and last model has been put forth by White Lessmann, and Christoph [61] in 1975. Actually their work emcompasses not so much a model, but rather a numerical method of calculating wall shear in a three-dimensional turbulent boundary layer.

They begin by rotating their coordinate system such that x is in the freestream direction. Wall shear components then exist in the freestream direction τ_{x_w}, and in the cross flow direction, τ_{z_w}, and are related by

$$\tau_{z_w} = \rho\zeta'\tau_{x_w} \text{ where } \zeta' = \tan\theta' \tag{99}$$

and θ' is the angle between the freestream and wall shear directions. In a manner similar to Eq. 21, one may write

$$\tau_x \simeq \tau_{x_w} + \frac{1}{h_1}\frac{\partial p}{\partial x} y \tag{100}$$

where h_1 is the streamwise metric. Utilizing Eq. 13, Eq. 21 may be rewritten in the form

$$\frac{du^+}{dy^+} = \frac{(1 + \alpha' y^+)^{1/2}}{\kappa y^+} \tag{101}$$

where $\alpha' = \frac{\nu}{\rho u^{*3} h_1}\frac{\partial p}{\partial x}$ and the nondimensionalized quantities are

defined as before. Integration results in the streamwise velocity approximation:

$$u^+ = \frac{1}{\kappa} [2(S - S_o) + \ln(\frac{S - 1}{S + 1} \frac{S_o + 1}{S_o - 1})] \qquad (102)$$

where $S = (1 + \alpha' y^+)^{1/2}$ and S_o is chosen to be $S_o = (1 + 0.1108\ \alpha')^{1/2}$ to enable Eq. 102 to reduce to the similarity law for the logarithmic region for a zero pressure gradient. For the cross flow component White, et al. use a slightly modified version of the simple unilateral hodograph proposed by Mager [62]:

$$w^+ = u^+ \zeta' (1 + \frac{y^+}{q^+})^2 \qquad (103)$$

where $w^+ = \frac{w}{w^*}$ and $w^* = \sqrt{\tau_{z_w}/\rho}$. It is accurately noted that the Mager hodograph does not allow for S-shaped profiles.

The three-dimensional turbulent boundary layer equations for continuity, streamwise momentum, and cross flow momentum are invoked. The velocities u and w are assumed to be known from Eqs. 102 and 103, where v is determined from continuity. Integration of the two momentum equations results in two coupled first-order partial differential equations in terms of the dependent variables, streamwise wall shear and ζ'. A solution requires:

1) $q(x,y)$ and four of its derivatives
2) $h_1(x,y)$ and two of its derivatives
3) $h_2(x,y)$ and its streamwise derivative.

It should be noted that none of these quantities is easily obtained from experimental data. Comparison was made with experiments by Klinksiek and Pierce [63] in a doubly-curved duct and by Johnston [48] in flow over a flat plate impinging against a back wall. Agreement was lacking in the quantitative sense, but good in the qualitative sense. No measurements of wall shear, direct or indirect, were made.

D. WALL SHEAR STRESS MEASUREMENT TECHNIQUES

In the last fifty years nearly fifty investigators have attempted to measure wall shear in incompressible turbulent boundary layers. This number does not include numerous investigations in compressible flow or those with mass injection. All but seven of these investigations have dealt with two-dimensional flows.

For two-dimensional flows the techniques employed include: floating element devices [38, 64-77], Preston tubes [78-82,37,38,39, 64,72], Stanton tubes [84-86], sublayer fences [87-89], razor blades [90-92, 72], heated elements [93-102], and electrochemical meters [103,104]. The floating element technique, comprising almost a third of the total, is difficult to use, but only it can provide a direct measurement of wall shear stress. All other techniques rely on the assumed existence and form of near-wall similarity to infer wall shear stress.

The indirect techniques listed above may generally be divided into two groups: 1) those which infer wall shear stress through pressure measurements and 2) those which infer wall shear stress

through heat or mass transfer rate measurements near the wall. Both groups rely in one form or another on the assumed existence of near-wall similarity, i.e.

$$q^+ = f(y^+).$$

For instance Preston tubes are simply pitot tubes laid on the wall. They may be used to measure dynamic pressure which is correlated with the local wall shear stress. Stanton tubes and the razor blade technique are somewhat similar to Preston tubes but are slightly smaller and may even be confined to the viscous sublayer. Heat and mass transfer techniques utilize near-wall similarity through Reynolds analogy. These methods sense flow conditions in the thin thermal or concentration layers, respectively, above the wall. These layers must remain within the viscous sublayer for accurate calibration. Miller [72], Rechenberg [82], and Pierce and Krommenhoek [52] provide more detailed discussions of these techniques.

The only technique that directly measures the wall shear stress is the floating element technique. In essence a small area of the wall is isolated and the force acting on that area is measured. This technique would appear to be the only one capable of resolving the question of near-wall similarity in three-dimensional flows; however floating element measurements can be very difficult due to a number of possible error sources.

Errors in the measurement of wall shear with the use of a

floating element device can be caused by a number of different occurrences [64,67,52,105]:

1) Misalignment of the floating disk with the surrounding wall can cause significant errors though these errors can be minimized through careful installation.
2) Secondary forces may be imposed on the edge or lip of the floating disk by penetration of the freestream pressure into the air gap. It is usually suggested that these errors can be minimized by minimizing the lip thickness, thereby decreasing the area over which the pressure may act. Everett [67] alone has suggested that a thicker lip will result in reducing the error. Regardless of how these errors may be minimized, they will remain significant when the wall shear approaches zero.
3) The pressure gradient will cause a pressure difference between the boundary layer above any point in the air gap and cause flow through it. These errors can be minimized but not entirely eliminated by sealing the floating element casing from the surroundings.

Of possibly less importance, other occurances include [64]:

4) The air gap will act as a roughness element in the smooth wall. Everett [67] suggests that the gap be reduced in size to minimize errors as is the usual

practice. Allen [105] however suggests that less error is encountered for larger gaps.

5) The shear stress measured is the mean shear stress over the area of the floating disk. If the flow geometry is large in comparison to the floating disk, this effect can be minimized.

6) The floating element can alter the geometry of the device according to its position and thus cause changes in the flow pattern through the air gap. It would therefore be advantageous if the floating element device were of the nulling type.

7) Even when the disturbance caused by the gap is ignored, there will be a shear stress transmitted through the shear layer. Hakkinen [106] suggests that a part of the gap area be considered effectively floating element area.

8) An imposed pressure gradient can result in a normal force acting on the floating element some distance from the disk's center. This normal force can therefore cause a moment that can introduce errors for large pressure gradients.

From the preceding list it can generally be concluded that largest errors for the floating element technique are derived from two sources: 1) element misalignment and 2) the pressure gradient imposed on the element.

Two experimental studies have been made concerning errors induced by floating element misalignment. Both of these studies were carried out in supersonic flows, and their applicability to subsonic flow is somewhat questionable. The results of Allen [105] and O'Donnell [107] are compared under similar flow situations in Fig. 14.

O'Donnell points out that on a smooth surface a misalignment error of 0.005 mm (0.0002 inches) can be felt by hand and that an error of 0.013 mm (0.0005 inches) can be readily seen. Therefore it certainly should be possible to keep these errors below ± 3% of the flush reading.

Pierce and Krommenhoek [52], Brown and Joubert [64], and Miller [72] have made experimental studies of pressure gradient effects on floating elements. These studies were made in small subsonic wind tunnels. The conditions studies are given in Table 2.

Both Pierce and Krommenhoek, and Brown and Joubert studied the effects of adverse pressure gradients. Miller studied both adverse and favorable pressure gradients. Figure 15 shows their results. The results of Pierce and Krommenhoek are based on 28 data where the wall shear stress was inferred from Clauser charts with Coles' constants and compared with a floating element device that could not be nulled. Brown and Joubert's results are based on more than 120 data, exhibiting much scatter, where the wall shear was inferred from Preston tubes using Patel's calibration and compared with a floating element device that was nulled by tipping the device. Miller's results for favorable pressure gradients were

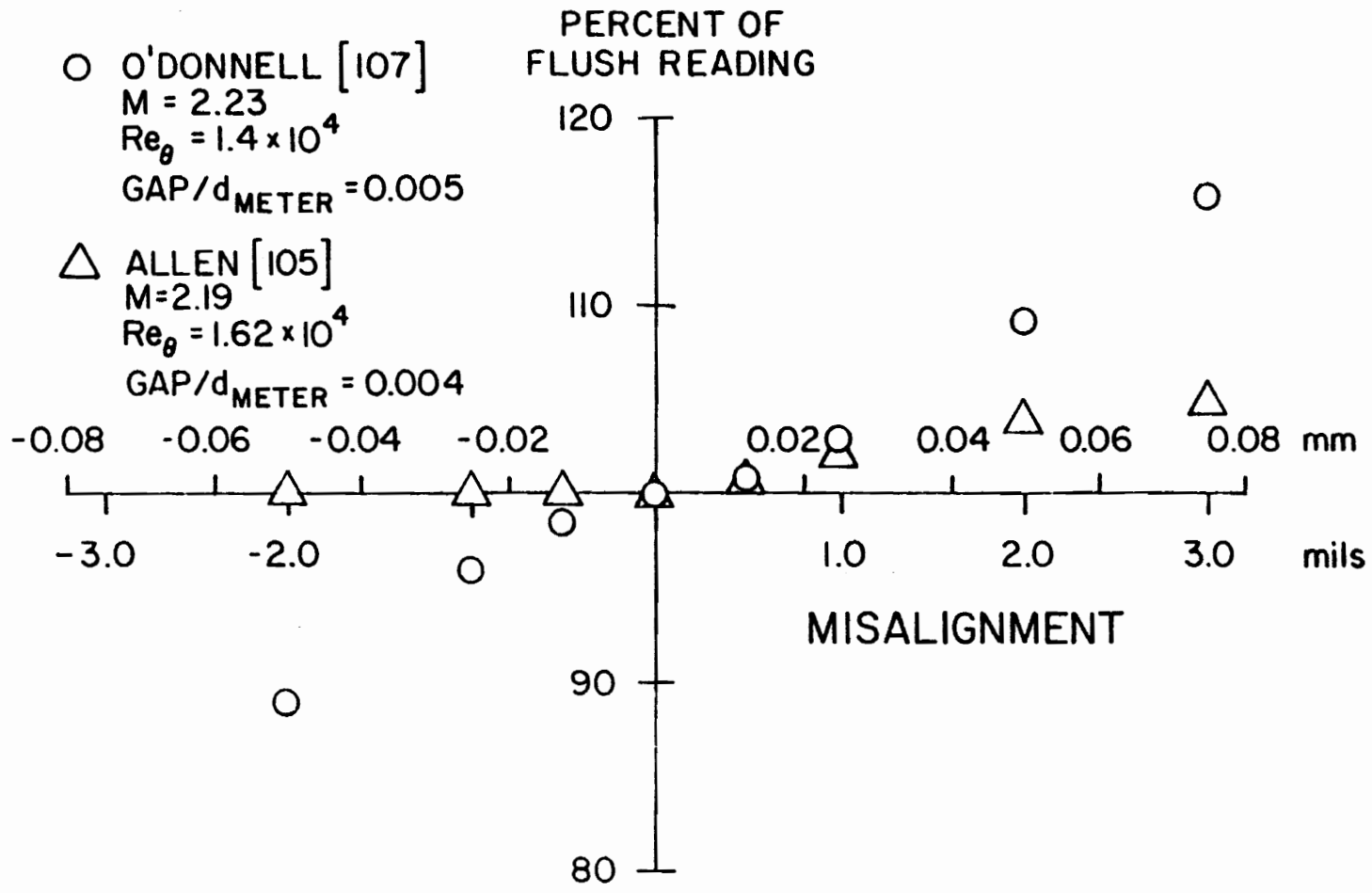

Figure 14. Comparison of Misalignment for Floating Element Devices

Table 2. Flow Conditions for Studies on Pressure Gradient Corrections for Floating Element Devices

Investigation	$R_{e_{unit}}$ (m^{-1})	$\frac{dp}{dx}$ ($\frac{kPa}{m}$)	$d_m u^*/\nu$	τ_w (Pa)
Pierce and Krommenhoek [52]	$8.2 \times 10^5 \rightarrow 28.2 \times 10^5$	$0 \rightarrow 2.0$	$1375 \rightarrow 2150$	$0.72 \rightarrow 1.77$
Brown and Joubert [64]	$6.6 \times 10^5 \rightarrow 39.4 \times 10^5$	$0 \rightarrow 11.0$	$500 \rightarrow 2500$	$0.24 \rightarrow 6.85$
Miller [72]	24.9×10^5	$-1.0 \rightarrow 3.6$	$1000 \rightarrow 2000$	$1.05 \rightarrow 6.11$

conversion factors

$ft^{-1} = 0.3048\ m^{-1}$

$lbf/ft^3 = 6.366 \times 10^{-2}$ kPa/m

$lbf/ft^2 = 0.02089$ Pa

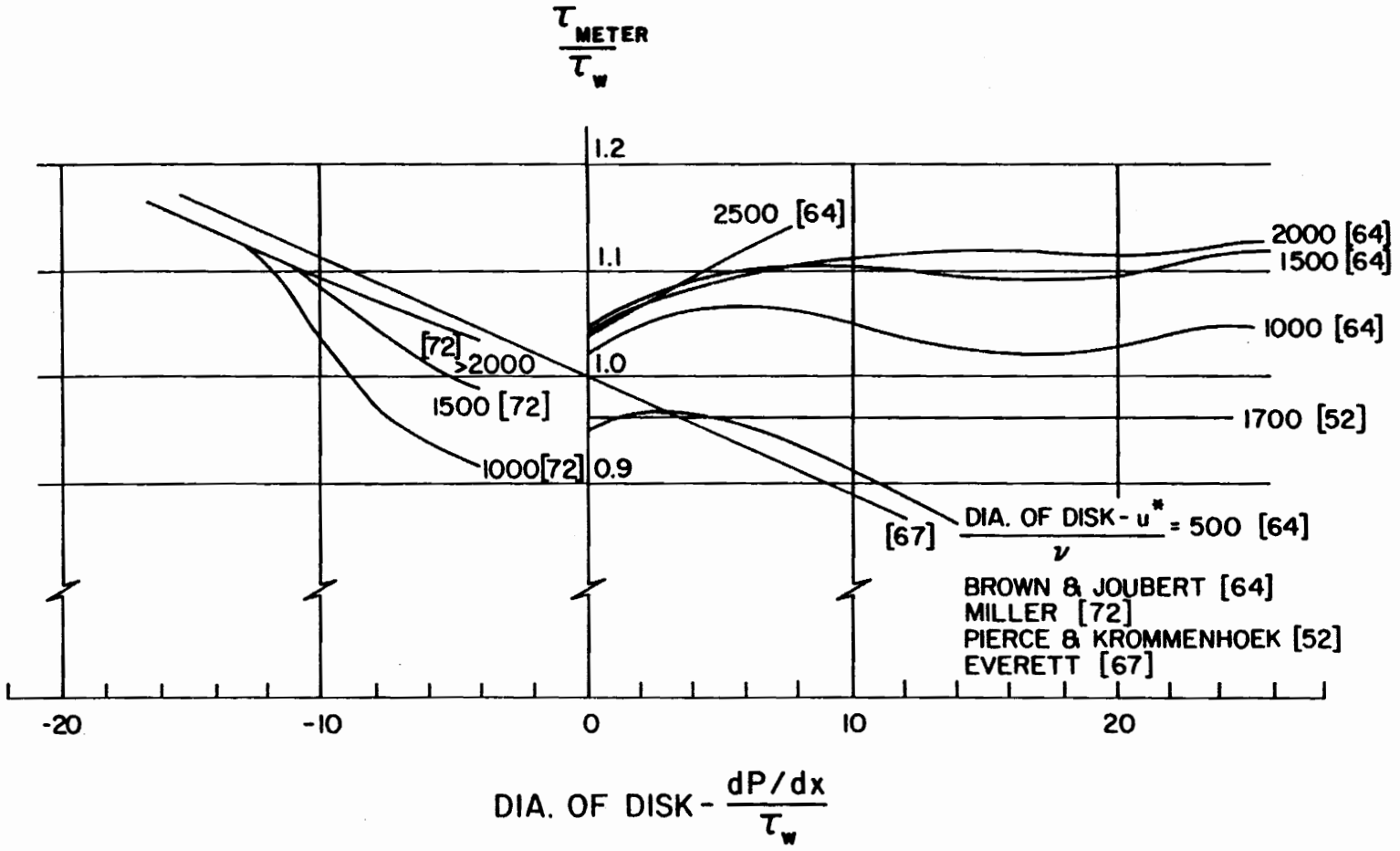

Figure 15. Pressure Gradient Corrections for Floating Element Devices

based on 9 data points. Miller used fully developed flow between two plates and calculated the wall shear stress with a momentum balance, i.e.,

$$\tau_w = \frac{d_p}{2} \frac{dp}{dx} \tag{104}$$

where the distance between plates, d_p, was 0.318 cm (0.125 in.) and 1.27 cm (0.5 in.). Miller's floating element was of the nulling type. Miller used a different tunnel for his adverse pressure gradient studies. There he compared wall shears using a Preston tube with Patel's calibration, a near-wall similarity plot for the logarithmic region using Patel's constants, and his floating element device corrected by + 10% using Brown and Joubert's results. Compared with the floating element results, the Preston tube measurements were reported to be 2 to 4% low, while the similarity plot gave results that were high by as much as 5%. The worst agreement was in accelerated flow regions. In addition, Fig. 15 shows the pressure correction suggested by Everett [67] which takes the form

$$\tau_w - \tau_{meter} = \frac{t}{2} \frac{dp}{dx} \tag{105}$$

where t is the thickness of the floating element lip. (A t = 0.64 mm (0.025 in.) and a diameter of disk d_m = 2.86 cm (1.125 in.) were assumed). The gap-to-disk diameter ratio was 0.0044 for the Pierce and Krommenhoek study, 0.004 for the Brown and Joubert study, and 0.0035 for Miller's work.

Examining Fig. 15 several observations can be made. Firstly, the studies of Pierce and Krommenhoek and of Brown and Joubert are apparently in conflict for equal values of $(d_m u^*/\nu)$. One suggests positive corrections associated with adverse pressure gradients while the other suggests negative corrections. Although not shown in Fig. 15, Pierce and Krommenhoek results show a constant +3 to +5% correction required up to a value of the parameter $(d_m \frac{dp/dx}{\tau_w}) \simeq 33$. The correction from there out to 51 increases to +17%. Everett's simple correction formula seems to support Pierce and Krommenhoek's results at least qualitatively. However, Miller's studies in adverse pressure gradients appear to support Brown and Joubert's results. In contradiction however, Miller's studies in favorable pressure gradients appear to be supported by Everett's formula.

The confusion, demonstrated in Fig. 15, that now exists in the literature on pressure gradient corrections makes application of correction factors for this study rather difficult. The confusion is heightened if one considers that, unlike the two-dimensional flow studied above, the direction of the pressure gradient in a three-dimensional flow is generally different from the wall shear stress direction. Obviously further work needs to be done in the area, although the manner in which an exacting experiment could be performed remains somewhat unclear to the author. For this study the pressure gradient parameter $(d_m \frac{dp/dx}{\tau_w})$ varies from ~ -0.3 in the two-dimensional cases to as much as ~ -22 for flow near the three-dimensional separation line. Typically this parameter is >-10 with

$(d_m u^*/\nu) \simeq 1500.$

For the zero pressure gradient case, Pierce and Krommenhoek's device read consistantly low by 3 to 5% when compared to wall shear determined from Clauser charts. Brown and Joubert's instrument read consistently high by 4 to 5% when compared to Preston tube measurements. These can be compared with Allen's instrument which read consistently low by 6% when compared to Preston tube measurements. Miller does not report any data for his device in a zero pressure gradient flow. It should be noted that: 1) these errors are calculated under the assumption that the near-wall similarity laws, the law of the wall constants, and the instruments that depend on them can provide exact wall shear values, and 2) an apparent ± 5% uncertainty can exist between very carefully designed and constructed floating element devices.

For three-dimensional flows the techniques employed for measurement of wall shear have been similar to those used in the two-dimensional case. The techniques employed include: Preston tubes [52,53,54, 108-110], Stanton tubes [57], sublayer fences [110,111], heated elements [52,112], and razor blades [53]. All the above are indirect measurement techniques and were calibrated in two-dimensional flows. Only the work of Pierce and Krommenhoek [52] includes three-dimensional measurements with a floating element device.

The direct force measurements by Pierce and Krommenhoek totaled five data points. Their test flow was the boundary layer confining a jet impinging on a back wall. They compared their results with

wall shear values inferred from a directionally sensitive heat meter, a Preston tube, and a yaw probe calibrated as a Preston tube. All the indirect devices were calibrated in a two-dimensional flow, and agreement between these devices and the floating element was within 5 to 10%. This would tend to indicate that the nondimensionalizing wall friction velocity is at least approximately related to wall shear in the same manner for both two- and three-dimensional flows. Regrettably, their experiment was flawed by :1) an insufficient number of measurements, 2) a lack of companion velocity profiles, 3) a lack of static pressure data in the neighborhood of the measuring location, and 4) the inability of the floating element to discern the direction of wall shear.

On this last point, some further discussion is required. As stated earlier, the direction of wall shear stress cannot be assumed to be the direction of flow at even small distances above the wall. Since evidence would suggest that the direction of the velocity vector generally changes continuously to the wall, the velocity vector direction is only an approximation to the wall shear direction that becomes less valid as the distance from the wall increases. Since the floating element device used by Pierce and Krommenhoek allowed movement of the floating disk in only one direction, a directionally sensitive heat meter was used to align the floating element. One would expect that the heat meter would respond to some average over the thermal boundary layer which should be very small; however, the degree to which this approximation is

valid is still in question.

Other than the work by Pierce and Krommenhoek, only Prahlad [54,109] has sought to address the problem of near-wall similarity in three-dimensional flows. Prahlad used Preston tubes calibrated in two-dimensional flows to infer wall shear in the limiting wall streamline direction as determined by yaw probes. The objection to yaw probes to determine wall shear direction would be even stronger than cited above for the heat meter. Prahlad studied the flow around a cylinder and an inclined plate. His results for small skews suggest that a nondimensionalizing wall friction velocity correlates his data. Since his measurement technique is indirect, it is impossible to conclude any direct relationship between the wall friction velocity and wall shear. Prahlad also noted two other results: 1) the effects of pressure gradients in three-dimensional flows appear to be qualitatively similar to those in two-dimensional flows, and 2) the larger Preston tubes give smaller values of wall shear than smaller Preston tubes. With regard to this last point, Prahlad states, "This deviation implies departures from wall similarity and consequent errors in the use of the Preston tube technique in these flows."

III. EXPERIMENTAL PROGRAM

A. INTRODUCTION

An experimental program was undertaken in a pressure driven three-dimensional turbulent boundary layer to measure: 1) direction and magnitude of wall shear stresses with an omnidirectional floating element device, 2) the velocity profile data over the measurement stations for wall shear stress, and 3) the static pressure field in the neighborhood of the wall shear stress measurements. The purpose of this experiment was to establish the instrumentation and experimental technique for measuring wall shear stress, and to obtain a complete set of data which would allow comparison of some existing near-wall similarity models for three-dimensional turbulent boundary layer flows. Working in reverse order, the instrumentation systems, their calibration, and experimental uncertainty will be discussed. But first there should be some discussion of the wind tunnel and flow configuration used for this experiment.

B. DESCRIPTION OF WIND TUNNEL AND FLOW CHARACTERISTICS

A careful survey of existing two- and three-dimensional data suggested the need for a tunnel of large flow section. A suitable tunnel would have a large cross section to allow for relatively large boundary layers while maintaining a substantial potential core, a low freestream turbulence level, and freestream velocities high enough to result in local wall shears that could be measured with

reasonable accuracy. The velocity and wall shear instrumentation should be capable of being precisely positioned. No existing facility adequately satisfied these requirements, so a new tunnel was designed and built.

The new wind tunnel is an open circuit type housed in a temperature-controlled laboratory. It has a rectangular test section 0.61 m (2 ft) high and 0.91 m (3 ft) wide. Figure 16 shows a sketch of the tunnel with its major dimensions. Air is drawn through the tunnel by a Twin City Fan and Blower Company BC-402 centrifugal fan powered by a 30-horsepower motor. Air speeds up to 25.9 m/sec (85 ft/sec) can be obtained. Lower air speeds can be maintained by adjustable louvers at the fan exit. To damp out fluctuations and obtain a relatively low turbulence flow, a nominally 2.54 cm (1 in.) diameter matrix of 15.24 cm (6 in.) long tubes and four fourteen-mesh screens are installed in the tunnel entrance. The screens are followed by a contraction, with an area ratio of 16:1, designed for zero acceleration at exit.

Core flow velocity fields were recorded with a United Sensor pitot probe. There was a 6% velocity deficit in the center region of the flow at the nozzle exit. Freestream velocity measurements were uniform within +2.5%, -1.4% of the main freestream velocity. At the test section there was a 1.5% velocity deficit in the center region of the flow and freestream velocity measurements were uniform within +1.0%, -1.2% of the mean value. The freestream turbulence has been measured at the test section to be 0.6 per cent.

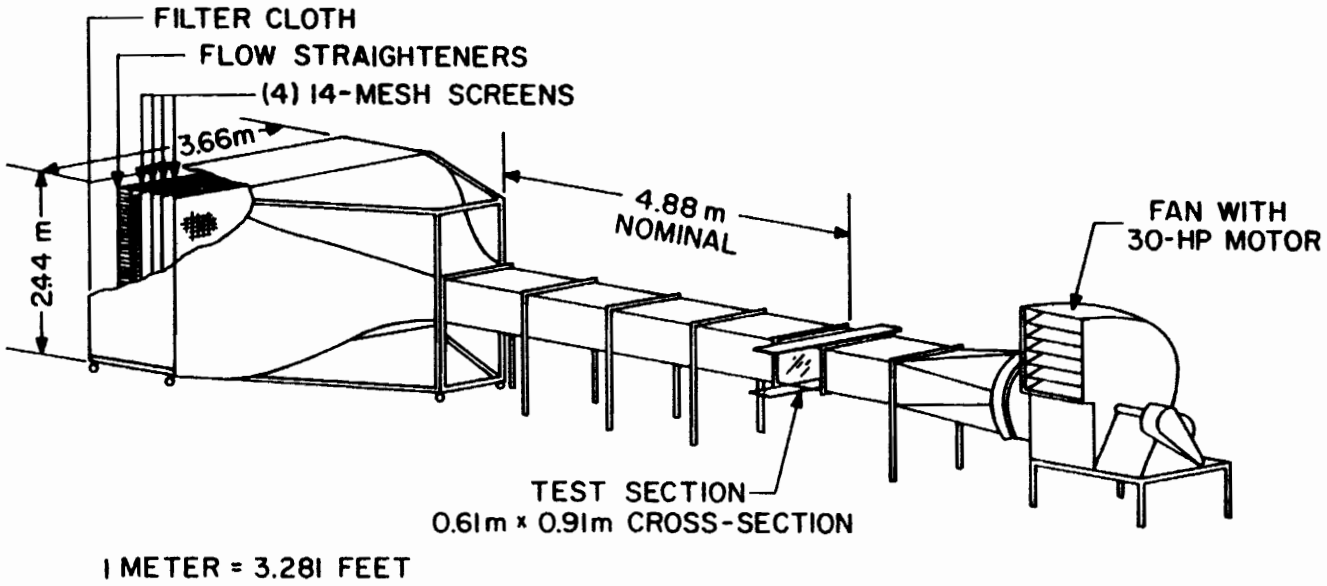

Figure 16. Wind Tunnel

Additional design features of the new tunnel include removable tunnel sections and movable floor and ceiling plates in the test section. The flow is tripped on all four sides by circular metal rods located at the outlet of the contraction where the unit Reynolds number of the flow is measured. The distance between the trip and the test section may be lengthened from its nominal length of 4.88 m (16 ft) by rolling the wheeled contraction section back and adding short sections of tunnel. Both the floor and ceiling of the tunnel contain sliding metal plates. The top plate houses the velocity probe traversing system, while the bottom plate houses the wall shear meter. The bottom plate may also be replaced by a plate containing 52 static pressure taps.

Though there are numerous types of three-dimensional flows and configurations for producing them, it was decided to study the flow around a cylinder with a trailing edge placed normal to the floor of the tunnel as shown in Fig. 17. The advantages of this configuration are: 1) a wide range of skewing can be studied, 2) though a pressure driven flow, the pressure gradients should be relatively small so that their effects on the floating element wall shear measurements should be minimized, and 3) this setup represents a large general class of three-dimensional flows. The cylinder itself has a diameter of 12.7 cm (5 in.), is 25.4 cm (10 in.) high, and has a tapered end that trails to a sharp edge. The overall length of the body is 29.2 cm (11.5 in.). The body was positioned in the tunnel by use of a sting that was secured approximately 2.44 m

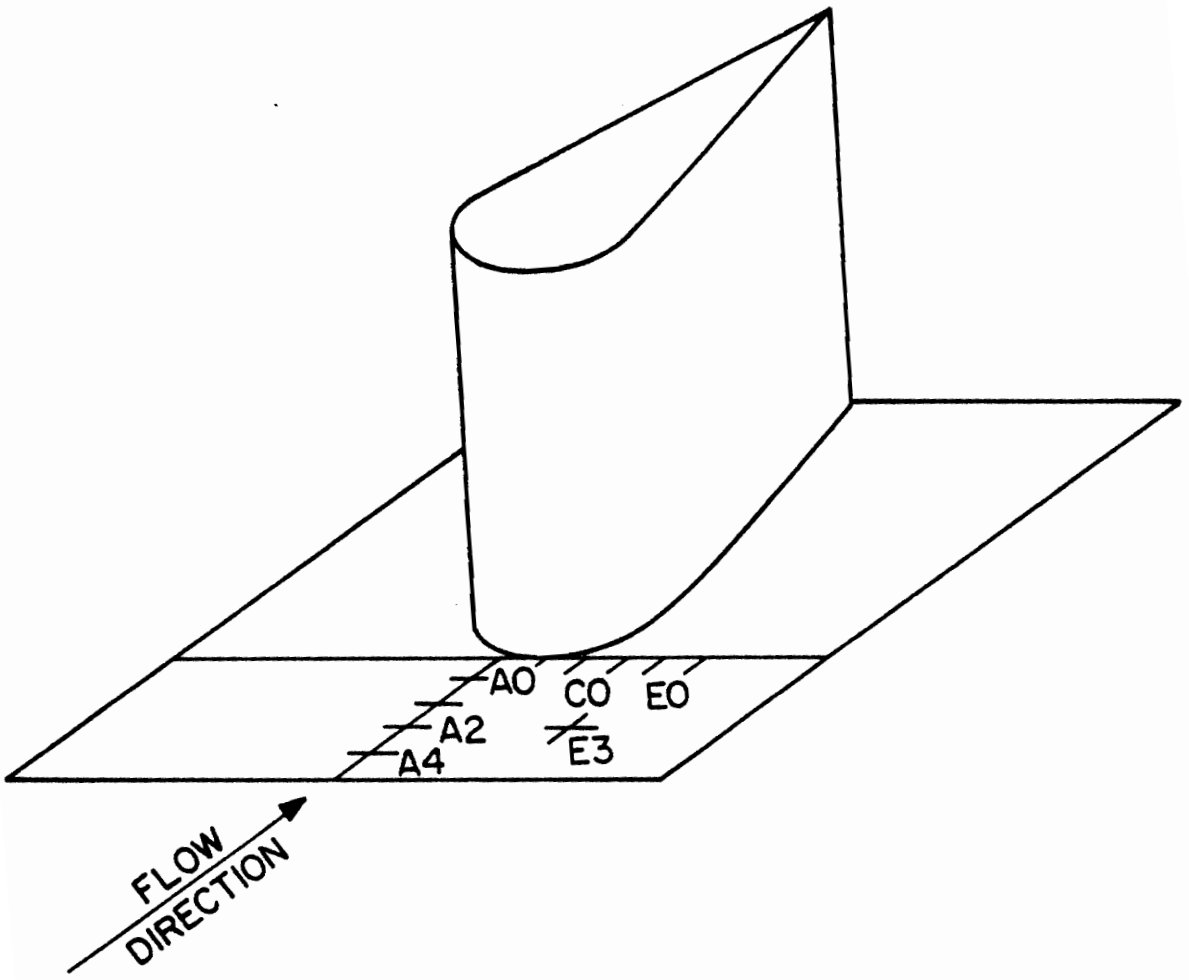

Figure 17. Flow Geometry

(8 ft) downstream of the test section.

C. STATIC PRESSURE MEASUREMENTS

The first of the measurement systems required was the static pressure measurement system. As mentioned earlier, the floor of the test section can be replaced with an aluminum plate containing 52 static pressure taps in a 15.2 x 61.0 cm (6 x 24 in.) grid on 5.1 cm (2 in.) centers. The holes are 0.40 mm (0.0156 in.) diameter, and much effort was expended in the fabrication to insure: 1) that the hole edges would be sharp, 2) that the plate would be flat and smooth, and 3) that no leakage or blockage of the ports would occur.

The heart of the system is a ± 0.69 kPa (±0.1 lbf/in^2) bi-directional differential capacitance type pressure transducer, model 237 built by Setra Systems, Inc. Manufacturer's specifications include:

Full Range Output.	±2.5 volts
Non-linearity.	< ±0.25% of full range output, (best straight line method)
Hysteresis	< ±0.1% of full range output, (infinite resolution)

The pressure transducer was installed in a 48-port Scanivalve sampling valve, model 48J9/OETM/S4-48. This allows the one pressure transducer

to sample 44 static pressure taps in 1 to 0.1 second intervals. (No difference in operating characteristics was noted within this time interval.) Figure 18 is a schematic of the static pressure measurement system. The signal from the transducer is fed into a Vidar model 240 voltage to frequency converter. From there the signal is fed into a Hewlett Packard model 5326A counter and read out on a Hewlett Packard model 5050A printer. Of the four remaining ports available on the Scanivalve device, three were left idle while the last one was used as a calibration port.

Calibration was carried out by attaching the calibration port to a known pressure source. This source was produced by carefully regulating the flow of laboratory supplied air through a small pipe with static pressure taps installed along its length. Control over the flow rate was obtained with three pressure regulators installed in series. The pressure transducer, through the calibration port, as well as a micromanometer were attached to one of the pressure taps in the small pipe. Thus the pressure transducer could easily and frequently be calibrated against a steady pressure source of known value as given by the manometer.

Figure 19 shows a typical calibration curve for the static pressure measurement system. The manufacturer's calibration is also shown. Several calibrations were made and the linear curve shown was demonstrated to be repeatable. By introducing known voltages into the voltage to frequency converter, it was shown that the upward shift in data was not caused by an error introduced in

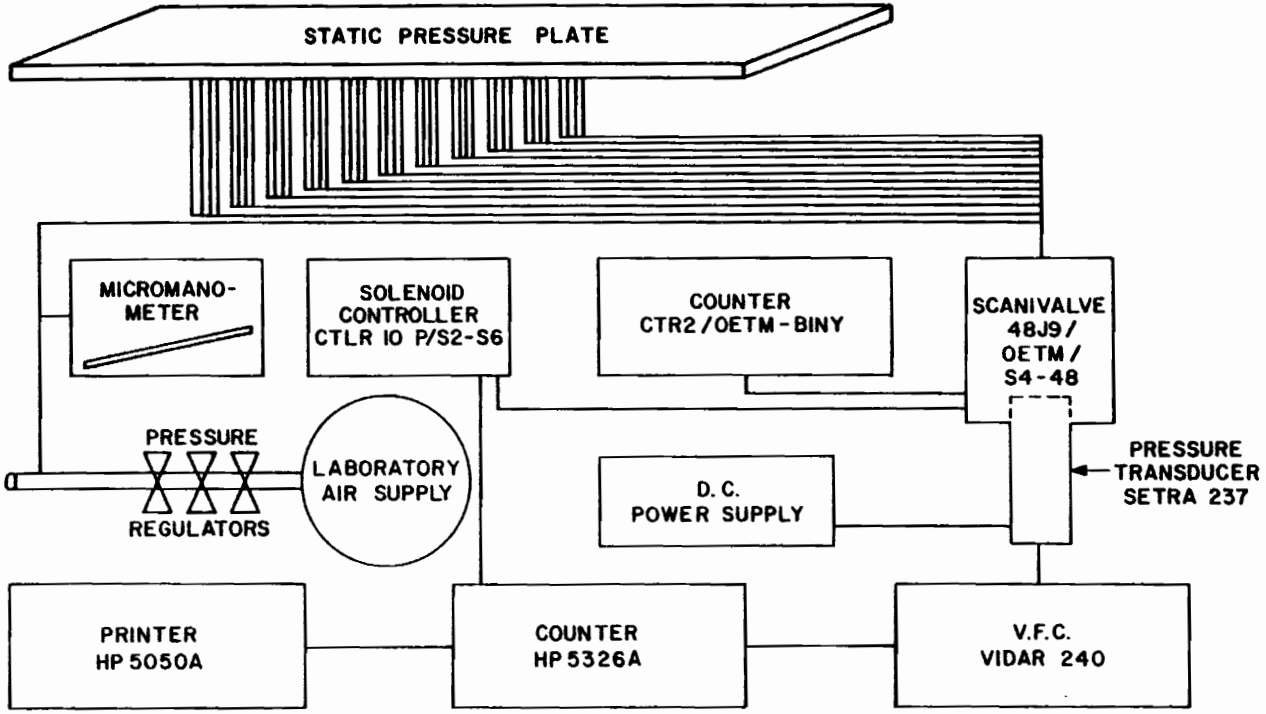

Figure 18. Static Pressure Measurement System

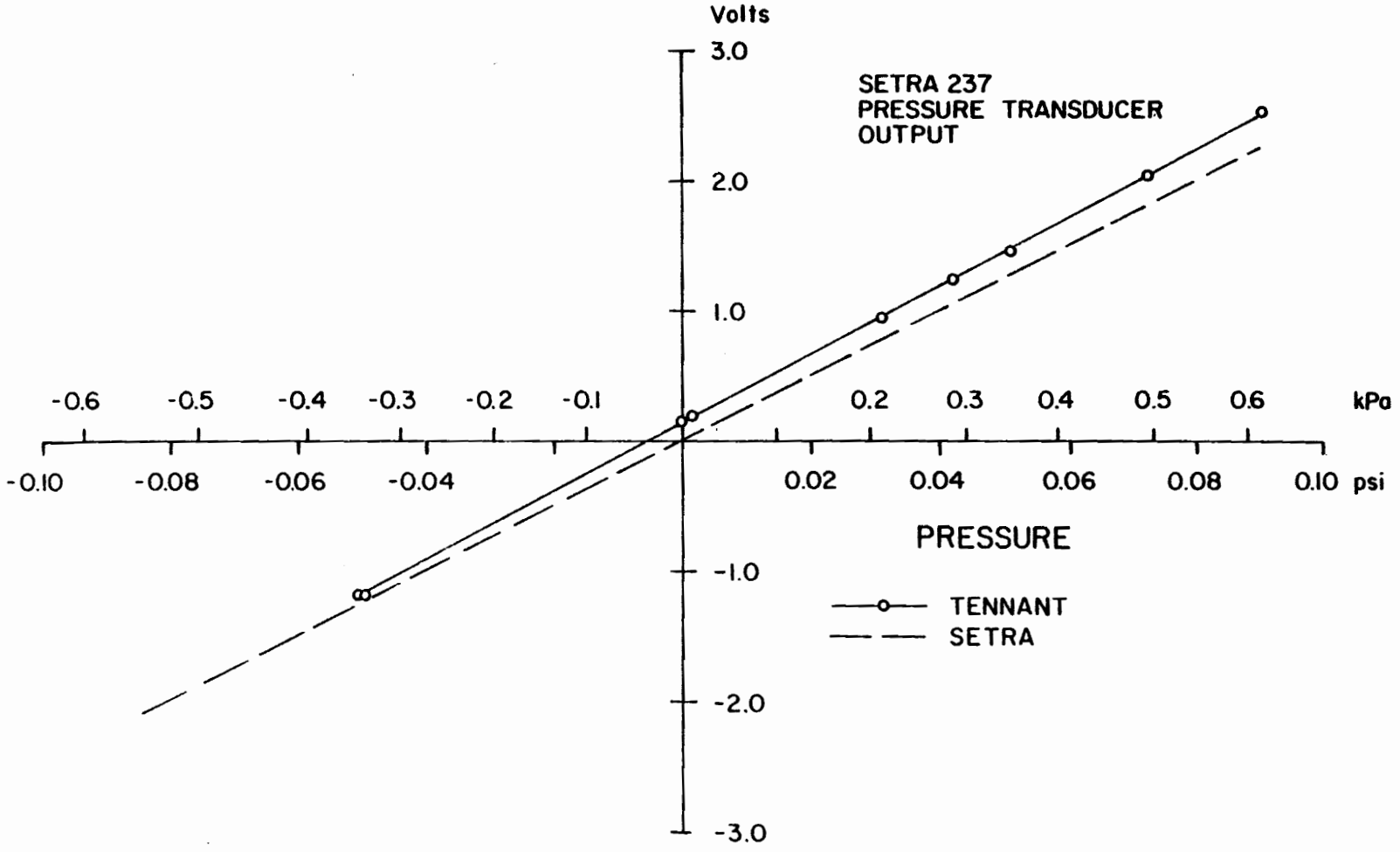

Figure 19. Typical Setra 237 Pressure Transducer Calibration Curve

the signal conditioning. It was therefore concluded that the manufacturer's curve was in error.

Since the desired result of static pressure measurements for this study is the estimation of pressure gradients, it is not so important that the precise value of pressure be measured. Rather it is important that precise measurement of the relative values of pressure be made. Therefore it is the slope of the calibration curve that is important. In this sense too, the calibration shown in Fig. 18 differs from the manufacturer's curve, showing a 4.75% steeper slope.

Estimation of the uncertainty is difficult. Individual static pressure tap measurements under flow conditions were repeatable within ± 0.5%, which would indicate an uncertainty in the pressure gradient of ± 0.7%. This value of uncertainty would appear to be unrealistic, however, when one observes that any nonuniformity in the shape of the static pressure tap or any flow obstructions near the taps can cause errors that are difficult to estimate. It would appear that a more conservative estimate of the uncertainty in the pressure gradient might be ± 3%.

To minimize the effect of the error of any single static pressure measurement on the calculation of pressure gradients, the data were fitted to a fifth order least squares curve. At least four static pressure measurements were used at each grid location. Derivatives of the resulting equation were then calculated in directions along and normal to the axis of the tunnel. This

allowed the estimation of derivatives in any given direction desired.

D. VELOCITY MEASUREMENTS

Velocity measurements were made with a specially designed goose-neck, cobra, stagnation pressure, impact probe. The probe tip consists of three 0.51 mm (0.020 in.) OD tubes located on the vertical axis of rotation. The outside tubes are cut at an angle, and are nulled to determine the flow direction. The stagnation or total pressure is measured with the center tube, while the static pressure is sensed from a 0.40 mm (0.156 in.) diameter pressure tap located in the tunnel floor approximately 0.635 cm (0.25 in.) downstream of the impact probe tip. Velocity measurements from 0.254 mm (0.010 in.) to 12.7 cm (5.0 in.) distance from the floor of the tunnel in a nominally 7.6 cm (3.0 in.) boundary layer were obtained.

The probe is held in place and positioned by a specially designed traversing mechanism located on top of the tunnel. A Unislide translational screw manufactured by Velmax, Inc. provides for adjustment of the vertical position, while mating worm and spur gears allow for rotation of the probe around the vertical axis.

Figure 20 shows a schematic view of the entire velocity measurement system. The major components of this system are an electrical setup to indicate when the impact probe touches the tunnel floor, a differential pressure transducer setup to position the probe in the direction of flow, and a micromanometer setup for measuring the dynamic pressure and thus the velocity.

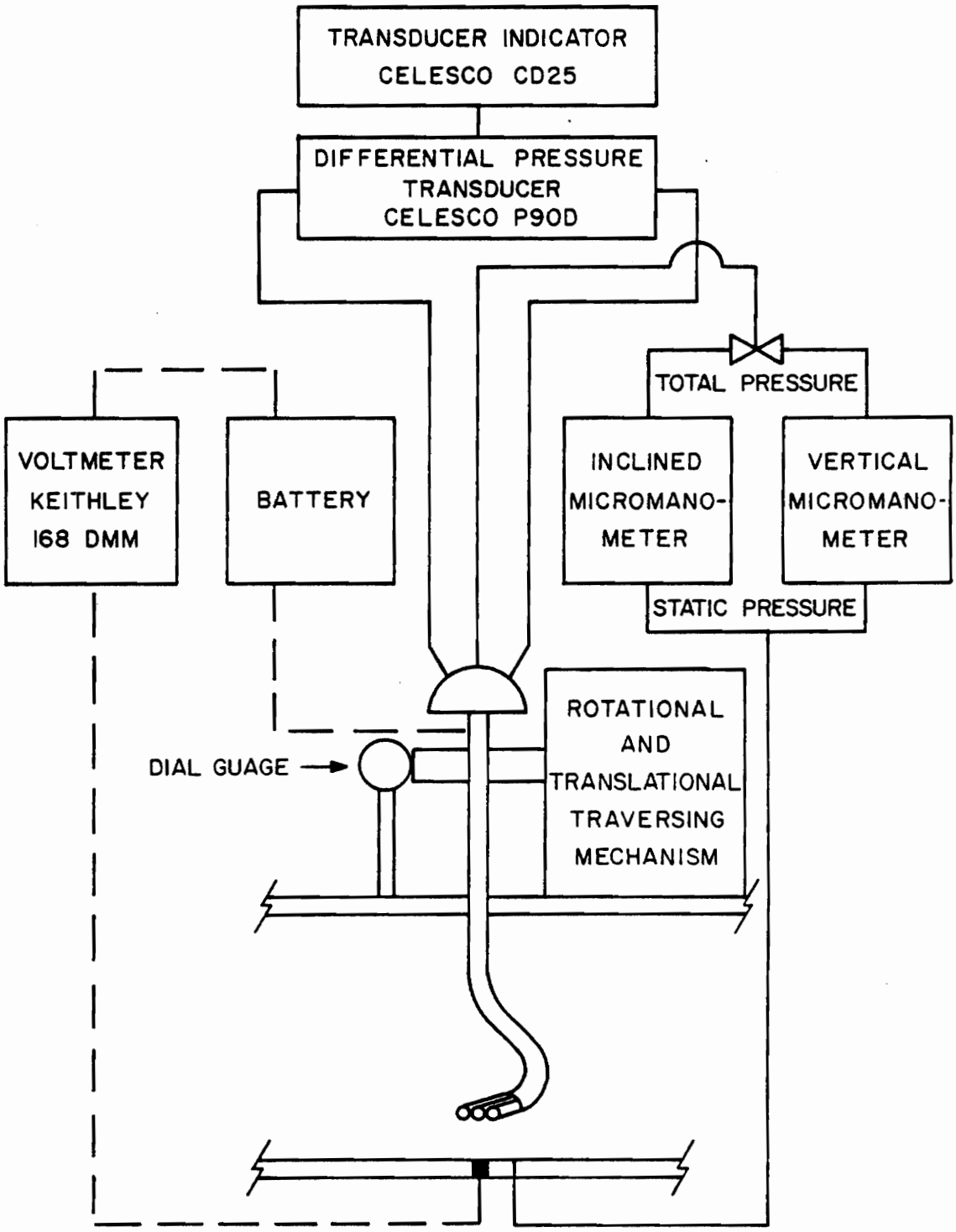

Figure 20. Velocity Measurement System

To position the impact probe vertically, the probe was lowered until the tunnel floor was touched by the probe tip. Attached to opposite terminals of a battery, the probe and a metal plug mounted flush with the floor of the tunnel completed an electrical circuit when contact was made. Sensed by a voltmeter mounted in series, contact could easily be noted within ±0.0127 mm (±0.0005 in.) as confirmed visually by a M-912 Horizontal-Vertical Cathetometer manufactured by Gaertner Scientific Corporation. Once contact was made, a Starrett dial gage was used to sense the probe's vertical location as the probe tip was moved away from the tunnel floor. It is estimated that this procedure resulted in an uncertainty of ±0.0127 mm (±0.0005 in.) in the vertical position of the probe.

The angular position of the probe was adjusted so that it was aligned with the local flow direction for any given vertical position. This was accomplished by nulling the two outside probe tubes with a differential pressure transducer. The transducer used was a sensitive ±0.25 Pa (±1.0 in. H_2O) variable reluctance type that was zeroed for zero flow conditions. Although this is a very linear device (± 1/2% of full scale best straightline), it was unnecessary to calibrate this device since it was used only for nulling pruposes. The angular position itself was determined by use of a protractor surrounding the probe shaft. The protractor could be read to a half-least count of 0.1 degree. However, an estimate of the uncertainty in angular measurement must await the introduction of two-dimensional measurements which will follow this

chapter.

The actual measurement of the dynamic pressure is sensed by two micromanometers installed in parallel between the center, total pressure, probe tube, and a static pressure tap in the tunnel floor. Using a three-way valve, either an inclined micromanometer with a range of 0 to 3.18 cm (1.250 in.) of water or a vertical micromanometer with a range of 0 to 15.24 cm (6.00 in.) of water can be utilized. The inclined manometer can be read to ±0.13 mm (±0.005 in.) of water, while the vertical manometer can be read to ±0.64 mm (±0.025 in.) of water. For readings closest to the wall, the errors contributed by the manometer should be no more than ±2.5%. The magnitude of this error is quickly reduced to < 1% as the probe is moved further from the wall. At 3.18 cm (1.250 in.) of water, the error would be ± 0.17%; whereas for the few data points surveyed in the outer flow by the vertical manometer a maximum error of ±0.80% would result.

In addition to the possible errors introduced by the manometer, an effect of vertical probe position on the static pressure measurements was noted. Figure 21 shows the correction required for dynamic pressure readings as a result of the effect of the vertical probe location on the static pressure measurement. The three cases of two-dimensional flow, symmetrical three-dimensional flow, and highly skewed three-dimensional flow are shown with the static pressure at a probe distance of 12.7 cm (5 in.) from the tunnel floor assumed as datum. Within the logarithmic region the largest

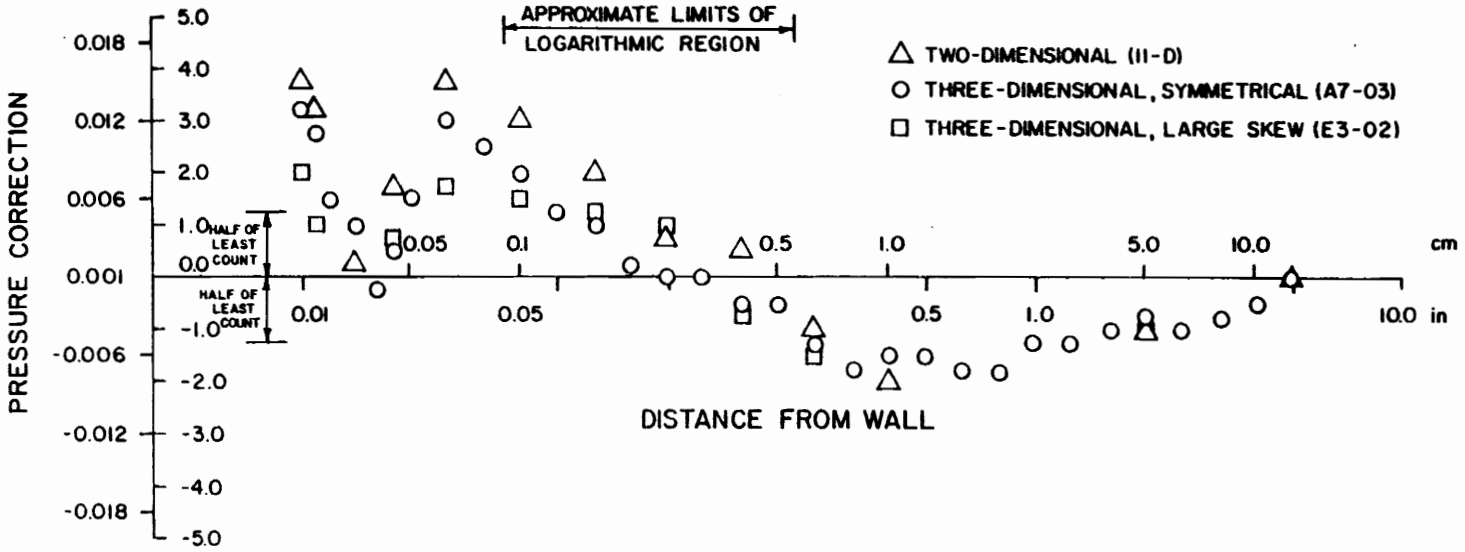

Figure 21. Corrections for Static Pressure

correction is -1.55% in velocity. Multiple tests comparing the inferred wall shear indicate that no significant differences result between using corrected or uncorrected data.

Finally, there are the inherent errors induced by the probe itself disturbing the flow. These errors result from viscous effects, normal velocity gradients, the proximity of the wall, and freestream turbulence effects. Some rather old studies have been carried out by Dean [113], Young and Maas [114], Livesey [115], MacMillan [116], and Davies [117]. Neither viscous nor turbulence effects appear to be significant to this research. The velocities being measured are large enough and the turbulence levels small enough to avoid these effects. As for pressure gradient effects near the wall, MacMillan suggests a correction for the vertical distance from the wall of 0.15 of the probe outside diameter (for d/D = .6 where d is the inside diameter and D the outside diameter of the probe). Young and Maas suggest a correction of 0.18 of the probe outside diameter (for d/D = 0.6), while Davies suggests no correction at all. Coles [35] in his analysis of the 1968 Stanford Conference data expressed deep concern over the advisability of these corrections and refrained from their use for that study, choosing rather to ignore very near-wall data. More recently studies by Gold [118] and Rule [119] have chosen to not include these displacement corrections.

For this study, no corrections of any kind have been made to the velocity data. While these corrections were available, they

were small in magnitude and sometimes of uncertain validity. As a result the uncertainty of any velocity measured in the logarithmic region is probably as high as ±2%, while that in the very near-wall region may reach as high as ±4%.

A final word should be said about the choice of an impact probe over other measuring systems, most notably the hot-wire. It is true that the hot-wire can provide greater spatial resolution. However two disadvantages should be noted. First, a hot-wire usually is calibrated versus an impact tube and manometer, thereby indirectly passing on certain errors associated with the impact tube. Secondly, as the wall is approached with a hot-wire, heat transfer between the probe and wall introduces error that tends to cloud the accuracy of such measurements. Since this near-wall region is indeed the one under study, it was felt that the increased complication of hot-wire measurements could not be justified in light of an uncertain gain in accuracy.

E. WALL SHEAR STRESS MEASUREMENTS

The most critical measurements for this study were the direct measurements of both magnitude and direction of wall shear stress in a three-dimensional turbulent boundary layer. While several investigators have indicated their intentions to directly measure wall shear stress in a three-dimensional flow (most notably Brown and Joubert [64]), no published studies have presented such measurements, with the one exception of Pierce and Krommenhoek's five data.

As the reader will no doubt discern in the following discussion, the lack of apparent success is not surprising. The problem is simply quite difficult.

Essentially the problem reduces to the accurate sensing of small displacements in arbitrary directions. Ten different types of displacement sensing systems were considered. Included were laser interferometers, optical photo cathode sensing devices, fiber optic sensors, Piezoresistive strain sensors, capacitance proximity probes, and eddy current proximity probes. These devices were judged on the basis of manufacturers' specifications and some limited comparative testing [120].

A Bently Nevada Model 2388-3000 series eddy current proximitor and model 300 probe were chosen for this work. These devices are capable of the resolution of 1.27 μm (50 μ in.) displacement and provide linearity of < 1% of full scale according to manufacturer's specifications. Their short term and long term drift characteristics are ±0.0391 μm/5 min (1.54 μin./5 min) and +0.624, -0.0 μm/7.5 hr (+24.6, -0.0 μin./7.5 hr) [121]. Their temperature sensitivity is 0.0264 μm/°C (1.88 μ inch/°F) [121]. The eddy current device was judged to have adequate sensitivity with the added convenience of simplicity and low cost.

A schematic of the omnidirectional floating element device is shown in Fig. 22. A circular disk 2.86 cm (1.125 in.) diameter is supported by a 21.6 cm (8.5 in.) long, 1.59 mm (0.0625 in.) diameter steel rod. The disk is separated from the surrounding

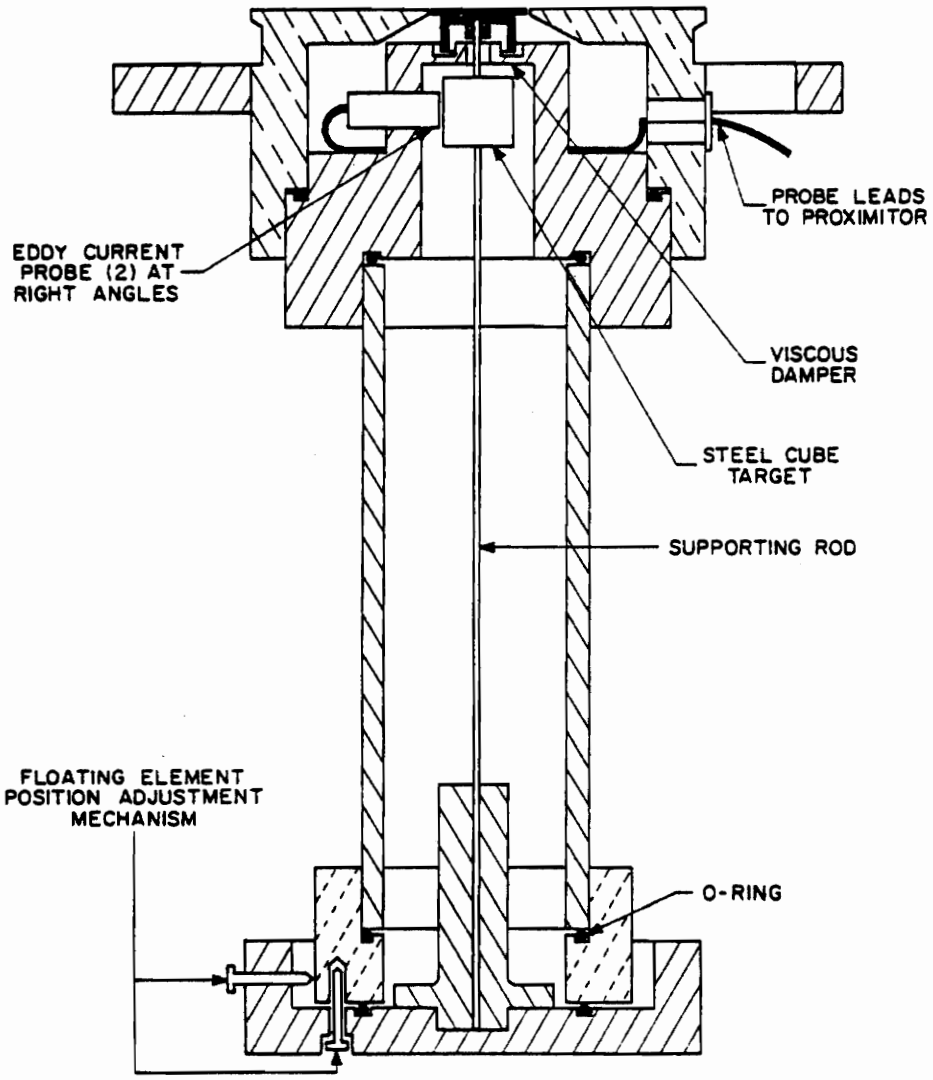

Figure 22. Omnidirectional Wall Shear Stress Measurement Device

wall by a 0.127 mm (0.005 in.) gap. Misalignment of the disk was measured to be less than 0.076 mm (0.003 in.) using shims, and was judged to be < 0.025 mm (0.001 in.) based on observation. As a fluid moves over the wall, the disk is allowed to move as the wall shear, as well as secondary forces acting upon the disk, dictate. Two eddy current devices (henceforth labeled channels A and B) located at right angles sense the displacement of a 2.0 cm (0.8 in.) steel cube target that is also supported by the rod. Resolution of the output signals of these eddy current devices results in the magnitude and direction of the wall shear stress. To prevent undue oscillations of the floating element, a viscous damper filled with 10,000 cs fluid is provided.

The entire wall shear stress measurement system is shown in Fig. 23. The output signal from the eddy current device is a d.c. voltage. Two voltage to frequency converters change the d.c. voltage signals to frequencies which are time averaged in frequency counters over 1 to 10 seconds.

For the researcher who may be contemplating building such a device, it may be useful to catalog some of the problems that were encountered in the development of the device just described. The aluminum welding rod used to support the floating element lacked rigidity and straightness and was replaced by a precise ground stainless steel rod. It was also necessary to reduce the length of the rod from 25.4 cm (10 in.) to 21.6 cm (8.5 in.) to obtain the desired force sensitivity. The original 4140 steel cube target,

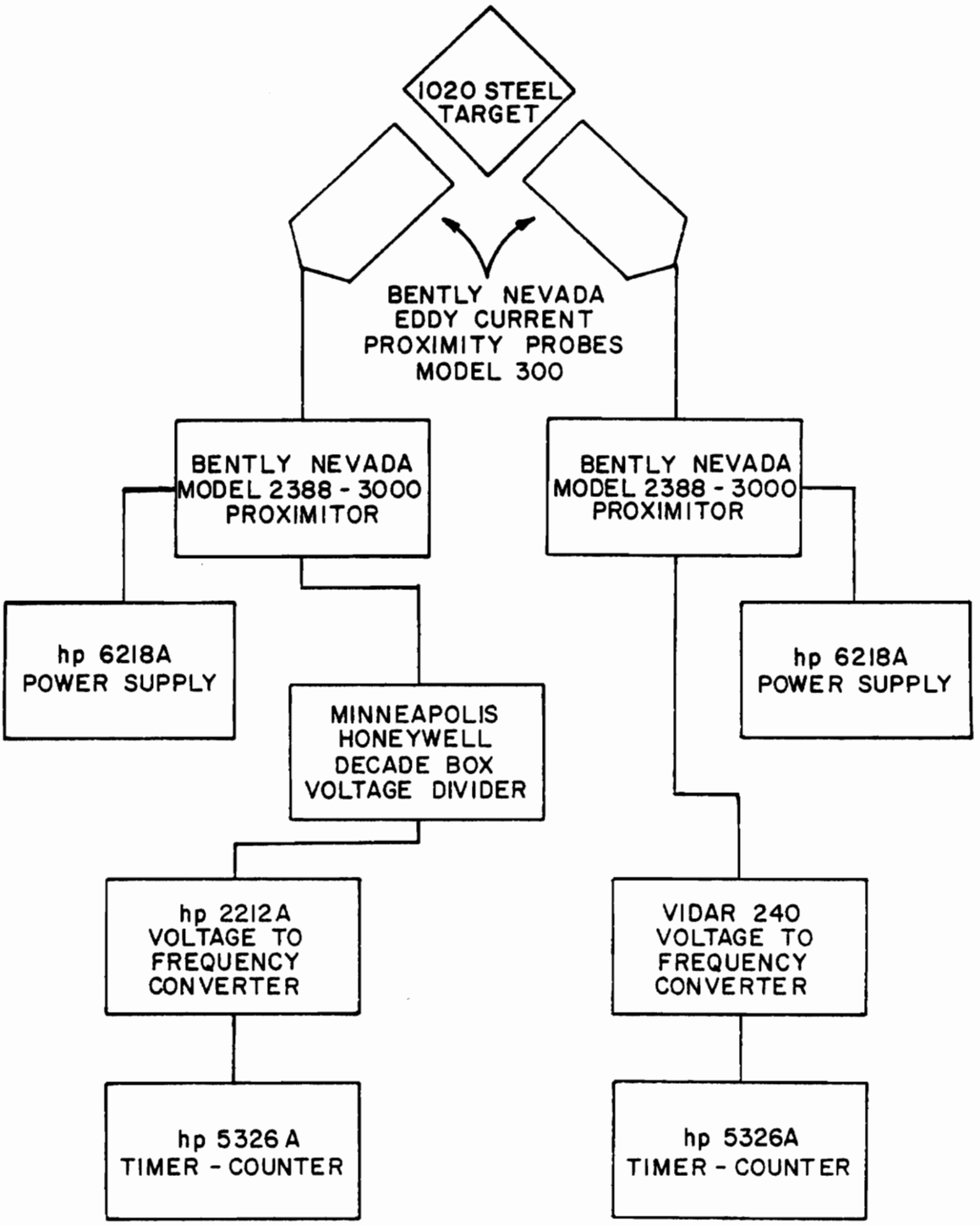

Figure 23. Wall Shear Stress Measurement System

1.27 cm (0.5 in.) on a side, was replaced with several other targets of varying composition, size, and design until a 1020 steel cube target 2.03 cm (0.8 in.) on a side with four, symmetrically drilled, 0.64 cm (0.25 in.) diameter, holes running in the same direction as the supporting rod was chosen. The target's increased size was necessary to eliminate observed interaction between the eddy current fields of the proximity probes, and because of the apparent ability of the proximity probes to 'sense' the edges of the smaller target. The holes were required to reduce the overall weight of the target. Efforts were also made to insure proper balancing of the target around its center axis. Three different viscous damping fluids were tried before the 10,000 cs fluid was chosen. Electrical problems encountered resulted in the need to: 1) provide the wiring with shielding to ground to eliminate stray signal interference, 2) electrically insulate the proximitors to prevent shorting, and 3) change the resistor decade box used with channel B in order to resolve an impedance mismatching problem. It was necessary to seal the entire lower portion of the device in a plastic bag to eliminate small leaks through the O-ring seals. One of the most intriguing problems was caused by a pressure differential between the area just below the floating element and the lower casing. The result was a periodic rise and then catastrophic fall of the output signals under flow conditions. Produced by bubbles growing and collapsing in the viscous damper, this problem was overcome by simply providing some venting holes between the various areas. Over six months of

intense effort were required to isolate, identify, and solve these problems.

Calibration of the system presented its own set of problems and challenges. It was first necessary to establish the linearity of the proximity probes and sensitivity to displacement using the 1020 steel target. Figure 24 shows the effect of displacement on proximitor output. Since channels A and B were operated between approximately 7.3 and 8.0 volts and 5.5 and 6.2 volts respectively when installed in the floating element device, they appeared to be acting well within their linear ranges with sensitivities of approximately 7.126 mV/μm (181 mV/mil). Displacement was measured by a precision micrometer in 0.0254 mm (0.001 in.) increments.

In order to gain confidence in the integrity and linearity of the floating element mechanism itself, the supporting rod was modeled with the use of a computer program called Line Solution Developer (LSD) [122]. This program is based on line-solution technology (transfer matrices or initial parameter theory) that allows for an accurate static solution for the deformation of elastic solids. The complex coupling of shear and normal forces as well as bending moments can be accurately predicted by this program. The results of that study indicated that: 1) the ideal system is linear 2) eccentric moments due to weight imbalances in the target or floating disk would have no effect on the linearity or sensitivity, 3) any initial bend in the supporting beam would have no effect on the linearity or sensitivity and 4) the nulling

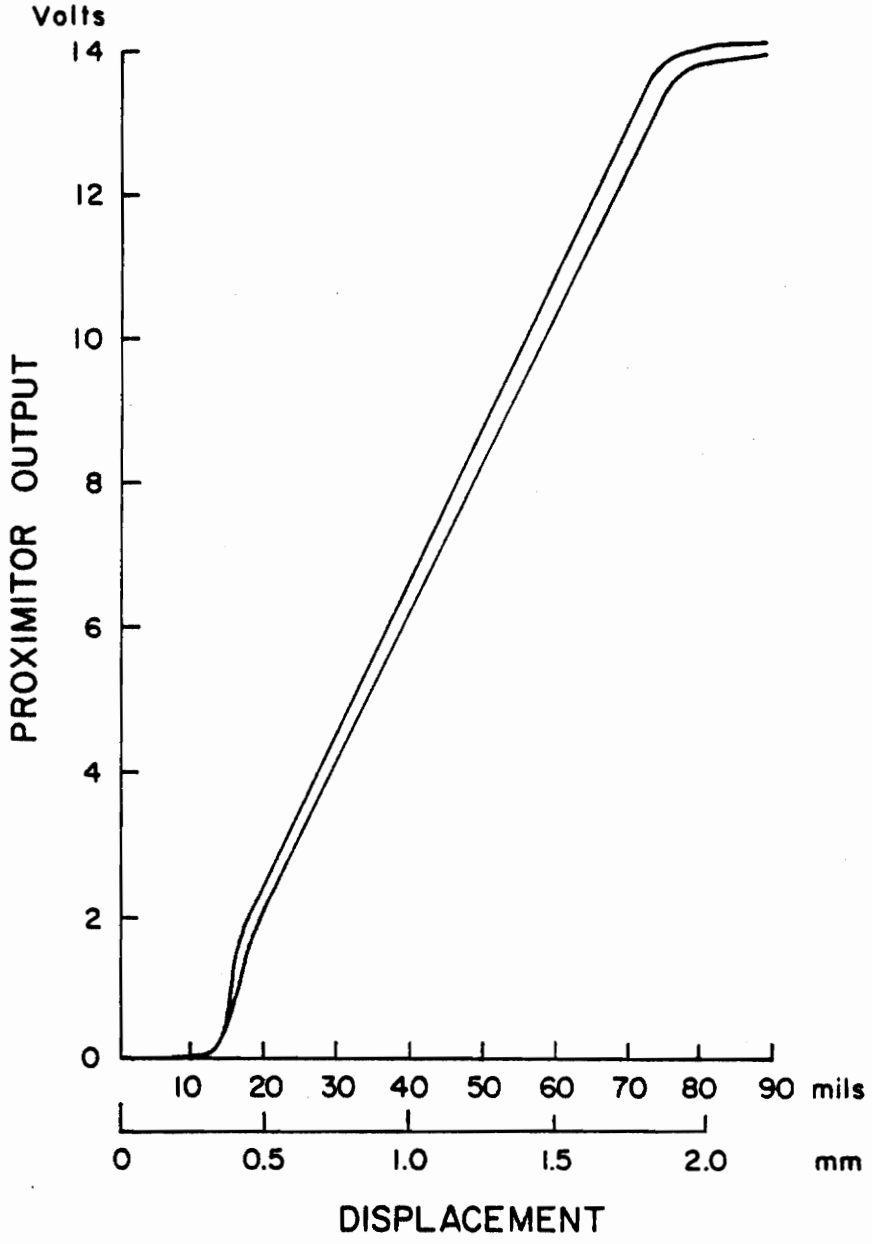

Figure 24. Displacement Calibration for Eddy Current Proximity Probes

method used in the static calibration technique to be discussed next would not affect the linearity or sensitivity of the device.

The static calibration technique required that small masses of predetermined weight be placed in a pan suspended by a 'string' connected through a pulley to a small post extending from the center of the floating element. Figure 25 shows a schematic of the system. Two vibrators were used to vibrate the pulley and calibration stand in order to minimize dry friction. The additional weight of the pan and string (actually human hair) were negated before the masses were added by changing the level of the entire device so that the floating element was recentered. By plotting the proximitor outputs versus the loading, calibration curves could be obtained.

Figure 26 shows a typical calibration curve. For this curve the linearity of channel A is < 0.9% of the full scale shown and channel B is < 0.6%, based on a least squares curve fit. If the sensitivity calculated for each calibration point is plotted versus the load, a better understanding of Fig. 26 results. Figure 27 reveals that: 1) considerably more scatter in the data occurs for small loadings than larger loadings, 2) the sensitivities for channels A and B are approximately the same at 6.501 mV/dyne (2.89×10^3 V/lbf) and 6.181 mV/dyne (2.750×10^3 V/lbf) respectively, and 3) all data, except for loadings below 10 dynes (22.48×10^{-6} lbf) falls within a ±2% error band while data above 50 dynes (112.4×10^{-6} lbf) falls within a ±1% error band. The scatter and increased uncertainty in the small weight calibration sensitivities are to be

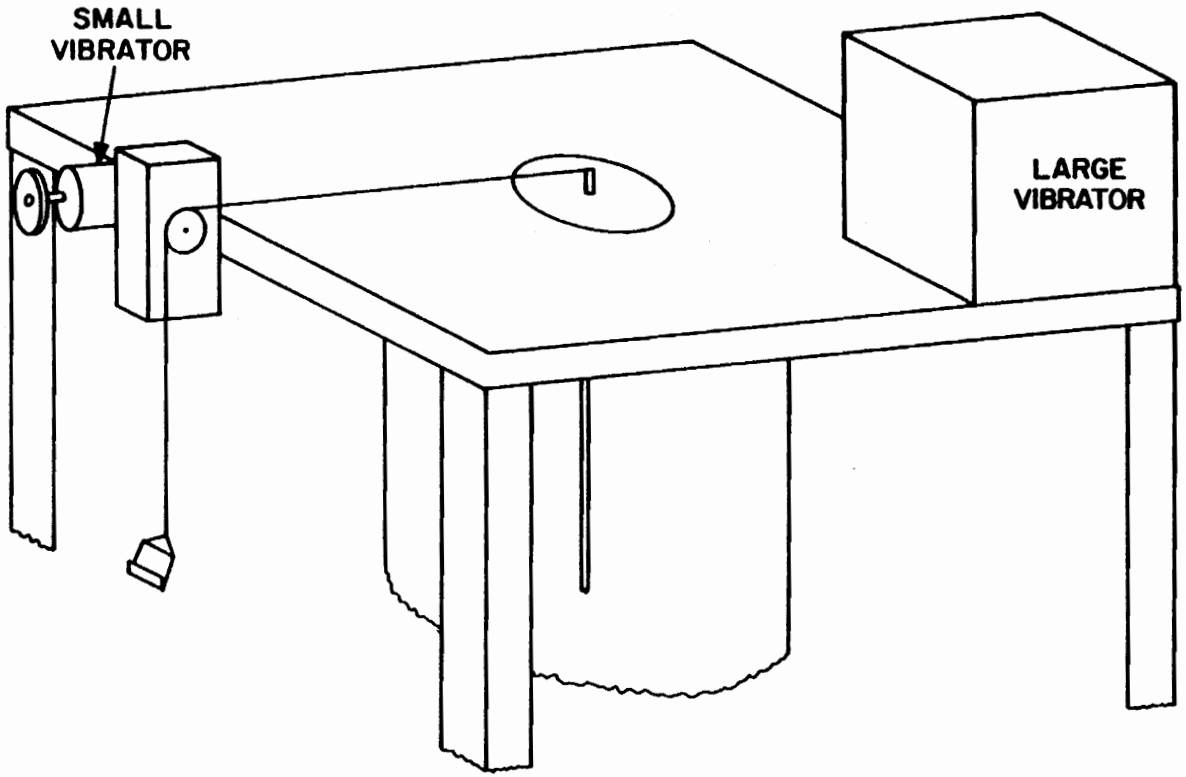

Figure 25. Wall Shear Meter Static Calibration Setup

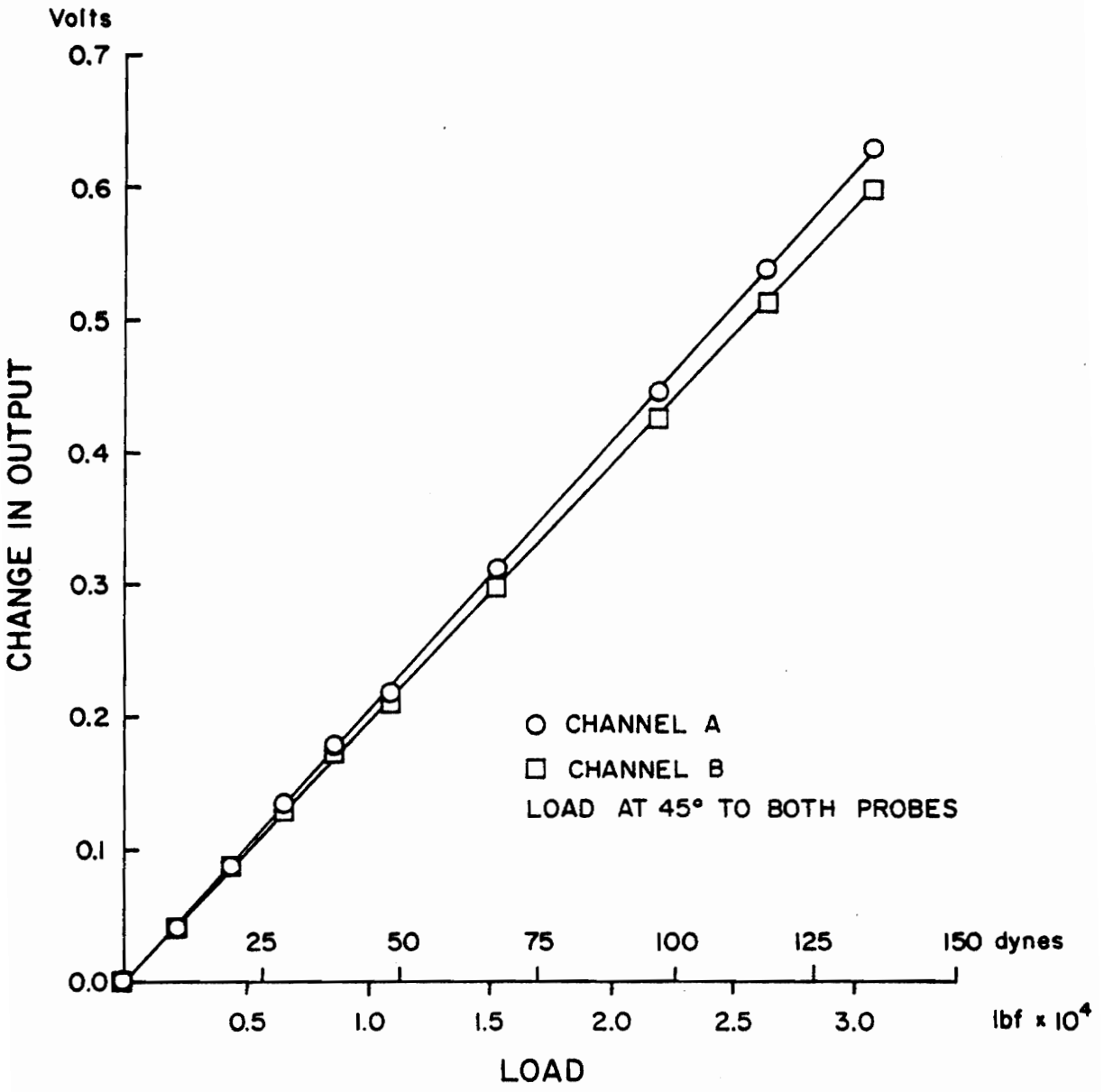

Figure 26. Floating Element Static Calibration Curve

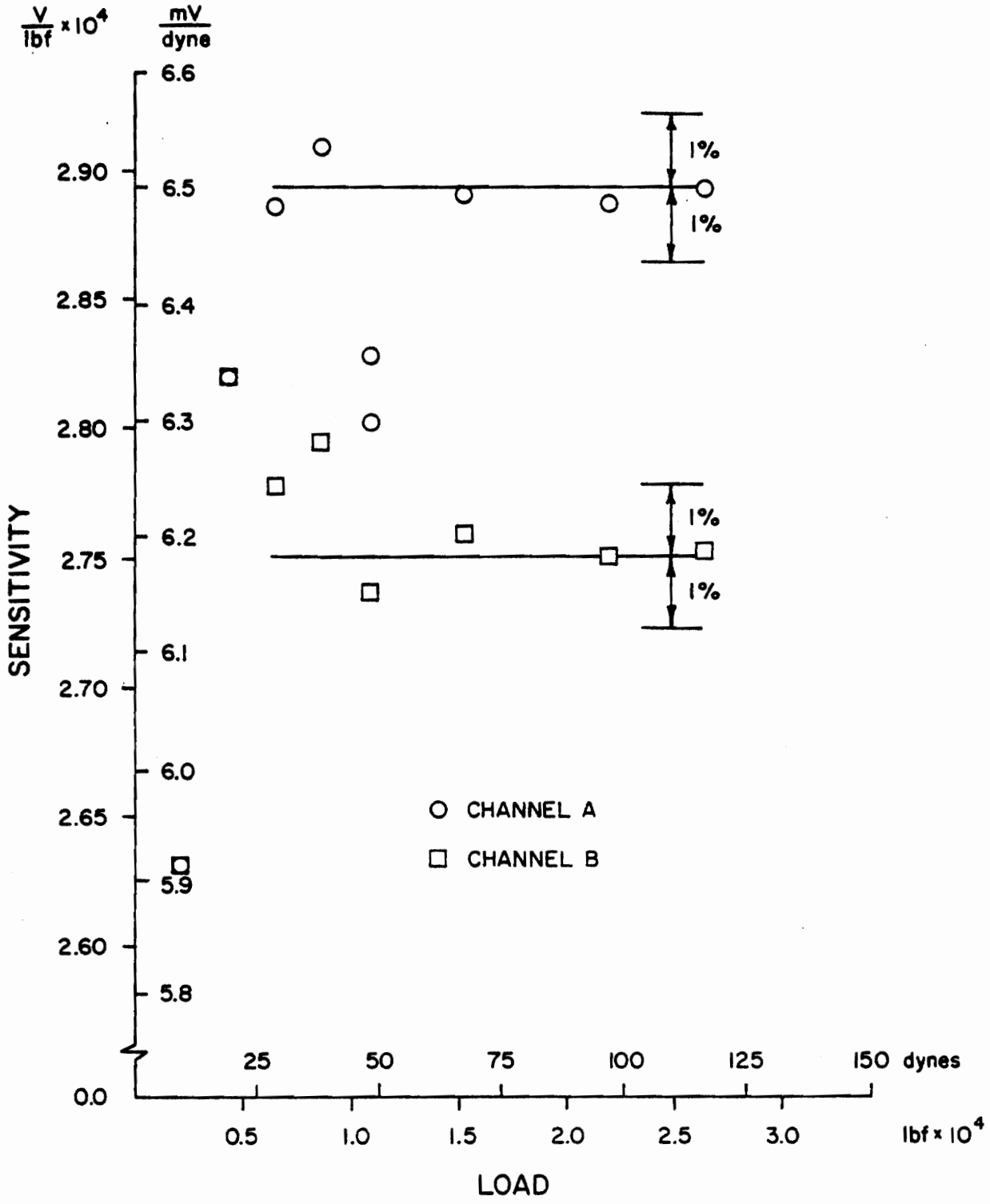

Figure 27. Floating Element Sensitivity Curve

expected since dry friction and other secondary forces become large when compared with the load.

Since the ability of the floating element device to discern angle is a direct function of its ability to sense loadings, the uncertainty in angular measurement can be estimated. If an uncertainty of $\pm 2\%$ is assumed for the sensitivities of each probe, the result would be a ± 1.2 degree uncertainty in the angle. Static calibrations at angles other than at 45° to each probe as well as two-dimensional flow measurements, to be discussed in the next chapter, support this uncertainty estimate.

Adequate repeatability is shown in Figs. 28 and 29. The sensitivities for channel A and B are 6.437 mV/dyne (2.863×10^3 V1bf) and 6.165 mV dyne (2.742×10^3 V/1bf) respectively. These values are $< 1\%$ and $< 0.3\%$ within the values determined in Figs. 26 and 27 for channels A and B respectively.

Static calibration by means of the pulley and string method proved to be difficult in practice so an alternative was considered. A method suggested by Headley [123] eliminates dry friction completely. Unfortunately, one set of problems is substituted for another. In Headley's method, accurate measurement of small angle changes is required. In addition the weight of the string and pan cannot be negated, but rather must be accounted for by accurate measurement of both and careful consideration of their contribution. Since the floating element device used here has a very limited range (~ 150 dynes (337.2×10^{-6} lbf)) due to the high sensitivity desired,

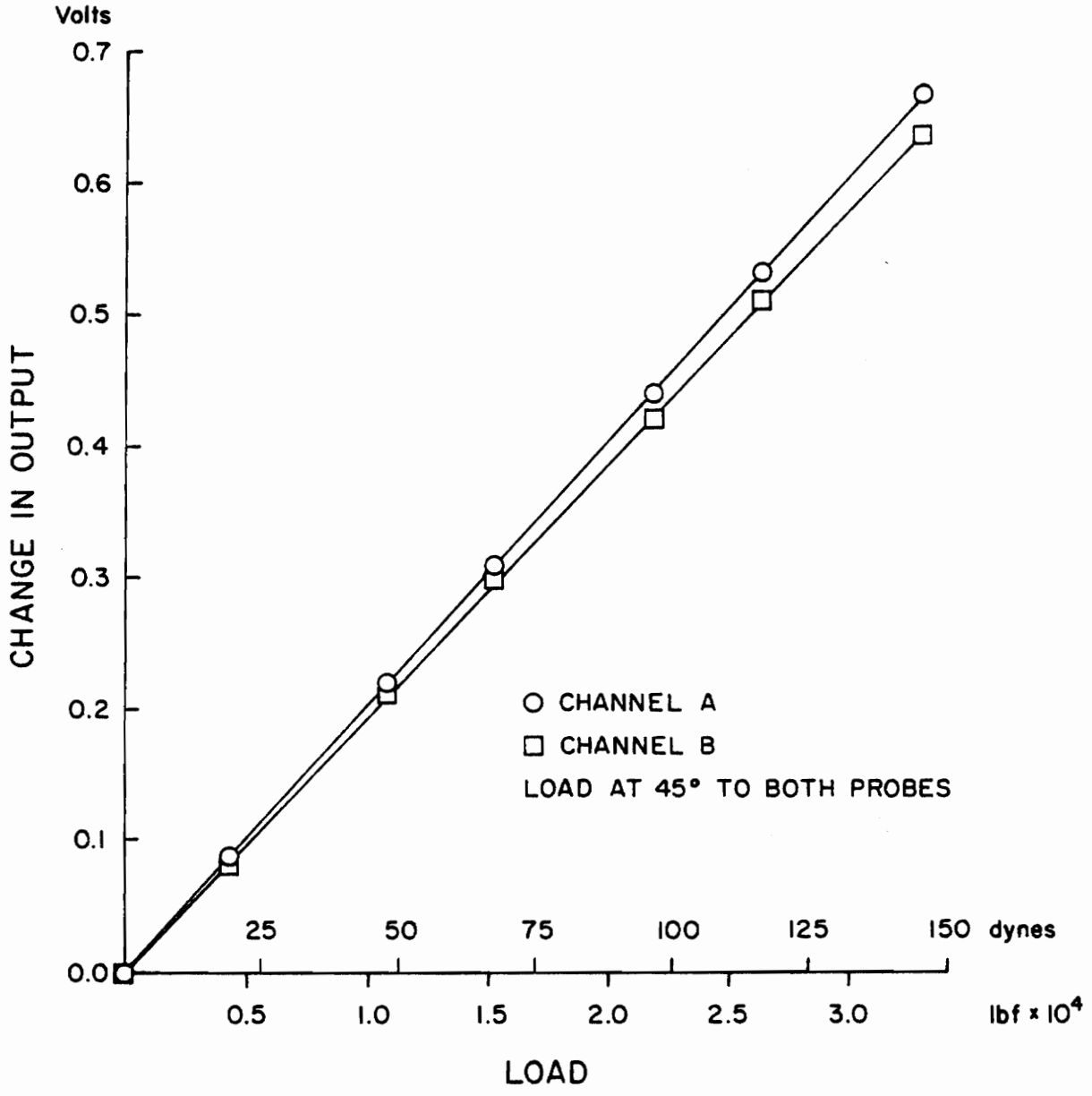

Figure 28. Floating Element Static Calibration Curve for Repeatability Check

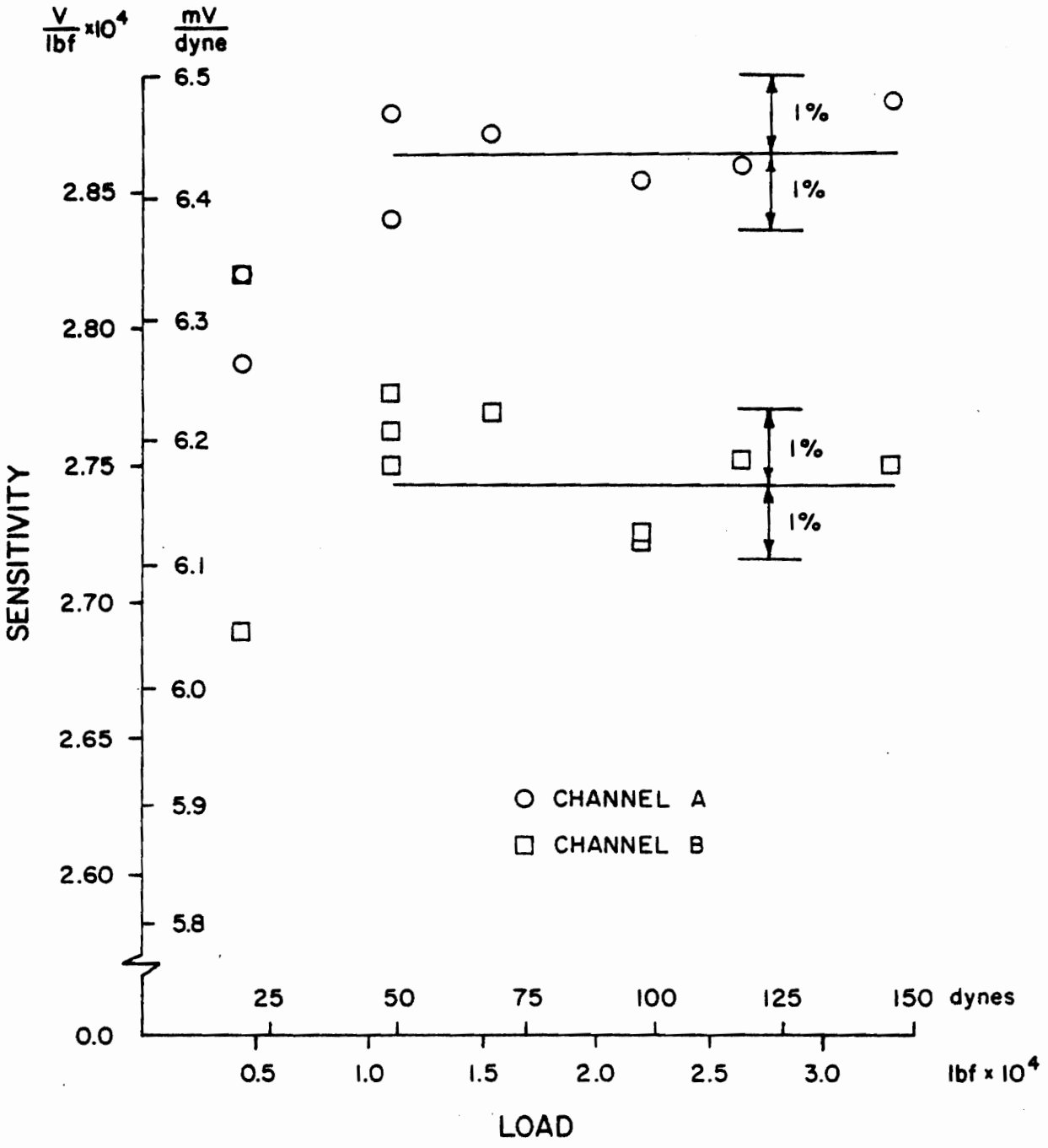

Figure 29. Floating Element Sensitivity Curve for Repeatability Check

the inability to negate these forces becomes a real disadvantage. Overall, even though several calibrations using Headley's method were obtained, the author felt no overriding advantage was to be gained by using his method.

The drift characteristics of these eddy current proximity probes were measured at constant temperature and found to be 6.3 mV/5 min and 1.2 mV/5 min for channels A and B respectively. The drift associated with channel A represents a change in sensed load of < 1 dyne/5 min (2.25×10^{-6} lbf/5 min) or < 2% of a typical loading of 50 dynes (112×10^{-6} lbf) experienced under flow conditions. The drift in channel B is obviously less and represents a change in sensed load of < .2 dynes/5 min (0.5×10^{-6} lbf/5 min) or < 0.5% of 50 dynes (112×10^{-6} lbf).

To minimize drift effects, an experimental procedure was introduced to minimize the time required to record measurements. Under zero flow conditions, the output for both probes was noted. The tunnel fan was then started, and the probe outputs allowed to stabilize. After the stabilized probe outputs were noted the fan was turned off. When zero flow conditions were reinstated the probe outputs were again noted. The time between the stabilized flow conditions and the reinstated zero flow conditions was less than three minutes. The difference between the output values at these last two conditions were used to calculate the wall shear stress.

Temperature stability was not judged to be a problem since during all wall shear measurements the temperature was kept at

25°C ± 1.1° (77°F ± 2°). Using the temperature sensitivity, 0.0264 μm/°C (1.88 μin./°F) cited earlier, the resulting effect on the probe output would be ± 0.68 mV which represents an uncertainty in the sensed load of ± 0.11 dynes (± 0.25 x 10^{-6} lbf) or < .5% of a 50 dynes (112 x 10^{-6} lbf) load.

To summarize, the omnidirectional wall shear meter has been shown to be linear by analytical calculations, a displacement calibration, and static loading calibrations. The static loading calibrations have also demonstrated excellent repeatability, magnitude and angle precision, and high sensitivity. Procedures have been implemented to reduce temperature and time drift effects to a minimum. As with the velocity measurements, no corrections were applied to the data gathered with this device. While certain corrections might be applicable (see Chapter II), their validity and method of application in the three-dimensional incompressible turbulent boundary layer flows studied here is uncertain.

F. EXPERIMENTAL PROCEDURE

The experimental program was completed chronologically in three separate parts: wall shear stress measurements, velocity profile measurements, and static pressure measurements. This separation was necessary since the physical requirements of individual measurement systems made a unified system impossible. In order to insure that the flow remained essentially the same regardless of which measurements were being made, the tunnel unit Reynolds number,

based on the freestream velocity measured at the tunnel entrance, was held to 1.445×10^6 m^{-1} ± 1.5% (4.403×10^5 ft^{-1} ± 1.5%). For the wall shear stress measurements the temperature was maintained at 25°C ± 1.1° (77°F ± 2°). For the velocity and static pressure measurements, the temperature was varied to maintain the desired unit Reynolds number. Uncertainty estimates for all measurements are given in Table 3.

It would have been preferable to keep the flow body obstruction stationary while moving the measurement devices. However this was not possible for this experiment since movement of the floating element required excessive time for releveling. Following the example of Prahlad [54], it was therefore decided to keep the measurement location stationary and to move the body around that location.

Every effort was made to insure the accurate placement of the body at each location. Attempts were made to obtain different wall shear measurements by slightly misaligning the body. These attempts showed that slight misalignments did not result in measurable changes in wall shear stress. Velocity measurements made after the body was removed and then replaced proved to be repeatable, indicating that body placement was not a problem.

Locations for data measurement were designated by two symbols. The first symbol was alphabetic and represents the location normal to tunnel axis with the centerline of the body designated as datuum with the symbol A. Moving away from the centerline in 2.54 cm (1 in.) increments, the symbols B, C, D, etc. are used. The second symbol

Table 3

Uncertainties in Measurements

Measurement	Uncertainty Interval
Static pressure	± 0.5%
Pressure gradient	± 3%
Vertical location of velocity probe	± 0.0127 mm (± 0.0005 in.)
Angle of flow	± 0.5°
Velocity	± 4% in transition region
	± 2% in logarithmic region
	< 1% in outer region
Wall shear stress	± 2%
Wall shear stress angle	± 1.2°

is numeric and represents the location along the tunnel axis with the leading portion of the body designated as datum with the symbol 0. Moving upstream from the leading edge in 2.54 cm (1 in.) increments, the symbols 1, 2, 3, etc. are used. Locations downstream of the leading edge are designated with minus numbers. As an example the location E3 was located 10.16 cm (4 in.) from the body centerline and 7.62 cm (3 in.) upstream of the leading edge as shown in Fig. 17. Run designations for velocity measurements are shown by a two-digit number added to the location designation.

For two-dimensional velocity measurements, runs are designated with a two-digit number followed by an Arabic numeral that indicates the tunnel unit Reynolds number as given in Table A5. These data will be discussed next.

IV. EXPERIMENTAL MEASUREMENTS

A. TWO-DIMENSIONAL MEASUREMENTS

Before three-dimensional studies could be undertaken, it was necessary to take measurements in a nominally two-dimensional flow in order to establish: 1) the uncertainty in the angular measurements for the velocity probe, 2) the repeatability for the velocity probe, 3) the uncertainty in the angular measurements for the omni-directional wall shear meter, 4) the repeatability for the wall shear meter, and 5) the validity of the static calibration for the wall shear meter. The two-dimensional results are all given in Appendix A. Tabular data for representative two-dimensional velocity profiles are found in Tables A1 through A3, while tabular data for the wall shear measurements are found in Table A4. Near-wall similarity plots of the velocity profiles are shown in Figs. A1 through A6. The unit Reynolds numbers for the velocity profiles are given in Table A5.

A series of fifteen velocity profiles were taken in a nominally two-dimensional flow when no body was introduced into the wind tunnel. Based on these measurements it was determined that: 1) the flow had a tendency to skew very slightly, an average of -0.8 degrees, as the tunnel floor was approached from a position 12.7 cm (5 in.) away, and 2) that the probable error in any angular measurement was ±0.25°. The uncertainty of angular measurement is then estimated to be ±0.5°. Concerning the former, this slight skewing appears to be a

real phenomenon of unknown origin. It was at first thought that the skewing was caused by a small tunnel misalignment (< 0.64 cm (0.25 in.)) which occurred in a wall junction just downstream of the test section; however, correction of this misalignment resulted in no measurable change in the degree of skewing. The addition of two sets of 15.24 cm (6 in.) long flow straighteners immediately preceding the fan inlet also had no effect. Since velocity profiles on either side of the centerline were symmetrical (the normal procedure for establishing two-dimensionality of a flow) and since all attempts to alter the flow were without success, it was decided to proceed with the very slight skew in the nominally two-dimensional flow. One can only speculate that the slight skewing is caused by asymmetric side-wall effects. It should be understood that most studies in nominally two-dimensional flows accept the two-dimensional status of the given flow without angular measurements of any kind. The repeatability of the velocity measurements was typical of that presented in Figs. A4 through A6 for runs 04-D, 05-D, and 06-D. These results are within the uncertainty limits established in Chapter III.

The angular sensitivity of the floating element device was also determined in the nominally two-dimensional flow. The floating element device was carefully aligned so that each proximity probe was displaced 45 degrees from the centerline of the tunnel. Hence for the two-dimensional flow, the wall shear angle should have been at 45 degrees to each proximity probe. In fact, of the sixteen such measurements taken, the maximum difference in the angular measurements

was +0.6, -1.0 degrees with a mean average of -0.4 degrees. The maximum difference noted between any wall shear magnitudes at similar unit Reynolds numbers was 2.5%, although typically the difference was ~ 1%. Since wall shear measurements at similar unit Reynolds numbers gave nearly the same measured angle, one might conclude that either the flow angle was a function of unit Reynolds number or that one or both proximity probes exhibit some long term changes in sensitivity. The latter is possible, but considered unlikely.

In order to obtain additional verification of the floating element proximity probe sensitivities as given by the static calibration in Chapter III, it was decided to undertake a dynamic calibration. In nominally two-dimensional flow, the tunnel unit Reynolds number based on the centerline velocity just downstream of the inlet nozzle was varied. Figure 30 is a resulting plot of wall shear stress versus unit Reynolds number. The data plotted include: 1) direct wall shear measurements using the omnidirectional wall shear meter developed for this study, 2) corresponding wall shear stress values inferred from Spalding's third order law of the wall with Patel's constants, averaging shear values from $50 \leq y^+ \leq 300$, 3) direct wall shear measurements by Rule [119], using the same floating element device developed by Pierce and Krommenhoek [52], and 4) corresponding wall shear stress values determined in the same way as for this study from velocity profiles taken by Rule [119]. Some scatter in data is observed, especially at higher Reynolds numbers.

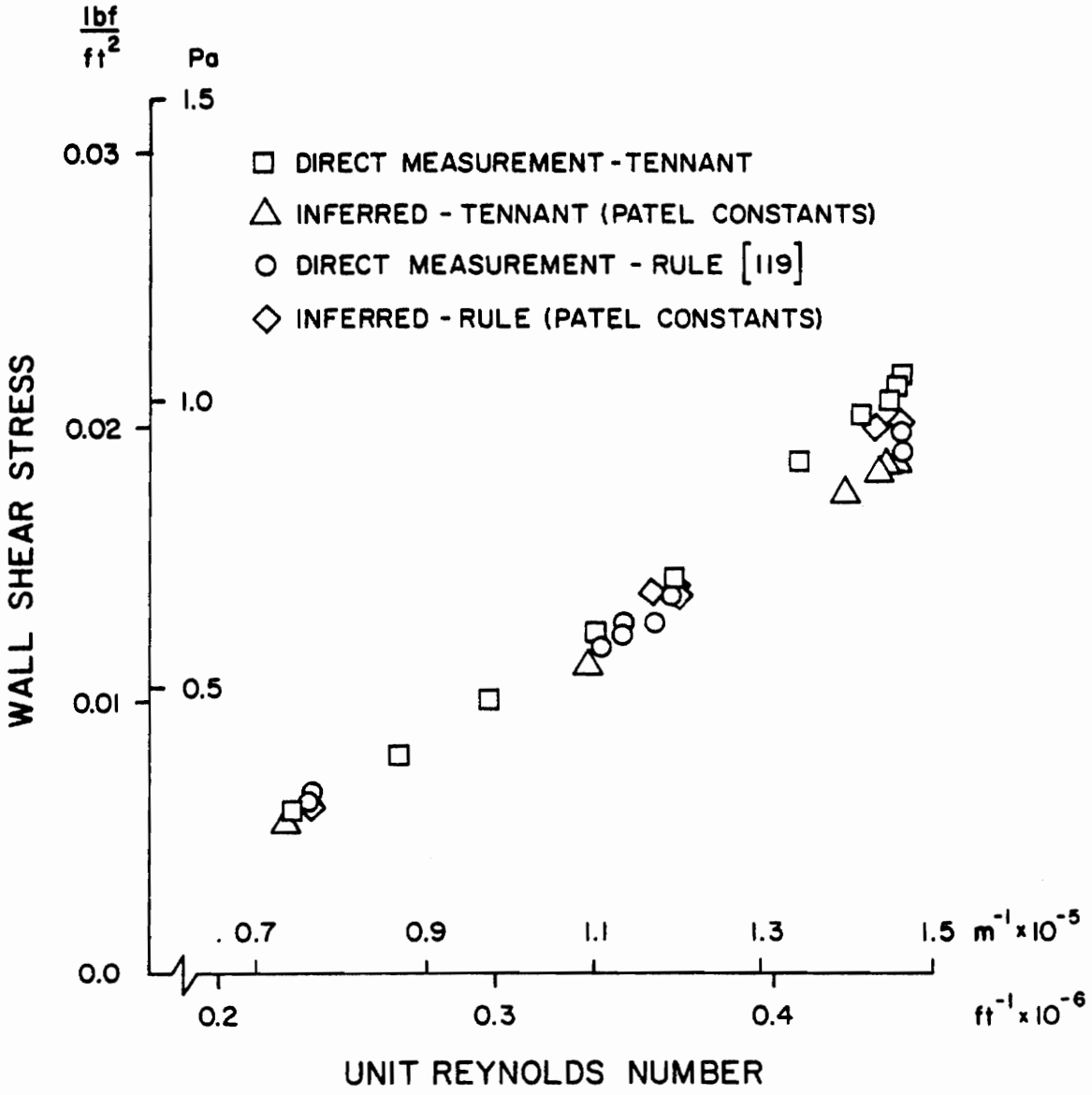

Figure 30. Dynamic Calibration of Floating Element Device

Rule's direct measurements appear to fall 1 to 5% below his inferred results and appear to compare favorably with the inferred measurements of this study. On the other hand, the omnidirectional wall shear meter appears to be high by about 10%. As noted in Chapter IID and confirmed here with Rule's data, an uncertainty in wall shear measurement of ± 5% exists in other carefully designed floating element devices reported in the literature. However, the omnidirectional wall shear meter results remain disturbing.

It is of special interest to note that if the constants suggested by the NPL Staff [39] are used instead of Patel's [37], agreement between the omnidirectional wall shear measurements and those inferred from velocity profile measurements is quite good as shown in Fig. 31. Independently, Brown and Joubert [64] noted that use of the NPL constants reconciled the differences noted between their directly measured and inferred wall shear stresses. Brown and Joubert, however, considered Patel's constants the more reliable and the discrepancy was attributed to slight secondary forces on the element.

To elaborate more on the use of NPL constants, it is informative to plot some of the two-dimensional velocity profiles on similarity plots, u^+ versus $\log_{10} y^+$, and compare these with the theoretical curves using Patel and NPL constants as shown in Figs. A1 through A6. The values of wall shear used in these plots are those which were measured by the omnidirectional wall shear meter. It should be obvious from these plots that the curves using the NPL constants

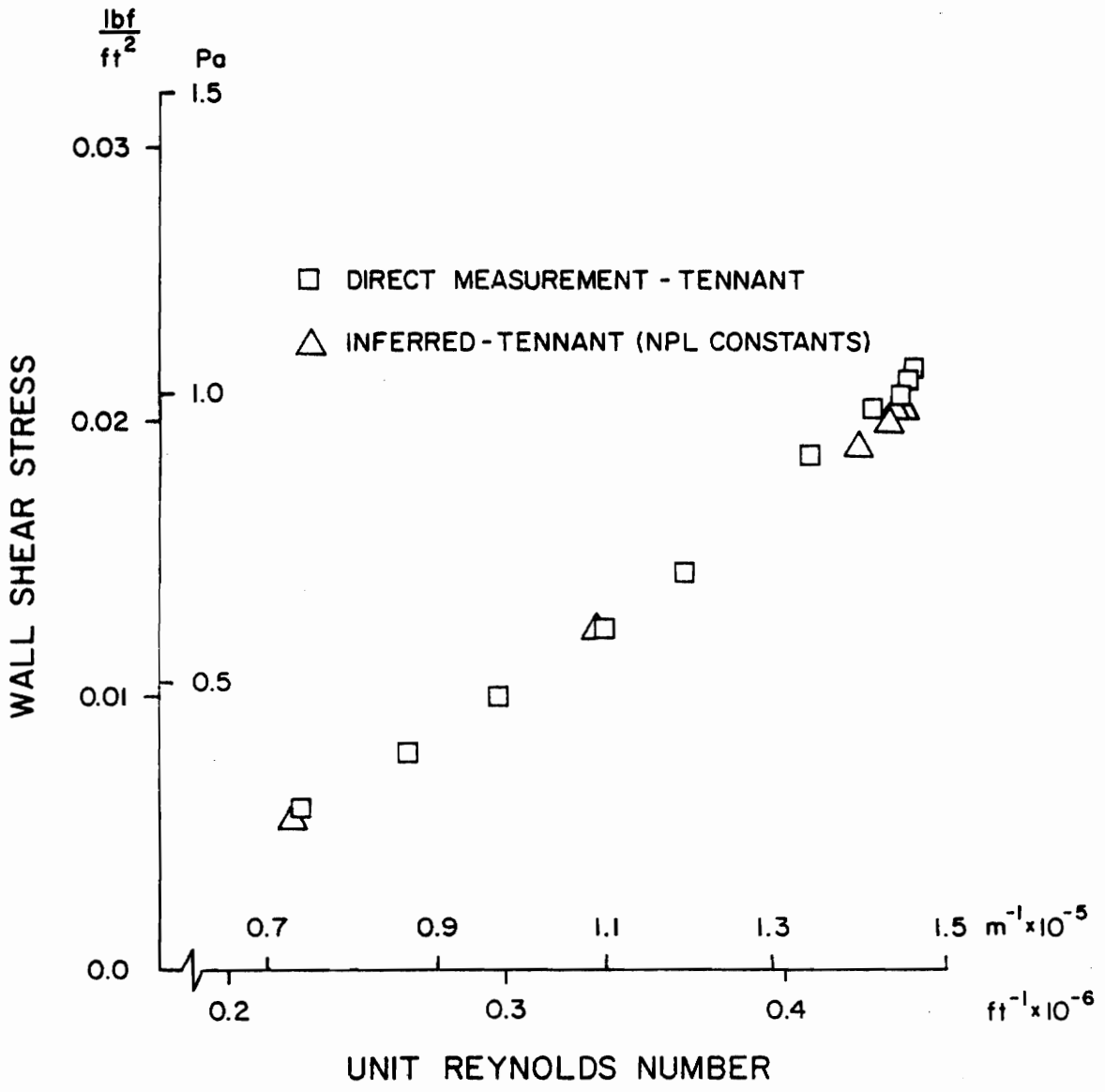

Figure 31. Dynamic Calibration of Floating Element Device Using NPL Constants

follow the data more closely than those using the Patel constants. The wall shear unit Reynolds numbers were matched as closely as possible with those for the velocity profiles. The wall shear unit Reynolds numbers were from 0.5% to 1.9% higher than those for velocity profiles. This would indicate that the wall shear stresses used were slightly high. Therefore, the velocity profile data shown should be raised by a very small amount; but much less than would be required to meet the Patel curves.

Another important feature to recognize about these two-dimensional similarity plots is the behavior of the data within the transition region, $10 \leq y^+ \leq 50$. As noted in Chapter II, much of the velocity data reported in the literature, e.g., Coles [36], shows a tendency to ride high in the transition region. Coles attributed this behavior to lack of certainty in the near-wall data. While this may be true, it is interesting to note that this trend does not appear as strong with the use of NPL constants. On the other hand, if the data were shifted upward to fit within the region $50 \leq y^+ \leq 300$ on Patel's curve, as is the normal practice, the data would definitely fall above the curve within the transition region.

One might be tempted at this point to account for the discrepancy with the use of the pressure gradient corrections for the floating element device discussed in Chapter II. As reported there, the pressure gradient for the two-dimensional case is favorable and very small ($d_m \frac{dP/dx}{\tau_w} \simeq -0.3$ with $d_m U^*/\nu \simeq 1500$). It would appear unlikely, in view of Fig. 15 and the small magnitude of the pressure

gradient, that the discrepancy can be attributed to a pressure gradient correction.

To reiterate: 1) use of the NPL constants reconciles the differences between the wall shear stress measured by the omnidirectional wall shear meter and those inferred from velocity profiles, 2) use of NPL constants similarly reconciled Brown and Joubert's results, 3) pressure gradient corrections applied to the floating element device appear to be unable to account for the discrepancy between measured and inferred wall shear stresses when Patel's constants are used, and 4) use of NPL constants lessens the tendency for the velocity profile data to ride high in the transition region. On the basis of these results, it was decided that NPL constants would be used for this study.

Because the use of the NPL constants is somewhat in contradiction to today's usually accepted views on the nature of two-dimensional near-wall similarity, a few additional words in defense of this decision are in order. Within the last twenty to twenty-five years a controversy has existed concerning the nature of near-wall similarity in pipe and flat plate boundary layer flows. The question in point is whether or not the constants, κ and C, in the logarithmic similarity law are universal. The issue was apparently settled in 1965 with the work of Patel [37], who argued convincingly in favor of the universality of the similarity law constants.

Patel pointed out that: 1) Preston tube calibrations by the

NPL Staff [39] and by Smith and Walker [38] seem to be in agreement with each other for results in a flat plate boundary layer flow, but in disagreement with Patel's results in pipe flow and some measurements over a symmetrical airfoil, and 2) similarity law constants suggested by Smith and Walker and the NPL Staff differ greatly. Patel suggested that the work of Head and Rechenberg [124] (with whose data Patel agrees) provides "quite conclusive evidence in favour of complete similarity of the law of the wall in the two cases (pipe flow and flat plate boundary layers)." Since Preston tube calibrations depend heavily on the logarithmic similarity law, Patel reasoned that errors in the measurement of wall shear stress and/or failure to use Pitot displacement corrections (used by Patel) must be at fault. Citing the work of Landweber [125] who re-analyzed Smith and Walker's data using displacement corrections, Patel stated that the "true values of A and B ... derived from the profiles corrected by Landweber are in fact in good agreement with the values 5.5 and 5.45 suggested here." These are equivalent to $\kappa = 0.42$ and $C = 5.45$.

Patel's position appears strong; however, a different view of the literature cited by Patel introduces a different conclusion. First, the work of Smith and Walker on a flat plate boundary layer can be examined. As Patel notes, Smith and Walker suggest that the similarity law constants are dependent on Reynolds number based on momentum thickness. Their results over a range of Reynolds numbers from 3500 to 60,000 indicate small changes in von Kármán's constant

to a low of 0.41 for low Reynolds numbers (< 20) while C values as low as 5.0 are reported in the low Reynolds number range. The Smith and Walker constants reported as 0.47 and 7.15 were the asymptotic values of κ and C, as Reynolds number becomes large.

As for the reanalysis by Landweber, his main objection to Smith and Walker's study concerned the Preston tube measurements which he viewed as of questionable validity. He noted however, that their "other velocity measurements, seem to be of high accuracy and consistency," and that their direct measurements using the floating element technique appeared to be excellent. While corrections (whose values has already been questioned in this study) to the velocity profiles did result in different constants, Landweber chose to include the data of Laufer [126] (pipe flow) and Landweber and Siao [127] (flat plate) in his determination of the new constants. If only the data of Smith and Walker at a $Re_x = 2 \times 10^6$ is considered (an action which will be justified in the next paragraph), the resulting wall similarity constants are $\kappa = 0.45$ and $C = 6.10$. These values are closer to the NPL constants of $\kappa = 0.47$ and $C = 5.9$ than to Patel's values. Indeed the Landweber and Siao data fit these new constants well.

Carefully reading Patel's comments, one observes that no direct criticism is leveled at the NPL study. Rather it is discredited by association with Smith and Walker's work. The study by the NPL Staff actually represents the combined results of three reports by R. G. Pankhurst, E. F. Relf, W. S. Walker, P. Bradshaw, and

N. Gregory in two separate experimental studies on flat plate boundary layers. The work appears to this author to be thorough and careful, and includes measurements of the effective centers of the Preston tubes used. Stanton tubes were also used to confirm the results. Patel noted that different similarity constants were cited though "both sets of measurements were made in zero-pressure gradient flat-plate boundary layers at similar Reynolds numbers." In actuality the constants reported by the NPL staff were for the lowest tunnel velocity at $Re_x = 2.07 \times 10^6$. The constants originally attributed to Smith and Walker, again, were asymptotic values given for high Reynolds numbers, the equivalent of $Re_x = 30 \times 10^6$. In fact the original data reported by Smith and Walker at $Re_x = 2 \times 10^6$ are fitted quite well by the NPL constants. This would indicate that Landweber's corrections, at least at this lower Reynolds number, were small.

As for the work of Head and Rechenberg, their "conclusive evidence" of the universality of the similarity constants consisted of comparing the measurements of a Preston tube and a sublayer fence in a flat plate boundary layer after each had been calibrated in pipe flow. Since no differences appeared between the measurement techniques in the boundary layer flow, Head and Rechenberg concluded that the similarity constants in the pipe flow were the same as in the flat plate flow. First, it should be pointed out that the displacement corrects, which Patel desired Smith and Walker use to determine the 'true values' of the similarity constants, are absent from Head

and Rechenberg's study. Secondly, the inherent assumptions associated with their conclusions are 1) that the Preston tube was located in the logarithmic region and the sublayer fence within the viscous sublayer and 2) that the viscous sublayers do not differ in the pipe and flat plate boundary layer. The author's reservations about these techniques has already been stated; however, it must be emphasized that these results are indeed 'evidence' in support of Patel's hypothesis ... but not really 'conclusive'.

It would appear from the preceding discussion that, at the very least, a reasonable doubt can be raised concerning the universality of the similarity constants. Obviously, a definitive experiment is needed. Unfortunately, this author is again uncertain how such an experiment would be designed. At least until the present inherent uncertainties in wall shear measurement or inference techniques can be reduced for any one such technique, no definitive answer appears imminent.

B. THREE-DIMENSIONAL MEASUREMENTS

Measurements of the magnitude and direction of wall shear stress, corresponding velocity profiles, and the surrounding static pressure field were made in a three-dimensional turbulent boundary layer flow. The area extending 17.8 cm (7 in.) upstream to 12.7 cm (5 in.) downstream and 20.3 m (8 in.) to one side of the leading portion of a cylinder with a trailing edge was studied. All three-dimensional tabulated data are found in Appendix B. Table B17 gives the

location, magnitude, and direction of all three-dimensional wall shear measurements. Table B18 gives the location and magnitude of measured gradients for wall shear stress, angle of wall shear stress, and static pressure as well as wall shear angles. Tables B1 through B6 give tabulated data for the three-dimensional velocity profiles, and Table B19 gives the unit Reynolds numbers.

Repeatability for the velocity measurements is demonstrated by comparing individual runs at stations A7, E7, E5, E3, and E1 in Tables B1 through B2 and B5 through B9. The two runs A7-03P and E3-03P in Tables B2 and B-8 have been corrected by use of the static pressure corrections discussed in Chapter IID. Comparison of these runs with the uncorrected data in runs A7-03 and E3-03 in Tables B1 and B8 show that the corrections are very small. In addition to the data shown, an additional five velocity profiles were taken at station E3 with the result that the same degree of repeatability demonstrated between runs E3-01 and E3-02 was obtained. Neither the freestream angle nor the angle of skew ever varied more than ±0.2 degrees from the mean. Differences noted in the velocity magnitudes are within the uncertainty intervals cited in Chapter III.

Along the centerline, at stations designated with an A7, where the flow should be pseudo-two-dimensional, there continues, as was the case in the two-dimensional flow, to be slight negative skewing, -0.40 degrees on the average. These results include data from two profiles at station A7 not included in Tables B1 through B16.

Repeatability is demonstrated for the direct wall shear measurements in Table B17. At least two wall shear measurements were taken at every station where velocity profiles were obtained. Again station E3 may be used as a typical comparison location. There the angle of the wall shear never varied more than ± 0.2 degrees and the magnitude of the wall shear never varied more than ± 0.75%. The stations designated with a minus sign preceding the arabic letter are located on the opposite side of the plane of symmetry. For station E3, its equivalent location on the opposite side of the body is station -E3. There the angle of shear was ~ 2.8 degrees less than at station E3, and the shear stress magnitude was ~ 3.8% higher.

Along the centerline at station A7, the angle of wall shear averaged 1.2 degrees. This can be compared with the -0.4 degree angle of skew noted in the velocity profiles at this station. These results are comparable within the experimental uncertainties established earlier in this chapter and in Chapter III for the individual measurement techniques.

A better view of the consistency of the wall shear data may possibly be obtained from Fig. 32. There the wall shear vectors are plotted showing their positions relative to the cylinder. The results appear to be plausible and consistent. As the leading portion of the body is approached, a reversal of the wall shear angle is noted between stations A2 and A4. From the oil flow pattern studies by East and Hoxey [53] and Dechow [128], the three-dimensional separation line was expected to occur upstream

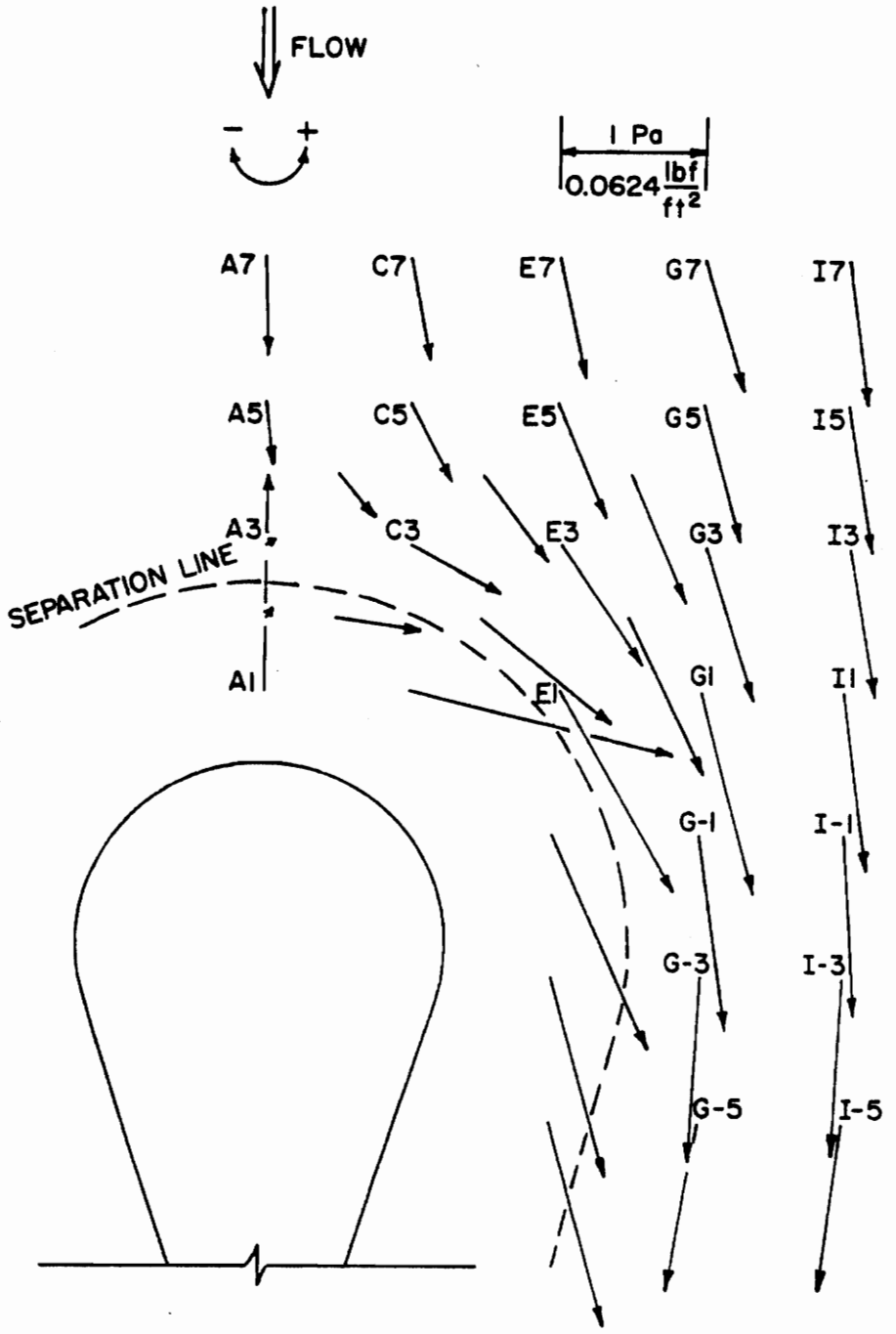

Figure 32. Wall Shear Stress Field

of the leading portion of the cylinder at a distance approximately equal to one-half the diameter of the cylinder. Though it is not possible to pinpoint the location of separation from Fig. 31, these results appear consistent and a dashed line has been added consistent with East and Hoxey and Dechow's results as an approximation of the three-dimensional separation line. Since the nature of the flow within the separated region is much different, and even more complex than the unseparated flow, no attempts were made to measure either velocity profiles or pressure gradients within this region. The wall shear in the unseparated region appears well behaved as its angle turns first away from the body as the flow approaches and moves around the cylinder, and then turns toward the body as the flow reverses direction to follow the trailing edge.

Pressure gradients, as estimated by the procedure outlined in Chapter III, are also shown in the form of a field map in Fig. 33. Only pressure gradients estimated at corresponding locations where velocity profiles were taken are reported. As the leading portion of the cylinder is approached along the plane of symmetry, the pressure gradient is adverse. As the flow moves around the body the pressure gradient turns clockwise, first normal and later opposite to the freestream velocity direction. Thus the pressure gradient becomes a favorable pressure gradient in the two-dimensional sense, i.e., the direction of the wall shear and pressure gradient are opposite. Still later as the flow moves further down the circumference of the cylinder and along the cylinder's

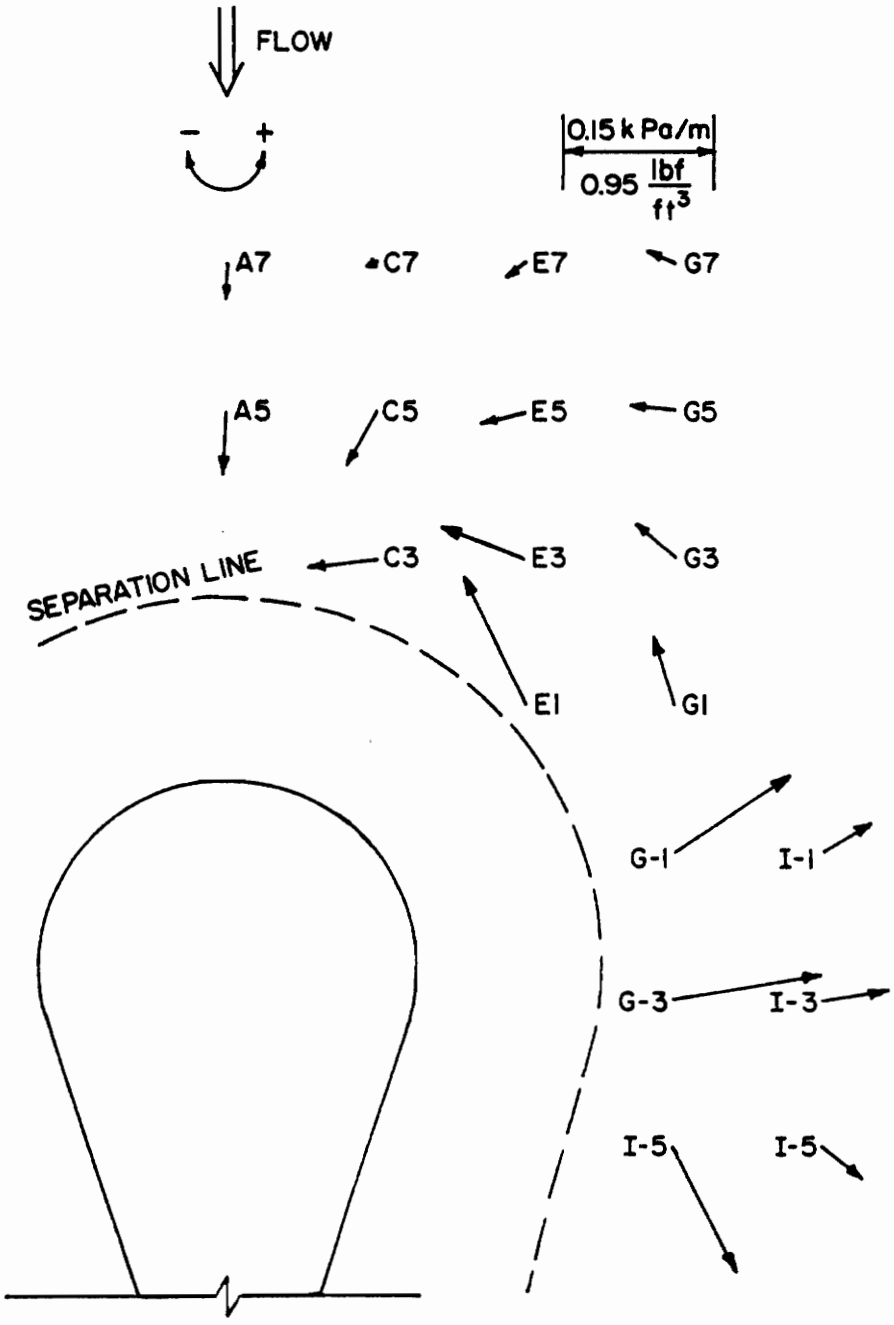

Figure 33. Pressure Gradient Field

trailing edge, the pressure gradient continues to rotate in the clockwise direction until adverse pressure gradient conditions are again encountered. As noted in Chapter III, the static pressure measurements showed a high degree of repeatability and the consistent results shown here for the pressure gradient estimates appear to confirm their validity.

V. COMPARISON OF THREE-DIMENSIONAL NEAR-WALL SIMILARITY MODELS

Comparisons were made among nine of the three-dimensional near-wall similarity models discussed in Chapter II. Omitted were the models by East [60] and White et al. [61]. East's model was omitted because no three-dimensional effects are noted for his near-wall similarity plot until values of $y^+ > 200$ in contradiction to three-dimensional velocity profile behavior noted here and in the literature, and because no measurements were made of the gradient of the angle of rotation of the shear stress vector at the wall, a parameter required by East's model. White, Lessmann, and Christoph put forth a model that requires derivatives of the velocity vector and two of the form metrics. While these parameters may be readily available when numerical solutions are being considered, derivatives of experimental data, e.g., the velocity profile, are very difficult to obtain with certainty since extensive smoothing techniques are required. For this reason, the model of White et al. was omitted from comparison.

For the remaining nine models, near-wall similarity plots were constructed and are included in Appendix B, Figs. B1 through B31. All the similarity plots shown have been nondimensionalized by a wall friction velocity based on the direct wall shear measurements. For all models studied except the model of Chandrashekar and Swamy [55], NPL constants were used. Chandrashekar and Swamy specified their own constants, as given in Chapter II, and these were used

with their model. For each station, five figures are shown. The first figure shows the models of Johnston [48], Coles [36], and East and Hoxey [53]. The second figure shows the Hornung and Joubert [51], freestream profile [52], and Prahlad [54] models. Perry and Joubert's model [56] is shown in the third figure. The fourth figure actually has two parts, one for the freestream profile, the other for the crossflow profile as required by the model of Chandrashekhar and Swamy [55]. The last figure also has freestream and crossflow profiles, and shows the model of van den Berg [6]. For convenience, each of the models has been designated as shown in Table 4.

The models of Perry and Joubert and van den Berg require that the pressure gradient be known. Since pressure gradient data were not available at stations I7, I5, I3, and I1, no comparisons of these models were made at those stations.

Four general areas can be segregated for comparison purposes: 1) along the plane of symmetry 2) in areas of small flow skewing, 3) in areas of large flow skewing, and 4) in areas of bilateral skewing. Along the plane of symmetry (the A-stations) the flow is pseudo-two-dimensional with a rapidly increasing adverse pressure gradient as separation is approached. Areas of small skewing include stations C7, E7, G7, and I7. Here the flow is nearly two-dimensional, and the pressure gradients are small. Even this far from the body the pressure gradients have begun to rotate in a counterclockwise direction from favorable to adverse as shown in

Table 4

Designations for Three-Dimensional

Near-Wall Similarity Models

Model Designation	Model
J	Johnston [48]
C	Coles [36]
E&H	East and Hoxey [53]
H&J	Hornung and Joubert [51]
FP	Freestream Profile [52]
P	Prahlad [54]
P&J	Perry and Joubert [56]
C&S	Chandrashekhar and Swamy [55]
B	van den Berg [6]

Fig. 33. As the cylinder is approached the flow skews more, and the pressure gradient grows while its direction of rotation is apparently reversed. At stations E3 and G3 for instance the pressure gradient is favorable in the two-dimensional sense. Following around the body and down its trailing edge the pressure gradient continues to rotate in the clockwise direction, becoming essentially adverse in the two-dimensional sense. For stations G-3, I-3, G-5, and I-5 the flow is bilaterally skewed.

Certain analytical model performance characteristics may be anticipated for given areas. For plane of symmetry flows or those with little skewing, one would expect that the flow could be modeled accurately. Since these flows are pseudo-two-dimensional, the analytical near-wall similarity models should be expected to reduce to the two-dimensional case.

On the other hand, for flows that exhibit bilateral skewing, one would expect that the models would not respond properly, since no near-wall similarity model examined in this study makes allowance for bilateral skewing.

Surrounding the cylinder is a separation line initiating a horseshoe-shaped vortex that curls away from the wall and then in toward the cylinder. As this separated region is approached one would expect the pressure gradients to be severe. Thus the ability to measure wall shear stress and to model the flow situation analytically within areas near separation are both diminished.

Indeed the results anticipated in the preceding paragraphs are

basically confirmed. Along the plane of symmetry station A7, Figs. B1 through B3, the similarity plots are much like the two-dimensional case except that the adverse pressure gradient forces an earlier departure from the logarithmic profile. Models J, C, E&H, H&J, FP, and P are indistinguishable from one another. Model P&J accounts for the adverse pressure gradient effect, and, at least qualitatively, properly corrects the theoretical curve to fit the departure. For the C&S model, the freestream, u-component, similarity plot appears satisfactory; however, the crossflow, w-component, similarity model fails to model the data. Finally model B, that accounts for both pressure gradient and inertial effects, models both the u- and w-components fairly well. (Note that u and w for van den Berg's model are in the wall-shear-stress and normal-to-wall-shear-stress directions respectively.) One may question why the u-component plot shows a downward curve typical of a favorable pressure gradient. The answer, of course, lies in the inertial effects which often tend to dominate. If only pressure gradient effects are considered, model B gives similar results to those of P&J.

As the separation line is approached along the plane of symmetry at station A5, Figs. B4-1 through B4-6, the adverse pressure gradient becomes stronger. Models J, C, E&H, H&J, FP, and P again all give similar results that show poor agreement between the measured data and the theoretical curve as does the C&S model. Models P&J and B appear to model this situation as least as well as at station A7.

Looking now at areas of small skewing, stations C7, E7, G7, and I7 are shown in Figs. B5, B9, B17, and B25. Moving from station C7 to I7, one notices a lessening of the departure noted at station A7, so that at stations G7 and I7 the deviation from the two-dimensional similarity law is small. This is due to a reduction in pressure gradient effects and amount of skewing. The C&S model continues to be unable to model the w-component similarity plot, while the B model shows a lessening of the inertial effects as one moves from stations C7 to I7.

One of the most interesting areas for study are those with large flow skewing such as stations C3, E3, and E1 shown in Figs. B7, B12, and B15. Here the pressure gradients are relatively large and favorable in the two-dimensional sense. For these stations models J, C, E&H, H&J, FP, and P tend to fan out and diverge and fall below the data as does the C&S model. The P&J model appears to approximate the data more closely. Both the C&S and B models both continue to have difficulty with their respective w-component similarity plots.

Finally for the area along side the body where the velocity profiles become bilaterally skewed, stations G-3, I-3, G-5, and I-5, shown in Figs. B22, B30, B23, and B31, may be studied. Here the J, C, E&H, H&J, FP, and P models again give similar results that tend to show pseudo-two-dimensional behavior for the I stations furthest from the body. The G stations are nearer the cylinder and the separated region, and there the agreement is poor. The P&J,

C&S, and B models also show poor agreement for the G stations.

Overall, certain characteristics or trends exhibited by the various models can be noted. First, the models of J, C, E&H, H&J, FP, and P may be lumped together in the sense that: 1) they are all three-dimensional near-wall similarity models that use an equivalent velocity in the two-dimensional near-wall similarity law, and 2) they all give approximately the same results. These results are, in a qualitative sense, good for nearly two-dimensional flows (flows with small skewing), poor for velocity profiles with large skews, and poor for velocity profiles that are near separation. Of these it can be generally stated that the model of J better approximates the data.

For the C&S model the u-component similarity profiles are probably as good as the first six models; however, the w-component similarity profile consistently fails. It would appear that the wall shear component in the cross flow direction is consistently underestimated by the C&S model. Since the C&S model was compared by its originators only with wall shear stresses inferred from Preston tube and razor blade measurements, it could be that the angle of wall shear was underestimated. In light of the previous discussion within this study of the dangers of assuming that the wall shear direction is in fact the direction of the velocity vector, even at small distances from the wall, this underestimation of the wall shear angle would appear plausible.

As for the B model, the striking result is the sensitivity that the model shows to both pressure gradient and inertial effects. It must be noted that the relatively poor agreement shown may be due to this author's inability to accurately estimate the pressure, wall shear, and wall shear angle gradients required for this model. Taking derivatives of experimental data is often risky.

Finally, the last model to be discussed is the P&J model. This model does not take into account inertial effects but does consider pressure gradient effects. Referring to Fig. 9, one observes that only the model of P&J shows the same characteristic deviations from the two-dimensional near-wall similarity law that the three-dimensional velocity profile data of this study show. Agreement is sometimes less than good, and, in the bilaterally skewed region, admittedly poor. However, of the nine models studied here, the P&J model must be judged best overall.

As a whole the results of this study give evidence in support of the hypothesis that near-wall similarity exists in three-dimensional turbulent boundary layers. The form of the applicable three-dimensional near-wall similarity law is apparently approximated by the Perry and Joubert model and requires, at least, the input of velocity profile data and pressure gradient data. The area of flow where Perry and Joubert's model fails is near separation.

The reader must be cautioned that these preliminary results should not be considered definitive. On the one hand, the measurements presented here are somewhat clouded by the controversy over

near-wall similarity constants, the use of pressure gradient corrections for floating element devices, the use of displacement corrections for velocity probes, and so on. While all these items have been addressed, the author must admit that uncertainty remains. On the other hand, assuming the measurements of this study strictly are valid, this investigation has been necessarily limited in its scope and thus in its ability to provide conclusive evidence. Only one pressure-driven three-dimensional flow configuration was studied. Certainly different flow configurations as well as shear-driven flows will have to be investigated before the question of three-dimensional near-wall similarity can be resolved more fully.

In judging the relative merits of the nine three-dimensional similarity models, their ability to infer wall shear stress is also of importance. As discussed previously, one of the important uses of two-dimensional near-wall similarity is in determining wall shear stress from velocity profile data. Certainly it would be useful if a three-dimensional similarity model could be used to determine wall shear stress in the same manner.

Seven of the models considered, those by J, C, E&H, H&J, FP, P, and C&S, are easy to use and require input of only velocity profile data from which the wall shear stress can be determined. Unfortunately, none of these models works well in flows with large skews. On the other hand, the model of B requires velocity profile, pressure gradient, wall shear gradient, and wall shear angle gradient data as input. In short, one must know the wall shear

stress before the B model is used; wall shear cannot be determined from this model. Somewhere in between the first seven models and the B model lies the P&J model. Required for the P&J model are velocity profile, pressure gradient, and wall shear angle data. The problem here, of course, is determining the direction of wall shear stress. It would appear unlikely, in light of previous discussion, that estimating the direction of wall shear stress from velocity measurements near the wall or from any other indirect method would be appropriate.

However, possibly another solution exists. Suppose a three-dimensional velocity profile is fitted to the P&J model by shifting the curves for various Θ's along the two-dimensional similarity law for the logarithmic region as shown in Fig. 9. Then the value of the parameter $q^*/\alpha\nu$ would give the wall shear stress and the value of Θ would give the wall shear stress direction. This method would clearly be preferable to varying the inertial terms in the B model until a curve fit was realized. More than one variable, those dependent on the wall shear stress gradient and the wall shear stress angle gradient, would need to be varied, and therefore existence of a unique solution would be questionable.

VI. CONCLUSIONS

A large scale wind tunnel, a precision velocity measurement system, an automated static pressure measurement system, and an omnidirectional floating element wall shear stress meter, the first of its kind, were designed, built, and calibrated for this study. A comprehensive set of data was measured for the three-dimensional case of plane, incompressible, turbulent boundary layer flow around a vertical cylinder with a trailing edge. Included were over one hundred direct measurements of wall shear stress, over thirty corresponding velocity profiles, and the neighboring static pressure field. Using these measured data, comparisons were made among nine near-wall similarity models. On the basis of these studies, several conclusions can be drawn.

1) The direct measurement of magnitude and direction for wall shear stress is very difficult. The accuracy of such measurements remains somewhat clouded by problems primarily associated with static calibration and pressure gradient corrections. Even among several carefully constructed and calibrated floating element devices, differences of approximately $\pm 5\%$ are common.
2) The results of this study for nominally two-dimensional flows supports the hypotheses of either the nonuniversality or continued elusiveness of unique values for the two-dimensional near-wall similarity law constants. The

results of this investigation based on direct measurements of wall shear stress suggest the use of the similarity constants $\kappa = 0.47$ and $C = 5.9$ given by the NPL staff [39] be considered for flat-plate boundary layers. Use of these constants also appears to eliminate the general trend toward departure from the two-dimensional near-wall similarity law within the transition region. Whether the two-dimensional similarity constants are functions of Reynolds number or not, as suggested by Smith and Walker [38], was neither confirmed nor disproven by this study.

3) Of the nine three-dimensional near-wall similarity models examined, the model by Perry and Joubert [56] appears to best approximate the measured data. Their model is relatively simple and considers pressure gradient effects.
4) In general, all the three-dimensional near-wall similarity models examined were able to model the flow behavior where pressure gradients and three-dimensional effects were small, but failed in varying degrees in flows that exhibited large skew.
5) All the three-dimensional near-wall similarity models examined were unable to model flows near separation. This is not surprising in that two-dimensional similarity fails near separation as well.

It is beleived that this study is the first step toward the ultimate goal of determining the existence and (if confirmed) form and extent of near-wall similarity in three-dimensional turbulent boundary layers. Evidence from this study would tend to support the hypothesis of three-dimensional near-wall similarity, at least for regions moderately remote from separation. The form of the three-dimensional near-wall similarity law apparently must consider pressure gradient effects at least, and appears to be approximated by the model suggested by Perry and Joubert. A definitive answer must await compilation of much more data gathered in various flow configurations for both pressure-driven and shear-driven, three-dimensional, turbulent boundary layers. It is hoped that the omni-directional wall shear meter developed in this study will prove to be a valuable tool in gathering that data.

BIBLIOGRAPHY

1. Spalding, D. B., "A Single Formula for the Law of the Wall," Trans. ASME, Journal of Applied Mechanics, Vol. 83, Sept. 1961, pp. 455-458.

2. Bradshaw, P., "Complex Turbulent Flows," Trans. ASME, Journal of Fluids Engineering, Vol. 97 (I), 1975, pp. 146-154.

3. Clauser, F., "Turbulent Boundary Layers in Adverse Pressure Gradients," Journal of Aeronautical Science, Vol. 21, No. 2, February 1954, pp. 91-108.

4. Nash, J. F., and V. C. Patel, Three-Dimensional Turbulent Boundary Layers, SBC Technical Books, 1972.

5. Chandrashekhar, N., "Some Studies on Three-Dimensional Turbulent Boundary Layers," Ph.D. Dissertation, Department of Applied Mechanics, Indian Institute of Technology, Madras, India, October, 1974.

6. van den Berg, B., "The Law of the Wall in Two- and Three-Dimensional Turbulent Boundary Layers," National Aerospace Laboratory, The Netherlands, TR 72111 U, January, 1973.

7. Cooke, J. C., and M. G. Hall, "Boundary Layers on Three-Dimensions," Royal Aircraft Establishment Report Aero. 2635, February, 1960.

8. Gruschwitz, E., "Turbulente Reibungsschichten Mit Secundärströmung," Ingenieur-Archiv., Vol. 6, 1935.

9. Johnston, J. P., "Experimental Studies in Three-Dimensional Turbulent Boundary Layers," Report MD-34, Department of Mechanical Engineering, Stanford University, Stanford, California, July, 1976.

10. Von Kármán, T., "Mechanische Ähnlichkeit und Turbulenz," Proceedings Third International Congress for Applied Mechanics, Stockholm, 1930.

11. Prandtl, L., "Neuere Ergebnisse der Turbulenzforschung," Z. Ver. Dtsch. Ing., Vol. 77, 1933, pp. 105-114, (translation NACA Tech. Mem. 720).

12. Hinze, J. O., Turbulence, 2 ed., McGraw Hill, New York, 1975.

13. Townsend, A. A., "Equilibrium Layers and Wall Turbulence," Journal of Fluid Mechanics, Vol. 11, 1961, pp. 97-120.

14. Millikan, C. B., "A Critical Discussion of Turbulent Flows in Channels and Circular Tubes," Proc. 5th Int. Congr. Appl. Mech., Cambridge, Mass., 1938, pp. 386-392.

15. Clauser, F. H., The Turbulent Boundary Layer," Advances in Applied Mechanics, Vol. 4, 1956, pp. 1-51.

16. Kleinstein, G., "Generalized Law of the Wall and Eddy-Viscosity Model for Wall Boundary Layers," AIAA Journal, Vol. 5, No. 8, August 1967, pp. 1402-1407.

17. Reichardt, H., "Vollstandige Darstelling der turbulenten Geschwindigkeitsverteilung in glatten Leitungen," Z. Angew. Math. Mech., Vol. 31, No. 7, 1951, pp. 208-219.

18. Elrod, H. G. Jr., "Note on the Turbulent Shear Stress Near a Wall," J. of the Aero. Sciences, Vol. 24, June 1957, pp. 468-469.

19. Rotta, J., "Das in Wandnähe gültige Geschwindigkeitsgesetz turbulenter Strömungen," Ing. Arch., Vol. 18, 1950, pp. 277-279.

20. Deissler, R. G., "Analysis of Turbulent Heat Transfer, Mass Transfer, and Friction in Smooth Tubes at High Prandtl and Schmidt Numbers," NACA TR 1210, 1955.

21. van Driest, E. R., "On Turbulent Flow Near a Wall," J. of Aero. Sci., Vol. 23, Nov. 1956, pp. 1007-1011.

22. Mellor, G. L., "Review of the Empirical Content of Some Turbulent Boundary Layer Prediction Methods," Proc. Symp. Fluidics and Internal Flows, Vol., Penn. State Univ., 1968, pp. 151-175.

23. Rasmussen, M. L., "On Compressible Turbulent Boundary Layer in the Presence of Favourable Pressure Gradients," Journal of Fluids Engineering, ASME Paper 75-WA/HT-53, 1975.

24. Green, J. E., "A Note on the Turbulent Boundary Layer at Low Reynolds Number in Incompressible Flow at Constant Pressure," RAE unpublished report, 1971.

25. Dean, R. B., "A Single Formula for the Complete Velocity Profile in a Turbulent Boundary Layer," Trans. ASME, Journal of Fluid Engineering, Dec. 1976, pp. 723-727.

26. Coles, D., "The Law of the Wake in the Turbulent Boundary Layer," Journal of Fluid Mechanics, Vol. 1, 1956, pp. 191-227.

27. Finley, P. J., Khoo Chong Phoe, and Chon Jeck Poh, "Velocity Measurements in a Thin Turbulent Water Layer," La Houille Blanche, Vol. 21, 1966, pp. 713-721.

28. Granville, P. S., "A Modified Law of the Wake for Turbulent Shear Layers," Naval Ship Research and Development Center - 4639, Bethesda, Maryland, May 1975.

29. Patel, V. C., "A Unified View of the Law of the Wall Using Mixing-Length Theory," Aeronautical Quarterly, Vol. 24, February 1973, pp. 55-70.

30. McDonald, H., "The Effect of Pressure Gradient on the Law of the Wall in Turbulent Flow," Journal of Fluid Mechanics, Vol. 35, part 2, 1969, pp. 311-336.

31. Mellor, G. L., "The Effects of Pressure Gradients on Turbulent Flow Near a Smooth Wall," Journal of Fluid Mechanics, Vol. 24, part 2, 1966, pp. 255-274.

32. Bradshaw, P., D. H. Ferriss, and N. P. Atwell, "Calculation of Boundary-Layer Development Using the Turbulent Energy Equation," Journal of Fluid Mechanics, Vol. 28, 1967, pp. 593-616.

33. Townsend, A. A., The Structure of Turbulent Shear Flows, Cambridge University Press, 1956.

34. Bradshaw, P., "A Simple Method for Determining Turbulent Skin Friction From Velocity Profiles," Journal of Aerospace Sciences, Vol. 20, December, 1959, p. 841.

35. Kline, S. J., and F. Schraub, "A Study of the Structure of the Turbulent Boundary Layer With and Without Longitudinal Pressure Gradients," Thermosciences Division, Stanford University Report MD-12, 1965.

36. Coles, D., "The Young Person's Guide to the Data," Proceedings Computation of Turbulent Boundary Layers - 1968, AFOSR-IFP-Stanford Conference Vol. II, 1968, pp. 1-45.

37. Patel, V. C., "Calibration of the Preston Tube and Limitations on Its Use in Pressure Gradients," Journal Fluid Mechanics, Vol. 23, part 1, 1965, pp. 185-208.

38. Smith, D. W., and J. H. Walker, "Skin Friction Measurements in Incompressible Flow," NASA TR R-26, 1959.

39. Staff of the N.P.L.,"On the Measurement of Local Surface Friction on a Flat Plate by Means of Preston Tubes," A.R.C. R & M 3185, May, 1958.

40. Laufer, J., "Investigation of Turbulent Flow in a Two-Dimensional Channel," NACA TN 2123, July, 1950.

41. Doench, F., "Divergente und Konvergente turbulente Stroemungen mit kleinen Oeffnungswinkeln," Fosch.-Arb. Geb. Ing.-Wes., Heft 282, 1926.

42. Klebanoff, P. S., and F. W. Diehl, "Some Features of Artifically Thickened Fully Developed Turbulent Boundary Layers with Zero Pressure Gradient," NACA TN 2475, 1951.

43. Schultz-Grunow, F. Von, "Neues Reibungswiderstands gesetz für glatte Platten," Luftfahrtforschung, Band 7, 5.239, 1940 (translation NACA TM 986).

44. Lindgren, E. R., and J. Chao, "Average Velocity Distribution of Turbulent Pipe Flow with Emphasis on the Viscous Sublayer," Physics of Fluids, Vol. 12, 1969, pp. 1364-1371.

45. Laufer, J., "The Structure of Turbulence in Fully Developed Pipe Flow," NACA TR 1174, 1954.

46. Pierce, F. J., and D. S. Gold, "Near-Wall Velocity Measurements for Wall Shear Inference in Turbulent Flows," Flow Measurement in Open Channels and Closed Conduits, NBS Special Publication 484, Vol. 2, October 1977, pp. 621-648.

47. Kuethe, A., P. McKee, and W. Curry, "Measurements in the Boundary Layer with Zero Pressure Gradient," NACA TN 1946, 1949.

48. Johnston, J. P., "On the Three-Dimensional Turbulent Boundary Layer Generated by Secondary Flow," Trans. ASME, Journal of Basic Engineering, Vol. 82, March 1960, pp. 233-248.

49. Rogers, B. K., and M. R. Head, "Measurement of Three-Dimensional Turbulent Boundary Layers," The Aero. Journal of the Royal Aero. Society, Vol. 73, September, 1969, pp. 796-798.

50. Pierce, F. J., and J. L. East, "Near-Wall Collateral Flow in Three-Dimensional Turbulent Boundary Layers," AIAA Journal, Vol. 10, No. 3, March, 1972, pp. 334-336.

51. Hornung, H. G., and P. N. Joubert, "The Mean Velocity in Three-Dimensional Turbulent Boundary Layers," Journal of Fluid Mechanics, Vol. 15, Part 3, 1963, pp. 368-384.

52. Pierce, F. J., and D. H. Krommenhoek, "Wall Shear Stress Diagnostics in Three-Dimensional Turbulent Boundary Layers," Interim Technical Report No. 2, ARO-D Project 6858E, Virginia Polytechnic Institute and State University, September, 1968.

53. East, L. F., and R. P. Hoxey, "Low-Speed Three-Dimensional Turbulent Boundary Layer Data," Parts 1 and 2, Aeronautical Research Council R & M 3653, March, 1969.

54. Prahlad, T. S., "Wall Similarity in Three-Dimensional Turbulent Boundary Layers," AIAA Journal, Vol. 6, No. 9, 1968, pp. 1772-1774.

55. Chandrashekhar, N., and N. V. C. Swamy, "Wall Shear Stress Inference for Three-Dimensional Turbulent Boundary Layer Velocity Profiles," Journal of Applied Mechanics, Vol. 43, March, 1976, pp. 20-27.

56. Perry, A. E., and P. N. Joubert, "A Three-Dimensional Turbulent Boundary Layers," Journal of Fluid Mechanics, Vol. 22, Part 2, 1965, pp. 285-304.

57. Van den Berg, B., and A. Elsenaar, "Measurements in a Three-Dimensional Incompressible Turbulent Boundary Layer in an Adverse Pressure Gradient under Infinite Swept Wing Conditions," National Aerospace Laboratory TR 72072 U, The Netherlands, August, 1972.

58. Vermeulen, A., "Measurements of Three-Dimensional Turbulent Boundary Layers," Ph.D. Thesis, Cambridge University, 1971.

59. Coles, D., "The Law of the Wall in Turbulent Shear Flow," 50 Jahre Grenzschichtforschung, (Ed.) H. Görtler und W. Tollmien, Friedr, Vieweg and Sohn, Braunschweig, 1955, pp. 153-163.

60. East, L. F., "A Prediction of the Law of the Wall in Compressible Three-Dimensional Turbulent Boundary Layers," Royal Aircraft Establishment Technical Report 72178, 1972.

61. White, F. M., R. C. Lessmann, and G. H. Christoph, "A Three-Dimension Integral Method for Calculating Incompressible Turbulent Skin Friction," Trans. ASME, Journal of Fluids Engineering, Vol. 97, December, 1975, pp. 550-557.

62. Mager, A., "Generalization of Boundary Layer Momentum Integral Equations to Three-Dimensional Flows, Including Those of a Rotating Disk," NACA TN 2310, 1951.

63. Klinksiek, W. F., and F. J. Pierce, "Simultaneous Lateral Skewing in a Three-Dimensional Turbulent Boundary Layer," Trans. ASME, Journal of Basic Engineering, Vol. 92, March, 1970, pp. 83-90.

64. Brown, K. C., and P. N. Joubert, "The Measurement of Skin Friction In Turbulent Boundary Layers with Adverse Pressure Gradients," Journal of Fluid Mechanics, Vol. 35, Part 4, 1969, pp. 732-757.

65. Dhawan, S., "Direct Measurements of Skin Friction," NACA TN 2567, 1952.

66. Dickinson, J., and V. Ozarapoglu, "The Determination of Turbulent Skin Friction," Progress Report DRB 9550-23 Universite Laval, Canada, 1969.

67. Everett, H. U., "Calibration of Skin Friction Balance Discs for Pressure Gradient," Defense Research Laboratory, DRL-426, CF-2708, August, 1958.

68. Fowke, J. G., "Development of a Skin-Friction Balance to Investigate Sources of Error in Direct Skin-Friction Measurements," M.S. Thesis, University of Virginia, 1969.

69. Franklin, R. E., "A Force-Displacement Indicator for a Drag Balance," Ministry of Aviation, Aeronautical Research Council, C.P. No. 549, London, 1961.

70. Furuya, Y., I. Nakamura, H. Osaka, and H. Honda,"The Spanwise Non-Uniformity of Nominally Two-Dimensional Turbulent Boundary Layer II--Wall Shear Stress and Flow Field," JSME Bulletin, Vol. 18, July, 1975, pp. 673-680.

71. Kempf, G., "Neue Ergebnisse der Widerstands forschung," Werft Reederei Hafen, 10, 1929, pp. 234-239.

72. Miller, B. L. P., "The Measurement of Wall Shearing Stress in Turbulent Boundary Layers," Ph.D. Thesis, University of Leicester, Great Britain, August, 1972.

73. Morsy, M. G., "An Instrument for the Direct Measurement of the Local Shear Stress on Circular Cylinders," Journal of Physics, Part E - Scientific Instruments, Vol. 7, February, 1974, pp. 83-86.

74. Paros, J. M., "Application of the Force-Balance Principle to Pressure and Skin Friction Sensors," 16th Annual Technical Meeting Proceedings, Institute of Environmental Science, 1970, pp. 363-368.

75. Schultz-Grunow, F., "New Frictional Resistance Law for Smooth Plates," NACA TM 956, 1950.

76. Smith, S. L., C. J. Lawn, and M. J. Hamlin, "The Direct Measurement of Wall Shear Stress in an Annulus," C.E. G.B. RD/B/N 1232, 1968.

77. White, J. K., and R. E. Franklin, "Measurements of Skin-Friction in an Annulus by the Floating Element Technique," A.R.C. 25 661, F.M. 3419, February 24, 1964.

78. Ferriss, D. H., "Preston Tube Measurements in Turbulent Boundary Layers and Fully Developed Pipe Flow," ARC-CP-831, 1965.

79. Head, M. R., and I. Rechenberg, "The Preston Tube as a Means of Measuring Skin Friction," Journal of Fluid Mechanics, Vol. 14, 1962, pp. 1-17.

80. Preston, J. H., "The Determination of Turbulent Skin Friction by Means of Pitot Tubes," J. Roy. Aer. Soc., Vol. 38, February 1954, pp. 109-121.

81. Rechenberg, I., "The Measurement of Turbulent Wall Shear Stress," Zeitschrift für Flugwissenschaften, Vol. 11, 11, November, 1963. (A.R.A. Library Translation No. 11)

82. Samuel, A. E., and P. N. Joubert, "A Boundary Layer Developing in an Increasing Adverse Pressure Gradient," Journal of Fluid Mechanics, Vol. 66, 1974, pp. 481-505.

83. Abarbanel, S. S., R. J. Hakkinen, and L. Trilling, "Use of a Stanton Tube for Skin-Friction Measurements," NASA MEMO 2-17-59W, March, 1969.

84. Bradshaw, P., and N. Gregory, "The Determination of Local Turbulent Skin Friction from Observations in the Viscous Sub-Layer," ARC R & M 3203, 1961.

85. Stanton, T. E., D. Marshall, and C. N. Bryant, "On the Conditions at the Boundary of a Fluid in Turbulent Motion," Proceedings Royal Society, London, Vol. 97, 1920.

86. Konstantinov, N. I., and G. L. Dragnysh, "The Measurement of Friction Stress on a Surface," English Translation, DSIR RTS 1499, 1960.

87. Wanschkuhn, P., and V. I. Vasanta Ram, "Turbulent Boundary Layer Behind a Separation Zone," Zeitschrift für Flugwissenschaften, Vol. 23, January 1975, pp. 1-9.

88. Wash-Weber, J. L., and G. C. Oates, "An Instrument for Skin-Friction Measurements in Thin Boundary Layers," ASME Paper No. 71-FE-27, 1971.

89. Wills, J. A. B., "Note on a Method of Measuring Skin Friction," A.R.C. 24, No. 655, 1963.

90. East, L. F., "Measurement of Skin Friction at Low Subsonic Speeds by the Razor-Blade Technique," Aeronautical Research Council R & M 3525, 1968.

91. Pai, B. R., and J. H. Whitelaw, "Simplification of the Razor-Blade Technique and its Application to the Measurement of Wall-Shear Stress in Wall-Jet Flows," Aero. Quarterly, Vol. 20, November 1969, pp. 355-364.

92. Wyatt, L. A., and L. F. East, "Low Speed Measurements of Skin Friction on a Slender Ring," A.R.C. R & M 3499, 1968.

93. Ludwieg, H., and W. Tillmann, "Investigations of the Wall-Shearing Stress in Turbulent Boundary Layers," NACA TM 1285, May, 1950.

94. Armistead, R. A. Jr., and J. J. Keyes Jr., "A Study of Wall-Turbulance Phenomena Using Hot-Film Sensors," Trans. ASME, Journal of Heat Transfer, Series C. Vol. 90, No. 2, February, 1968, pp. 13-21.

95. Bellhouse, B. J., and D. L. Schultz, "Determination of Mean and Dynamic Skin Friction, Separation, and Transition in Low-Speed Flow with a Thin-Film Heated Element," Journal of Fluid Mechanics, Vol. 24, Part 2, 1966, pp. 379-400.

96. Bellhouse, B. J., and D. L. Schultz, "The Measurement of Fluctuating Skin Friction in Air with Heated Thin-Film Gauges," Journal of Fluid Mechanics, Vol. 32, Part 4, 1968, pp. 675-680.

97. Brown, G. L., "Theory and Application of Heated Films for Skin Friction Measurement," Proceedings of the 1967 Heat Transfer and Fluid Mechanics Institute, Stanford University Press, Stanford, California, 1967, pp. 361-381.

98. Drinkuth, R. H.,and F. J. Pierce, "Directional Heat Meter for Wall Shear Stress Measurements in Turbulent Boundary Layers," Review of Scientific Instruments, Vol. 37, June, 1966, pp. 740-741.

99. Fage, A., and V. M. Falkner, "On the Relation Between Heat Transfer and Surface Friction for Laminar Flow," Aeronautical Research Council R & M No. 1408, April, 1931.

100. Liepmann, H. W., and G. T. Skinner, "Shearing-Stress Measurements by Use of a Heated Element," NACA Technical Note 3268, November, 1954.

101. Ludwieg, H., "Instrument for Measuring the Wall Shearing Stress of Turbulent Boundary Layers," NACA Technical Memorandum 1284, May, 1950,(translated from Ingenier Arch., Vol. 17, 1949), pp. 207-218.

102. Owen, F. K., "Transition Experiments on a Flat Plate at Subsonic and Supersonic Speeds," AIAA Journal, Vol. 8, March, 1970, pp. 518-523.

103. Kashinskiy, O. N., S. S. Kutateladze, and V. A. Mukhin, "Skin Friction in a Turbulent Boundary Layer with a Positive Pressure Gradient," NASA Translation from Z. H. Prikl. Mekh. Tekh. Fiz. (USSR), No. 6, November December, 1974, pp. 92-96.

104. Mitchell, J. E.,and T. J. Hanratty, "A Study of Turbulence at a Wall Using an Electrochemical Wall Shear Stressmeter," Journal of Fluid Mechanics, Vol. 26, Part 1, 1966, pp. 199-221.

105. Allen, J. M., "Experimental Study of Error Sources in Skin Friction Balance Measurements," Trans. ASME, Journal of Fluid Engineering, Vol. 99, March, 1977, pp. 192-204.

106. Hakkinen, R. J., "Measurements of Turbulent Skin Friction on a Flat Plate at Transonic Speeds," NACA TN 3486, 1955.

107. O'Donnell, F. B., Jr., "A Study of the Effect of Floating-Element Misalignment on Skin-Friction-Balance Accuracy," Defense Research Laboratory, DRL-515, CR-10, March, 1964.

108. Power, J. L., "Wall Shear Stress and Mean-Velocity Measurements in a Three-Dimensional Turbulent Boundary Layer," Naval Ship and Development Center Report 4056, September, 1973.

109. Prahlad, T. S., "Yaw Characteristics of Preston Tubes," AIAA Journal, Vol. 10, No. 3, March, 1972, pp. 357-359.

110. Hebbar, K. S., and W. L. Melnik, "Measurements in the Near-Wall Region of a Relaxing Three-Dimensional Low Speed Turbulent Air Boundary Layer," University of Maryland, T. R. No. AE-76-1, July, 1976.

111. Vagt, J. D., and H. Fernholz, "Use of Surface Fences to Measure Wall Shear Stress in Three-Dimensional Boundary Layers," The Aeronautical Quarterly, Vol. 24, 1973, pp. 87-91.

112. McCroskey, W. J., and E. J. Durbin, "Flow Angle and Shear Stress Measurements Using Heated Films and Wires," Trans. ASME, Journal of Basic Engineering, Vol. 94, March, 1972, pp. 46-52.

113. Dean, R. C., Jr., Aerodynamics Measurements, Gas Turbine Laboratory, Massachusetts Institute of Technology, Eagle Enterprise, 1958.

114. Young, A. B., and J. N. Maas, "The Behavior of a Pitot-Tube in a Transverse Pressure Gradient," ARC R & M No. 1770, 1936.

115. Livesey, J. L., "The Behavior of Transverse Cylindrical and Forward Facing Total Pressure Probes in Transverse Total Pressure Gradients," Journal of Aeronautical Science, Vol. 23, 1956.

116. MacMillan, F., "Experiments on Pitot-Tubes in Shear Flow," ARC R & M No. 3028, 1956.

117. Davies, P. O. A. L., "The Behavior of a Pitot Tube in Transverse Shear," Journal of Fluid Mechanics, Vol. 3, 1958, pp. 441-456.

118. Gold, D. S., "Near-Wall Velocity Measurements in Two-Dimensional Turbulent Boundary Layers," M.S. Thesis, Va. Polytechnic Inst. and State Univ., Blacksburg, Virginia, December, 1974.

119. Rule, J. A., Jr., "Near-Wall Similarity and Wall Shear Stress Measurements in a Two-Dimensional Wind Tunnel," M.S. Thesis, Va. Polytechnic Inst. and State Univ., Blacksburg, Virginia, August, 1976.

120. Pierce, F. J., M. H. Tennant, and J. A. Rule, "Near-Wall Similarity in Three-Dimensional Turbulent Flows-Experimental Systems," Int. Rpt. NSF Grant ENG 73-03737-A01, (VPI & SU Rpt. VPI-E-76-16, available NTIS), August, 1976.

121. Lagace, L. J., personal communication, Mechanical Technology Incorporated, March 24, 1976.

122. Pilkey, W. D., "Manual for the Response of Structural Members," IIT Research Institute, Vols. I and II, August, 1969.

123. Headley, J. W., "A Simple Calibration Technique for Skin Friction Balances," AIAA Journal, Vol. 4, October, 1966, p. 1862.

124. Head, M. R., and I. Rechenberg, "The Preston Tube as a Means of Measuring Skin Friction," Journal of Fluid Mechanics, Vol. 14, 1962, pp. 1-17.

125. Landweber, L., "Reanalysis of Boundary-Layer Data on a Flat Plate," written discussion of Ninth International Toning Tank Conference, Paris, 1960. Iowa Institute of Hydraulic Research, State University of Iowa, 1960.

126. Laufer, J., "The Structure of Turbulence in Fully Developed Pipe Flow," NACA Tech. Note 2954, June, 1953.

127. Landweber, L., and T. T. Siao, "Comparison of Two Analyses of Boundary Layer Data on a Flat Plate," Journal of Ship Research, Vol. 1, March, 1958, pp. 21-33.

128. Dechow, R., "Mittlere Geschwindigkeit und Reynoldsscher Spannungstensor in der dreidimensionalen turbulenten Wandgrenzschicht vor einen stehenden Zylinder," dissertation, Universität (TH) Karlsruhe, April, 1966.

APPENDIX A

TWO-DIMENSIONAL DATA AND COMPARISONS

TABLE A 1. TWO-DIMENSIONAL BOUNDARY LAYER PROFILES FOR RUN NUMBERS 01A AND 01B.

RUN NUMBER 2D-01-A
Q FREESTREAM = 13.33 M/S
KINEMATIC VISCOSITY
= 0.0000170 SQ M/S
FREESTREAM
ANGLE = 0.0 DEGREES

Y (CM)	Q (M/S)	ALPHA (DEGREES)
0.025	3.70	-0.6
0.028	3.99	-0.6
0.030	4.27	-0.6
0.036	4.53	-0.6
0.041	5.00	-0.6
0.046	5.23	-0.6
0.051	5.44	-0.6
0.063	5.85	-0.6
0.081	6.22	-0.6
0.102	6.58	-0.6
0.127	6.75	-0.6
0.163	7.08	-0.6
0.203	7.39	-0.6
0.254	7.70	-0.6
0.317	7.99	-0.6
0.406	8.27	-0.6
0.508	8.54	-1.0
0.635	8.80	-1.0
0.813	9.06	-1.0
1.016	9.30	-1.0
8.128	13.16	-0.4
10.160	13.33	-0.4
12.700	13.33	0.0

RUN NUMBER 2D-01-B
Q FREESTREAM = 19.79 M/S
KINEMATIC VISCOSITY
= 0.0000170 SQ M/S
FREESTREAM
ANGLE = 0.0 DEGREES

Y (CM)	Q (M/S)	ALPHA (DEGREES)
0.025	6.40	-0.2
0.028	6.92	-0.2
0.030	7.08	-0.2
0.036	7.54	-0.2
0.041	7.98	-0.2
0.046	8.40	-0.2
0.051	8.67	-0.2
0.063	9.05	-0.2
0.081	9.54	-0.8
0.102	10.01	-0.8
0.127	10.34	-0.8
0.163	10.67	-0.8
0.203	10.98	-1.0
0.254	11.49	-1.2
0.317	11.88	-1.2
0.406	12.35	-1.2
0.508	12.80	-1.2
0.635	13.16	-1.2
0.813	13.58	-1.2
1.016	13.91	-1.2
8.128	19.67	-0.2
10.160	19.79	-0.2
12.700	19.79	0.0

CONVERSION FACTORS
1 IN. = 2.54 CM
1 FT/S = 0.3048 M/S
1 SQ FT/S = 0.0929 SQ M/S

TABLE A 2. TWO-DIMENSIONAL BOUNDARY LAYER PROFILES FOR RUN NUMBERS 01E AND 04D.

RUN NUMBER 2D-01-E
Q FREESTREAM = 24.79 M/S
KINEMATIC VISCOSITY
= 0.0000170 SQ M/S
FREESTREAM
ANGLE = 0.0 DEGREES

Y (CM)	Q (M/S)	ALPHA (DEGREES)
0.025	9.30	-1.0
0.028	9.66	-1.0
0.030	9.77	-0.8
0.036	10.23	-0.2
0.041	10.67	-0.2
0.046	11.09	-0.2
0.051	11.39	-0.4
0.063	11.88	-0.6
0.081	12.44	-0.8
0.102	12.89	-0.8
0.127	13.32	-0.8
0.163	13.83	-0.8
0.203	14.31	-0.8
0.254	14.78	-0.8
0.317	15.31	-1.0
0.406	15.89	-1.0
0.508	16.39	-0.8
0.635	16.86	-0.8
0.813	17.40	-0.6
1.016	17.91	-0.6
8.128	24.55	0.0
10.160	24.79	0.0
12.700	24.79	0.0

RUN NUMBER 2D-04-D
Q FREESTREAM = 25.64 M/S
KINEMATIC VISCOSITY
= 0.0000169 SQ M/S
FREESTREAM
ANGLE = 0.0 DEGREES

Y (CM)	Q (M/S)	ALPHA (DEGREES)
0.025	9.77	-0.4
0.028	10.00	-0.4
0.030	10.23	-0.4
0.036	10.77	-0.4
0.041	11.29	-0.4
0.046	11.59	-0.4
0.051	11.78	-0.4
0.063	12.25	-0.4
0.081	12.44	-0.4
0.102	13.15	-0.4
0.127	13.57	-0.4
0.163	14.15	-0.4
0.203	14.55	-0.4
0.254	15.23	0.2
0.317	15.67	0.0
0.406	16.24	0.0
0.508	16.86	0.0
0.635	17.33	0.0
0.813	17.97	0.0
1.016	18.47	0.0
1.270	18.96	0.0
1.626	19.60	0.0
2.032	20.23	0.0
2.540	21.01	0.0
3.175	21.80	0.0
4.064	22.72	0.0
5.080	23.36	0.0
6.350	24.32	0.0
8.128	25.46	0.0
10.160	25.64	0.0

CONVERSION FACTORS
1 IN. = 2.54 CM
1 FT/S = 0.3048 M/S
1 SQ FT/S = 0.0929 SQ M/S

TABLE A 3. TWO-DIMENSIONAL BOUNDARY LAYER PROFILES FOR RUN NUMBERS 05D AND 06D.

RUN NUMBER 2D-05-D
Q FREESTREAM = 25.64 M/S
KINEMATIC VISCOSITY = 0.0000169 SQ M/S
FREESTREAM ANGLE = 0.0 DEGREES

Y (CM)	Q (M/S)	ALPHA (DEGREES)
0.025	9.52	-1.2
0.028	10.43	-1.2
0.030	10.65	-1.2
0.036	11.06	-1.2
0.041	11.57	-1.2
0.046	11.86	-1.2
0.051	12.14	-1.2
0.063	12.51	-1.2
0.081	13.04	-1.2
0.102	13.47	-1.2
0.127	13.88	-1.2
0.163	14.37	-1.2
0.203	14.83	-1.2
0.254	15.36	-1.2
0.317	15.79	-1.2
0.406	16.36	-1.2
0.508	16.90	-1.0
0.635	17.43	-1.0
0.813	17.94	-1.0
1.016	18.44	-1.0
1.270	19.05	-1.0
1.626	19.63	-1.0
2.032	20.20	-0.4
2.540	20.87	-0.4
3.175	21.67	-0.4
4.064	22.74	-0.4
5.080	23.33	0.0
6.350	24.51	0.0
8.128	25.42	-0.2
10.160	25.64	0.0
12.700	25.64	0.0

RUN NUMBER 2D-06-D
Q FREESTREAM = 25.62 M/S
KINEMATIC VISCOSITY = 0.0000168 SQ M/S
FREESTREAM ANGLE = 0.0 DEGREES

Y (CM)	Q (M/S)	ALPHA (DEGREES)
0.025	9.63	-1.0
0.028	10.09	-1.0
0.030	10.31	-1.0
0.036	10.85	-1.0
0.041	11.26	-1.0
0.046	11.75	-1.0
0.051	11.94	-1.0
0.063	12.41	0.0
0.081	13.03	0.0
0.102	13.45	0.0
0.127	13.95	0.0
0.163	14.35	0.0
0.203	14.89	0.0
0.254	15.41	0.0
0.317	15.92	0.0
0.406	16.48	0.0
0.508	16.95	0.0
0.635	17.54	0.0
0.813	18.24	0.0
8.128	25.62	0.0
10.160	25.62	0.0
12.700	25.62	0.0

CONVERSION FACTORS
1 IN. = 2.54 CM
1 FT/S = 0.3048 M/S
1 SQ FT/S = 0.0929 SQ M/S

Table A4

Two-Dimensional Wall Shear Stress Measurements

Re_{unit} x $10^5(m^{-1})$	$\rho(kg/m^3)$	$\tau_w(Pa)$	β(degrees)
0.742	1.102	0.28	-1.0
0.742	1.102	0.29	-1.3
0.871	1.102	0.39	-0.6
0.871	1.102	0.38	-0.6
0.977	1.102	0.47	-0.9
0.977	1.102	0.48	-1.0
1.104	1.102	0.60	-0.1
1.104	1.102	0.60	-0.7
1.195	1.102	0.70	0.2
1.195	1.102	0.70	-0.1
1.342	1.102	0.90	0.0
1.342	1.102	0.90	0.2
1.416	1.102	0.98	0.3
1.416	1.102	0.98	0.4
1.450	1.100	1.00	0.5
1.458	1.102	1.02	0.2
1.462	1.105	1.05	0.2

Conversion Factors

$ft^{-1} = 3.281\ m^{-1}$

$lbm/ft^3 = 16.026\ kg/m^3$

$lbf/ft^2 = 47.847\ Pa$

Table A5

Tunnel Reynolds Numbers for Two-Dimensional Velocity Profiles

Run	$Re_{unit} \times 10^5 (m^{-1})$
01-A	0.683
01-B	1.015
01-E	1.299
04-D	1.339
05-D	1.341
06-D	1.344

Conversion Factor

$ft^{-1} = 3.281\ m^{-1}$

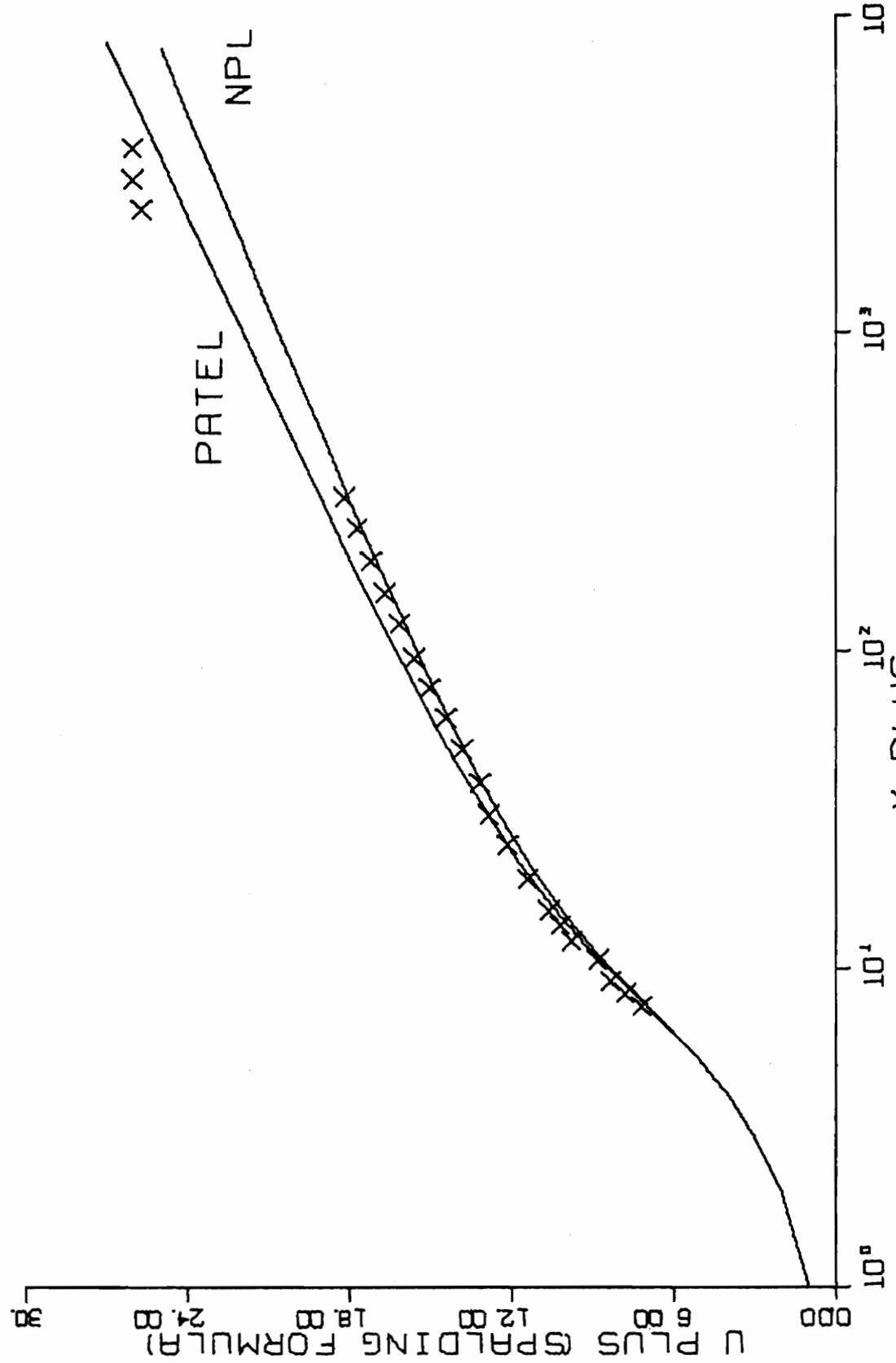

FIG. A 1. TWO-DIMENSIONAL SIMILARITY PLOT-RUN 01-A.

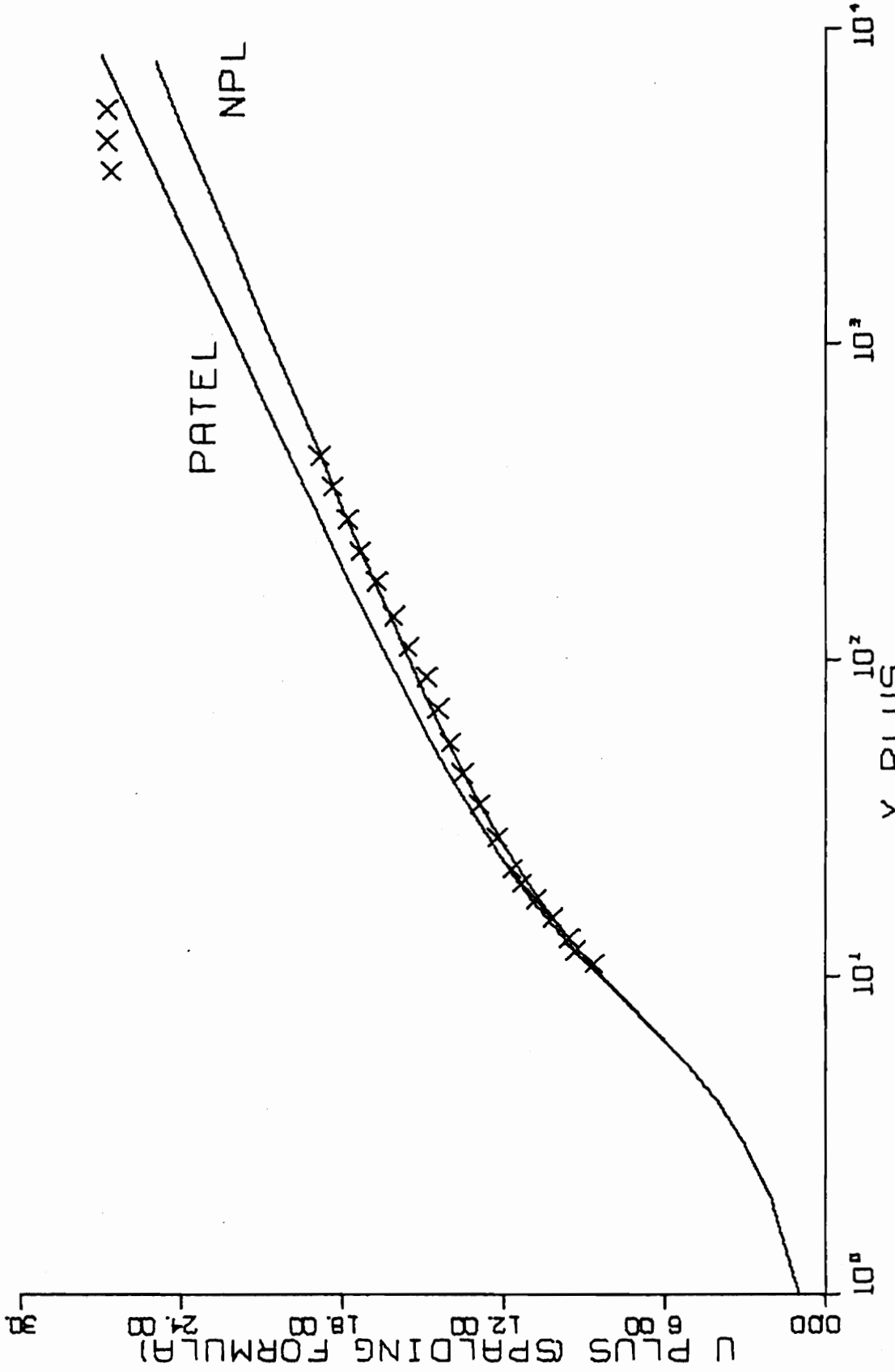

FIG. A 2. TWO-DIMENSIONAL SIMILARITY PLOT-RUN 01-B.

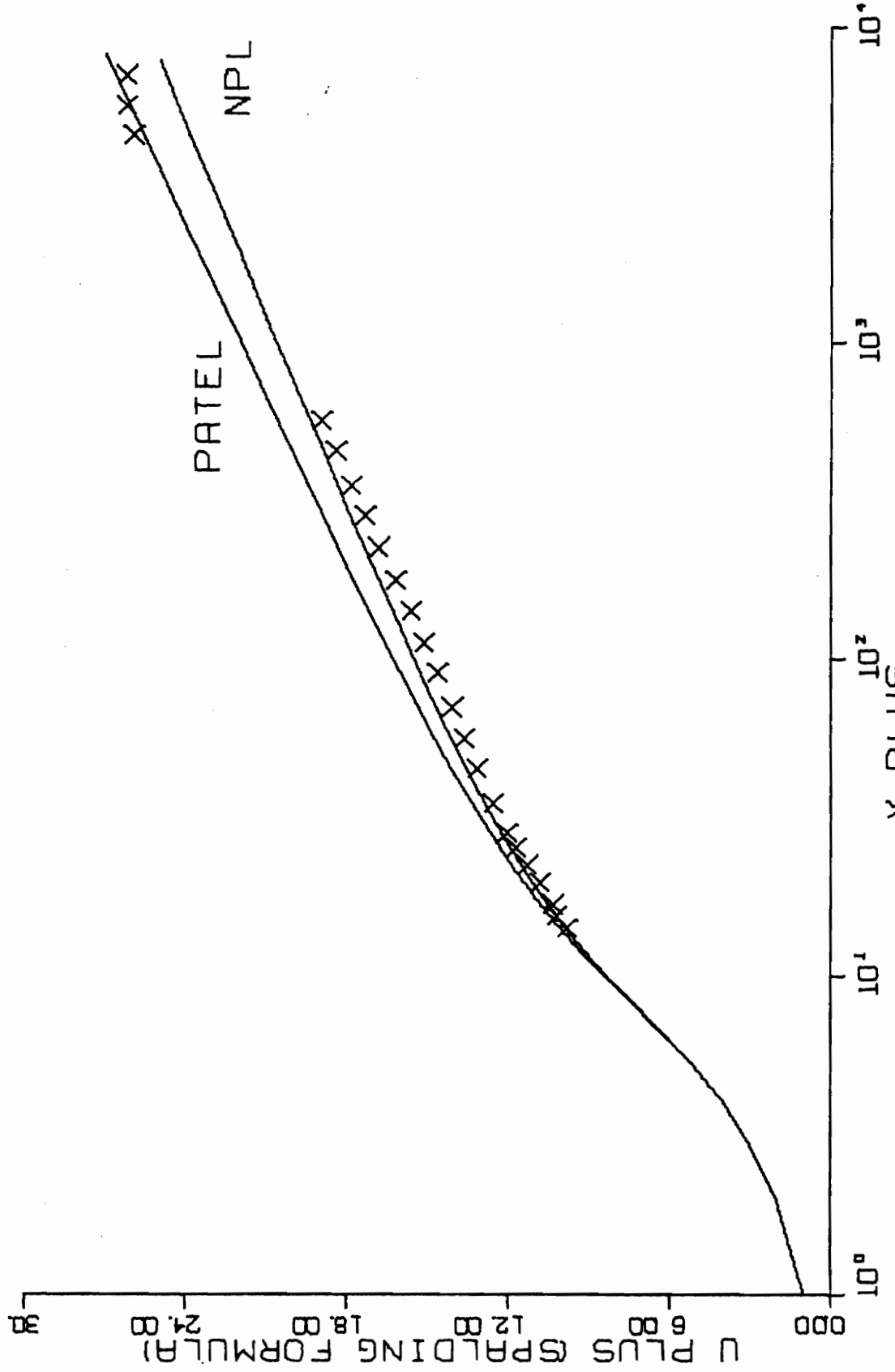

FIG. A 3. TWO-DIMENSIONAL SIMILARITY PLOT-RUN 01-E.

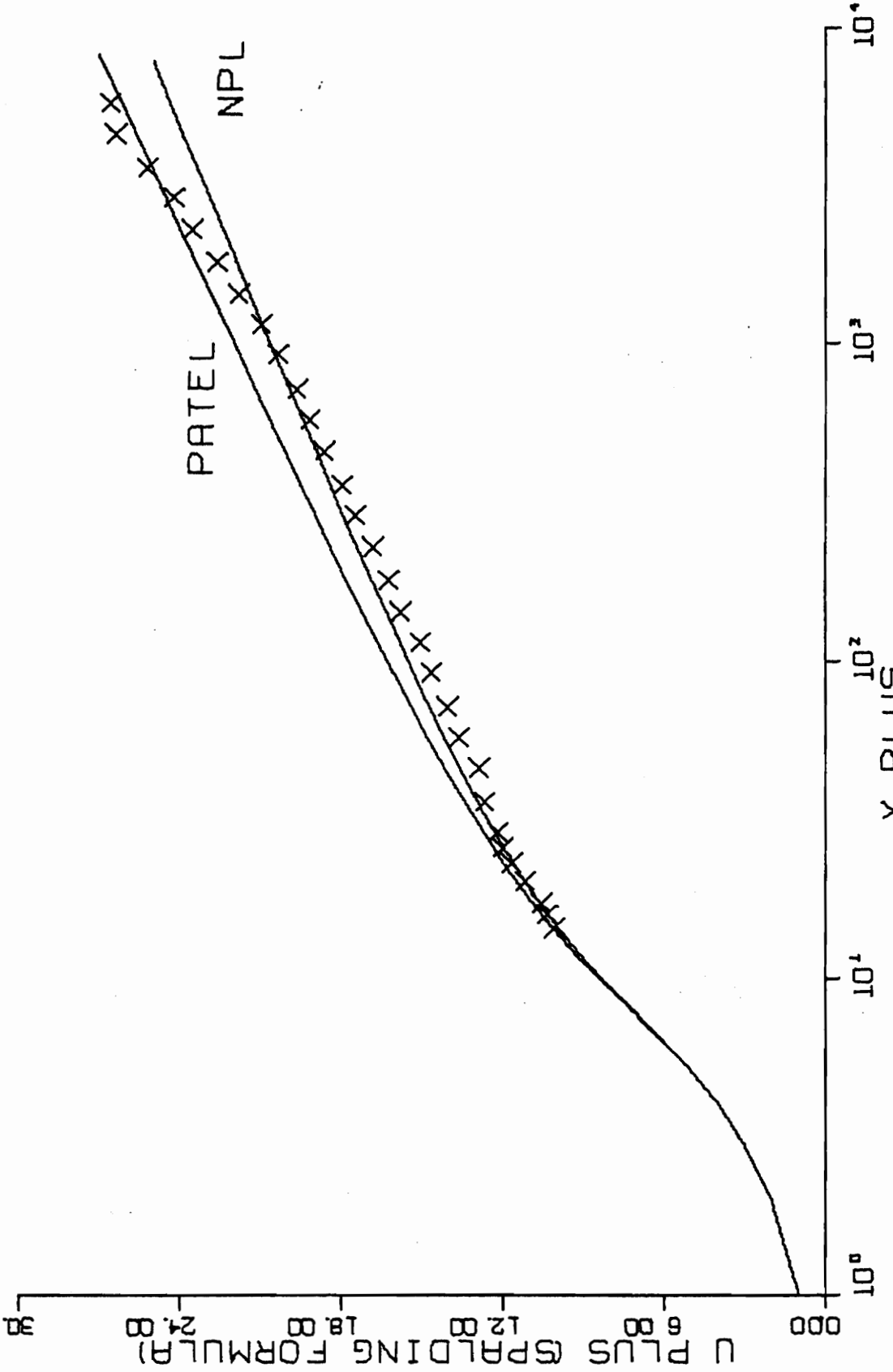

FIG. A 4. TWO-DIMENSIONAL SIMILARITY PLOT-RUN 04-D.

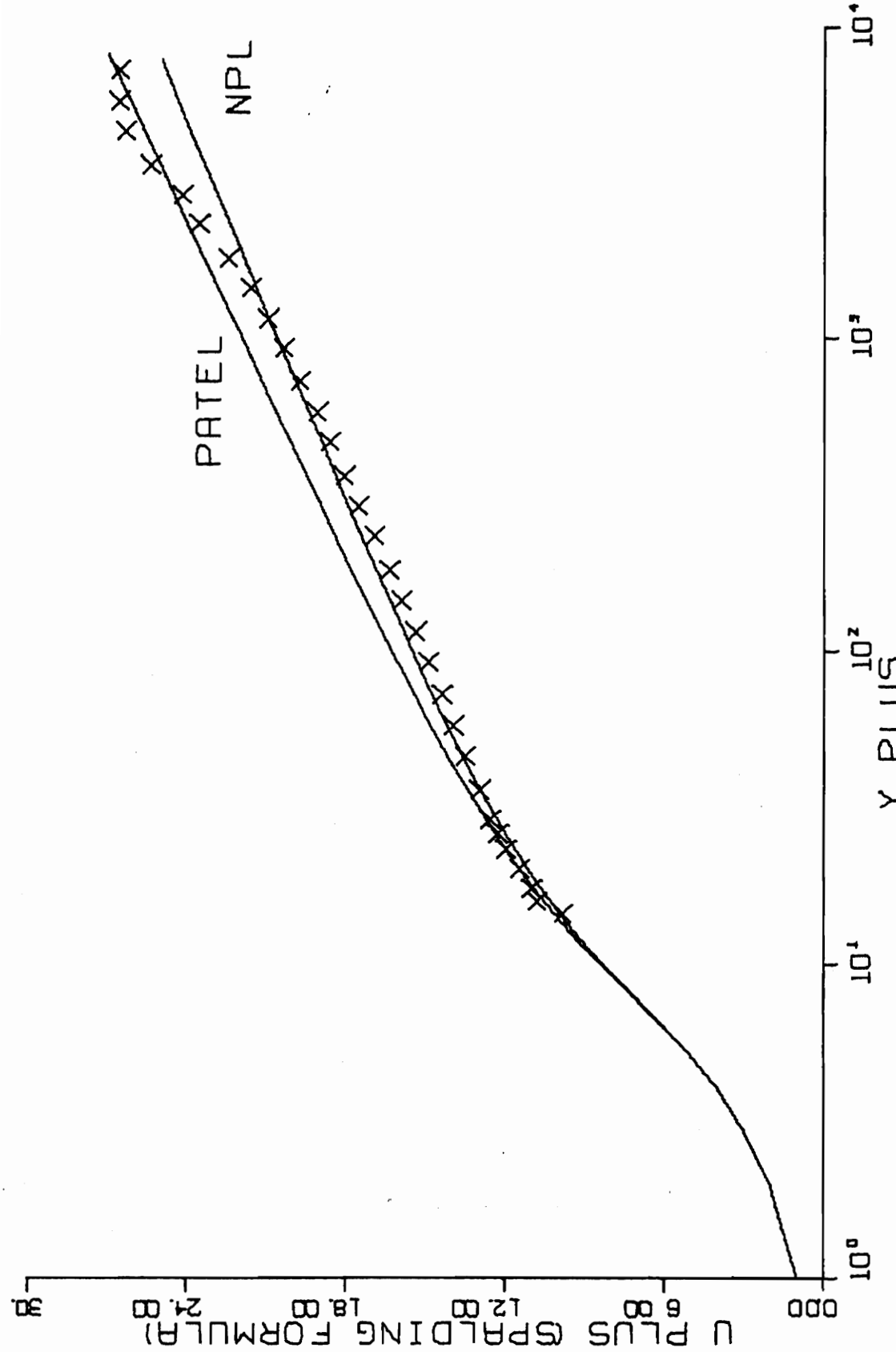

FIG. A 5. TWO-DIMENSIONAL SIMILARITY PLOT-RUN 05-D.

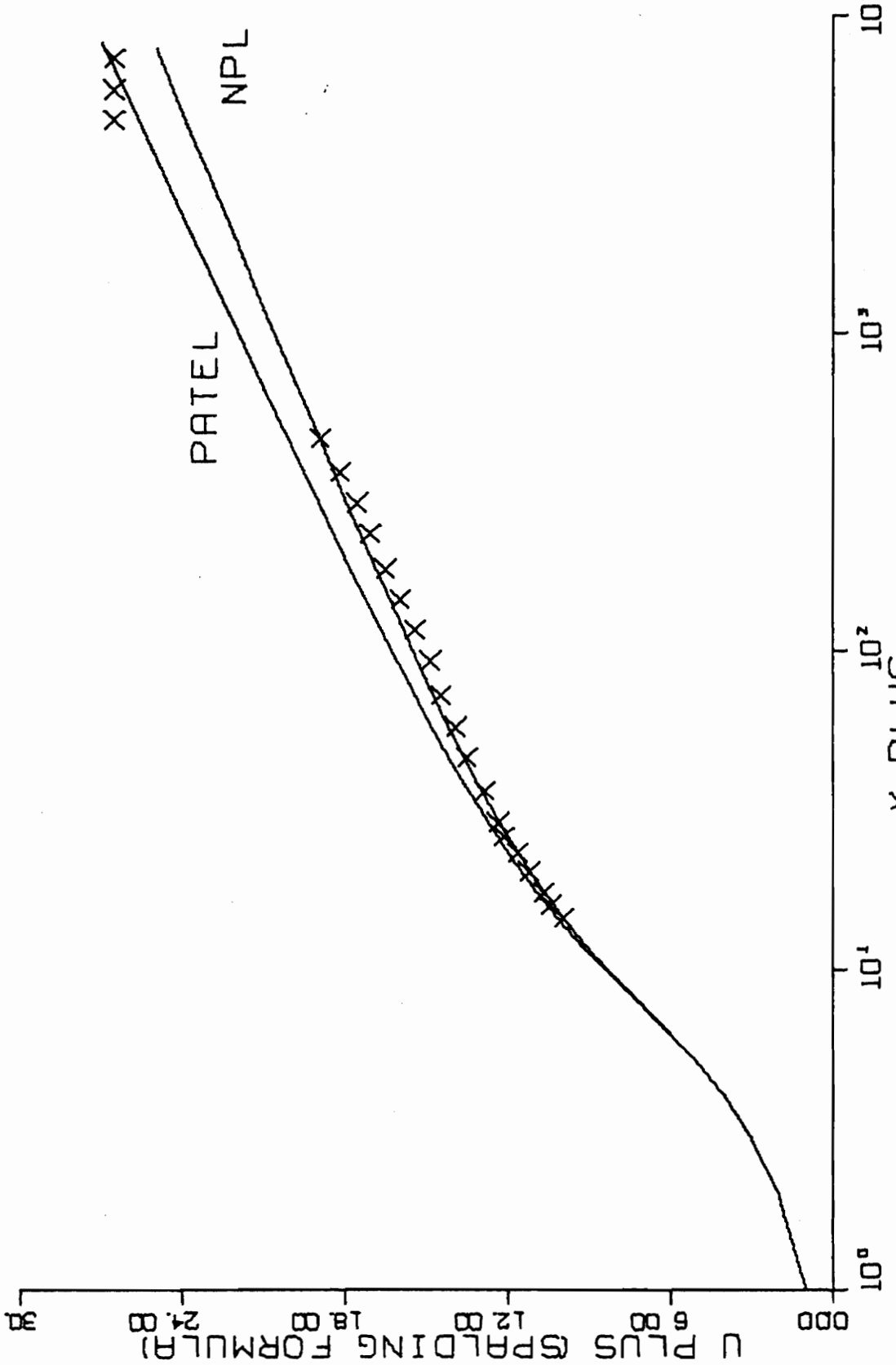

FIG. A 6. TWO-DIMENSIONAL SIMILARITY PLOT-RUN 06-D.

APPENDIX B

THREE-DIMENSIONAL DATA AND COMPARISONS

TABLE B1. THREE-DIMENSIONAL BOUNDARY LAYER PROFILES FOR RUN NUMBERS A7-01 AND A7-03.

RUN NUMBER A7-01
Q FREESTREAM = 23.94 M/S
KINEMATIC VISCOSITY = 0.0000166 SQ M/S
FREESTREAM ANGLE = -0.2 DEGREES

Y (CM)	Q (M/S)	ALPHA (DEGREES)
0.025	7.19	-1.4
0.028	7.79	-1.4
0.030	8.07	-1.4
0.036	8.74	-1.4
0.041	9.00	-1.0
0.046	9.24	-1.0
0.051	9.48	-1.0
0.063	9.95	-1.0
0.081	10.39	-1.0
0.102	10.81	-1.0
0.127	11.22	-1.2
0.163	11.71	-1.2
0.203	12.18	-1.2
0.254	12.63	-1.2
0.317	13.16	-1.2
0.406	13.82	-1.2
0.495	14.38	-1.2
0.622	14.92	-1.2
0.800	15.51	-1.2
1.003	16.15	-1.2
1.257	16.63	-1.0
1.613	17.36	-1.0
2.019	17.99	-1.0
2.527	18.79	-0.8
3.162	19.67	-0.6
4.051	20.67	-0.6
5.067	21.78	-0.4
6.337	22.84	-0.4
8.115	23.71	0.0
10.147	23.94	-0.4
12.687	23.94	0.0

RUN NUMBER A7-03
Q FREESTREAM = 23.77 M/S
KINEMATIC VISCOSITY = 0.0000167 SQ M/S
FREESTREAM ANGLE = -0.2 DEGREES

Y (CM)	Q (M/S)	ALPHA (DEGREES)
0.025	7.36	0.2
0.028	7.67	0.2
0.030	7.81	0.2
0.036	8.50	0.2
0.041	9.02	0.2
0.046	9.27	0.2
0.051	9.51	0.2
0.063	9.97	0.2
0.081	10.42	0.0
0.102	10.74	0.0
0.127	11.25	0.0
0.163	11.74	0.0
0.203	12.12	0.0
0.254	12.66	0.0
0.317	13.10	0.0
0.406	13.69	0.0
0.508	14.18	0.0
0.635	14.88	0.0
0.813	15.55	0.0
1.016	16.05	0.0
1.270	16.67	0.0
1.626	17.33	0.0
2.032	18.04	0.0
2.540	18.78	0.2
3.175	19.66	0.2
4.064	20.83	0.4
5.080	21.99	0.4
6.350	23.09	0.4
8.128	23.53	0.4
10.160	23.77	0.2
12.700	23.77	0.0

CONVERSION FACTORS
1 IN. = 2.54 CM
1 FT/S = 0.3048 M/S
1 SQ FT/S = 0.0929 SQ M/S

TABLE B2. THREE-DIMENSIONAL BOUNDARY LAYER PROFILES FOR RUN NUMBERS A7-03P AND A5-01.

RUN NUMBER A7-03P
Q FREESTREAM = 23.77 M/S
KINEMATIC VISCOSITY
= 0.0000167 SQ M/S
FREESTREAM
ANGLE = -0.2 DEGREES

Y (CM)	Q (M/S)	ALPHA (DEGREES)
0.025	7.75	0.2
0.028	7.96	0.2
0.030	8.01	0.2
0.036	8.58	0.2
0.041	8.99	0.2
0.046	9.31	0.2
0.051	9.63	0.2
0.063	10.24	0.2
0.081	10.63	0.0
0.102	10.90	0.0
0.127	11.37	0.0
0.163	11.84	0.0
0.203	12.17	0.0
0.254	12.68	0.0
0.317	13.10	0.0
0.406	13.66	0.0
0.508	14.12	0.0
0.635	14.80	0.0
0.813	15.45	0.0
1.016	15.95	0.0
1.270	16.58	0.0
1.626	17.25	0.0
2.032	17.95	0.0
2.540	18.70	0.2
3.175	19.59	0.2
4.064	20.78	0.4
5.080	21.95	0.4
6.350	23.06	0.4
8.128	23.51	0.4
10.160	23.76	0.2
12.700	23.77	0.0

RUN NUMBER A5-01
Q FREESTREAM = 23.48 M/S
KINEMATIC VISCOSITY
= 0.0000166 SQ M/S
FREESTREAM
ANGLE = -0.8 DEGREES

Y (CM)	Q (M/S)	ALPHA (DEGREES)
0.025	5.99	-1.0
0.028	6.35	-1.0
0.030	6.53	-1.0
0.036	7.02	-1.0
0.041	7.49	-1.0
0.046	7.78	-1.0
0.051	7.92	-1.0
0.063	8.20	-1.0
0.081	8.73	-0.8
0.102	9.11	-0.8
0.127	9.47	-0.8
0.163	9.93	-0.8
0.203	10.37	-0.6
0.254	10.80	-0.6
0.317	11.50	-0.6
0.406	11.98	-0.6
0.508	12.62	-0.6
0.635	13.31	-0.6
0.813	13.97	-0.6
1.016	14.51	-0.6
1.270	15.19	-0.6
1.626	15.99	-0.4
2.032	16.67	-0.4
2.540	17.52	-0.2
3.175	18.40	-0.2
4.064	19.58	-0.2
5.080	20.64	0.0
6.350	21.90	0.2
8.128	23.15	0.2
10.160	23.48	0.2
12.700	23.48	0.0

CONVERSION FACTORS
1 IN. = 2.54 CM
1 FT/S = 0.3048 M/S
1 SQ FT/S = 0.0929 SQ M/S

TABLE B3. THREE-DIMENSIONAL BOUNDARY LAYER PROFILES FOR RUN NUMBERS C7-01 AND C5-01.

RUN NUMBER C7-01
Q FREESTREAM = 24.21 M/S
KINEMATIC VISCOSITY
= 0.0000167 SQ M/S
FREESTREAM
ANGLE = 0.4 DEGREES

Y (CM)	Q (M/S)	ALPHA (DEGREES)
0.025	7.51	3.8
0.028	8.22	3.8
0.030	8.49	3.6
0.036	9.01	3.4
0.041	9.38	3.4
0.046	9.73	3.4
0.051	9.96	3.4
0.063	10.29	3.0
0.081	10.72	2.8
0.102	11.13	2.8
0.127	11.53	2.8
0.163	12.01	2.2
0.203	12.56	2.2
0.254	13.00	2.0
0.317	13.51	1.8
0.406	14.16	1.6
0.503	14.63	1.4
0.630	15.16	1.0
0.808	15.82	1.0
1.011	16.38	0.8
1.265	16.99	0.8
1.621	17.64	0.4
2.027	18.27	0.4
2.535	19.11	0.4
3.170	19.92	0.4
4.059	20.91	0.4
5.075	21.96	0.4
6.345	23.06	0.4
8.123	23.98	0.2
10.155	24.21	0.2
12.695	24.21	0.0

RUN NUMBER C5-01
Q FREESTREAM = 23.45 M/S
KINEMATIC VISCOSITY
= 0.0000166 SQ M/S
FREESTREAM
ANGLE = 2.0 DEGREES

Y (CM)	Q (M/S)	ALPHA (DEGREES)
0.025	6.87	8.4
0.028	7.19	8.4
0.030	7.34	8.4
0.036	7.78	8.4
0.041	8.21	8.4
0.046	8.61	8.4
0.051	8.74	8.4
0.063	8.99	7.8
0.081	9.48	7.8
0.102	9.83	6.8
0.127	10.27	6.6
0.163	10.81	6.0
0.203	11.21	5.6
0.254	11.61	5.2
0.317	12.17	4.8
0.406	12.80	4.2
0.508	13.32	3.6
0.635	13.90	3.2
0.813	14.61	2.6
1.016	15.13	2.2
1.270	15.86	2.0
1.626	16.41	1.8
2.032	17.15	1.2
2.540	17.92	1.2
3.175	18.83	0.6
4.064	19.93	0.4
5.080	21.08	0.4
6.350	22.23	0.2
8.128	23.55	0.0
10.160	23.45	0.0
12.700	23.45	0.0

CONVERSION FACTORS
1 IN. = 2.54 CM
1 FT/S = 0.3048 M/S
1 SQ FT/S = 0.0929 SQ M/S

TABLE B4. THREE-DIMENSIONAL BOUNDARY LAYER PROFILES FOR RUN NUMBERS C3-01 AND E7-01.

RUN NUMBER C3-01
Q FREESTREAM = 23.05 M/S
KINEMATIC VISCOSITY
= 0.0000167 SQ M/S
FREESTREAM
ANGLE = 5.4 DEGREES

Y (CM)	Q (M/S)	ALPHA (DEGREES)
0.025	5.61	30.8
0.028	6.00	30.8
0.030	6.36	30.8
0.036	6.71	30.8
0.041	7.04	30.0
0.046	7.20	29.6
0.051	7.35	29.6
0.063	7.65	27.4
0.081	7.80	27.0
0.102	8.35	25.2
0.127	8.62	24.6
0.163	9.00	22.4
0.203	9.37	20.2
0.254	9.72	17.8
0.317	10.17	16.6
0.406	10.71	14.2
0.508	11.43	12.5
0.635	12.00	11.0
0.813	12.82	9.4
1.016	13.42	8.4
1.270	14.23	6.8
1.626	14.93	5.4
2.032	15.81	4.4
2.540	16.64	3.4
3.175	17.62	2.8
4.064	18.80	2.0
5.080	19.90	1.6
6.350	21.27	0.8
8.128	22.66	0.6
10.160	23.05	0.2
12.700	23.05	0.0

RUN NUMBER E7-01
Q FREESTREAM = 24.68 M/S
KINEMATIC VISCOSITY
= 0.0000167 SQ M/S
FREESTREAM
ANGLE = 1.6 DEGREES

Y (CM)	Q (M/S)	ALPHA (DEGREES)
0.025	8.89	5.0
0.028	9.38	5.0
0.030	9.50	5.4
0.036	9.96	5.4
0.041	10.41	5.4
0.046	10.52	5.4
0.051	10.73	5.4
0.063	11.24	4.8
0.081	11.54	4.6
0.102	11.92	4.0
0.127	12.57	4.0
0.163	12.92	4.0
0.203	13.44	3.6
0.254	13.93	3.2
0.317	14.41	3.2
0.406	14.94	2.8
0.508	15.47	2.6
0.635	16.04	2.2
0.813	16.52	2.0
1.016	17.06	2.0
1.270	17.58	1.6
1.626	18.21	1.6
2.032	19.00	1.6
2.540	19.58	1.0
3.175	20.38	1.0
4.064	21.45	1.0
5.080	22.02	1.0
6.350	23.03	0.6
8.128	24.22	0.2
10.160	24.68	0.2
12.700	24.68	0.0

CONVERSION FACTORS
1 IN. = 2.54 CM
1 FT/S = 0.3048 M/S
1 SQ FT/S = 0.0929 SQ M/S

TABLE B5. THREE-DIMENSIONAL BOUNDARY LAYER PROFILES FOR RUN NUMBERS E7-02 AND E5-01.

RUN NUMBER E7-02
Q FREESTREAM = 24.50 M/S
KINEMATIC VISCOSITY
= 0.0000168 SQ M/S
FREESTREAM
ANGLE = 1.6 DEGREES

Y (CM)	Q (M/S)	ALPHA (DEGREES)
0.025	8.38	4.8
0.028	8.78	4.8
0.030	9.03	4.8
0.036	9.52	4.8
0.041	10.09	4.8
0.046	10.31	4.8
0.051	10.64	4.8
0.063	11.06	4.6
0.081	11.56	4.6
0.102	11.94	4.2
0.127	12.32	3.8
0.163	12.77	3.8
0.203	13.29	3.6
0.254	13.71	3.4
0.317	14.27	3.0
0.406	14.82	2.6
0.508	15.35	2.4
0.635	15.93	2.4
0.813	16.48	1.8
1.016	17.02	1.6
1.270	17.55	1.6
1.626	18.18	1.4
2.032	18.79	0.8
2.540	19.50	0.8
3.175	20.41	0.6
4.064	21.44	0.6
5.080	22.47	0.4
6.350	23.65	0.4
8.128	24.26	0.4
10.160	24.50	0.0
12.700	24.50	0.0

RUN NUMBER E5-01
Q FREESTREAM = 24.48 M/S
KINEMATIC VISCOSITY
= 0.0000168 SQ M/S
FREESTREAM
ANGLE = 3.4 DEGREES

Y (CM)	Q (M/S)	ALPHA (DEGREES)
0.025	8.51	9.4
0.028	9.15	9.4
0.030	9.63	9.4
0.036	9.97	9.4
0.041	10.20	9.4
0.046	10.42	9.4
0.051	10.63	9.4
0.069	11.05	9.0
0.081	11.45	8.6
0.104	11.84	8.0
0.127	12.22	8.0
0.163	12.58	7.2
0.203	12.94	6.6
0.254	13.45	6.6
0.317	13.94	5.6
0.406	14.42	5.0
0.508	14.96	4.6
0.635	15.48	4.0
0.813	16.19	3.6
1.016	16.68	3.2
1.270	17.01	3.0
1.626	17.73	2.6
2.032	18.48	2.0
2.540	19.14	2.0
3.175	20.12	1.8
4.064	21.16	1.2
5.080	22.25	0.8
6.350	23.29	0.6
8.128	24.24	0.6
10.160	24.48	0.0
12.700	24.48	0.0

CONVERSION FACTORS
1 IN. = 2.54 CM
1 FT/S = 0.3048 M/S
1 SQ FT/S = 0.0929 SQ M/S

TABLE B6. THREE-DIMENSIONAL BOUNDARY LAYER PROFILES FOR RUN NUMBERS E5-02 AND E3-01.

RUN NUMBER E5-02
Q FREESTREAM = 24.24 M/S
KINEMATIC VISCOSITY
= 0.0000167 SQ M/S
FREESTREAM
ANGLE = 3.4 DEGREES

Y (CM)	Q (M/S)	ALPHA (DEGREES)
0.025	8.64	9.2
0.028	8.77	9.2
0.030	9.02	9.2
0.036	9.51	9.2
0.041	9.97	9.2
0.046	10.31	9.2
0.051	10.63	9.0
0.063	10.74	9.0
0.081	11.45	8.6
0.102	11.65	7.8
0.127	12.03	7.4
0.163	12.58	6.8
0.203	13.11	6.6
0.254	13.45	6.4
0.317	13.94	5.6
0.406	14.26	5.0
0.508	14.89	4.6
0.635	15.55	4.4
0.813	15.91	3.6
1.016	16.74	3.2
1.270	17.14	2.8
1.626	17.79	2.6
2.032	18.48	2.0
2.540	19.02	1.6
3.175	20.06	1.6
4.064	20.94	1.2
5.080	22.15	1.0
6.350	23.39	0.4
8.128	23.77	-0.2
10.160	24.24	-0.4
12.700	24.24	0.0

RUN NUMBER E3-01
Q FREESTREAM = 24.49 M/S
KINEMATIC VISCOSITY
= 0.0000168 SQ M/S
FREESTREAM
ANGLE = 6.4 DEGREES

Y (CM)	Q (M/S)	ALPHA (DEGREES)
0.025	8.77	18.0
0.028	9.28	18.0
0.030	9.63	18.0
0.036	10.20	18.0
0.041	10.53	18.0
0.046	10.85	17.4
0.051	11.16	17.4
0.063	11.46	16.8
0.081	11.84	16.2
0.102	12.04	15.6
0.127	12.41	15.0
0.163	12.77	14.2
0.203	13.12	13.0
0.254	13.54	12.6
0.317	13.95	11.6
0.406	14.66	10.4
0.508	15.12	9.4
0.635	15.56	8.4
0.813	15.92	7.0
1.016	16.55	6.4
1.270	17.02	5.8
1.626	17.80	4.8
2.032	18.49	4.0
2.540	19.15	3.2
3.175	19.90	2.4
4.064	21.43	2.2
5.080	22.26	1.8
6.350	23.26	0.6
8.128	24.26	0.2
10.160	24.49	0.2
12.700	24.49	0.0

CONVERSION FACTORS
1 IN. = 2.54 CM
1 FT/S = 0.3048 M/S
1 SQ FT/S = 0.0929 SQ M/S

TABLE B7. THREE-DIMENSIONAL BOUNDARY LAYER PROFILES FOR RUN NUMBERS E3-03 AND E3-03P.

RUN NUMBER E3-03
Q FREESTREAM = 24.51 M/S
KINEMATIC VISCOSITY
= 0.0000167 SQ M/S
FREESTREAM
ANGLE = 6.4 DEGREES

Y (CM)	Q (M/S)	ALPHA (DEGREES)
0.025	9.03	18.0
0.028	9.28	18.0
0.030	9.52	18.0
0.033	9.76	18.0
0.036	9.99	18.0
0.041	10.54	18.0
0.046	10.75	17.8
0.051	10.96	17.2
0.063	11.37	16.8
0.081	11.85	16.2
0.102	12.23	15.6
0.127	12.59	15.0
0.163	13.04	14.2
0.203	13.30	13.0
0.254	13.63	12.2
0.317	14.12	11.4
0.406	14.59	10.6
0.508	15.20	9.4
0.635	15.79	8.4
0.813	16.28	7.8
1.016	16.83	6.4
1.270	17.29	5.8
1.626	17.94	4.8
2.032	18.68	4.2
2.540	19.28	3.4
3.175	20.25	2.6
4.064	21.29	2.0
5.080	22.38	1.4
6.350	23.52	0.6
8.128	24.04	0.2
10.160	24.51	0.2
12.700	24.51	0.0

RUN NUMBER E3-03P
Q FREESTREAM = 24.51 M/S
KINEMATIC VISCOSITY
= 0.0000167 SQ M/S
FREESTREAM
ANGLE = 6.4 DEGREES

Y (CM)	Q (M/S)	ALPHA (DEGREES)
0.025	9.20	18.0
0.028	9.42	18.0
0.030	9.64	18.0
0.033	9.85	18.0
0.036	10.05	18.0
0.041	10.58	18.0
0.046	10.81	17.8
0.051	11.06	17.2
0.063	11.50	16.8
0.081	11.97	16.2
0.102	12.34	15.6
0.127	12.69	15.0
0.163	13.12	14.2
0.203	13.36	13.0
0.254	13.70	12.2
0.317	14.14	11.4
0.406	14.58	10.6
0.508	15.14	9.4
0.635	15.70	8.4
0.813	16.18	7.8
1.016	16.74	6.4
1.270	17.20	5.8
1.626	17.85	4.8
2.032	18.60	4.2
2.540	19.21	3.4
3.175	20.19	2.6
4.064	21.24	2.0
5.080	22.34	1.4
6.350	23.48	0.6
8.128	24.02	0.2
10.160	24.50	0.2
12.700	24.51	0.0

CONVERSION FACTORS
1 IN. = 2.54 CM
1 FT/S = 0.3048 M/S
1 SQ FT/S = 0.0929 SQ M/S

TABLE 88. THREE-DIMENSIONAL BOUNDARY LAYER PROFILES FOR RUN NUMBERS E1-01 AND E1-02.

RUN NUMBER E1-01
Q FREESTREAM = 26.08 M/S
KINEMATIC VISCOSITY
= 0.0000169 SQ M/S
FREESTREAM
ANGLE = 11.0 DEGREES

Y (CM)	Q (M/S)	ALPHA (DEGREES)
0.025	12.05	25.0
0.028	12.87	25.0
0.030	13.13	25.0
0.036	13.47	25.2
0.041	13.88	25.2
0.046	14.21	25.4
0.051	14.44	25.4
0.063	14.98	25.2
0.081	15.36	25.2
0.102	15.65	25.4
0.127	15.87	24.2
0.163	16.08	23.6
0.203	16.29	22.4
0.254	16.50	21.4
0.317	16.63	19.8
0.406	16.90	17.6
0.508	17.30	15.8
0.635	17.69	13.4
0.813	18.14	11.4
1.016	18.63	9.4
1.270	19.23	7.6
1.626	19.87	6.0
2.032	20.54	4.6
2.540	21.24	3.8
3.175	22.03	2.6
4.064	23.04	1.6
5.080	23.57	1.4
6.350	24.75	0.6
8.128	25.87	0.2
10.160	26.08	-0.2
12.700	26.08	0.0

RUN NUMBER E1-02
Q FREESTREAM = 26.09 M/S
KINEMATIC VISCOSITY
= 0.0000169 SQ M/S
FREESTREAM
ANGLE = 10.6 DEGREES

Y (CM)	Q (M/S)	ALPHA (DEGREES)
0.025	12.24	24.8
0.028	12.87	24.8
0.030	13.13	25.2
0.036	13.56	25.2
0.041	13.97	25.4
0.046	14.37	25.8
0.051	14.60	25.6
0.063	15.06	25.6
0.081	15.65	25.6
0.102	15.94	25.6
0.127	16.15	25.2
0.163	16.29	24.0
0.203	16.50	23.0
0.254	16.64	21.8
0.317	16.91	20.4
0.406	17.11	17.8
0.508	17.37	16.4
0.635	17.82	14.0
0.813	18.20	11.8
1.016	18.69	9.8
1.270	19.17	8.0
1.626	19.87	6.0
2.032	20.54	5.2
2.540	21.08	3.6
3.175	22.09	2.8
4.064	23.24	1.8
5.080	23.58	1.2
6.350	24.75	1.0
8.128	25.87	-0.2
10.160	26.09	0.0
12.700	26.09	0.0

CONVERSION FACTORS
1 IN. = 2.54 CM
1 FT/S = 0.3048 M/S
1 SQ FT/S = 0.0929 SQ M/S

TABLE B9. THREE-DIMENSIONAL BOUNDARY LAYER PROFILES FOR RUN NUMBERS G7-01 AND G5-01.

RUN NUMBER G7-01
Q FREESTREAM = 25.17 M/S
KINEMATIC VISCOSITY = 0.0000168 SQ M/S
FREESTREAM ANGLE = 2.0 DEGREES

Y (CM)	Q (M/S)	ALPHA (DEGREES)
0.025	9.03	3.8
0.028	9.75	3.8
0.030	9.98	3.8
0.036	10.53	3.8
0.041	10.85	3.8
0.046	11.06	3.4
0.051	11.26	3.6
0.063	11.84	3.6
0.081	12.31	3.4
0.102	12.77	3.4
0.127	13.37	3.2
0.163	13.79	3.0
0.196	14.11	3.0
0.246	14.66	2.4
0.310	15.19	2.4
0.399	15.71	2.0
0.500	16.13	2.0
0.627	16.75	1.6
0.805	17.22	1.6
1.008	17.67	1.4
1.262	18.30	1.2
1.618	18.79	1.0
2.024	19.44	0.8
2.532	20.18	0.6
3.167	20.95	0.6
4.056	21.91	0.4
5.072	22.82	0.4
6.342	23.79	0.4
8.120	24.72	0.0
10.152	25.17	0.0
12.692	25.17	0.0

RUN NUMBER G5-01
Q FREESTREAM = 24.94 M/S
KINEMATIC VISCOSITY = 0.0000168 SQ M/S
FREESTREAM ANGLE = 2.4 DEGREES

Y (CM)	Q (M/S)	ALPHA (DEGREES)
0.025	9.51	7.4
0.028	9.98	7.4
0.030	10.18	7.4
0.036	10.63	7.4
0.041	11.05	7.4
0.046	11.35	7.4
0.051	11.45	7.4
0.063	11.84	7.0
0.081	12.40	7.0
0.127	13.28	6.0
0.163	13.70	5.8
0.203	14.19	5.6
0.254	14.58	4.8
0.317	15.04	4.8
0.406	15.70	4.6
0.508	16.20	4.4
0.635	16.68	3.8
0.813	17.14	3.2
1.016	17.73	2.8
1.270	18.29	2.6
1.626	18.78	2.0
2.032	19.38	2.0
2.540	20.06	2.0
3.175	20.95	1.6
4.064	21.90	1.4
5.080	22.95	1.2
6.350	23.30	0.4
8.128	24.71	0.4
10.160	24.94	0.2
12.700	24.94	0.0

CONVERSION FACTORS
1 IN. = 2.54 CM
1 FT/S = 0.3048 M/S
1 SQ FT/S = 0.0929 SQ M/S

TABLE B10. THREE-DIMENSIONAL BOUNDARY LAYER PROFILES FOR RUN NUMBERS G3-01 AND G1-01.

RUN NUMBER G3-01
Q FREESTREAM = 25.40 M/S
KINEMATIC VISCOSITY
= 0.0000168 SQ M/S
FREESTREAM
ANGLE = 4.2 DEGREES

Y (CM)	Q (M/S)	ALPHA (DEGREES)
0.025	10.31	9.2
0.028	10.64	9.2
0.030	10.74	9.2
0.036	11.16	9.6
0.041	11.66	9.6
0.046	11.85	9.6
0.051	12.22	9.6
0.063	12.59	8.8
0.081	13.29	8.8
0.102	13.46	8.8
0.127	13.95	8.4
0.163	14.43	8.0
0.203	14.74	7.6
0.254	15.04	6.8
0.317	15.64	6.8
0.406	16.21	6.2
0.508	16.62	5.6
0.635	17.15	4.8
0.813	17.61	4.6
1.016	18.06	4.0
1.270	18.55	3.6
1.626	19.09	3.2
2.032	19.79	2.8
2.540	21.28	2.2
3.175	21.28	1.8
4.064	22.32	1.0
5.080	23.31	1.0
6.350	23.79	0.2
8.128	24.95	-0.2
10.160	25.40	0.0
12.700	25.40	0.0

RUN NUMBER G1-01
Q FREESTREAM = 26.46 M/S
KINEMATIC VISCOSITY
= 0.0000168 SQ M/S
FREESTREAM
ANGLE = 4.8 DEGREES

Y (CM)	Q (M/S)	ALPHA (DEGREES)
0.025	11.64	10.8
0.028	12.02	10.8
0.030	12.39	10.8
0.036	13.27	10.8
0.041	13.44	11.2
0.046	13.69	11.4
0.051	13.94	11.0
0.063	14.57	11.0
0.081	15.03	11.0
0.102	15.47	10.8
0.127	15.76	10.4
0.163	16.19	10.4
0.203	16.53	9.8
0.254	16.94	9.6
0.317	17.33	9.0
0.406	17.66	8.8
0.508	18.10	7.8
0.635	18.53	7.0
0.813	18.95	6.0
1.016	19.36	5.6
1.270	19.82	4.8
1.626	20.39	3.8
2.032	20.99	3.4
2.540	21.68	3.0
3.175	22.45	2.2
4.064	23.38	1.8
5.080	23.77	1.2
6.350	24.69	1.2
8.128	26.03	0.2
10.160	26.46	0.8
12.700	26.46	0.0

CONVERSION FACTORS
1 IN. = 2.54 CM
1 FT/S = 0.3048 M/S
1 SQ FT/S = 0.0929 SQ M/S

TABLE B11. THREE-DIMENSIONAL BOUNDARY LAYER PROFILES FOR RUN NUMBERS G-1-01 AND G-3-01.

RUN NUMBER G-1-01
Q FREESTREAM = 27.89 M/S
KINEMATIC VISCOSITY
= 0.0000167 SQ M/S
FREESTREAM
ANGLE = 3.6 DEGREES

Y (CM)	Q (M/S)	ALPHA (DEGREES)
0.025	13.09	6.8
0.028	13.76	6.8
0.030	14.08	7.4
0.036	14.86	7.4
0.041	15.31	8.0
0.046	15.60	7.8
0.051	15.89	7.8
0.063	16.58	8.2
0.081	17.12	8.2
0.102	17.77	9.0
0.127	18.14	9.2
0.163	18.63	9.4
0.203	19.11	9.2
0.254	19.46	9.2
0.317	19.92	9.2
0.406	20.20	7.6
0.508	20.48	8.0
0.635	20.70	7.4
0.813	21.07	6.2
1.016	21.34	5.2
1.270	21.76	4.4
1.626	22.07	3.2
2.032	22.62	2.8
2.540	23.16	2.0
3.175	23.26	1.2
4.064	24.21	1.0
5.080	25.12	0.6
6.350	26.22	0.0
8.128	27.28	-0.4
10.160	27.89	0.0
12.700	27.89	0.0

RUN NUMBER G-3-01
Q FREESTREAM = 28.48 M/S
KINEMATIC VISCOSITY
= 0.0000167 SQ M/S
FREESTREAM
ANGLE = -0.4 DEGREES

Y (CM)	Q (M/S)	ALPHA (DEGREES)
0.025	12.74	1.6
0.028	13.59	1.6
0.030	13.92	1.8
0.036	14.71	2.4
0.041	15.23	2.8
0.046	15.60	2.8
0.051	15.81	2.8
0.063	16.58	2.8
0.081	17.18	4.0
0.102	17.76	4.0
0.127	18.26	5.0
0.163	18.99	5.8
0.203	19.57	6.2
0.254	20.14	6.8
0.317	20.63	7.2
0.406	21.23	7.2
0.508	21.54	7.0
0.635	21.85	6.4
0.813	22.06	5.0
1.016	22.26	4.2
1.270	22.46	3.0
1.626	22.91	2.0
2.032	23.20	1.0
2.540	23.73	0.6
3.175	23.73	0.4
4.064	24.89	0.0
5.080	25.78	0.0
6.350	26.85	0.0
8.128	28.08	0.0
10.160	28.48	0.0
12.700	28.48	0.0

CONVERSION FACTORS
1 IN. = 2.54 CM
1 FT/S = 0.3048 M/S
1 SQ FT/S = 0.0929 SQ M/S

TABLE B12. THREE-DIMENSIONAL BOUNDARY LAYER PROFILES FOR RUN NUMBERS G-5-01 AND I7-01.

RUN NUMBER G-5-01
Q FREESTREAM = 27.87 M/S
KINEMATIC VISCOSITY
= 0.0000167 SQ M/S
FREESTREAM
ANGLE = -3.3 DEGREES

Y (CM)	Q (M/S)	ALPHA (DEGREES)
0.025	11.43	-2.8
0.028	11.63	-2.8
0.030	11.91	-2.8
0.036	12.73	-2.8
0.041	13.17	-2.8
0.046	13.59	-1.4
0.051	13.92	-1.4
0.063	14.55	-1.0
0.081	15.16	-0.2
0.102	15.74	0.4
0.127	16.30	0.8
0.163	17.11	1.6
0.203	17.76	2.2
0.254	18.50	3.0
0.317	19.10	4.0
0.406	19.91	4.6
0.508	20.52	5.2
0.635	20.96	4.6
0.813	21.28	4.4
1.016	21.49	3.2
1.270	21.54	2.0
1.626	21.95	0.8
2.032	22.26	0.0
2.540	22.81	-0.8
3.175	23.59	-1.2
4.064	23.97	-1.2
5.080	25.11	-0.8
6.350	26.21	-0.4
8.128	27.47	-0.4
10.160	27.87	-0.2
12.700	27.87	0.0

RUN NUMBER I7-01
Q FREESTREAM = 25.46 M/S
KINEMATIC VISCOSITY
= 0.0000170 SQ M/S
FREESTREAM
ANGLE = -6.1 DEGREES

Y (CM)	Q (M/S)	ALPHA (DEGREES)
0.025	9.30	3.6
0.028	9.89	3.6
0.030	10.23	3.6
0.036	10.88	3.6
0.041	11.29	3.6
0.046	11.49	3.6
0.051	11.88	3.6
0.063	12.25	3.6
0.081	12.80	3.2
0.102	13.24	3.2
0.127	13.66	2.8
0.163	14.07	2.8
0.203	14.55	2.6
0.254	15.01	2.4
0.317	15.53	2.2
0.406	16.04	2.2
0.495	16.66	1.8
0.622	17.20	1.8
0.800	17.65	1.4
1.003	18.16	1.2
1.257	18.66	1.2
1.613	19.26	1.0
2.019	19.84	0.8
2.527	20.57	0.8
3.162	21.44	0.8
4.051	22.32	0.6
5.067	23.12	0.4
6.337	24.09	0.4
8.115	25.24	0.2
10.147	25.46	0.0
12.687	25.46	0.0

CONVERSION FACTORS
1 IN. = 2.54 CM
1 FT/S = 0.3048 M/S
1 SQ FT/S = 0.0929 SQ M/S

TABLE B13. THREE-DIMENSIONAL BOUNDARY LAYER PROFILES FOR RUN NUMBERS I7-02 AND I5-01.

RUN NUMBER I7-02
Q FREESTREAM = 25.37 M/S
KINEMATIC VISCOSITY
= 0.0000168 SQ M/S
FREESTREAM
ANGLE = -6.5 DEGREES

Y (CM)	Q (M/S)	ALPHA (DEGREES)
0.025	9.51	3.8
0.028	9.97	3.8
0.030	10.20	3.8
0.036	10.63	3.8
0.041	11.05	3.8
0.046	11.45	3.8
0.051	11.74	3.8
0.063	12.21	3.8
0.081	12.75	3.4
0.102	13.10	3.2
0.127	13.61	3.2
0.163	14.10	3.0
0.203	14.57	3.0
0.254	15.03	2.4
0.317	15.47	2.4
0.406	16.05	2.2
0.508	16.60	2.0
0.635	17.14	2.0
0.813	17.72	1.8
1.016	18.16	1.4
1.270	18.65	1.4
1.626	19.25	1.4
2.032	19.94	1.2
2.540	20.61	1.4
3.175	21.42	0.6
4.064	22.40	1.2
5.080	23.38	0.6
6.350	24.24	1.0
8.128	24.93	0.8
10.160	25.37	0.4
12.700	25.37	0.0

RUN NUMBER I5-01
Q FREESTREAM = 25.64 M/S
KINEMATIC VISCOSITY
= 0.0000169 SQ M/S
FREESTREAM
ANGLE = -8.1 DEGREES

Y (CM)	Q (M/S)	ALPHA (DEGREES)
0.025	9.52	4.8
0.028	10.21	4.8
0.030	10.65	4.8
0.036	11.06	4.8
0.041	11.56	4.8
0.046	11.86	4.8
0.051	12.05	4.8
0.063	12.51	4.6
0.081	13.12	4.4
0.102	13.47	4.4
0.127	13.80	4.4
0.163	14.36	4.4
0.203	14.83	4.0
0.254	15.21	3.8
0.317	15.79	3.4
0.406	16.22	3.2
0.495	16.83	3.0
0.622	17.30	2.6
0.800	17.75	2.4
1.003	18.25	2.4
1.257	18.75	2.2
1.613	19.34	2.0
2.019	19.97	1.8
2.527	20.64	1.4
3.162	21.40	1.4
4.051	22.43	1.4
5.067	23.33	0.8
6.337	24.28	0.8
8.115	25.19	0.8
10.147	25.64	0.2
12.687	25.64	0.0

CONVERSION FACTORS
1 IN. = 2.54 CM
1 FT/S = 0.3048 M/S
1 SQ FT/S = 0.0929 SQ M/S

TABLE B14. THREE-DIMENSIONAL BOUNDARY LAYER PROFILES FOR RUN NUMBERS I3-01 AND I1-01.

RUN NUMBER I3-01
Q FREESTREAM = 25.78 M/S
KINEMATIC VISCOSITY
= 0.0000167 SQ M/S
FREESTREAM
ANGLE = -7.9 DEGREES

Y (CM)	Q (M/S)	ALPHA (DEGREES)
0.025	10.82	6.0
0.028	10.93	6.0
0.030	11.33	6.0
0.036	11.82	6.0
0.041	12.10	6.0
0.046	12.29	6.0
0.051	12.56	6.0
0.063	13.00	5.4
0.081	13.59	5.4
0.102	14.00	5.4
0.127	14.40	5.4
0.163	14.86	5.0
0.203	15.31	4.8
0.254	15.67	4.6
0.317	16.24	4.4
0.406	16.78	4.0
0.508	17.11	3.8
0.635	17.70	3.2
0.813	18.20	2.8
1.016	18.81	2.8
1.270	19.22	2.4
1.626	19.69	2.2
2.032	20.36	2.0
2.540	20.91	1.8
3.175	21.70	1.2
4.064	22.77	1.2
5.080	23.73	0.8
6.350	24.44	0.6
8.128	25.56	0.4
10.160	25.78	0.4
12.700	25.78	0.0

RUN NUMBER I1-01
Q FREESTREAM = 26.44 M/S
KINEMATIC VISCOSITY
= 0.0000167 SQ M/S
FREESTREAM
ANGLE = -4.1 DEGREES

Y (CM)	Q (M/S)	ALPHA (DEGREES)
0.025	11.03	4.6
0.028	11.23	4.6
0.030	11.53	4.6
0.036	12.11	5.2
0.041	12.56	5.6
0.046	12.92	4.8
0.051	13.09	5.4
0.063	13.76	4.8
0.081	14.32	5.2
0.102	14.79	4.8
0.127	15.16	5.2
0.163	15.68	5.0
0.203	16.03	4.8
0.254	16.58	4.4
0.317	17.05	4.4
0.406	17.57	4.4
0.508	18.02	4.2
0.635	18.39	3.8
0.813	18.93	3.4
1.016	19.35	3.0
1.270	19.86	2.6
1.626	20.37	2.2
2.032	20.97	2.2
2.540	21.60	1.8
3.175	22.37	1.6
4.064	23.31	1.4
5.080	23.74	1.0
6.350	24.90	2.8
8.128	26.01	0.0
10.160	26.44	-0.2
12.700	26.44	0.0

CONVERSION FACTORS
1 IN. = 2.54 CM
1 FT/S = 0.3048 M/S
1 SQ FT/S = 0.0929 SQ M/S

TABLE B15. THREE-DIMENSIONAL BOUNDARY LAYER PROFILES FOR RUN NUMBERS I-1-01 AND I-3-01.

RUN NUMBER I-1-01
Q FREESTREAM = 27.10 M/S
KINEMATIC VISCOSITY
= 0.0000168 SQ M/S
FREESTREAM
ANGLE = 1.6 DEGREES

Y (CM)	Q (M/S)	ALPHA (DEGREES)
0.025	11.45	1.6
0.028	11.55	2.2
0.030	11.74	2.2
0.036	12.58	2.2
0.041	13.10	2.8
0.046	13.36	2.8
0.051	13.69	2.8
0.063	14.34	2.8
0.081	14.96	3.0
0.102	15.40	3.0
0.127	15.91	3.2
0.163	16.40	3.8
0.203	16.87	3.8
0.254	17.40	4.0
0.317	17.79	3.8
0.406	18.41	3.8
0.508	18.84	3.8
0.635	19.25	5.2
0.813	19.77	2.8
1.016	20.11	2.8
1.270	20.61	2.2
1.626	21.05	2.0
2.032	21.63	1.8
2.540	22.20	1.4
3.175	22.99	1.2
4.064	23.53	0.8
5.080	24.47	0.8
6.350	25.38	0.4
8.128	26.68	0.2
10.160	27.10	0.0
12.700	27.10	0.0

RUN NUMBER I-3-01
Q FREESTREAM = 27.11 M/S
KINEMATIC VISCOSITY
= 0.0000168 SQ M/S
FREESTREAM
ANGLE = 0.0 DEGREES

Y (CM)	Q (M/S)	ALPHA (DEGREES)
0.025	11.45	-0.4
0.028	11.65	-0.4
0.030	12.03	-0.4
0.036	12.84	-0.4
0.041	13.28	-0.4
0.046	13.53	-0.4
0.051	13.78	0.2
0.063	14.34	0.4
0.081	15.04	-0.8
0.102	15.48	-1.2
0.127	15.98	-1.4
0.163	16.61	-0.6
0.203	17.14	-0.6
0.254	17.73	1.8
0.317	18.17	2.4
0.406	18.72	2.6
0.508	19.25	2.2
0.635	19.54	2.4
0.813	20.00	2.4
1.016	20.34	2.2
1.270	20.83	1.4
1.626	21.37	1.4
2.032	21.99	0.8
2.540	22.40	0.8
3.175	23.20	0.6
4.064	23.77	0.6
5.080	24.70	0.6
6.350	25.60	0.4
8.128	26.69	0.2
10.160	27.11	0.2
12.700	27.11	0.0

CONVERSION FACTORS
1 IN. = 2.54 CM
1 FT/S = 0.3048 M/S
1 SQ FT/S = 0.0929 SQ M/S

TABLE B16. THREE-DIMENSIONAL BOUNDARY LAYER PROFILE FOR RUN NUMBERS I-5-01.

RUN NUMBER I-5-01
Q FREESTREAM = 26.90 M/S
KINEMATIC VISCOSITY
= 0.0000168 SQ M/S
FREESTREAM
ANGLE = -1.6 DEGREES

Y (CM)	Q (M/S)	ALPHA (DEGREES)
0.025	10.53	-3.2
0.028	11.05	-3.2
0.030	11.55	-3.2
0.036	12.12	-3.2
0.041	12.31	-2.4
0.046	12.76	-2.4
0.051	13.02	-0.2
0.063	13.54	-2.6
0.081	14.27	-2.2
0.102	14.81	-2.2
0.127	15.34	-1.4
0.163	15.92	-1.2
0.203	16.41	-1.2
0.254	17.08	-0.4
0.317	17.67	0.0
0.406	18.36	0.4
0.508	18.91	0.4
0.635	19.38	1.0
0.813	19.84	1.0
1.016	20.24	0.8
1.270	20.62	0.6
1.626	21.11	0.2
2.032	21.80	0.2
2.540	22.31	0.0
3.175	23.01	0.0
4.064	23.30	0.4
5.080	24.48	0.4
6.350	25.39	0.4
8.128	26.48	0.0
10.160	26.90	0.0
12.700	26.90	0.0

CONVERSION FACTORS
1 IN. = 2.54 CM
1 FT/S = 0.3048 M/S
1 SQ FT/S = 0.0929 SQ M/S

Table B17

Three-Dimensional Wall Shear Stress Measurements

Station	Re_{unit} x 10^5(m^{-1})	ρ(kg/m^3)	τ_w(Pa)	β(degrees)
A9	1.369	1.115	0.79	1.1
A9	1.369	1.115	0.79	1.1
A7	1.375	1.115	0.69	1.5
A7	1.375	1.115	0.68	0.9
A5	1.363	1.113	0.41	3.7
A5	1.363	1.113	0.43	3.0
A4	1.347	1.104	0.25	5.4
A3	1.372	1.115	0.03	120.5
A3	1.372	1.115	0.04	120.8
A2	1.347	1.104	0.07	162.3
A1	1.342	1.100	1.51	178.7
B4	1.347	1.104	0.39	36.0
B3	1.347	1.104	0.37	74.3
B2	1.346	1.102	0.58	81.3
B1	1.343	1.100	1.72	67.7
C9	1.366	1.110	0.81	5.4
C9	1.366	1.110	0.81	5.3
C7	1.366	1.110	0.72	10.6
C7	1.366	1.110	0.71	11.1
C6	1.346	1.102	0.64	17.0
C5	1.366	1.110	0.60	71.2
C5	1.366	1.110	0.60	71.5
C4	1.346	1.102	0.58	42.0
C3	1.366	1.110	0.69	61.9
C3	1.366	1.110	0.69	61.9
C3	1.346	1.102	0.67	61.1
-C3	1.347	1.104	0.69	-56.2
C2	1.342	1.100	0.97	65.0
C1	1.346	1.100	1.87	76.3
D6	1.346	1.102	0.73	17.0
D5	1.342	1.100	0.71	25.4
D4	1.342	1.100	0.74	35.8
D3	1.346	1.102	0.86	46.7
D2	1.342	1.100	1.14	51.1
D1	1.342	1.100	1.78	40.1

Conversion Factors

ft^{-1} = 3.281 m^{-1}

lbm/ft^3 = 16.026 kg/m^3

lbf/ft^2 = 47.847 Pa

Table B17 (continued)

Three-Dimensional Wall Shear Stress Measurements

Station	$Re_{unit} \times 10^5 (m^{-1})$	$\rho (kg/m^3)$	τ_w (Pa)	β (degrees)
D0	1.346	1.102	1.97	47.1
E9	1.365	1.110	0.87	7.3
E9	1.365	1.110	0.87	7.4
E7	1.346	1.102	0.83	13.0
E7	1.346	1.102	0.85	12.7
E6	1.342	1.100	0.81	16.7
E5	1.349	1.104	0.85	22.6
E5	1.349	1.104	0.85	22.6
E4	1.342	1.100	0.86	28.2
E3	1.349	1.104	1.01	34.4
E3	1.349	1.104	1.01	34.6
E3	1.346	1.102	0.99	34.8
-E3	1.347	1.104	1.04	-31.8
E2	1.346	1.102	1.17	36.1
E1	1.349	1.104	1.60	30.2
E1	1.349	1.104	1.61	30.0
E0	1.342	1.100	1.64	24.9
E-1	1.342	1.100	1.63	23.3
E-1	1.342	1.100	1.65	24.4
E-3	1.341	1.099	1.44	15.8
E-5	1.345	1.100	1.46	15.2
F6	1.345	1.100	0.87	15.2
F5	1.341	1.099	0.90	19.5
F4	1.341	1.099	0.95	22.6
F3	1.341	1.099	1.03	25.8
F2	1.341	1.099	1.19	25.7
F1	1.341	1.099	1.42	21.5
F0	1.341	1.099	1.45	17.4
F-1	1.341	1.099	1.42	12.4
F-3	1.341	1.099	1.32	5.6
F-5	1.341	1.099	1.28	1.5
G9	1.349	1.104	0.94	7.1
G9	1.349	1.104	0.93	7.4
G7	1.346	1.102	0.94	16.8
G7	1.346	1.102	0.93	16.8

Conversion Factors

$ft^{-1} = 3.281\ m^{-1}$

$lbm/ft^3 = 16.026\ kg/m^3$

$lbf/ft^2 = 47.847\ Pa$

Table B17 (continued)

Three-Dimensional Wall Shear Stress Measurements

Station	$Re_{unit} \times 10^5 (m^{-1})$	$\rho (kg/m^3)$	τ_w (Pa)	β (degrees)
G6	1.341	1.099	0.92	12.8
G5	1.349	1.104	0.98	14.8
G5	1.349	1.104	0.98	15.2
G4	1.341	1.099	0.99	17.3
G3	1.350	1.105	1.10	18.2
G3	1.350	1.105	1.10	18.1
G3	1.345	1.102	1.10	18.0
G3	1.346	1.102	1.09	18.3
-G3	1.346	1.102	1.12	-17.6
G2	1.341	1.099	1.19	18.1
G1	1.346	1.104	1.35	14.3
G1	1.346	1.104	1.34	14.3
G-1	1.352	1.105	1.38	7.1
G-1	1.352	1.105	1.38	8.0
G-1	1.352	1.105	1.38	7.9
G-3	1.349	1.104	1.26	-2.2
G-3	1.349	1.104	1.27	-2.1
G-5	1.349	1.104	1.20	-9.9
G-5	1.349	1.104	1.20	-10.0
H1	1.345	1.102	1.26	10.5
H-1	1.342	1.100	1.24	5.3
H-3	1.342	1.100	1.19	-1.9
H-5	1.342	1.100	1.15	-8.8
I9	1.352	1.105	0.98	5.7
I9	1.352	1.105	0.98	6.0
I7	1.349	1.104	0.99	7.4
I7	1.349	1.104	1.00	8.0
I5	1.349	1.104	1.03	10.2
I5	1.349	1.104	1.03	9.9
I3	1.349	1.104	1.11	9.8
I3	1.349	1.104	1.10	9.9
I1	1.349	1.104	1.24	6.1
I1	1.349	1.104	1.23	6.9
I-1	1.349	1.104	1.24	2.1

Conversion Factors

$ft^{-1} = 3.281\ m^{-1}$

$lbm/ft^3 = 16.026\ kg/m^3$

$lbf/ft^2 = 47.847\ Pa$

Table B17 (continued)

Three-Dimensional Wall Shear Stress Measurements

Station	$Re_{unit} \times 10^5 (m^{-1})$	$\rho (kg/m^3)$	τ_w (Pa)	β (degrees)
I-1	1.349	1.104	1.25	2.5
I-1	1.342	1.100	1.20	3.5
I-3	1.349	1.104	1.21	-3.0
I-3	1.349	1.104	1.22	-2.7
I-5	1.346	1.100	1.16	-7.8
I-5	1.346	1.100	1.16	-8.0
J-1	1.345	1.102	1.17	2.0
J-2	1.345	1.102	1.17	-0.8
K-1	1.345	1.102	1.15	1.5

Conversion Factors

$ft^{-1} = 3.281\ m^{-1}$

$lbm/ft^3 = 16.026\ kg/m^3$

$lbf/ft^2 = 47.847\ Pa$

Table B18

Three-Dimensional Gradient and Angle Data

Station	$\partial P/\partial x$ (kPa/m)	$\partial P/\partial y$ (kPa/m)	$\partial \tau_w/\partial y$ (Pa/m)	$\partial \tau_w/\partial y$ (Pa/m)	$\partial \beta/\partial x$ (radiaus/m)	$\partial \beta/\partial y$ (radiaus/m)	β (degrees)
A7	0.31	-0.02	-4.02	-0.01	0.13	1.13	1.5
A5	0.61	-0.03	-6.29	3.77	0.32	3.18	3.4
C7	0.02	-0.14	-2.58	1.53	1.11	0.58	10.9
C5	0.53	-0.29	-0.68	4.10	2.68	1.01	26.4
C3	0.08	-0.69	3.22	9.78	4.29	-2.93	61.7
E7	0.14	-0.22	-0.76	2.35	1.08	0.27	12.1
E5	0.10	-0.43	1.88	3.82	1.41	0.77	22.5
E3	-0.31	-0.83	5.81	3.56	0.56	-2.25	34.5
E1	-1.34	-0.61	10.29	-6.70	-1.08	-1.91	30.1
G7	-0.13	-0.27	0.58	2.09	0.51	0.26	16.8
G5	-0.05	-0.45	2.65	2.38	0.24	-1.16	15.0
G3	-0.36	-0.39	3.11	0.37	-0.13	-1.39	18.2
G1	-0.71	-0.21	2.31	-3.67	-0.51	-1.27	14.3
G-1	-0.79	1.16	0.60	-3.07	-0.83	-0.78	7.9
G-3	-0.24	1.48	-1.64	-2.54	-1.00	-1.03	-2.1
G-5	1.27	0.63	-3.99	-3.16	-0.92	-1.34	-9.2
I7			0.70	0.32	0.26	0.67	7.2
I5			1.43	-0.88	0.11	1.06	10.1
I3			1.62	1.54	-0.17	-1.86	9.9
I1			1.27	-0.33	-0.43	-0.77	6.5
I-1	-0.31	0.47	0.42	-0.57	-0.56	0.13	2.3
I-3	-0.10	0.66	0.83	1.33	-0.53	0.85	-2.8
I-5	0.34	0.42	-2.37	2.69	-0.27	1.70	-7.9

Conversion Factors

kPa/m = 6.366 lbf/ft^3

Pa/m = 6.366 x 10^{-3} lbf/ft^3

radiaus/m = 0.3048 radiaus/ft

Table B19

Tunnel Reynolds Numbers for Three-Dimensional Velocity Profiles

Run	$Re_{unit} \times 10^5 (m^{-1})$
A7-01	1.366
A7-03	1.350
A7-03P	1.350
A5-01	1.370
C7-01	1.360
C5-01	1.366
C3-01	1.362
E7-01	1.353
E7-02	1.346
E5-01	1.347
E5-02	1.352
E3-01	1.347
E3-03	1.347
E3-03P	1.347
E1-01	1.340
E1-02	1.331
G7-01	1.349
G5-01	1.348
G3-01	1.346
G1-01	1.353
G-1-01	1.357
G-3-01	1.359
G-5-01	1.360
I7-01	1.330
I7-02	1.349
I5-01	1.339
I3-01	1.355
I1-01	1.360
I-1-01	1.354
I-3-01	1.346
I-5-01	1.347

Conversion Factor

$ft^{-1} = 3.281\ m^{-1}$

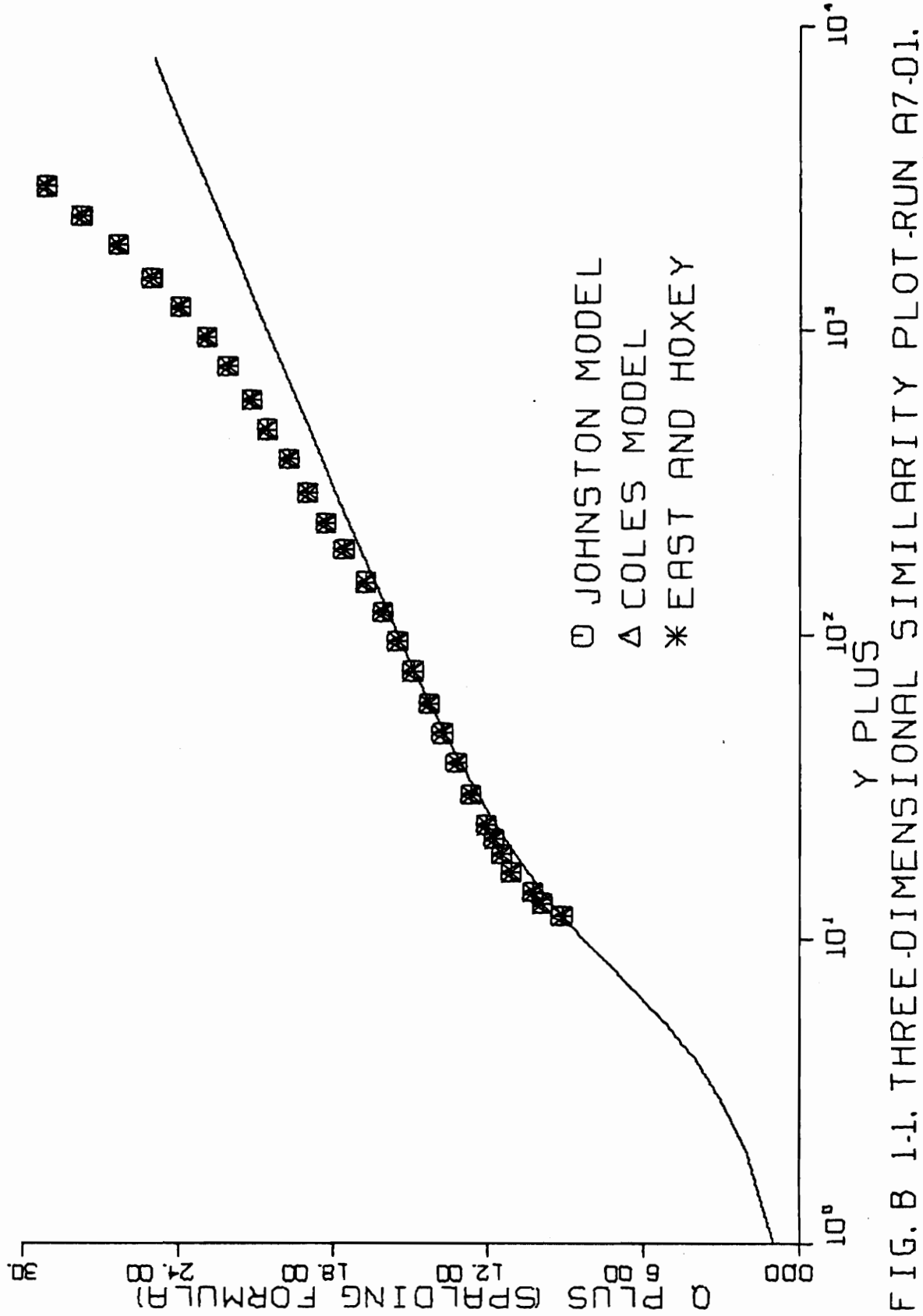

FIG. B 1-1. THREE-DIMENSIONAL SIMILARITY PLOT-RUN A7-01.

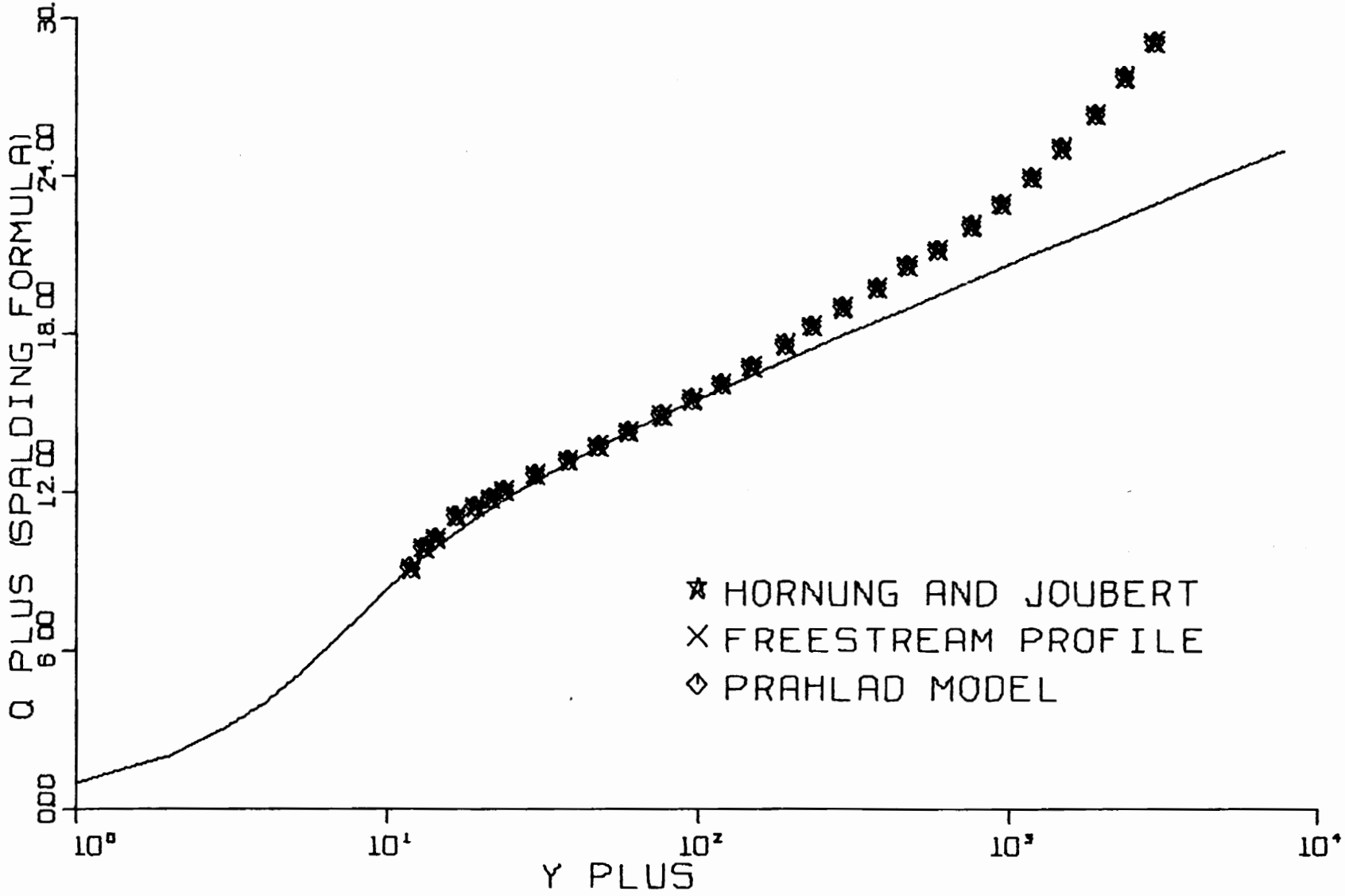

FIG. B 1-2. THREE-DIMENSIONAL SIMILARITY PLOT-RUN A7-01.

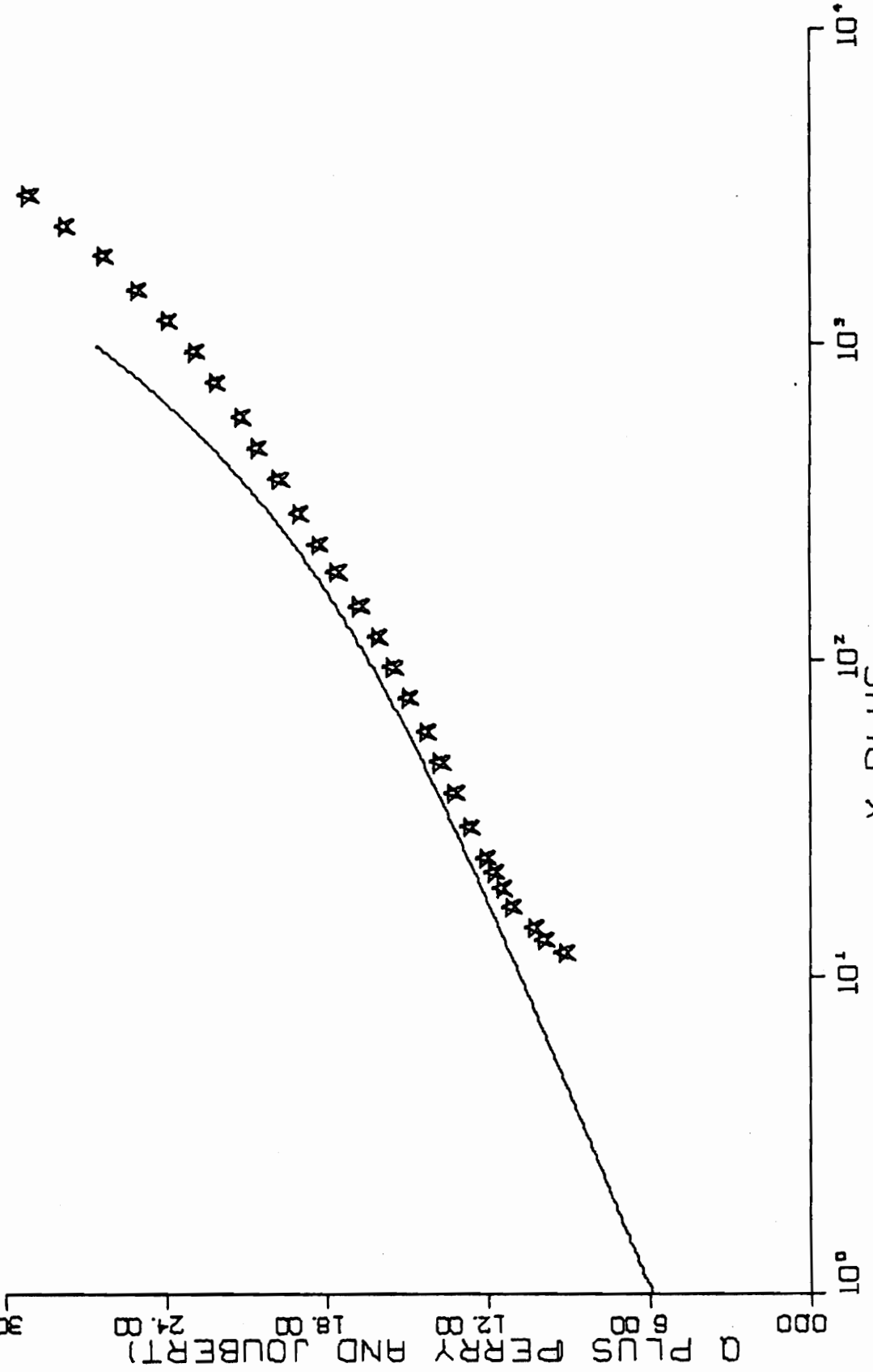

FIG. B 1-3. THREE-DIMENSIONAL SIMILARITY PLOT-RUN A7-01.

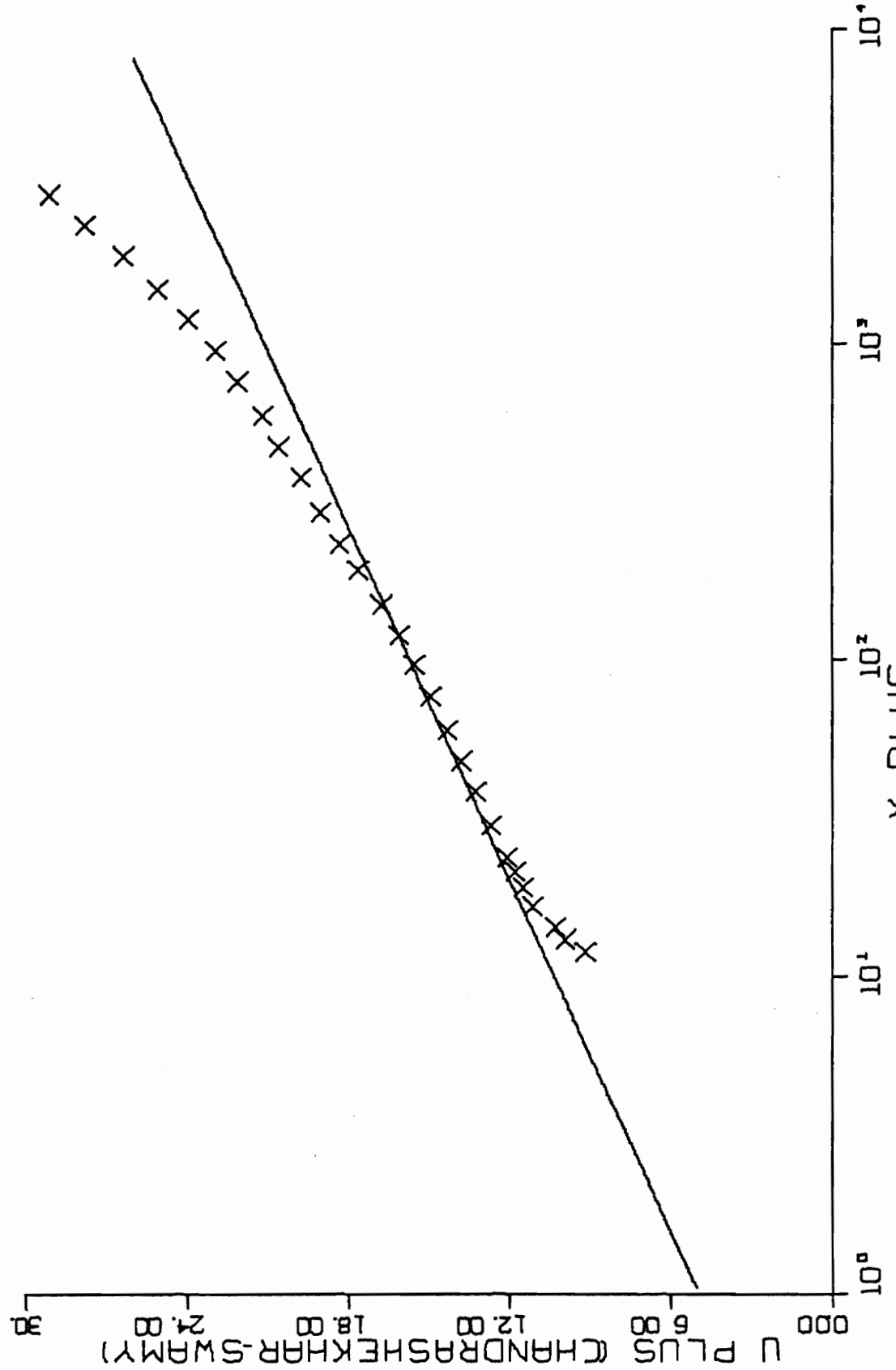

FIG. B 1-4. THREE-DIMENSIONAL SIMILARITY PLOT-RUN A7-01.

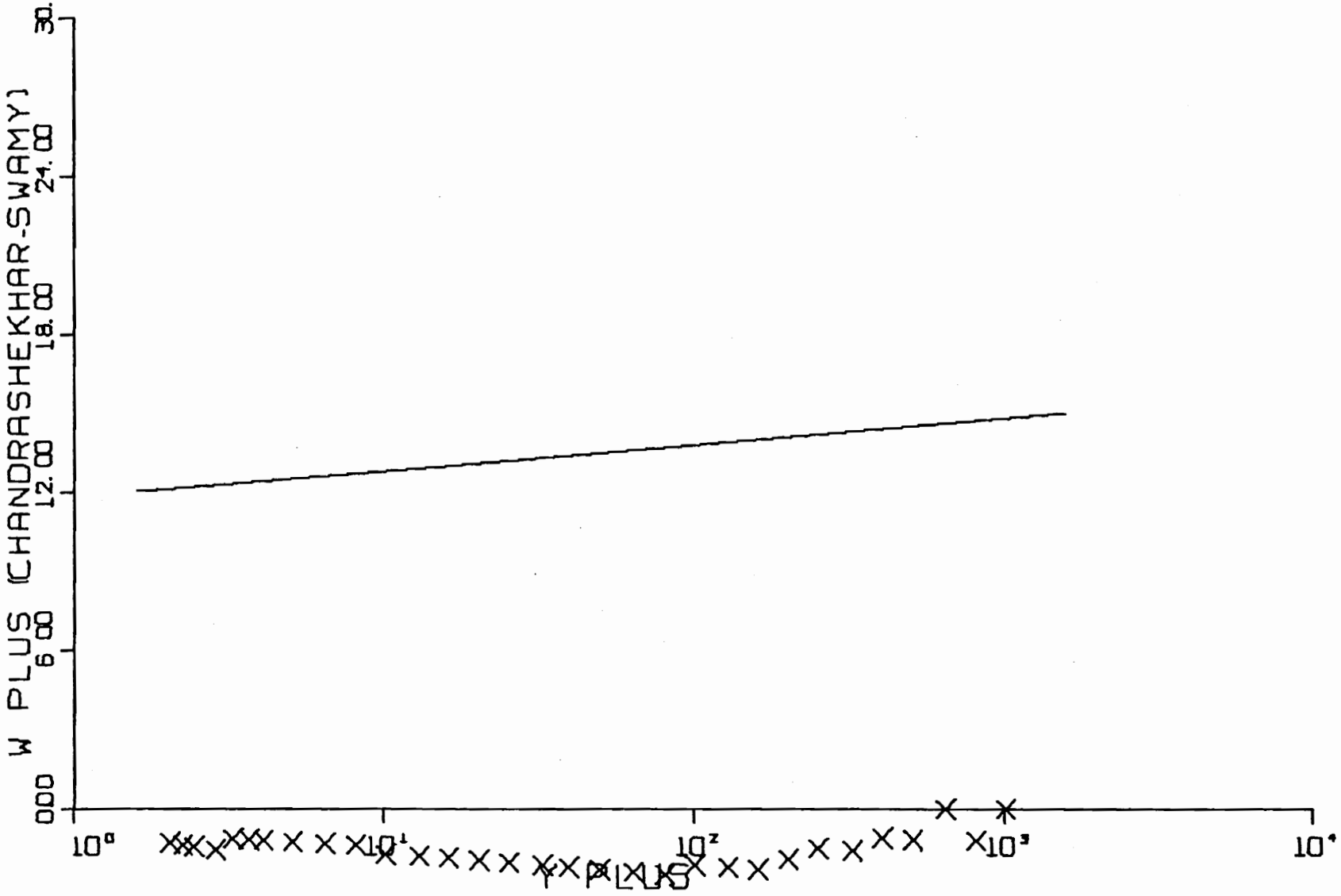

FIG. B 1-4. CONTINUED FOR RUN A7-01.

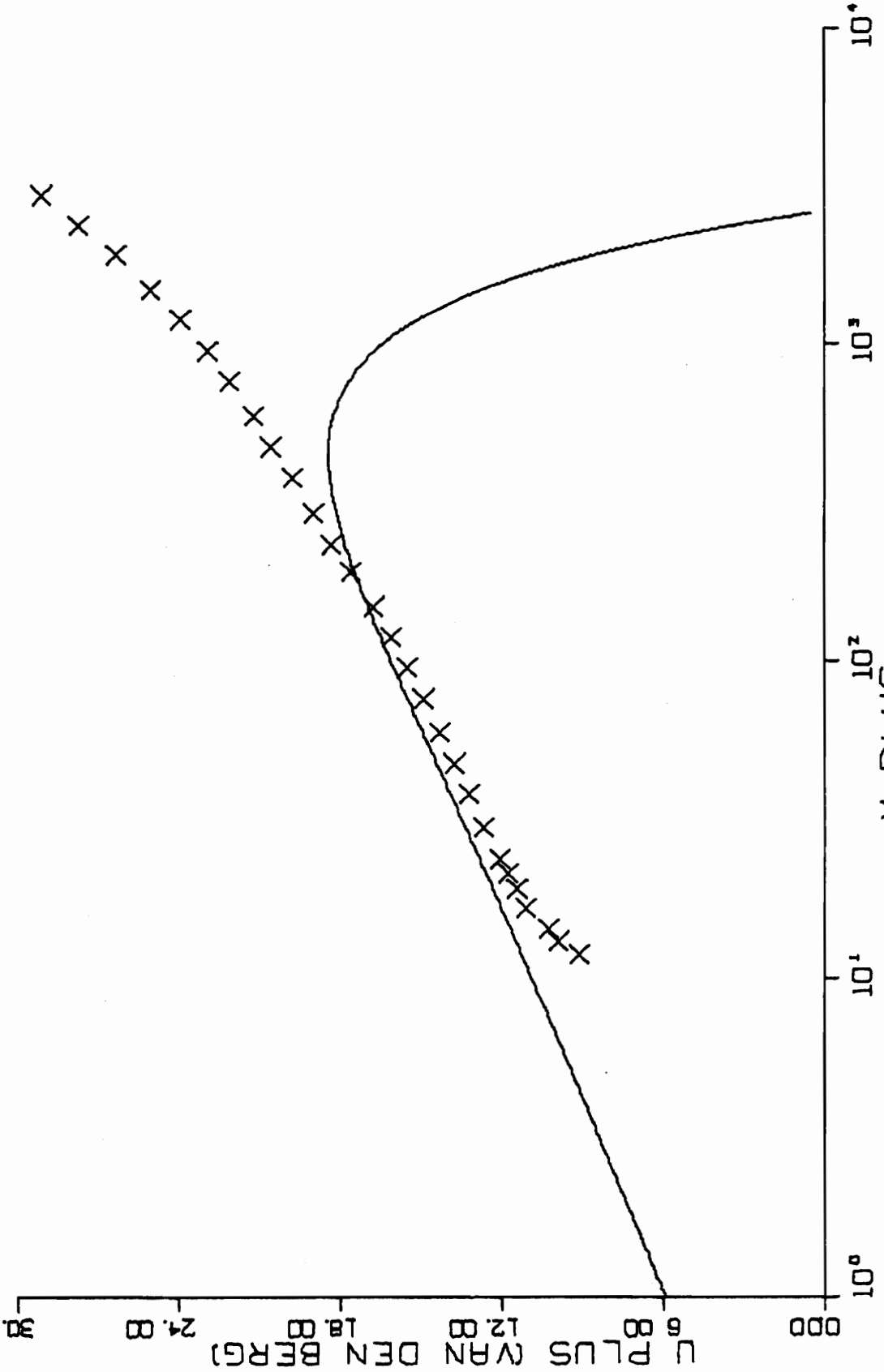

FIG. B 1-5. THREE-DIMENSIONAL SIMILARITY PLOT-RUN A7-01.

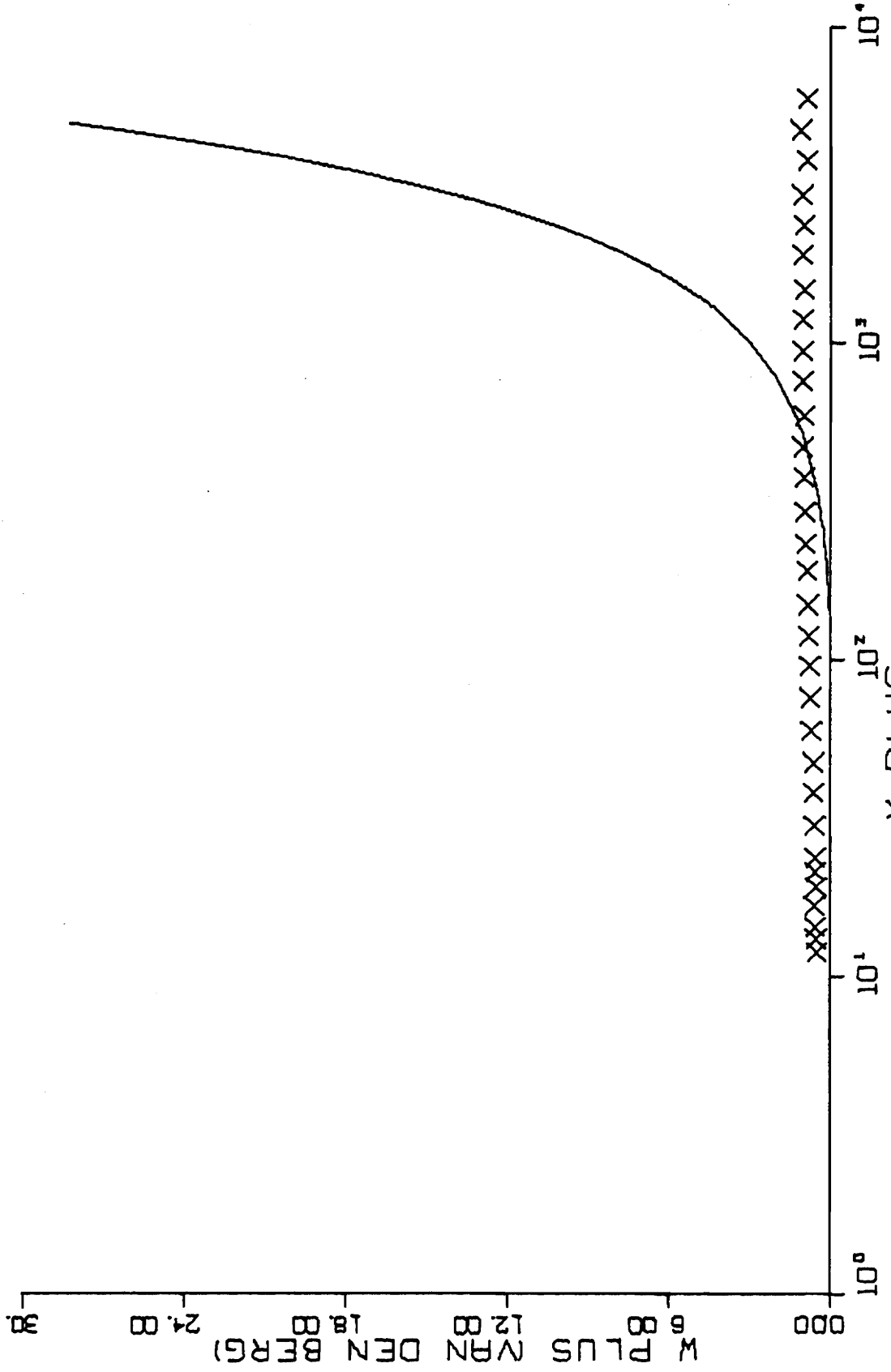

FIG. B 1-5. CONTINUED FOR RUN A7-01.

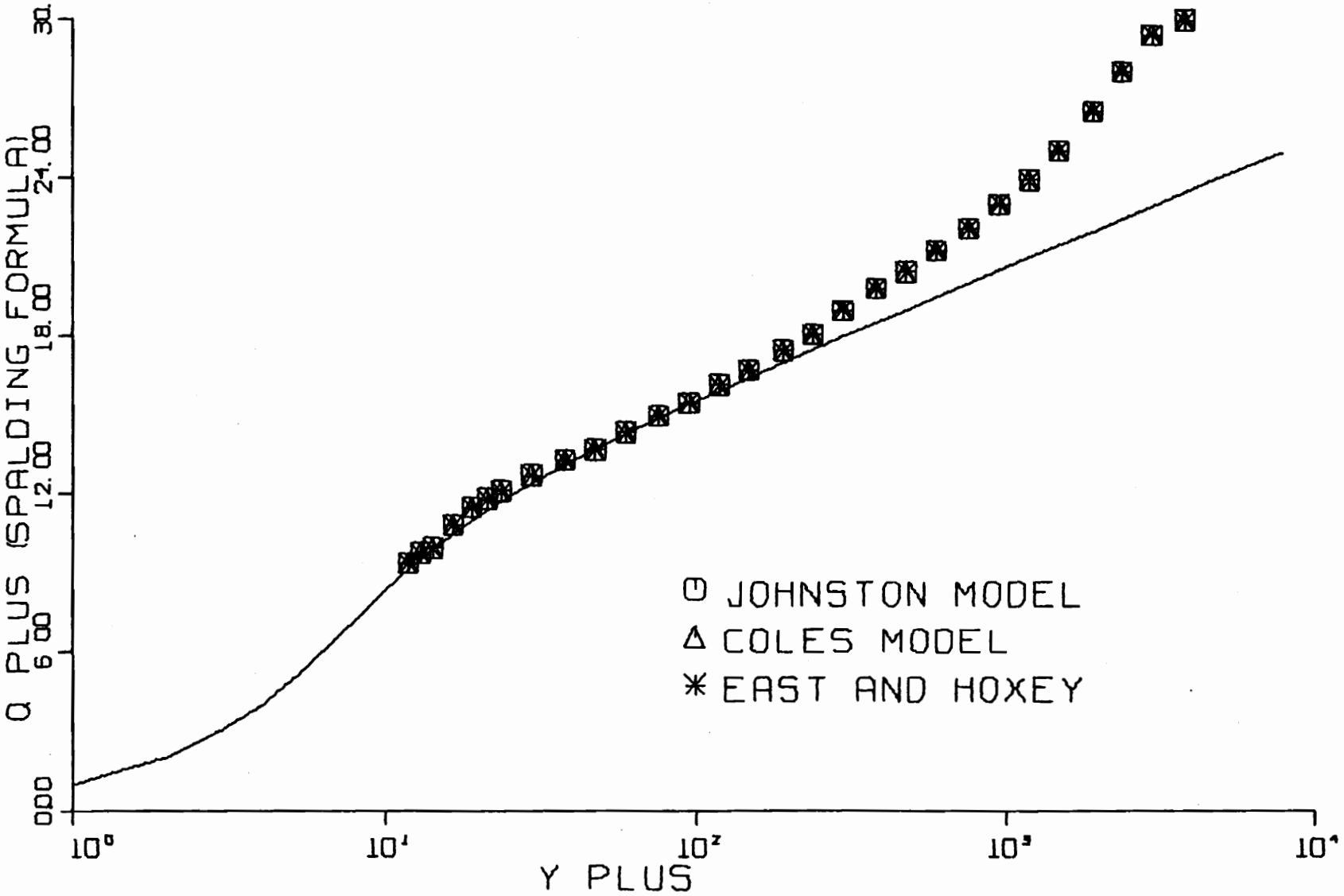

FIG. B 2-1. THREE-DIMENSIONAL SIMILARITY PLOT-RUN A7-03.

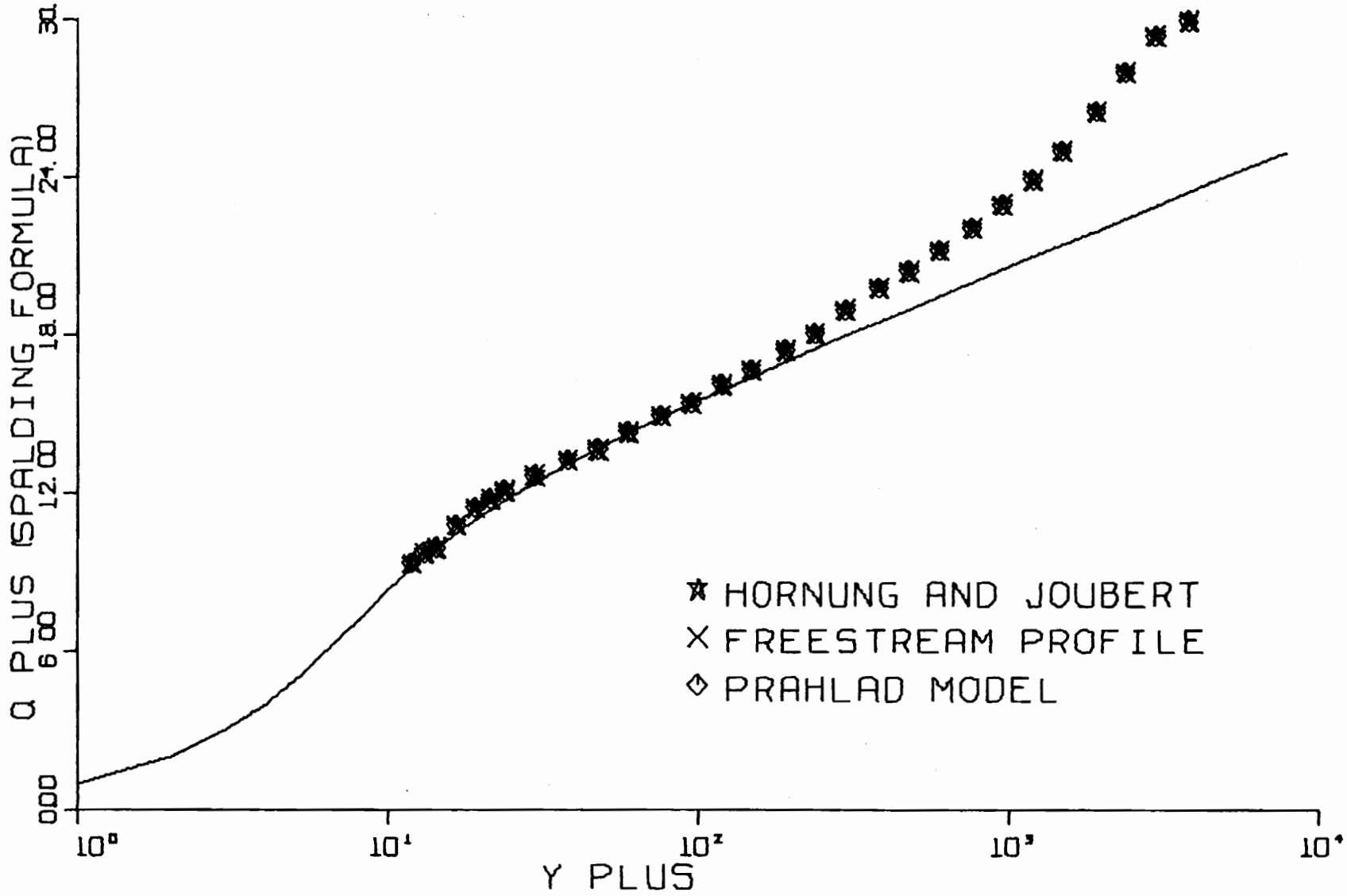

FIG. B 2-2. THREE-DIMENSIONAL SIMILARITY PLOT-RUN A7-03.

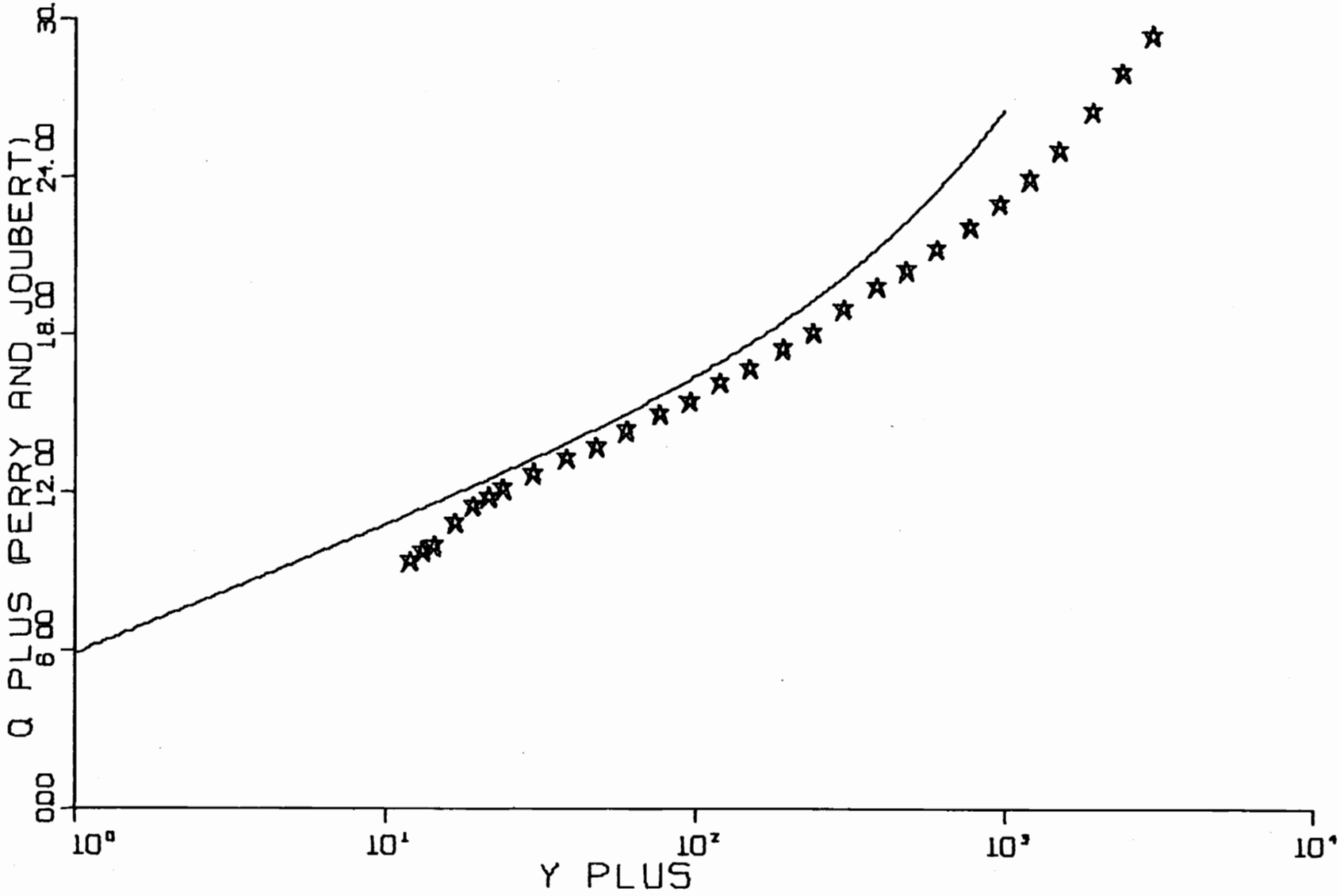

FIG. B 2-3. THREE-DIMENSIONAL SIMILARITY PLOT-RUN A7-03.

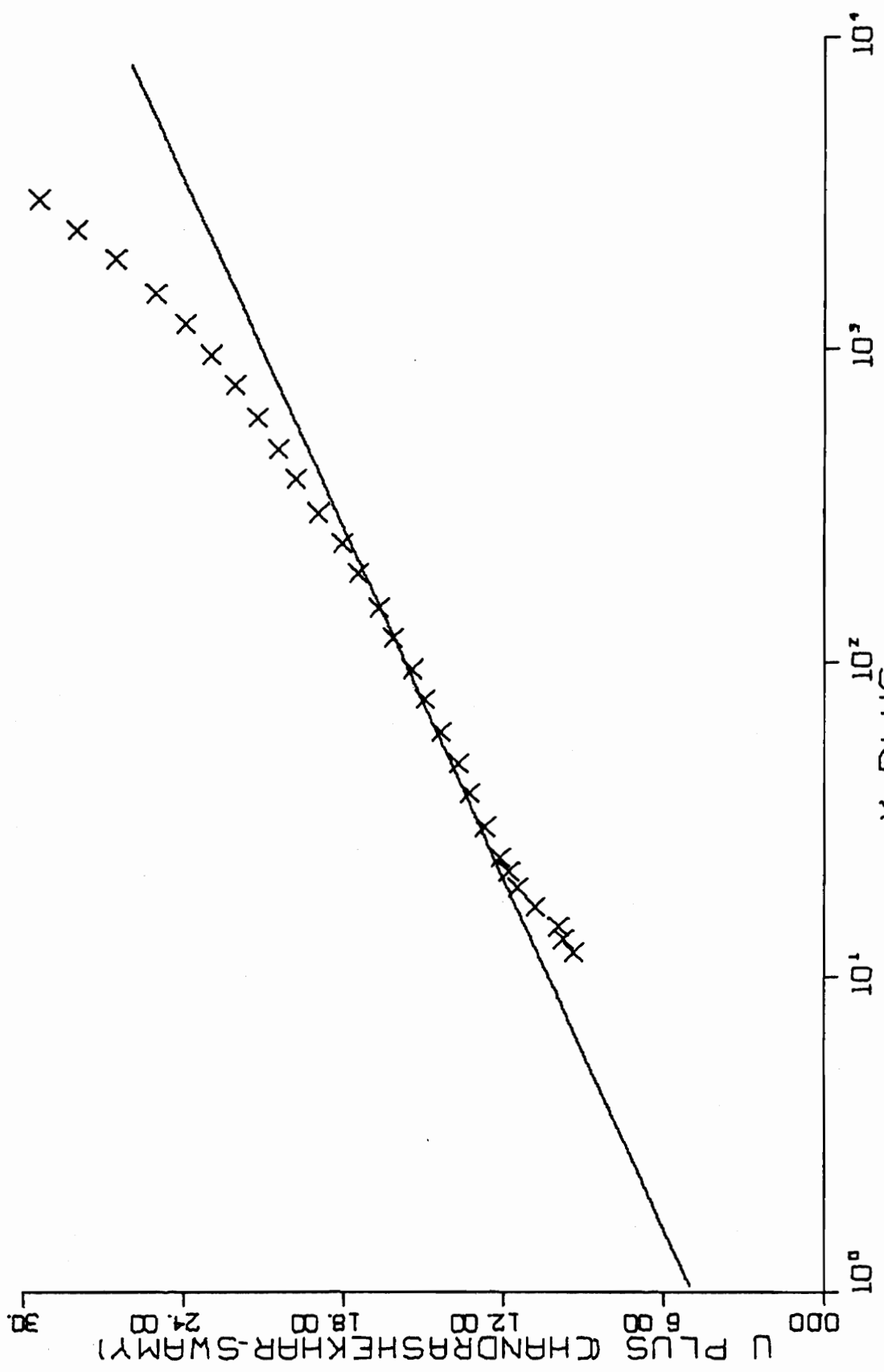

FIG. B 2-4. THREE-DIMENSIONAL SIMILARITY PLOT-RUN A7-03.

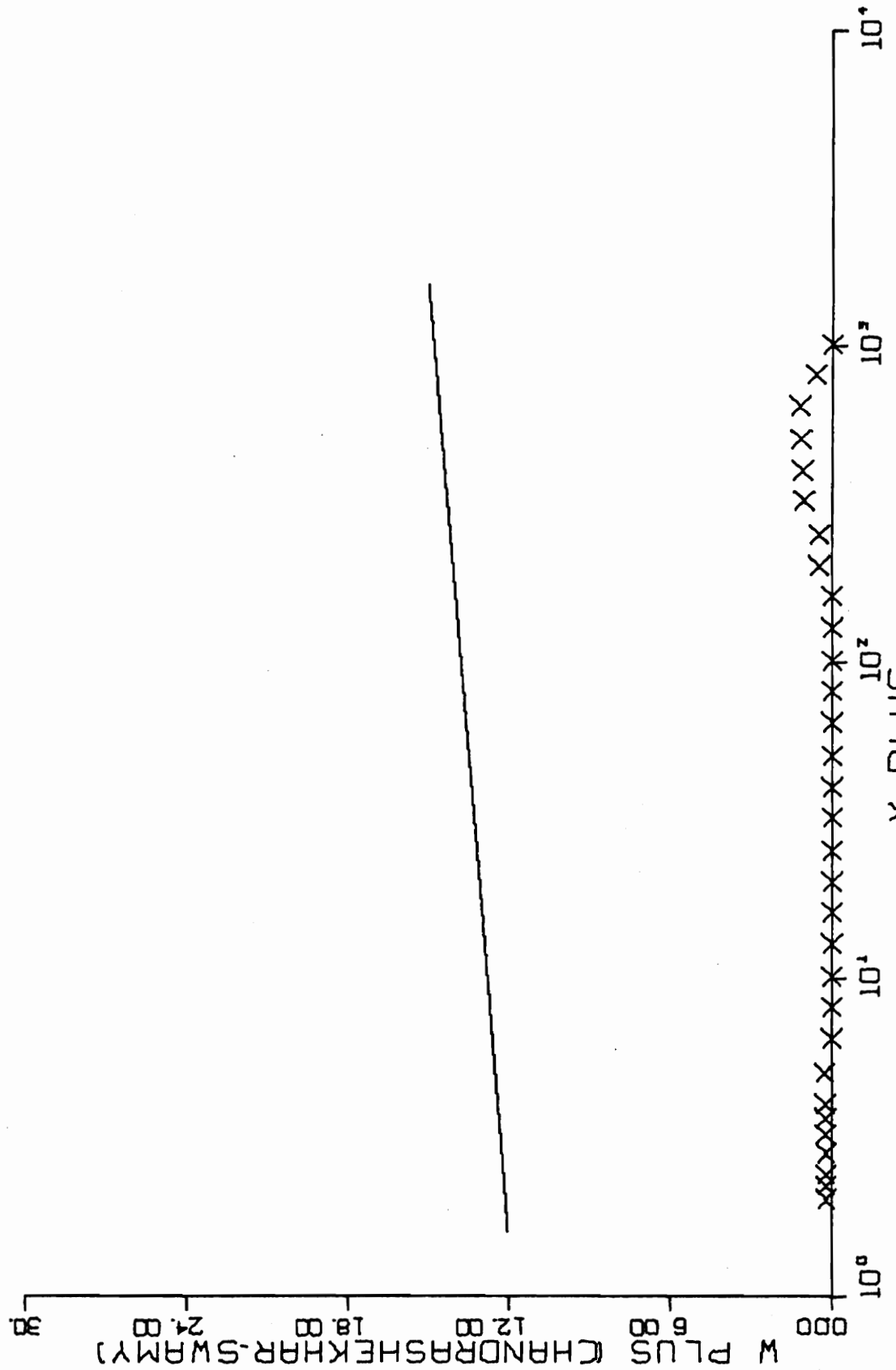

FIG. B 2-4. CONTINUED FOR RUN A7-03.

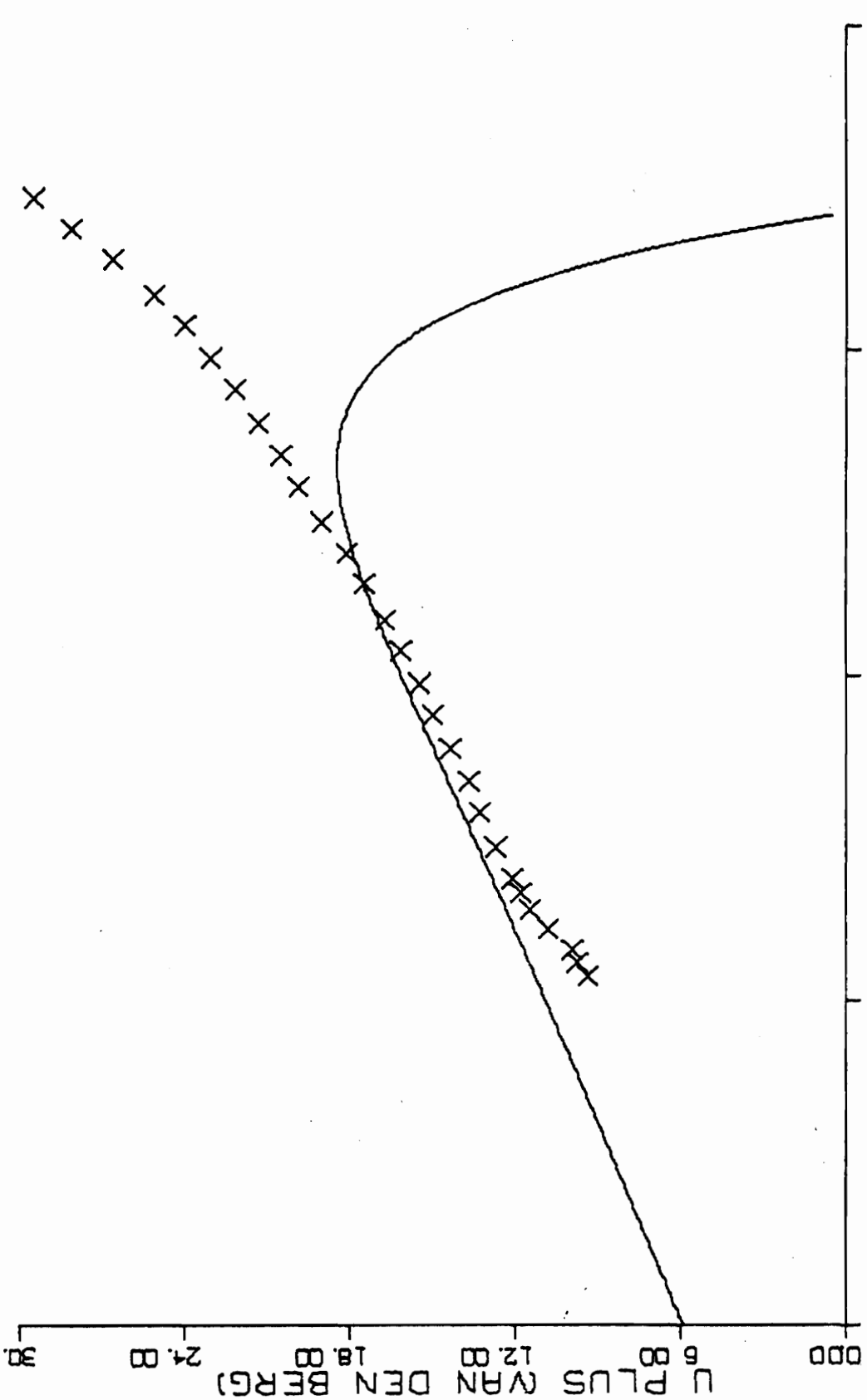

FIG. B 2-5. THREE-DIMENSIONAL SIMILARITY PLOT-RUN A7-03.

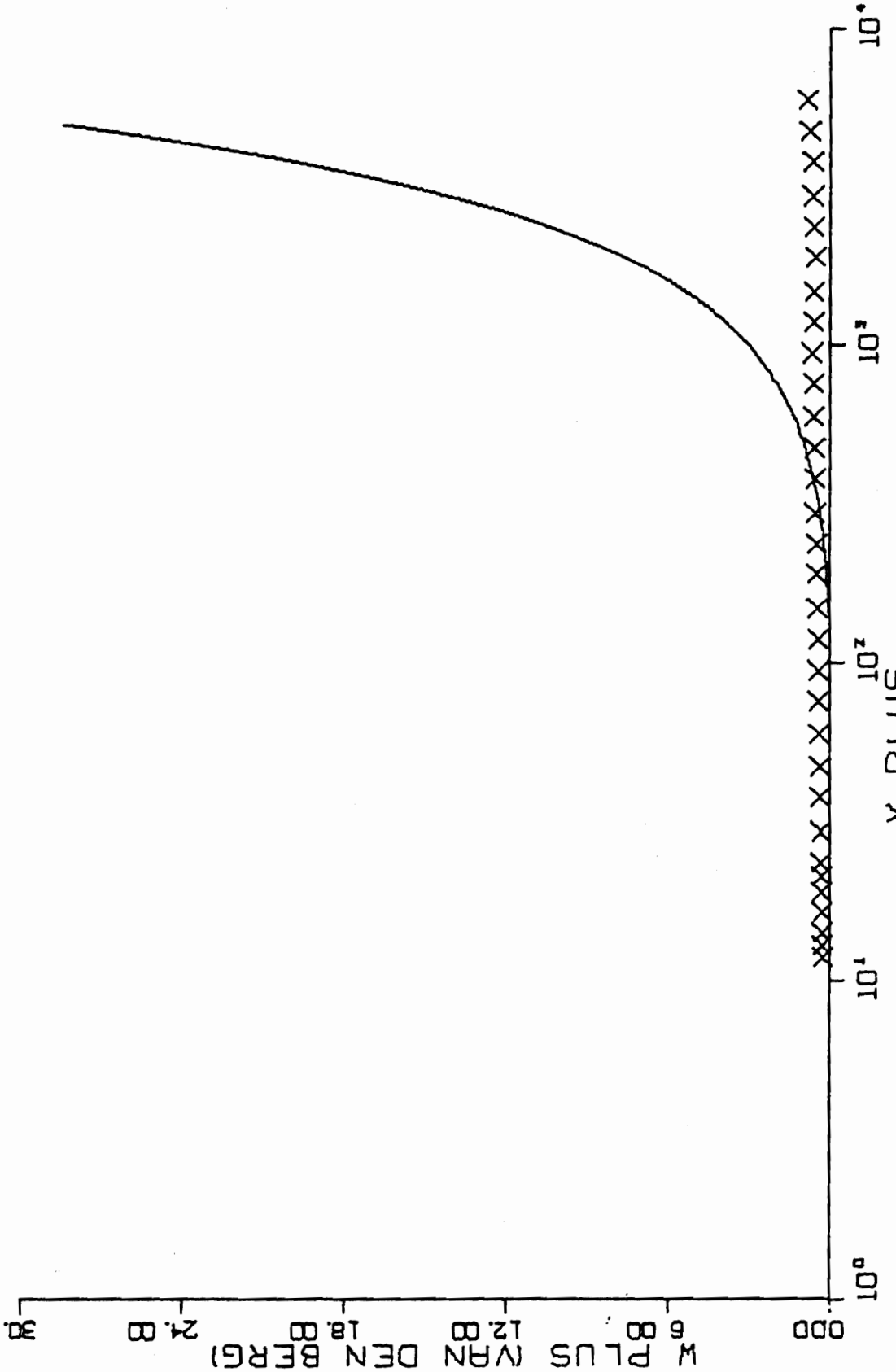

FIG. B 2-5. CONTINUED FOR RUN A7-03.

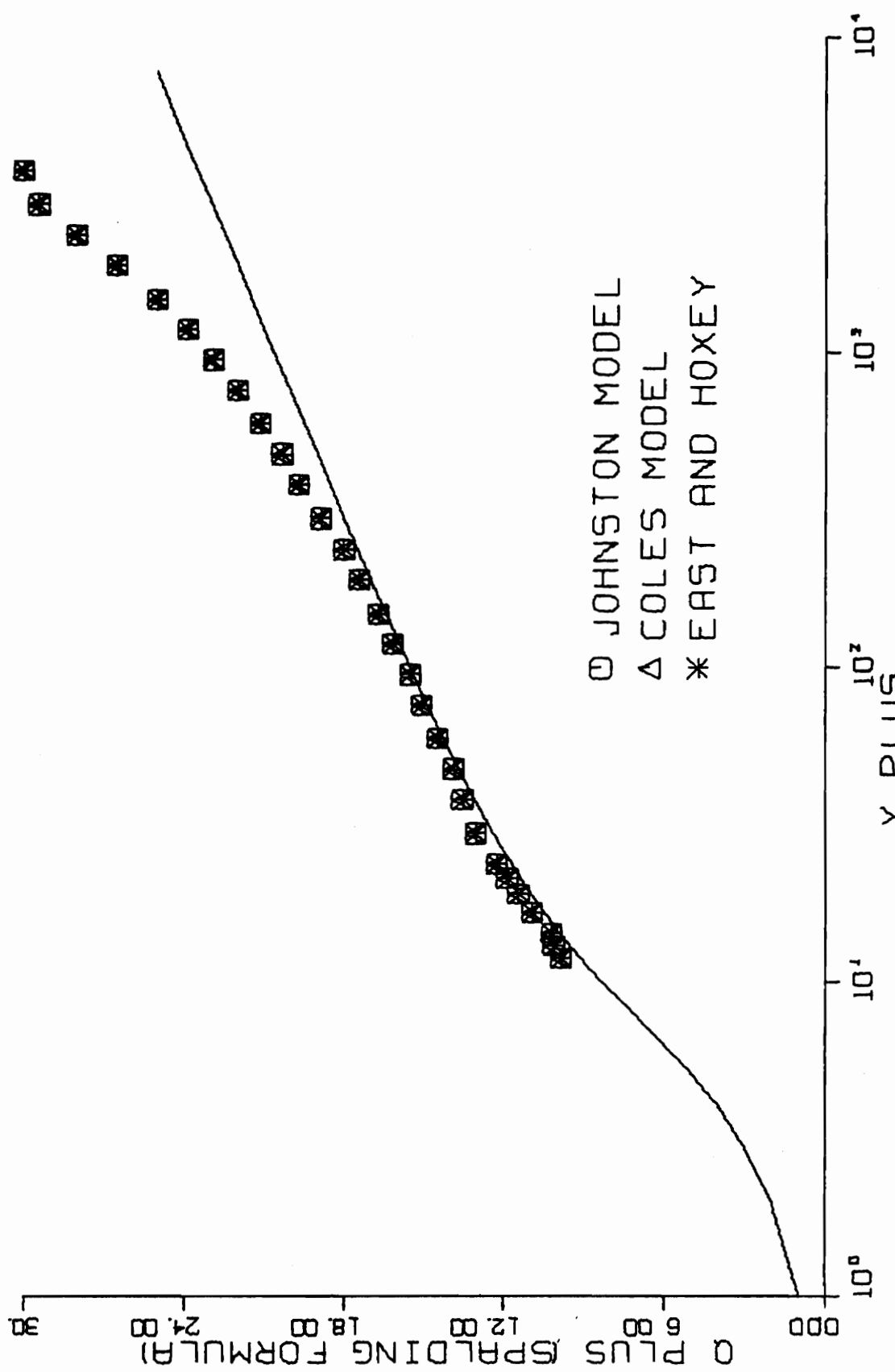

FIG. B3-1. THREE-DIMENSIONAL SIMILARITY PLOT-RUN A7-03P.

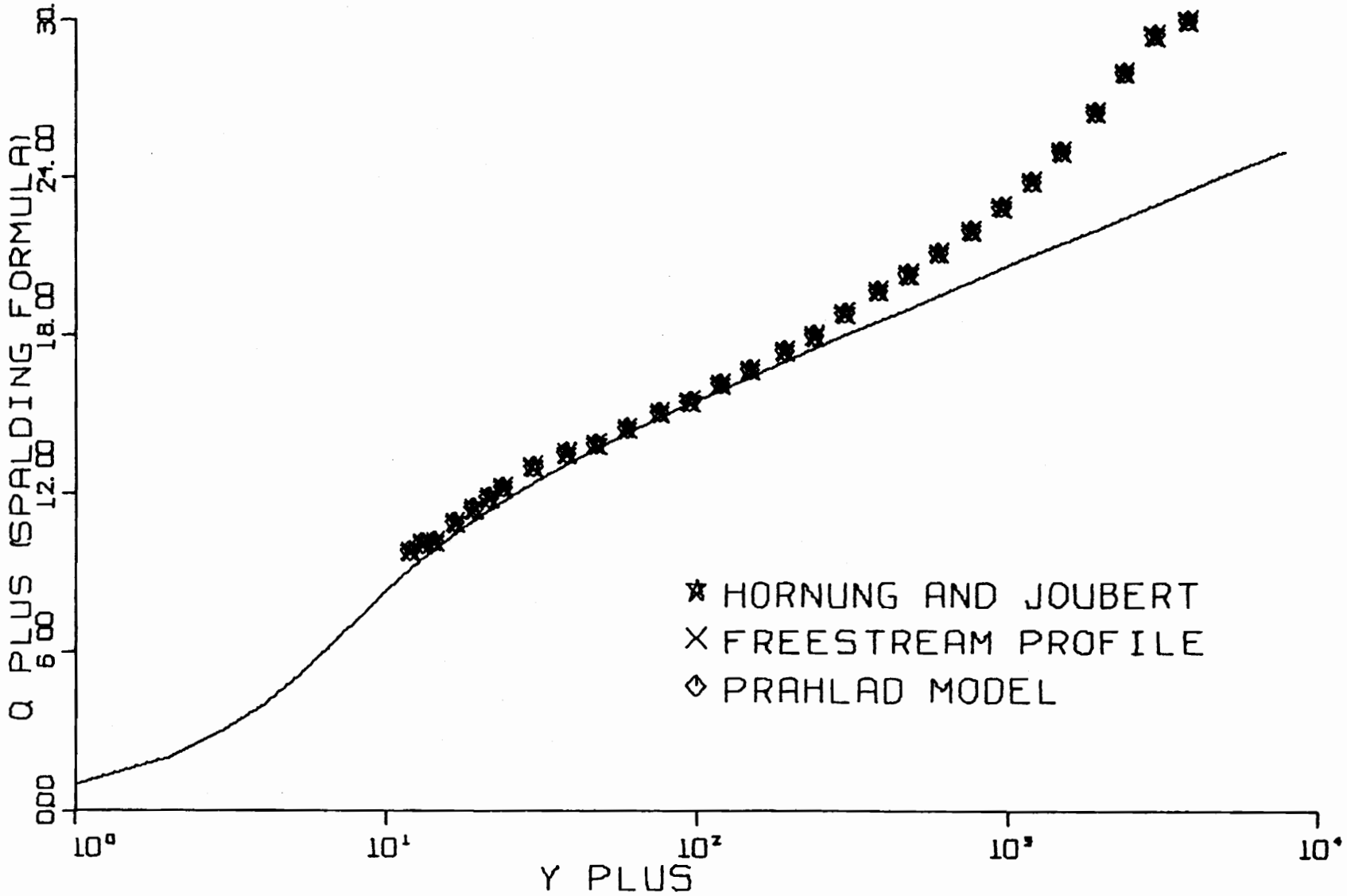

FIG. B3-2. THREE-DIMENSIONAL SIMILARITY PLOT-RUN A7-03P.

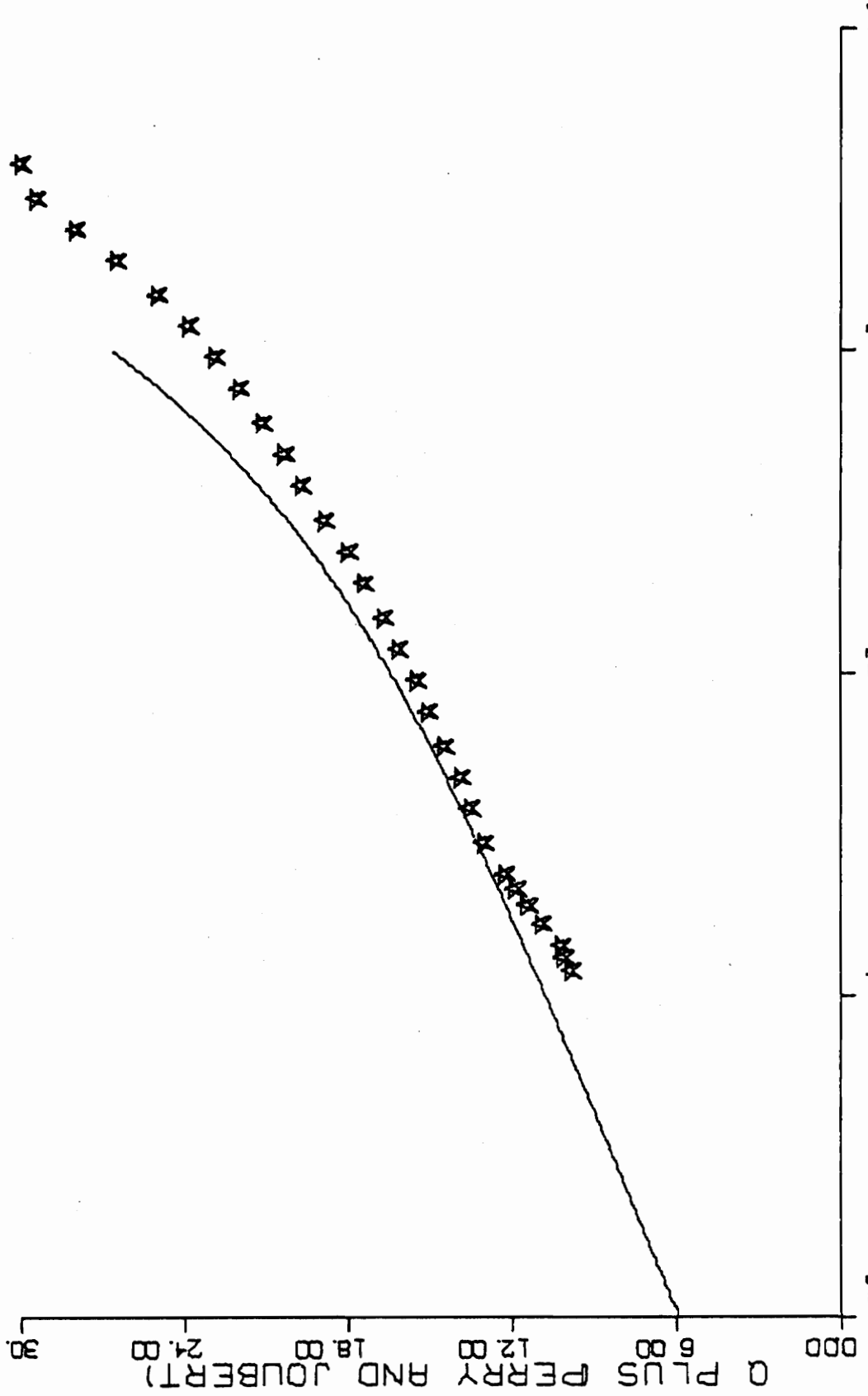

FIG. B3-3. THREE-DIMENSIONAL SIMILARITY PLOT-RUN A7-03P.

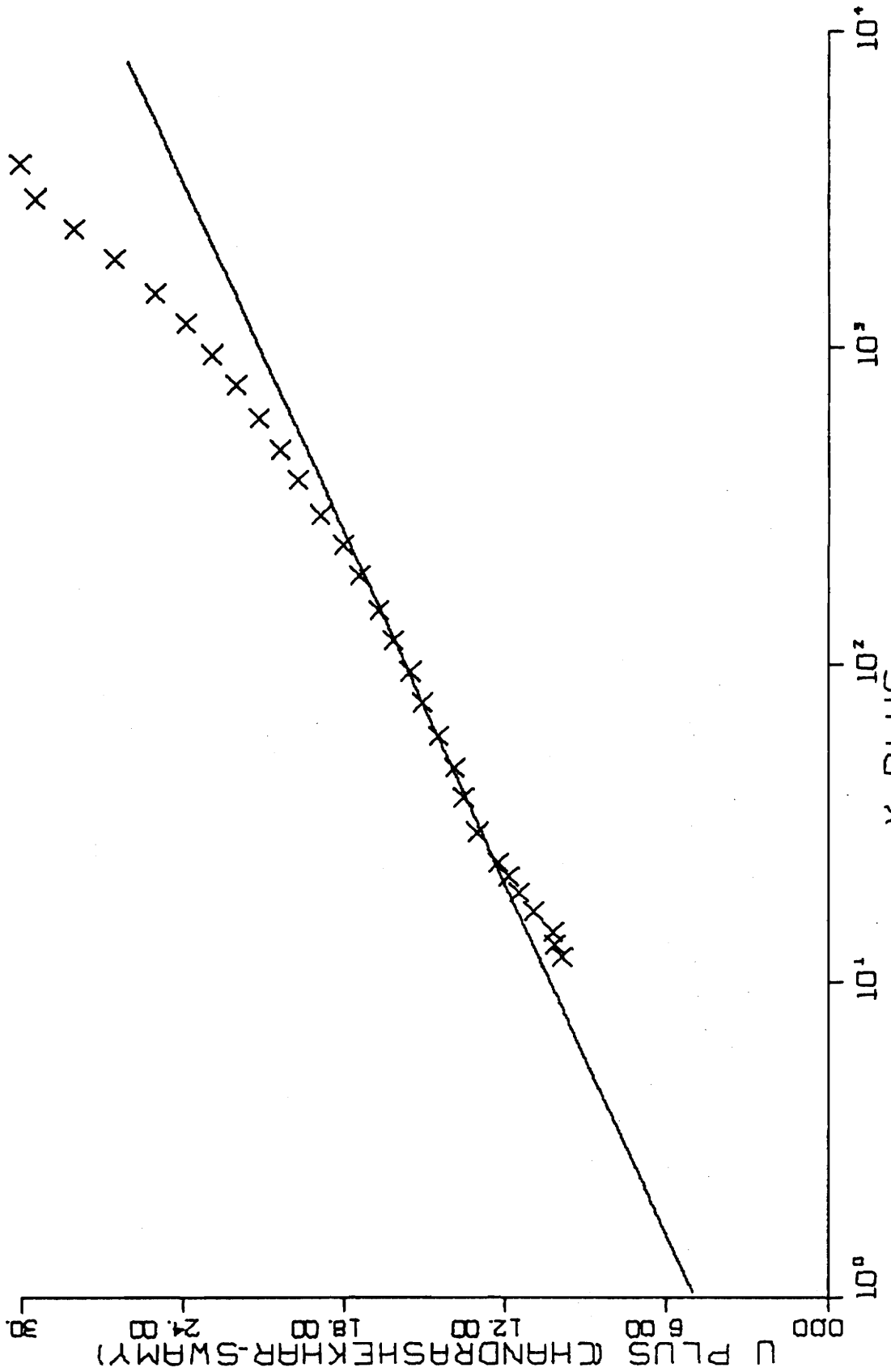

FIG. B3-4. THREE-DIMENSIONAL SIMILARITY PLOT-RUN A7.03P.

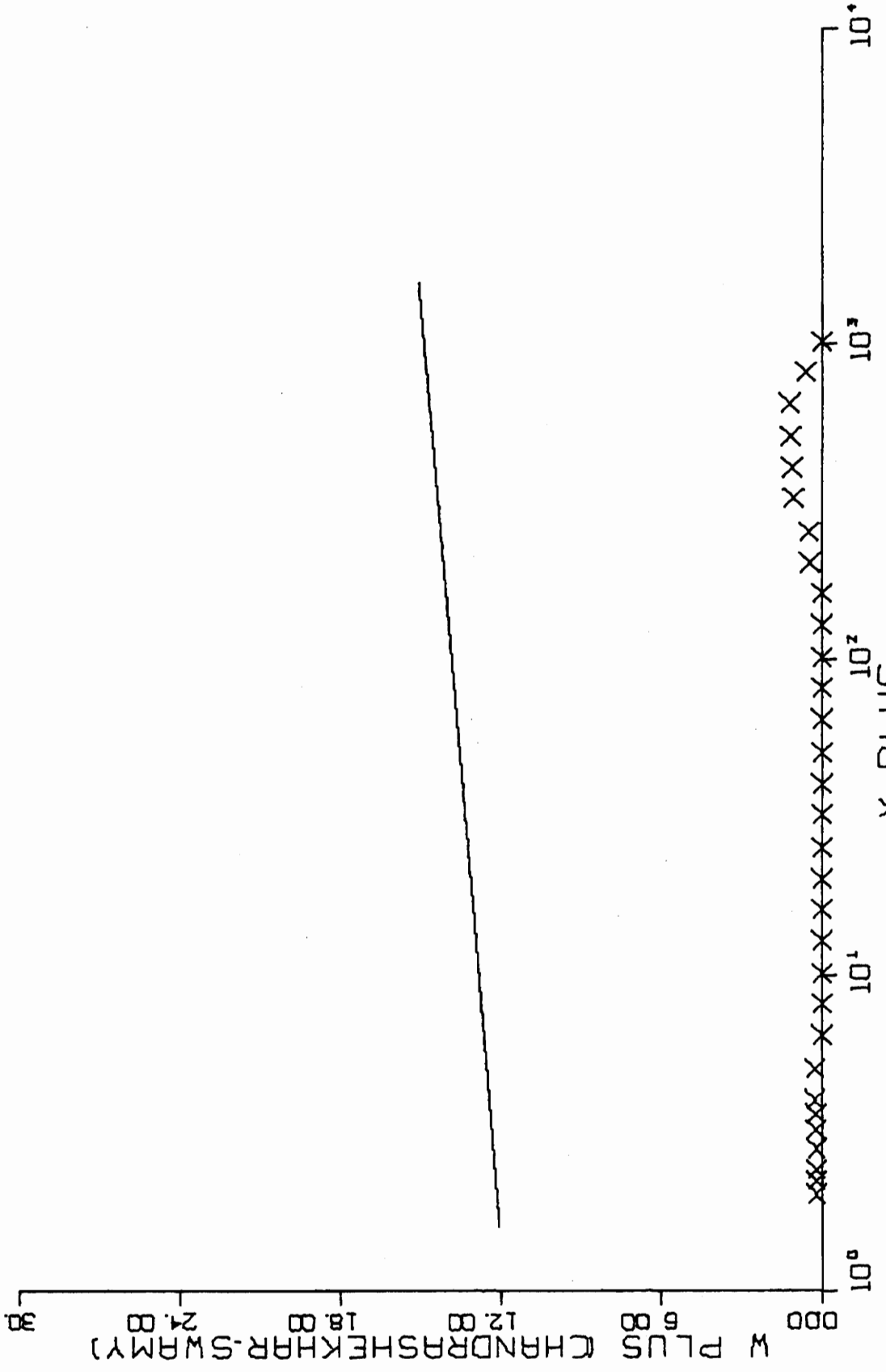

FIG. B 3-4. CONTINUED FOR RUN A7-03P.

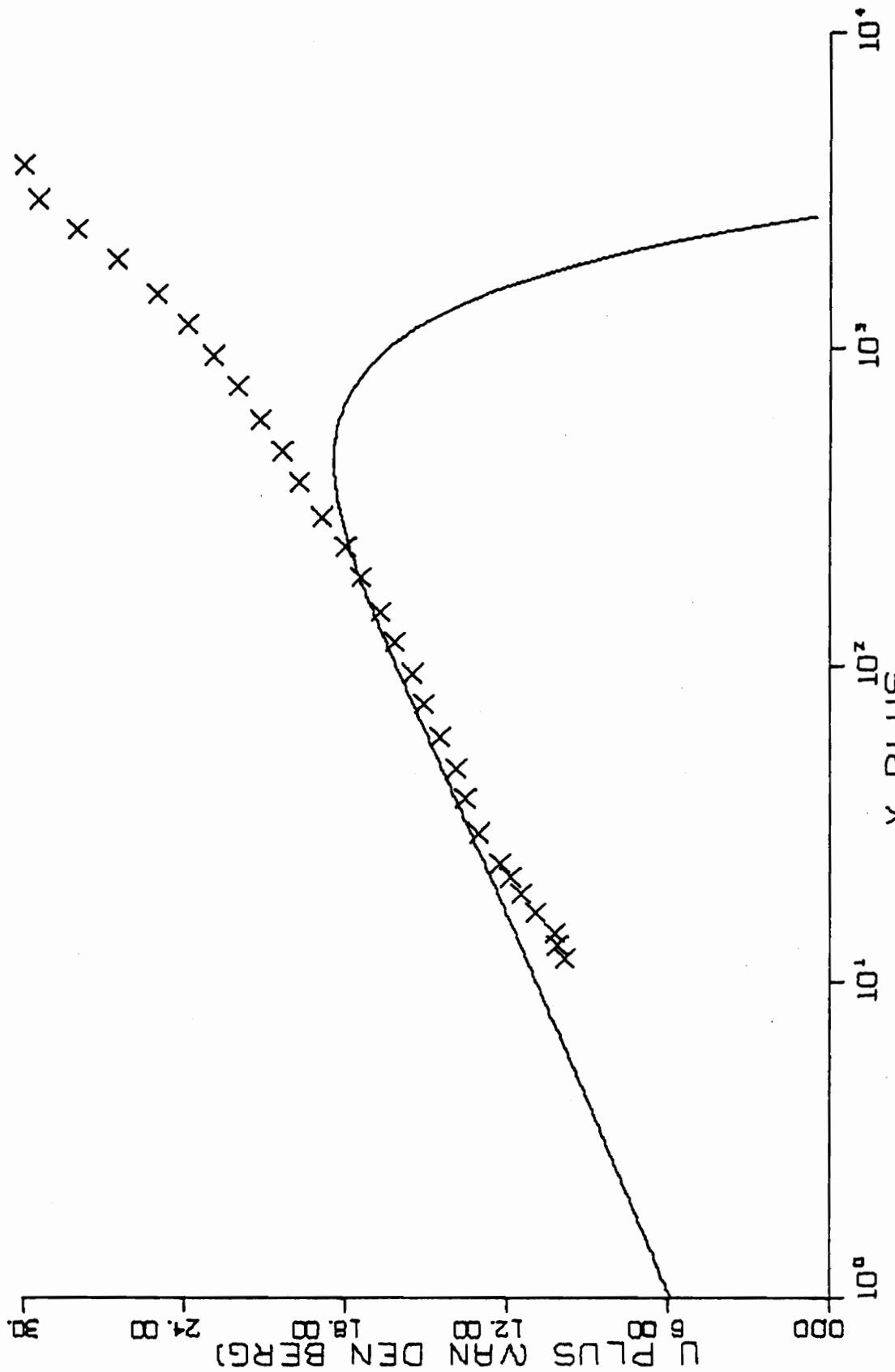

FIG. B3-5. THREE-DIMENSIONAL SIMILARITY PLOT-RUN A7-03P.

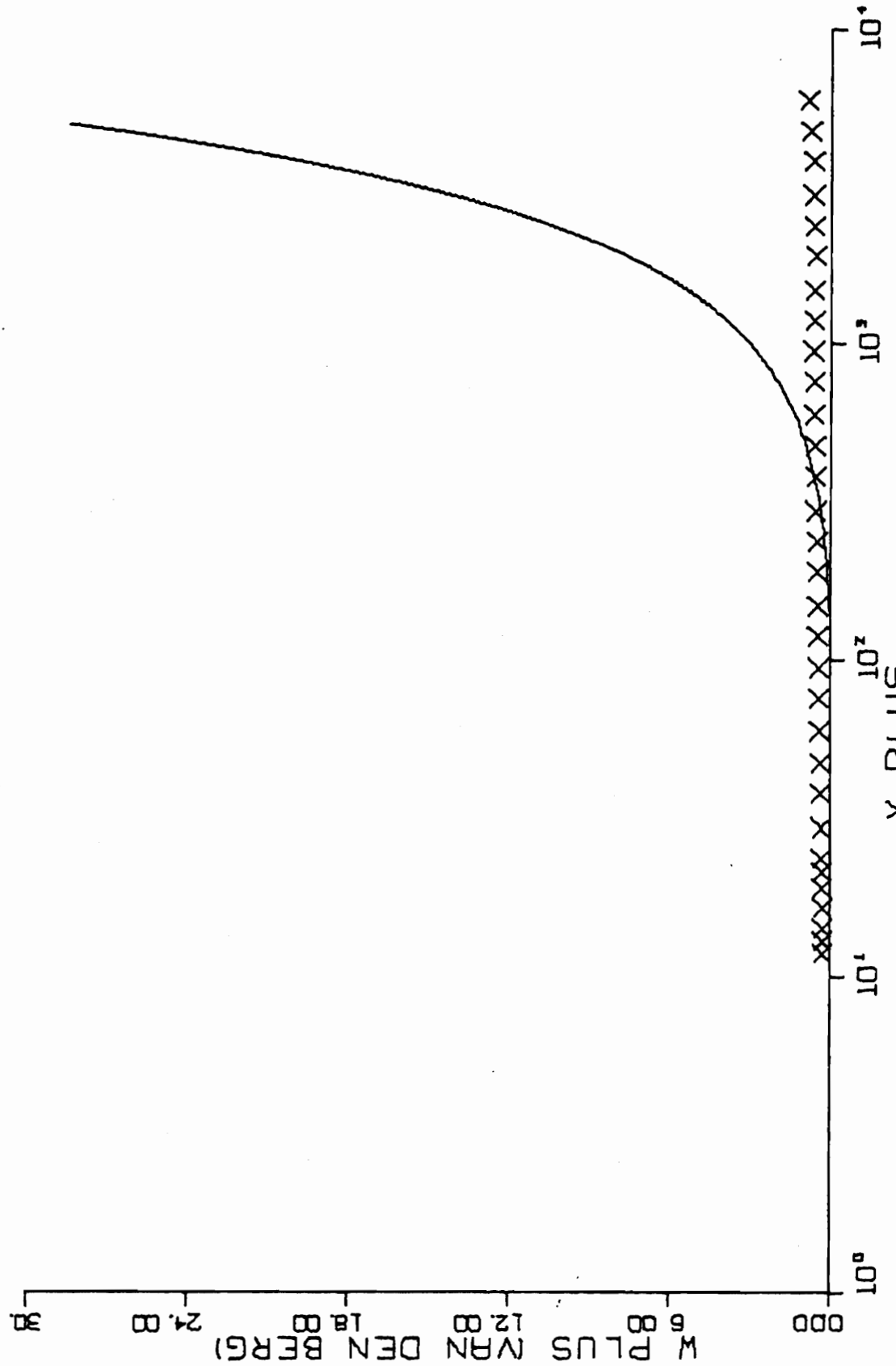

FIG. B 3-5. CONTINUED FOR RUN A7-03P.

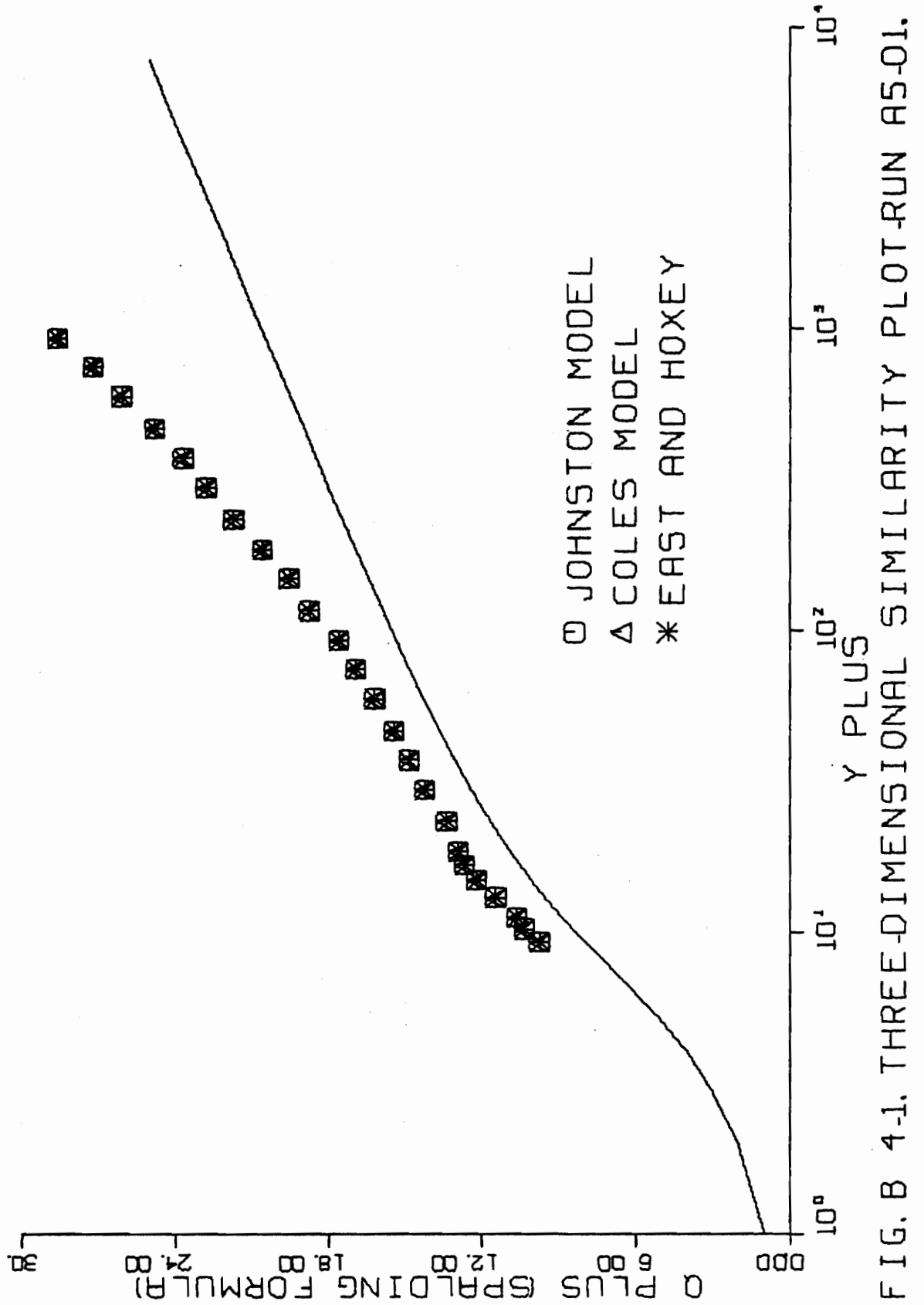

FIG. B 4-1. THREE-DIMENSIONAL SIMILARITY PLOT-RUN A5-01.

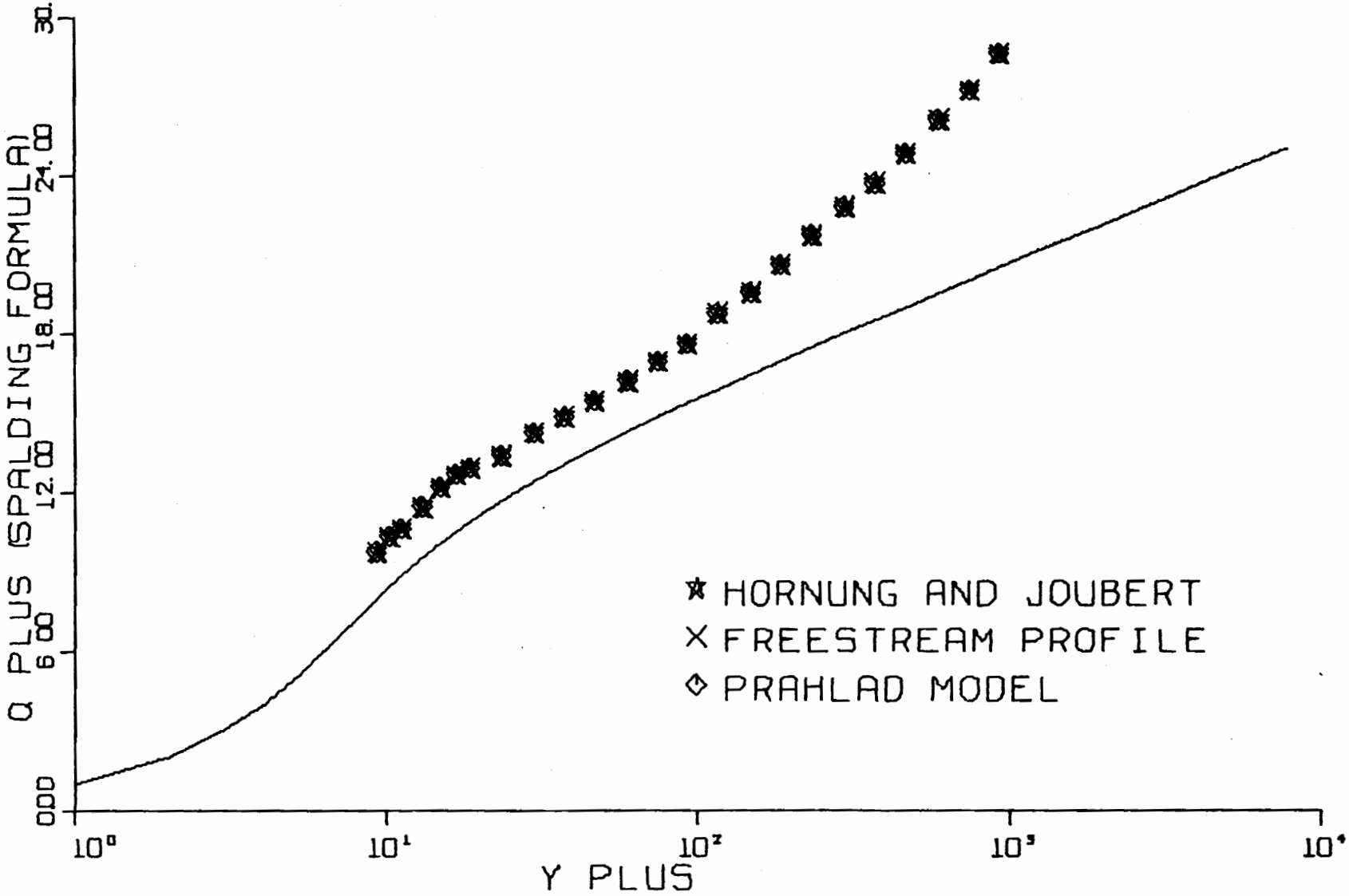

FIG. B 4-2. THREE-DIMENSIONAL SIMILARITY PLOT-RUN A5-01.

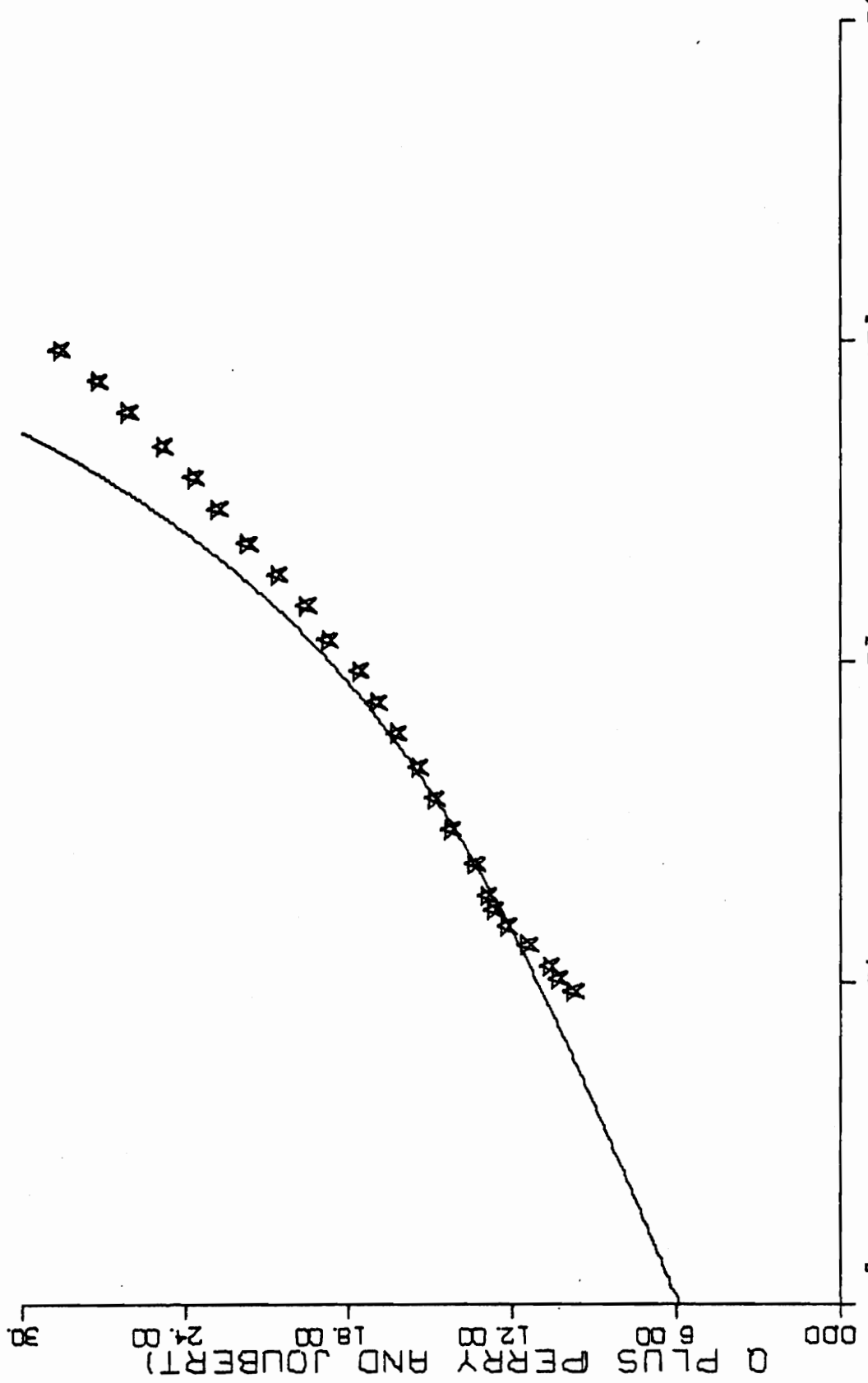

FIG. B 4-3. THREE-DIMENSIONAL SIMILARITY PLOT-RUN A5-01.

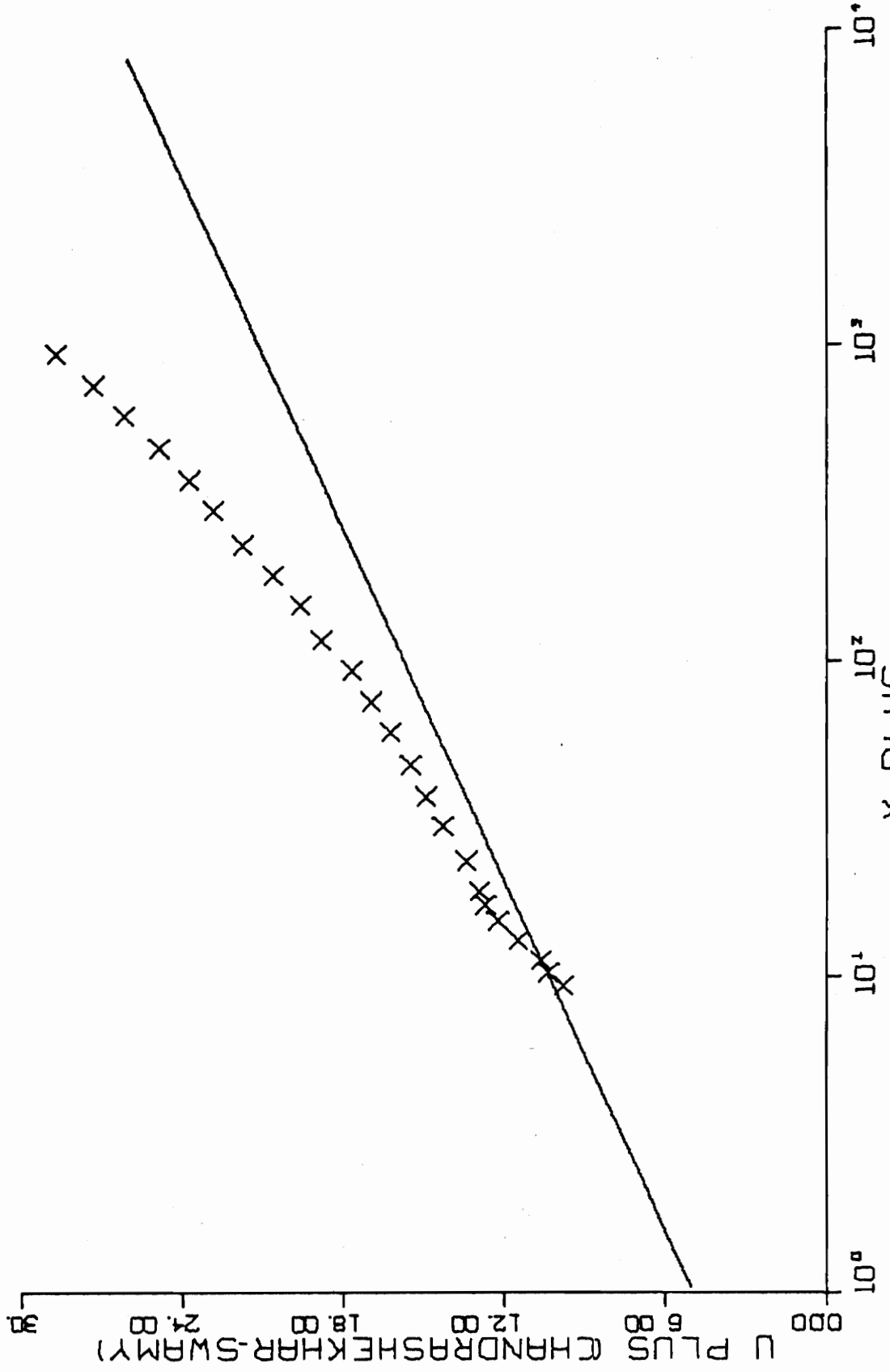

FIG. B 4-4. THREE-DIMENSIONAL SIMILARITY PLOT-RUN A5-01.

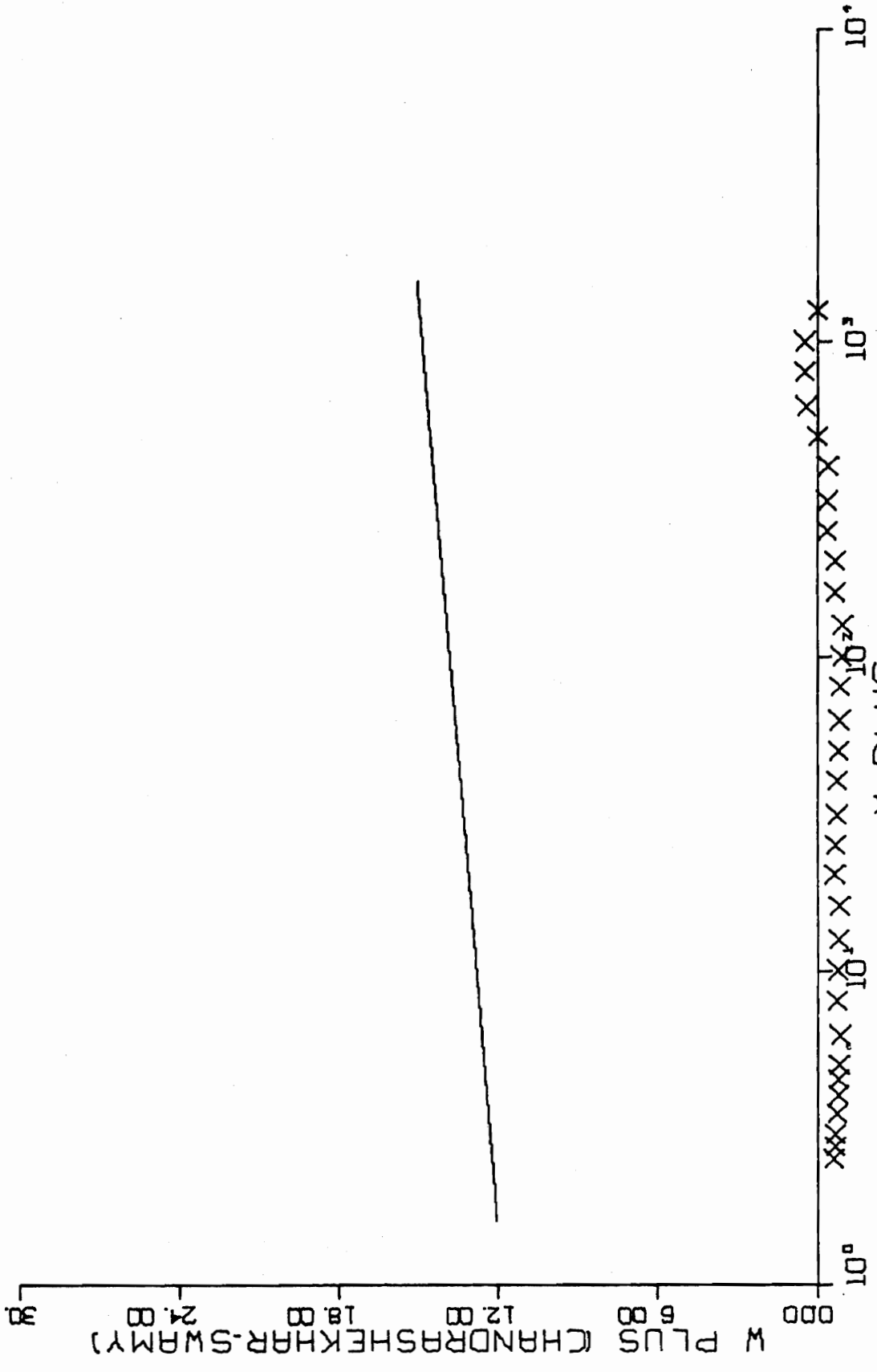

FIG. B 4-4. CONTINUED FOR RUN A5-01.

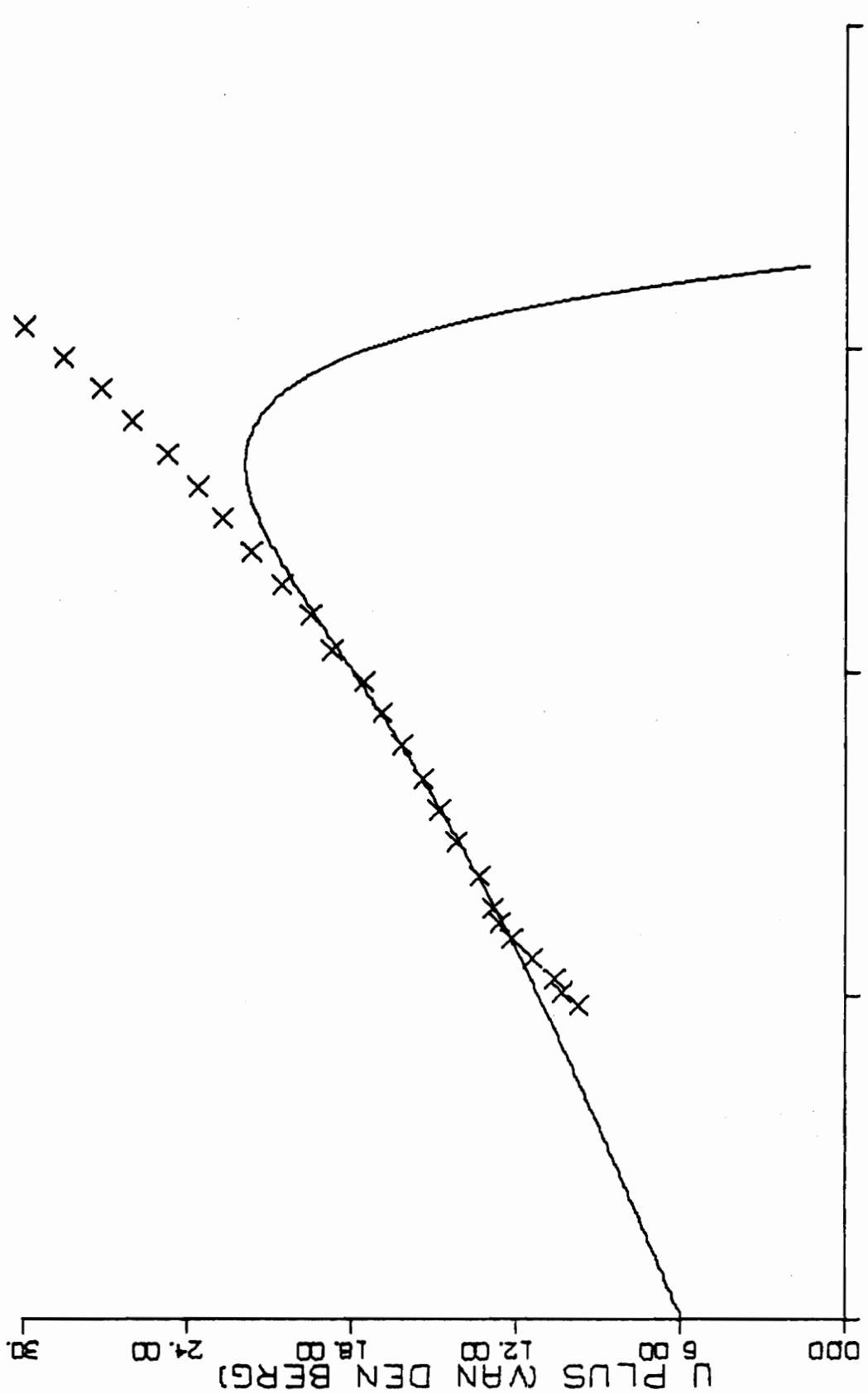

FIG. B 4-5. THREE-DIMENSIONAL SIMILARITY PLOT-RUN AS-01.

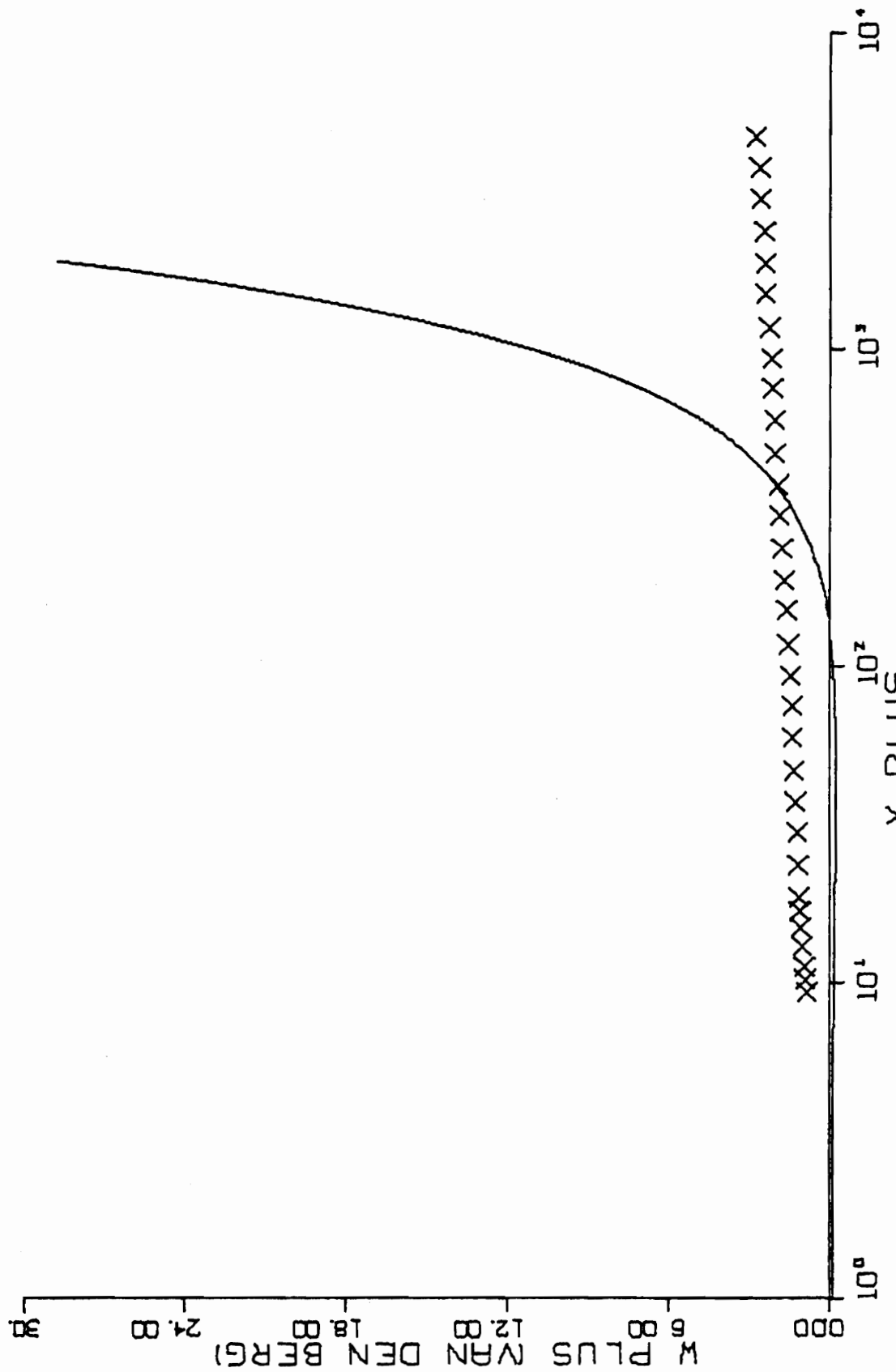

FIG. B 4-5. CONTINUED FOR RUN A5-01.

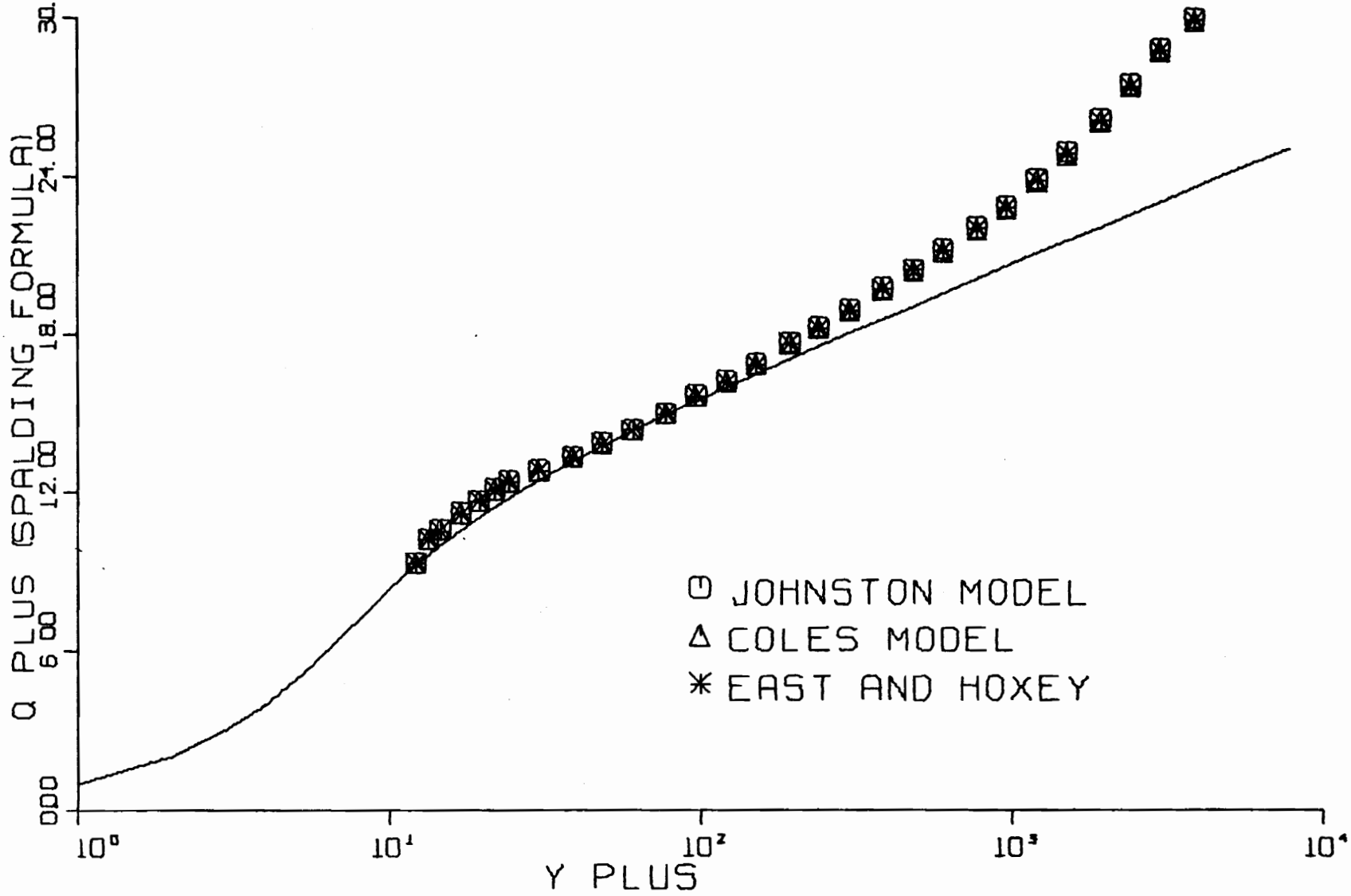

FIG. B 5-1. THREE-DIMENSIONAL SIMILARITY PLOT-RUN C7-01.

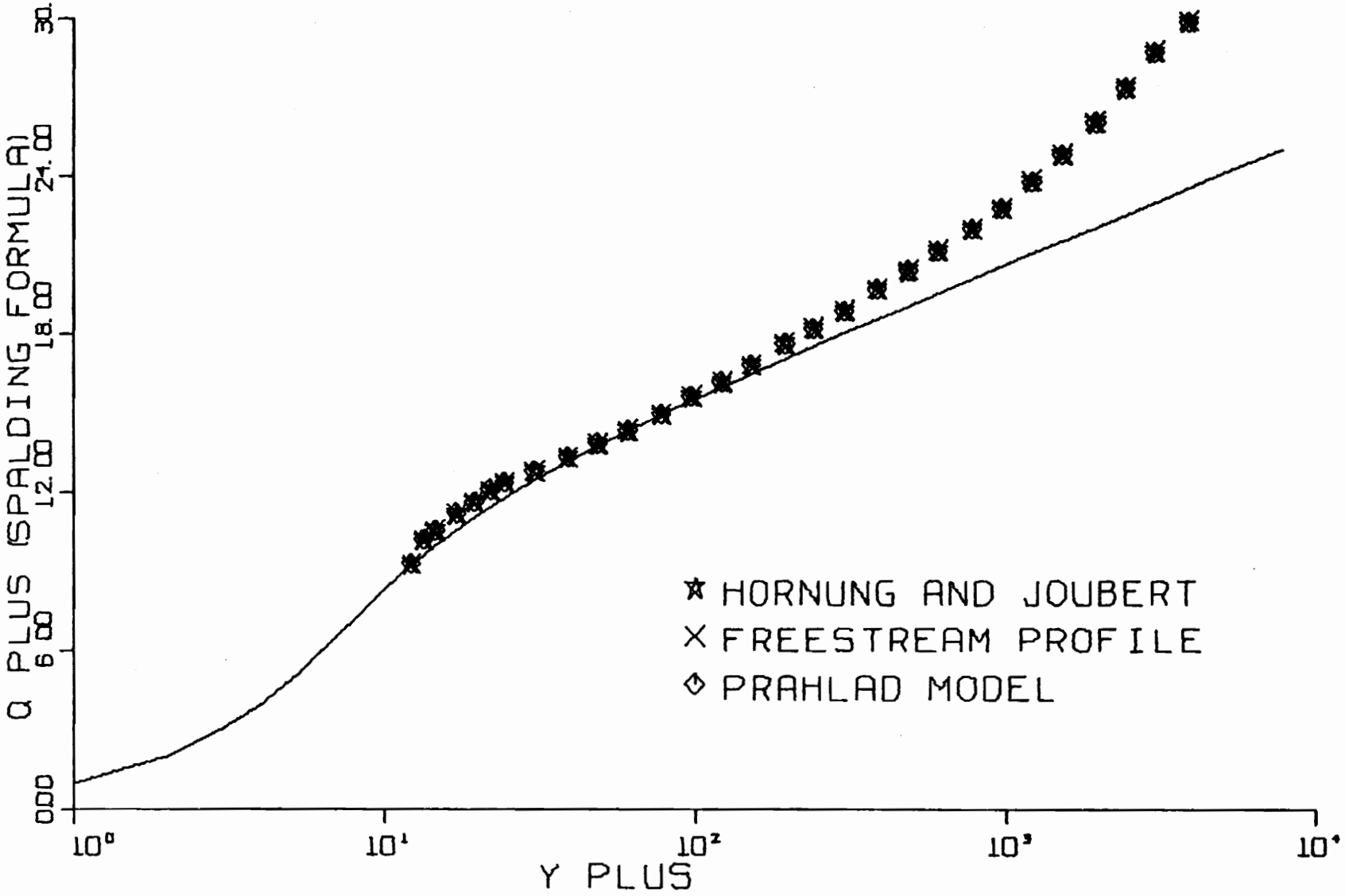

FIG. B 5-2. THREE-DIMENSIONAL SIMILARITY PLOT-RUN C7-01.

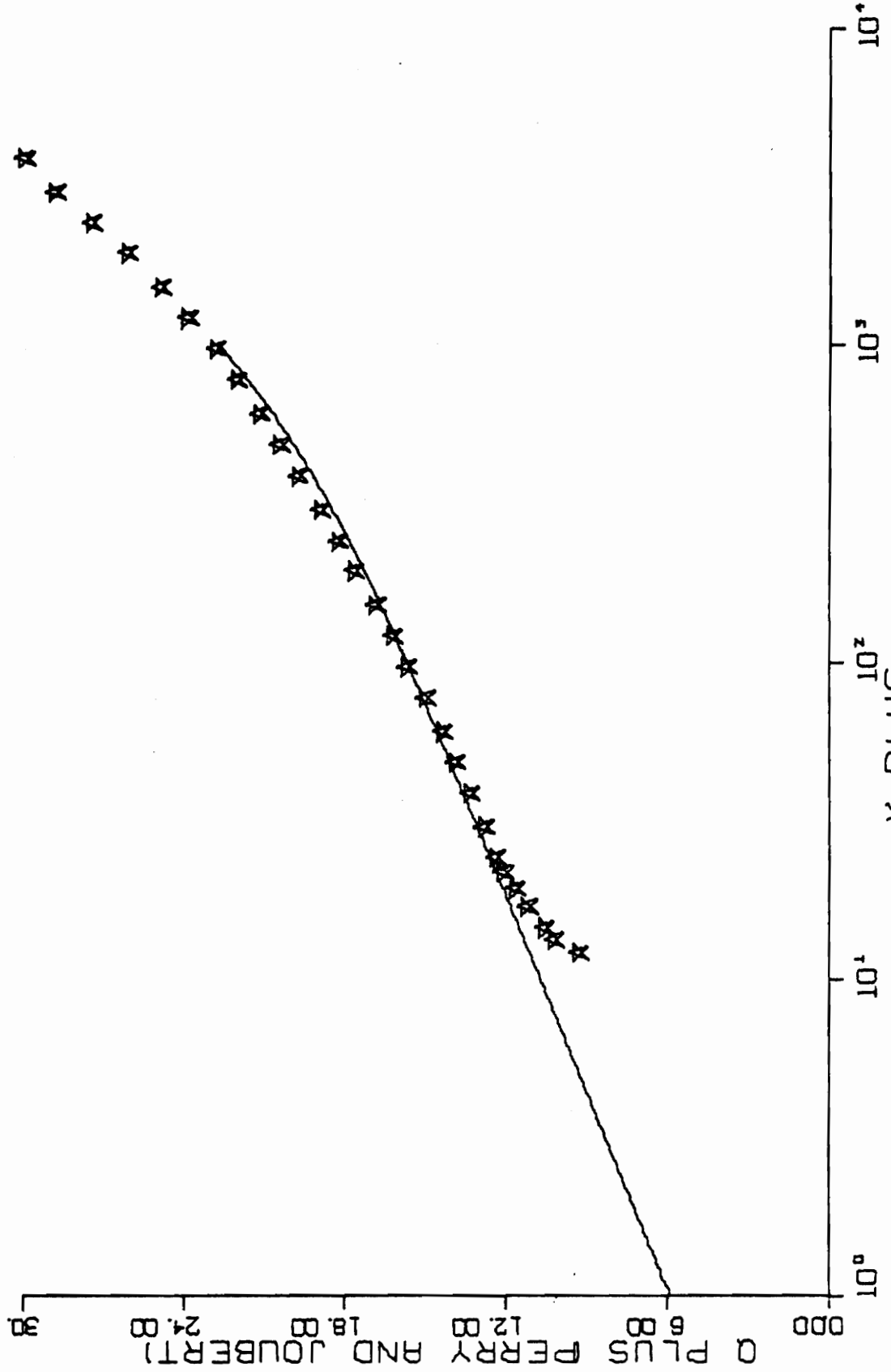

FIG. B 5-3. THREE-DIMENSIONAL SIMILARITY PLOT-RUN C7-01.

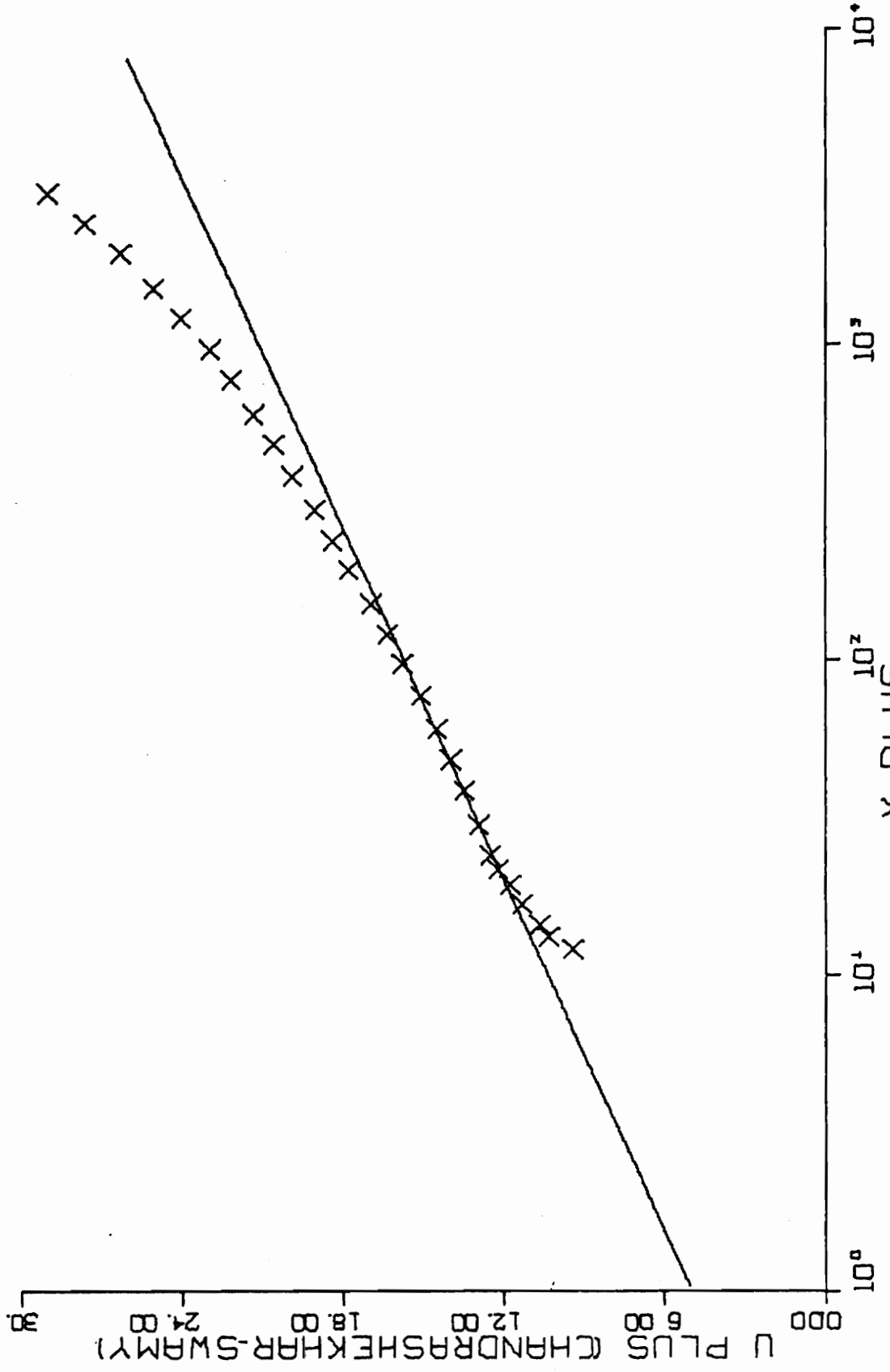

FIG. B 5-4. THREE-DIMENSIONAL SIMILARITY PLOT-RUN C7-01.

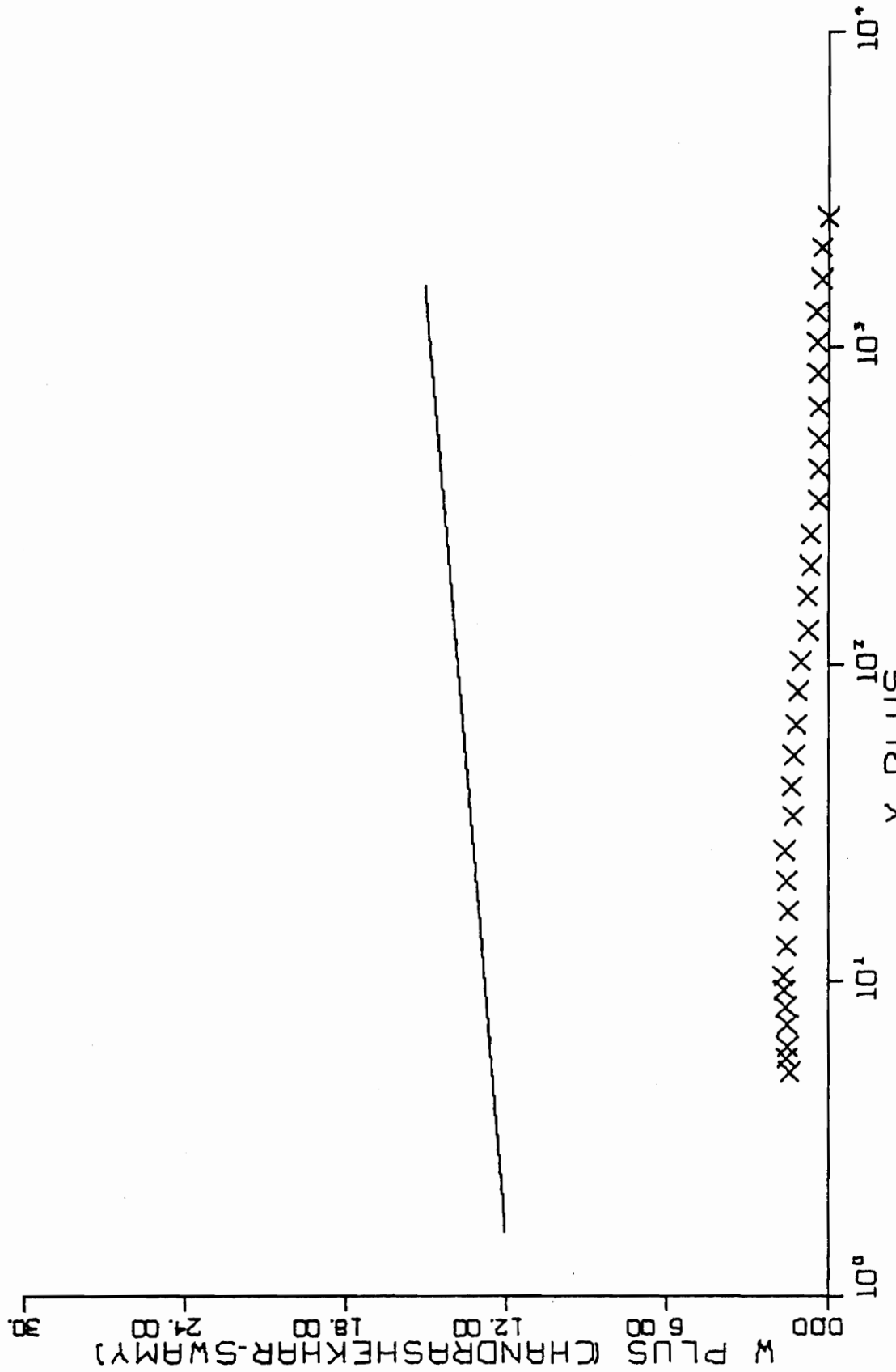

FIG. B 5-4. CONTINUED FOR RUN C7-01.

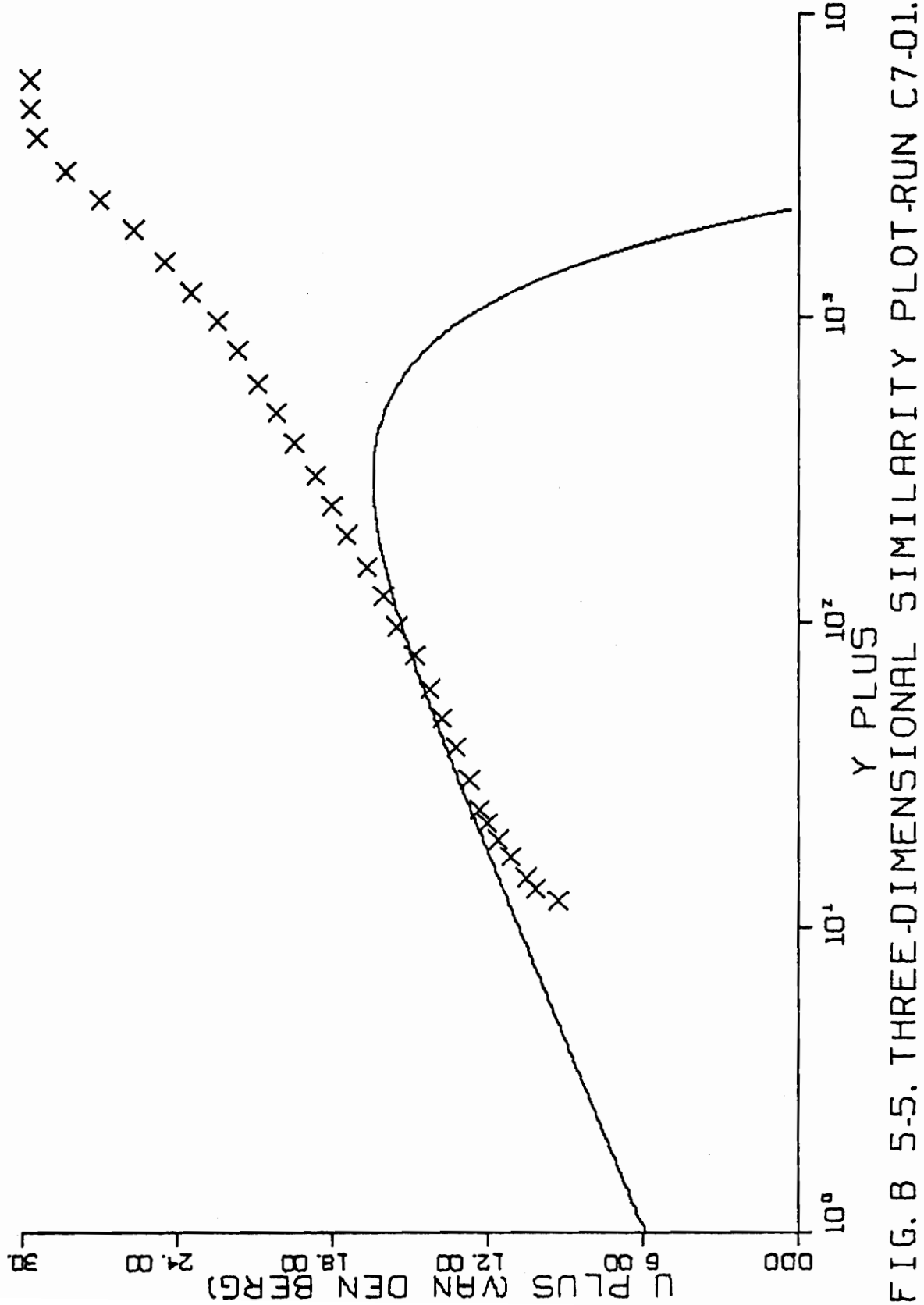

FIG. B 5-5. THREE-DIMENSIONAL SIMILARITY PLOT-RUN C7-01.

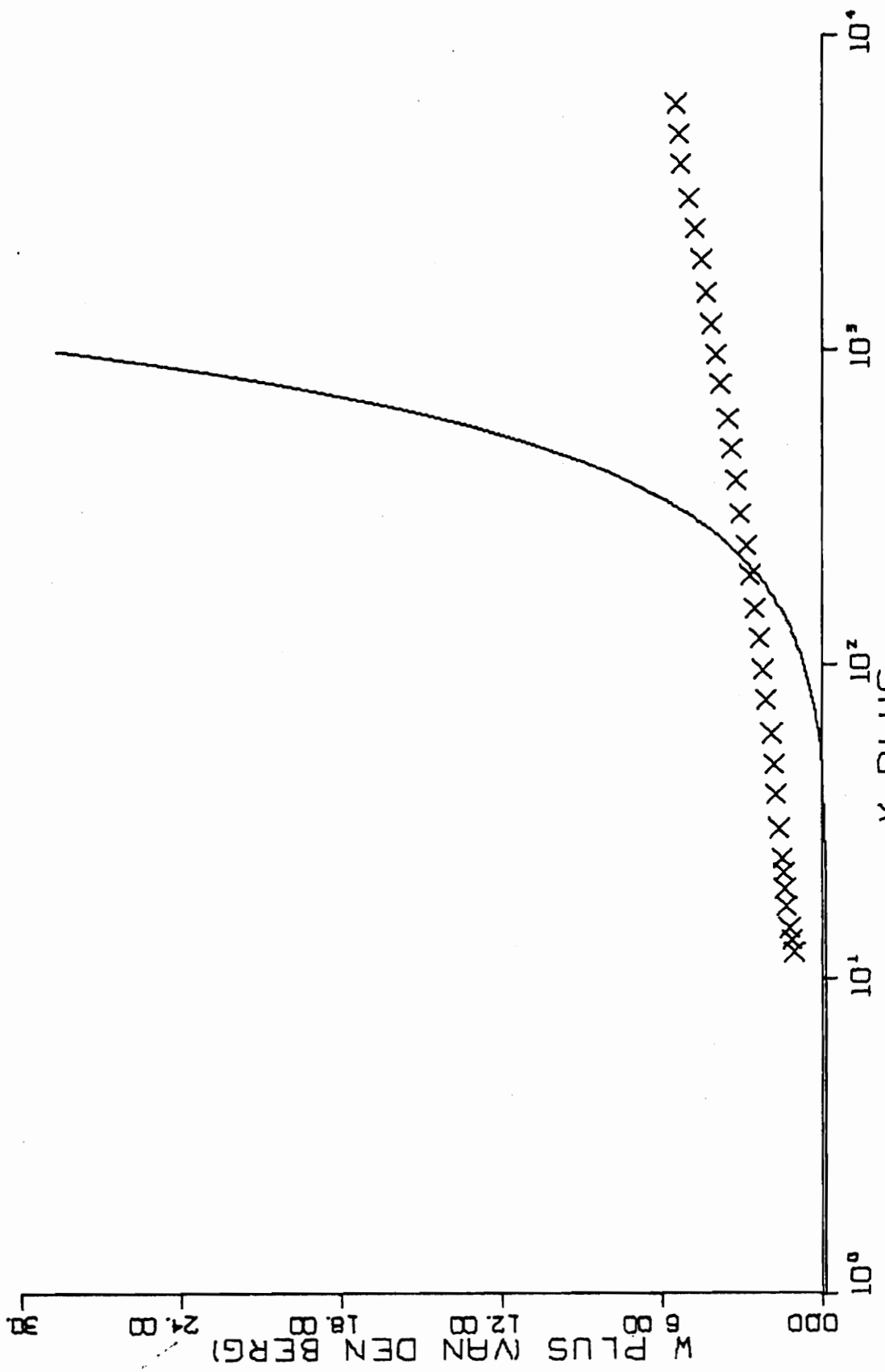

FIG. B 5-5. CONTINUED FOR RUN C7-01.

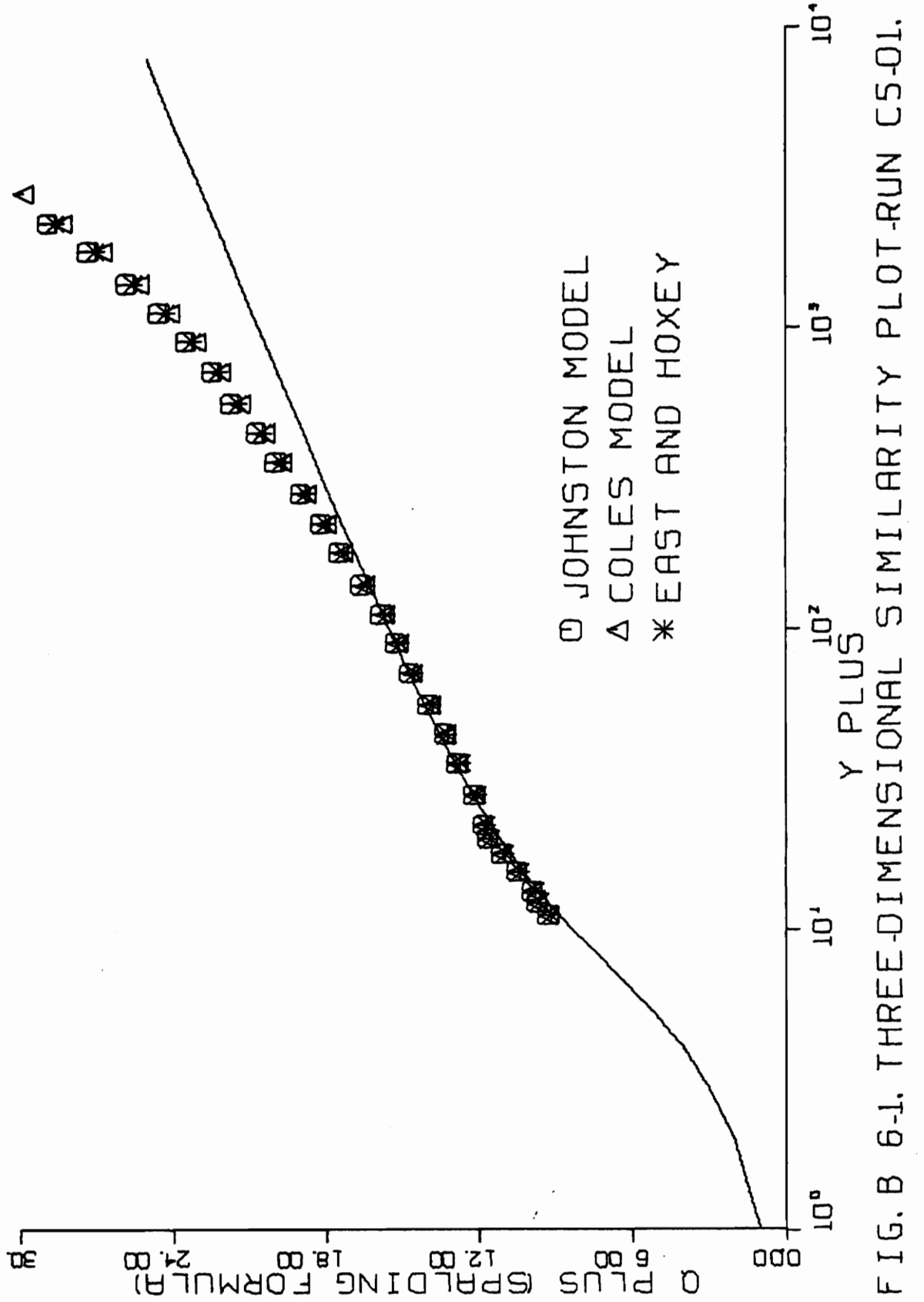

FIG. B 6-1. THREE-DIMENSIONAL SIMILARITY PLOT-RUN C5-01.

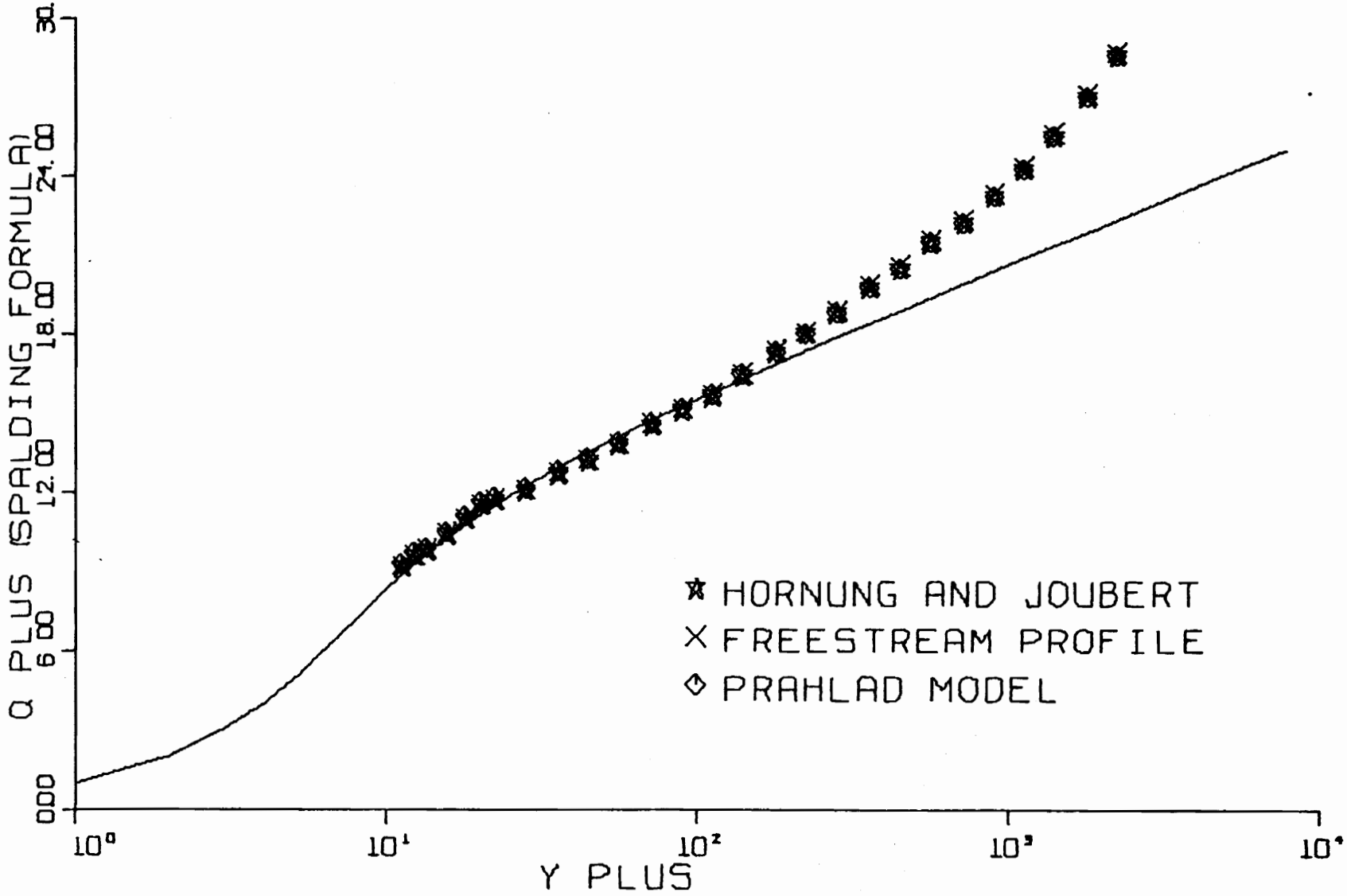

FIG. B 6-2. THREE-DIMENSIONAL SIMILARITY PLOT-RUN C5-01.

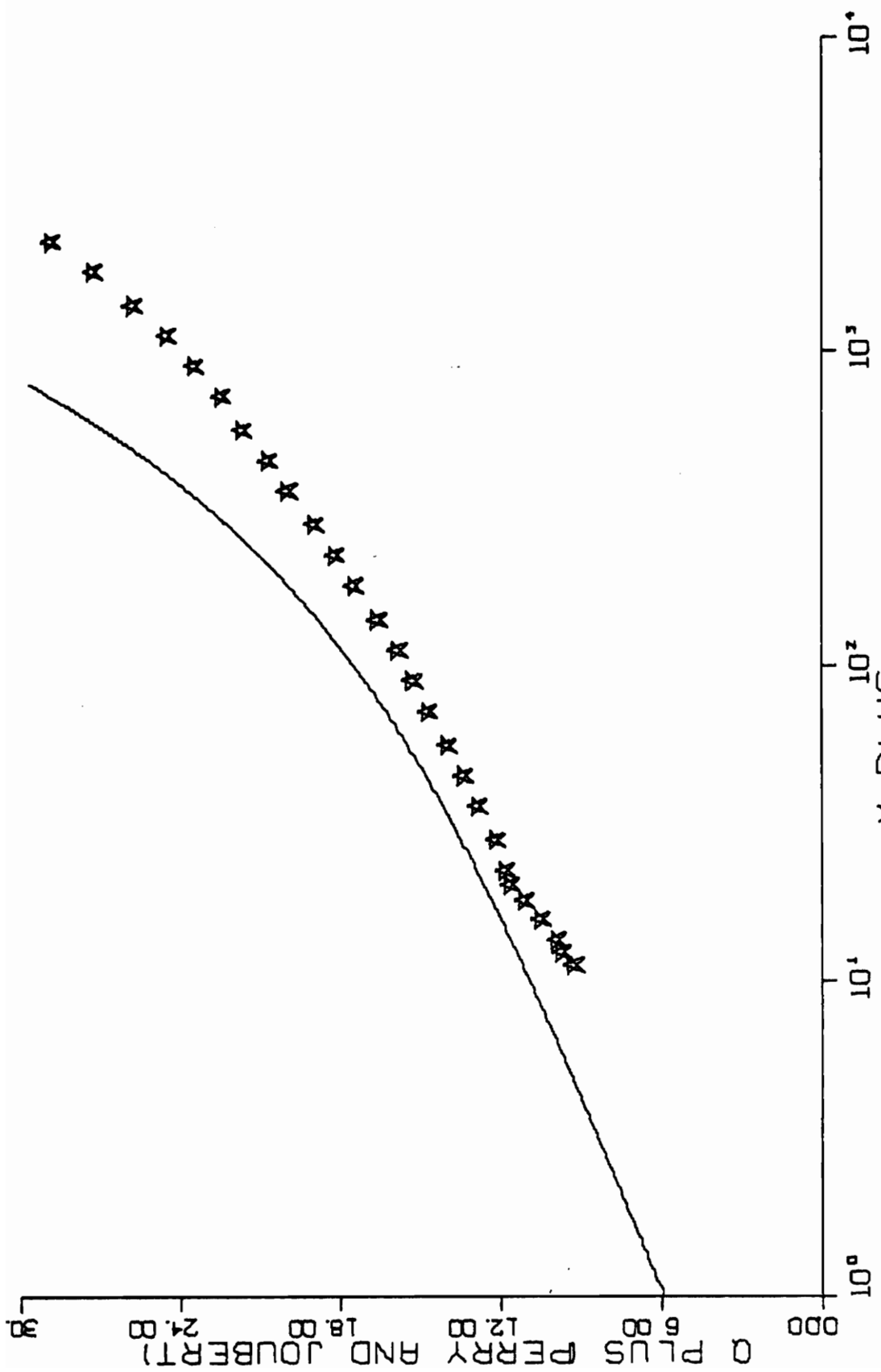

FIG. B 6-3. THREE-DIMENSIONAL SIMILARITY PLOT-RUN C5-01.

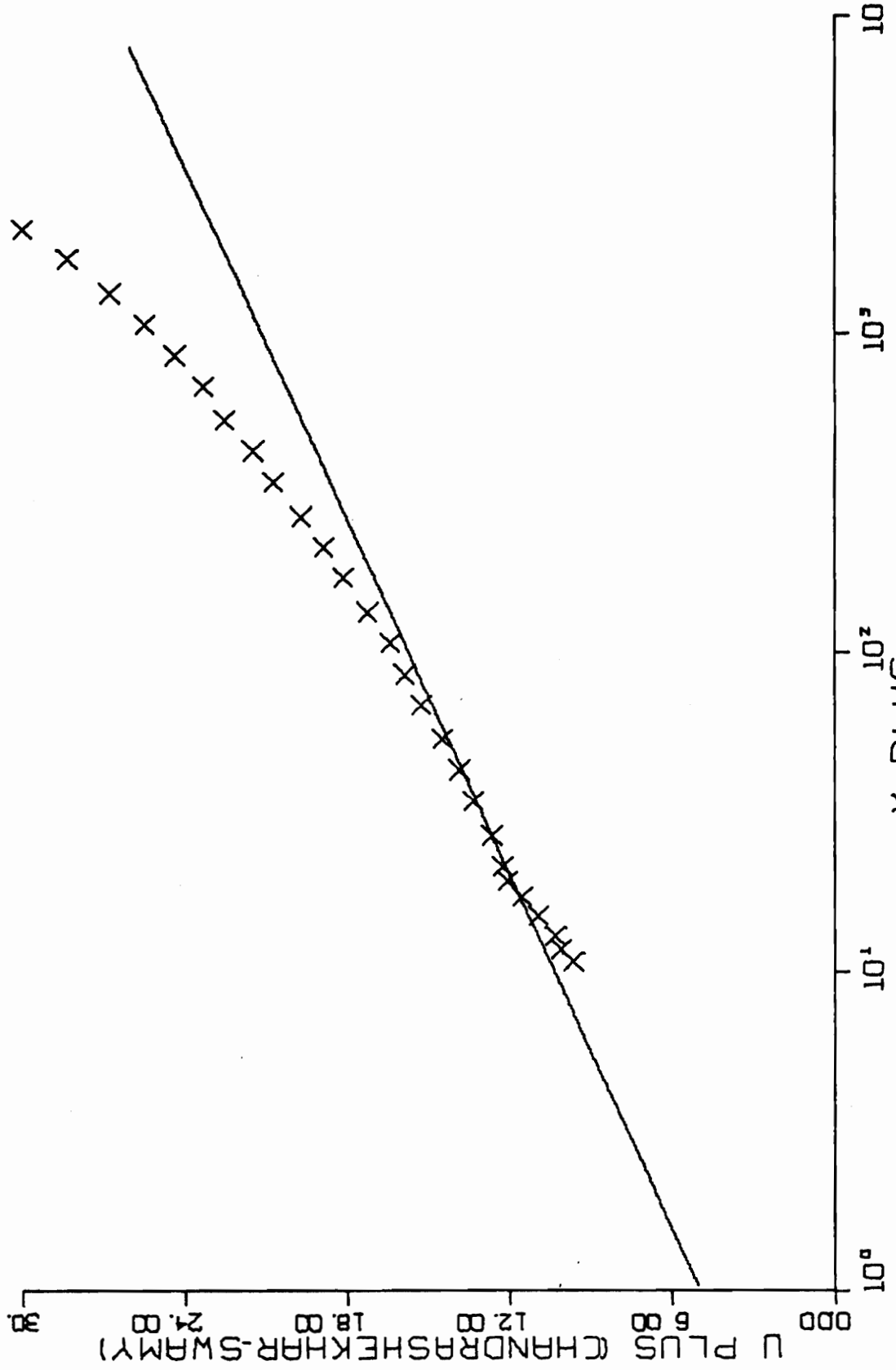

FIG. B 6-4. THREE-DIMENSIONAL SIMILARITY PLOT-RUN C5-01.

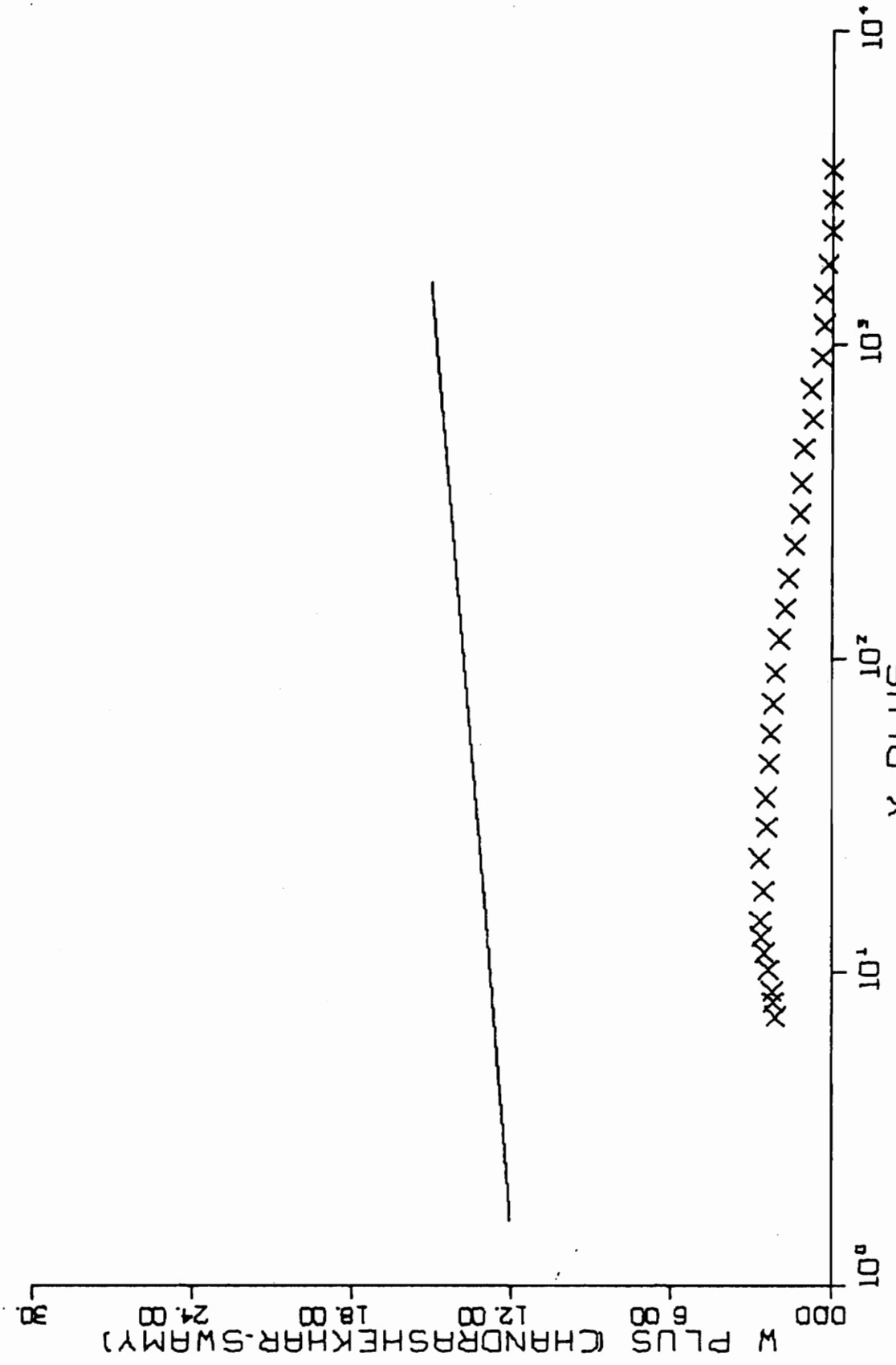

FIG. B 6-4. CONTINUED FOR RUN C5-01.

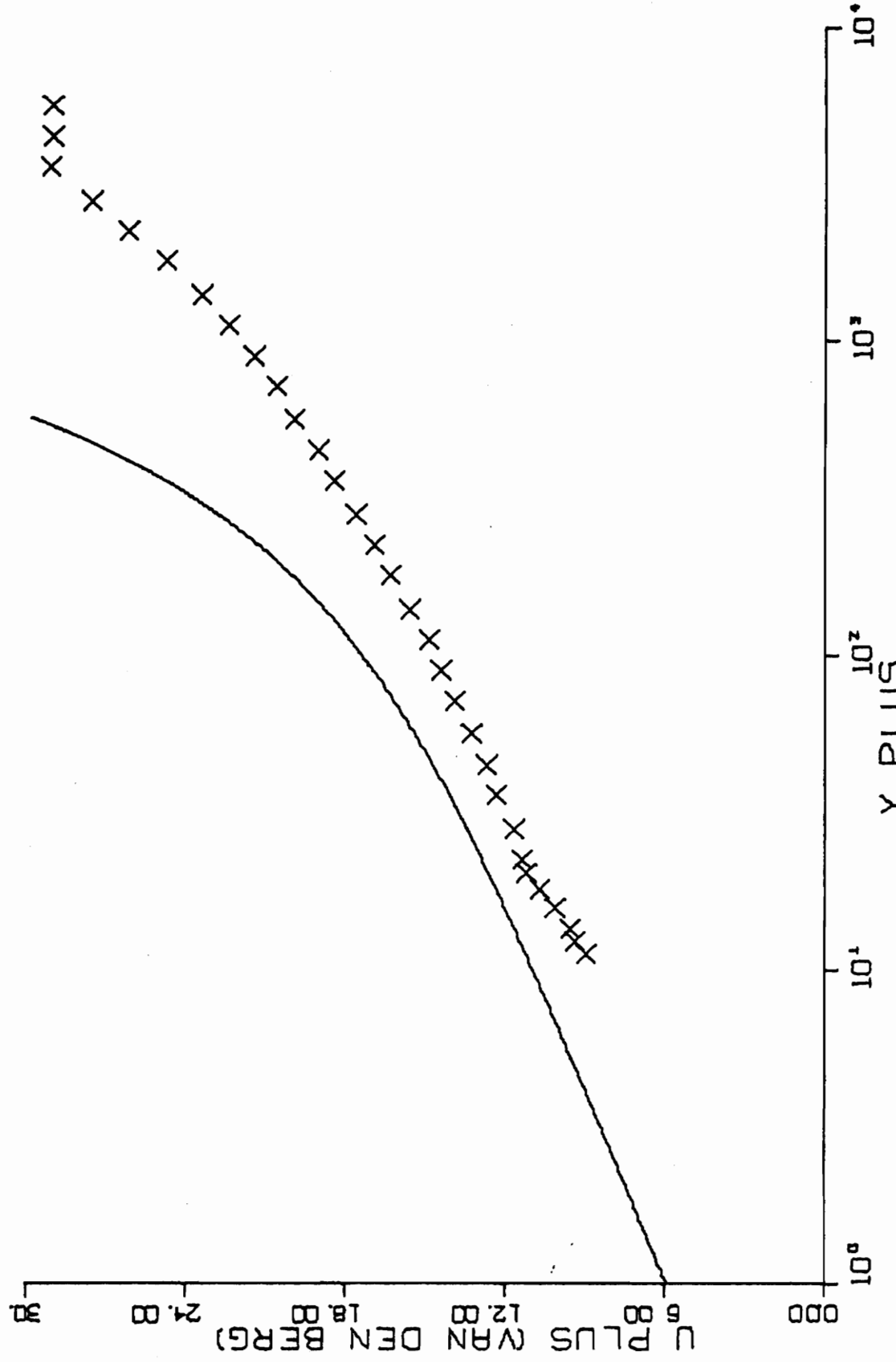

FIG. B 6-5. THREE-DIMENSIONAL SIMILARITY PLOT-RUN C5-01.

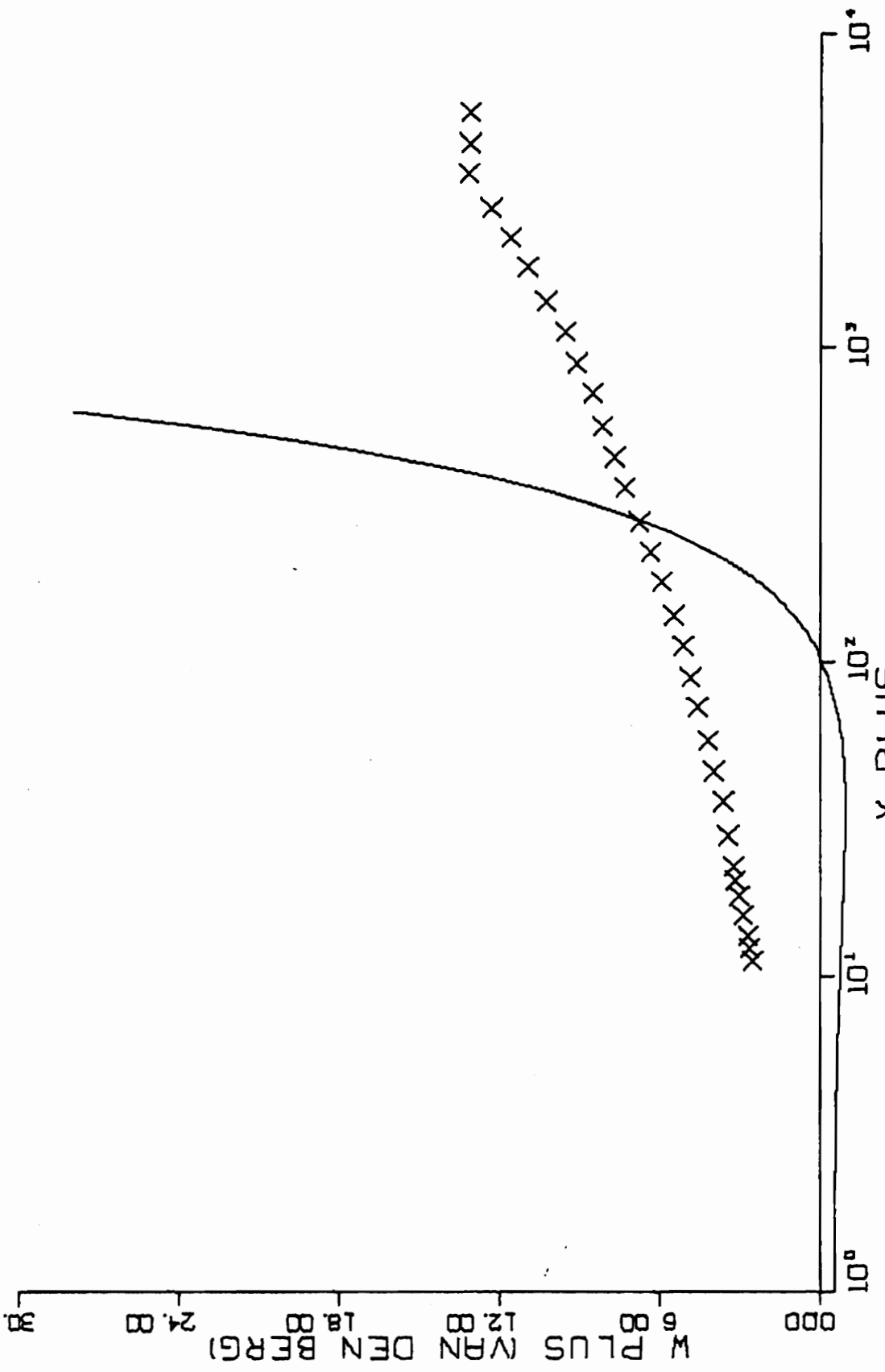

FIG. B 6-5. CONTINUED FOR RUN C5-01.

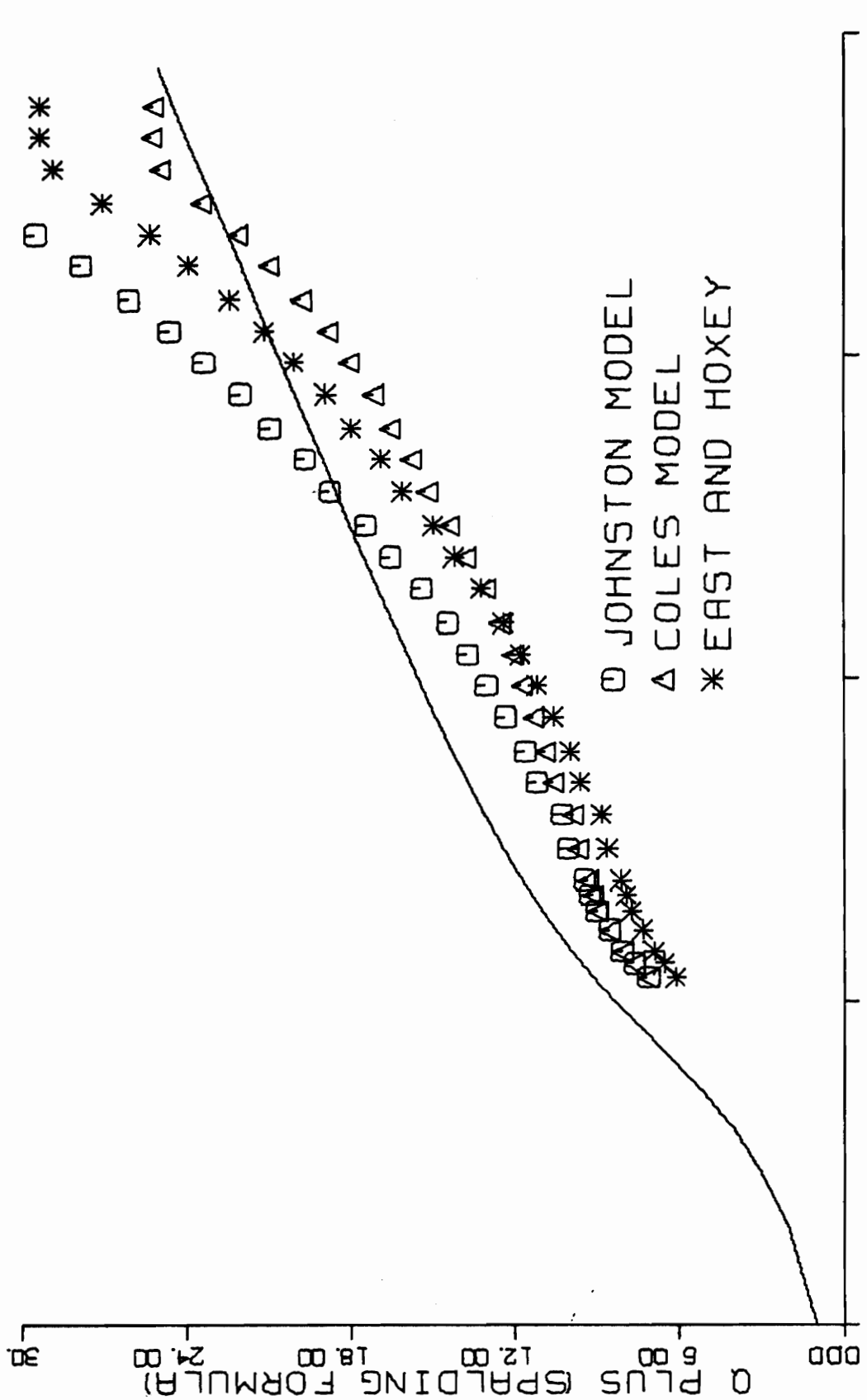

FIG. B 7-1. THREE-DIMENSIONAL SIMILARITY PLOT-RUN C3-01.

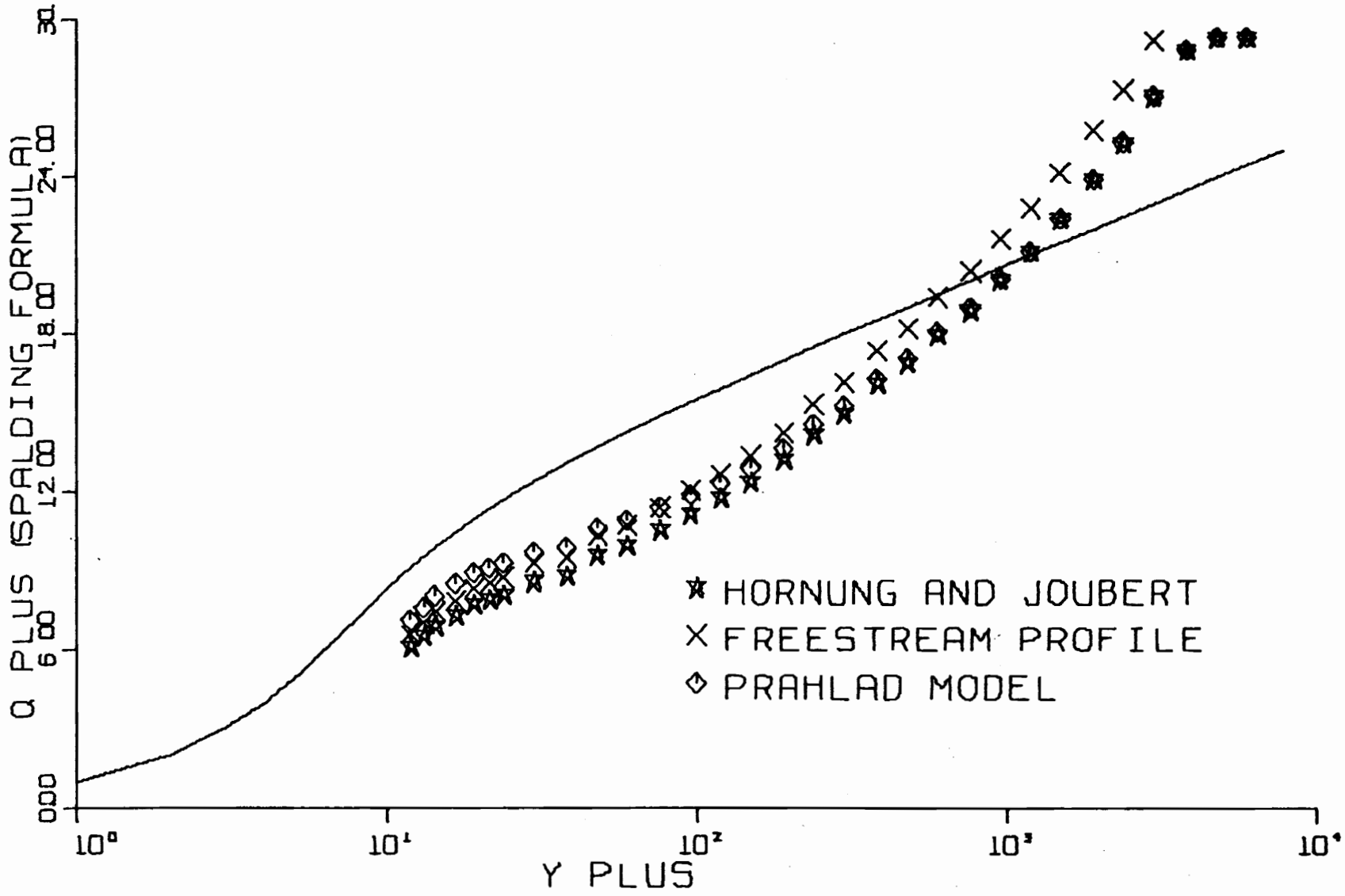

FIG. B 7-2. THREE-DIMENSIONAL SIMILARITY PLOT-RUN C3-01.

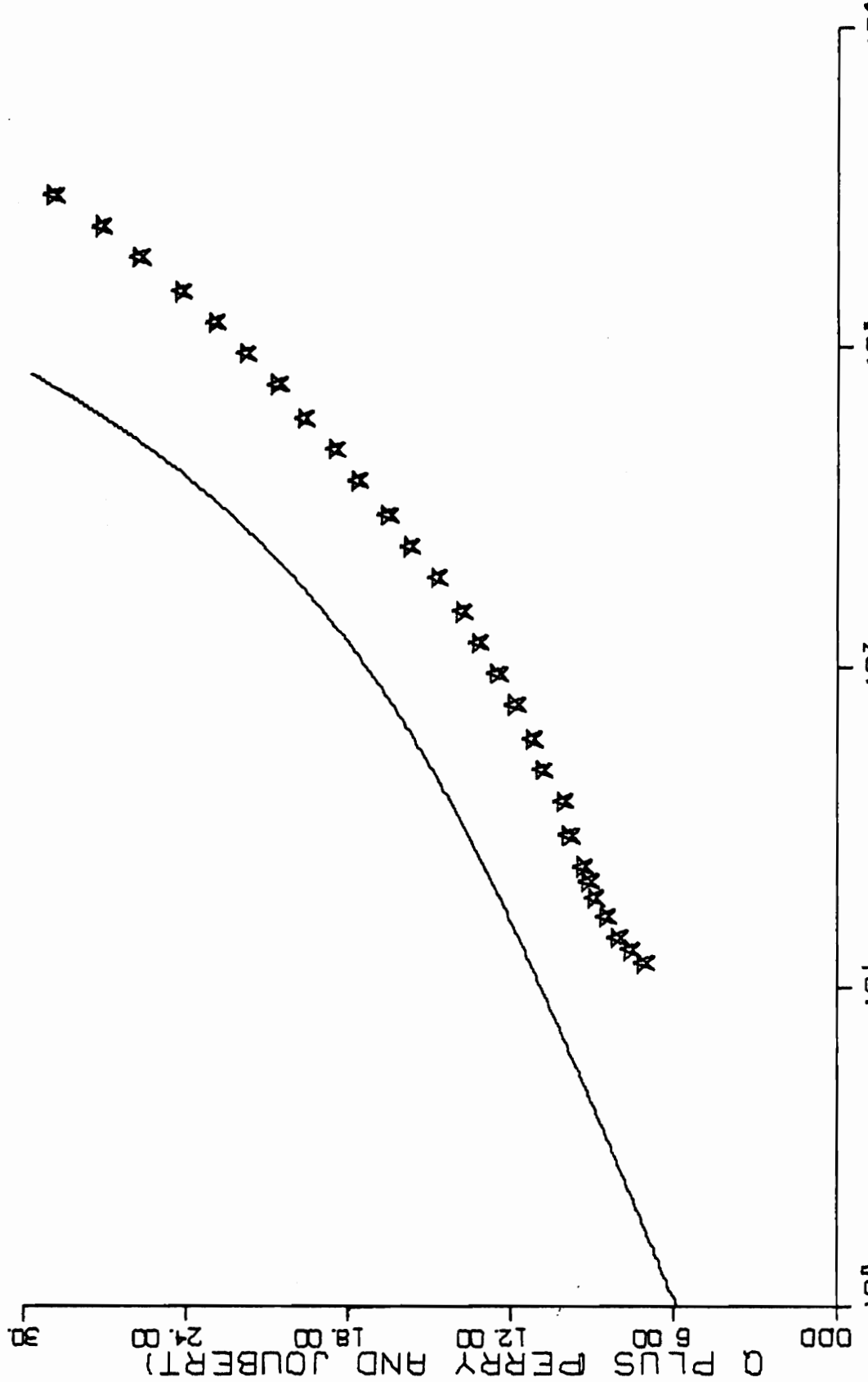

FIG. B 7-3. THREE-DIMENSIONAL SIMILARITY PLOT-RUN C3-01.

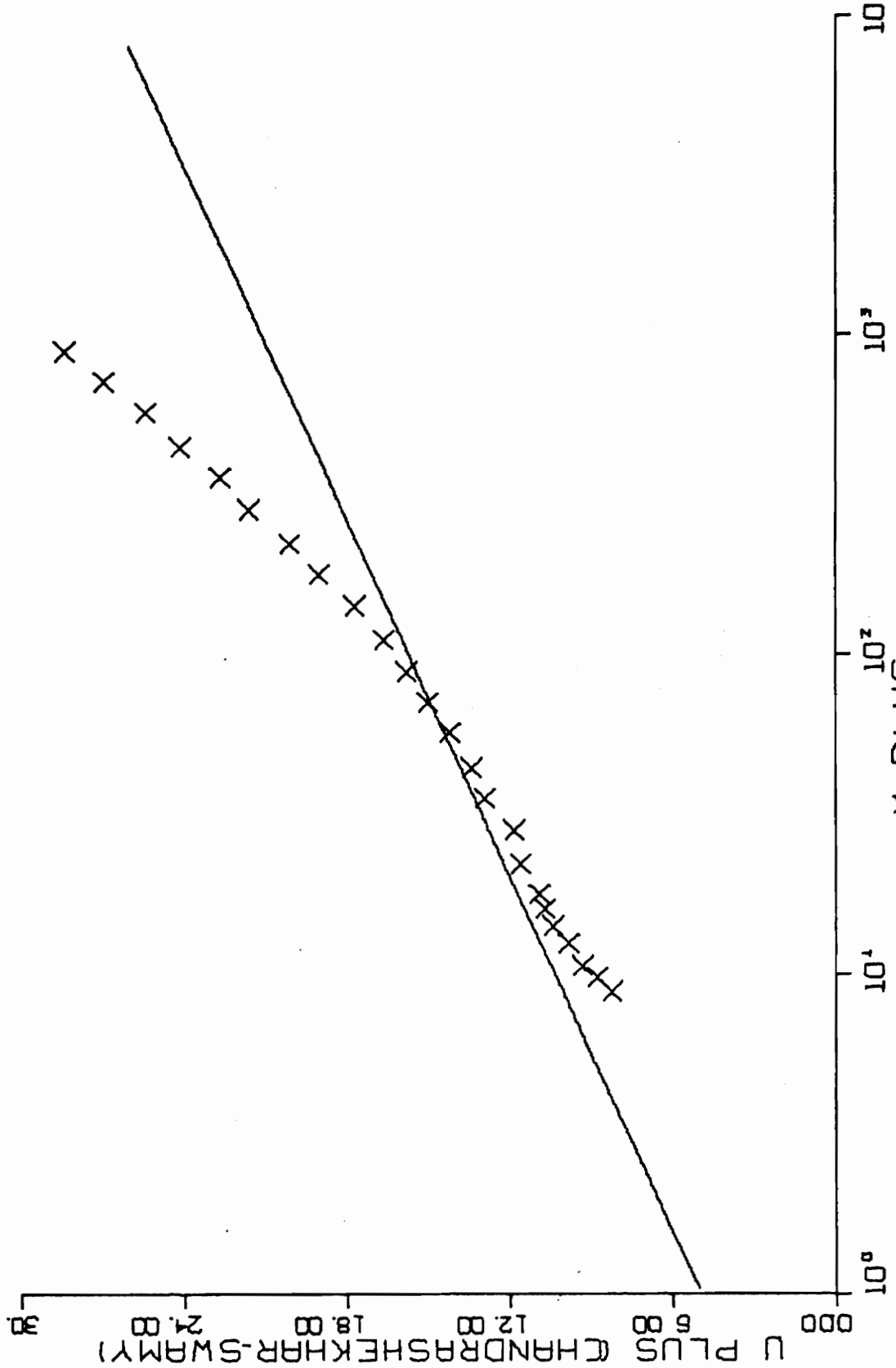

FIG. B 7-4. THREE-DIMENSIONAL SIMILARITY PLOT-RUN C3-01.

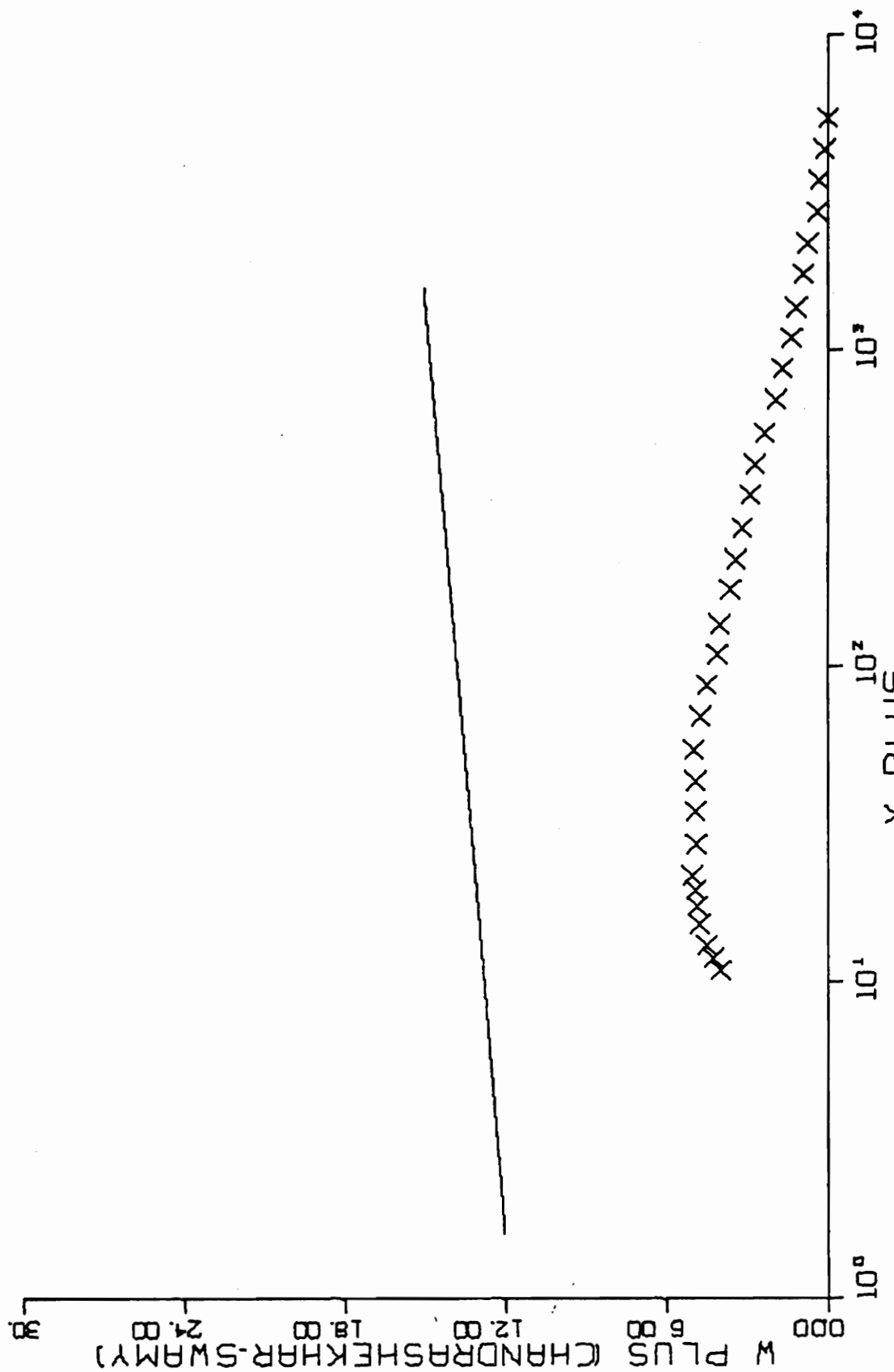

FIG. B 7-4. CONTINUED FOR RUN C3-01.

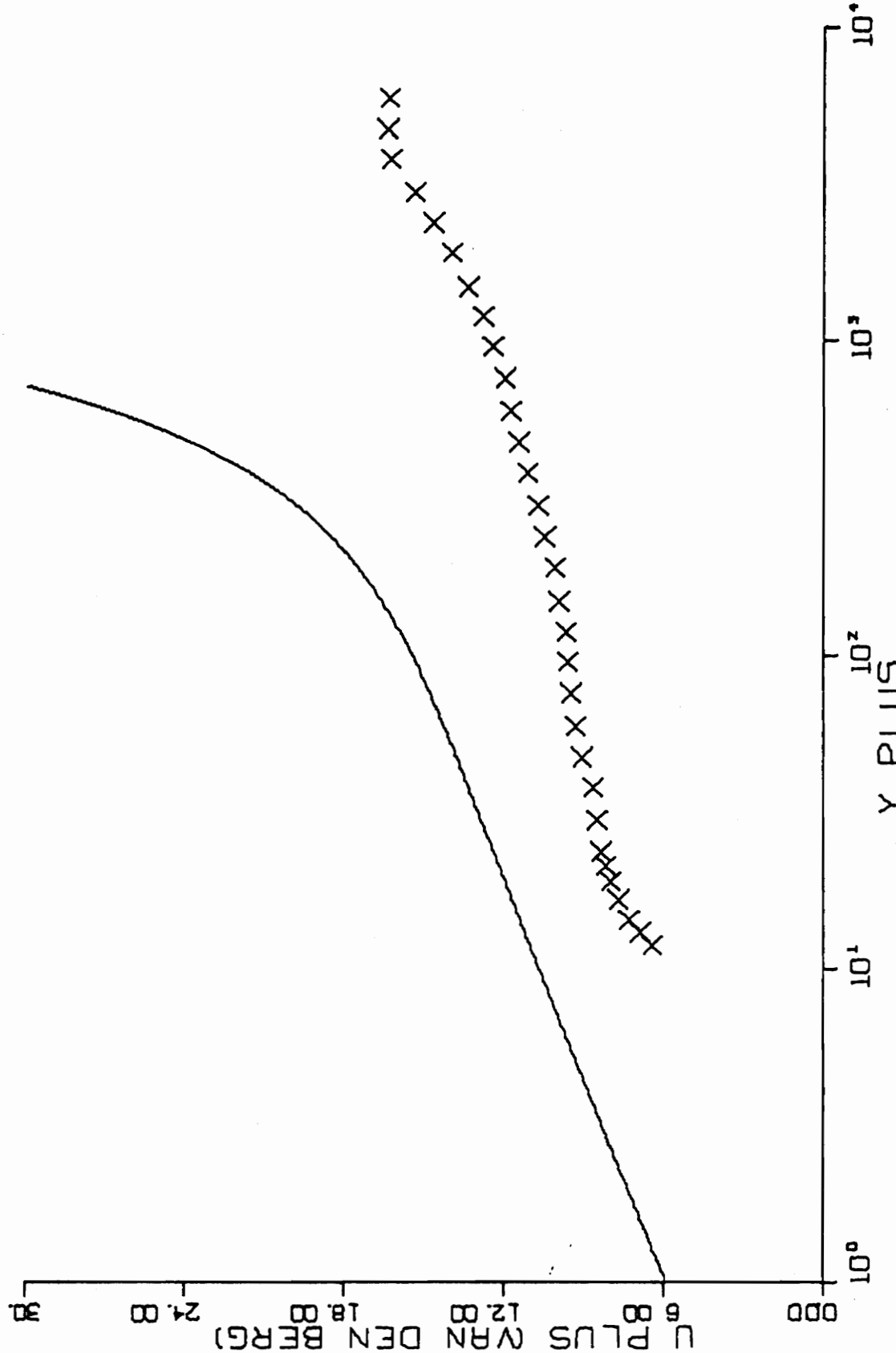

FIG. B 7-5. THREE-DIMENSIONAL SIMILARITY PLOT-RUN C3-01.

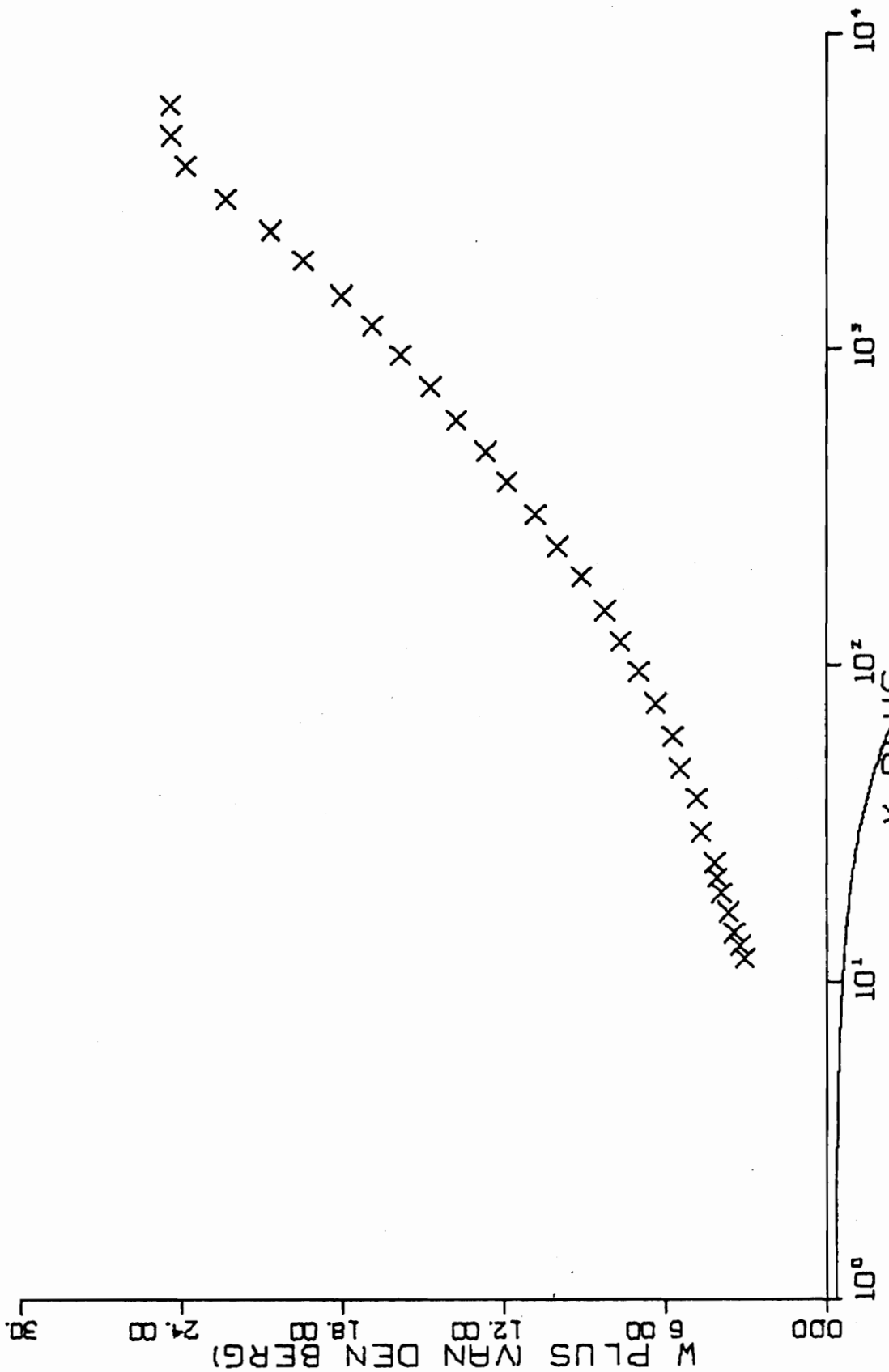

FIG. B 7-5, CONTINUED FOR RUN C3-01.

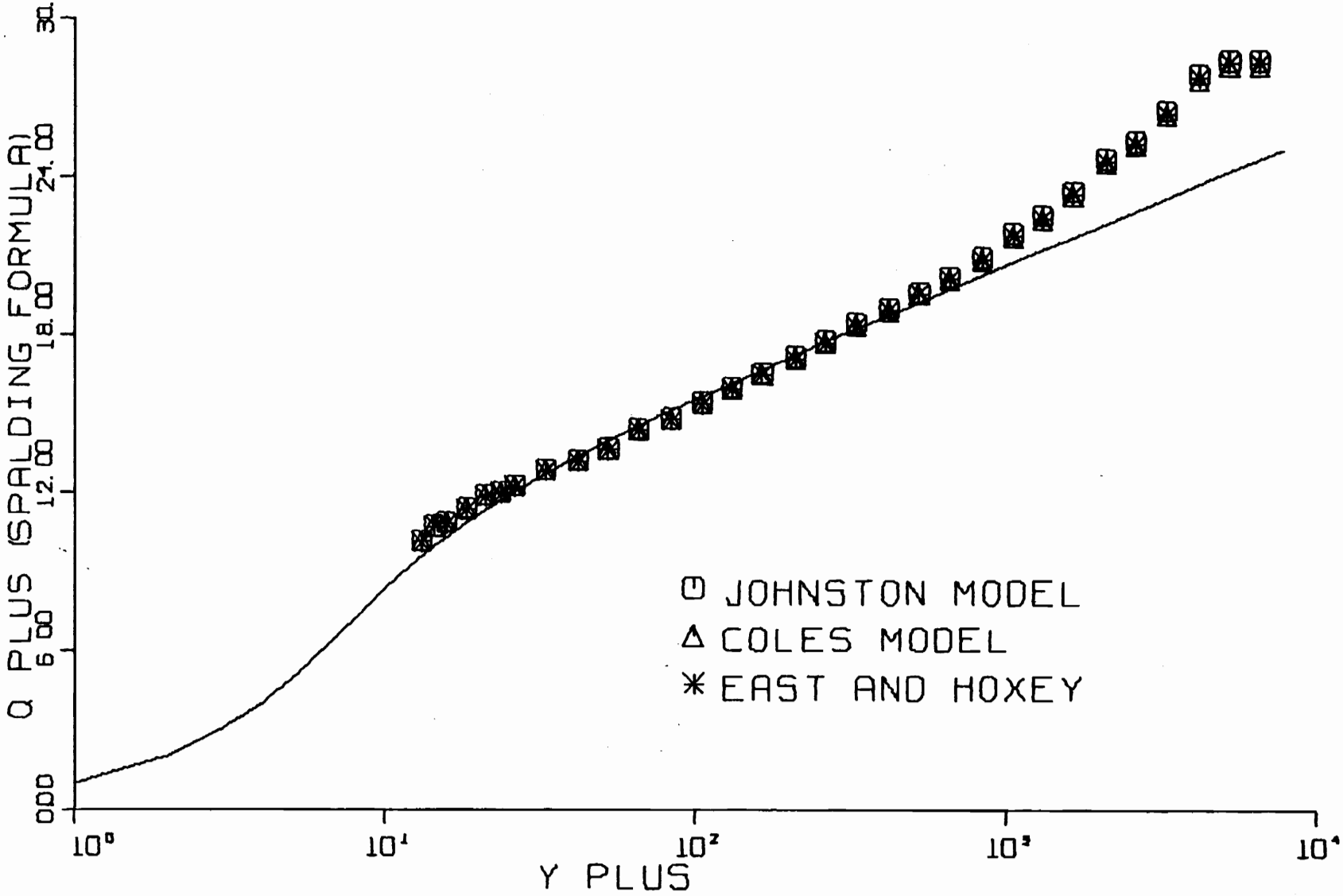

FIG. B 8-1. THREE-DIMENSIONAL SIMILARITY PLOT-RUN E7-01.

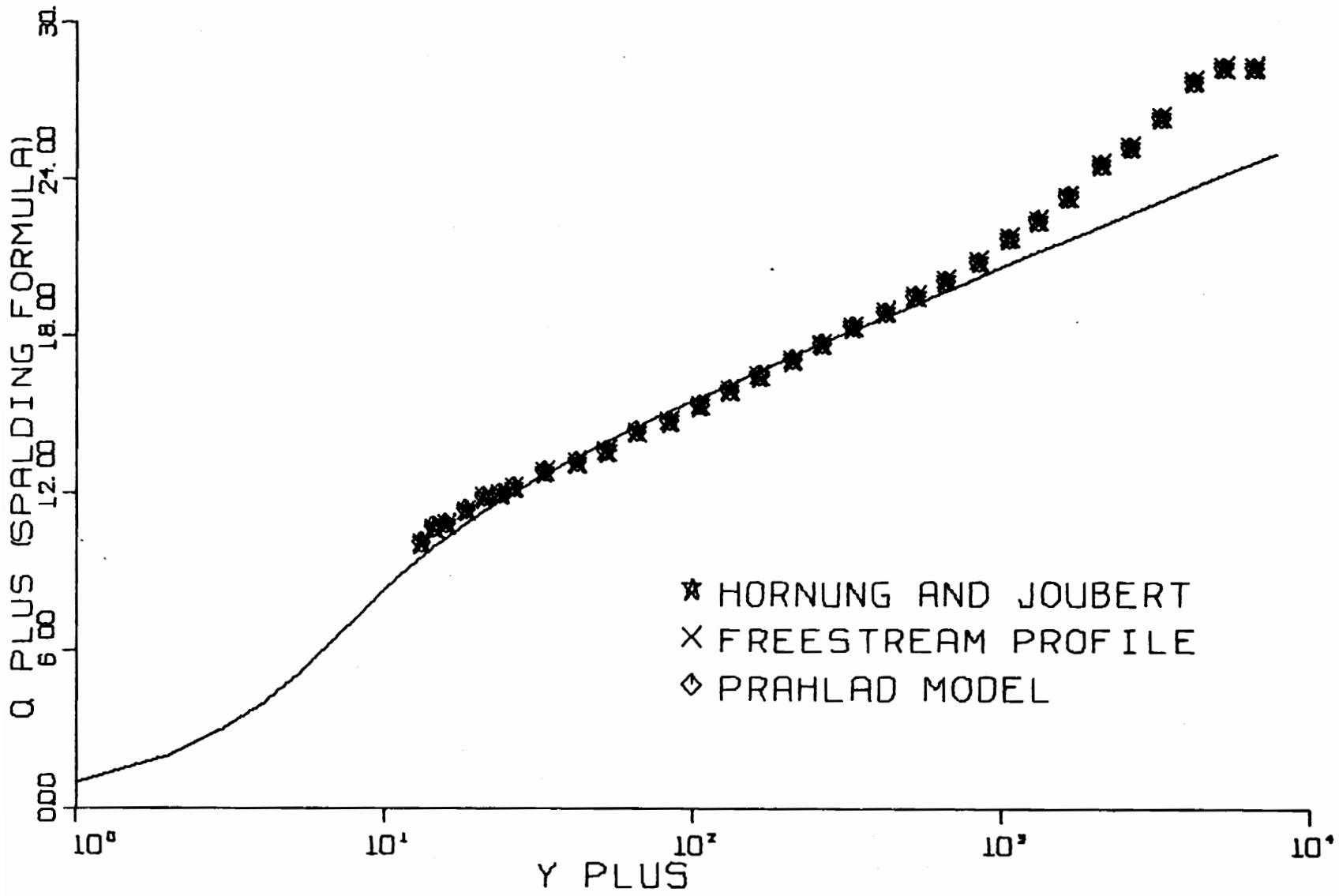

FIG. B 8-2. THREE-DIMENSIONAL SIMILARITY PLOT-RUN E7-01.

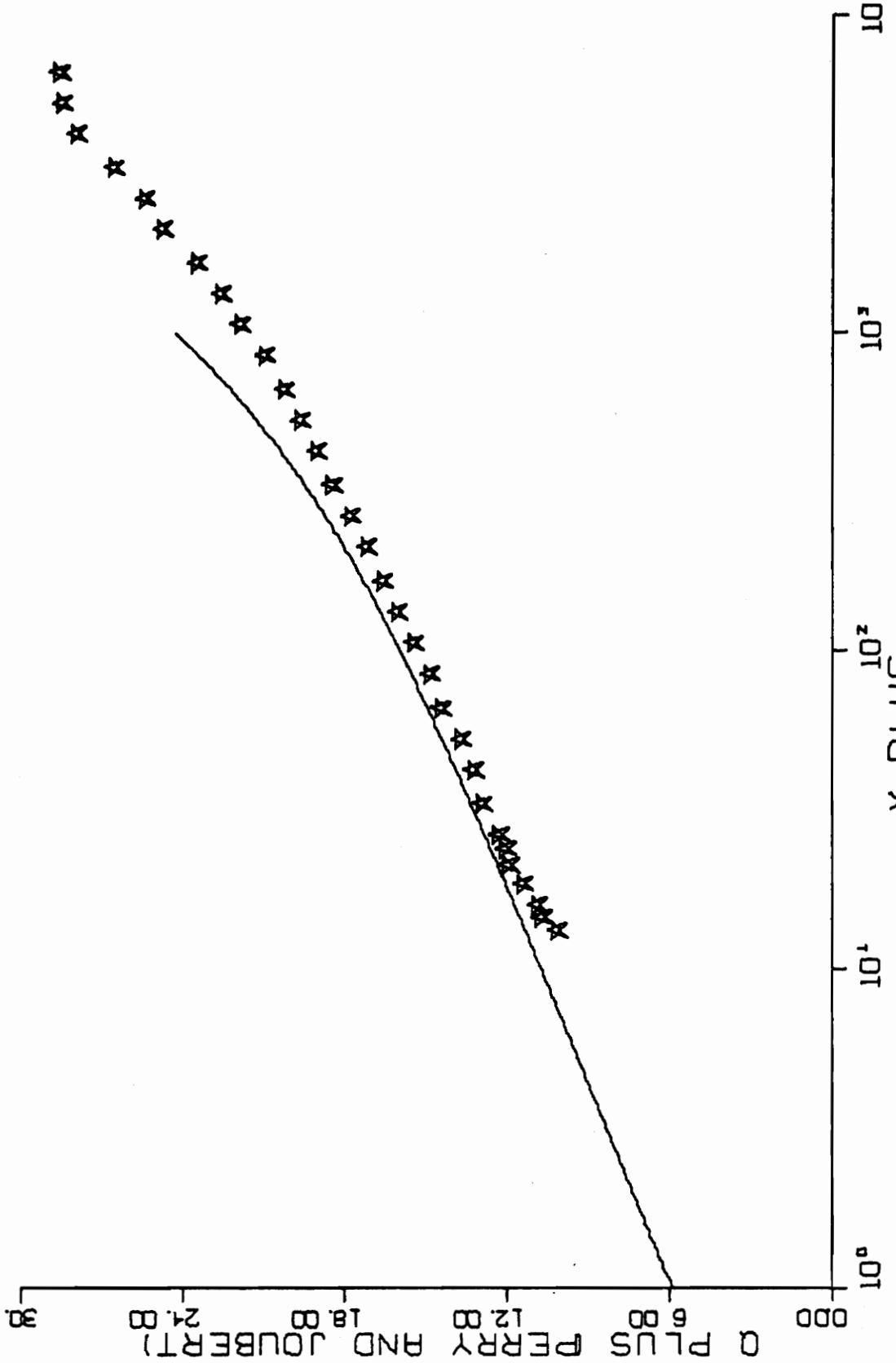

FIG. B 8-3. THREE-DIMENSIONAL SIMILARITY PLOT-RUN E7-01.

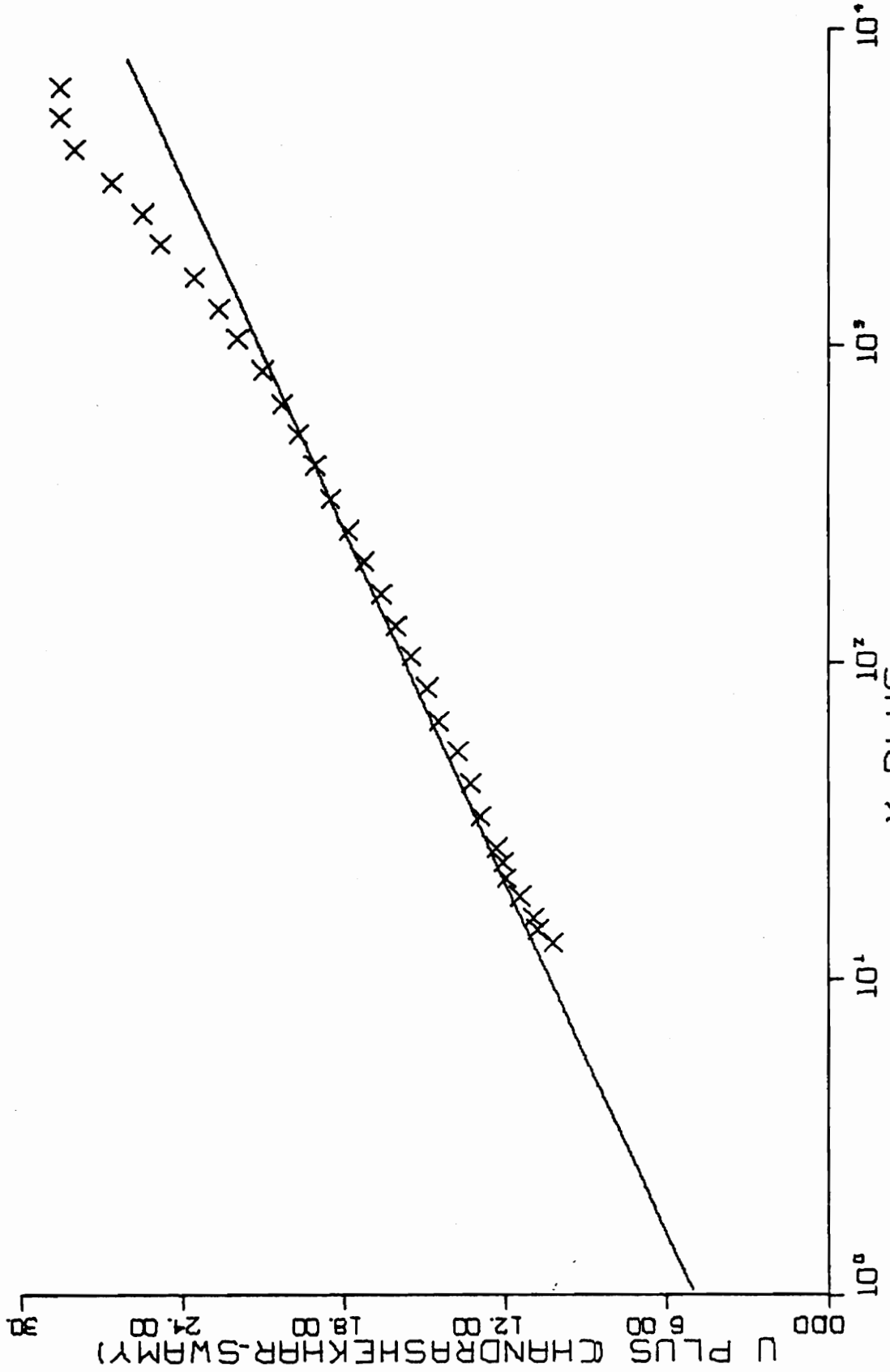

FIG. B 8-4. THREE-DIMENSIONAL SIMILARITY PLOT-RUN E7-01.

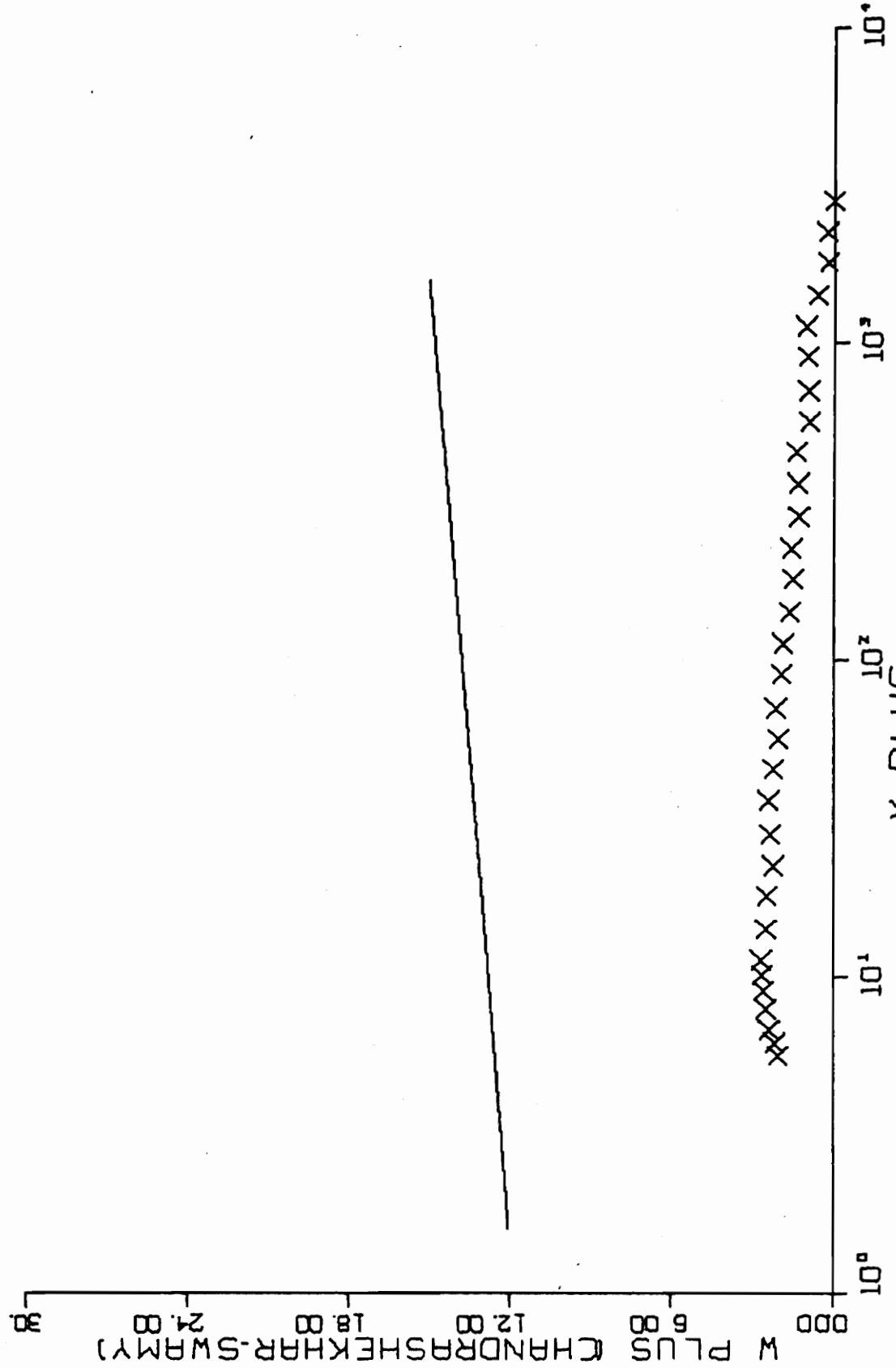

FIG. B 8-4. CONTINUED FOR RUN E7-01.

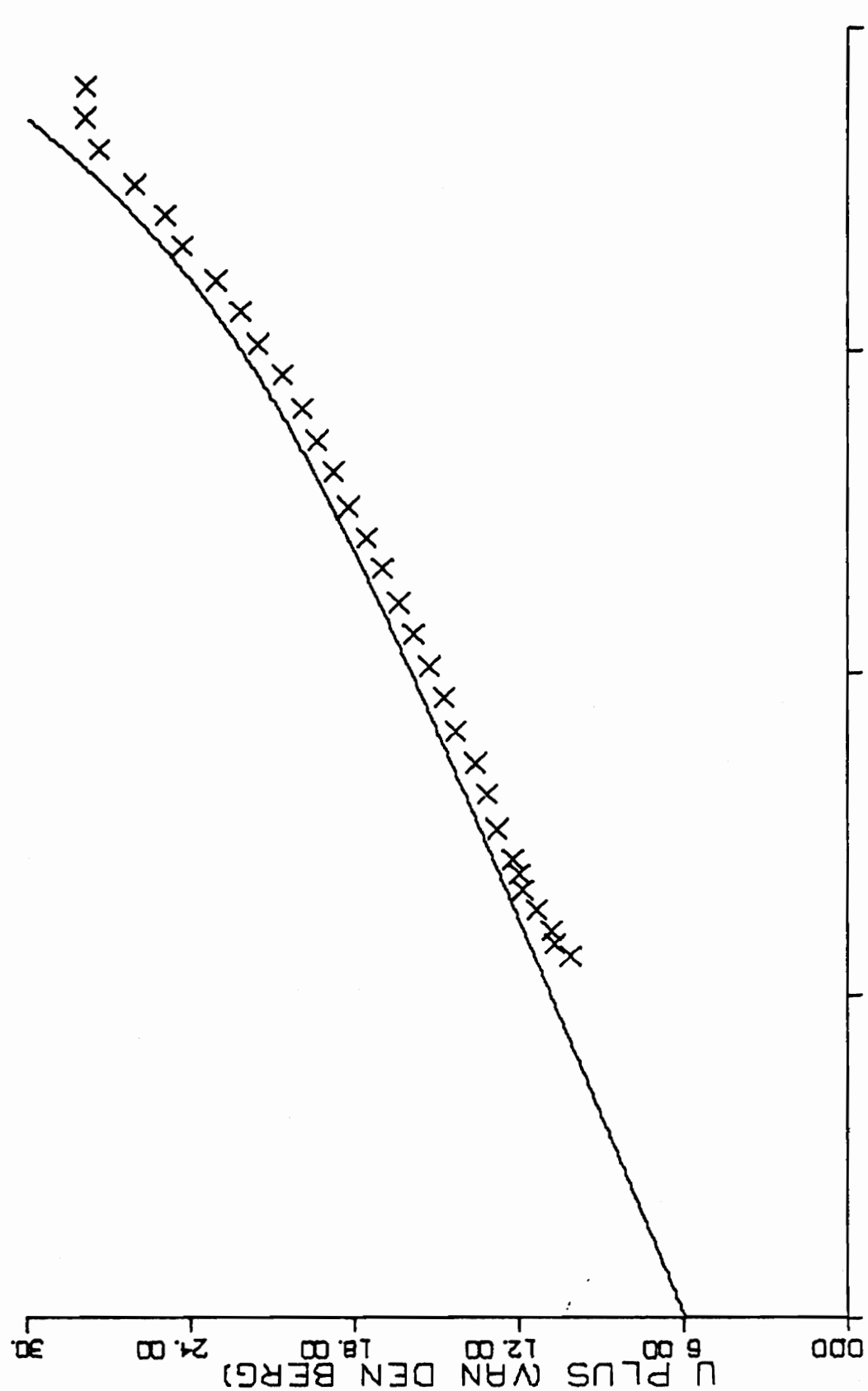

FIG. B 8-5. THREE-DIMENSIONAL SIMILARITY PLOT-RUN E7-01.

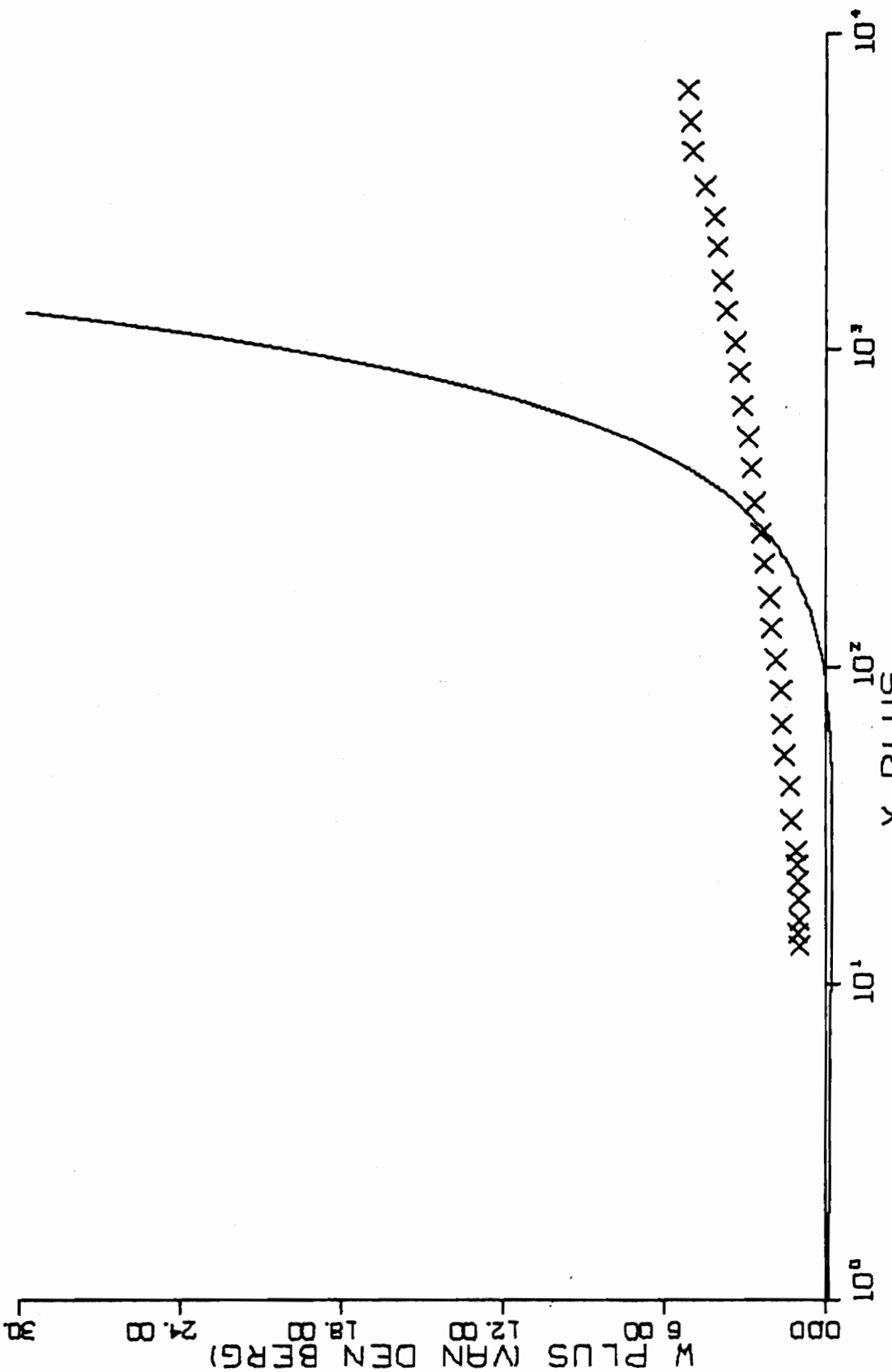

FIG. B 8-5. CONTINUED FOR RUN E7-01.

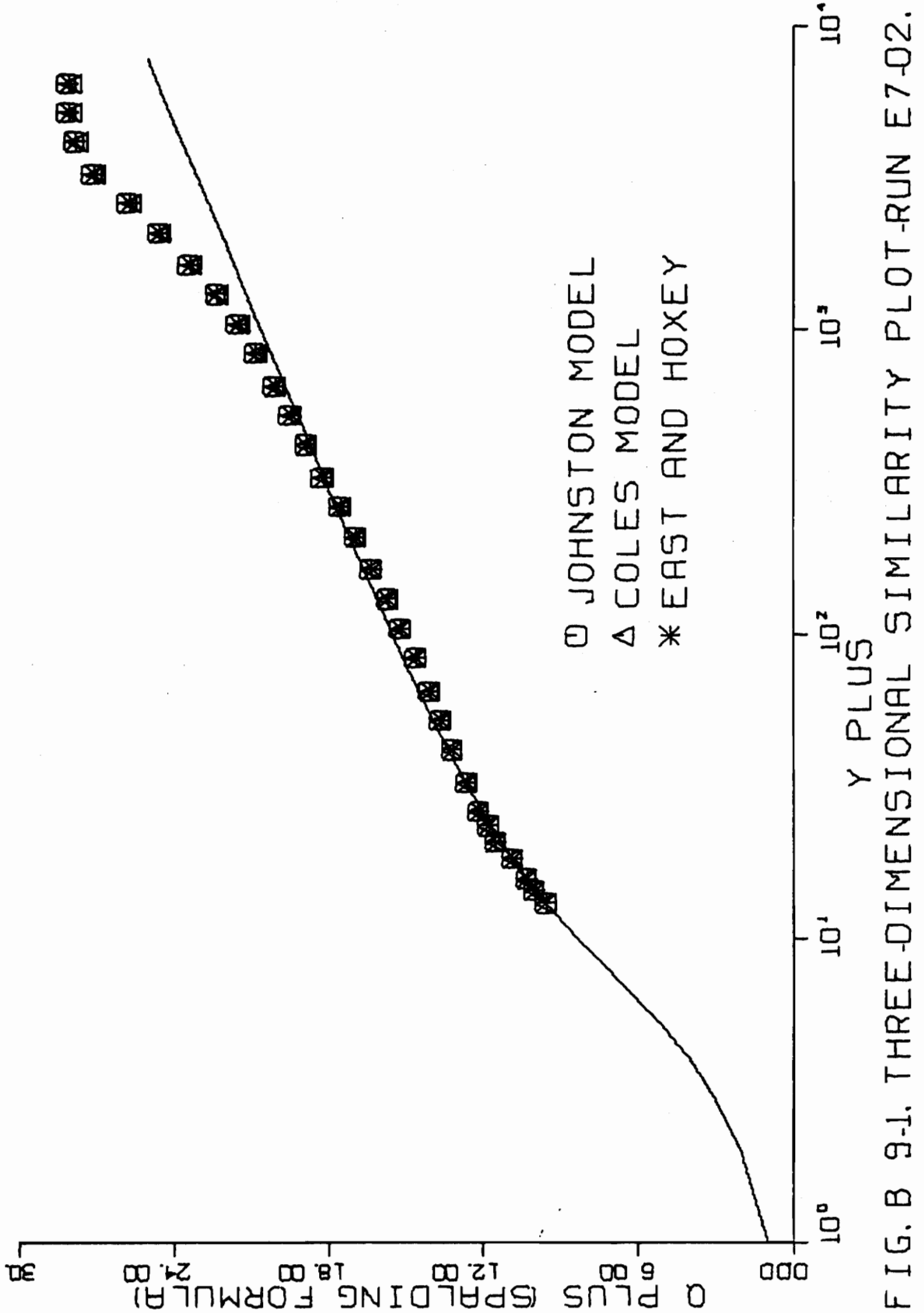

FIG. B 9-1. THREE-DIMENSIONAL SIMILARITY PLOT-RUN E7-02.

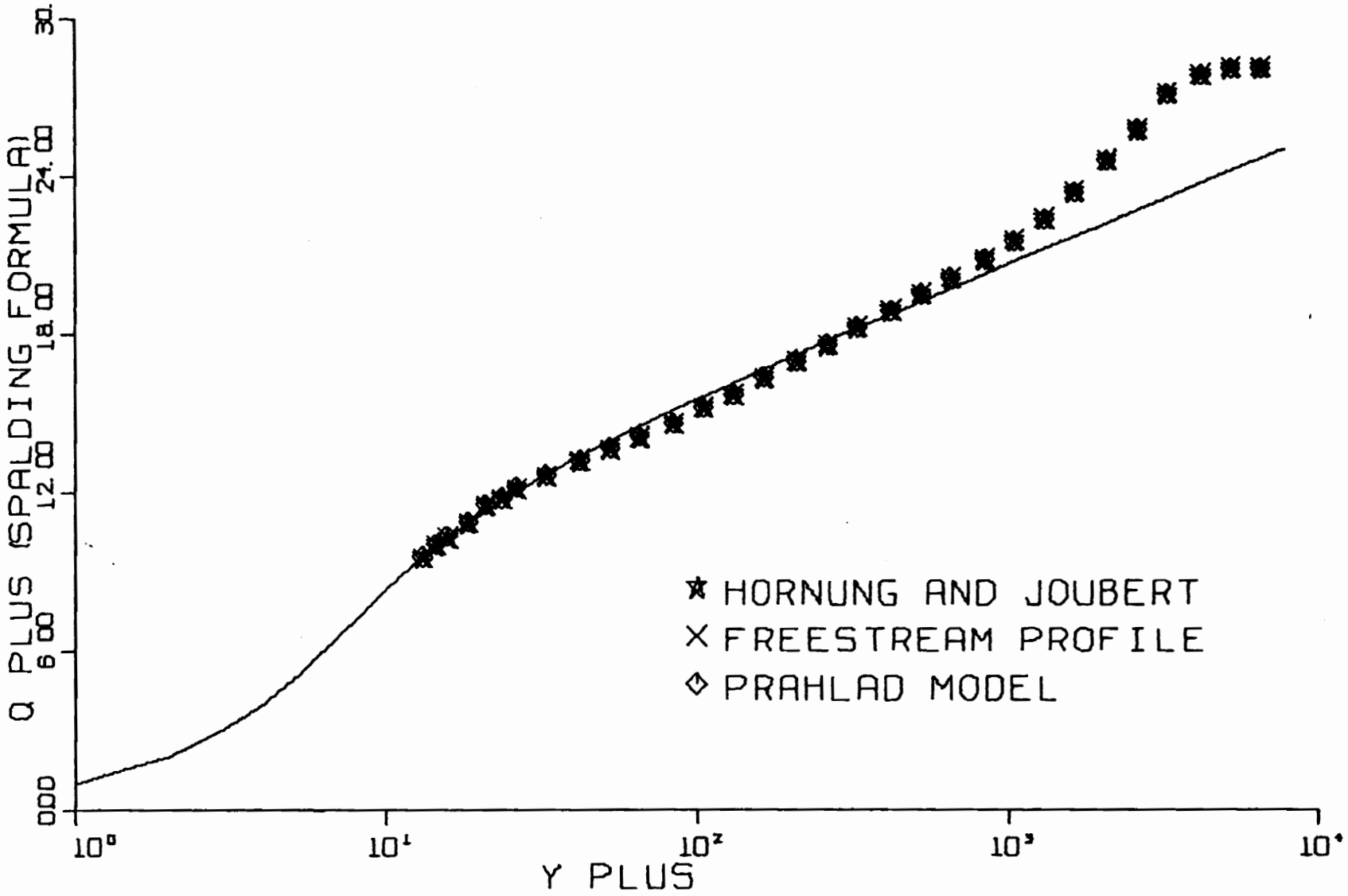

FIG. B 9-2. THREE-DIMENSIONAL SIMILARITY PLOT-RUN E7-02.

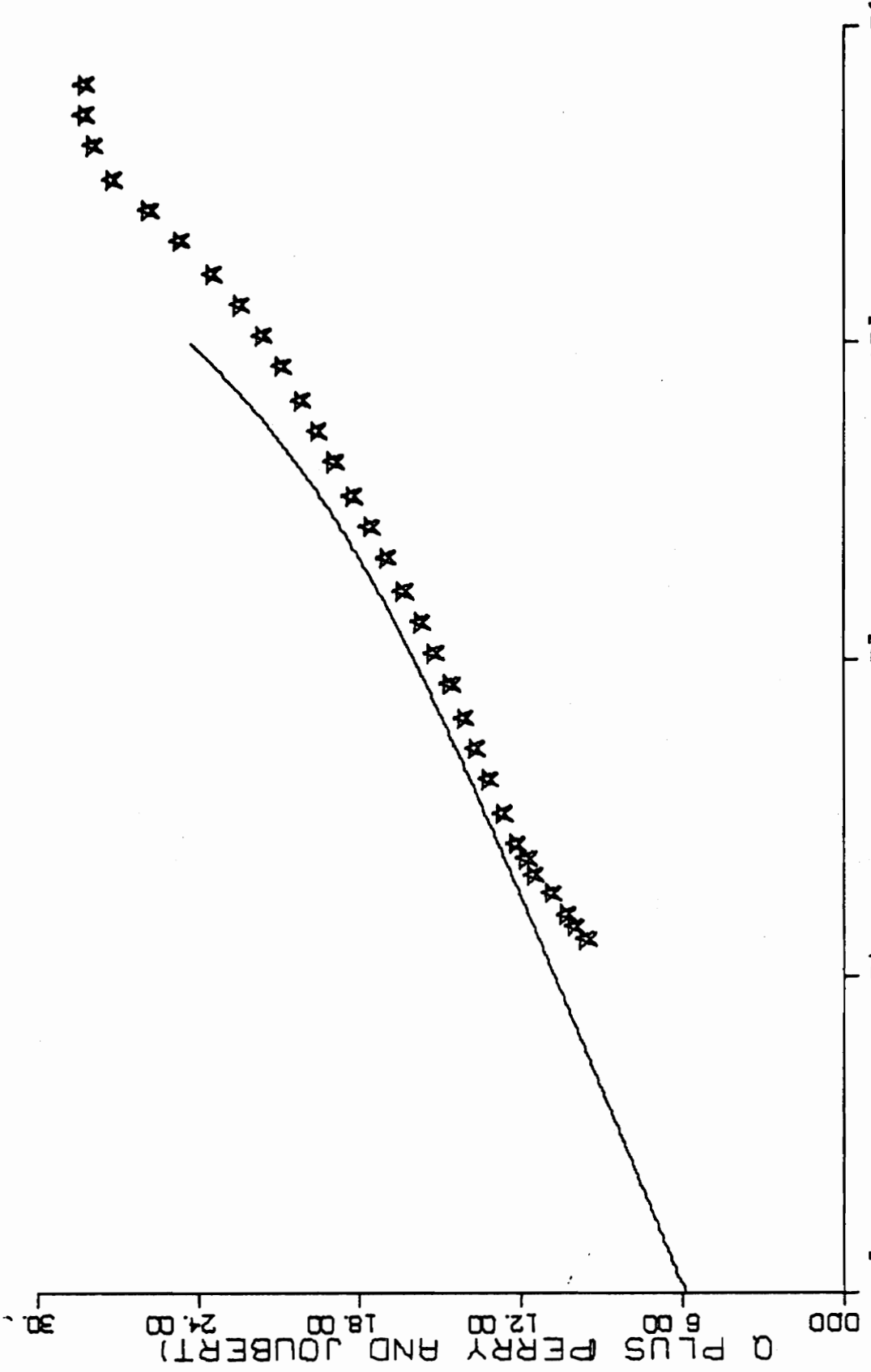

FIG. B 9-3. THREE-DIMENSIONAL SIMILARITY PLOT-RUN E7-02.

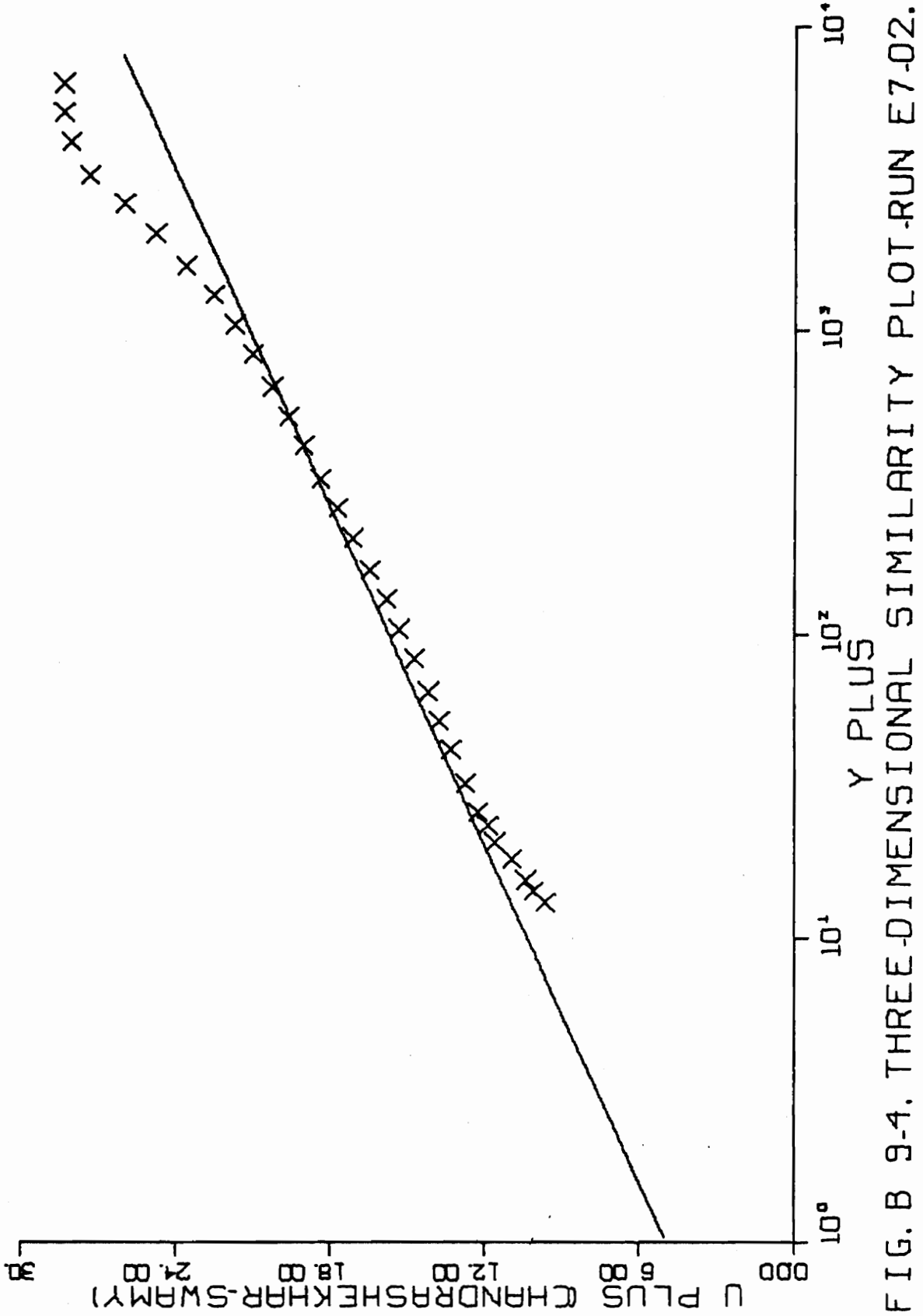

FIG. B 9-4. THREE-DIMENSIONAL SIMILARITY PLOT-RUN E7-02.

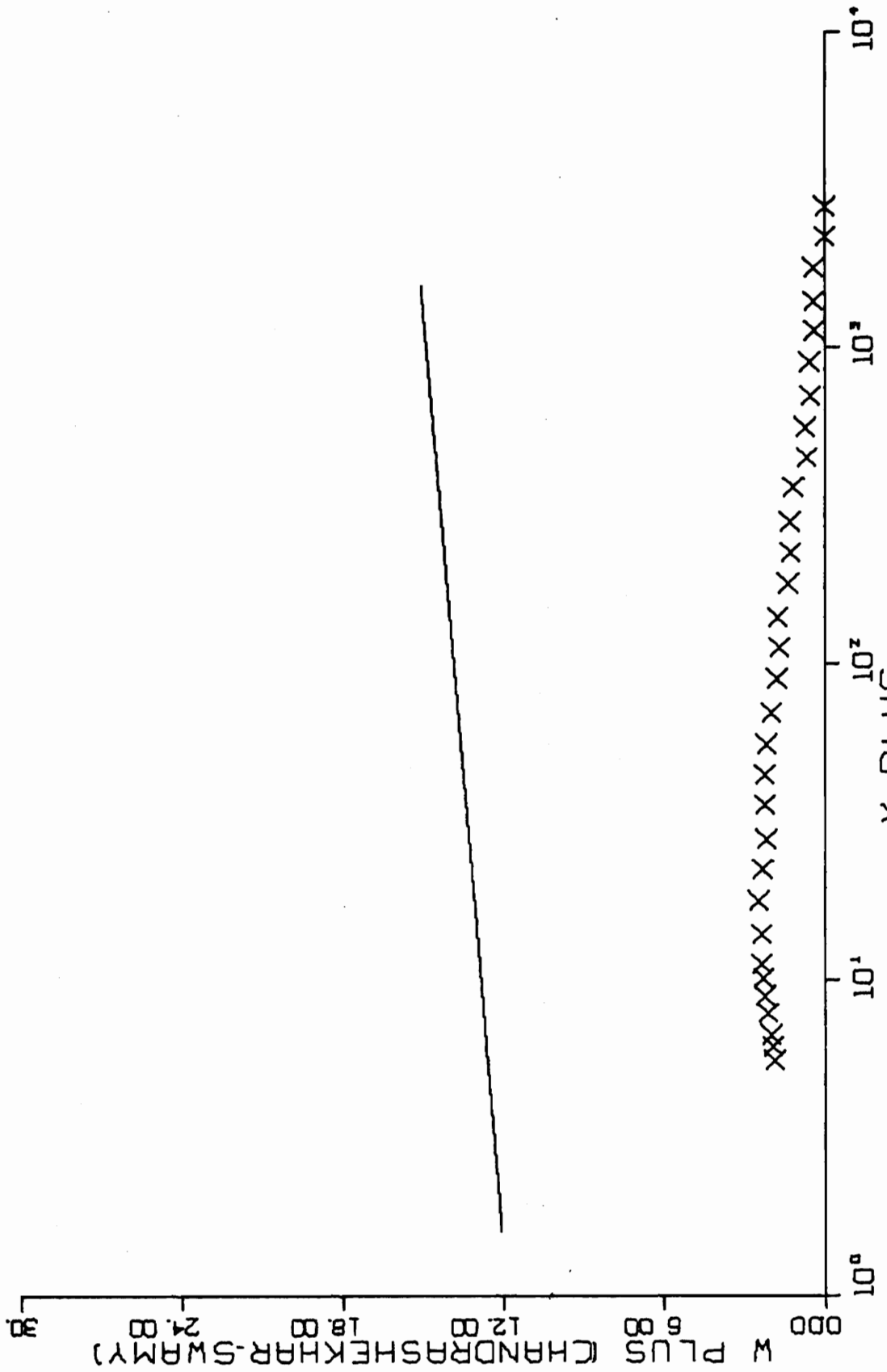

FIG. B 9-4. CONTINUED FOR RUN E7-02.

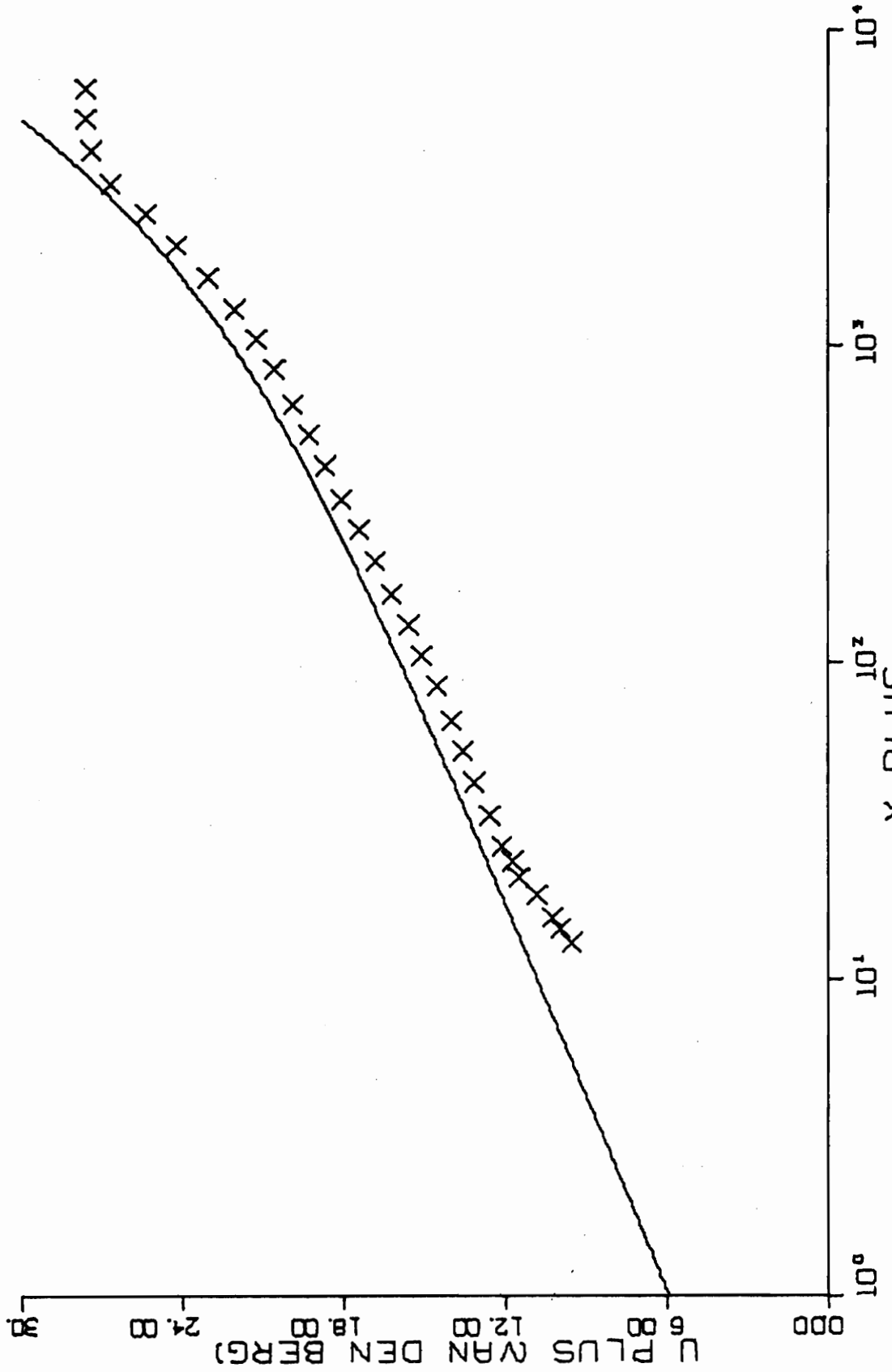

FIG. B 9-5. THREE-DIMENSIONAL SIMILARITY PLOT-RUN E7-02.

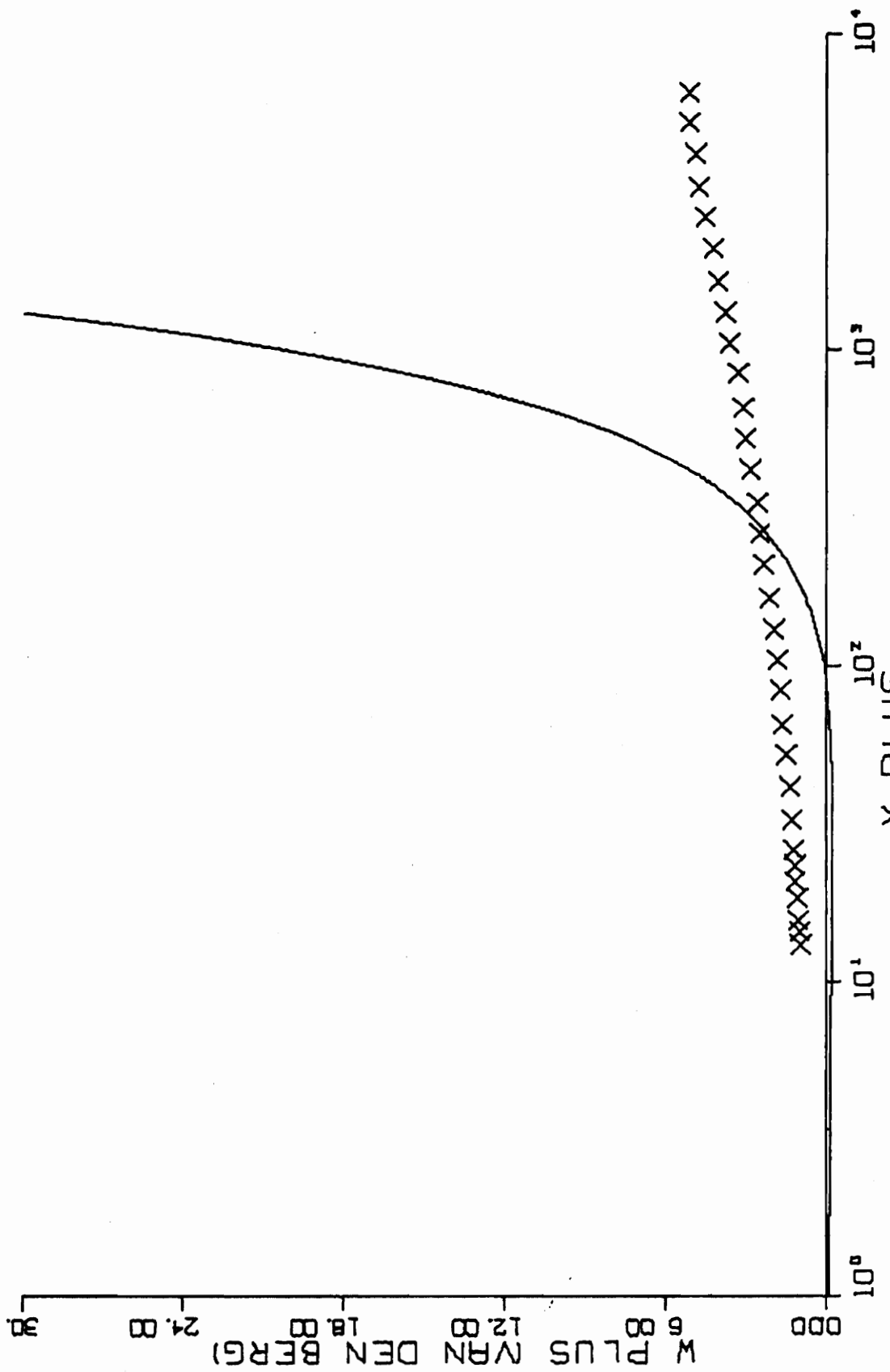

FIG. B 9-5. CONTINUED FOR RUN E7-02.

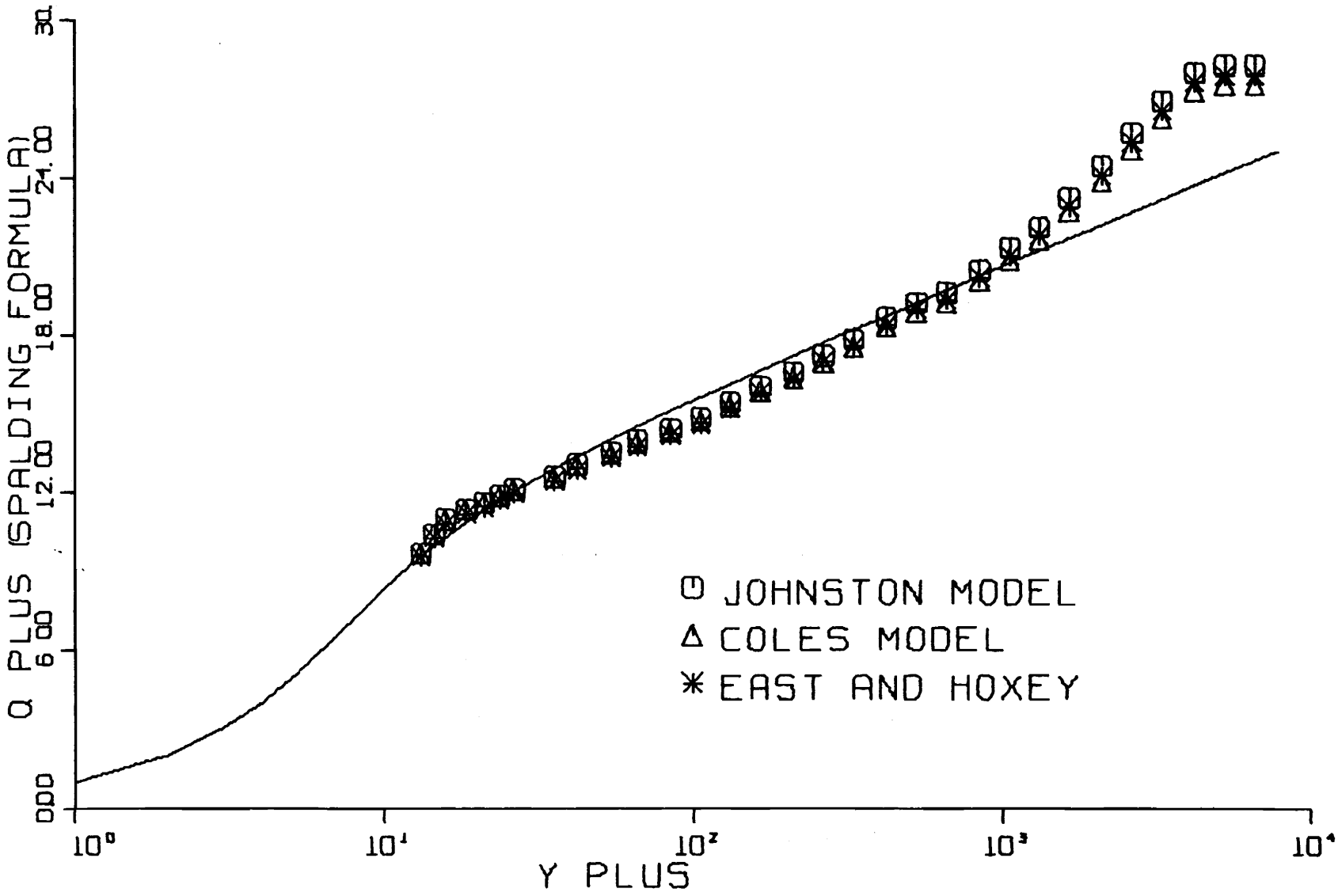

FIG. B10-1. THREE-DIMENSIONAL SIMILARITY PLOT-RUN ES-01.

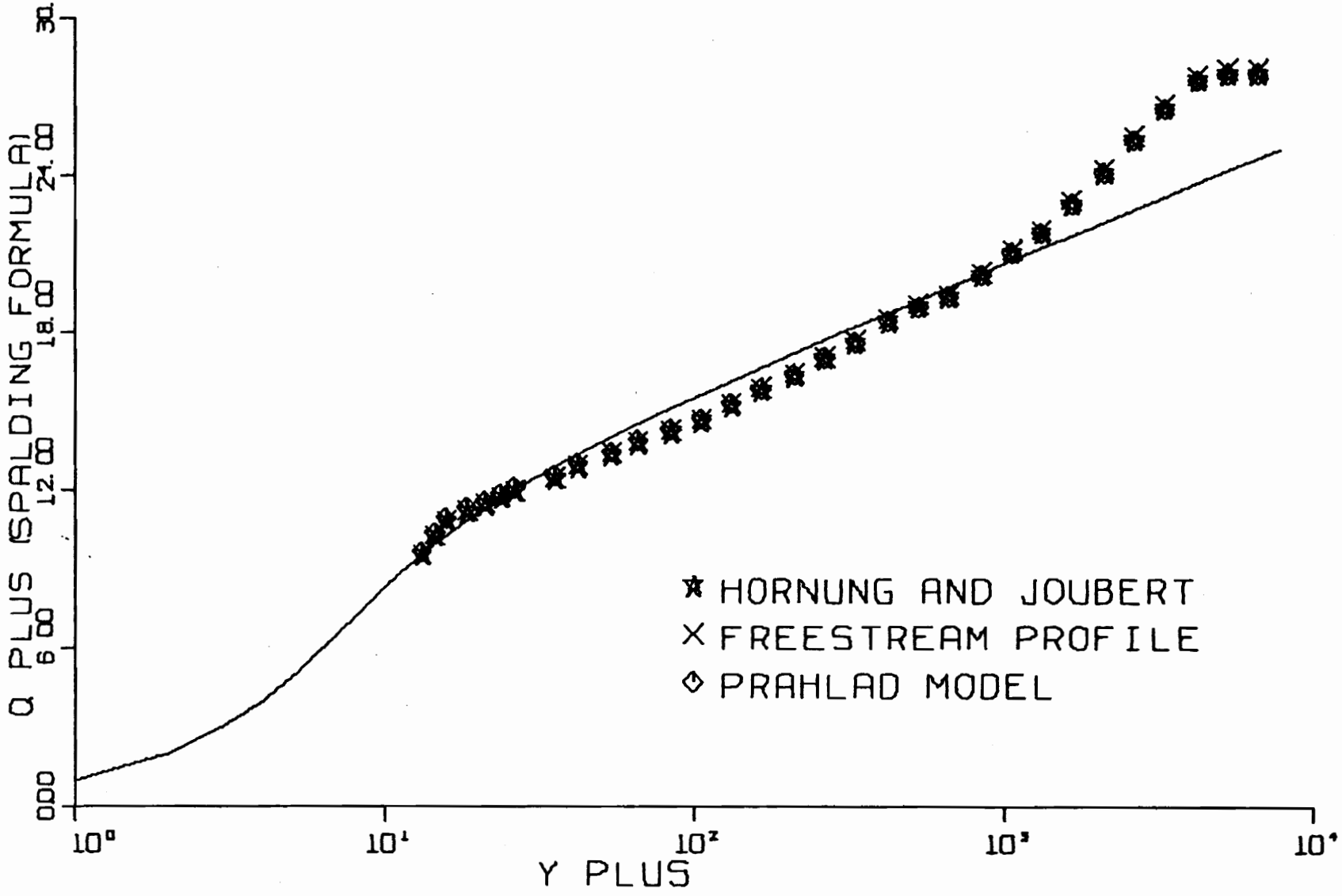

FIG. B10-2. THREE-DIMENSIONAL SIMILARITY PLOT-RUN ES-01.

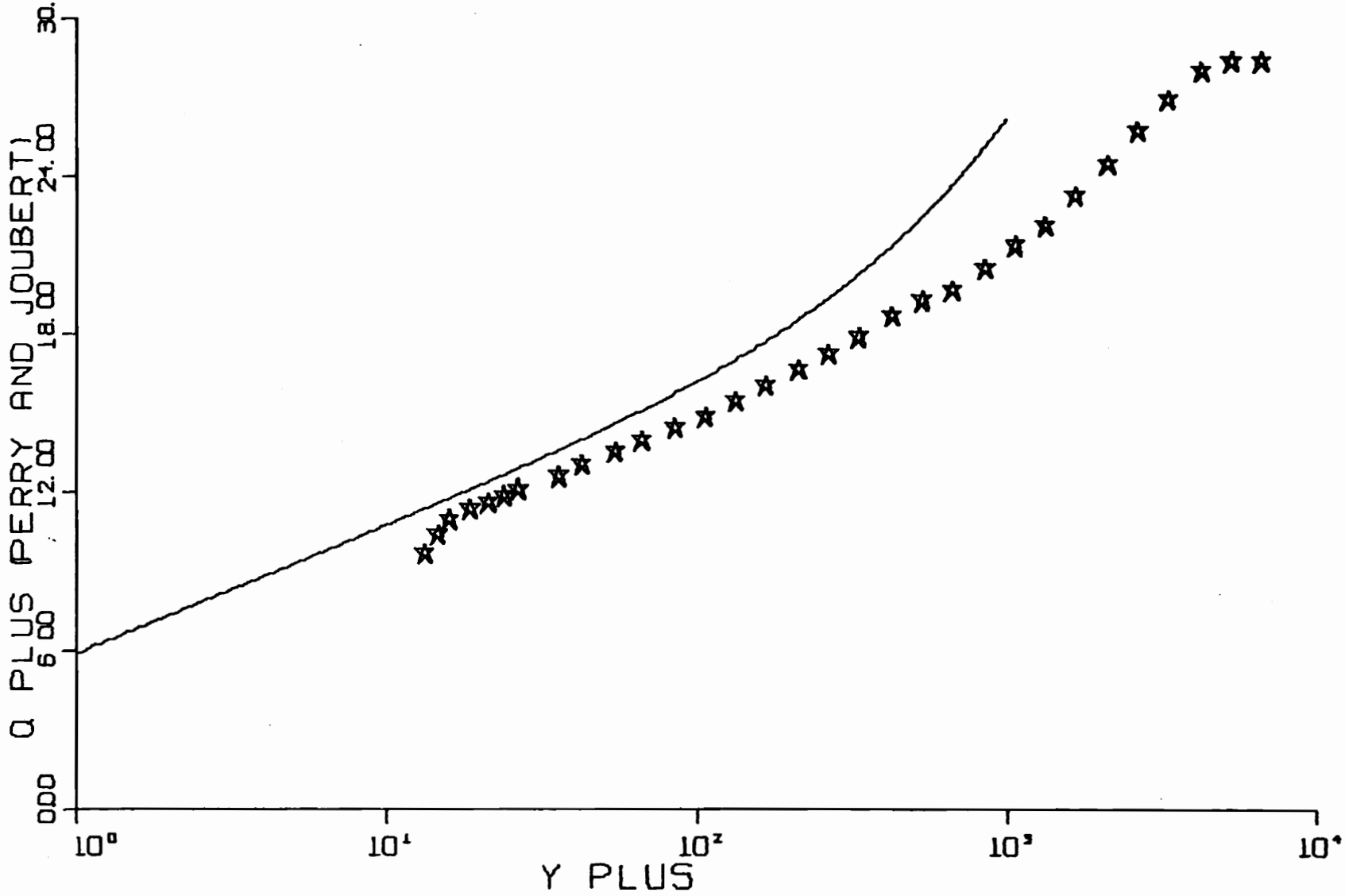

FIG. B10-3. THREE-DIMENSIONAL SIMILARITY PLOT-RUN E5-01.

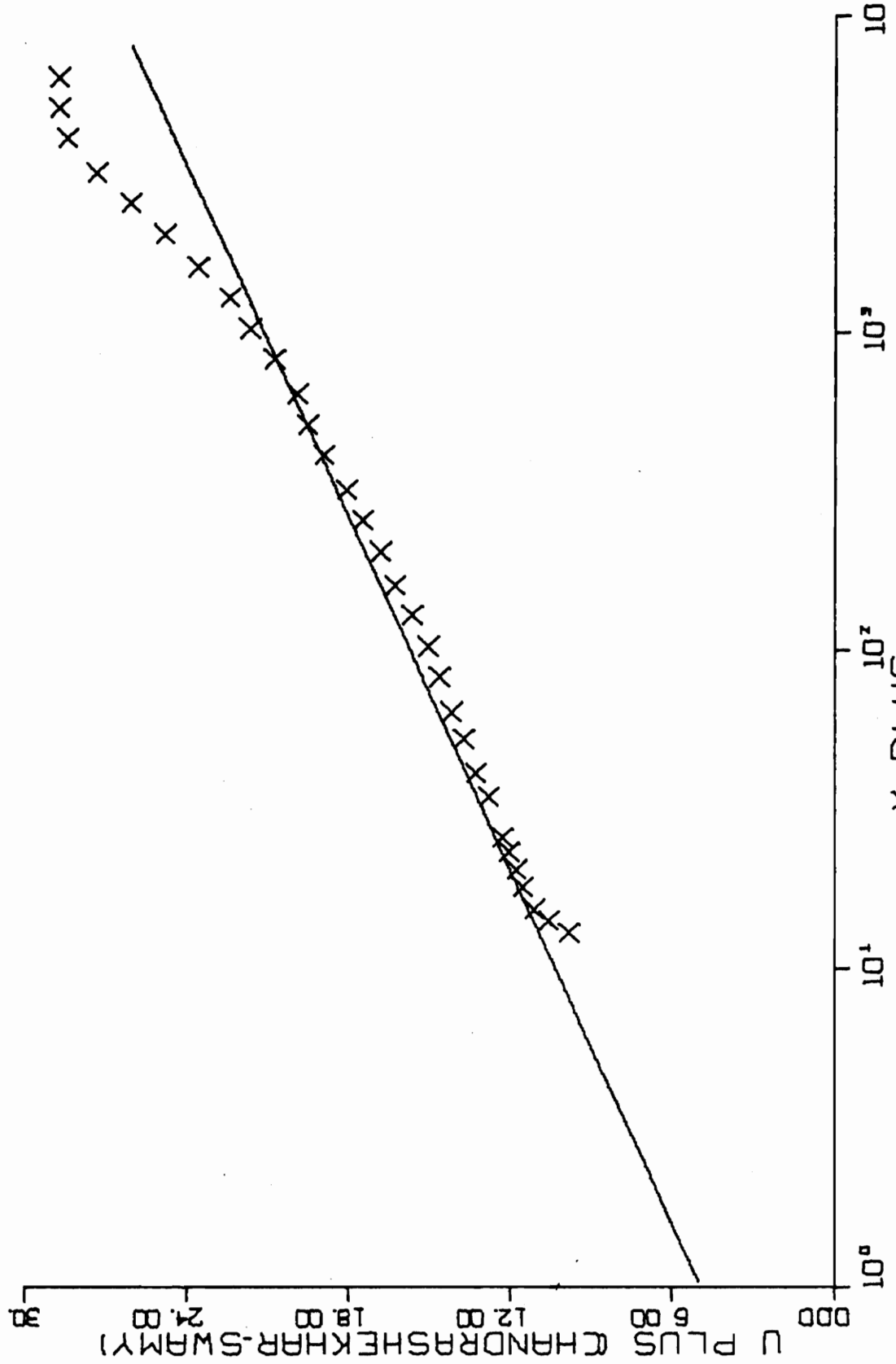

FIG. B10-4. THREE-DIMENSIONAL SIMILARITY PLOT-RUN E5-01.

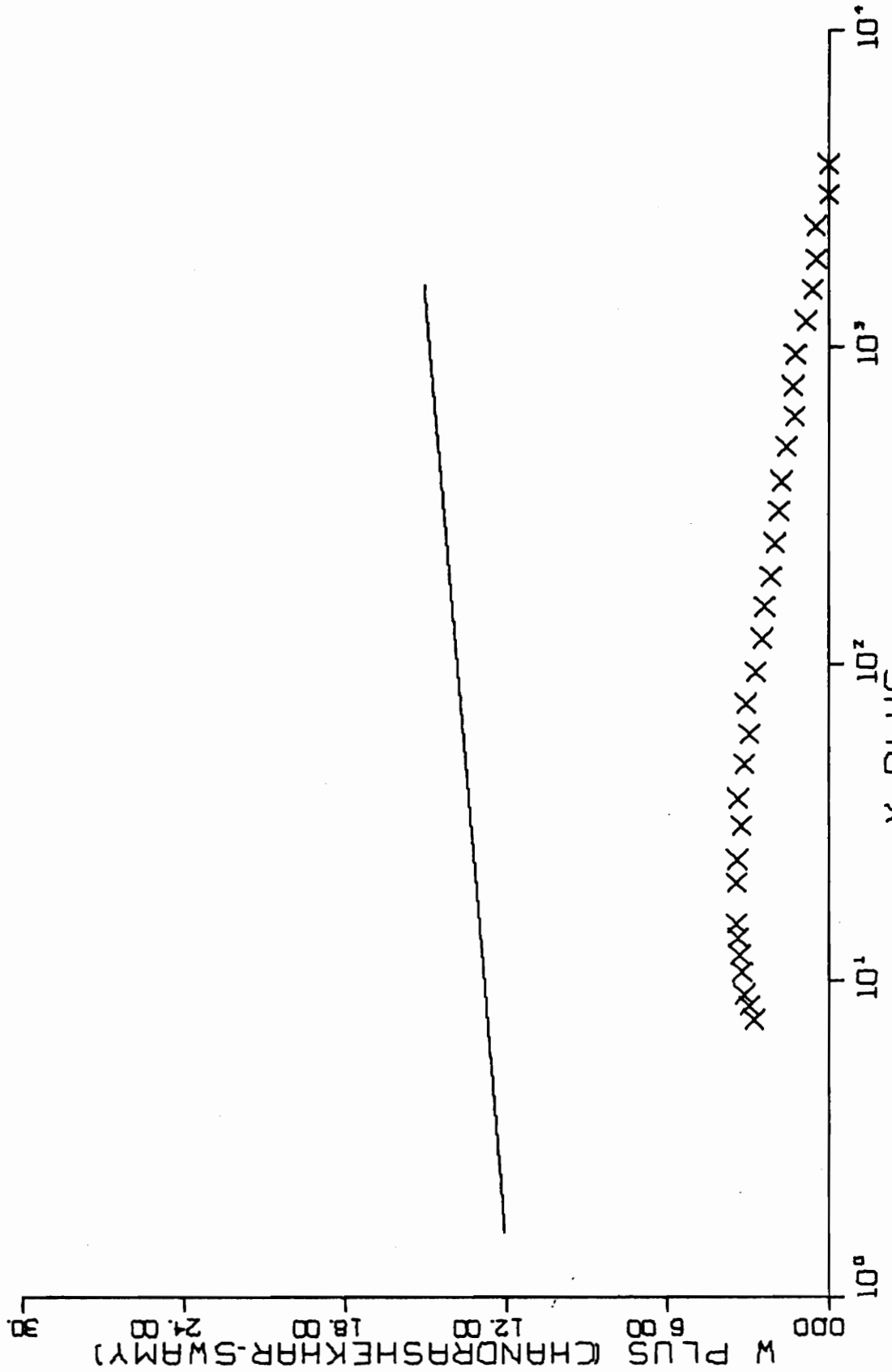

FIG. B10-4. CONTINUED FOR RUN E5-01.

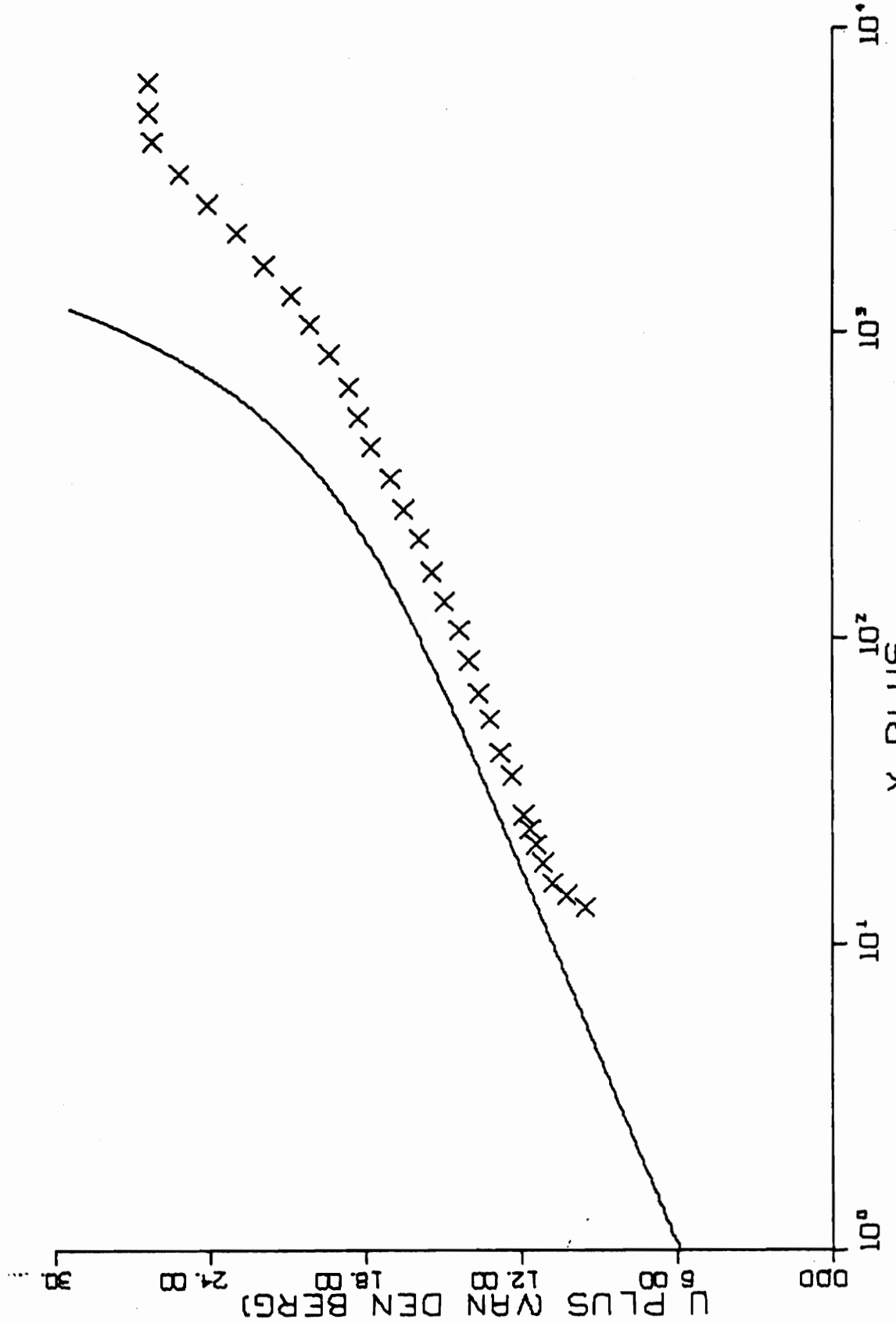

FIG. B10-5. THREE-DIMENSIONAL SIMILARITY PLOT-RUN E5-01.

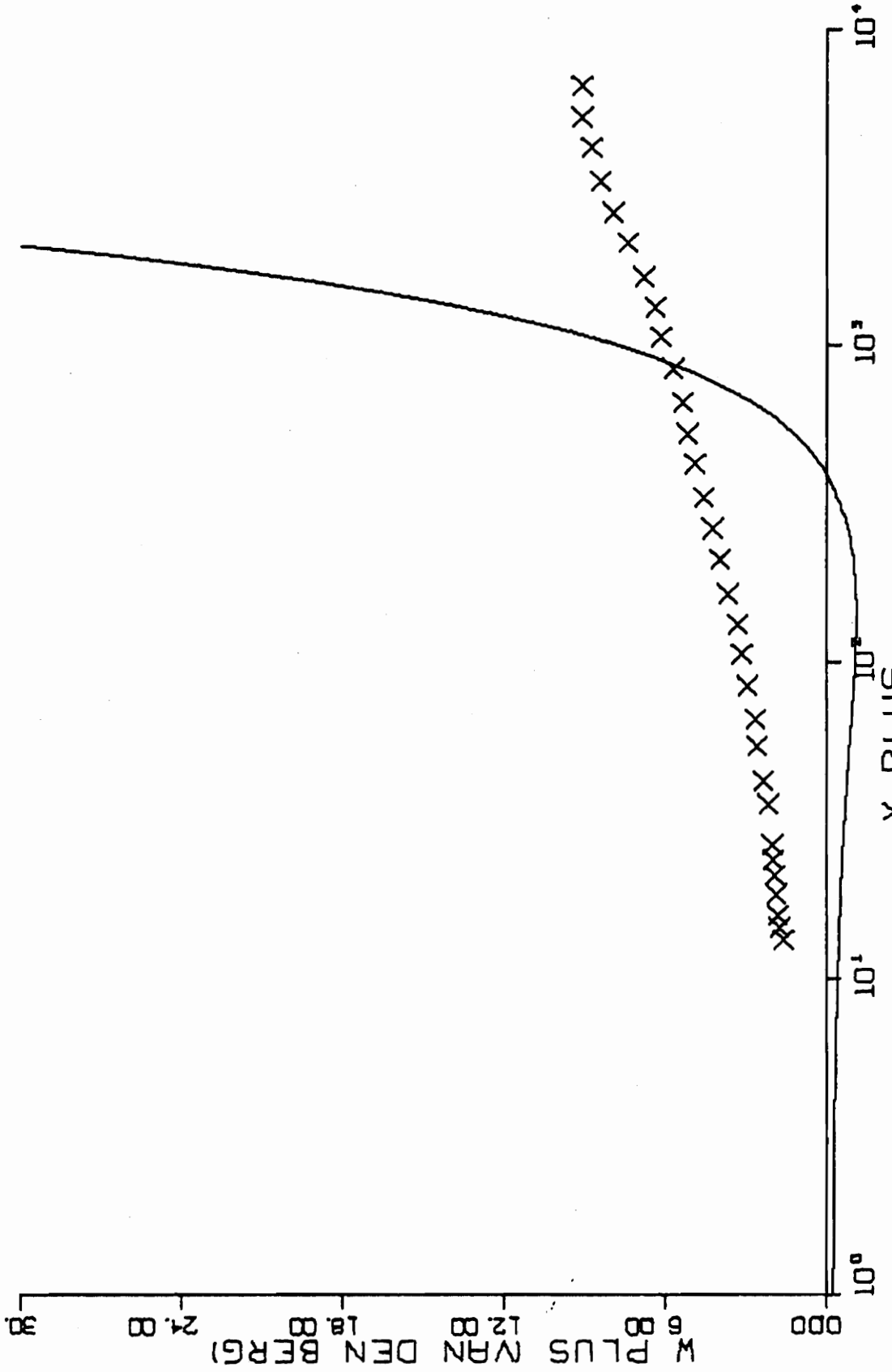

FIG. B10-5. CONTINUED FOR RUN E5-01.

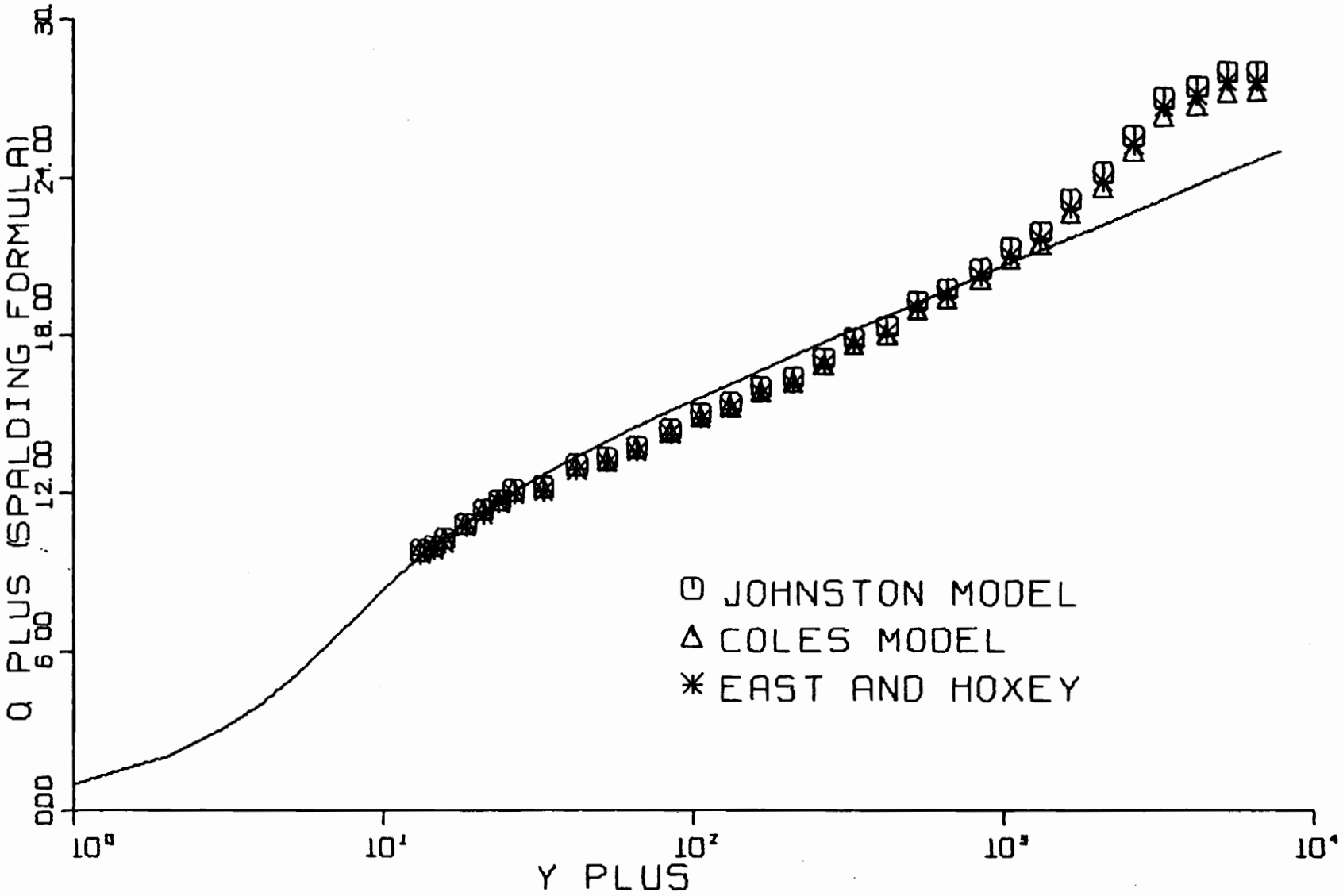

FIG. B11-1. THREE-DIMENSIONAL SIMILARITY PLOT-RUN E5-02.

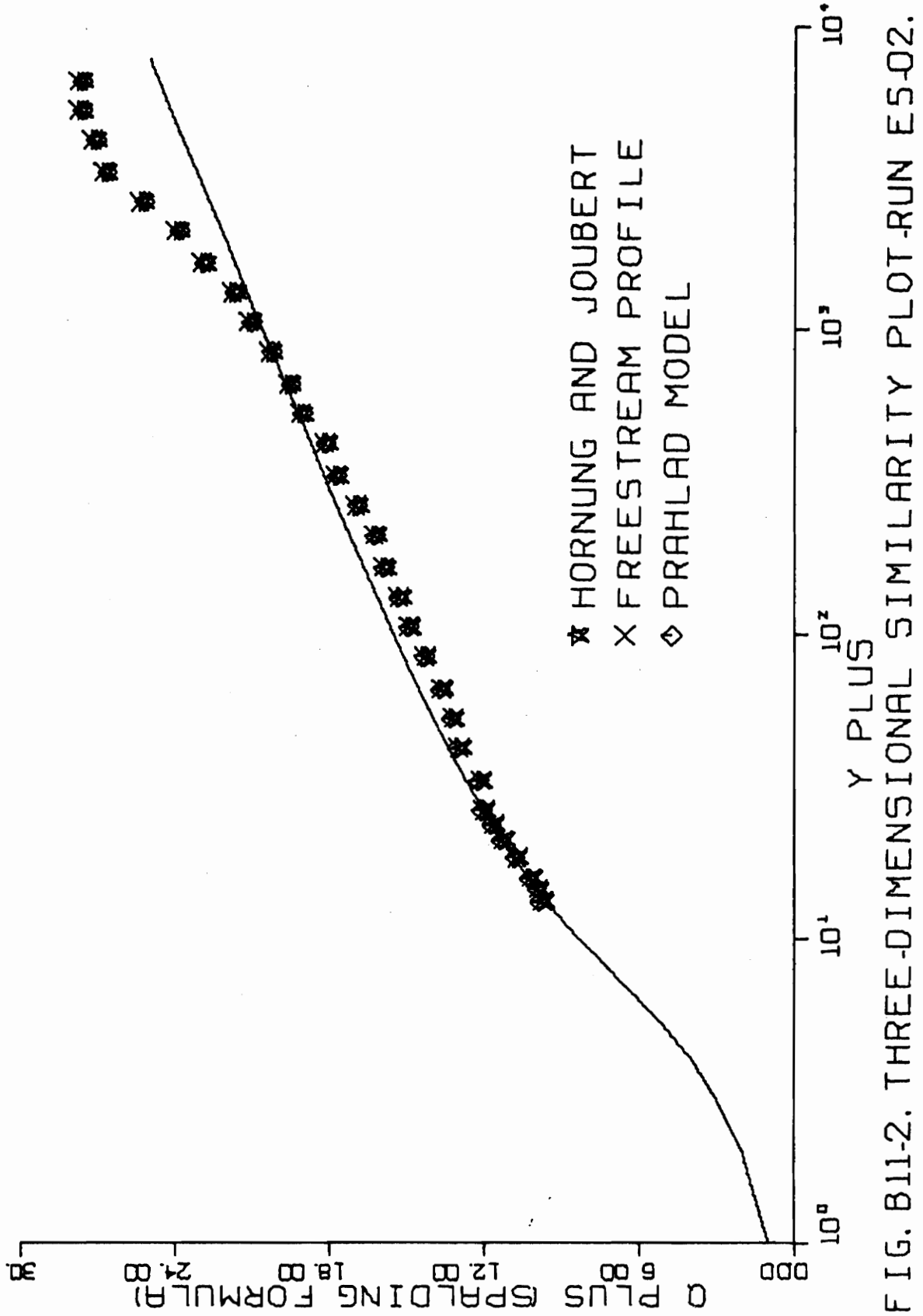

FIG. B11-2. THREE-DIMENSIONAL SIMILARITY PLOT-RUN ES-02.

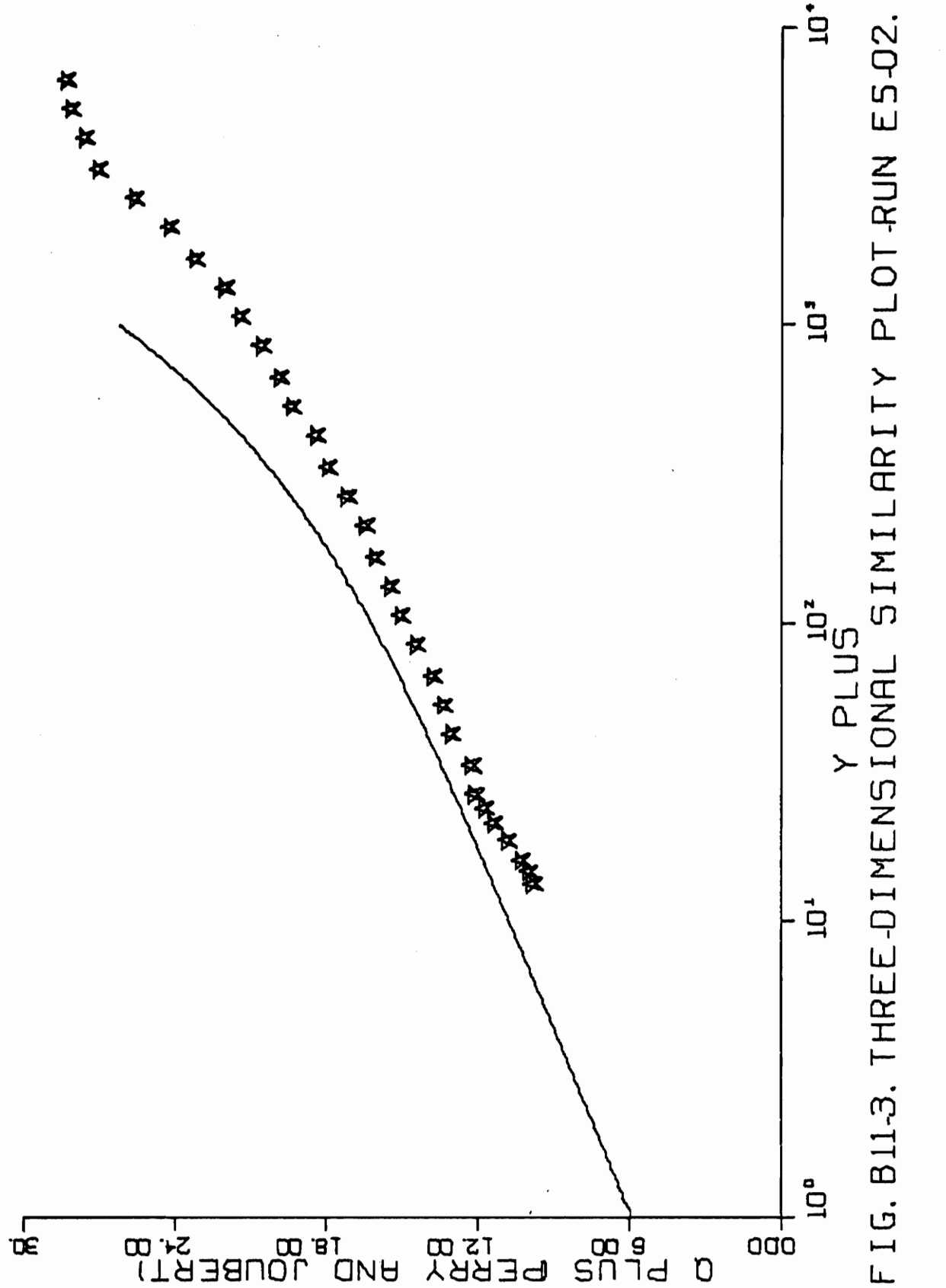

FIG. B11-3. THREE-DIMENSIONAL SIMILARITY PLOT-RUN ES-02.

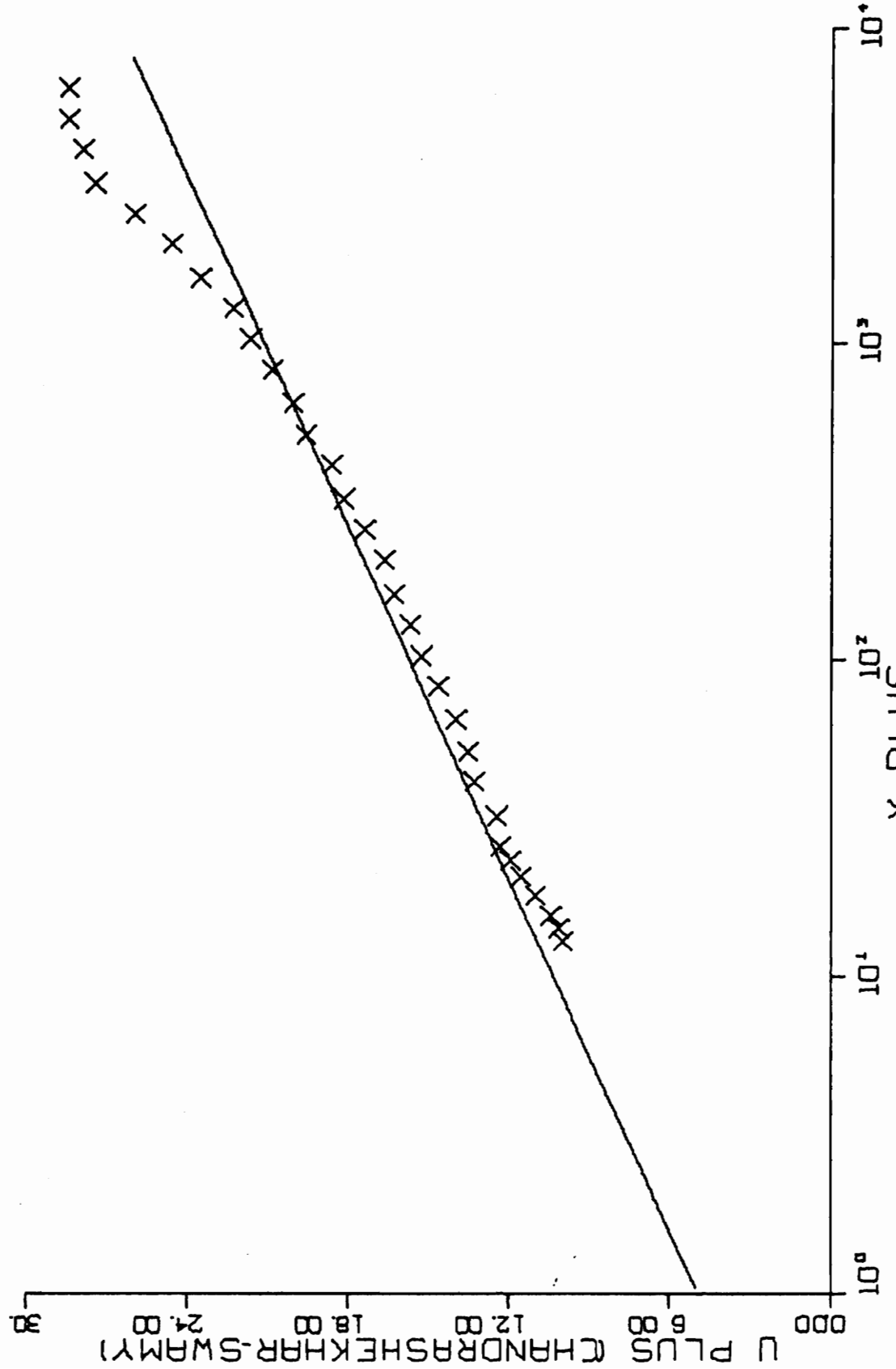

FIG. B11-4. THREE-DIMENSIONAL SIMILARITY PLOT-RUN E5-02.

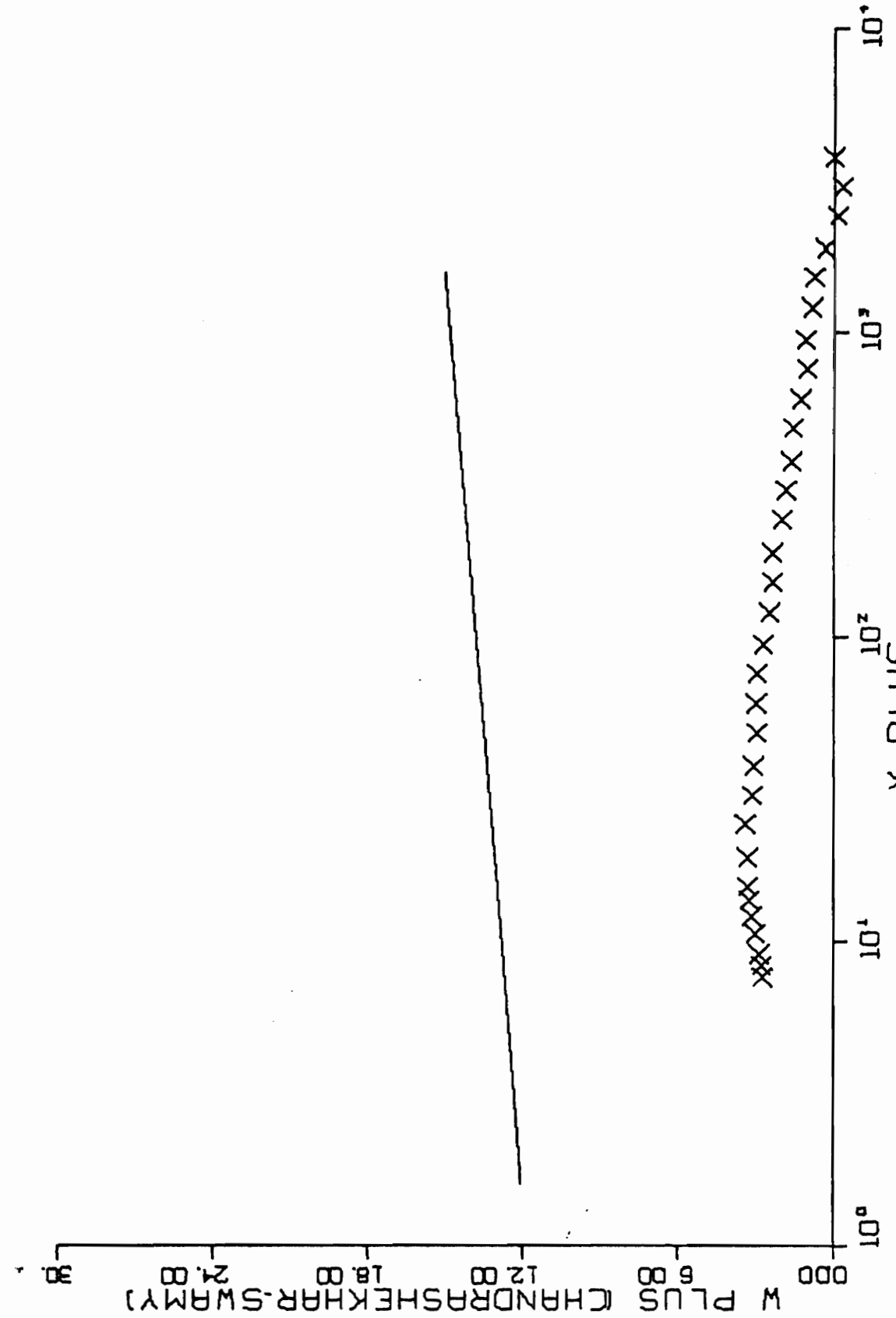

FIG. B11-4. CONTINUED FOR RUN E5-02.

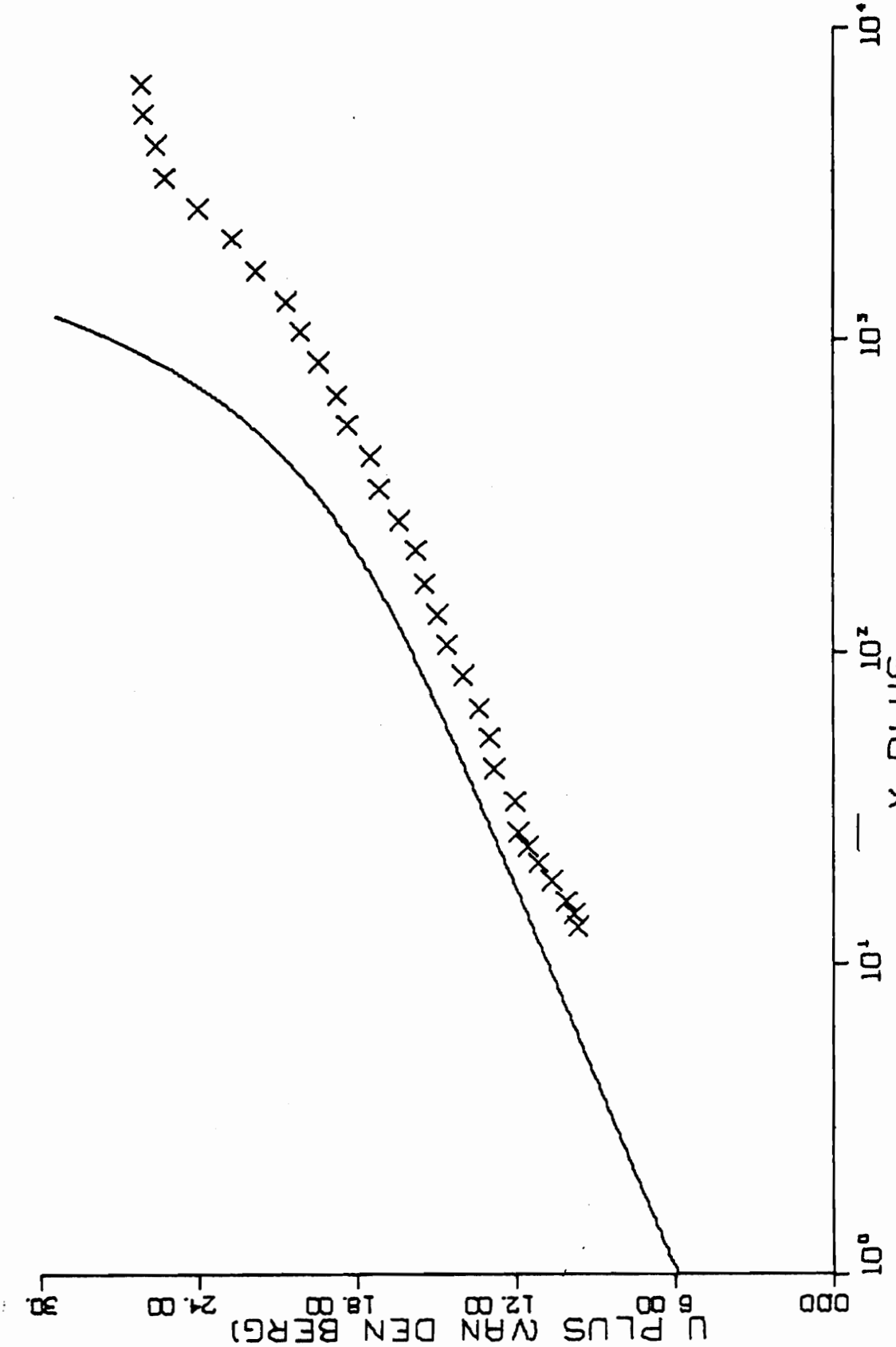

FIG. B11-5. THREE-DIMENSIONAL SIMILARITY PLOT-RUN ES-02.

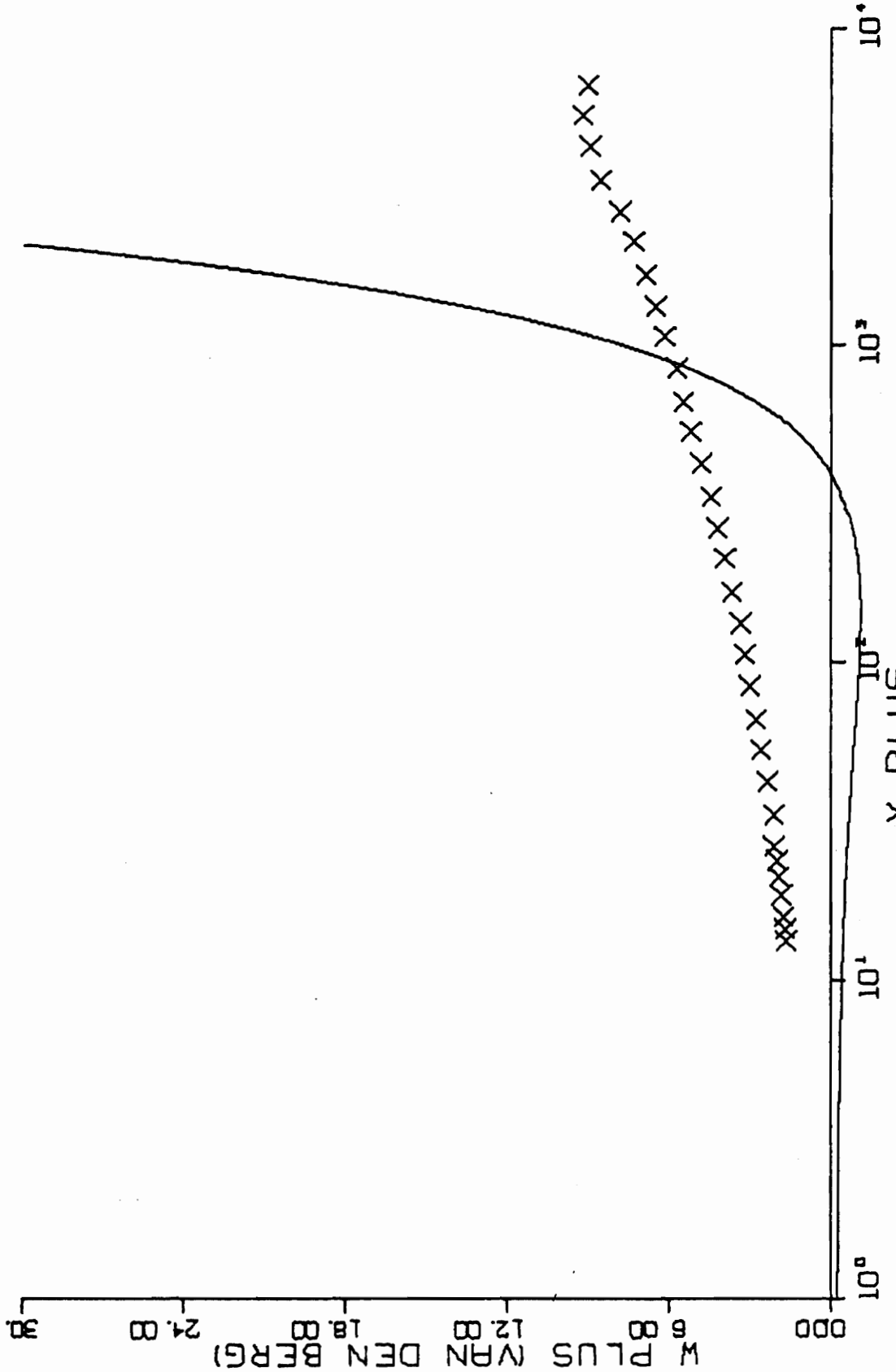

FIG. B11-5. CONTINUED FOR RUN E5-02.

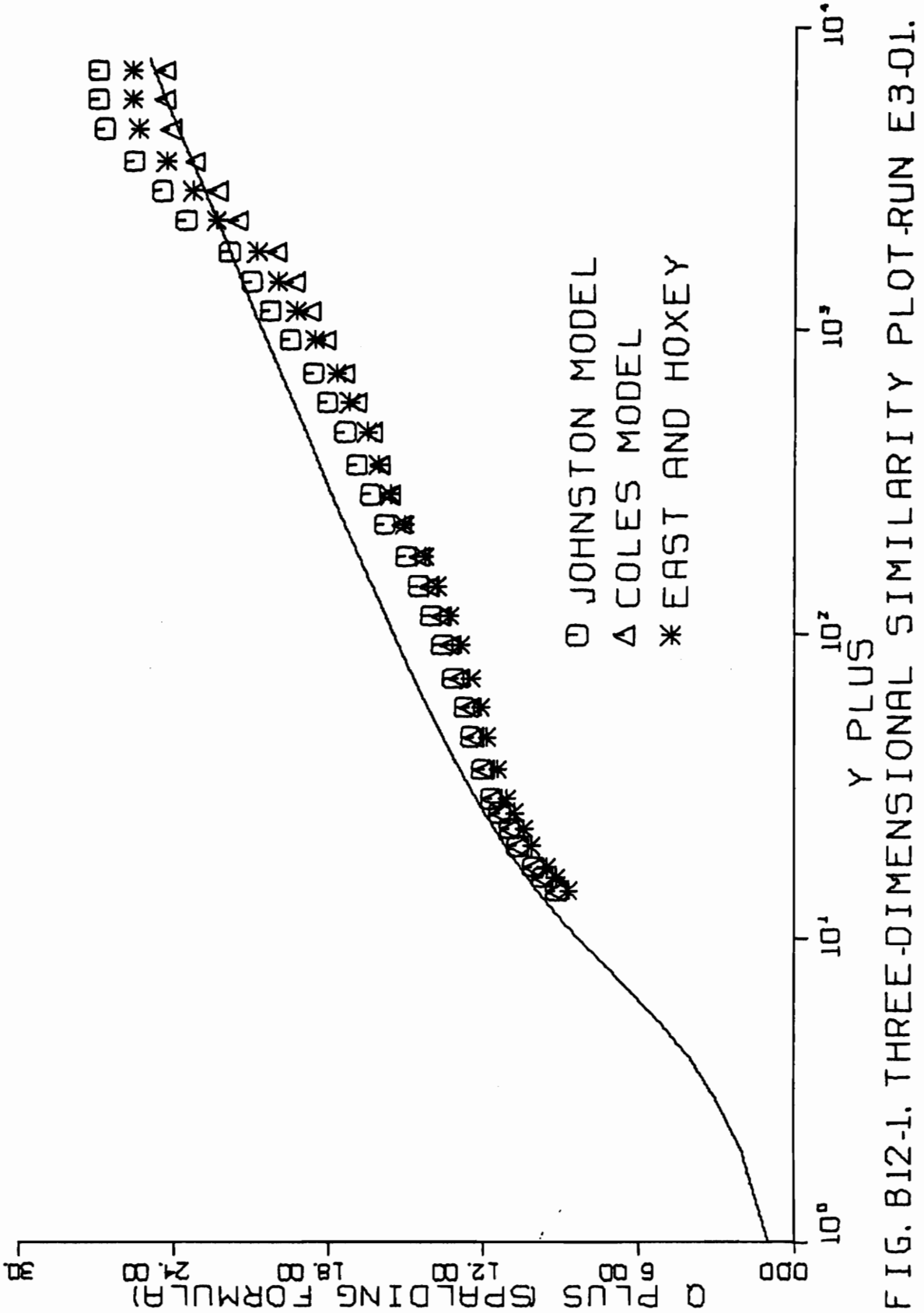

FIG. B12-1. THREE-DIMENSIONAL SIMILARITY PLOT-RUN E3-01.

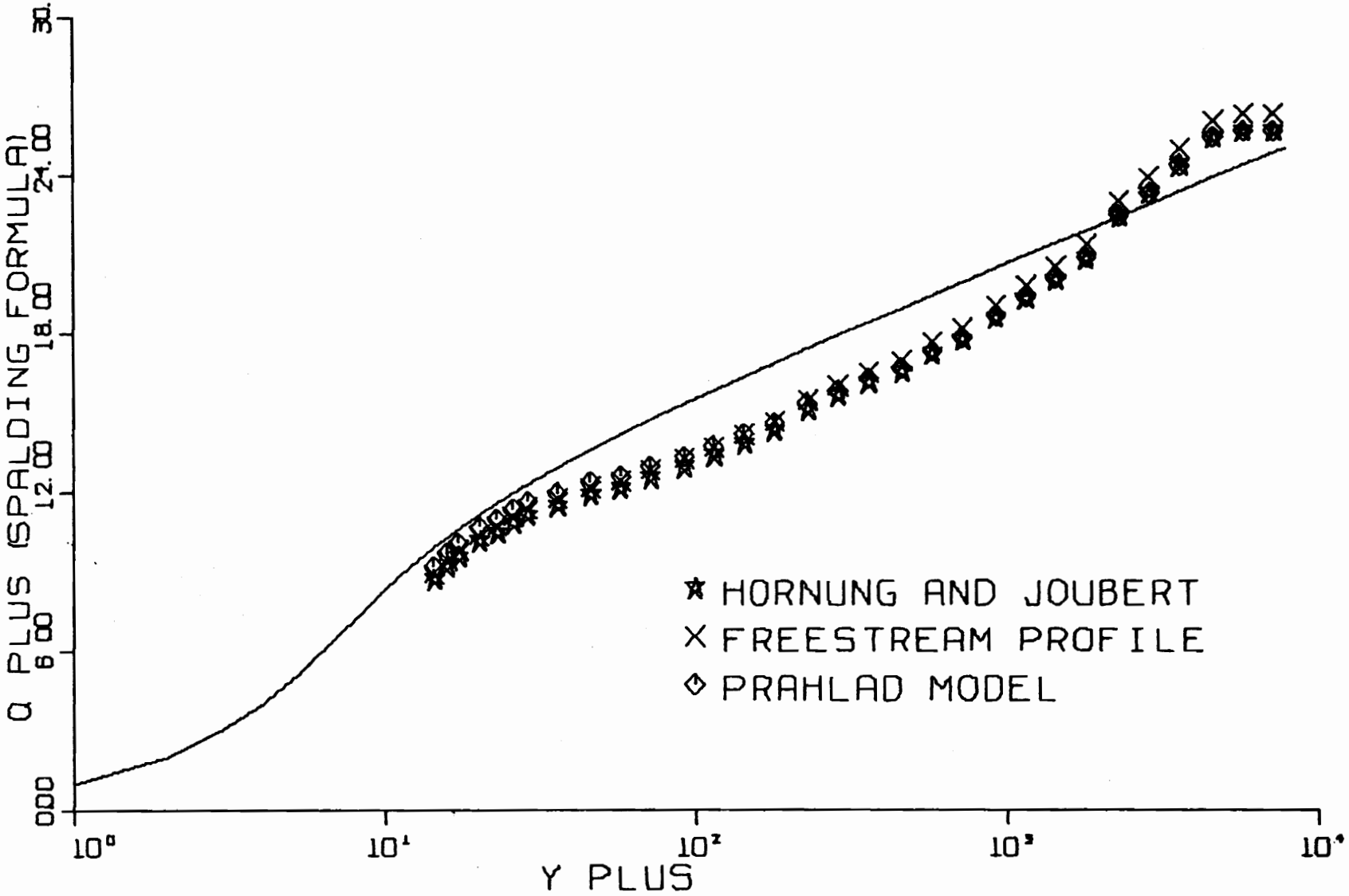

FIG. B12-2. THREE-DIMENSIONAL SIMILARITY PLOT-RUN E3-01.

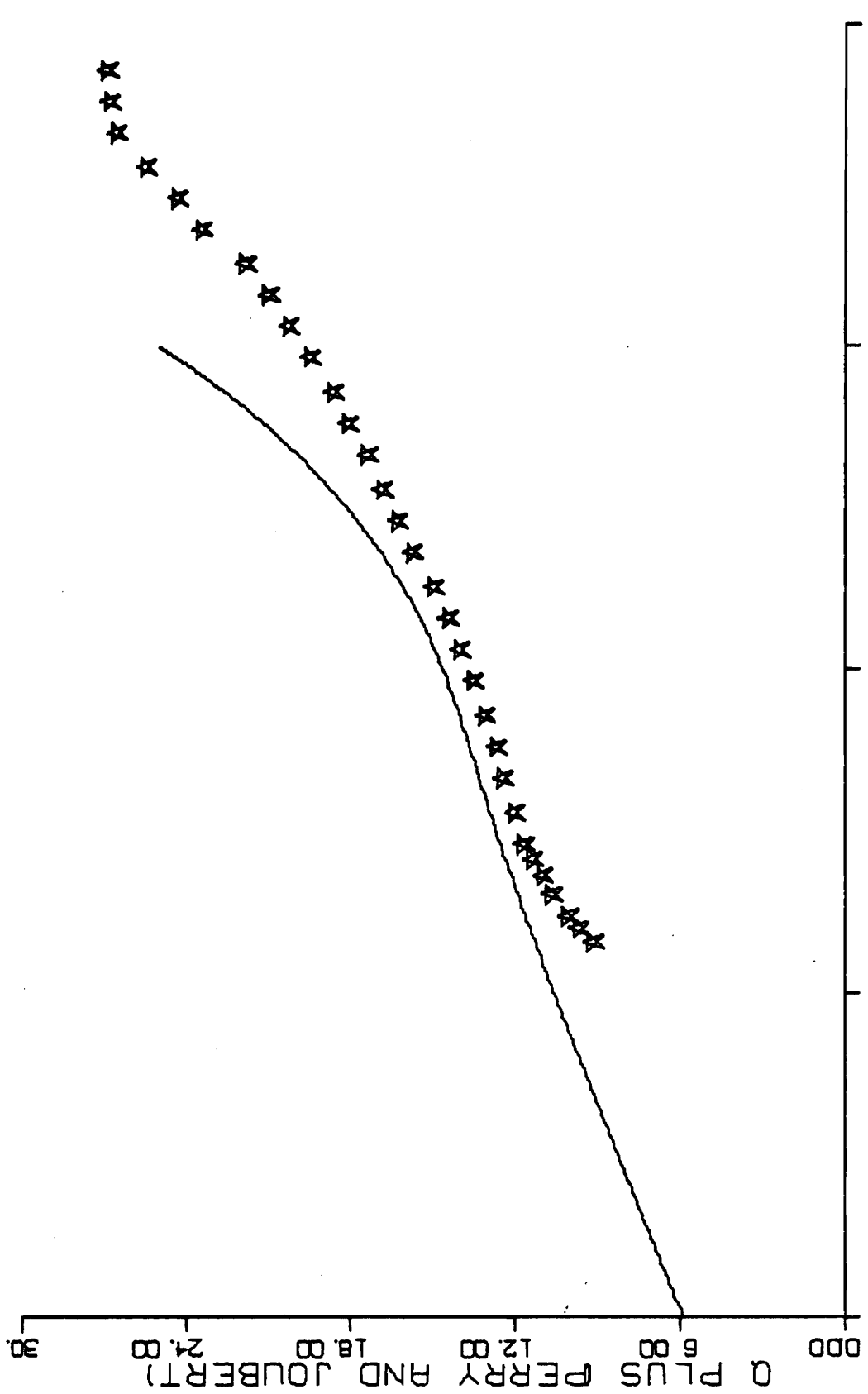

FIG. B12-3. THREE-DIMENSIONAL SIMILARITY PLOT-RUN E3-01.

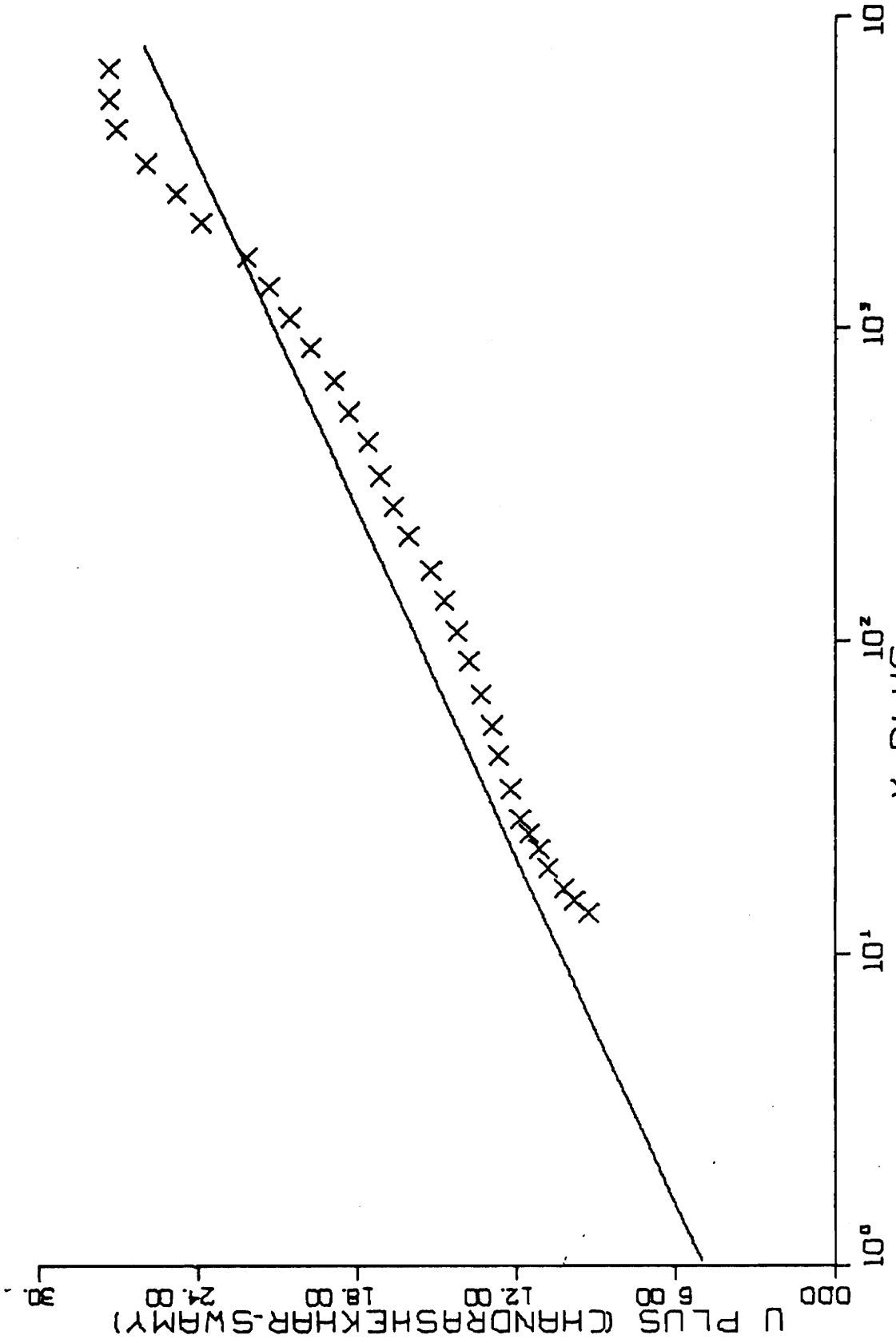

FIG. B12-4. THREE-DIMENSIONAL SIMILARITY PLOT-RUN E3-01.

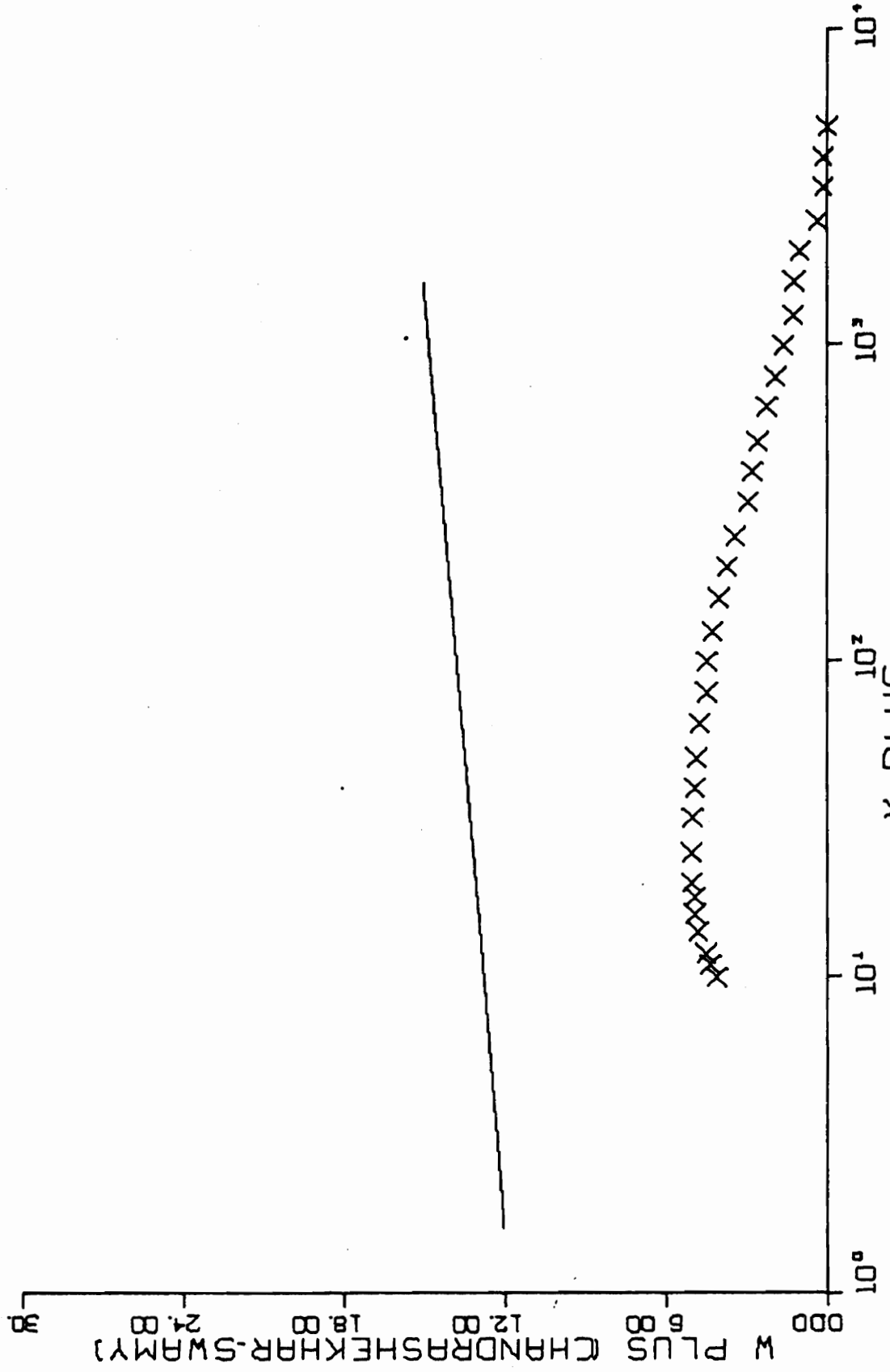

FIG. B12-4. CONTINUED FOR RUN E3-01.

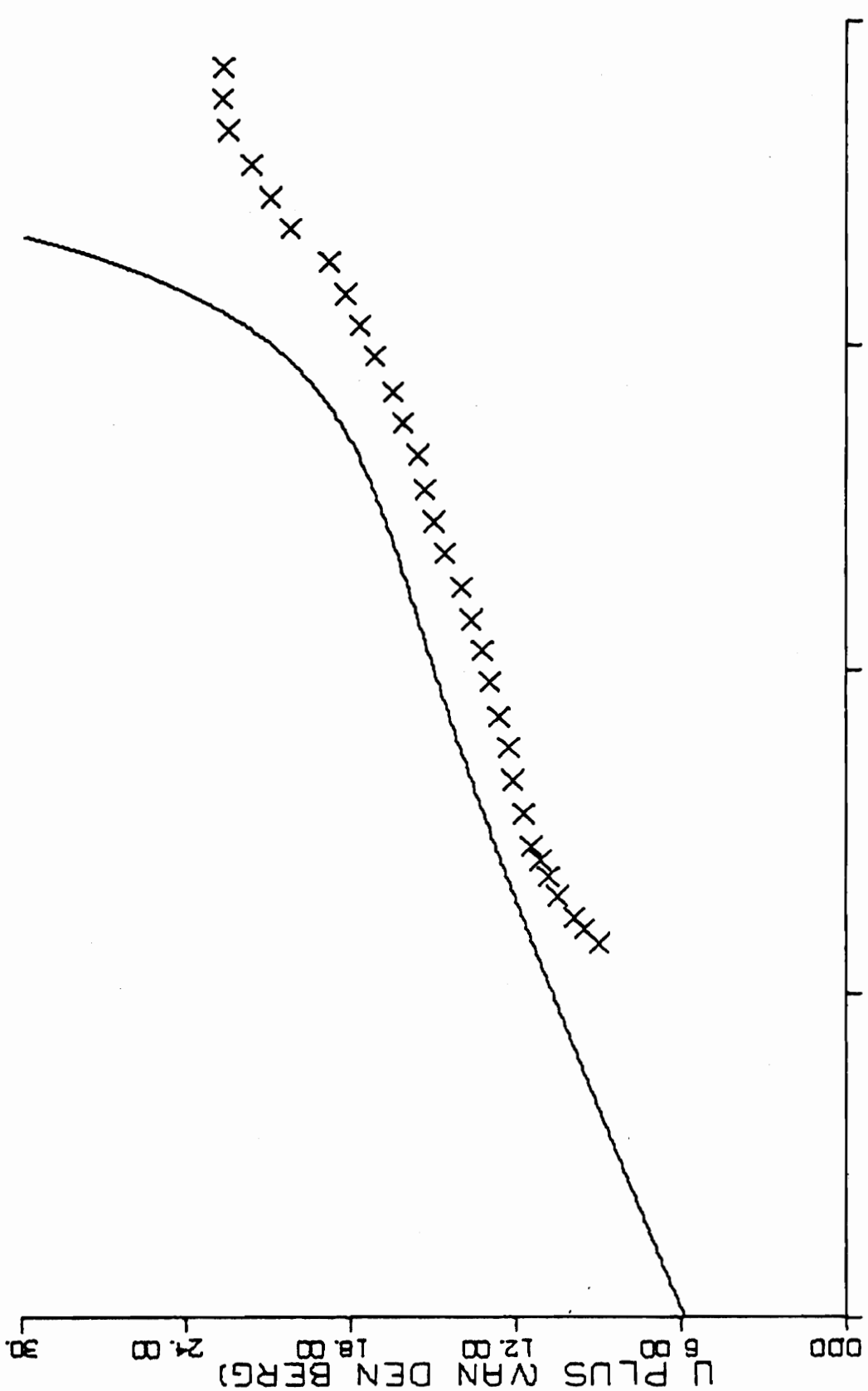

FIG. B12-5. THREE-DIMENSIONAL SIMILARITY PLOT-RUN E3-01.

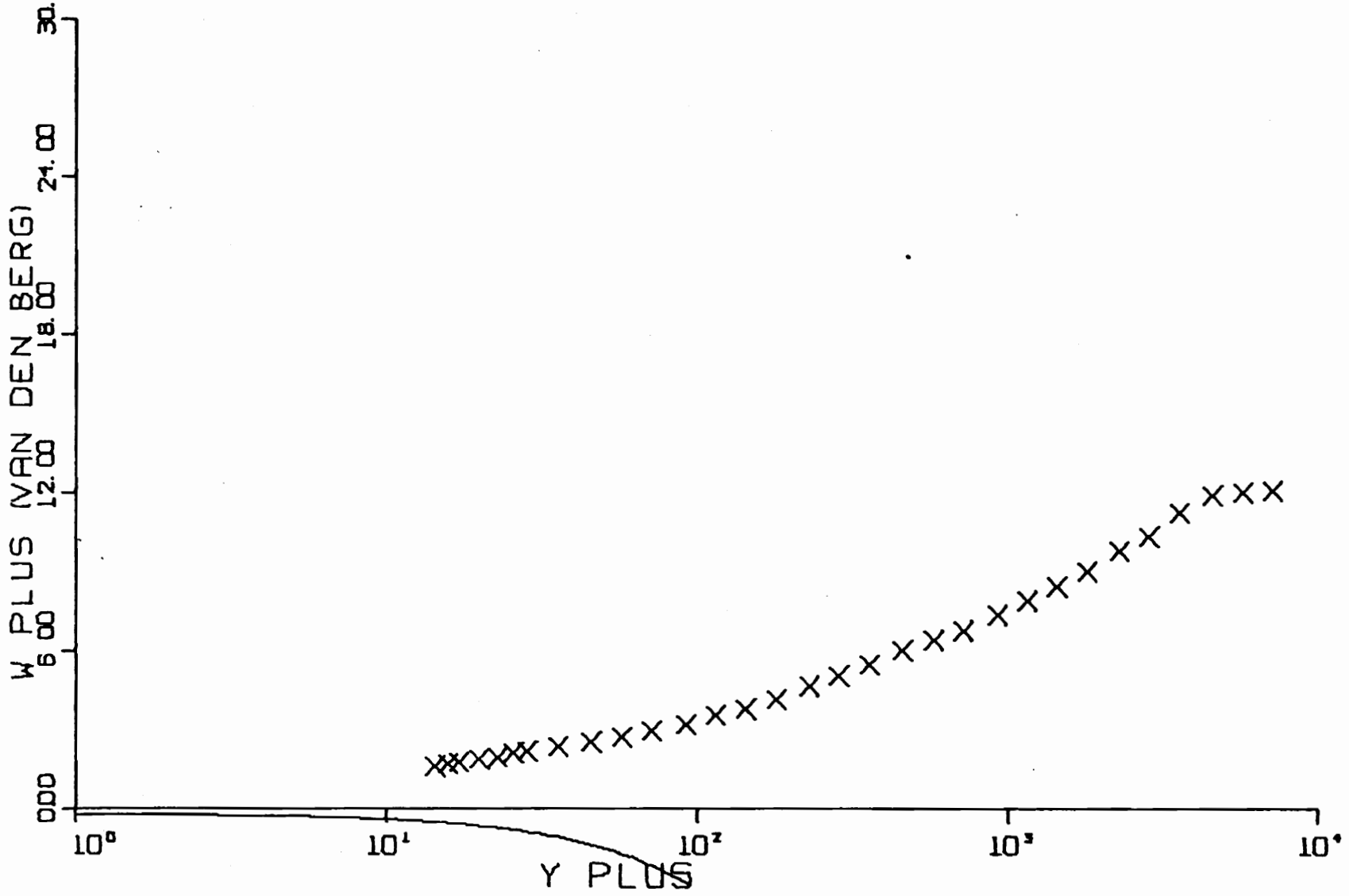

FIG. B12-5. CONTINUED FOR RUN E3-01.

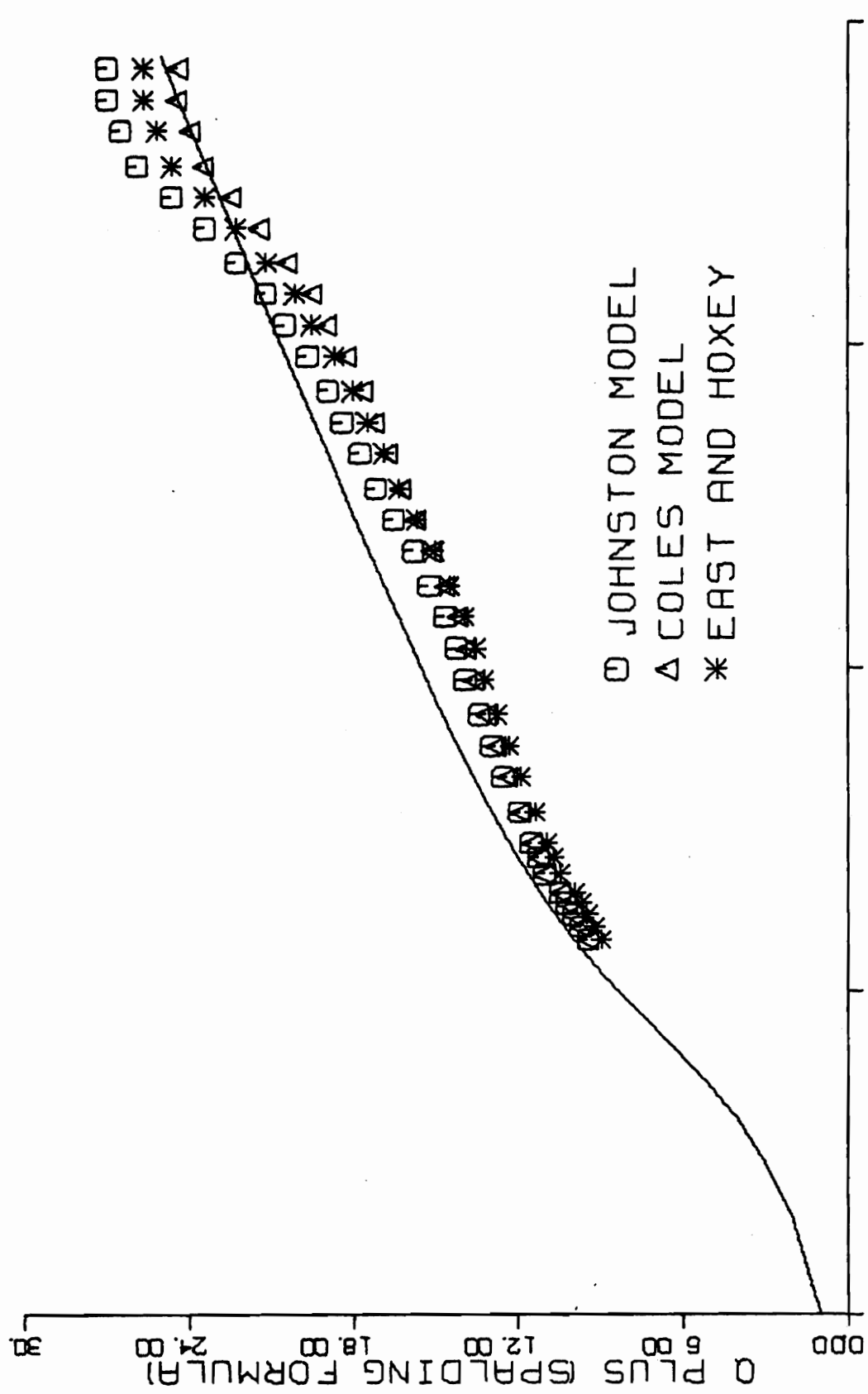

FIG. B13-1. THREE-DIMENSIONAL SIMILARITY PLOT-RUN E3-03.

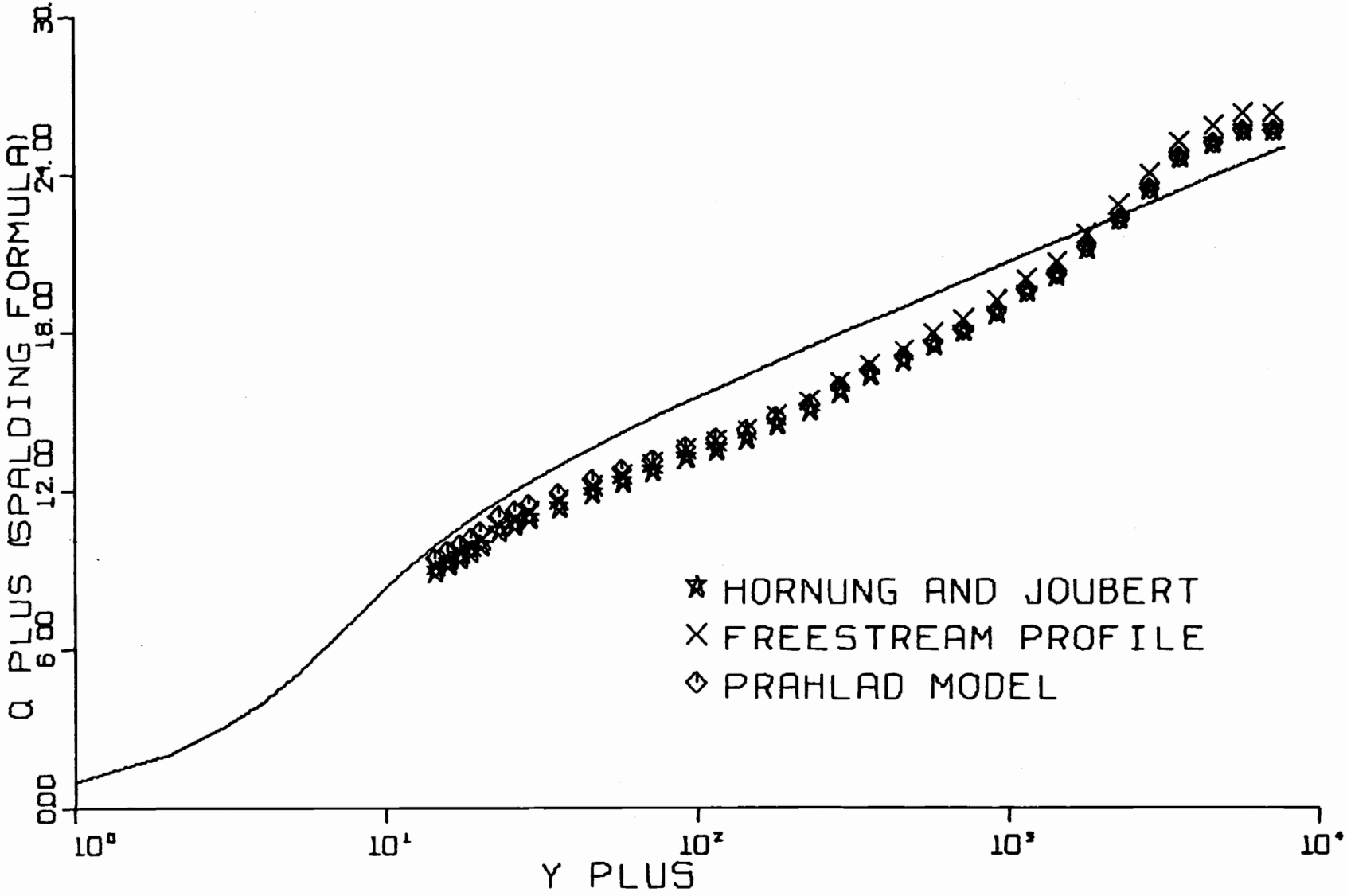

FIG. B13-2. THREE-DIMENSIONAL SIMILARITY PLOT-RUN E3-03.

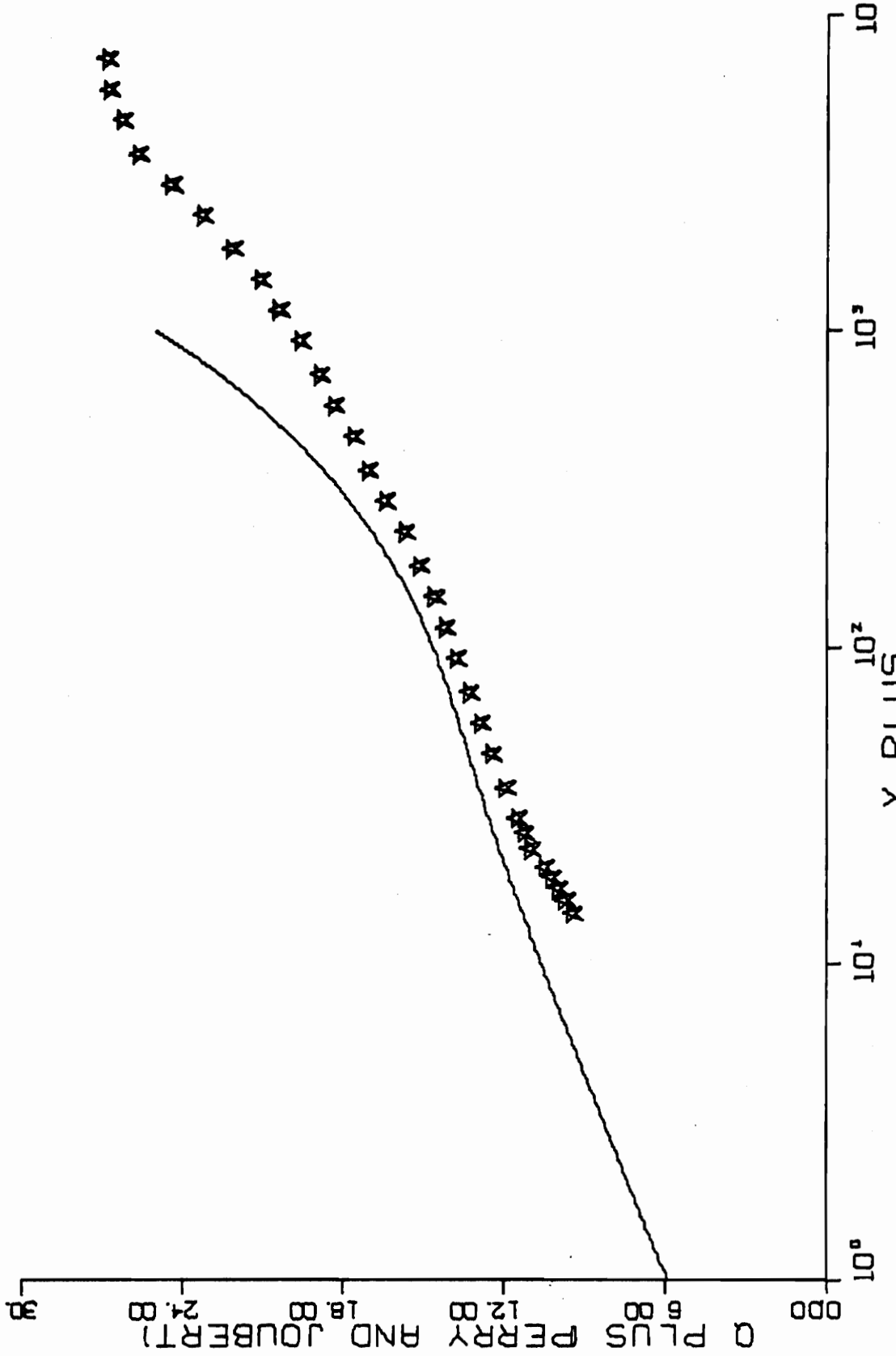

FIG. B13-3. THREE-DIMENSIONAL SIMILARITY PLOT-RUN E3-03.

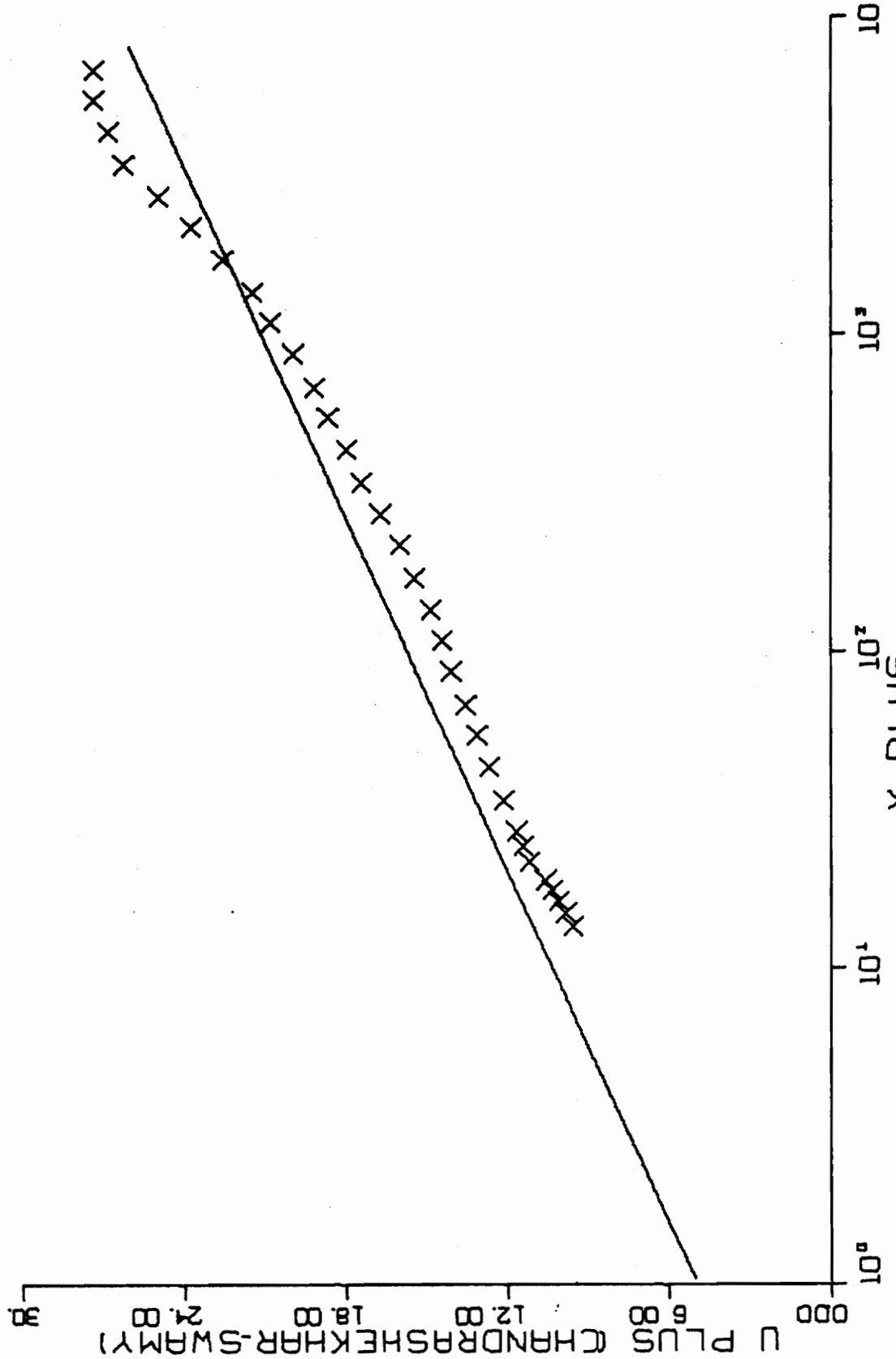

FIG. B13-4. THREE-DIMENSIONAL SIMILARITY PLOT-RUN E3-03.

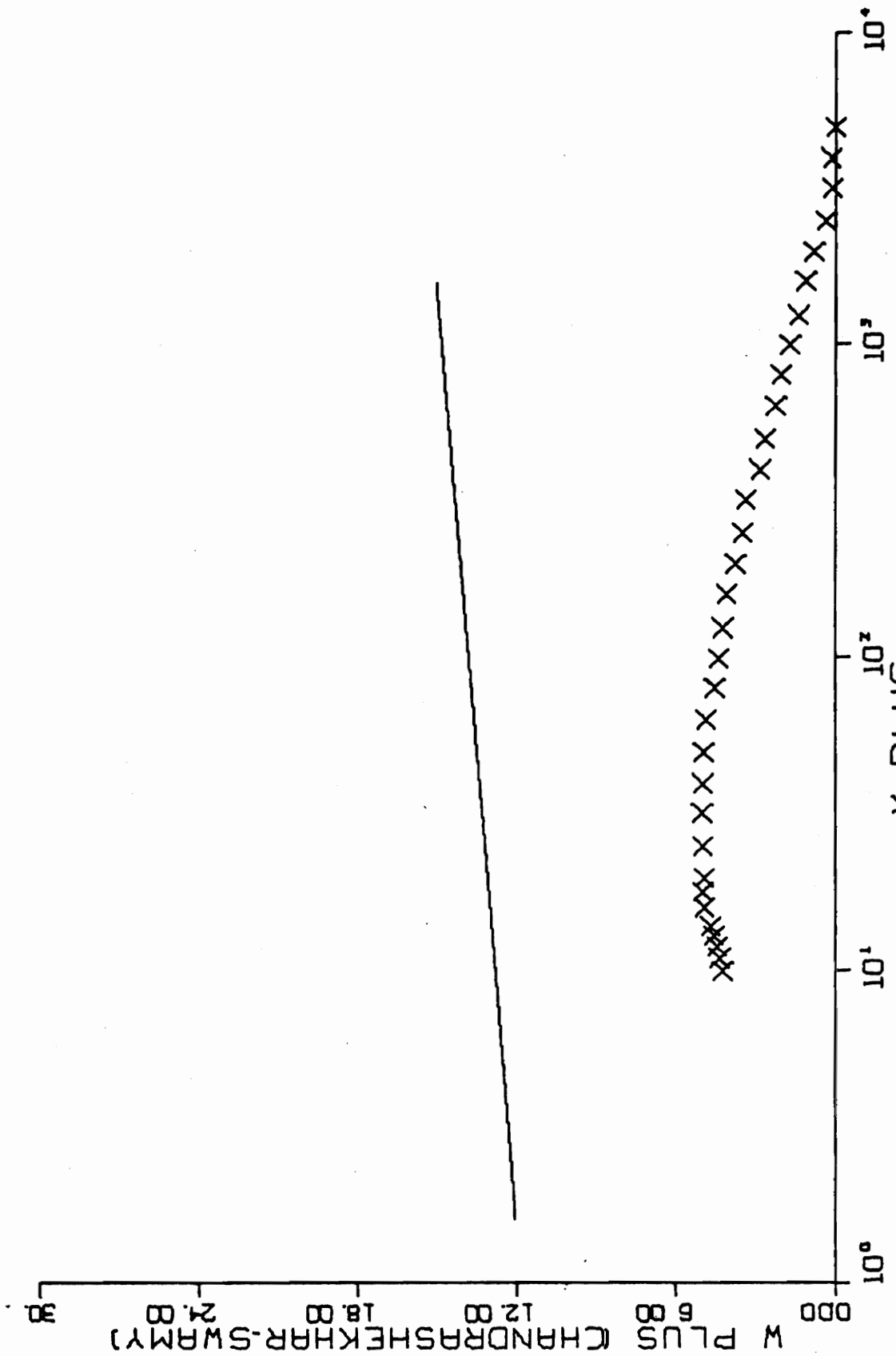

FIG. B13-4. CONTINUED FOR RUN E3-03.

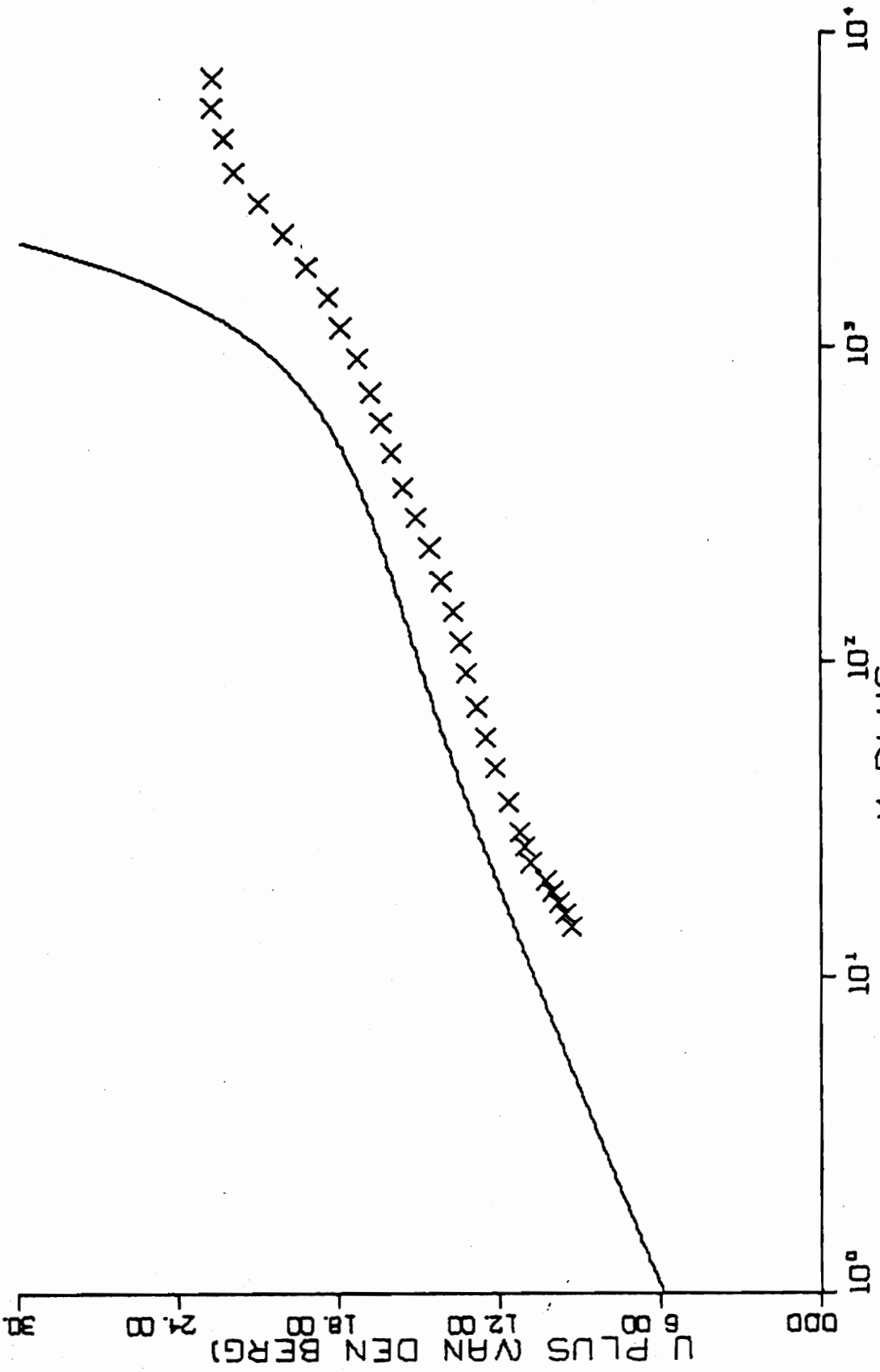

FIG. B13-5. THREE-DIMENSIONAL SIMILARITY PLOT-RUN E3-03.

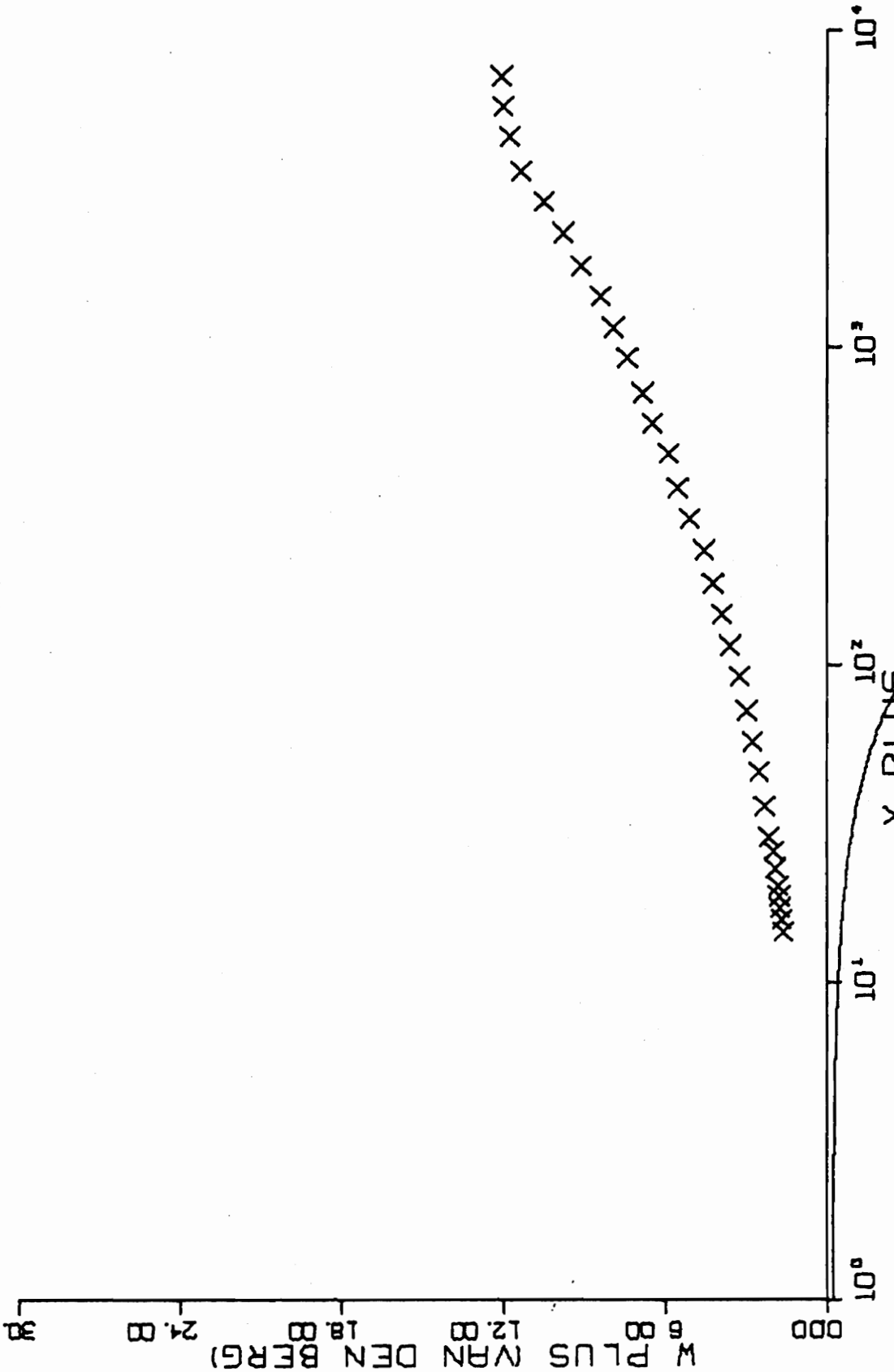

FIG. B13-5. CONTINUED FOR RUN E3-03.

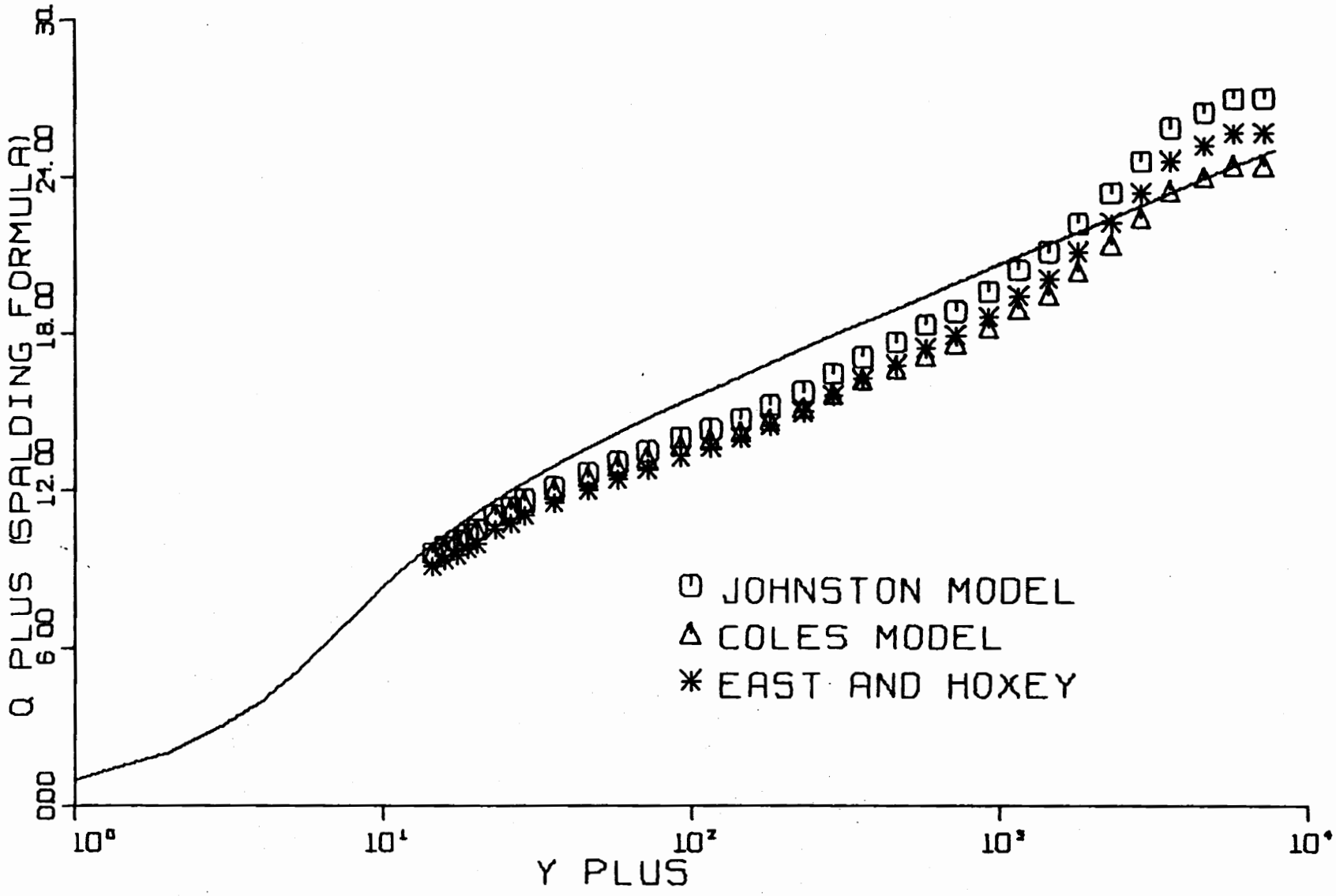

FIGB14-1. THREE-DIMENSIONAL SIMILARITY PLOT-RUN E3-03P.

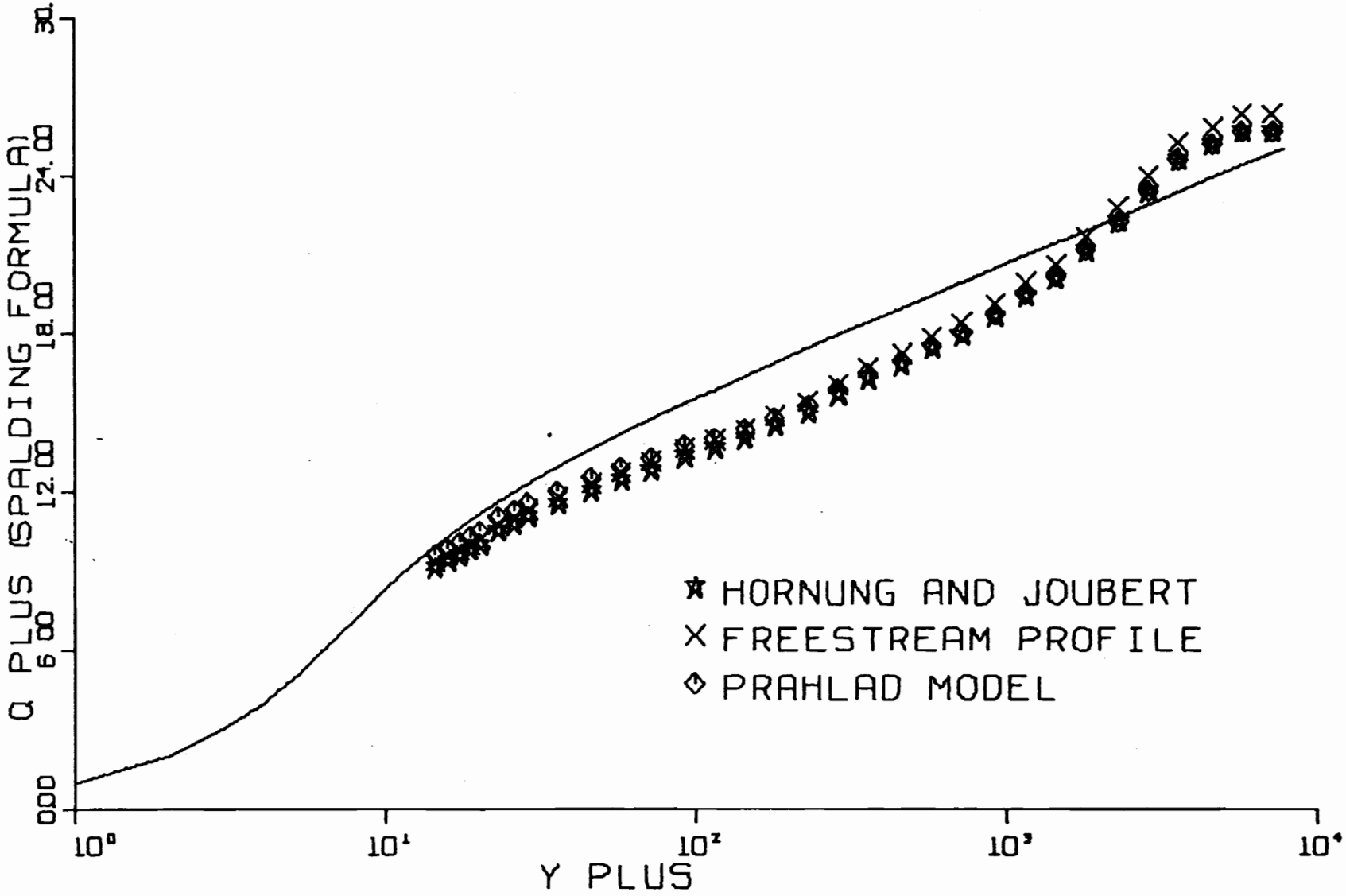

FIGB14-2. THREE-DIMENSIONAL SIMILARITY PLOT-RUN E3-03P.

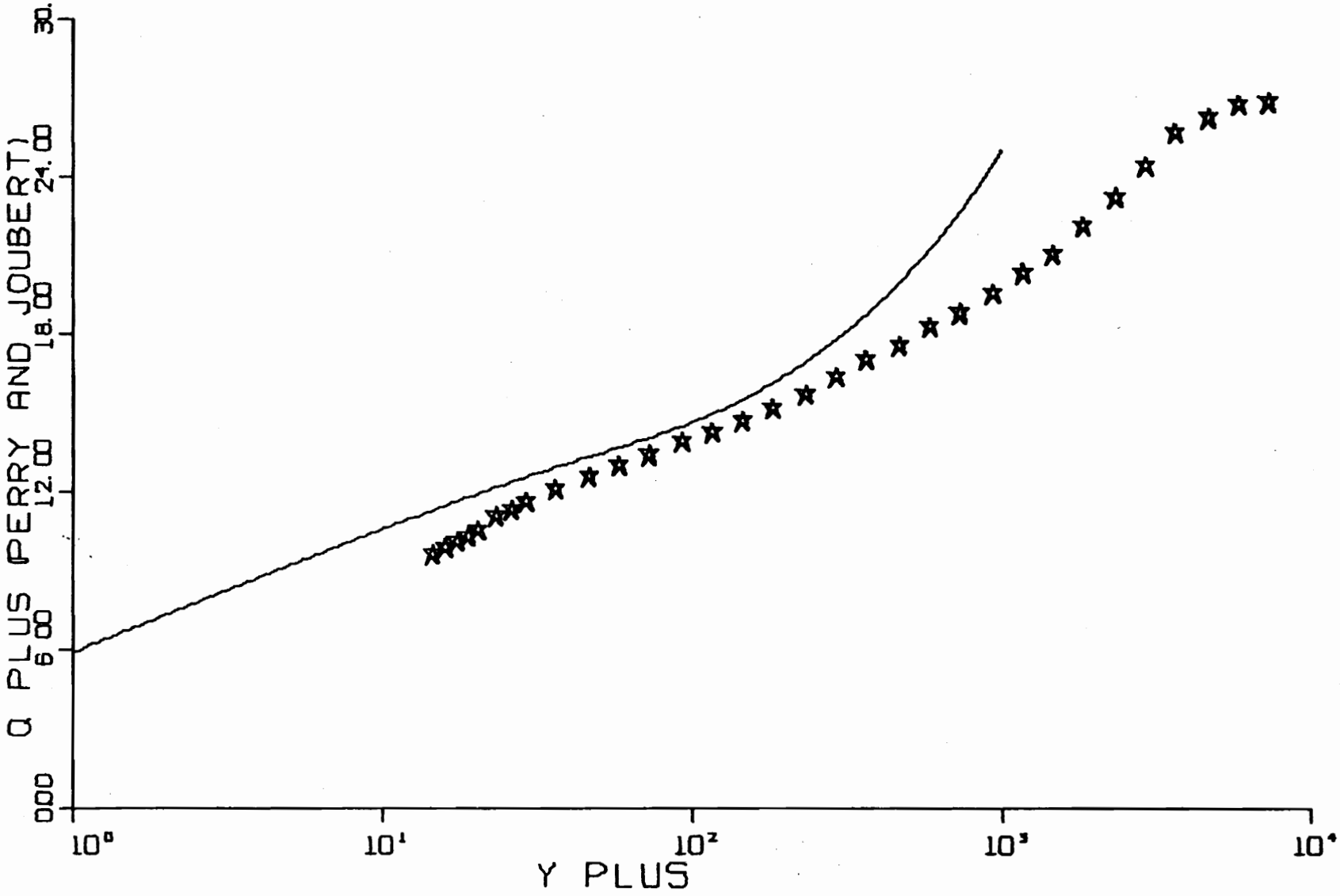

FIGB14-3. THREE-DIMENSIONAL SIMILARITY PLOT-RUN E3-03P.

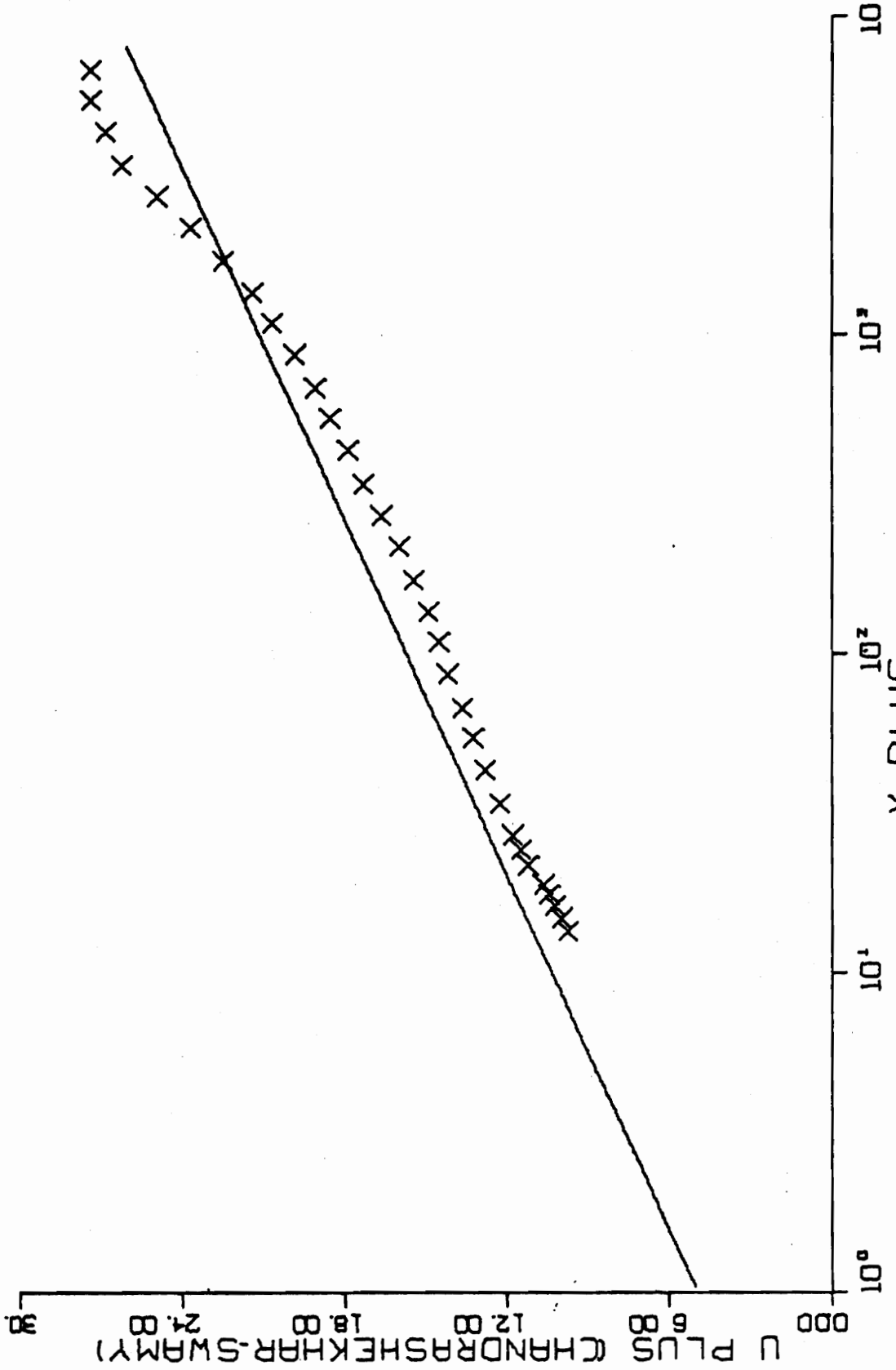

FIGB14-4. THREE-DIMENSIONAL SIMILARITY PLOT-RUN E3-03P.

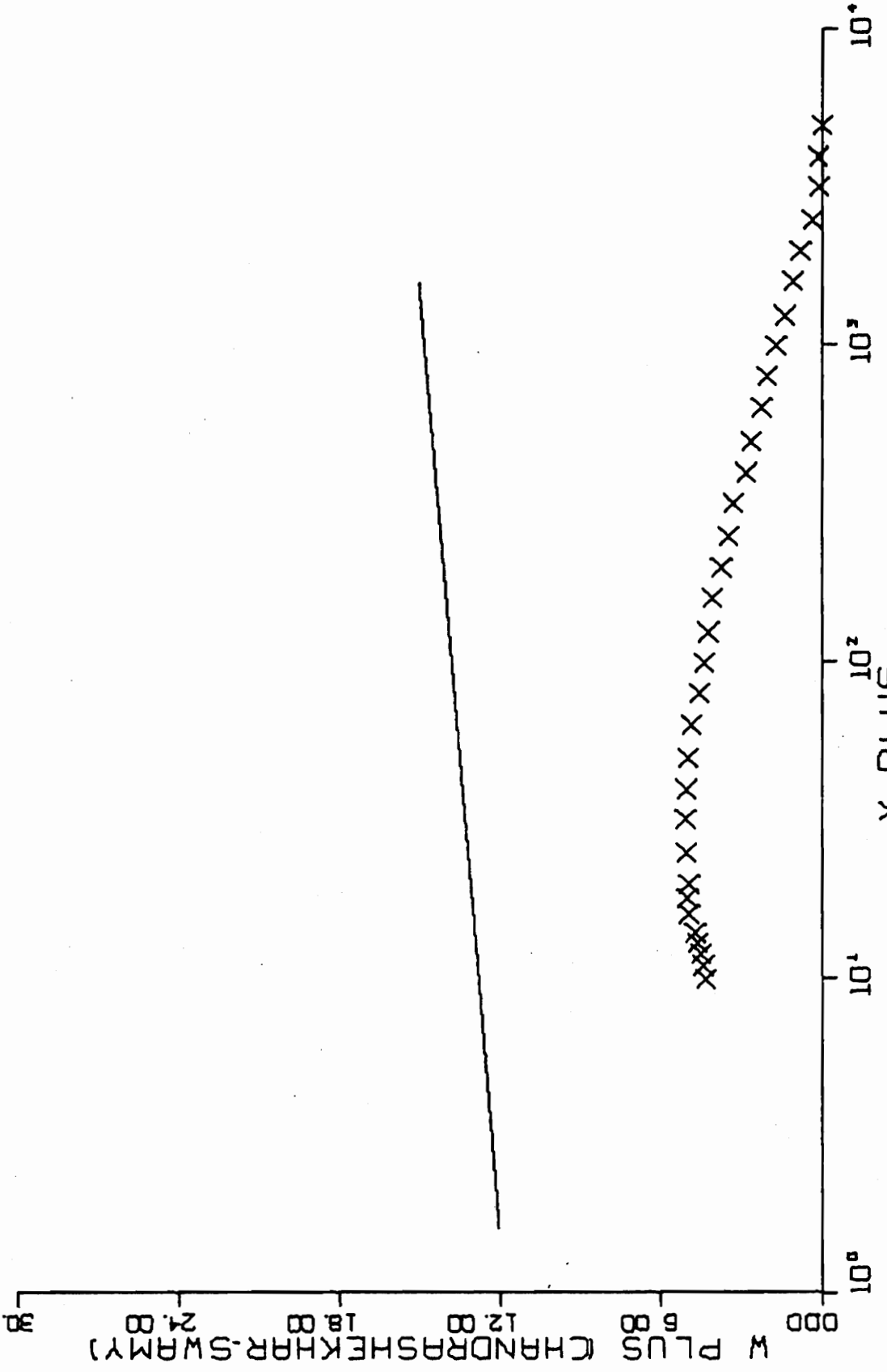

FIG. B14-4. CONTINUED FOR RUN E3-03P.

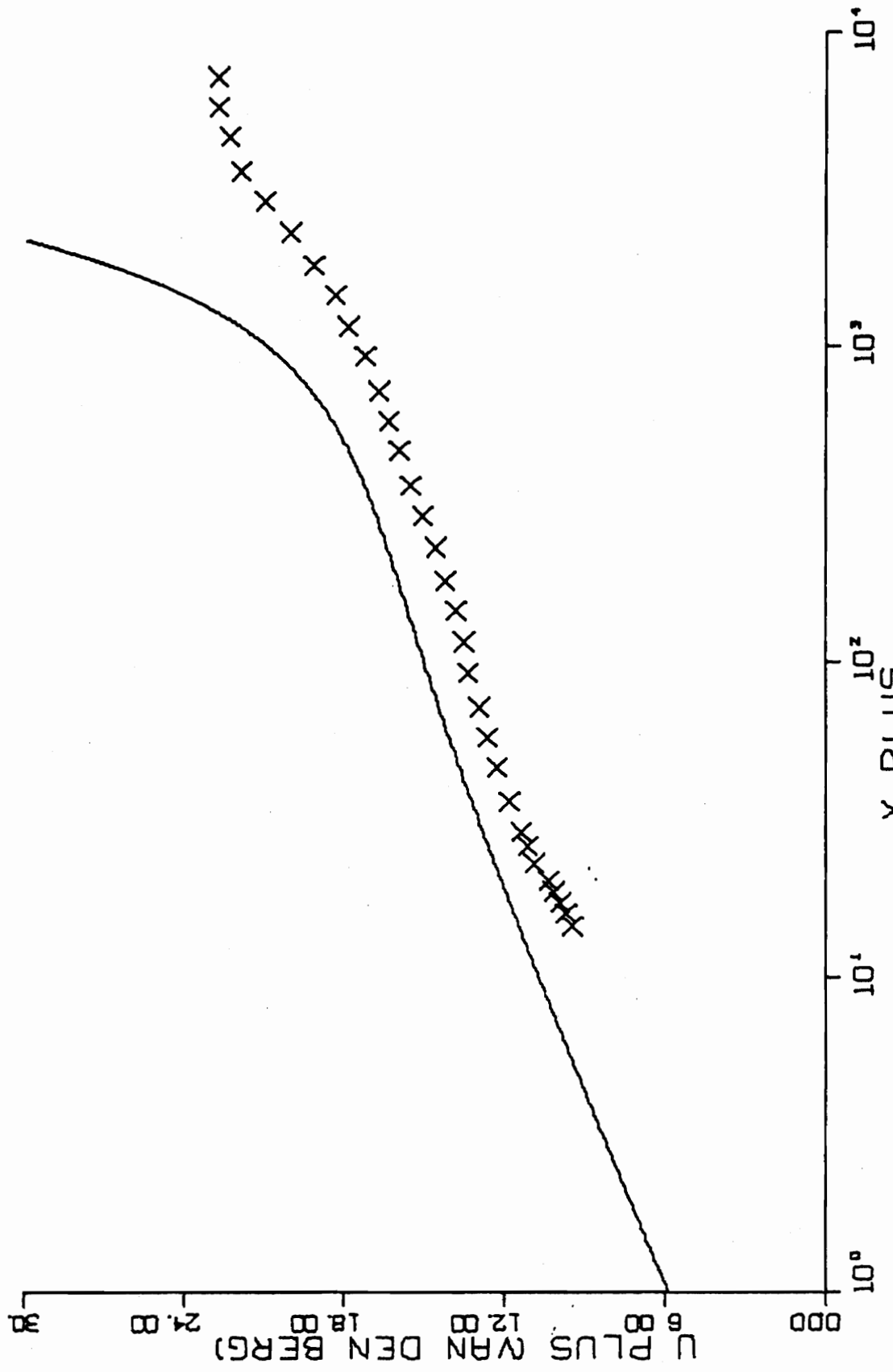

FIGB14-5. THREE-DIMENSIONAL SIMILARITY PLOT-RUN E3-03P.

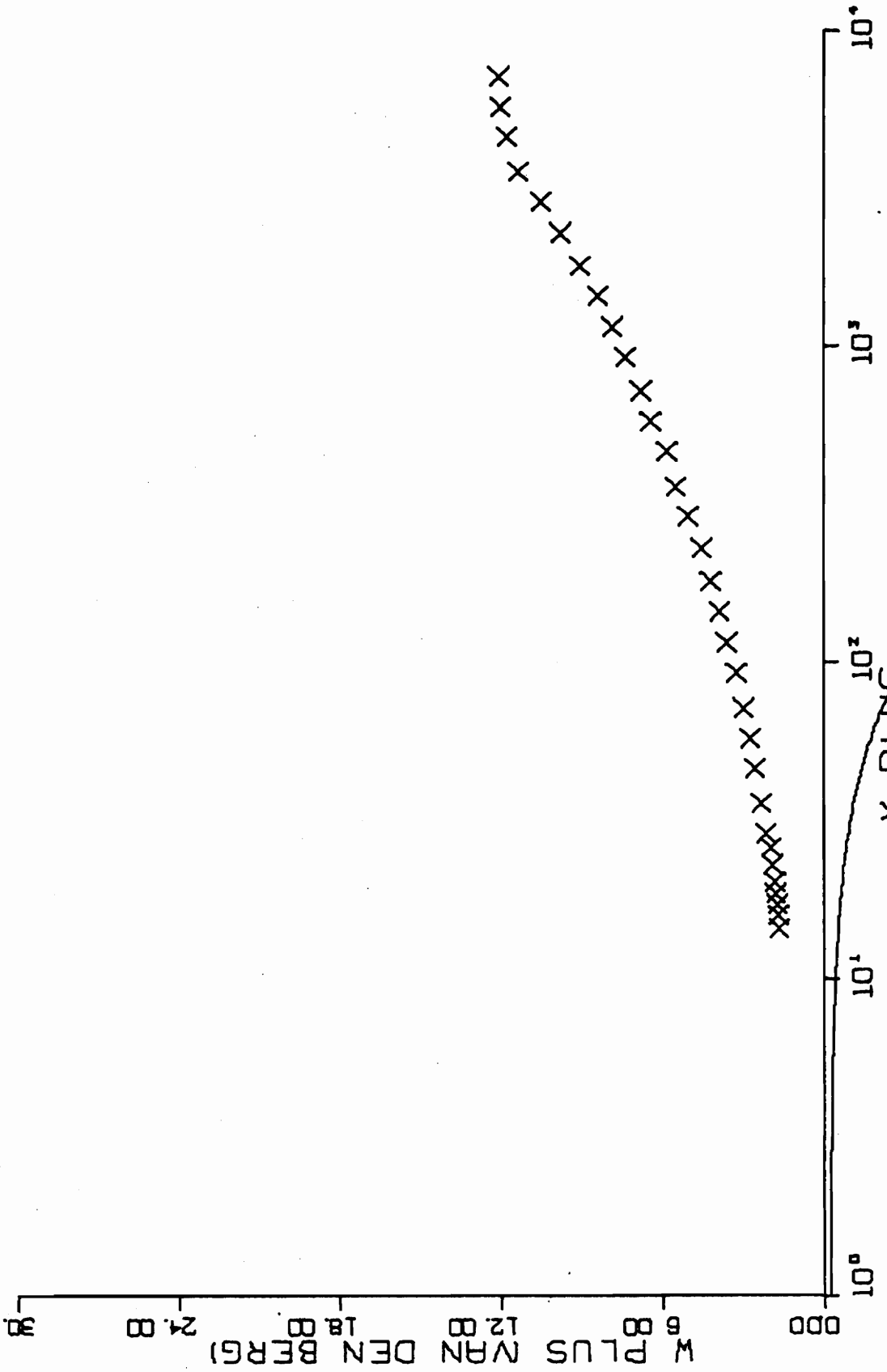

FIG. B14-5. CONTINUED FOR RUN E3-03P.

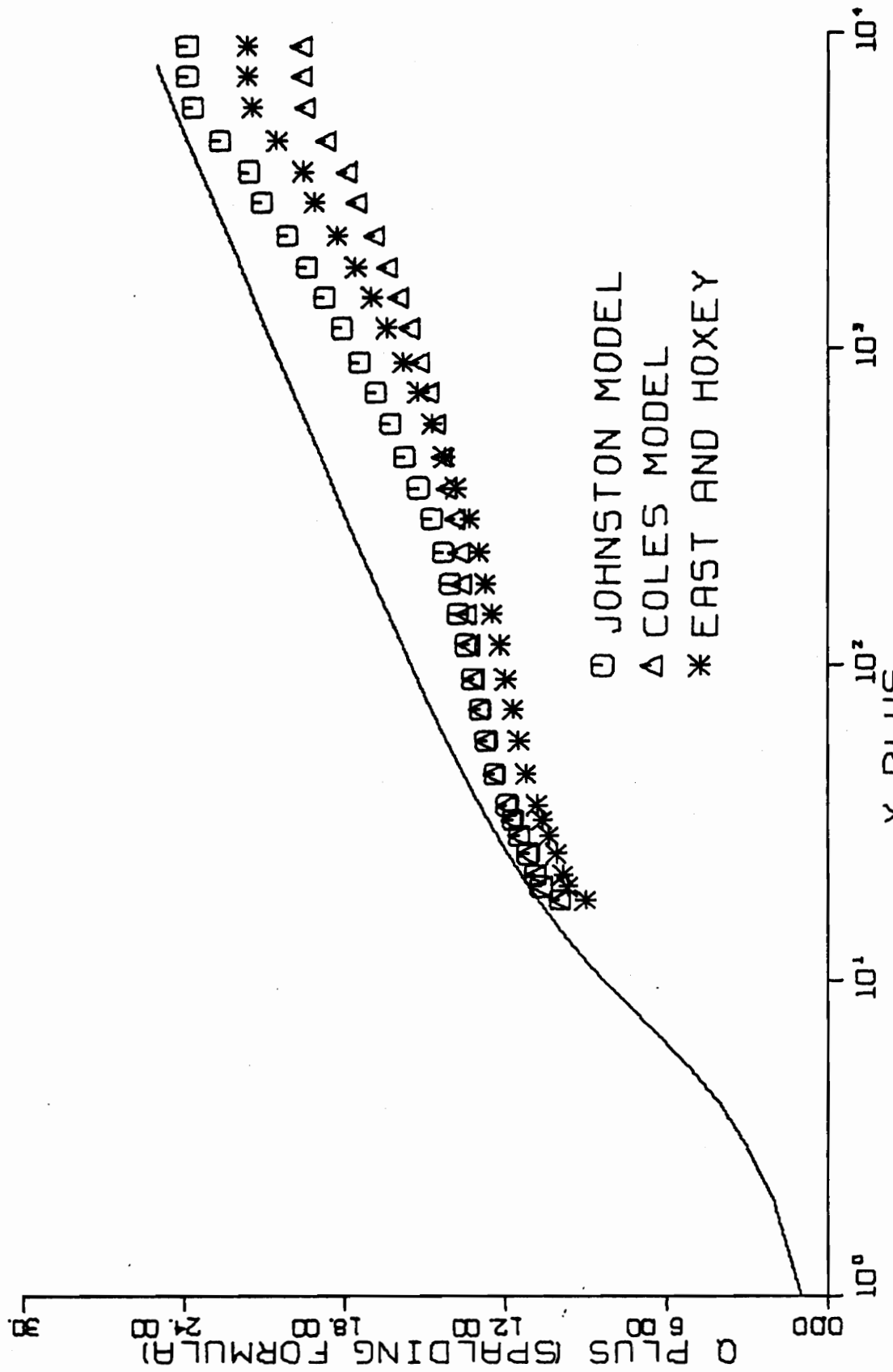

FIG. B15-1. THREE-DIMENSIONAL SIMILARITY PLOT-RUN E1-01.

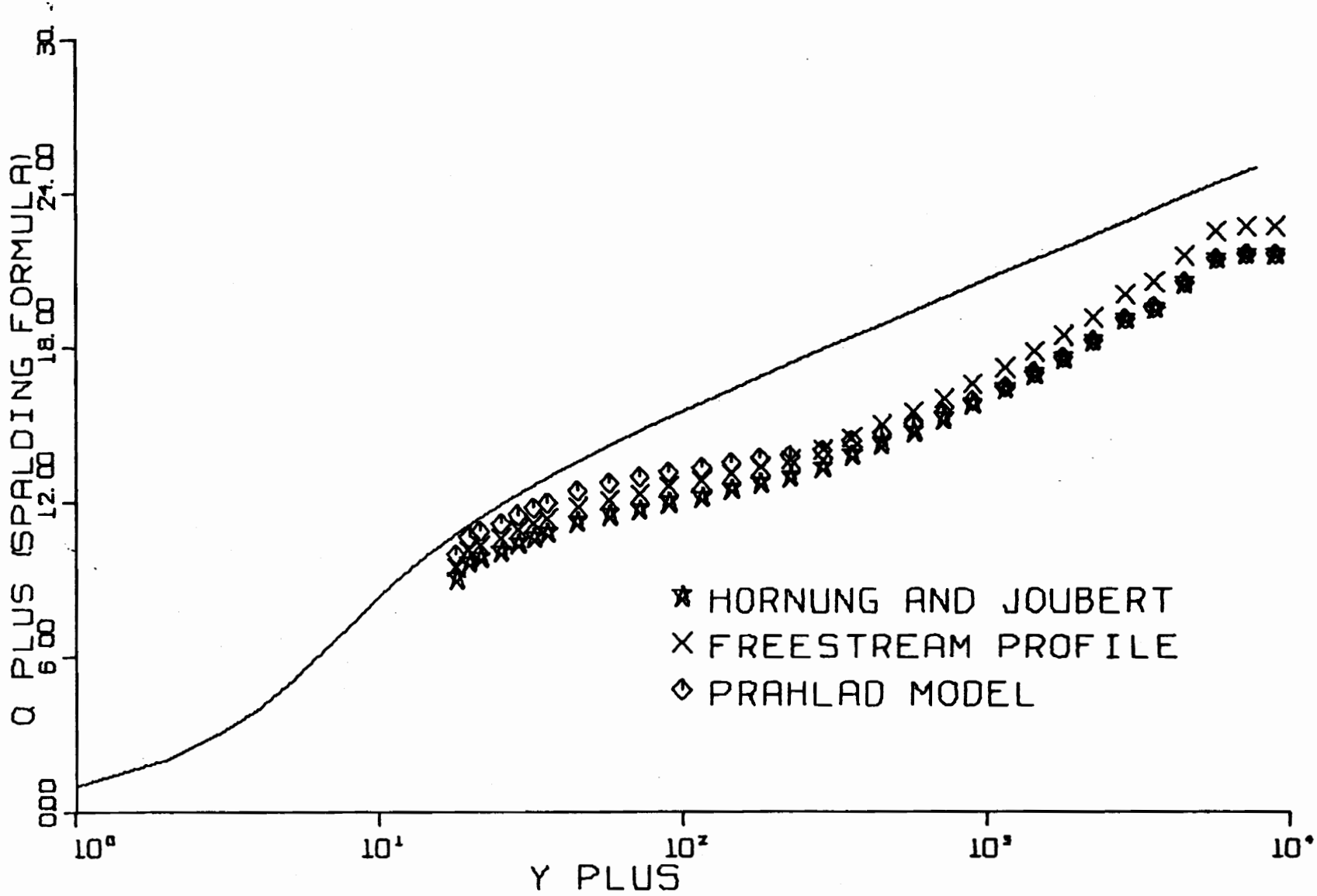

FIG. B15-2. THREE-DIMENSIONAL SIMILARITY PLOT-RUN E1-01.

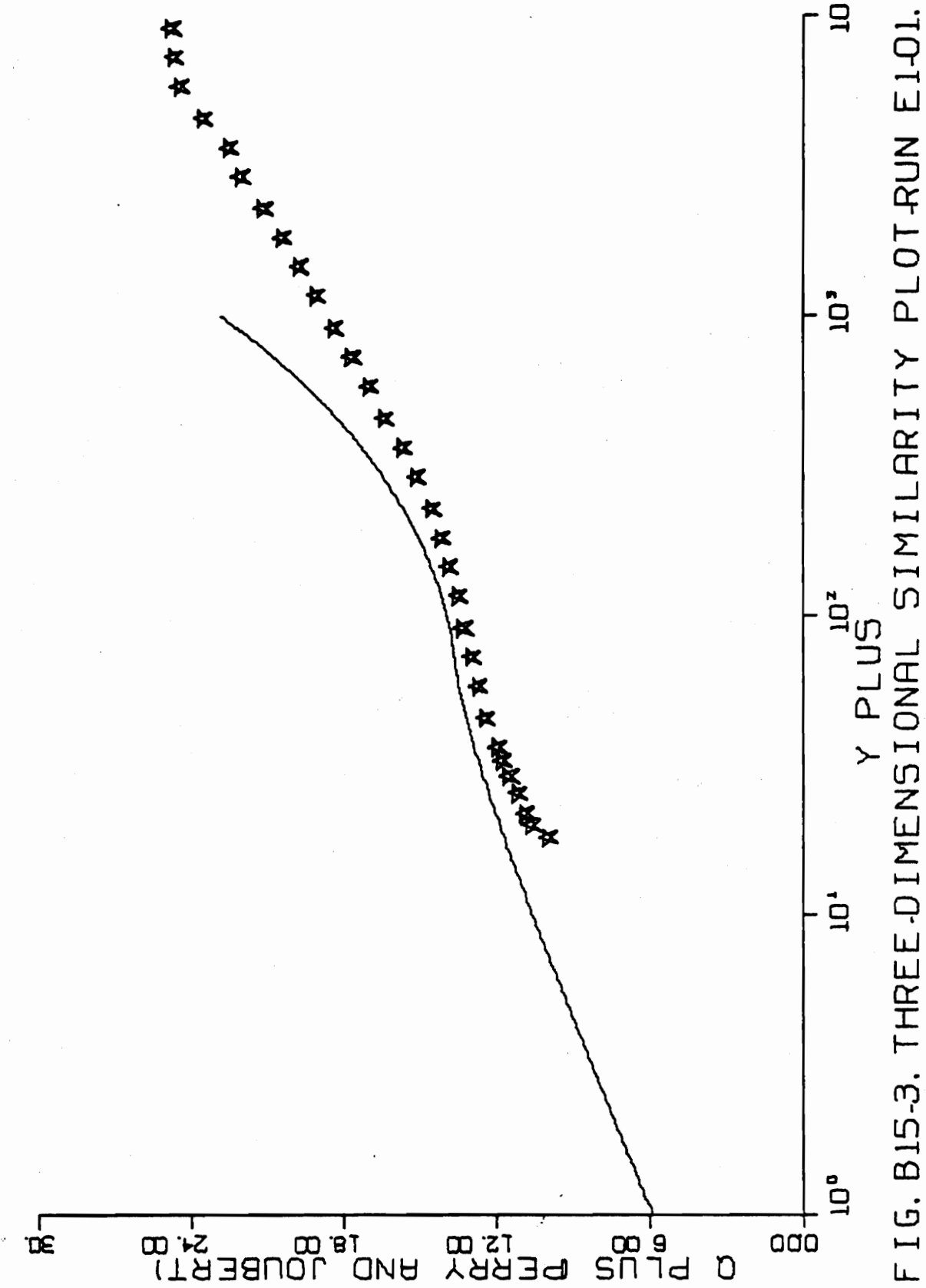

FIG. B15-3. THREE-DIMENSIONAL SIMILARITY PLOT-RUN E1-01.

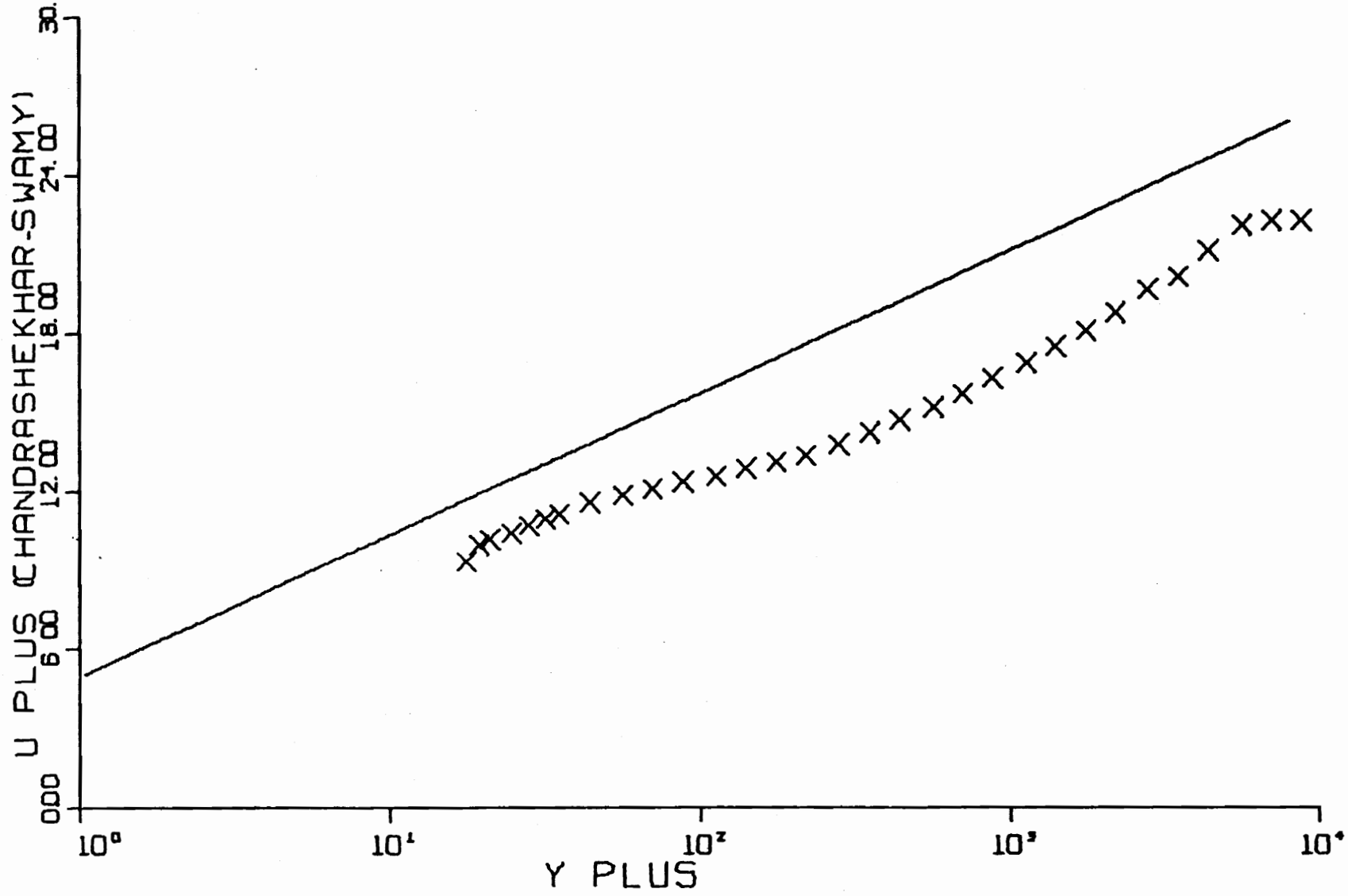

FIG. B15-4. THREE-DIMENSIONAL SIMILARITY PLOT-RUN E1-01.

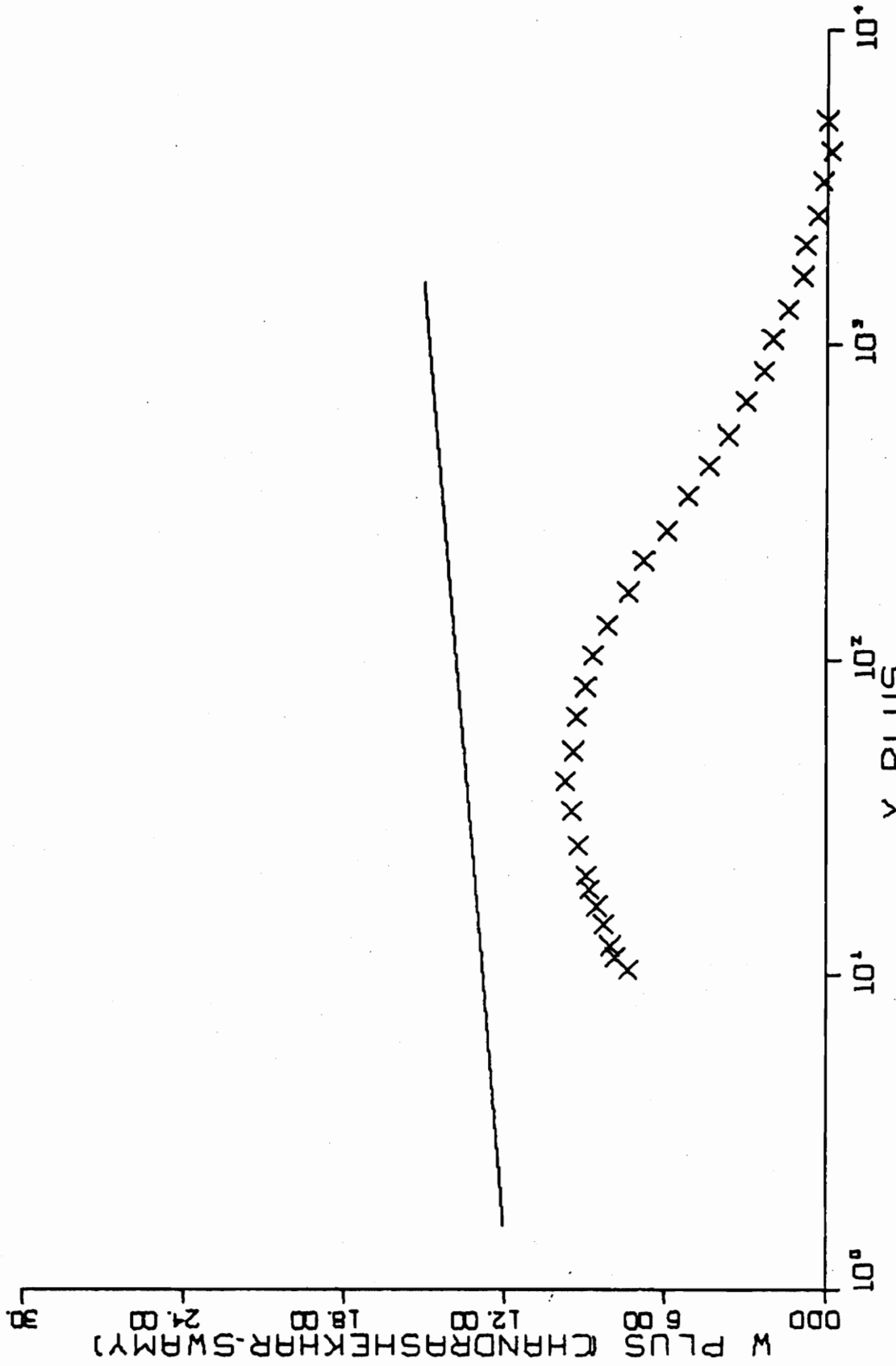

FIG. B15-4. CONTINUED FOR RUN E1-01.

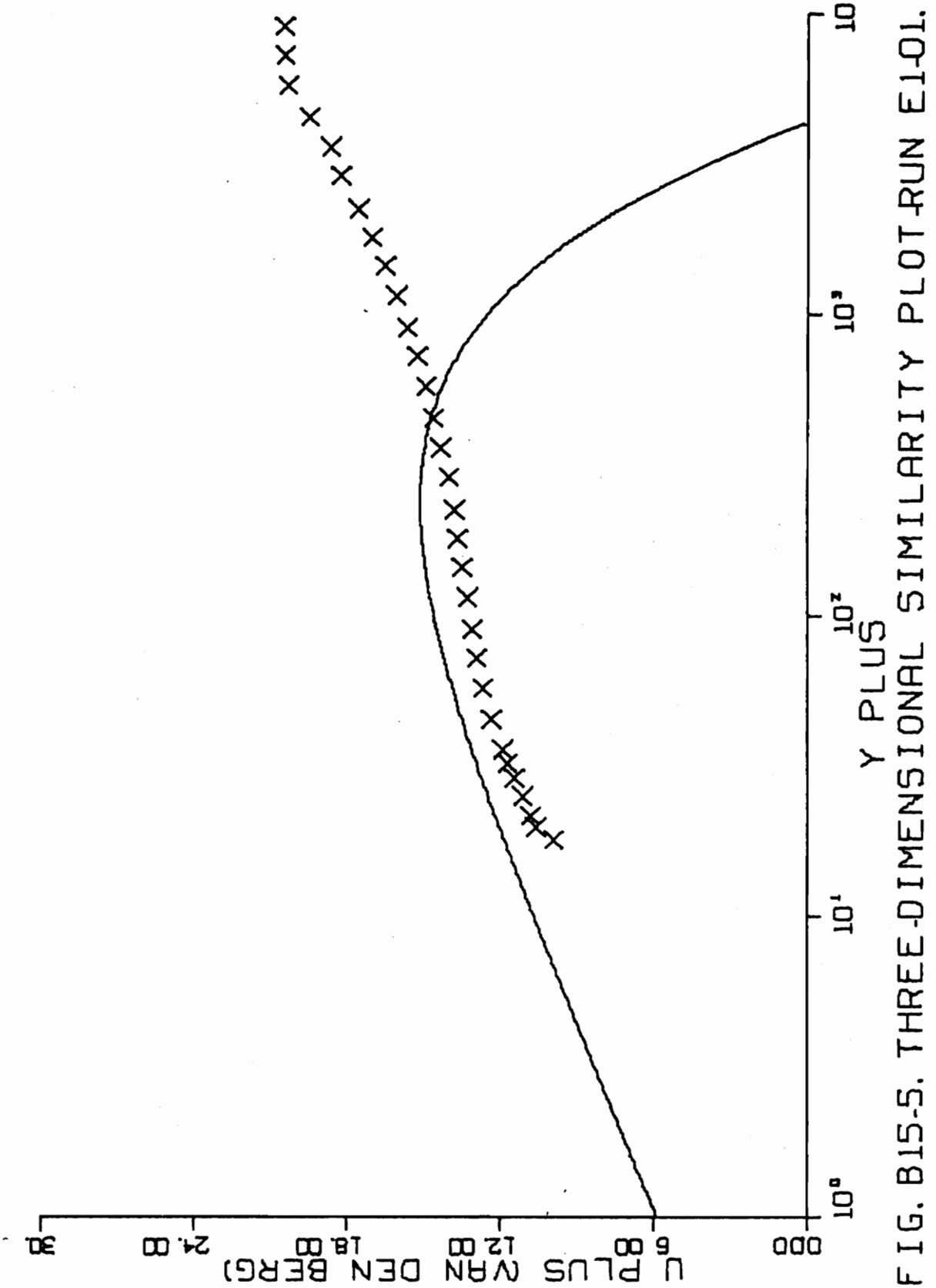

FIG. B15-5. THREE-DIMENSIONAL SIMILARITY PLOT-RUN E1-01.

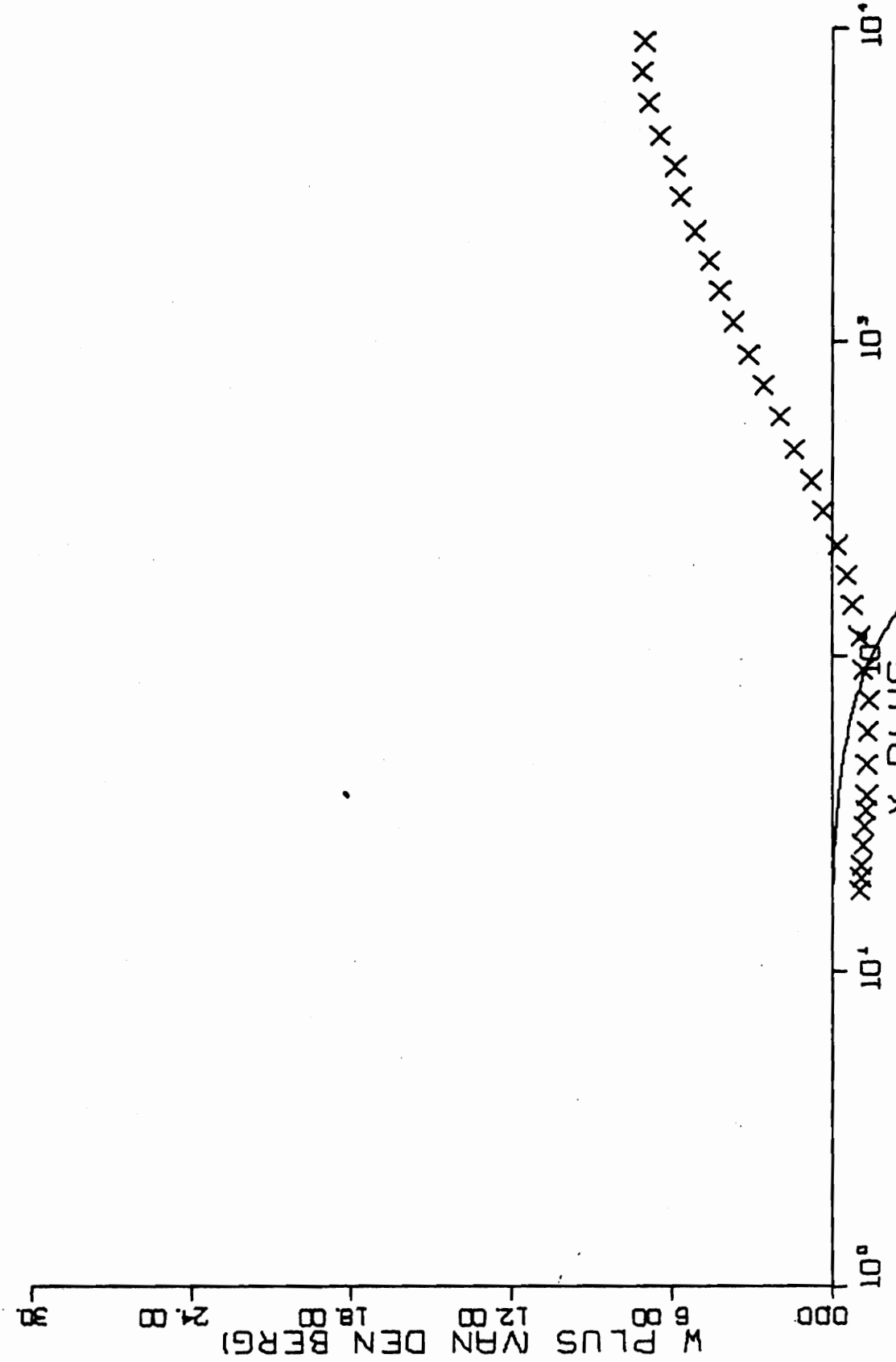

FIG. B15-5. CONTINUED FOR RUN E1-01.

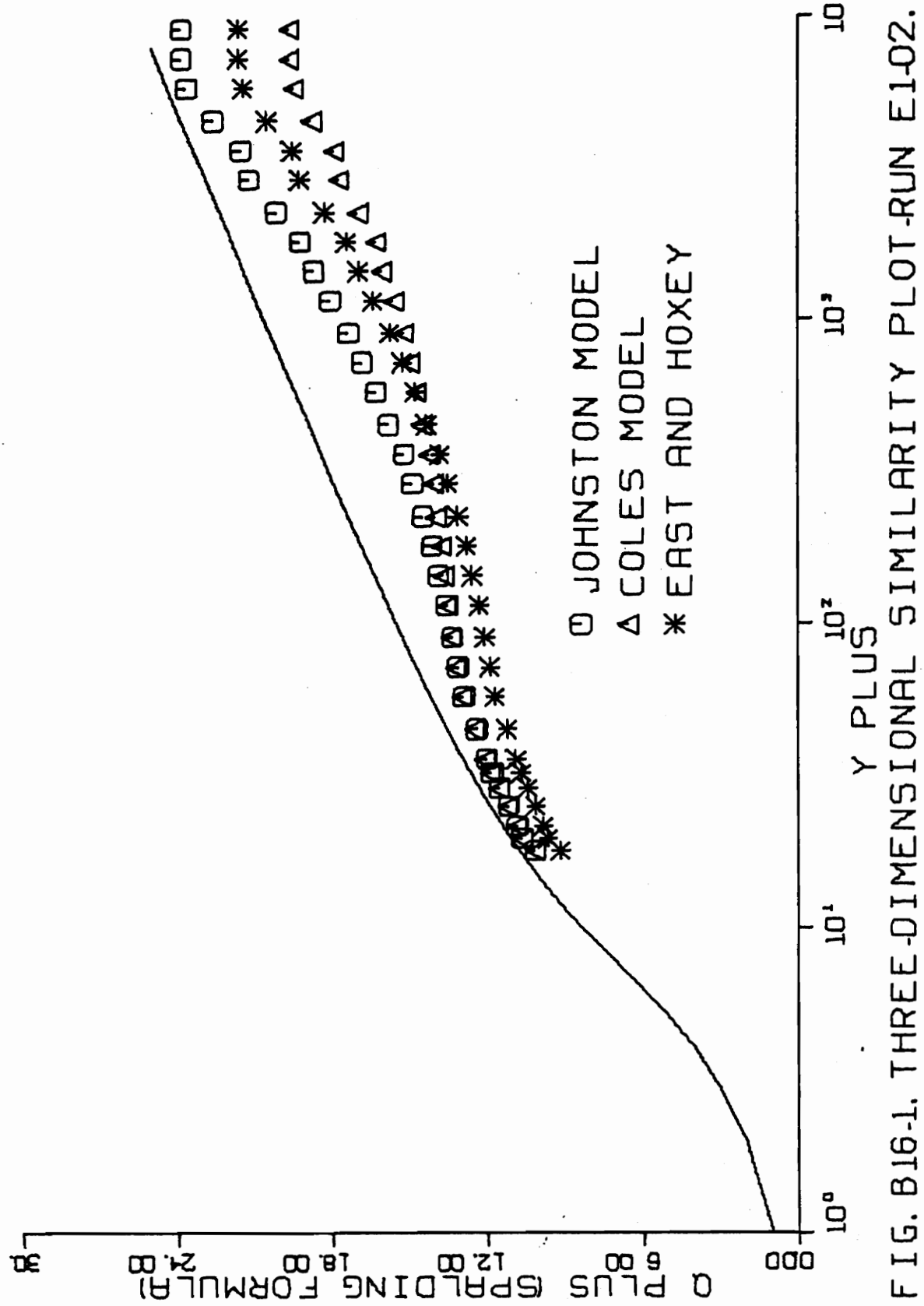

FIG. B16-1. THREE-DIMENSIONAL SIMILARITY PLOT-RUN E1-02.

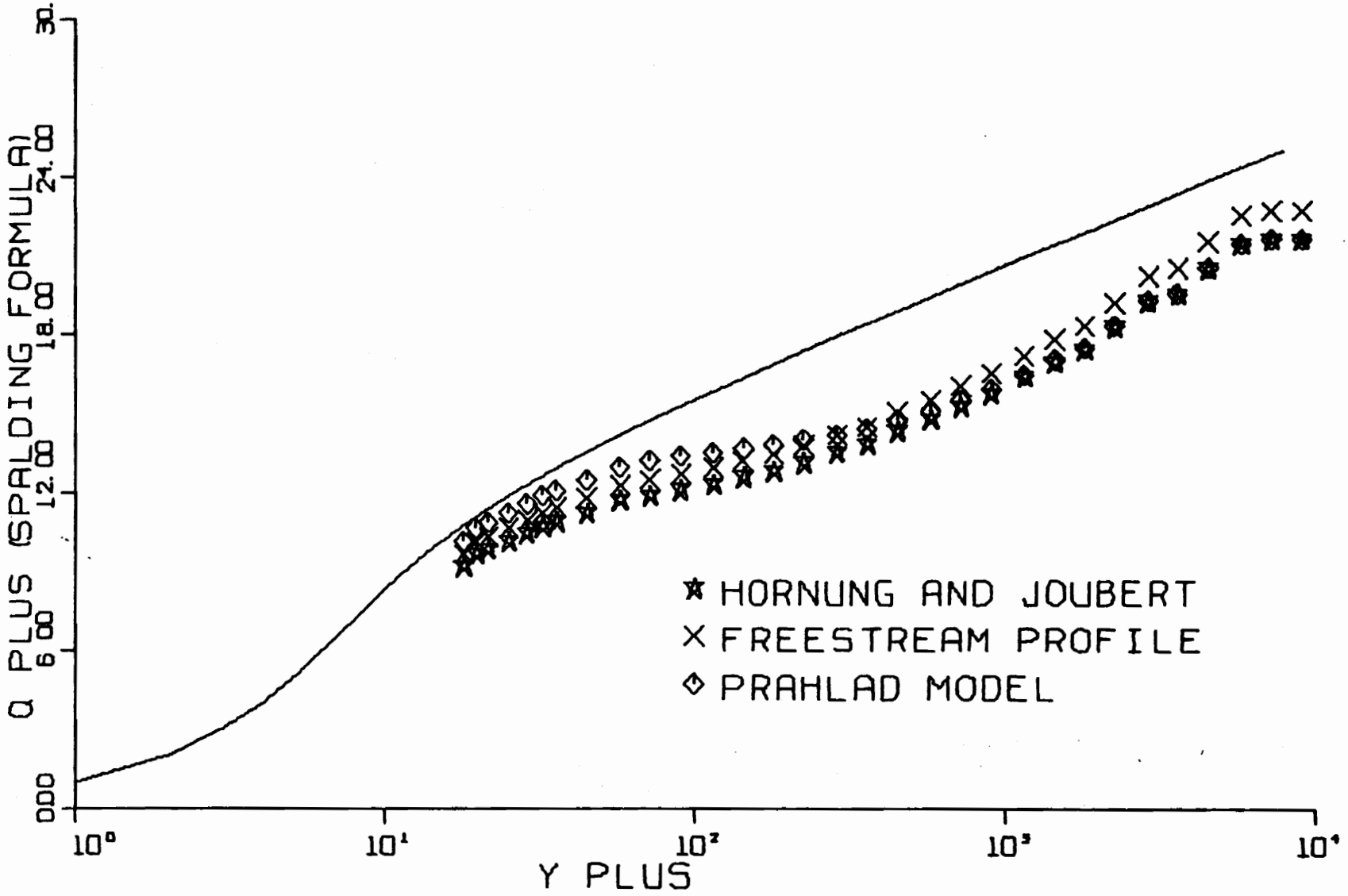

FIG. B16-2. THREE-DIMENSIONAL SIMILARITY PLOT-RUN E1-02.

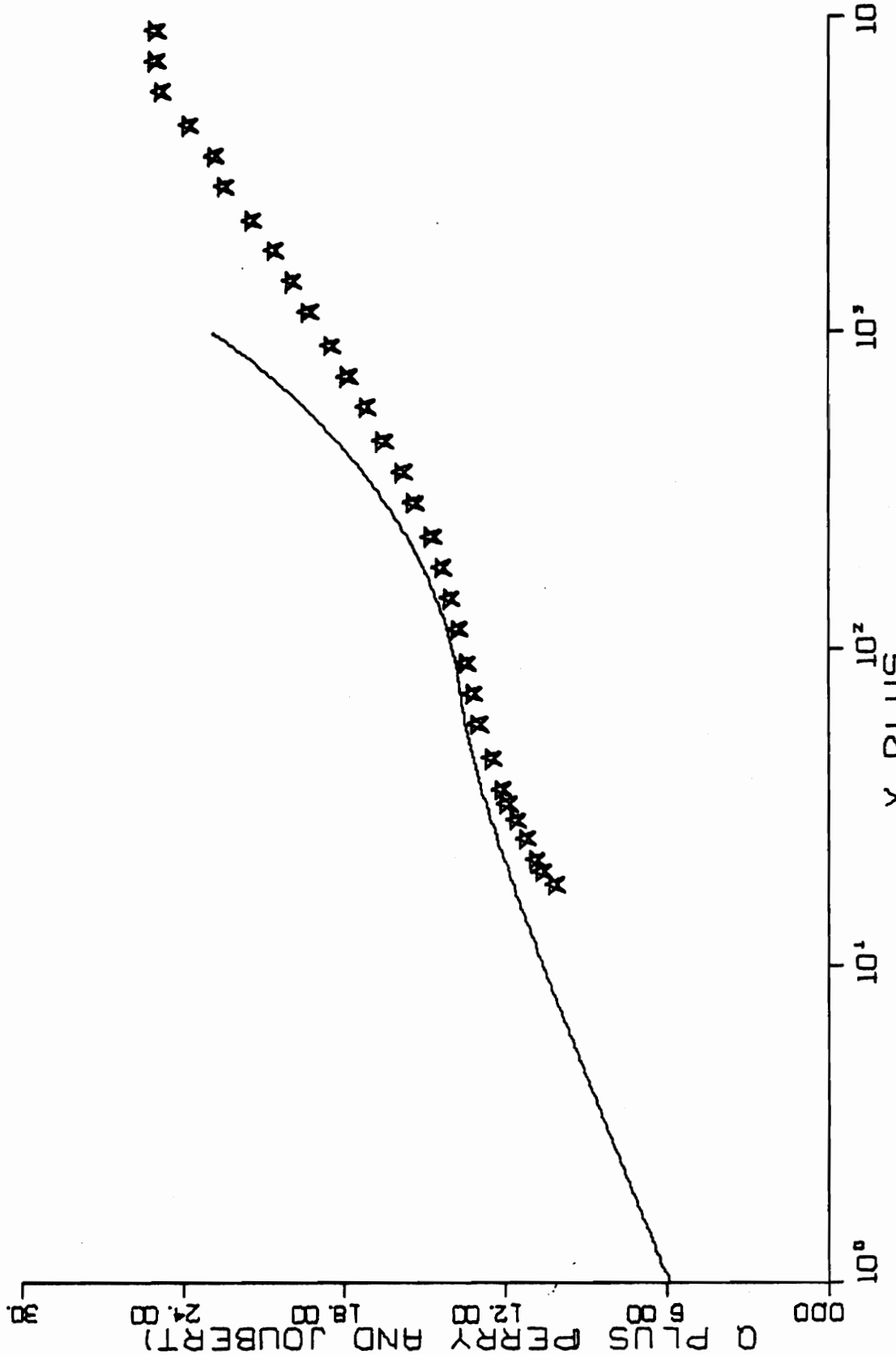

FIG. B16-3. THREE-DIMENSIONAL SIMILARITY PLOT-RUN E1-02.

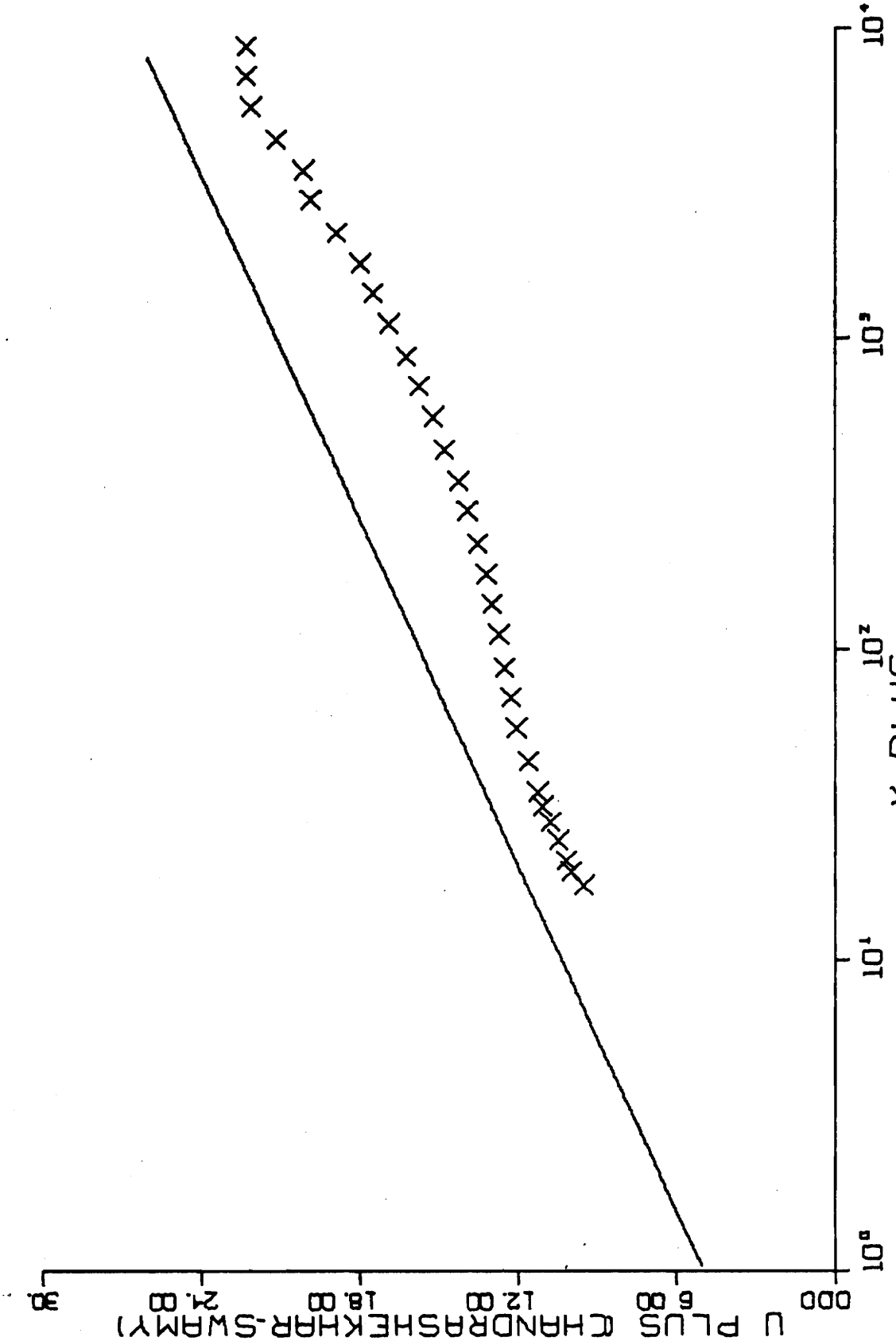

FIG. B16-4. THREE-DIMENSIONAL SIMILARITY PLOT-RUN E1-02.

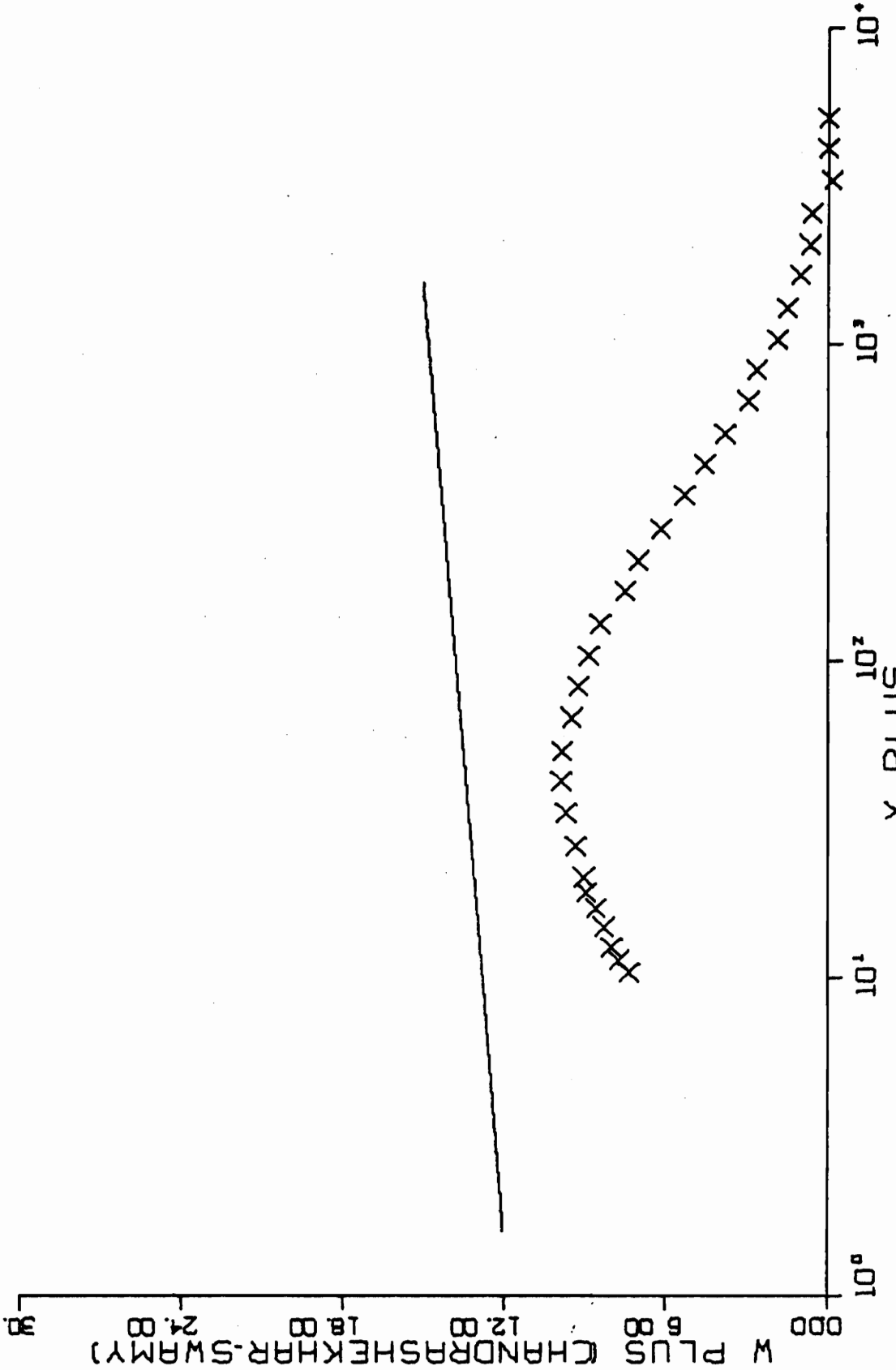

FIG. B16-4. CONTINUED FOR RUN E1-02.

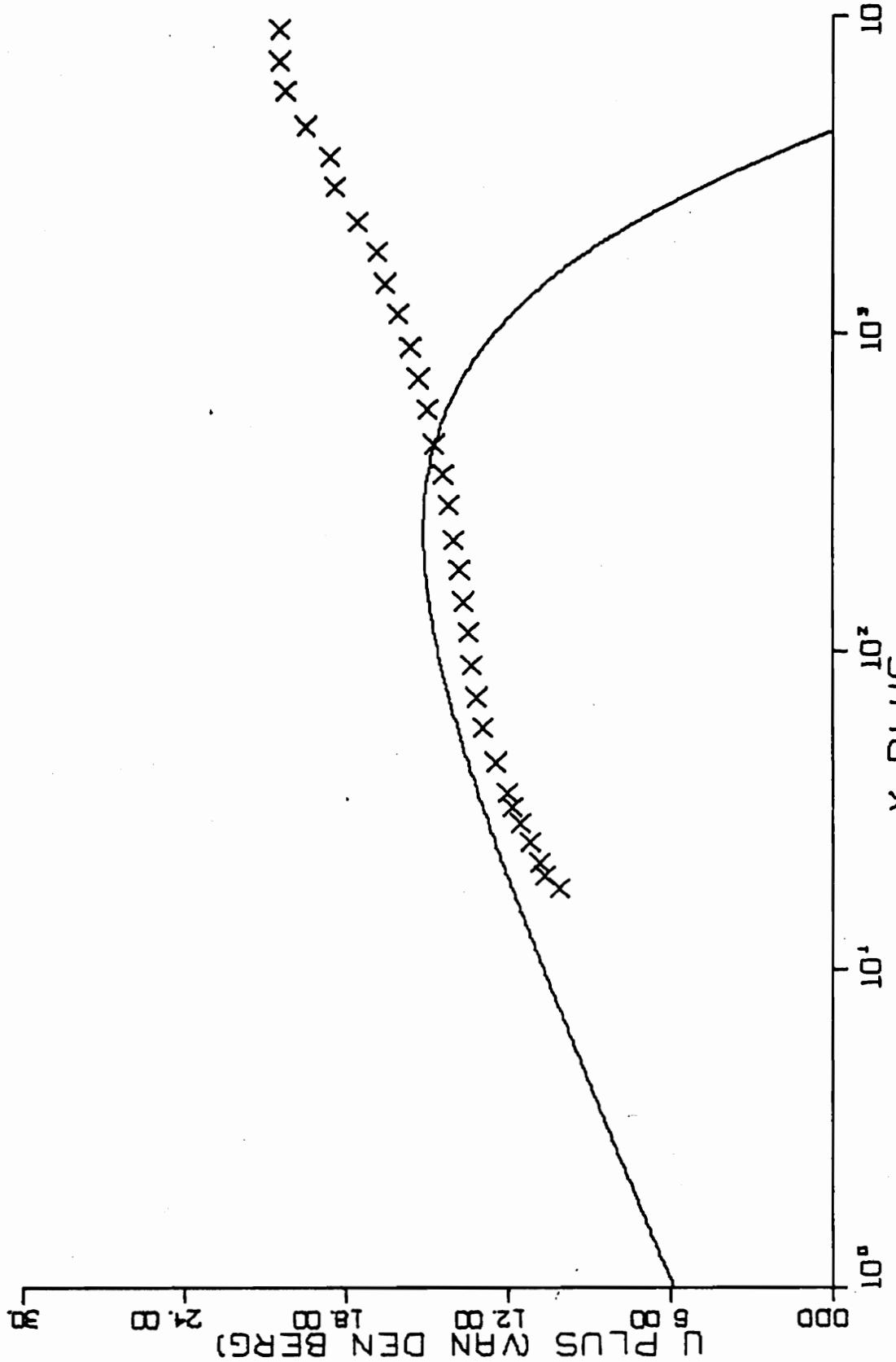

FIG. B16-5. THREE-DIMENSIONAL SIMILARITY PLOT-RUN E1-02.

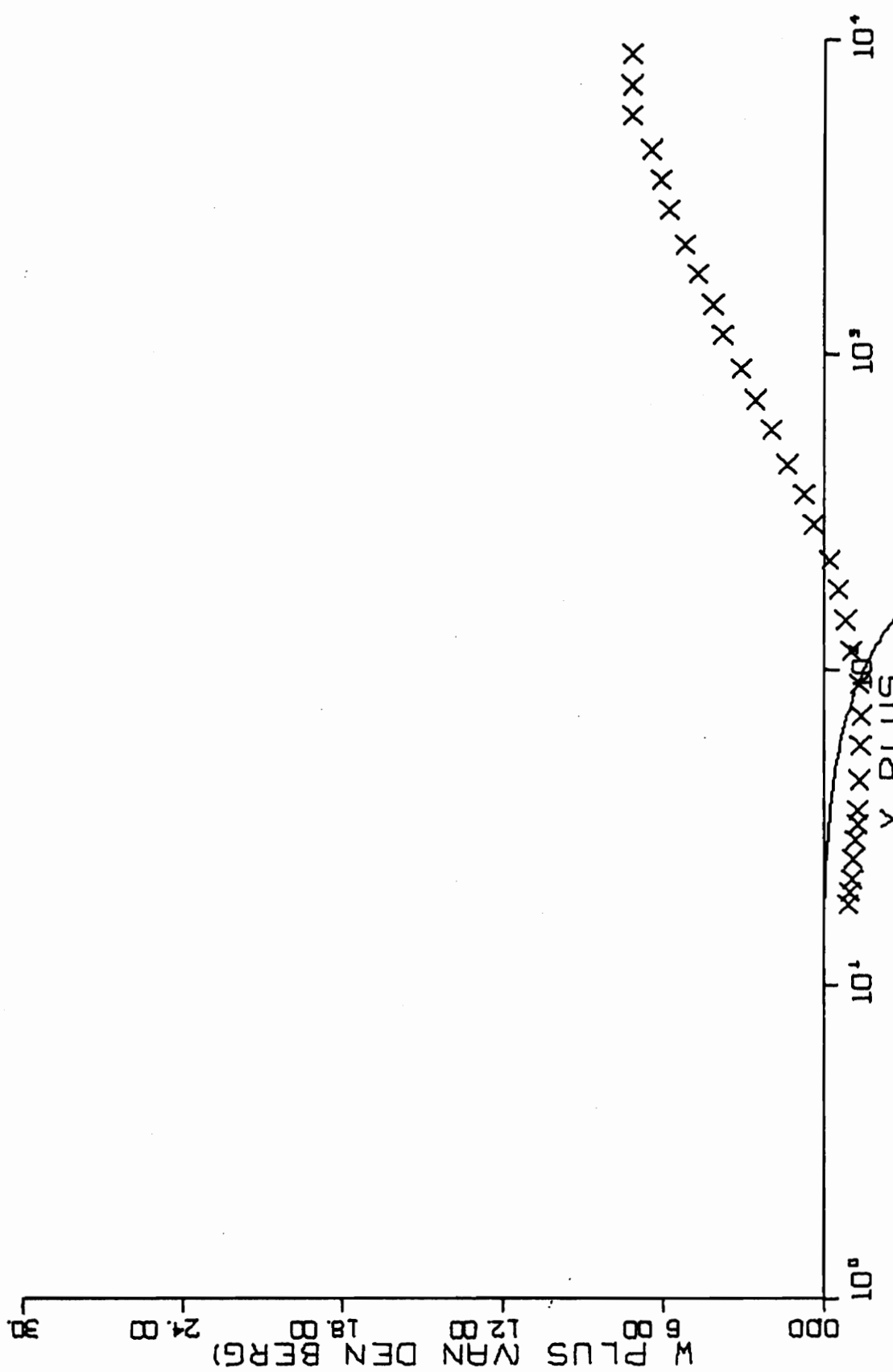

F.IG. B16-5. CONTINUED FOR RUN E1-02.

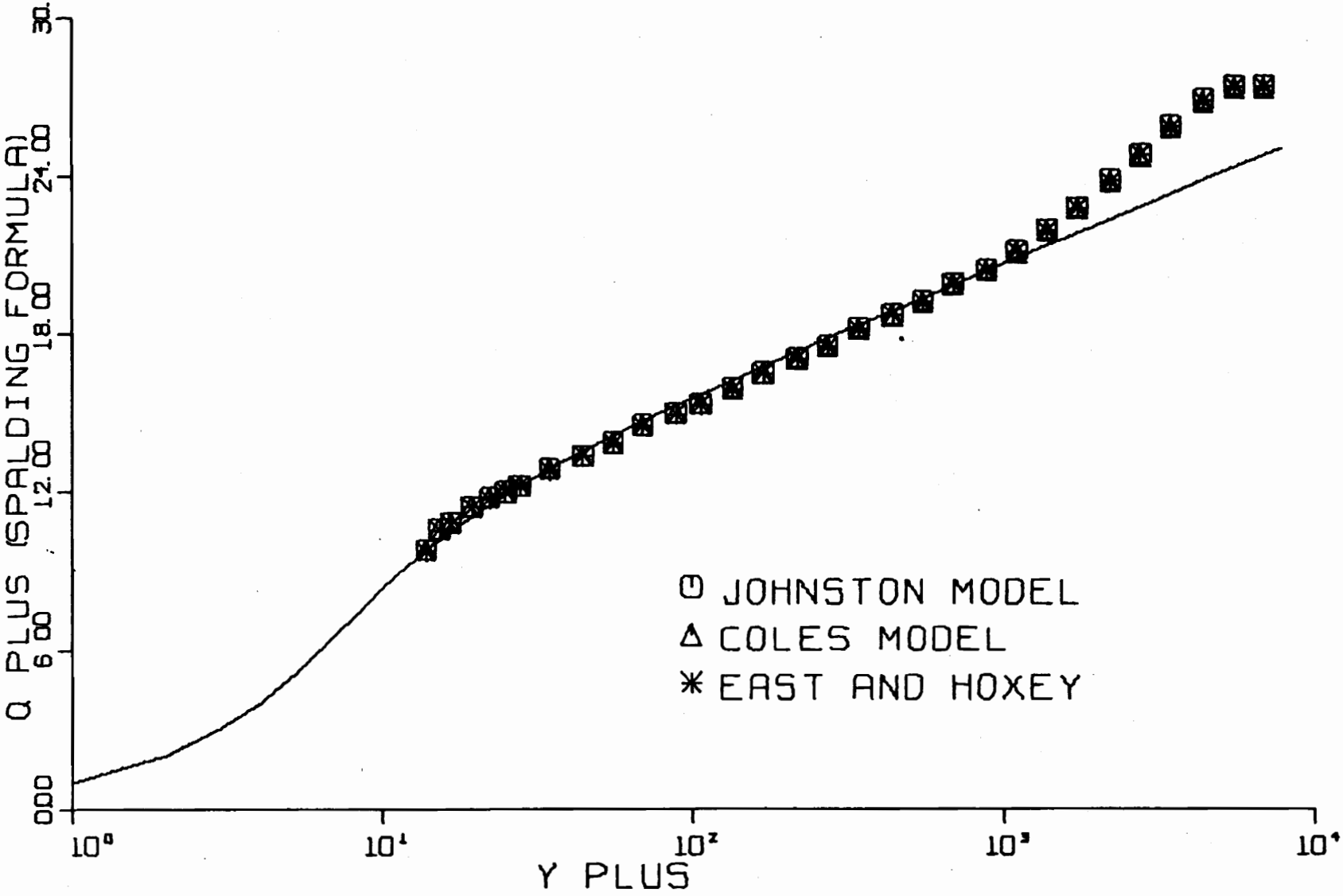

FIG. B17-1. THREE-DIMENSIONAL SIMILARITY PLOT-RUN G7-01.

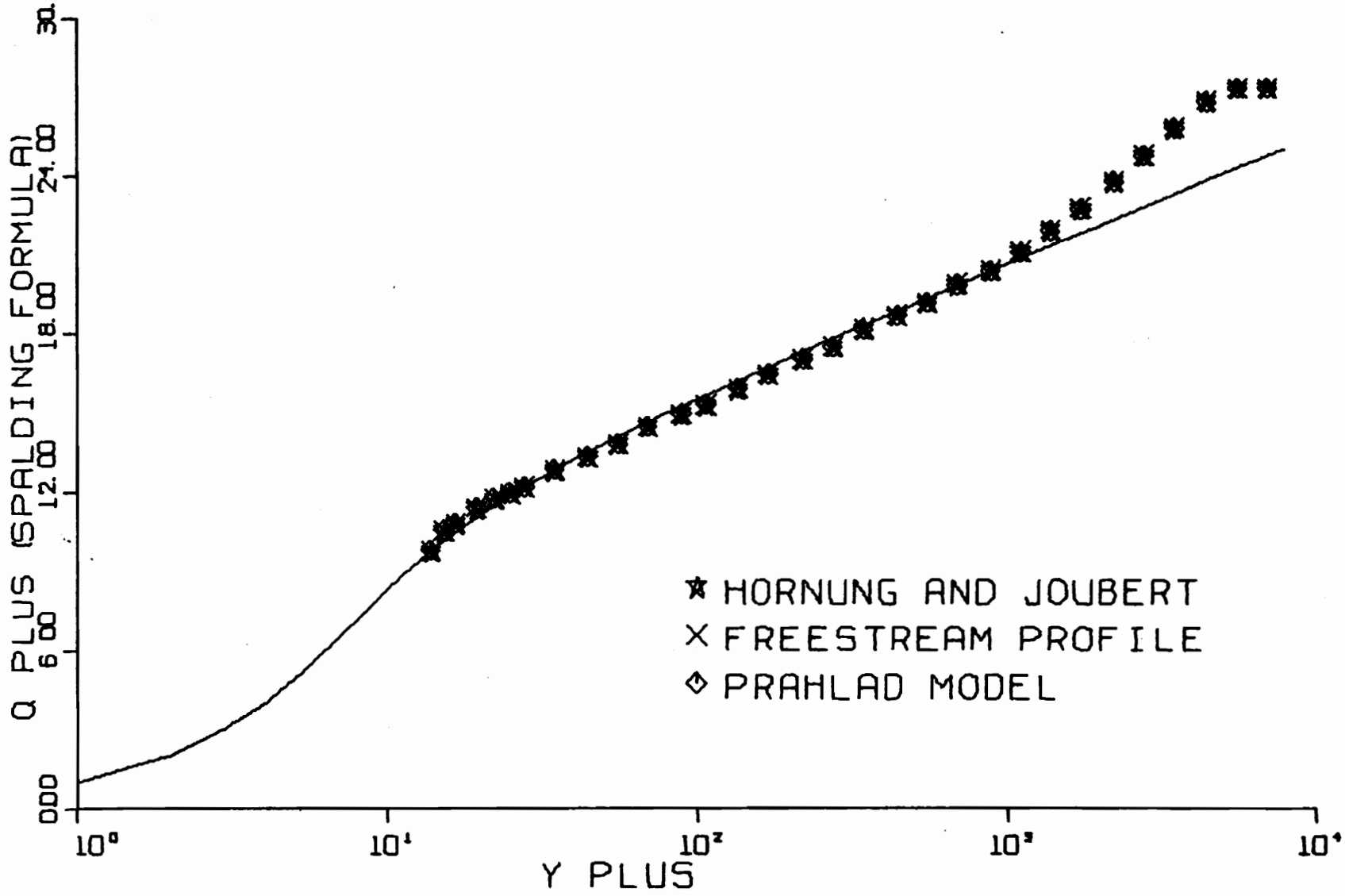

FIG. B17-2. THREE-DIMENSIONAL SIMILARITY PLOT-RUN G7-01.

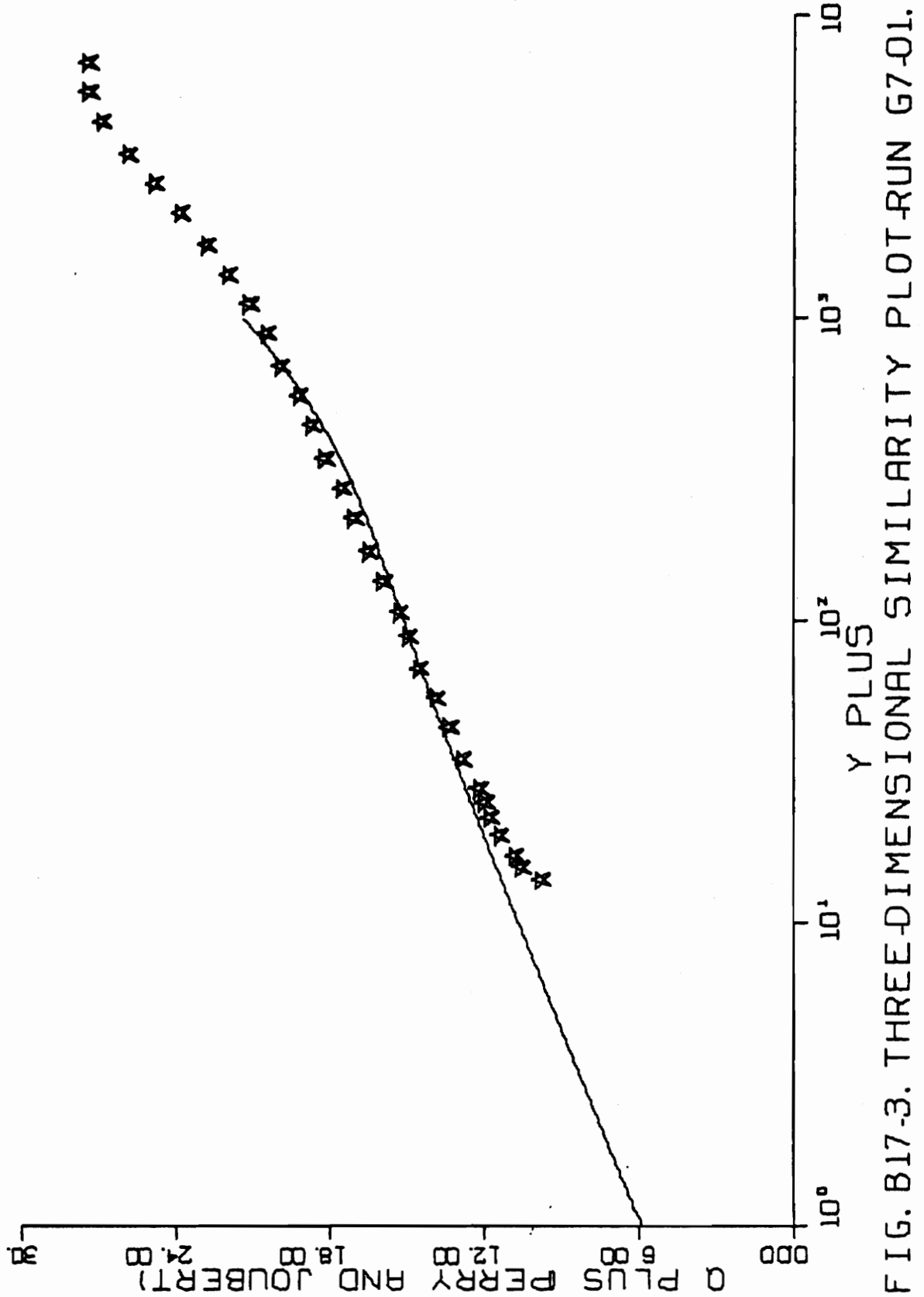

FIG. B17-3. THREE-DIMENSIONAL SIMILARITY PLOT-RUN G7-01.

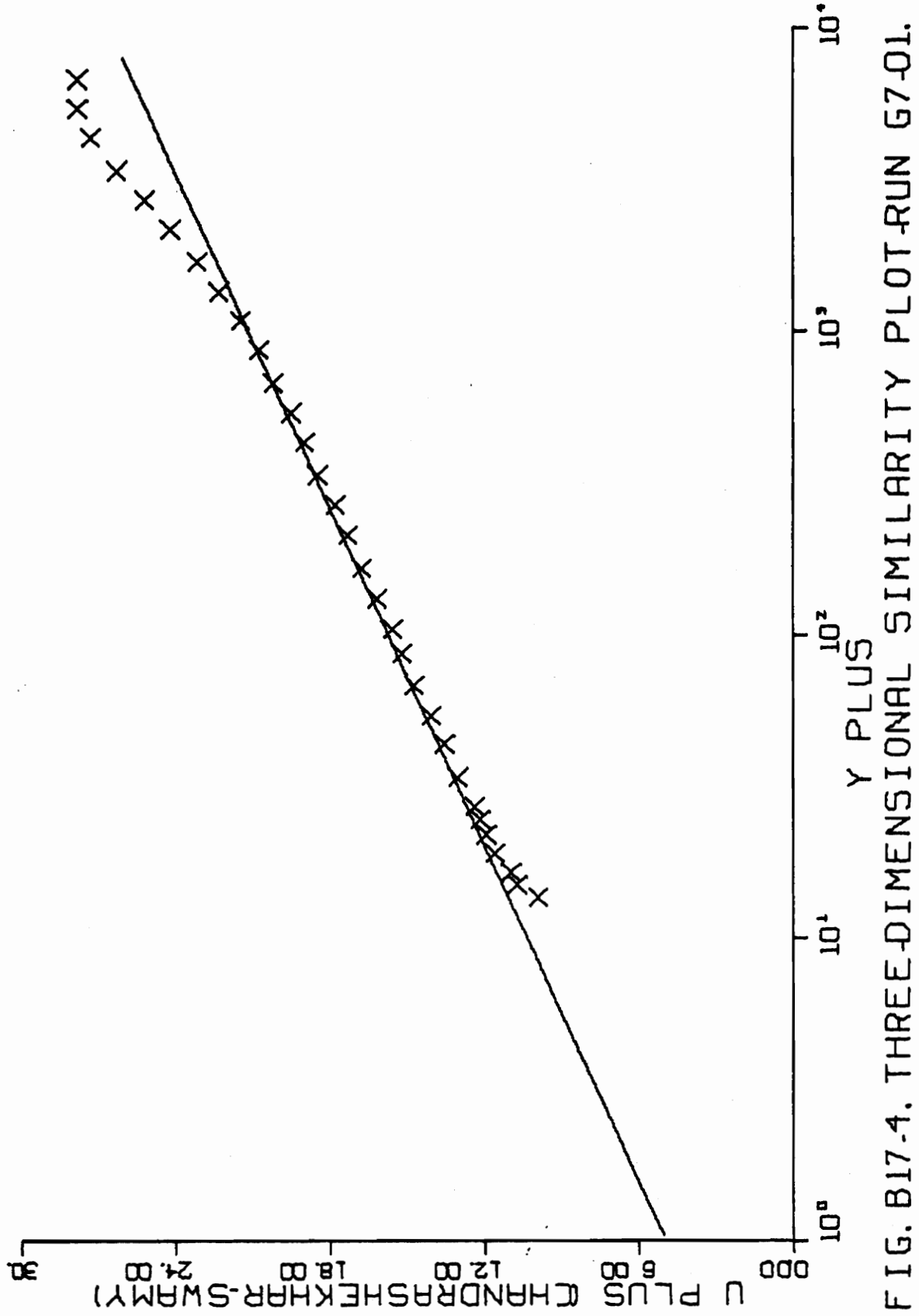

FIG. B17-4. THREE-DIMENSIONAL SIMILARITY PLOT-RUN G7-01.

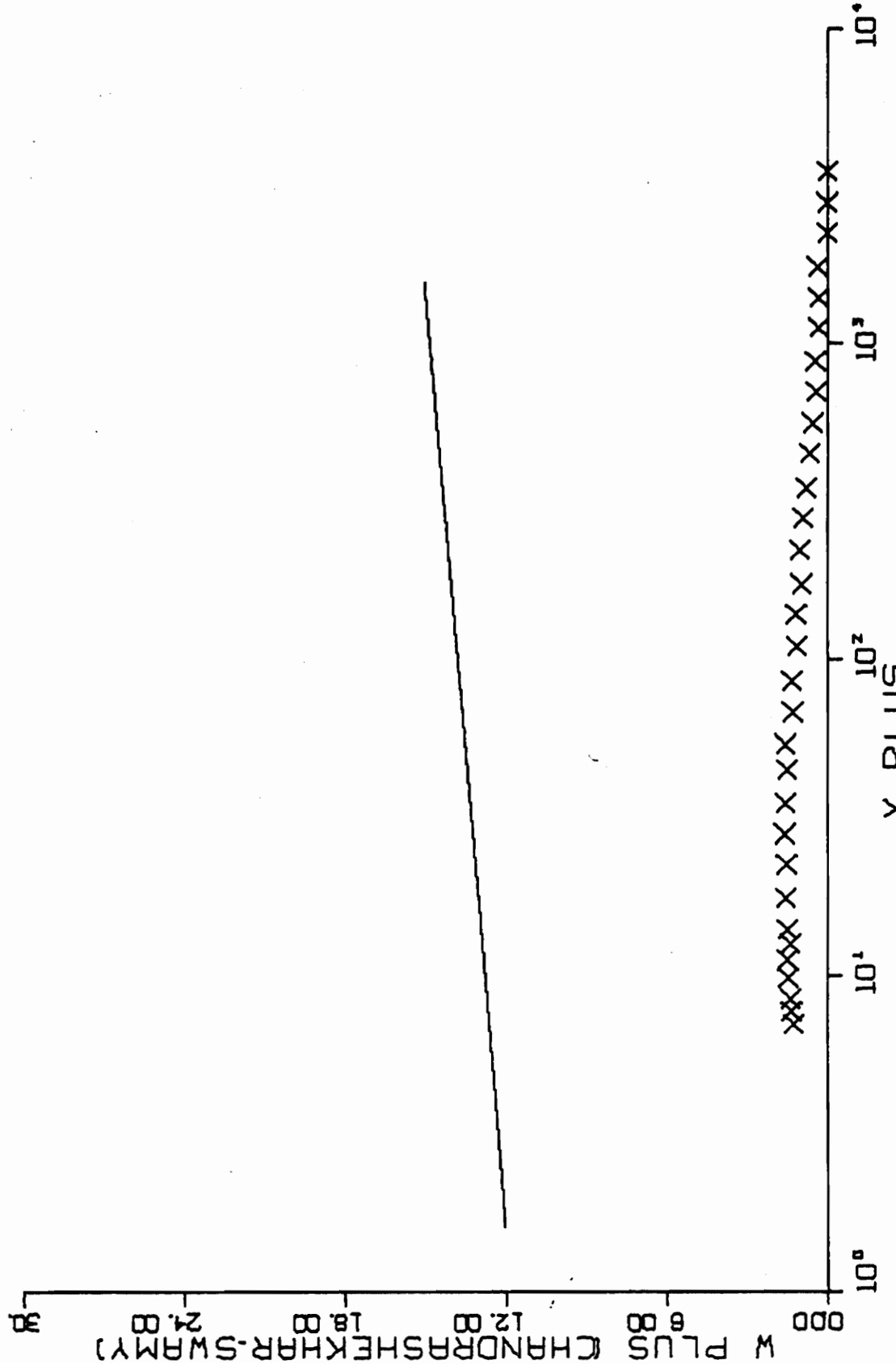

FIG. B17-4. CONTINUED FOR RUN G7-01.

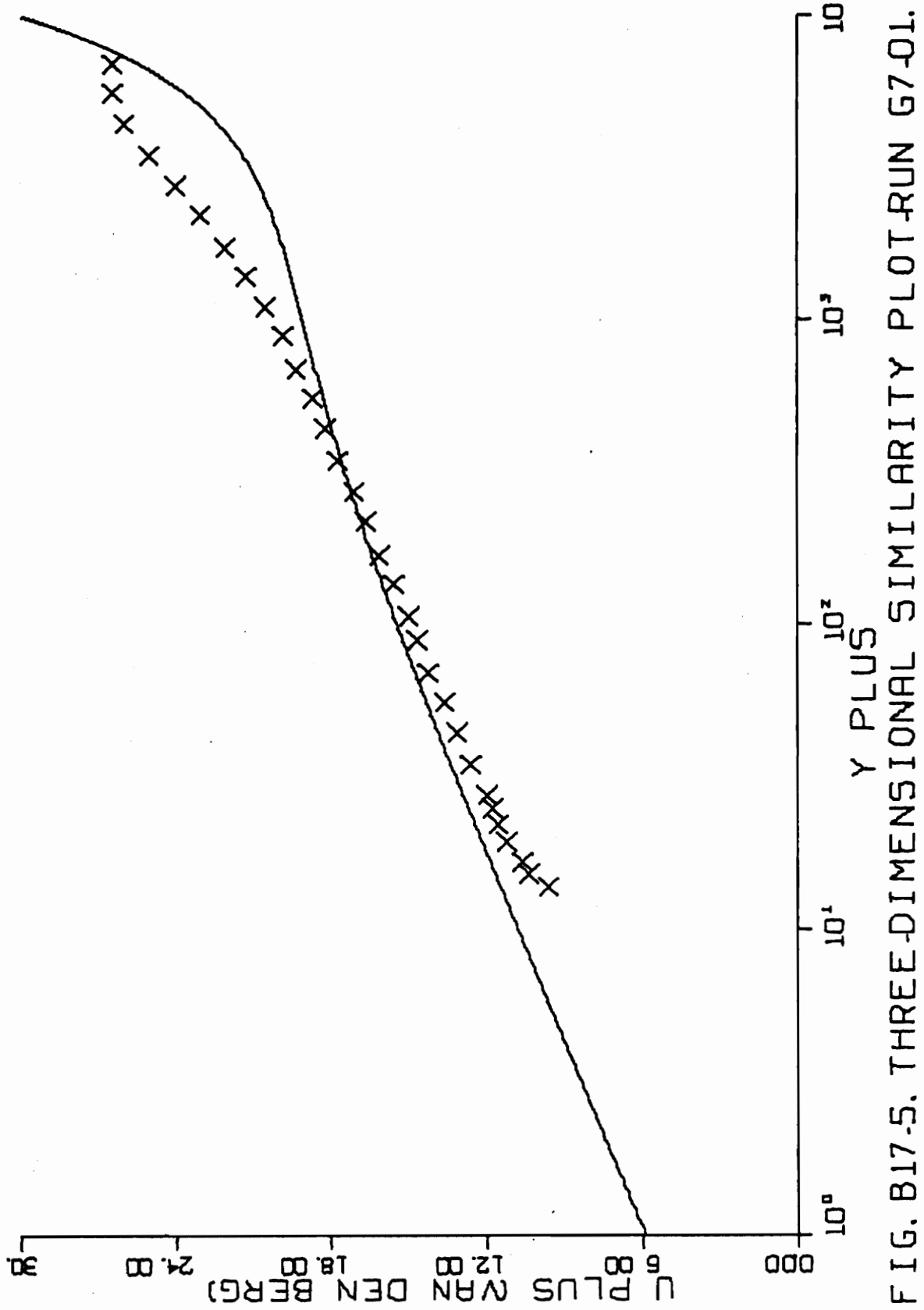

FIG. B17-5. THREE-DIMENSIONAL SIMILARITY PLOT-RUN G7-01.

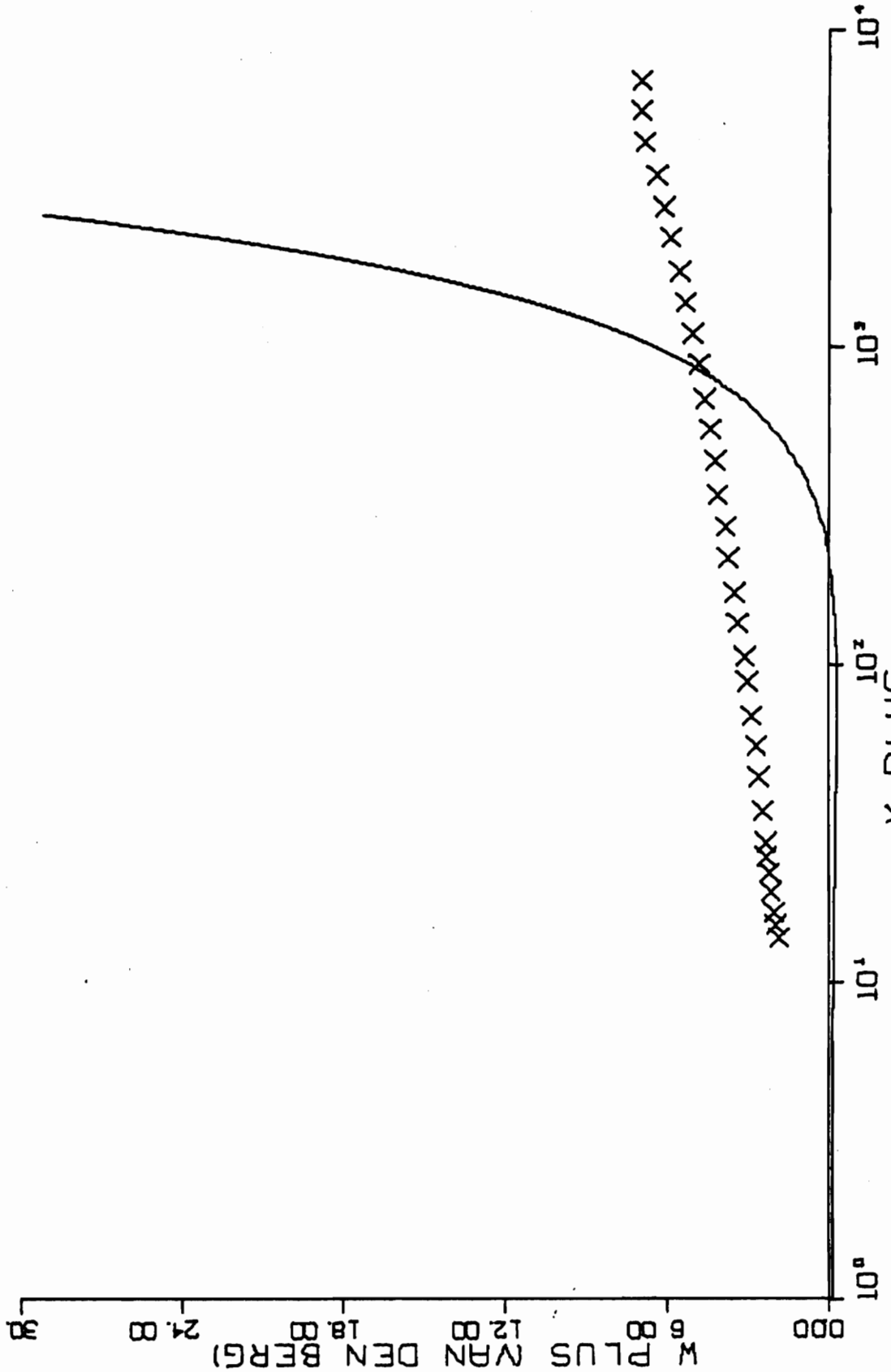

FIG. B17-5. CONTINUED FOR RUN G7-01.

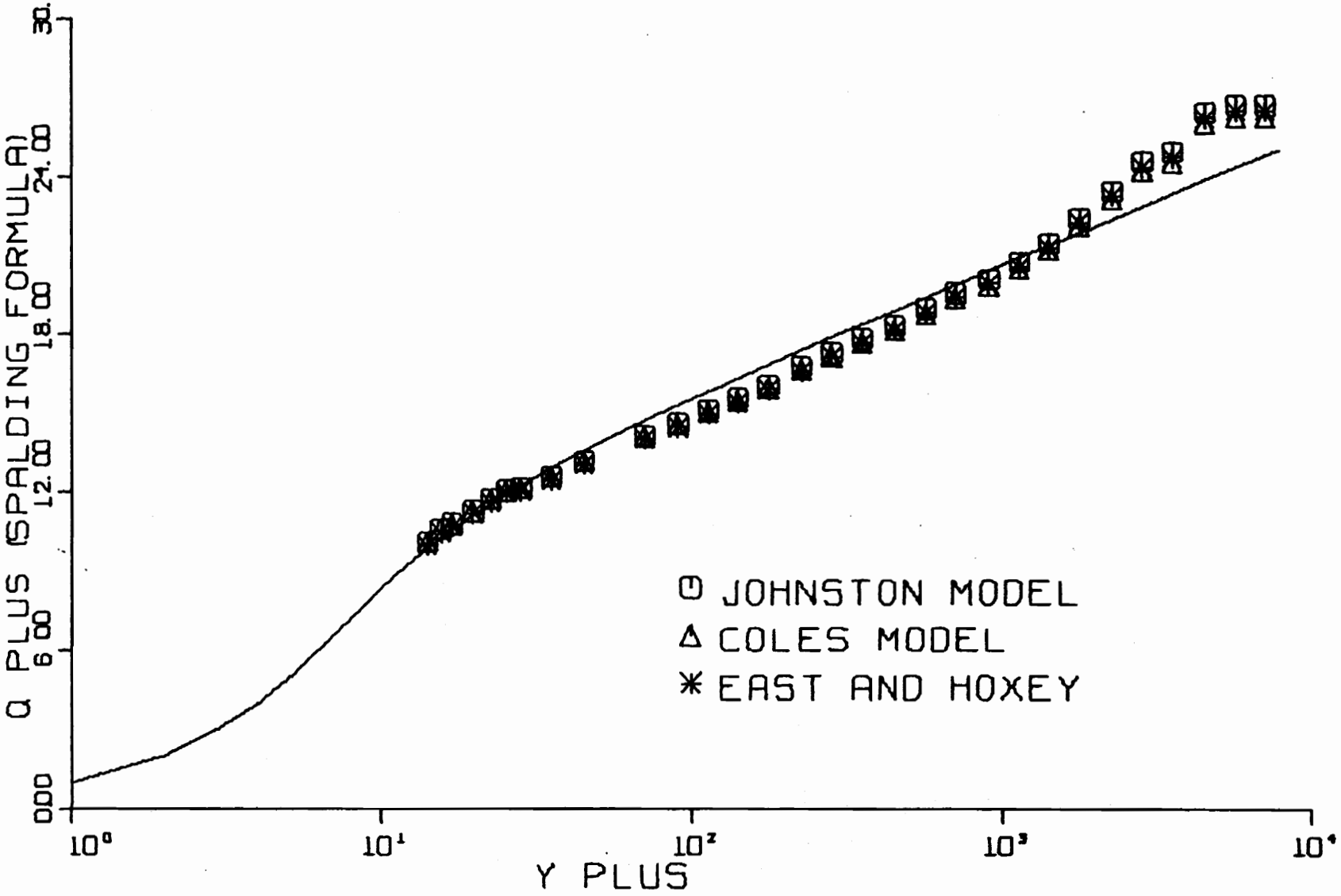

FIG. B18-1. THREE-DIMENSIONAL SIMILARITY PLOT-RUN G5-01.

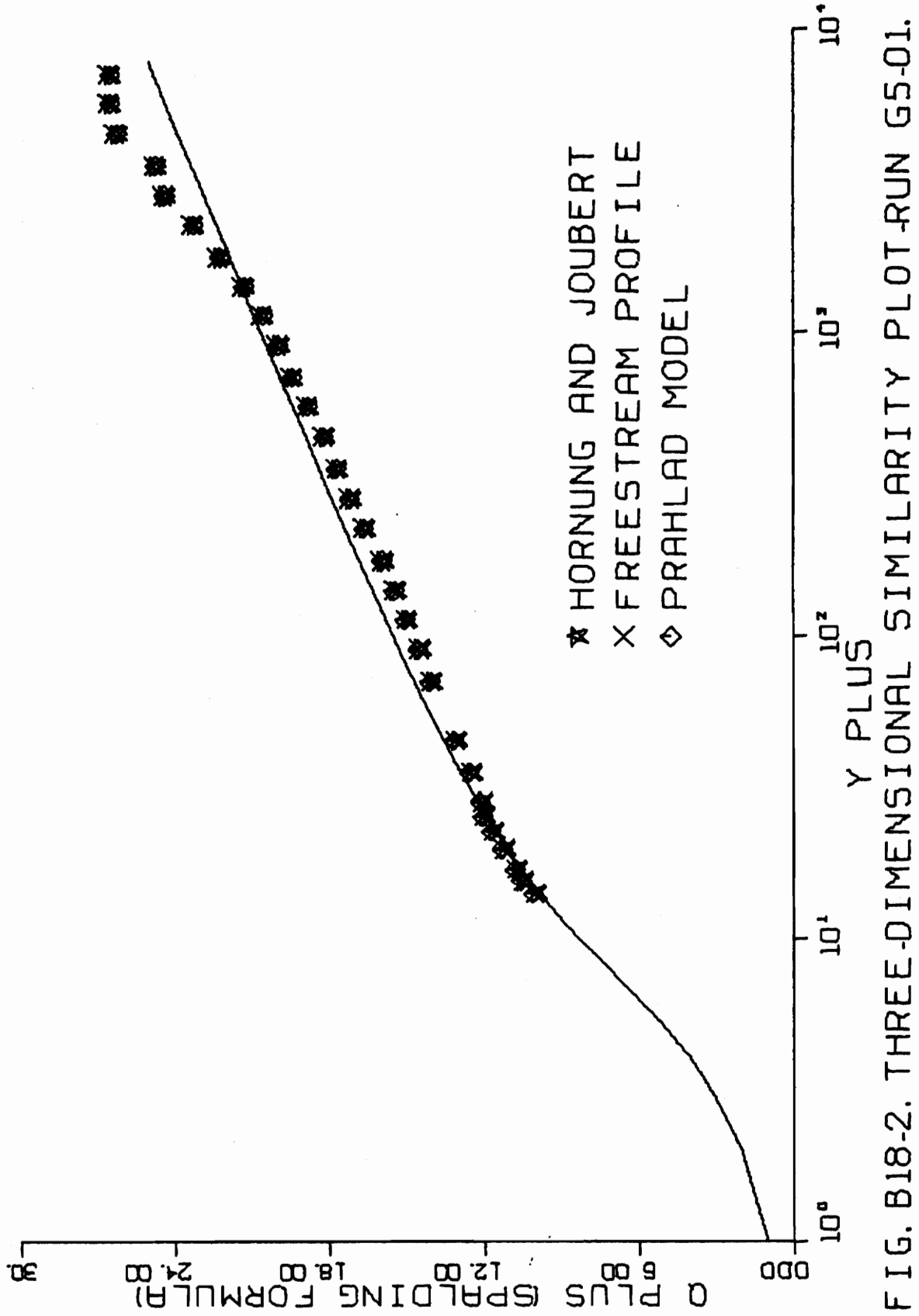

FIG. B18-2. THREE-DIMENSIONAL SIMILARITY PLOT-RUN G5-01.

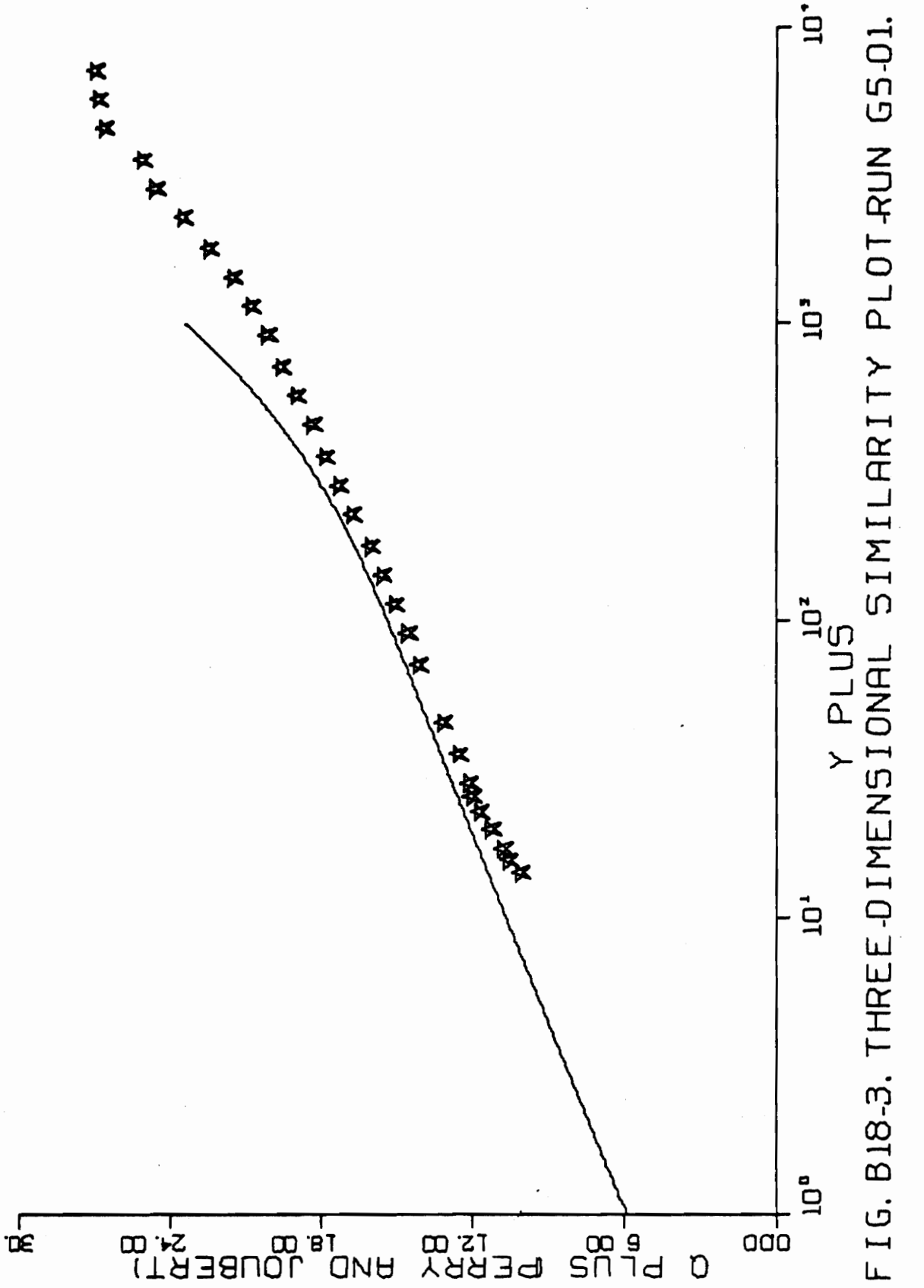

FIG. B18-3. THREE-DIMENSIONAL SIMILARITY PLOT-RUN G5-01.

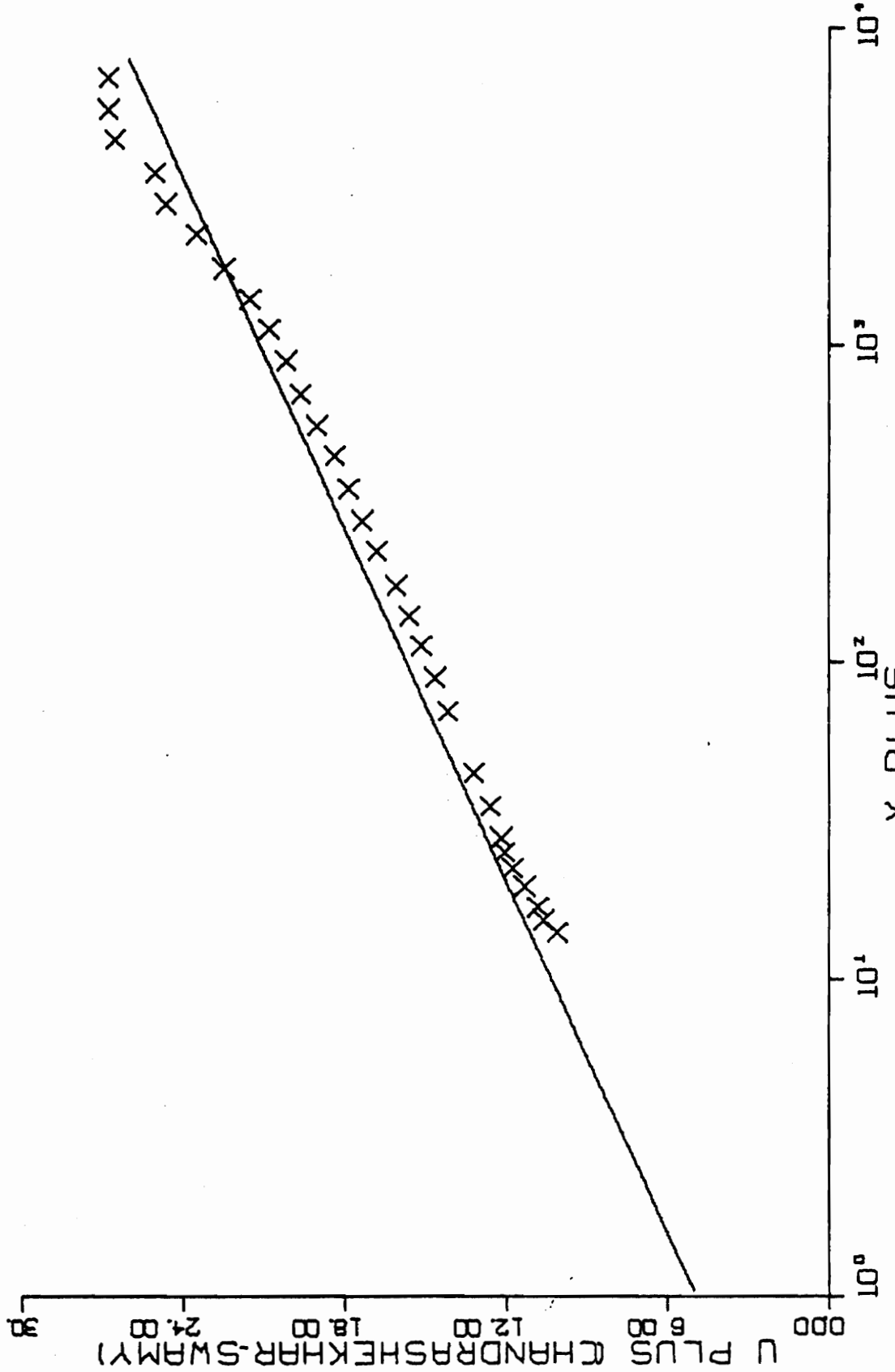

FIG. B18-4. THREE-DIMENSIONAL SIMILARITY PLOT-RUN G5-01.

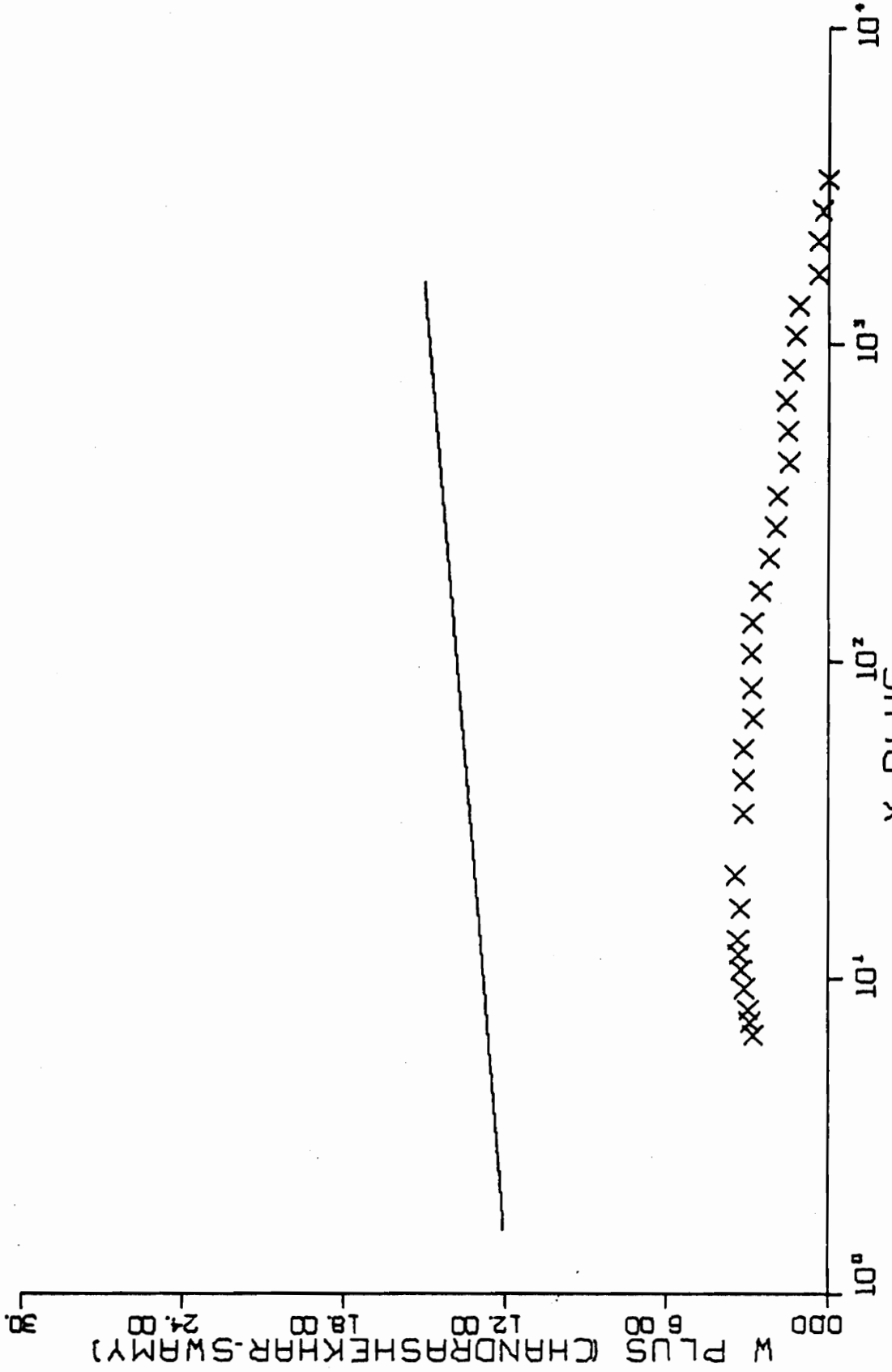

FIG. B18-4. CONTINUED FOR RUN G5-01.

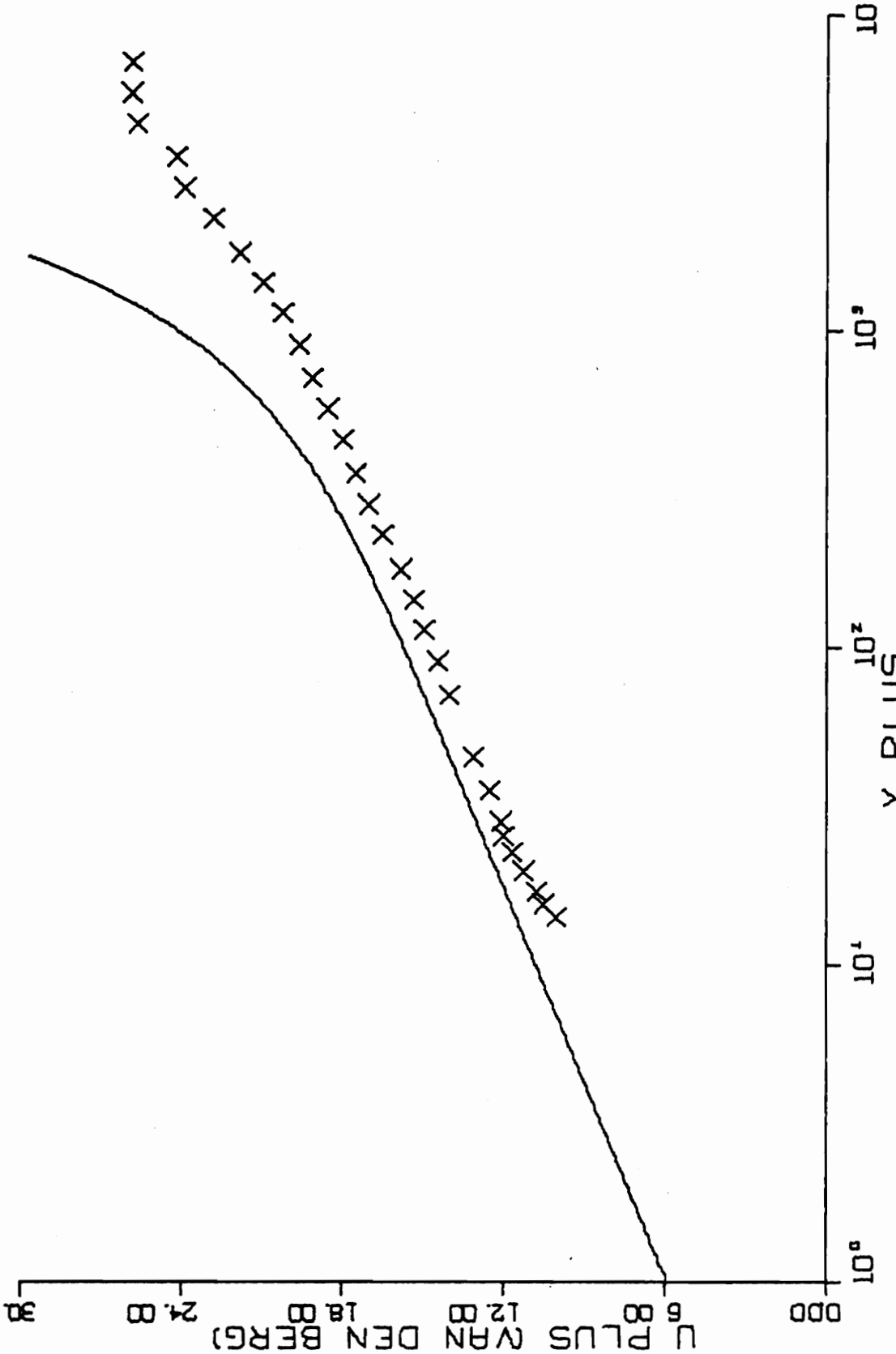

FIG. B18-5. THREE-DIMENSIONAL SIMILARITY PLOT-RUN G5-01.

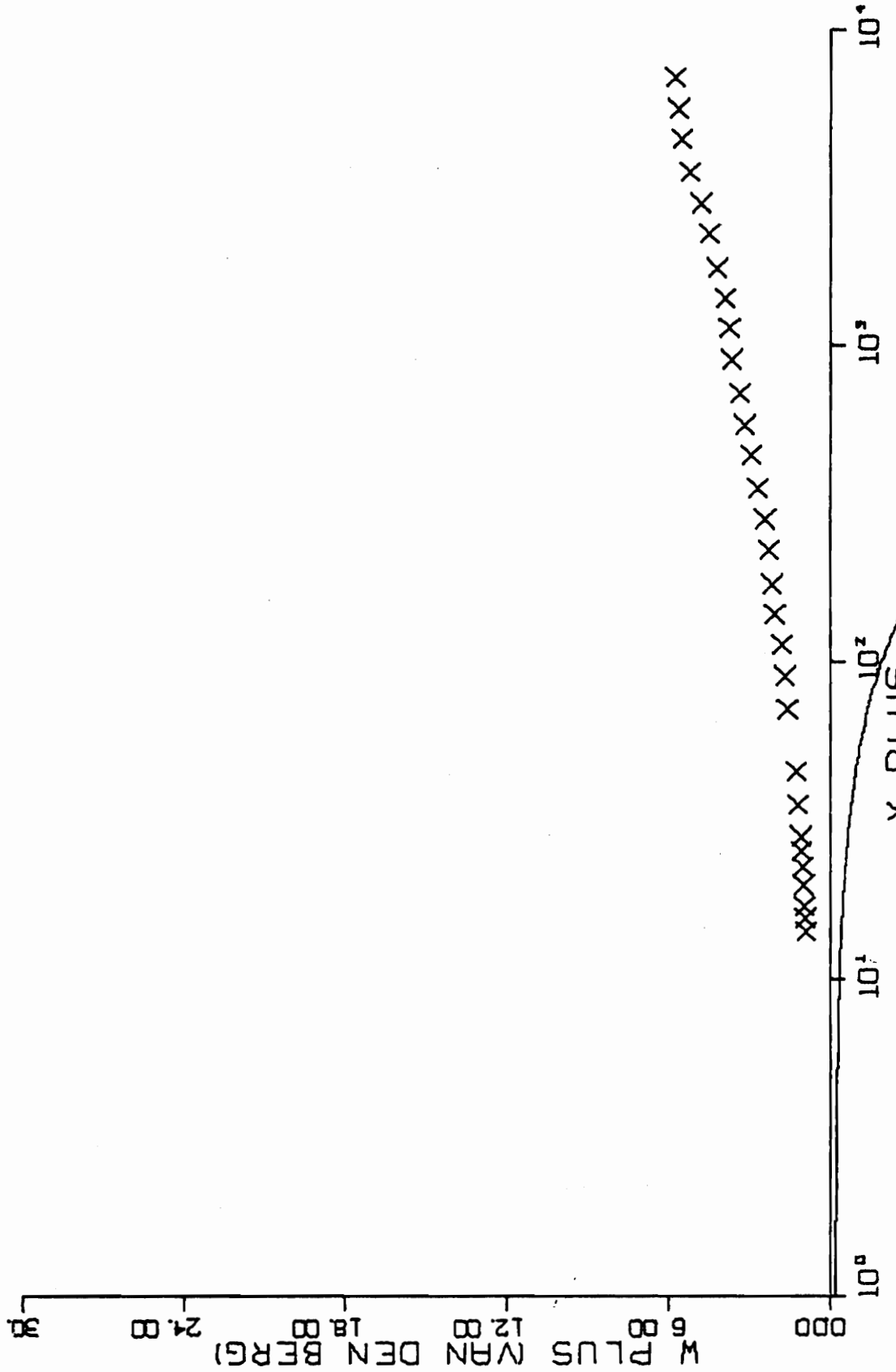

FIG. B18-5. CONTINUED FOR RUN G5-01.

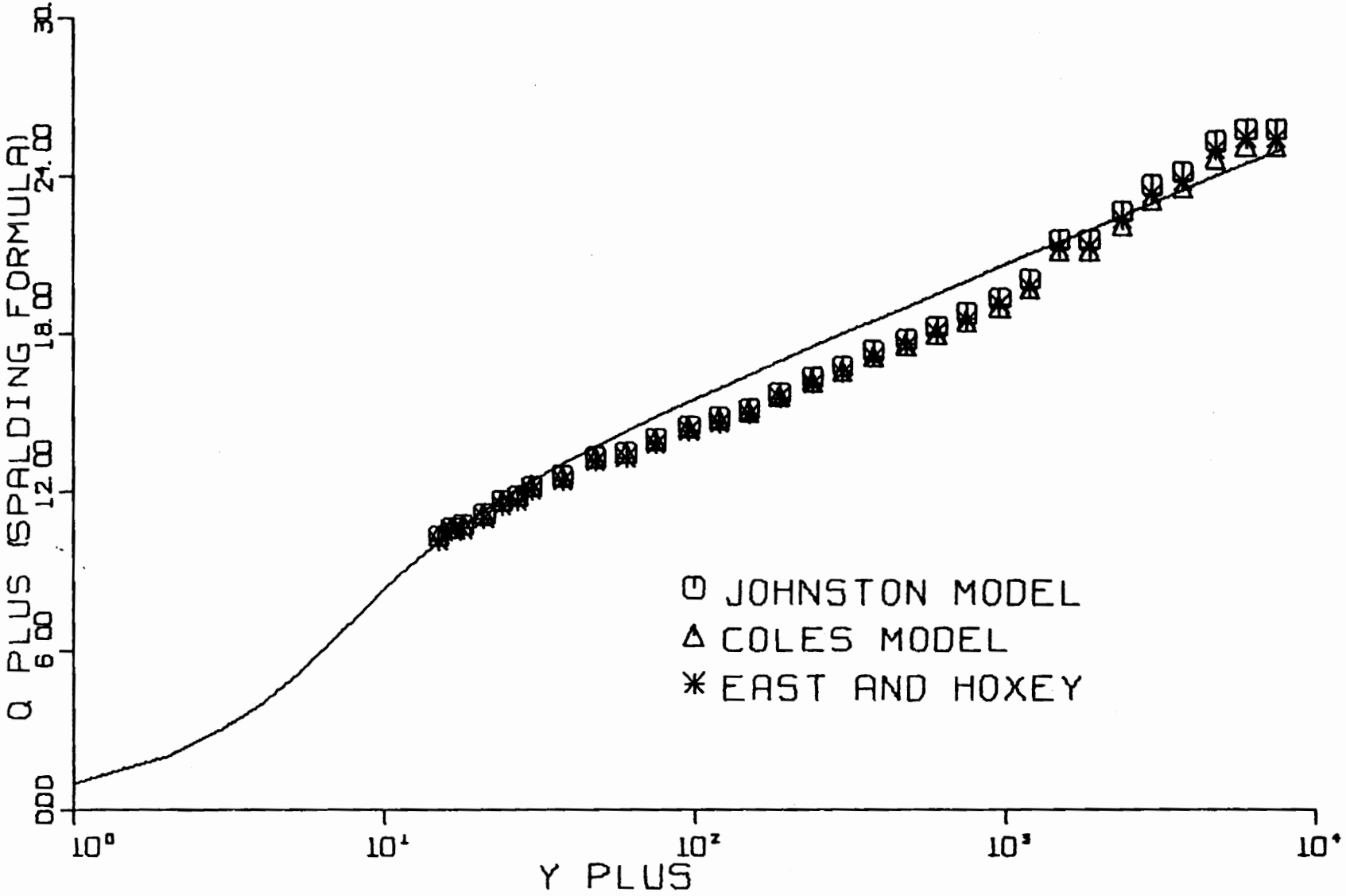

FIG. B19-1. THREE-DIMENSIONAL SIMILARITY PLOT-RUN G3-01.

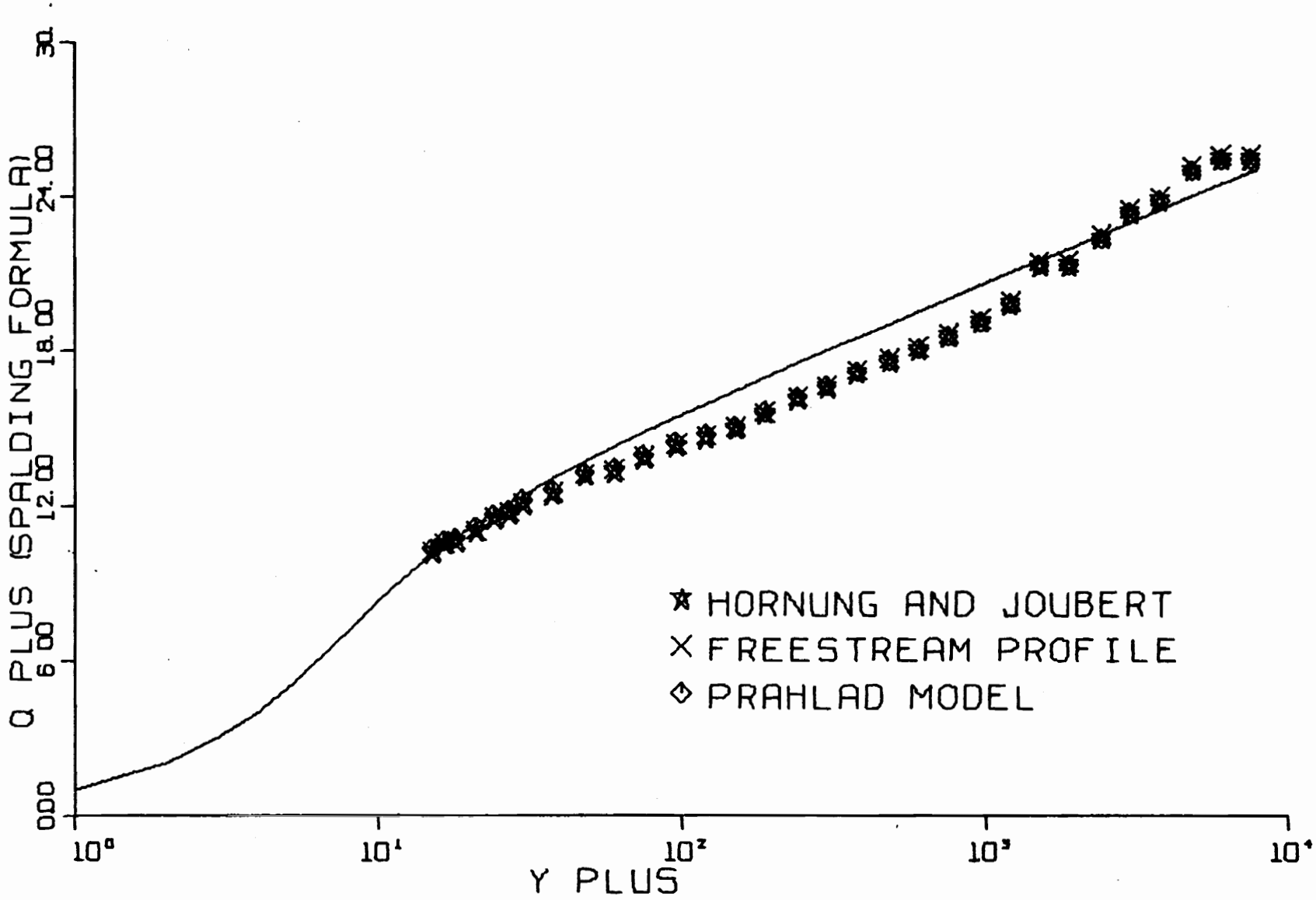

FIG. B19-2. THREE-DIMENSIONAL SIMILARITY PLOT-RUN G3-01.

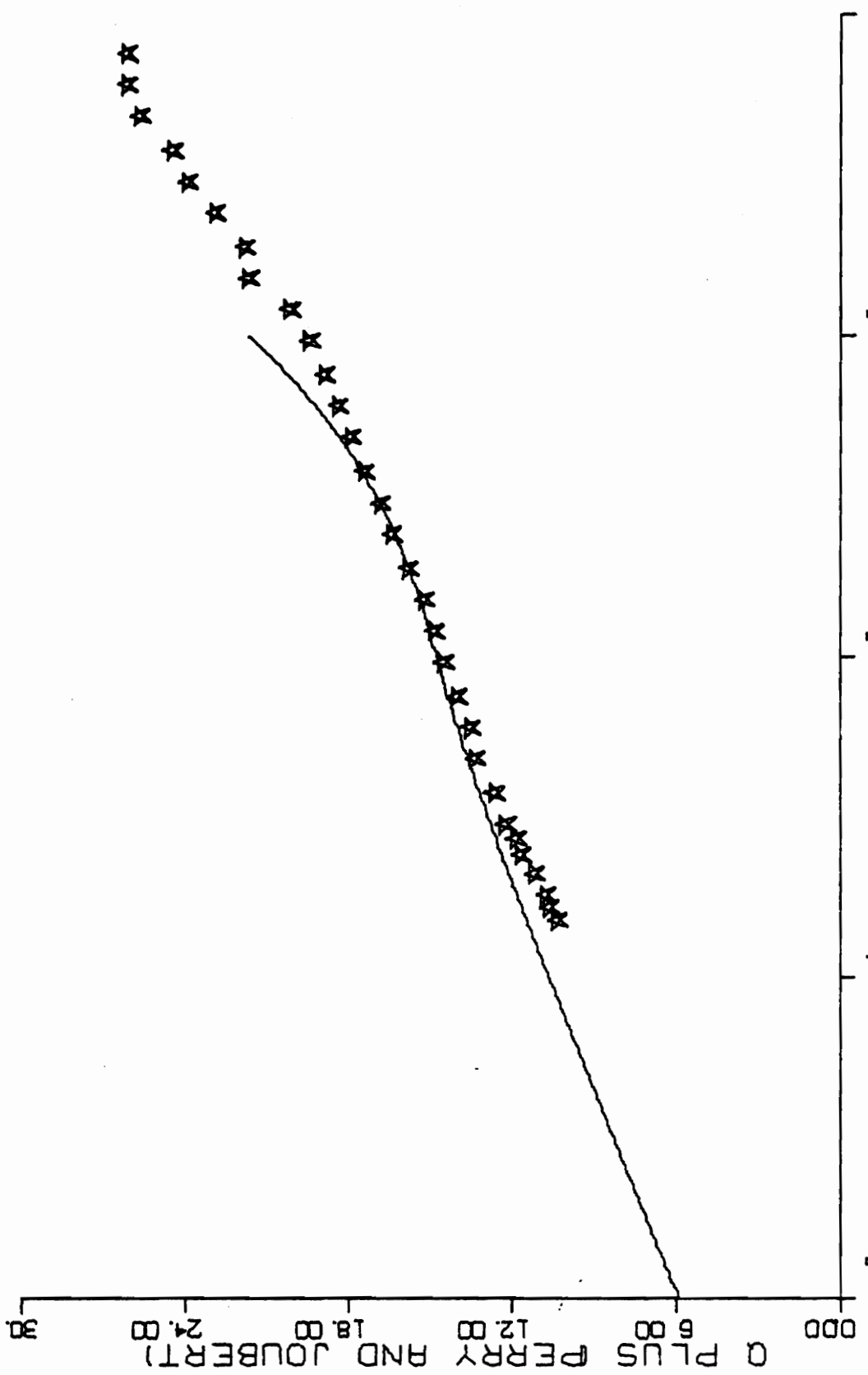

FIG. B19-3. THREE-DIMENSIONAL SIMILARITY PLOT-RUN G3-01.

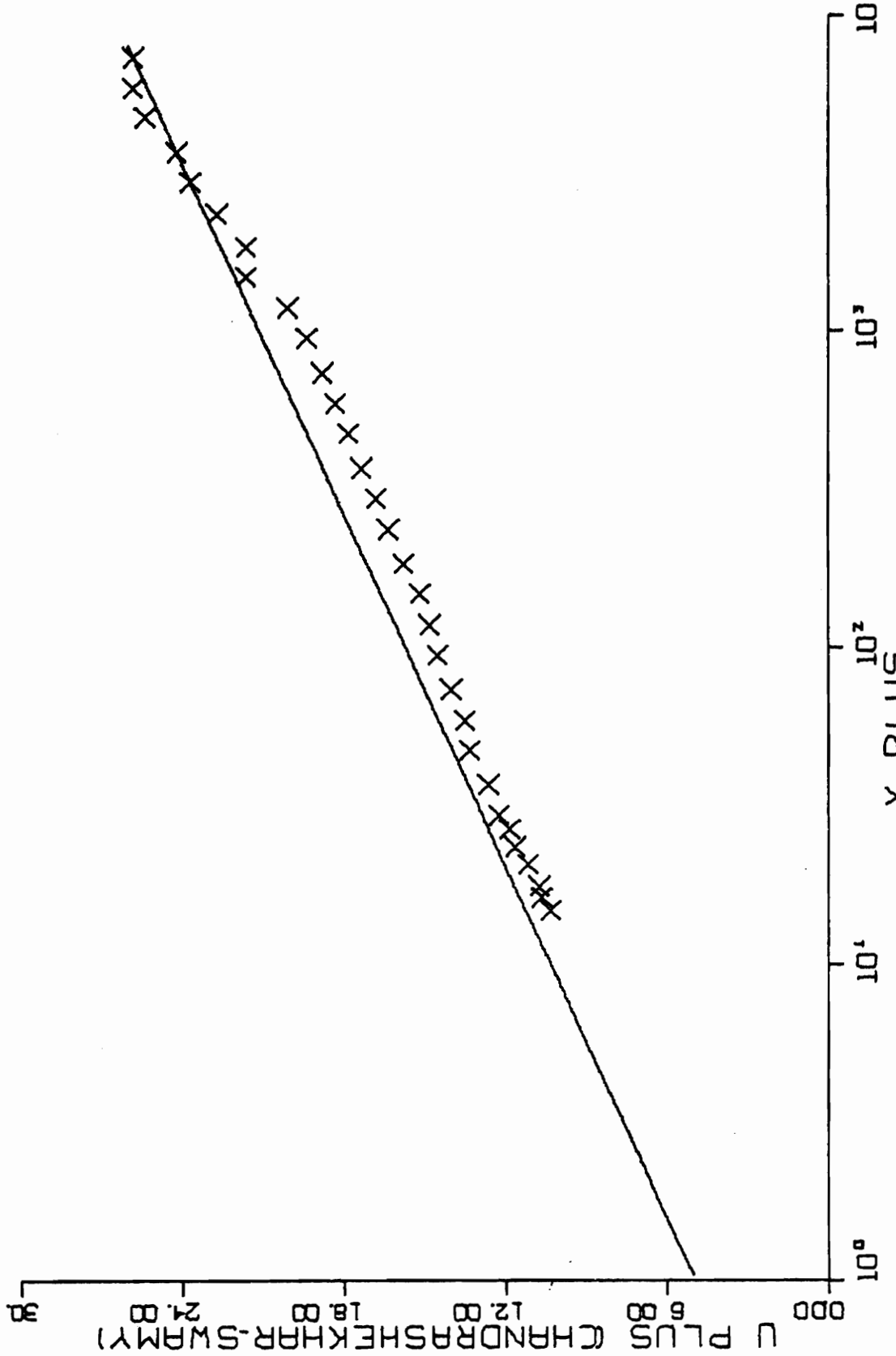

FIG. B19-4. THREE-DIMENSIONAL SIMILARITY PLOT-RUN G3-01.

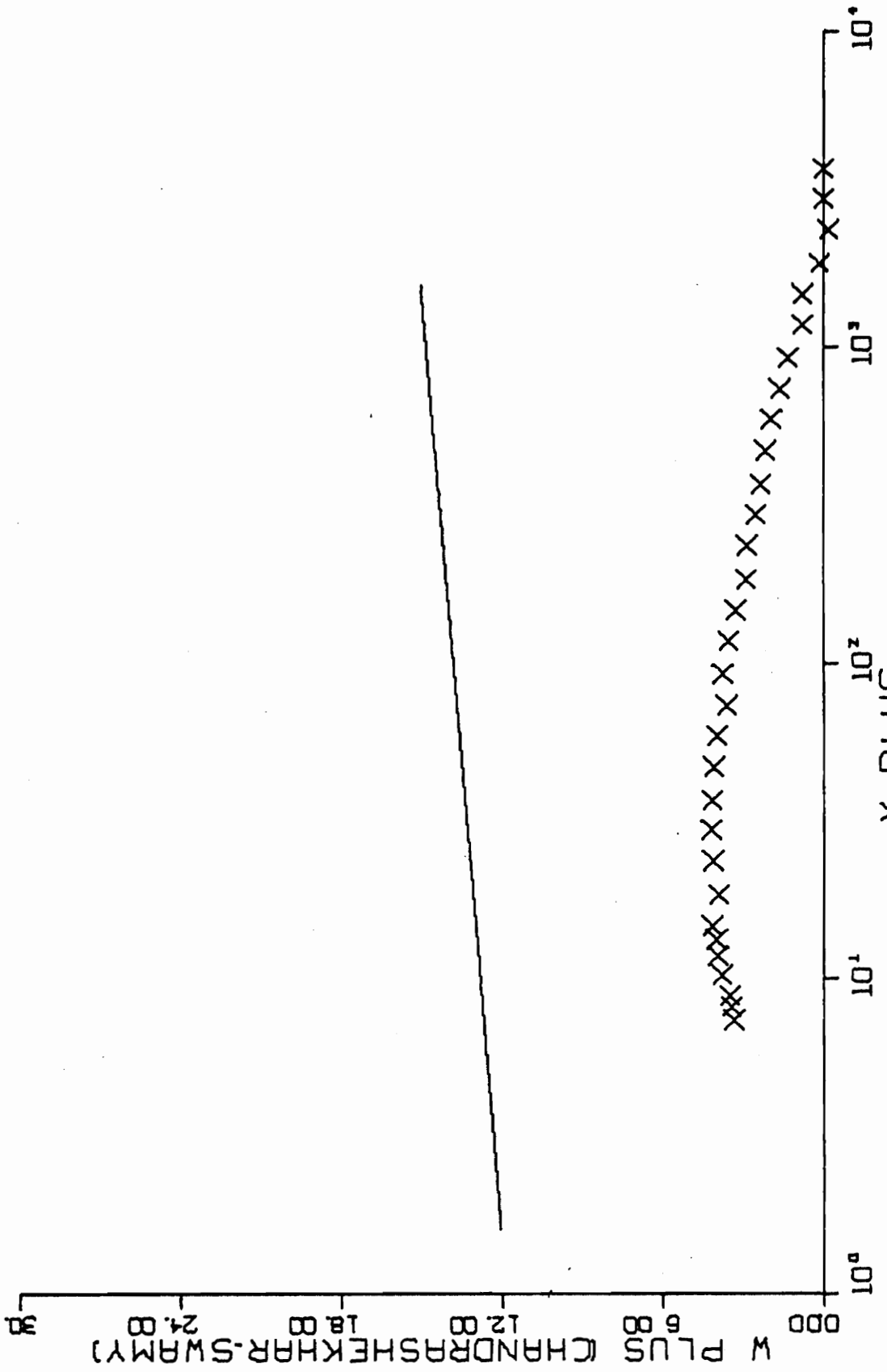

FIG. B19-4. CONTINUED FOR RUN G3-01.

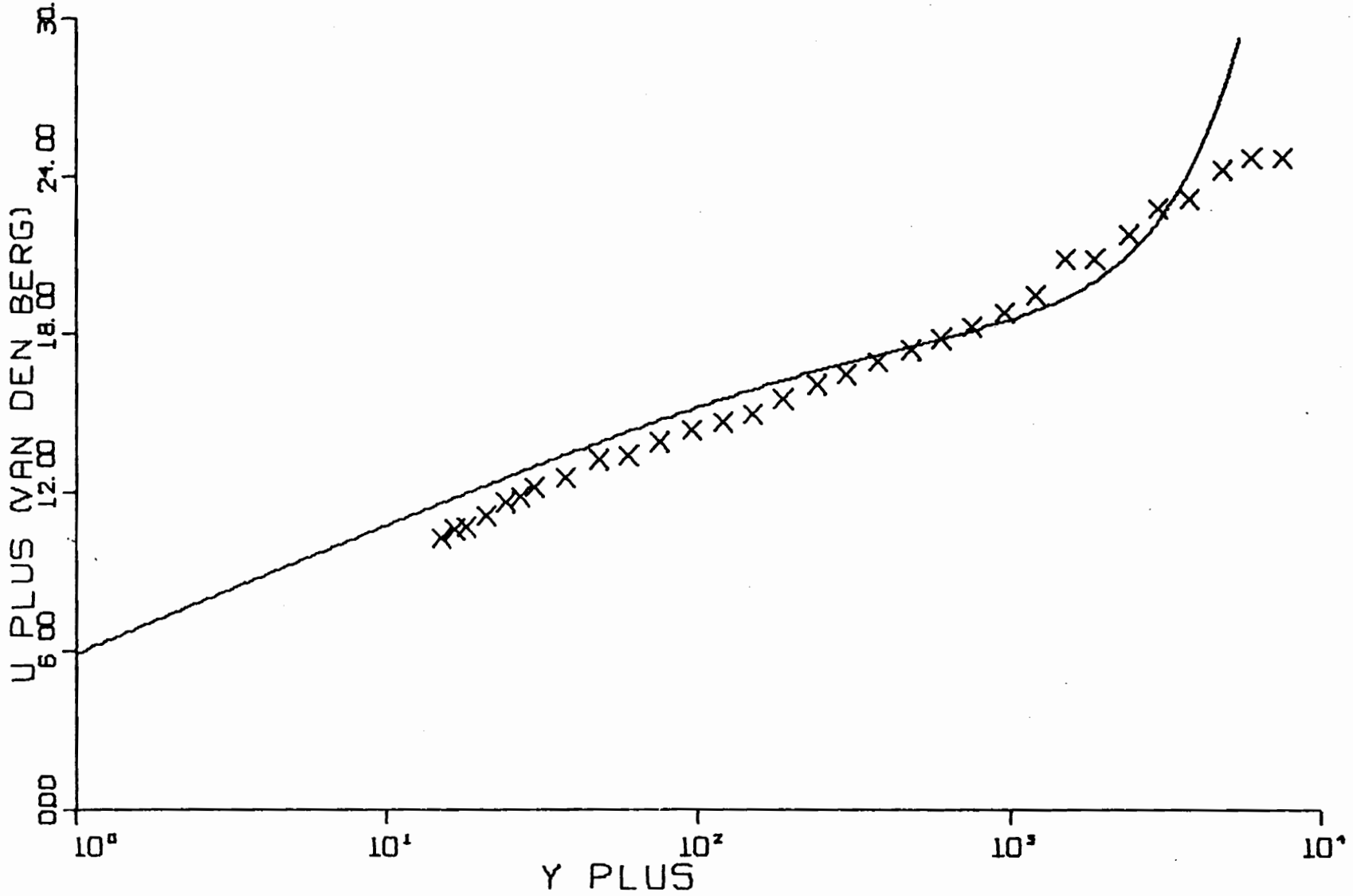

FIG. B19-5. THREE-DIMENSIONAL SIMILARITY PLOT-RUN G3-01.

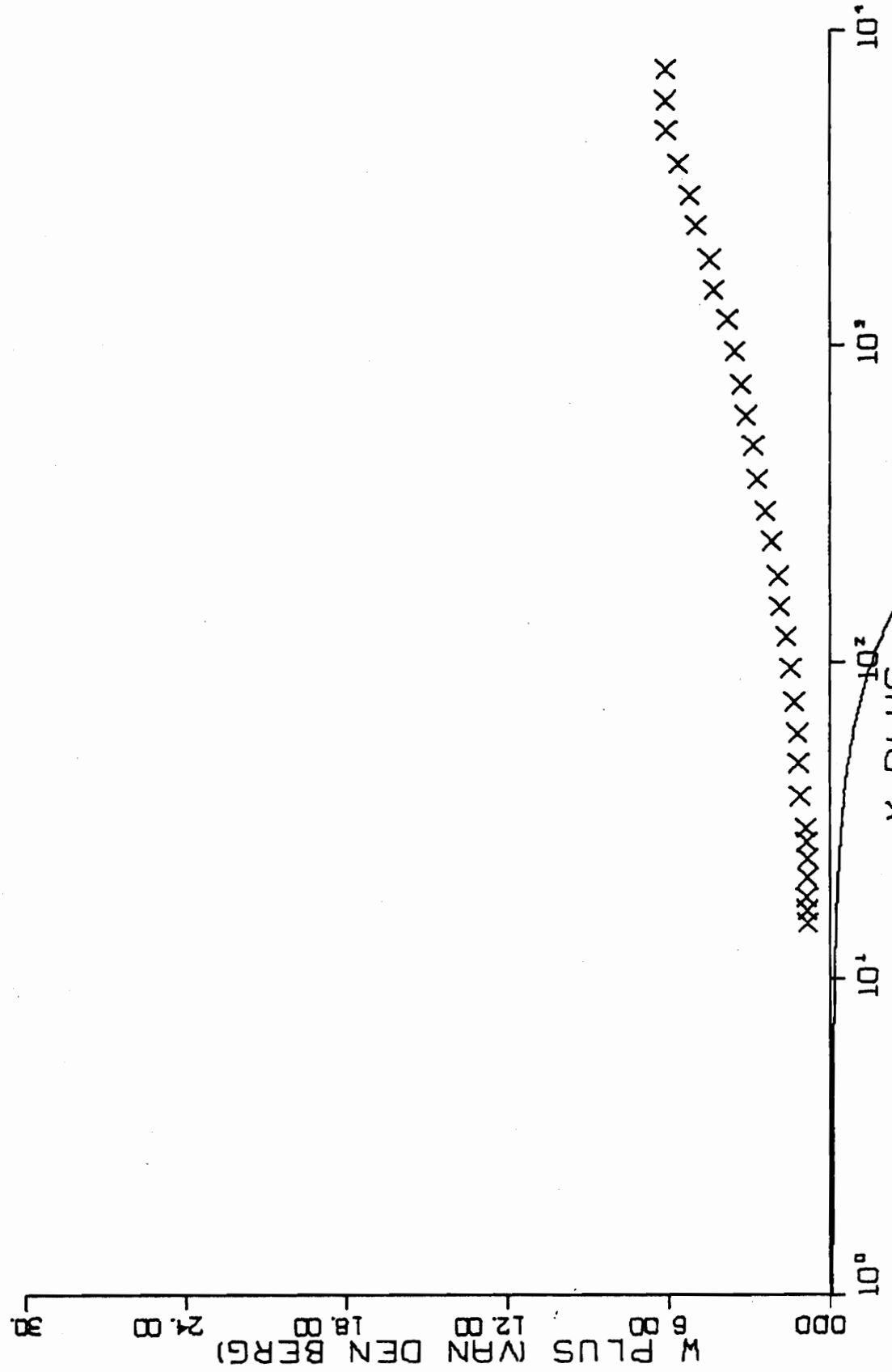

FIG. B19-5. CONTINUED FOR RUN G3-01.

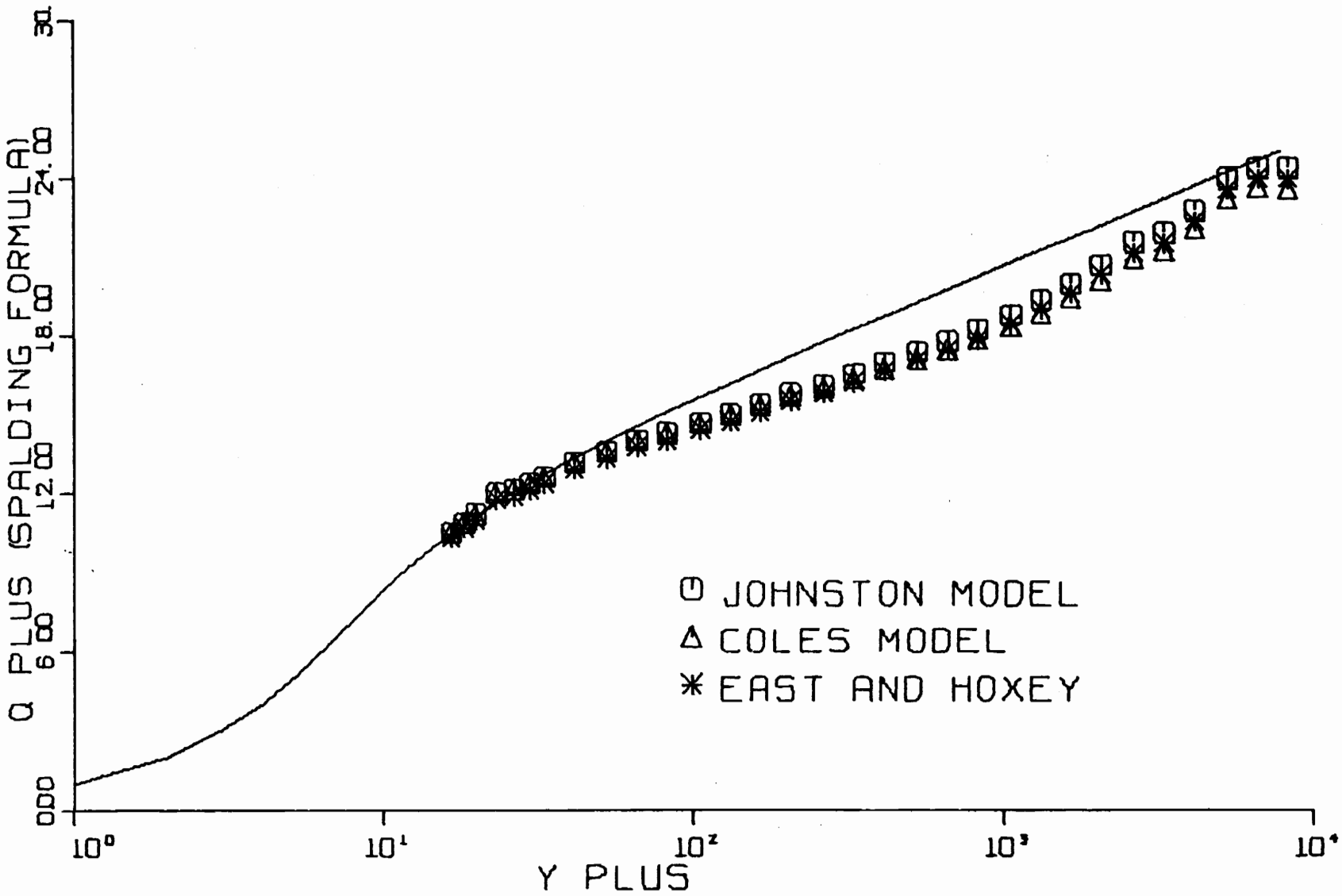

FIG. B20-1. THREE-DIMENSIONAL SIMILARITY PLOT-RUN G1-01.

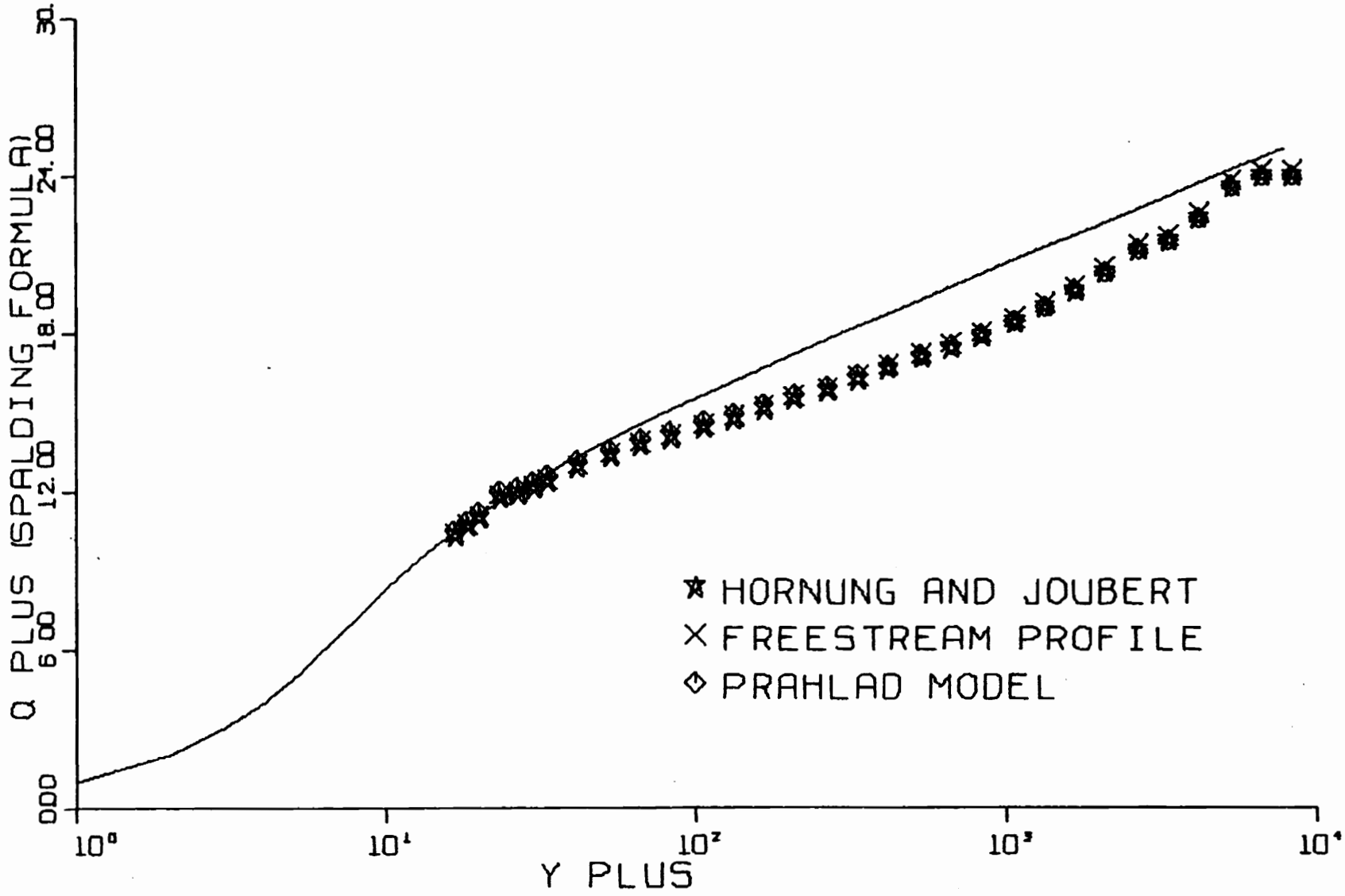

FIG. B20-2. THREE-DIMENSIONAL SIMILARITY PLOT-RUN G1-01.

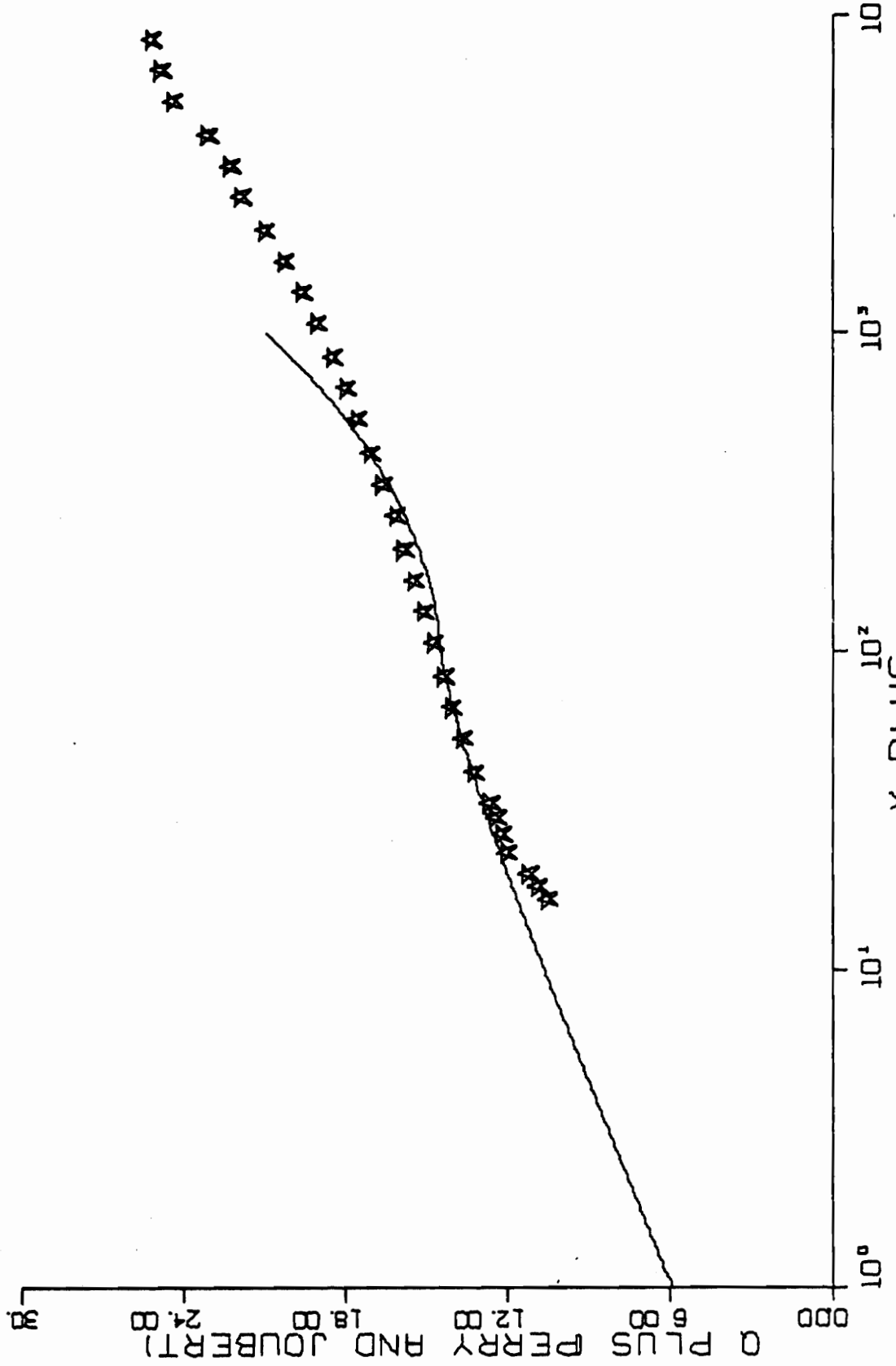

FIG. B20-3. THREE-DIMENSIONAL SIMILARITY PLOT-RUN G1-01.

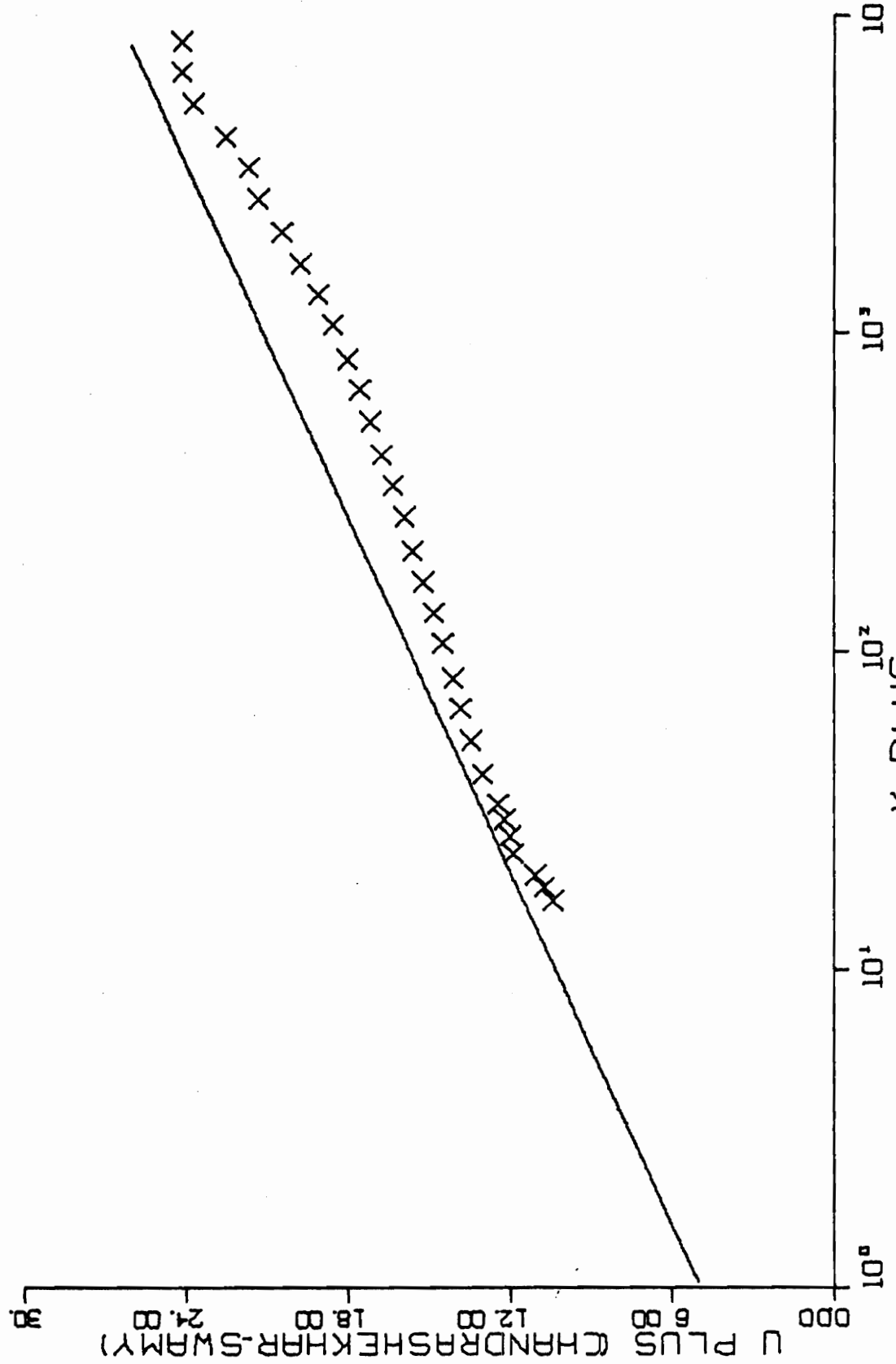

FIG. B20-4. THREE-DIMENSIONAL SIMILARITY PLOT-RUN G1-01.

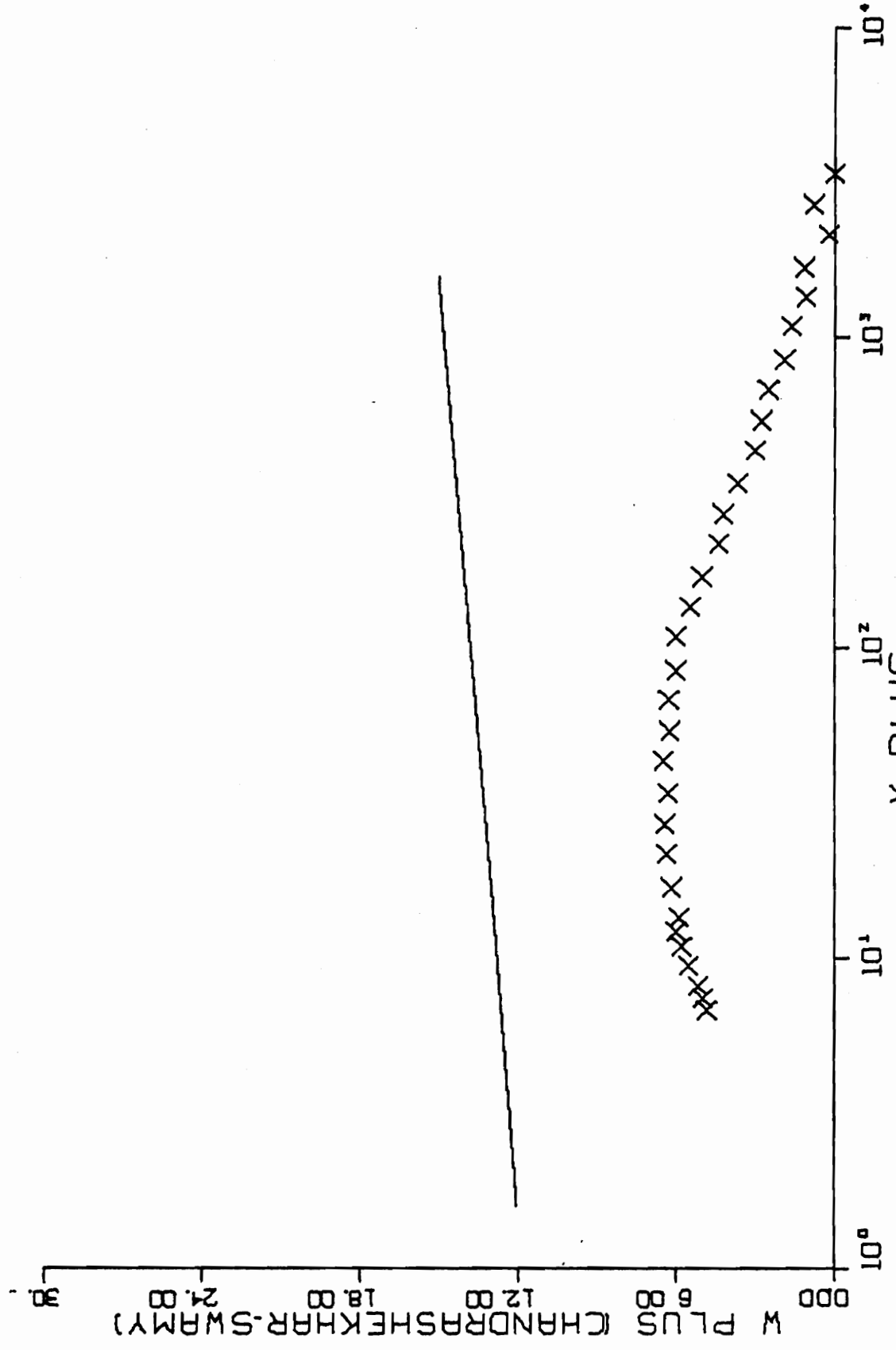

FIG. B20-4. CONTINUED FOR RUN G1-01.

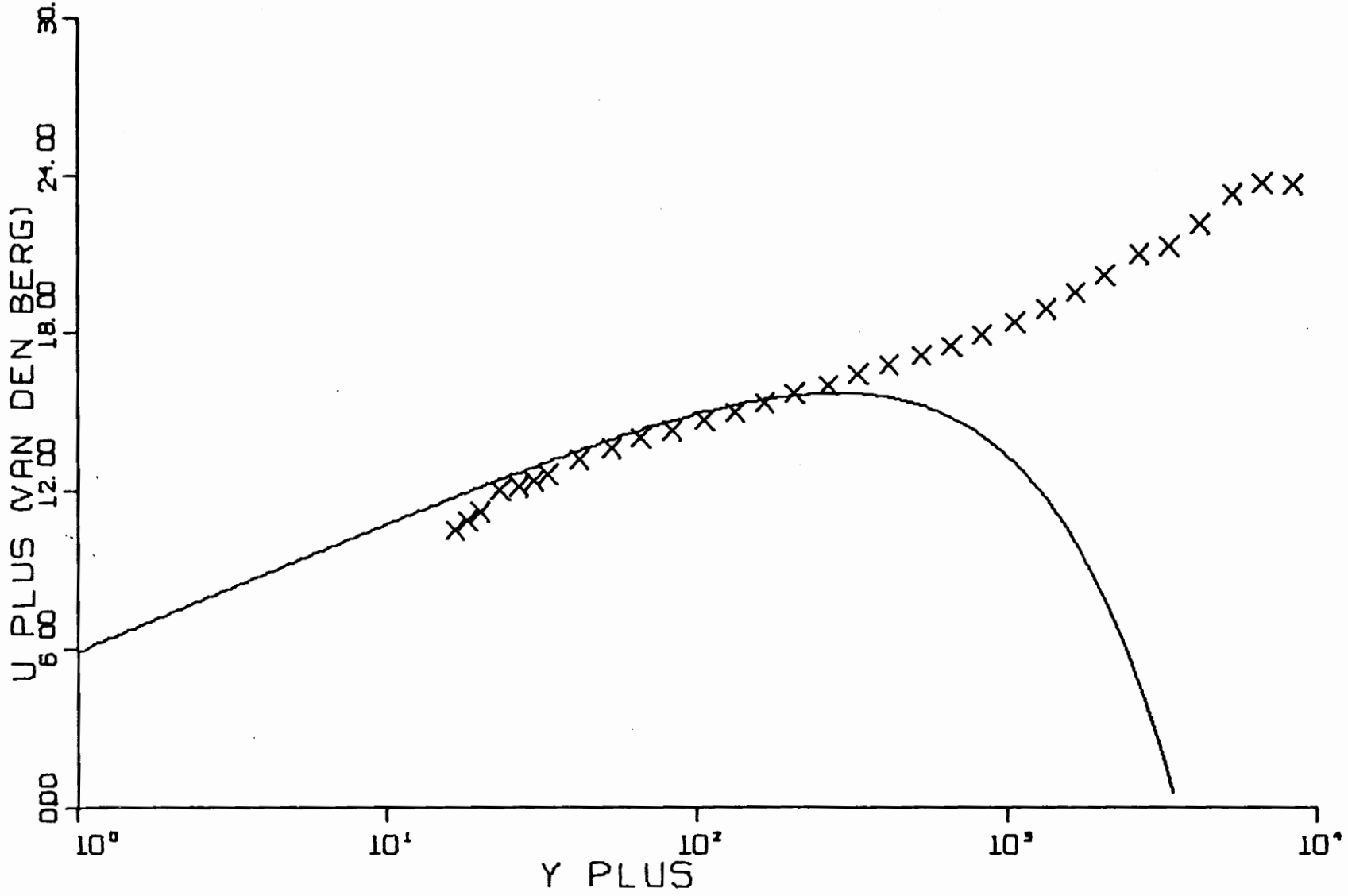

FIG. B20-5. THREE-DIMENSIONAL SIMILARITY PLOT-RUN G1-01.

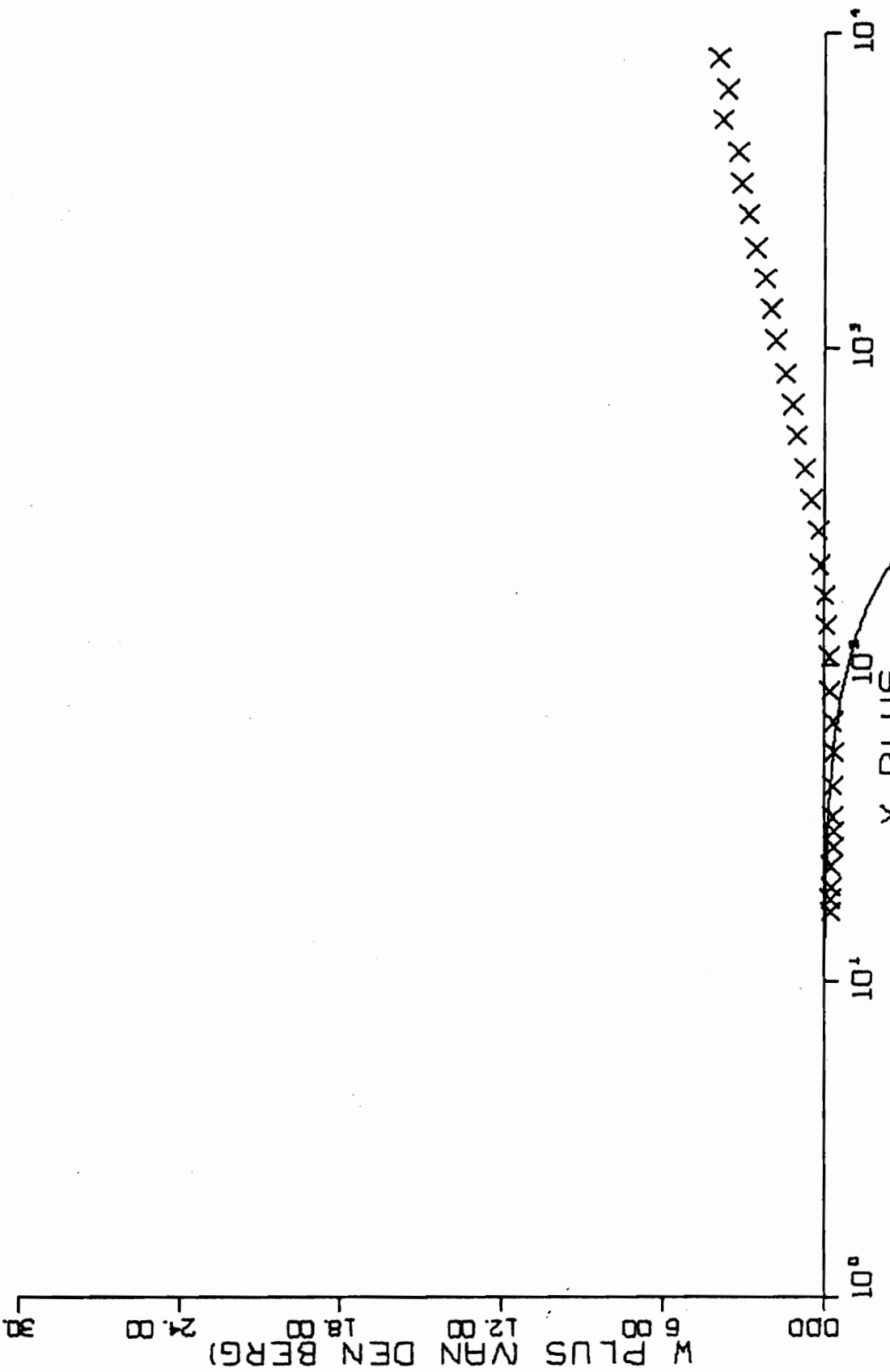

FIG. B20-5. CONTINUED FOR RUN G1-01.

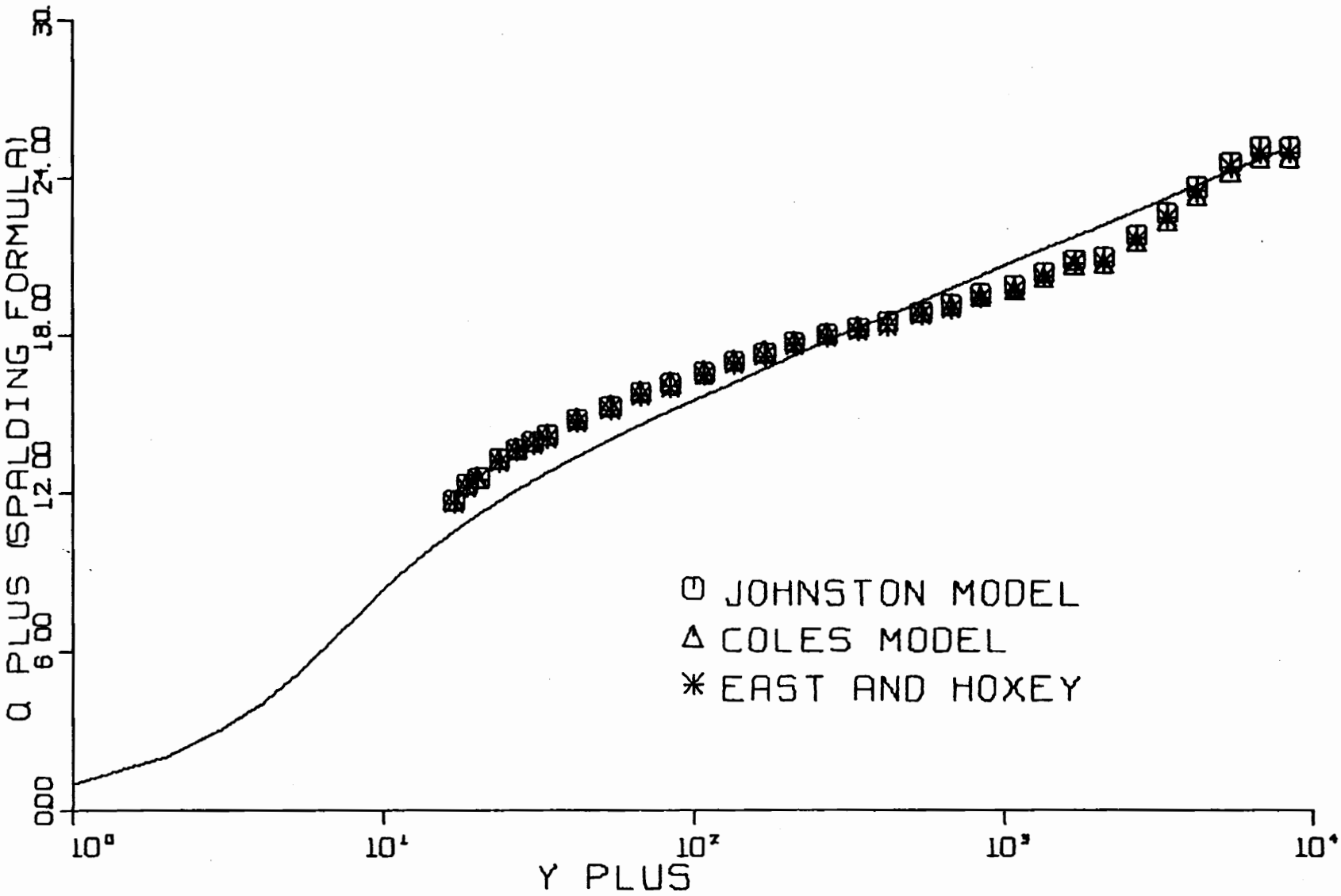

FIG. B21-1. THREE-DIMENSIONAL SIMILARITY PLOT-RUN G-1-01.

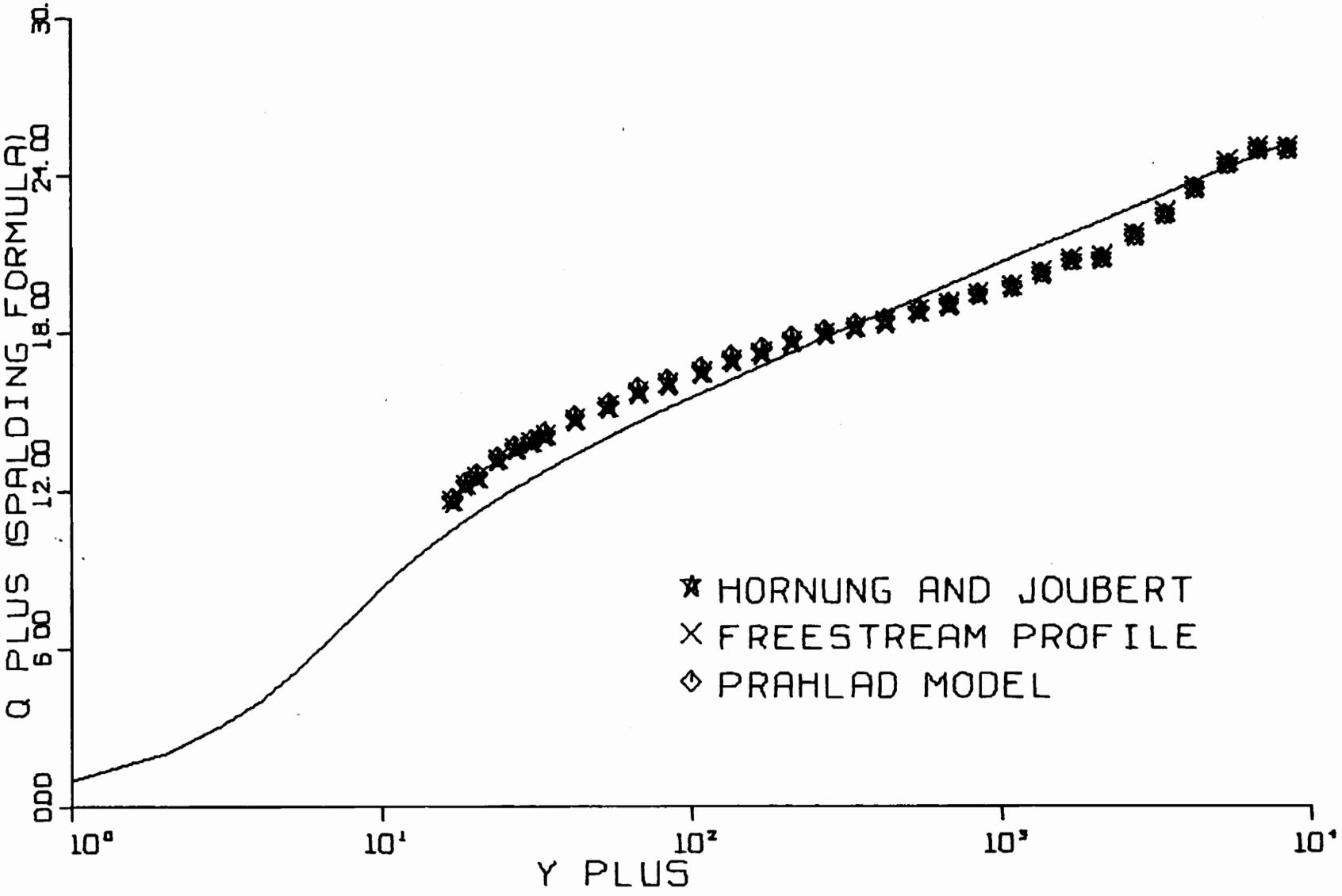

FIG. B21-2. THREE-DIMENSIONAL SIMILARITY PLOT-RUN G-1-01.

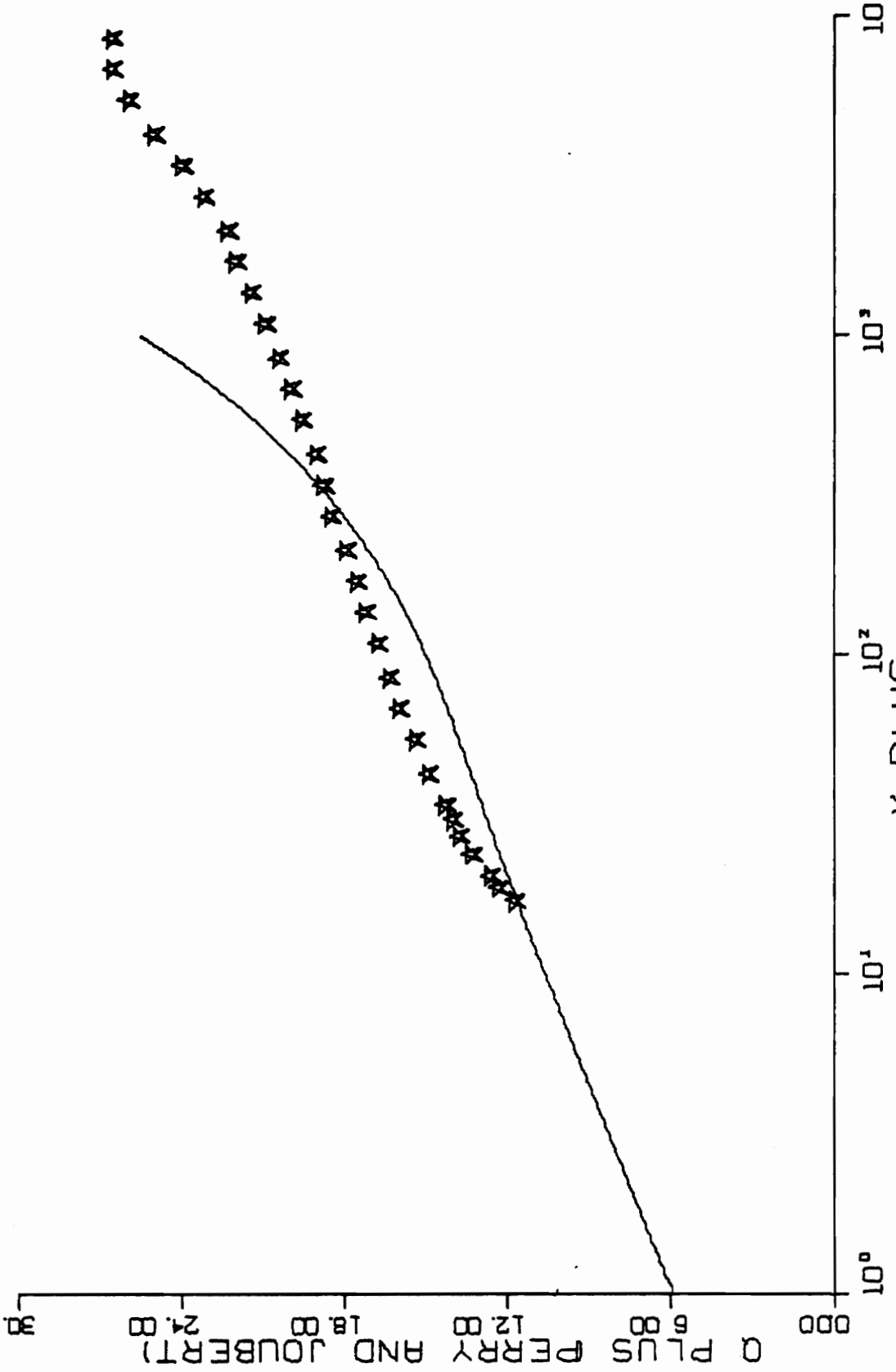

FIG. B21-3. THREE-DIMENSIONAL SIMILARITY PLOT-RUN G-1-01.

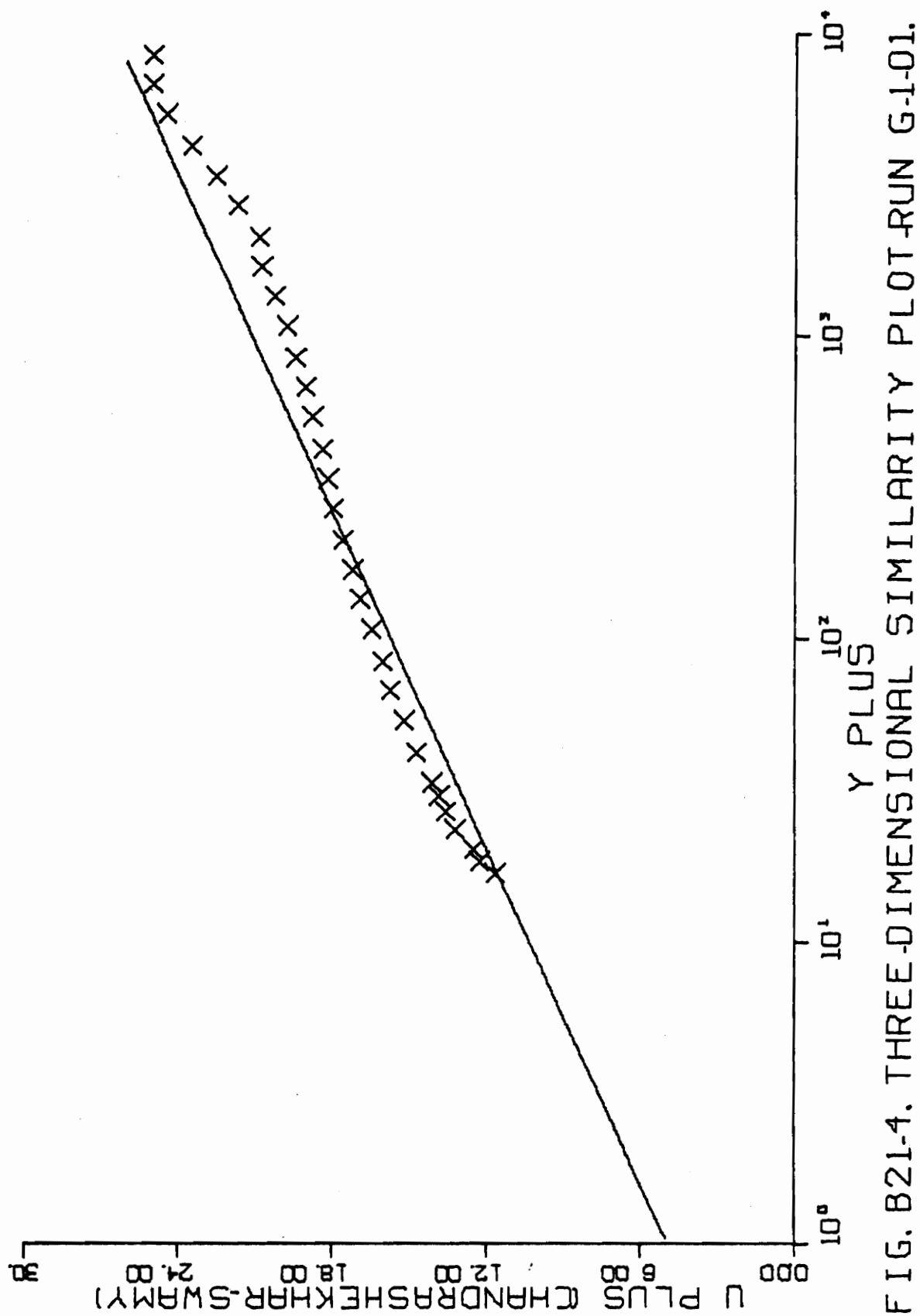

FIG. B21-4. THREE-DIMENSIONAL SIMILARITY PLOT-RUN G-1-01.

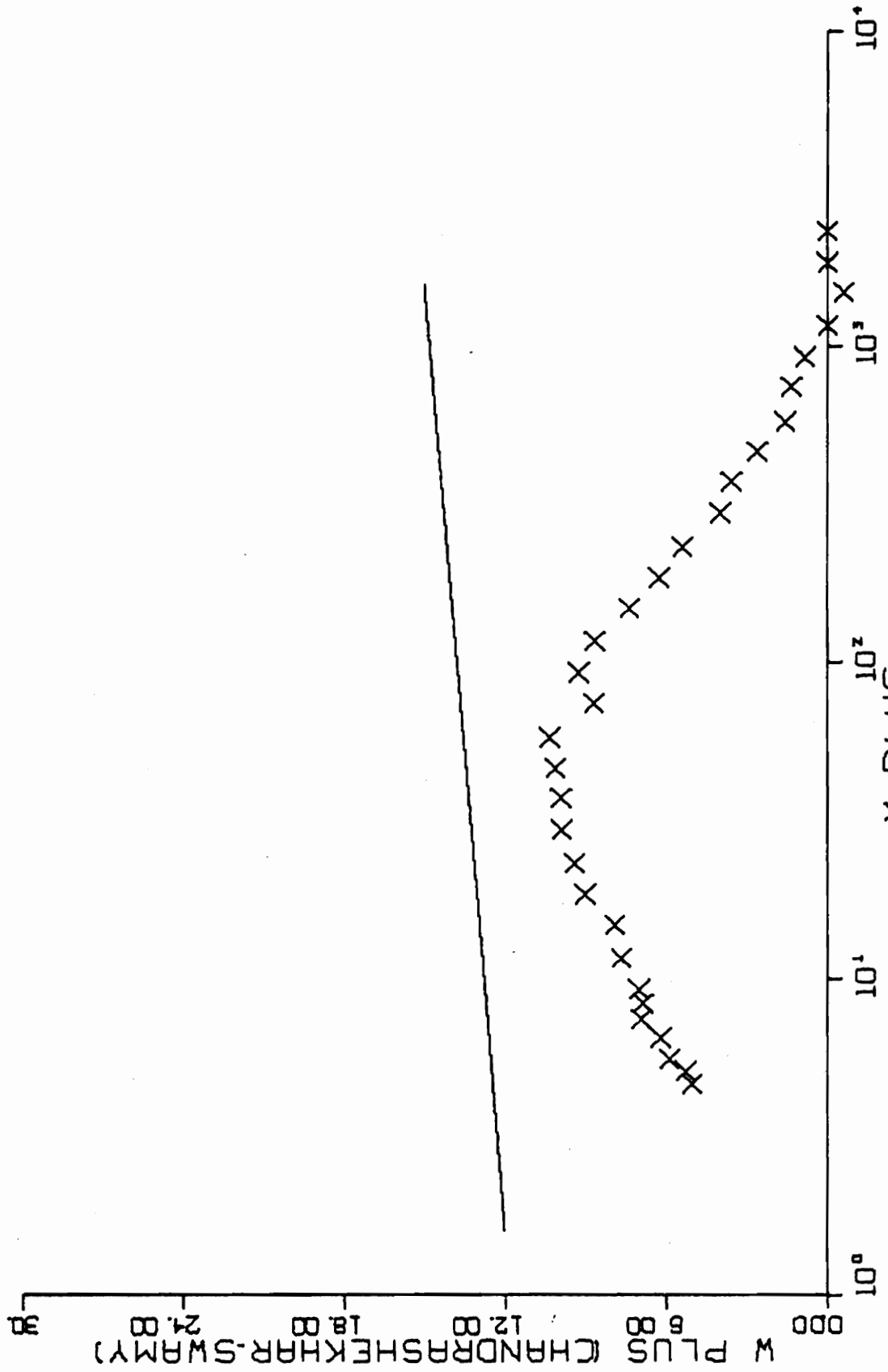

FIG. B21-4. CONTINUED FOR RUN G-1-01.

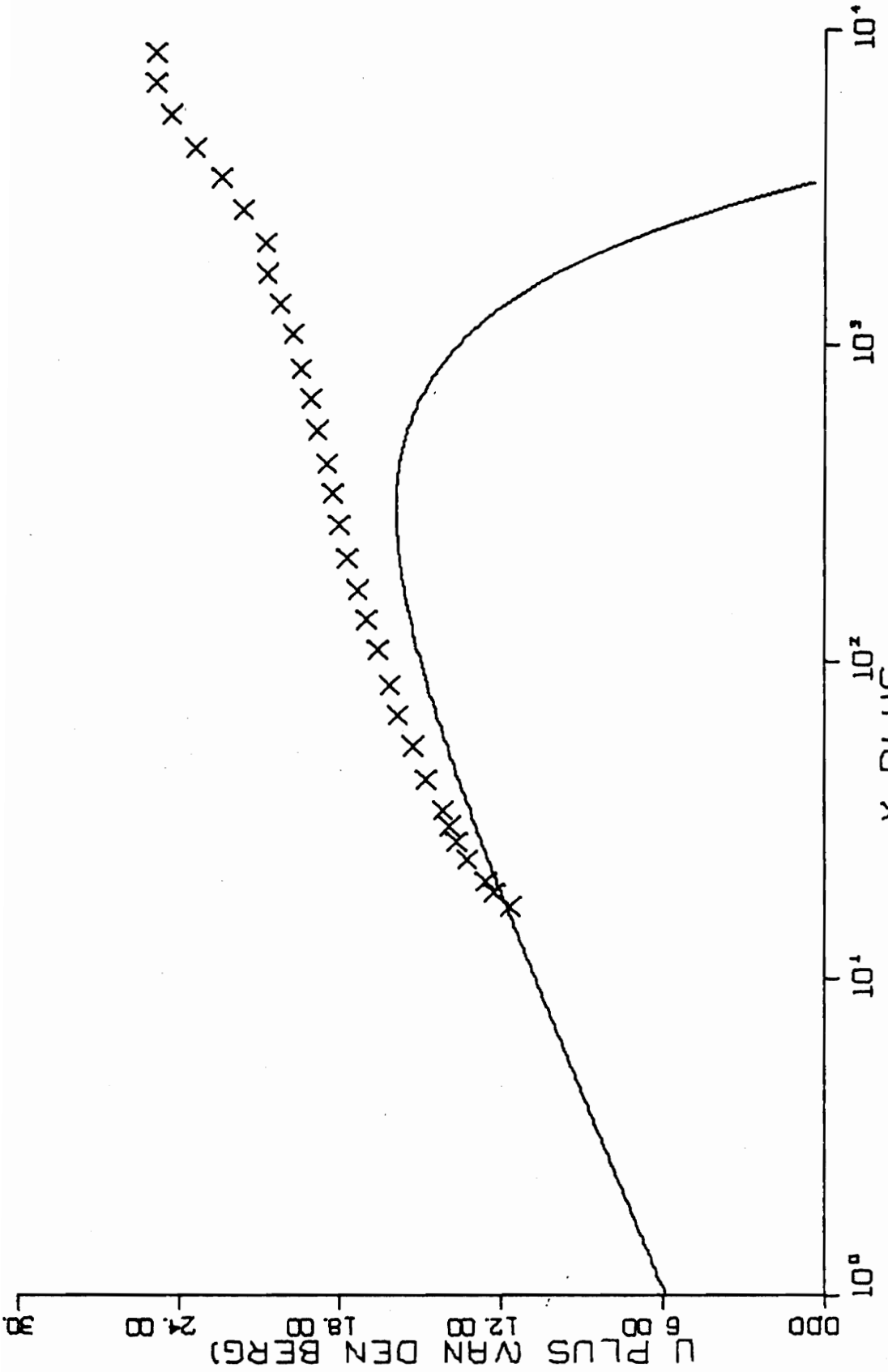

FIG. B21-5. THREE-DIMENSIONAL SIMILARITY PLOT-RUN G-1-01.

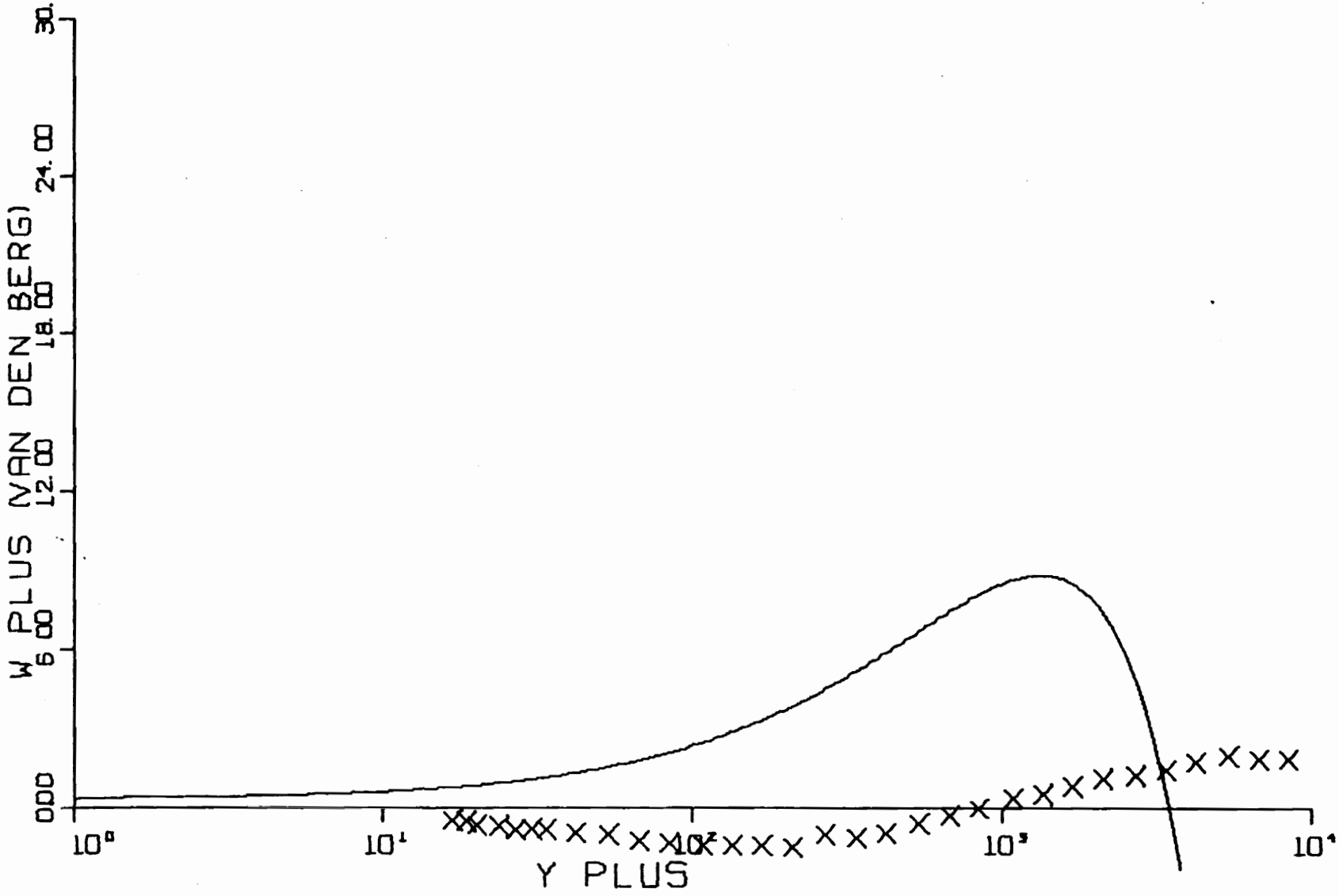

FIG. B21-5. CONTINUED FOR RUN G-1-01.

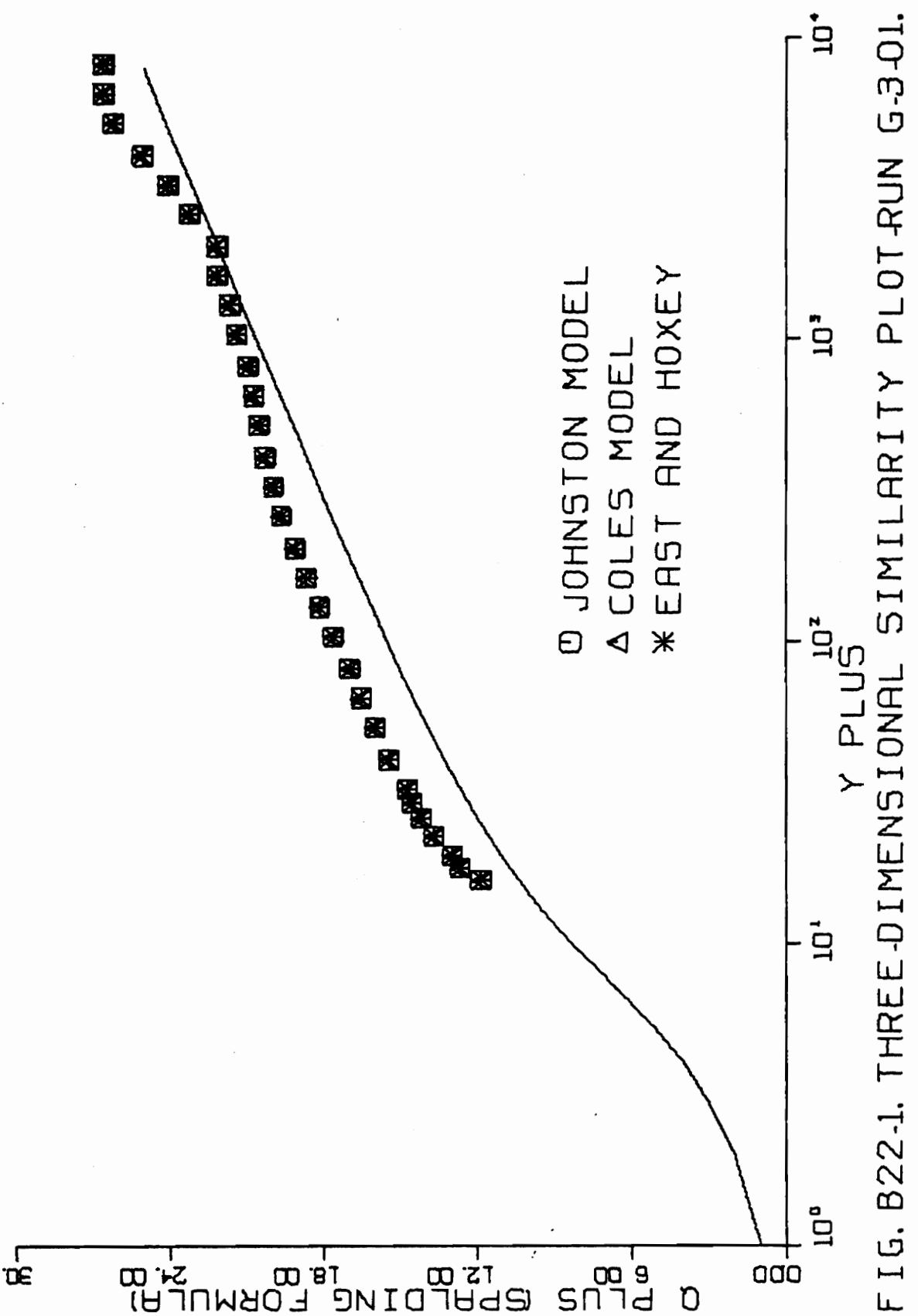

FIG. B22-1. THREE-DIMENSIONAL SIMILARITY PLOT-RUN G-3-01.

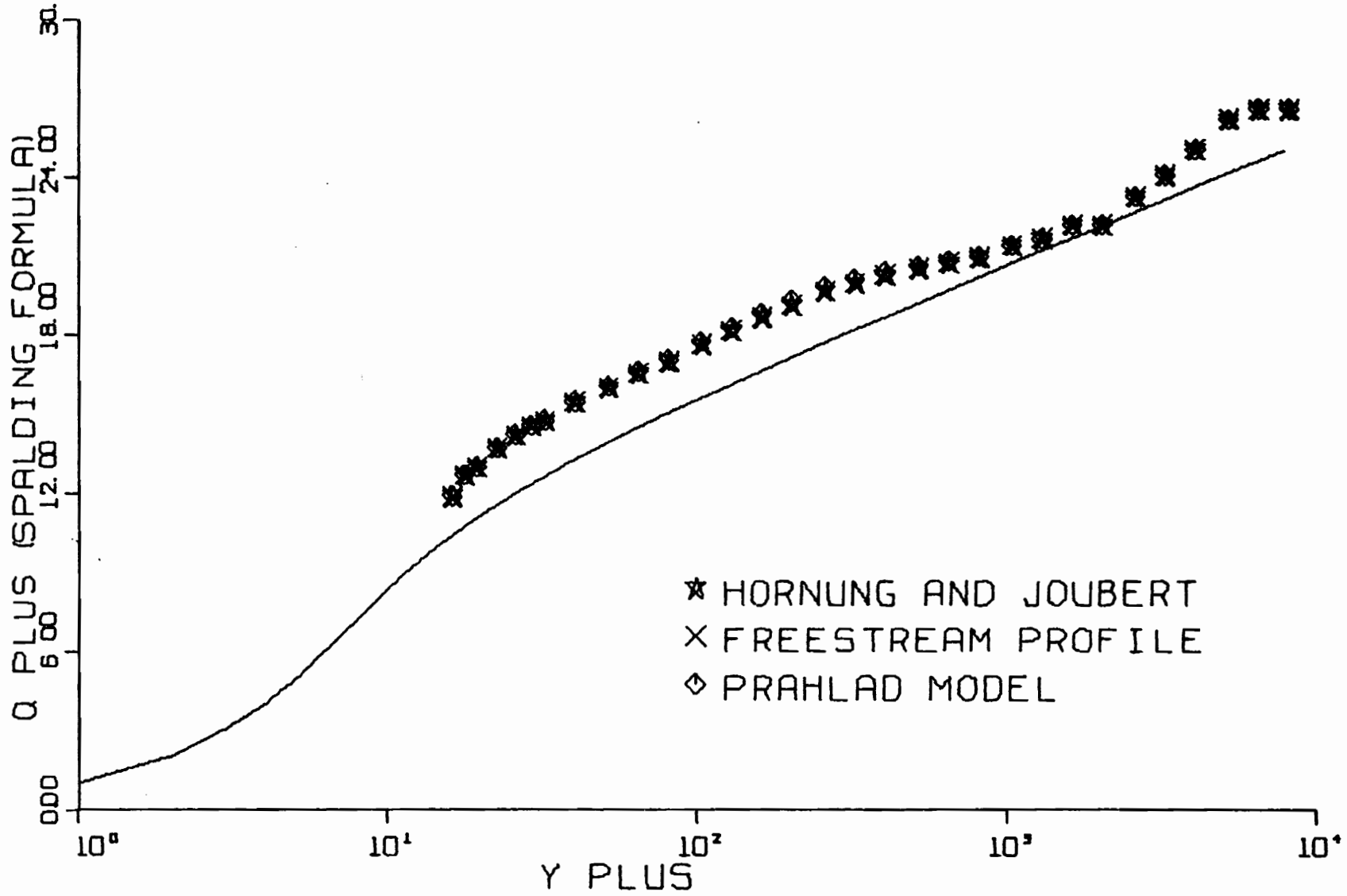

FIG. B22-2. THREE-DIMENSIONAL SIMILARITY PLOT-RUN G-3-01.

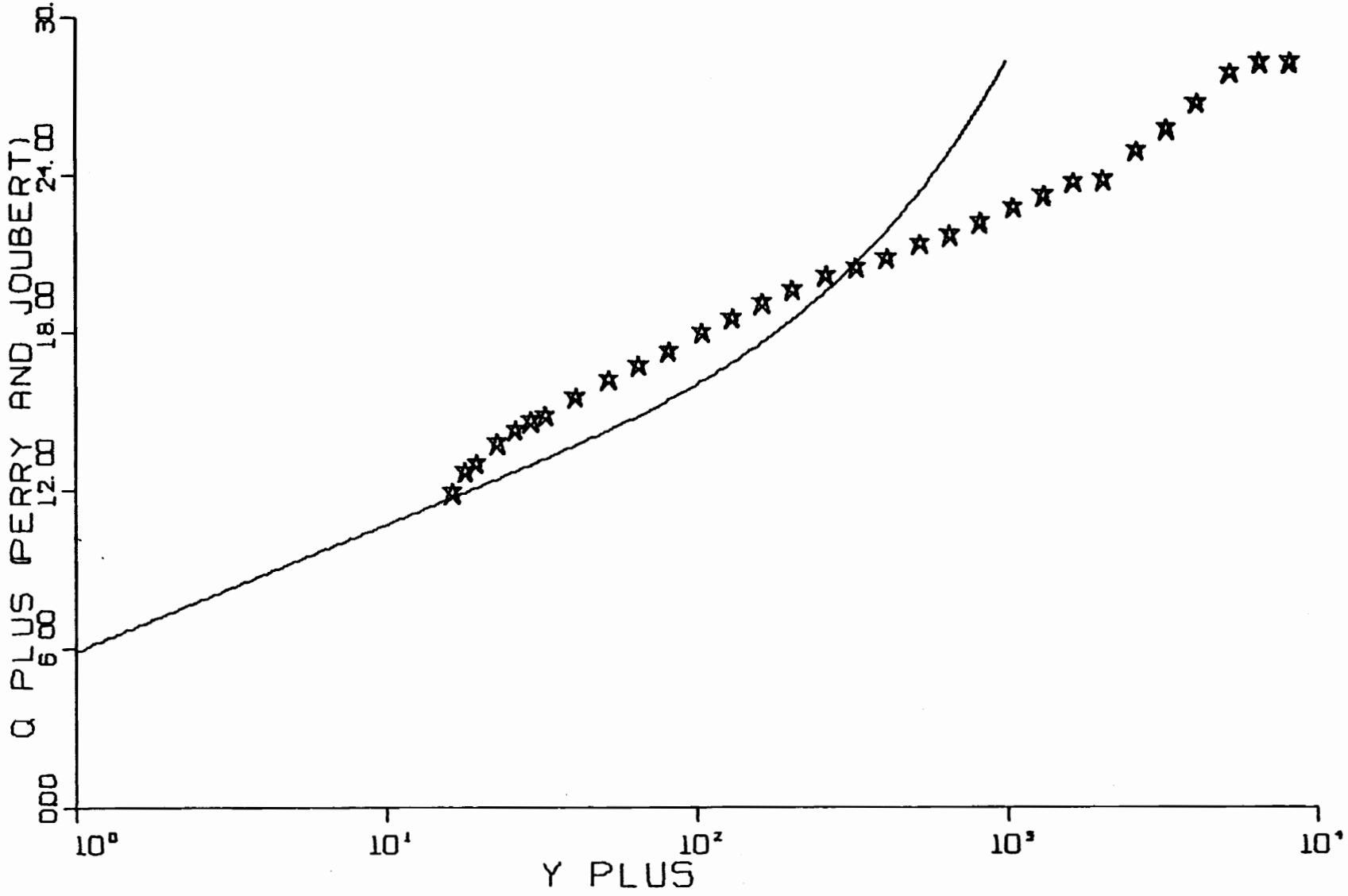

FIG. B22-3. THREE-DIMENSIONAL SIMILARITY PLOT-RUN G-3-01.

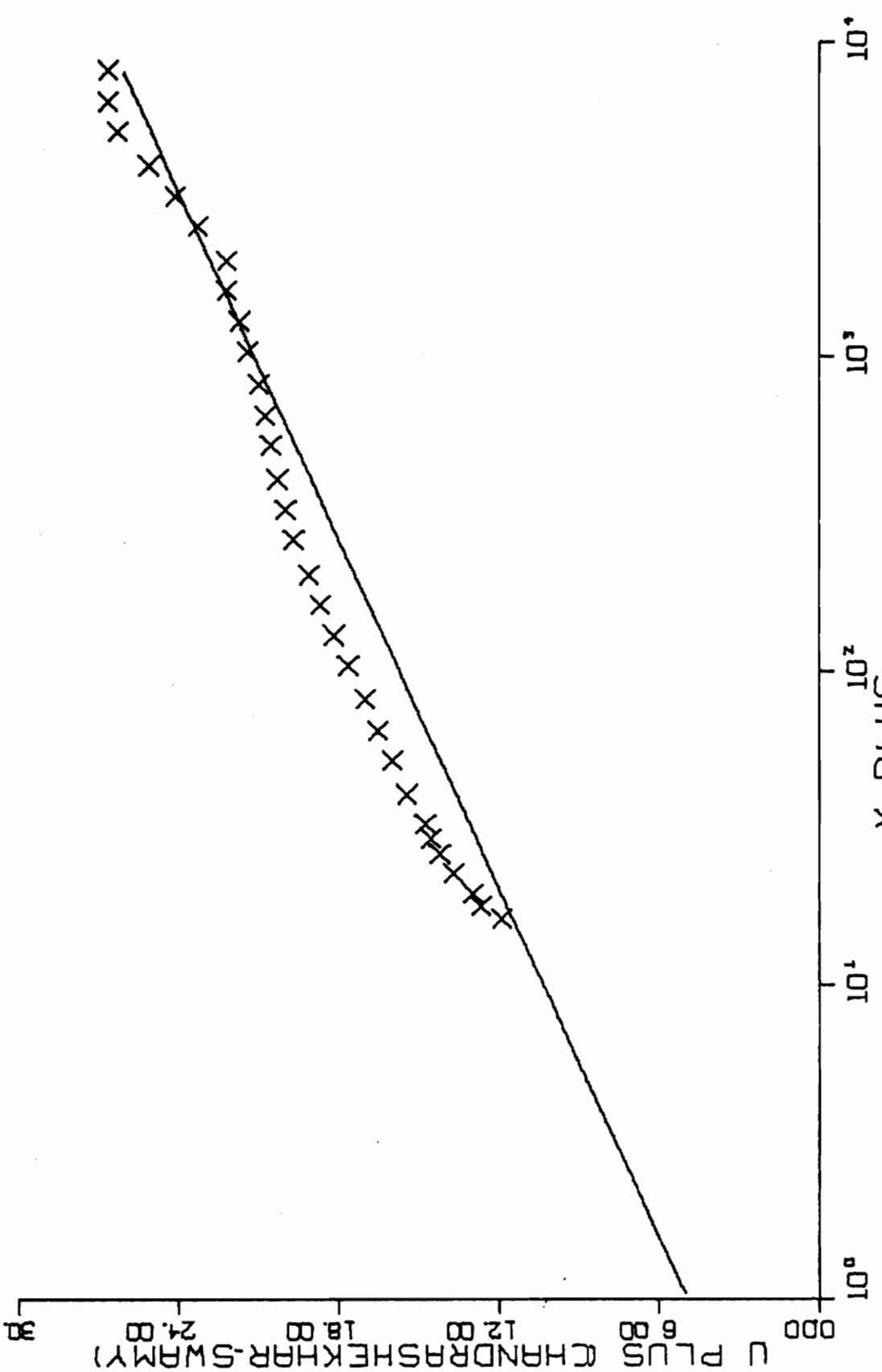

FIG. B22-4. THREE-DIMENSIONAL SIMILARITY PLOT-RUN G-3-01.

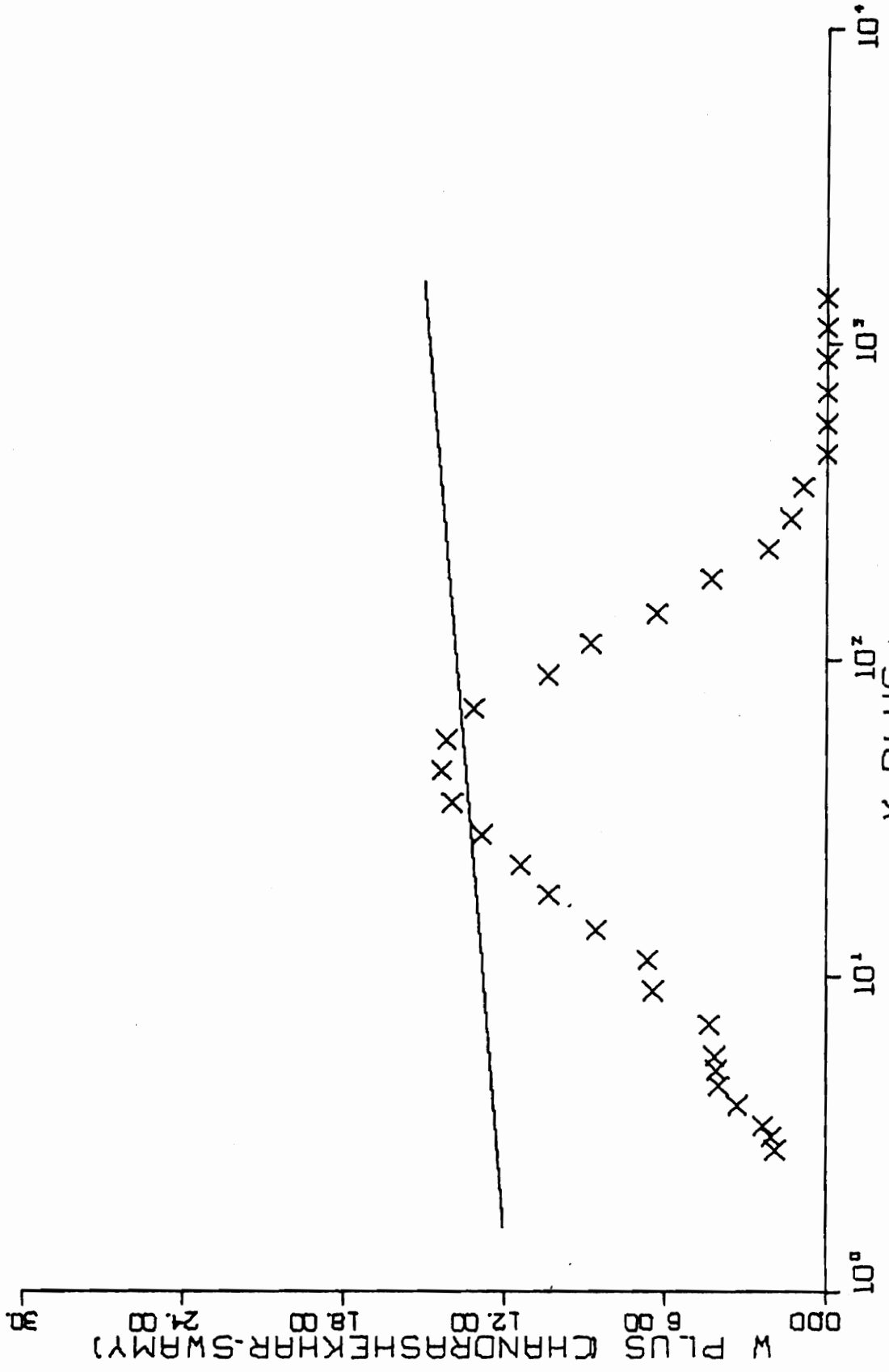

FIG. B22-4. CONTINUED FOR RUN G-3-01.

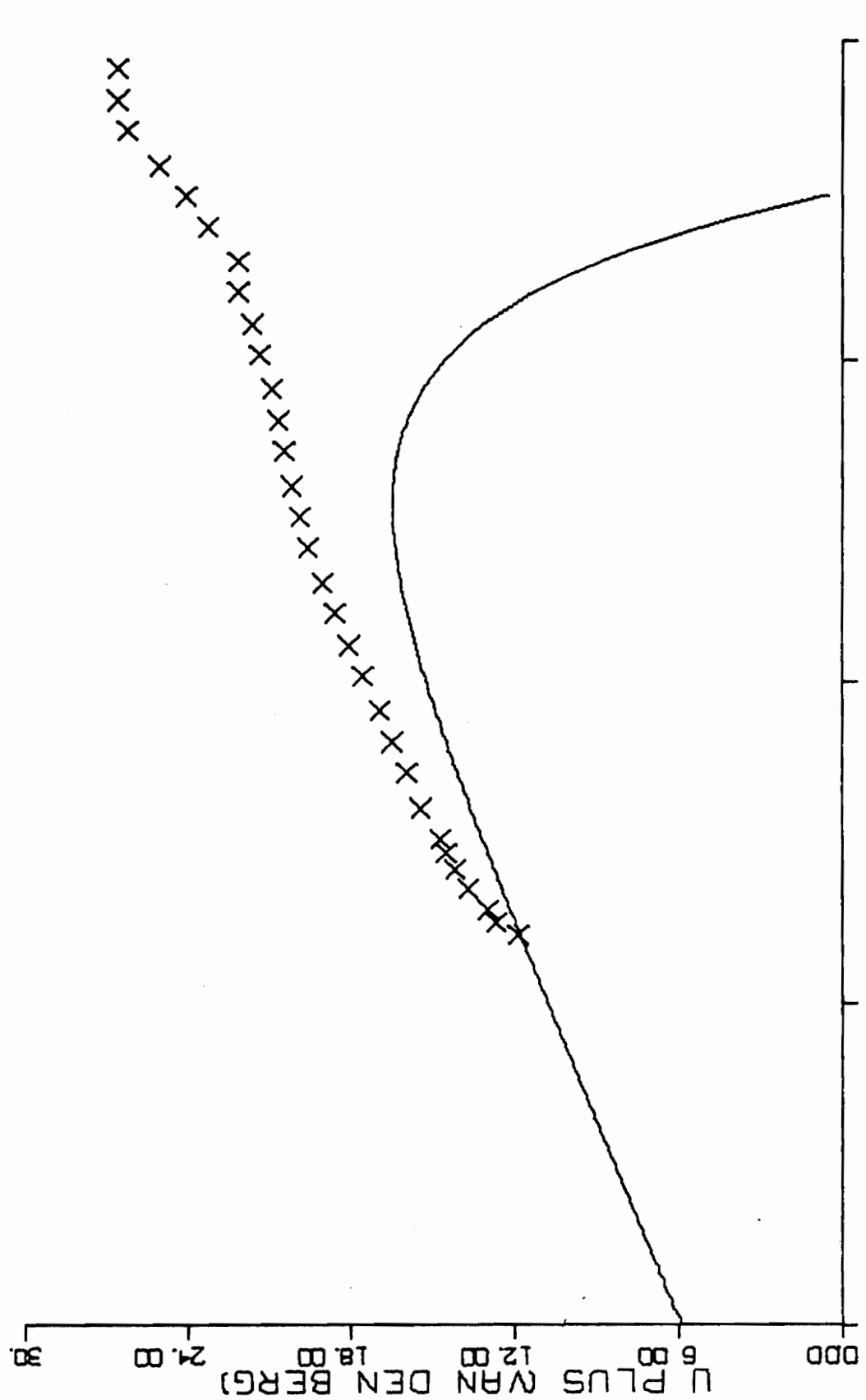

FIG. B22-5. THREE-DIMENSIONAL SIMILARITY PLOT-RUN G-3-01.

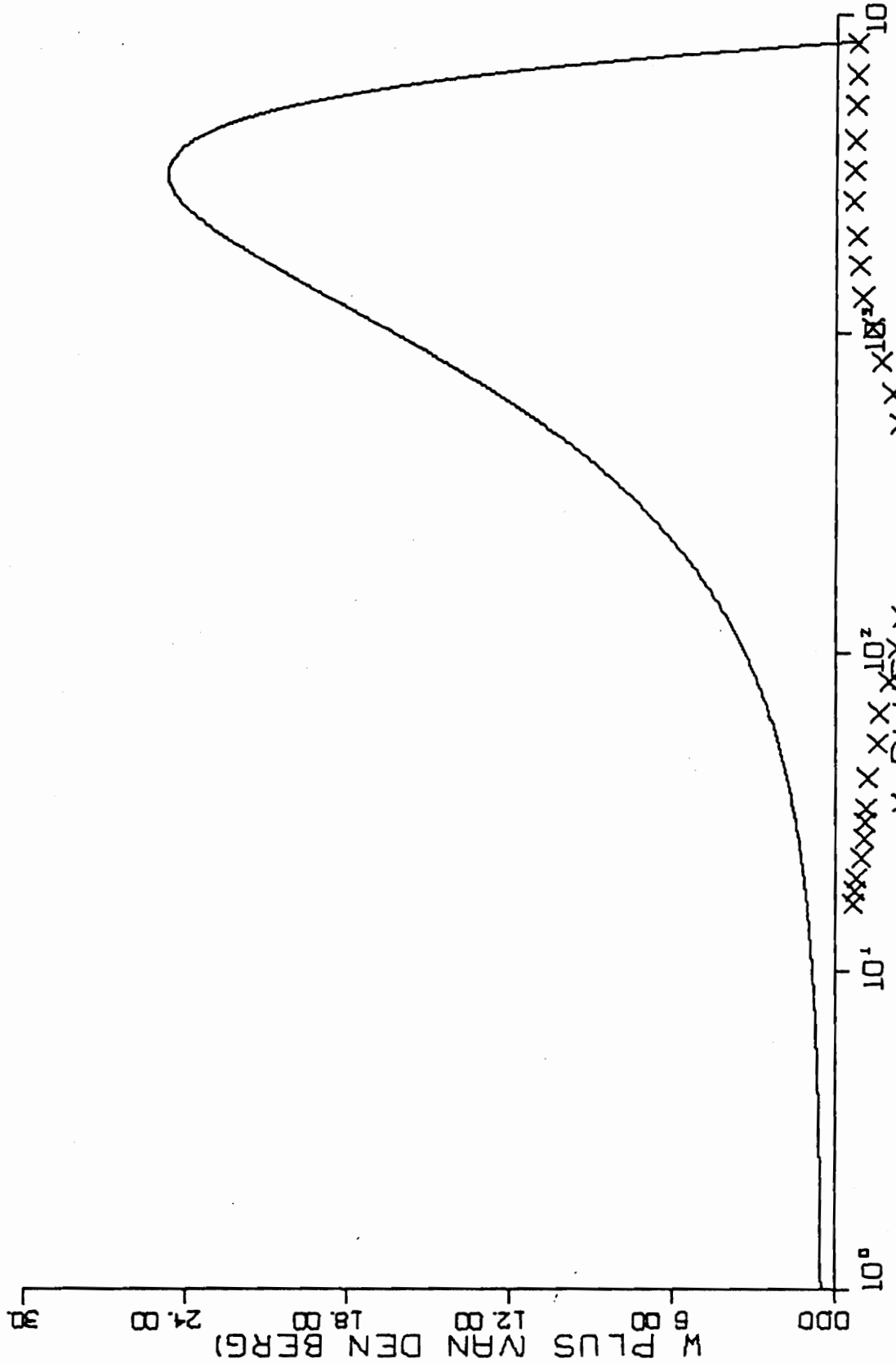

FIG. B22-5. CONTINUED FOR RUN G-3-01.

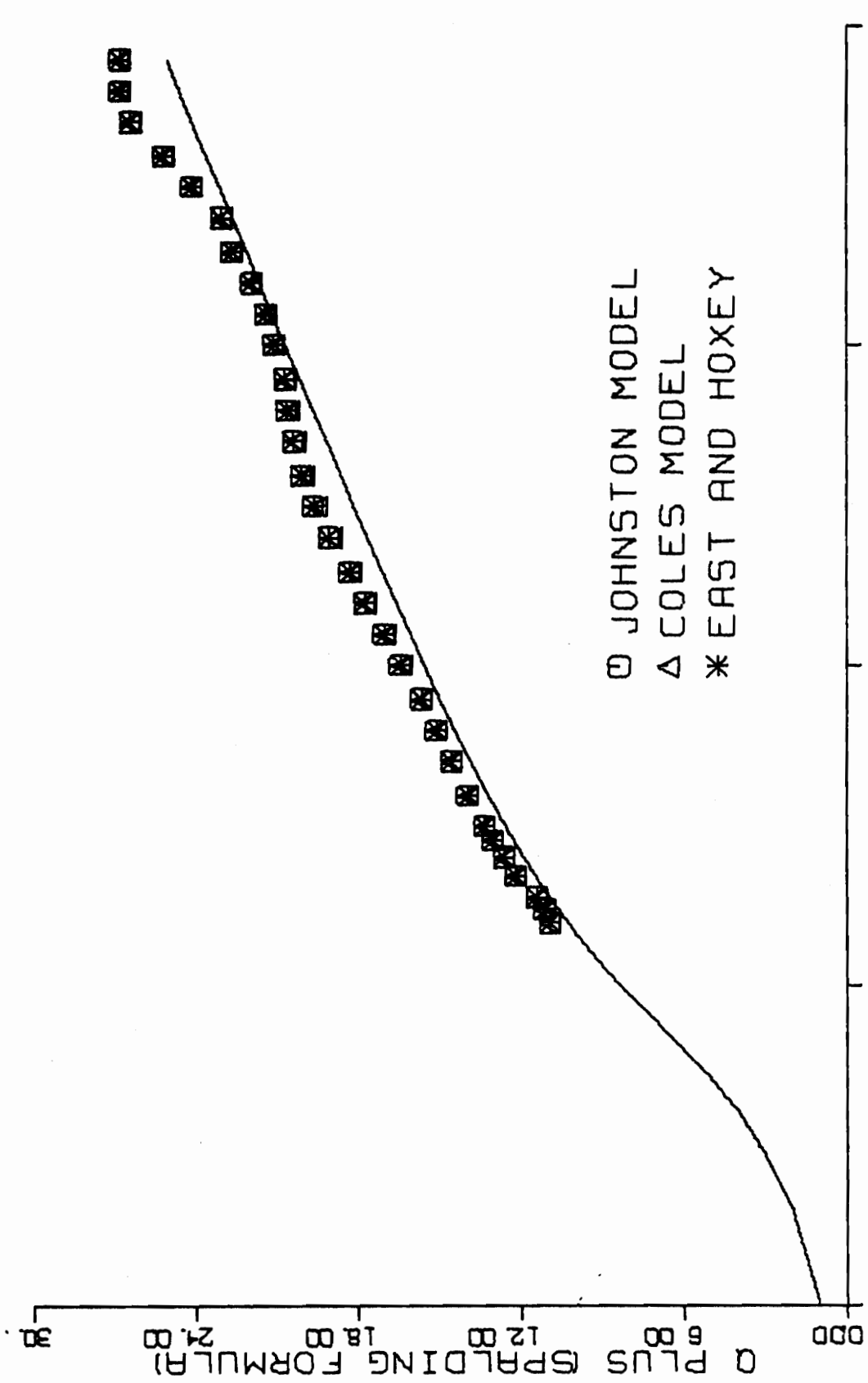

FIG. B23-1. THREE-DIMENSIONAL SIMILARITY PLOT-RUN G-5-01.

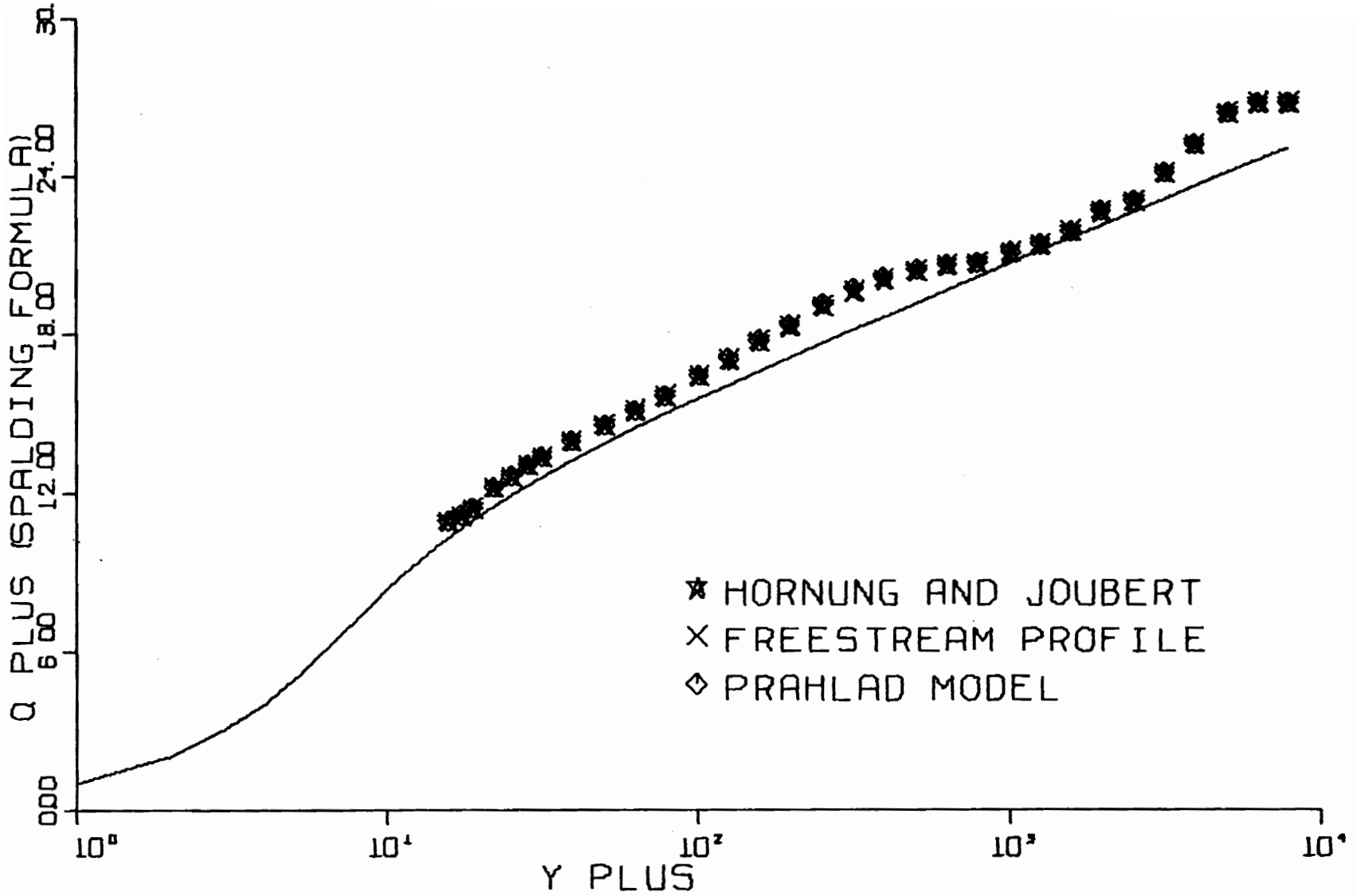

FIG. B23-2. THREE-DIMENSIONAL SIMILARITY PLOT-RUN G-5-01.

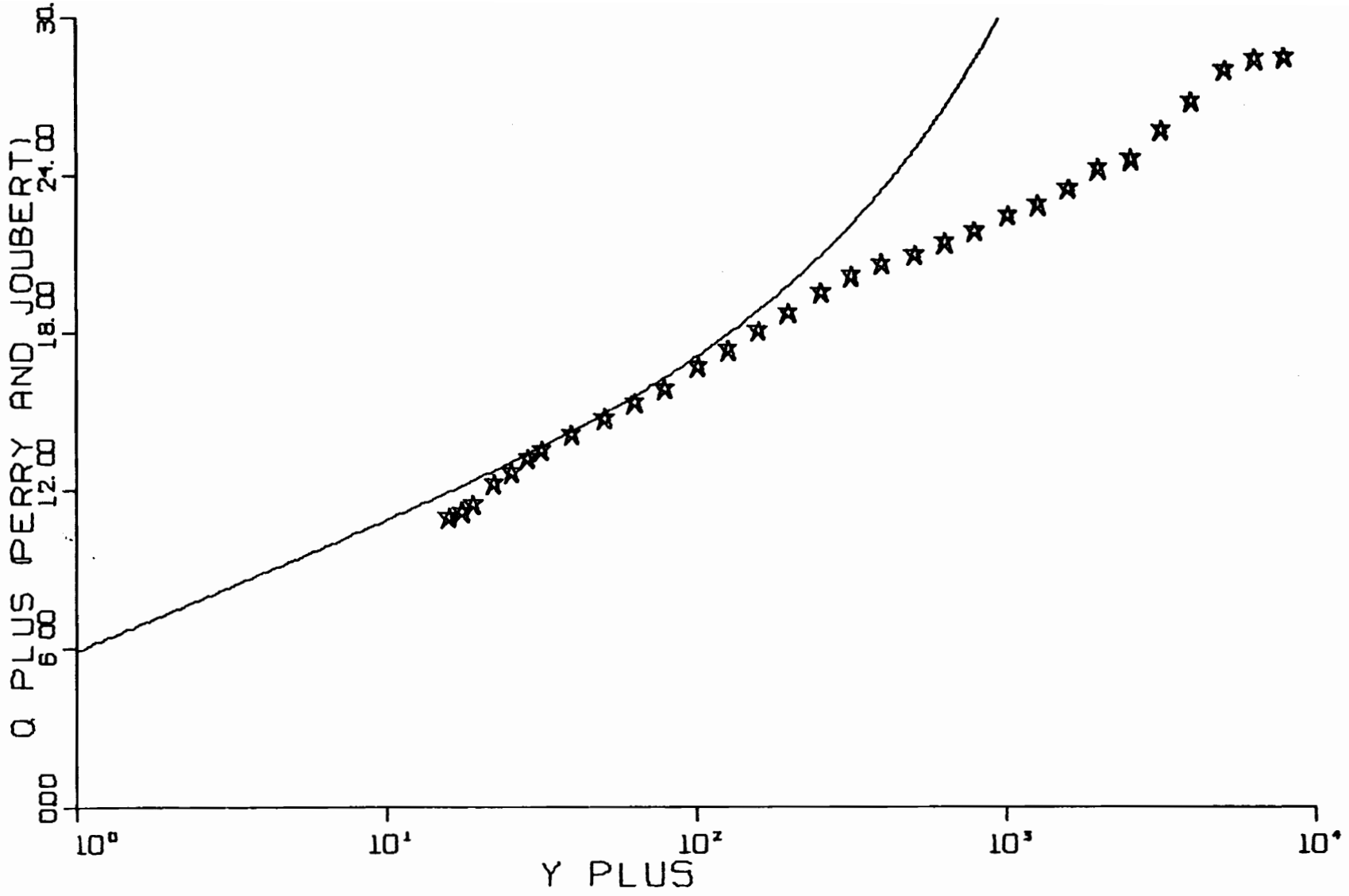

FIG. B23-3. THREE-DIMENSIONAL SIMILARITY PLOT-RUN G-5-01.

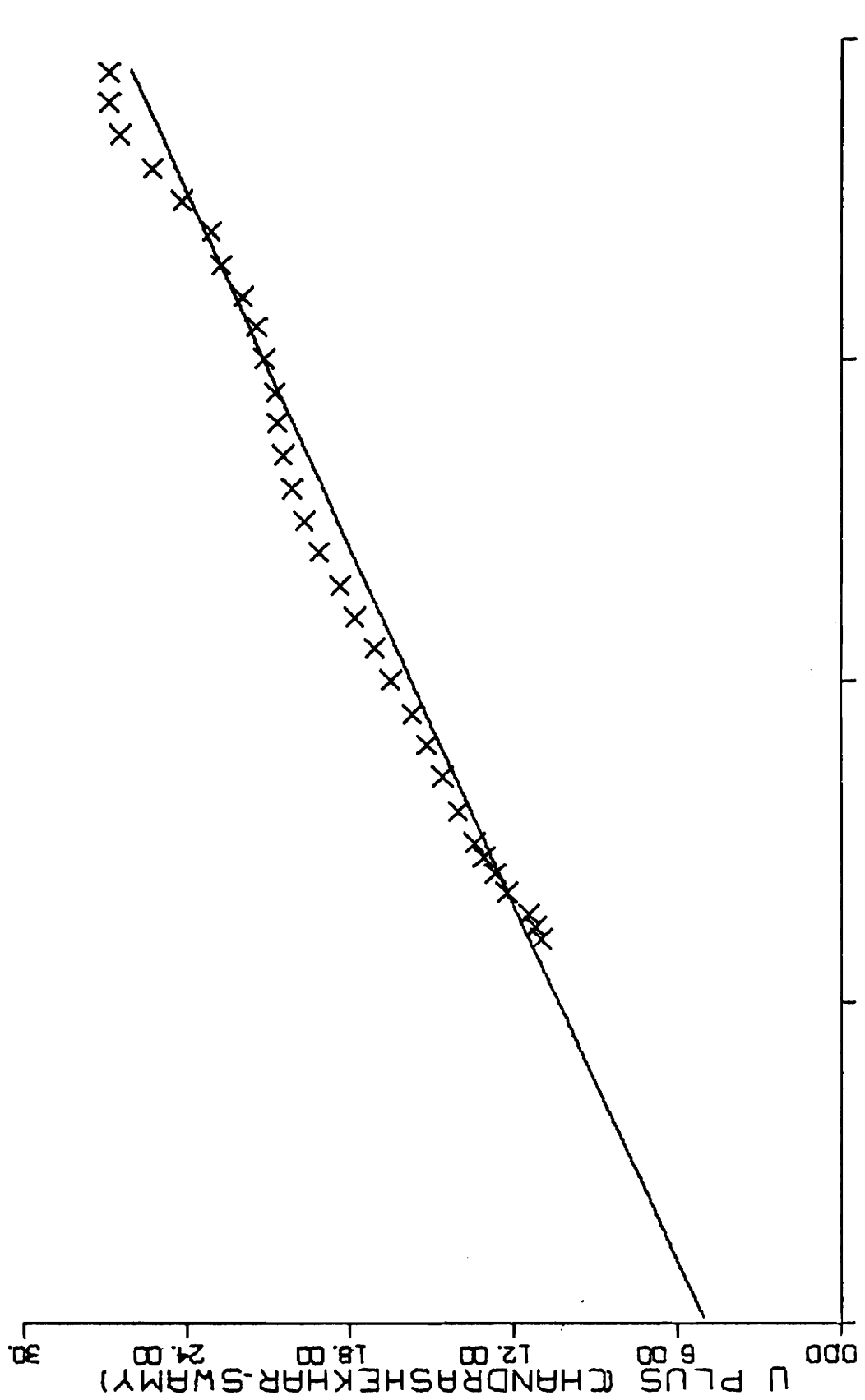

FIG. B23-4. THREE-DIMENSIONAL SIMILARITY PLOT-RUN G-5-01.

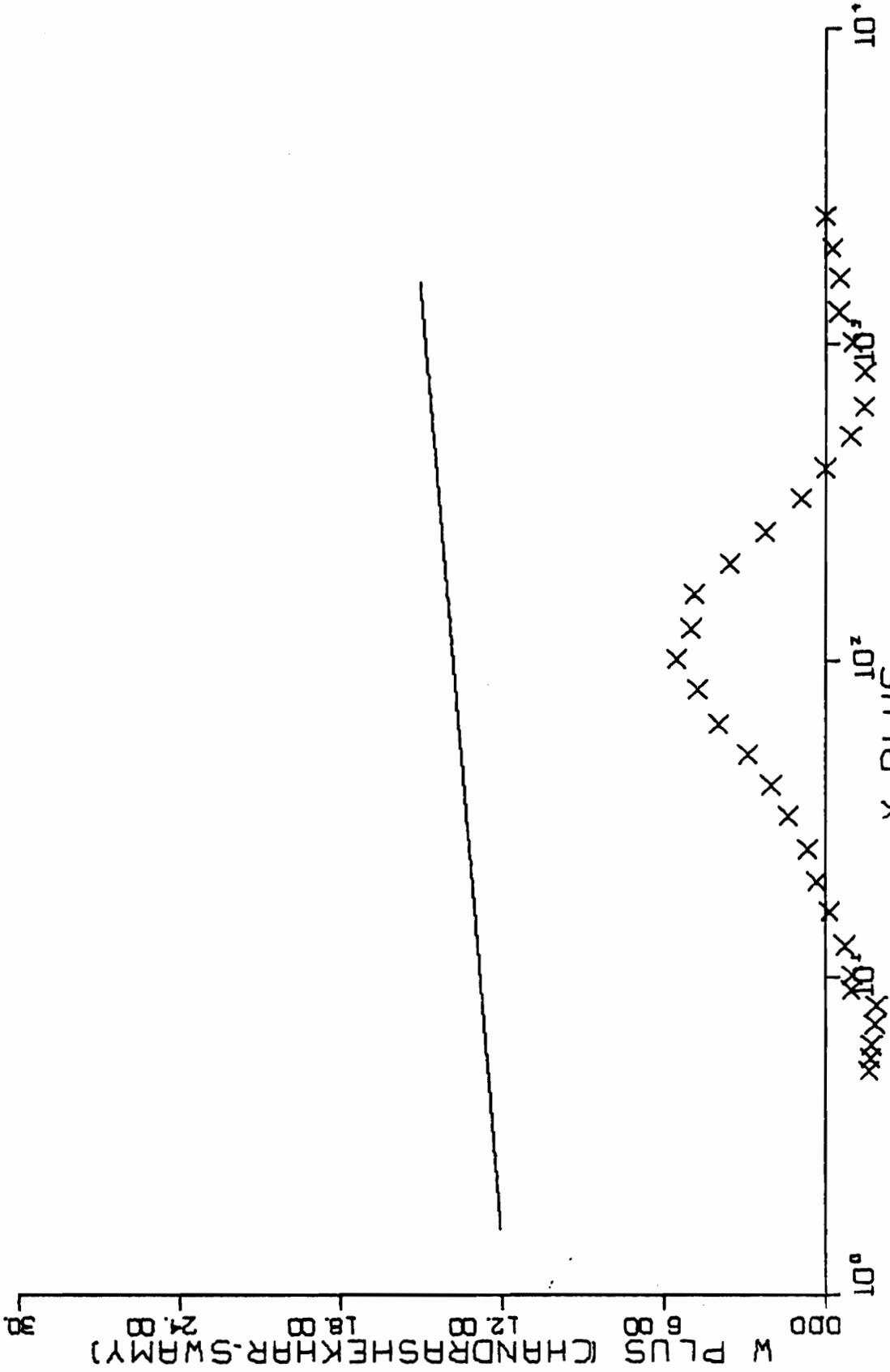

FIG. B23-4. CONTINUED FOR RUN G-5-01.

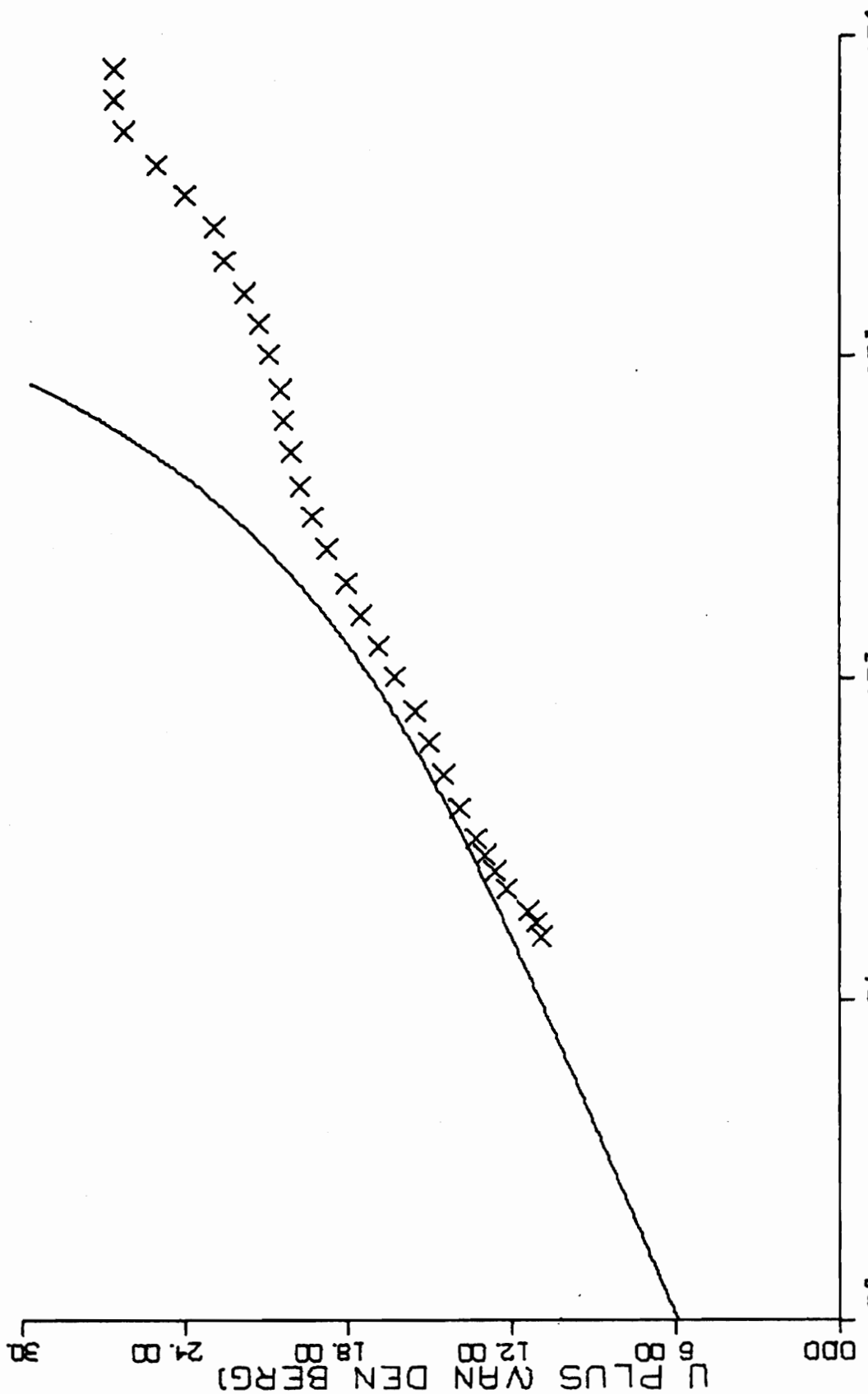

FIG. B23-5. THREE-DIMENSIONAL SIMILARITY PLOT-RUN G-5-01.

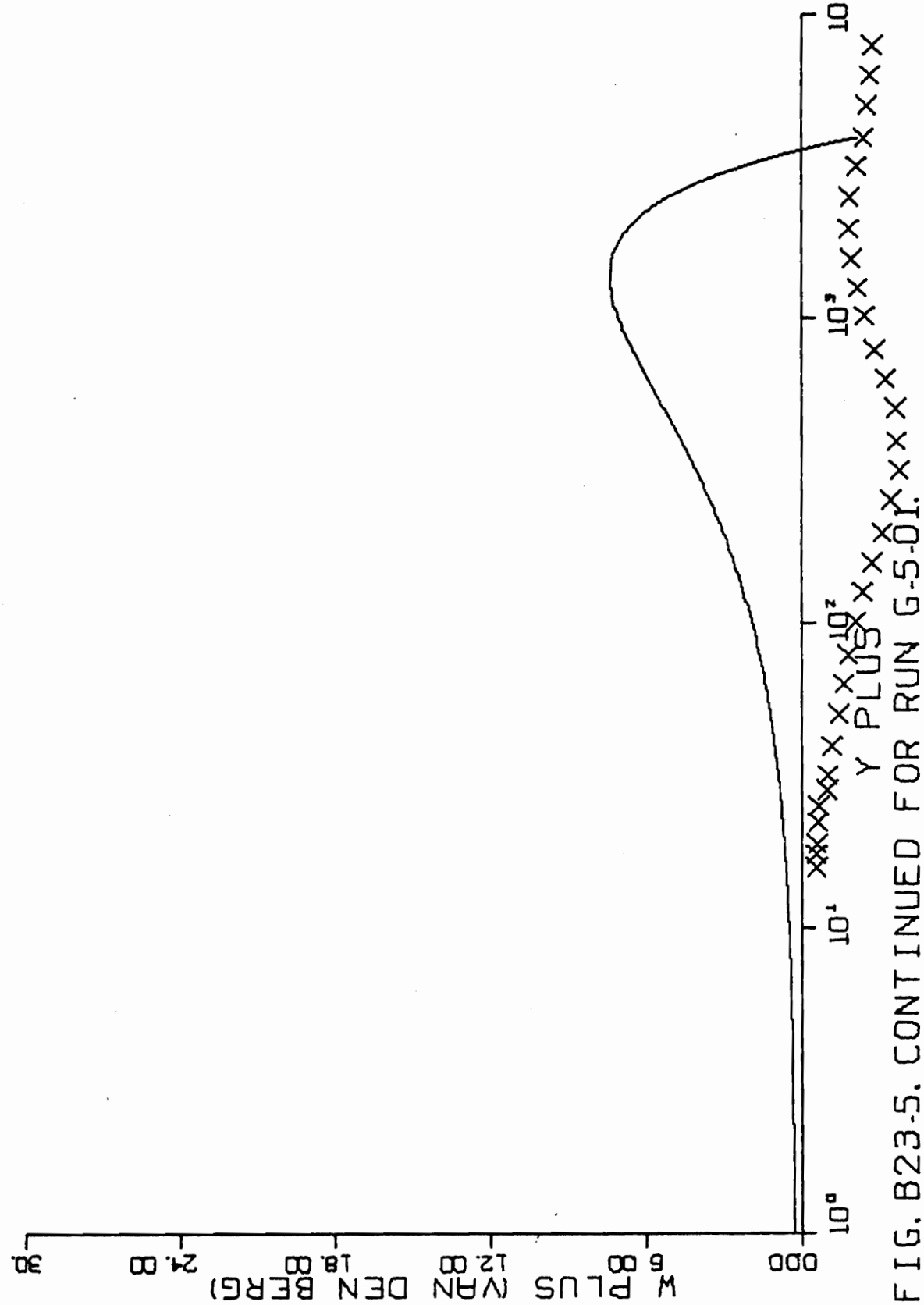

FIG. B23-5. CONTINUED FOR RUN G-5-01.

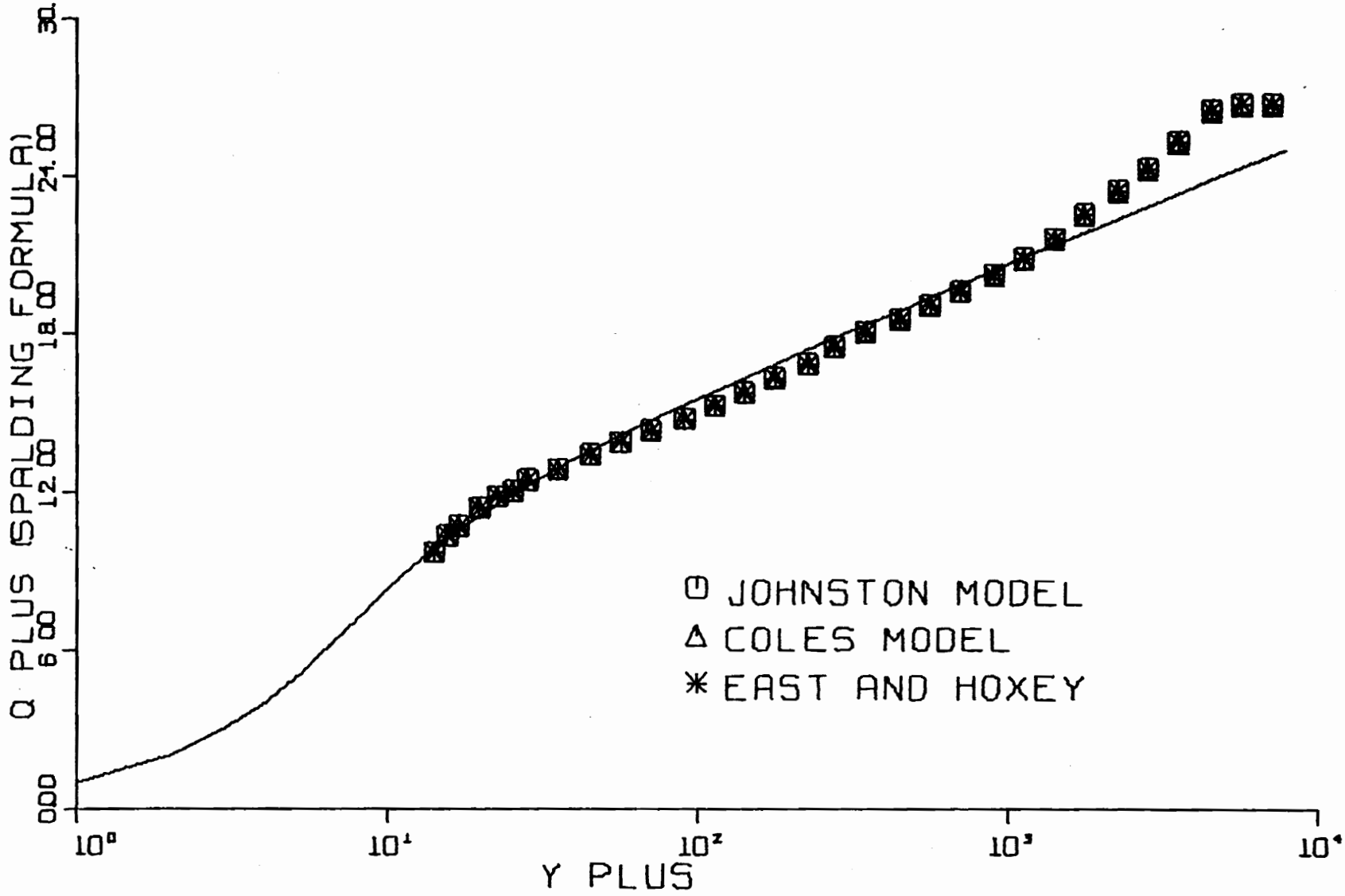

FIG. B24-1. THREE-DIMENSIONAL SIMILARITY PLOT-RUN I7-01.

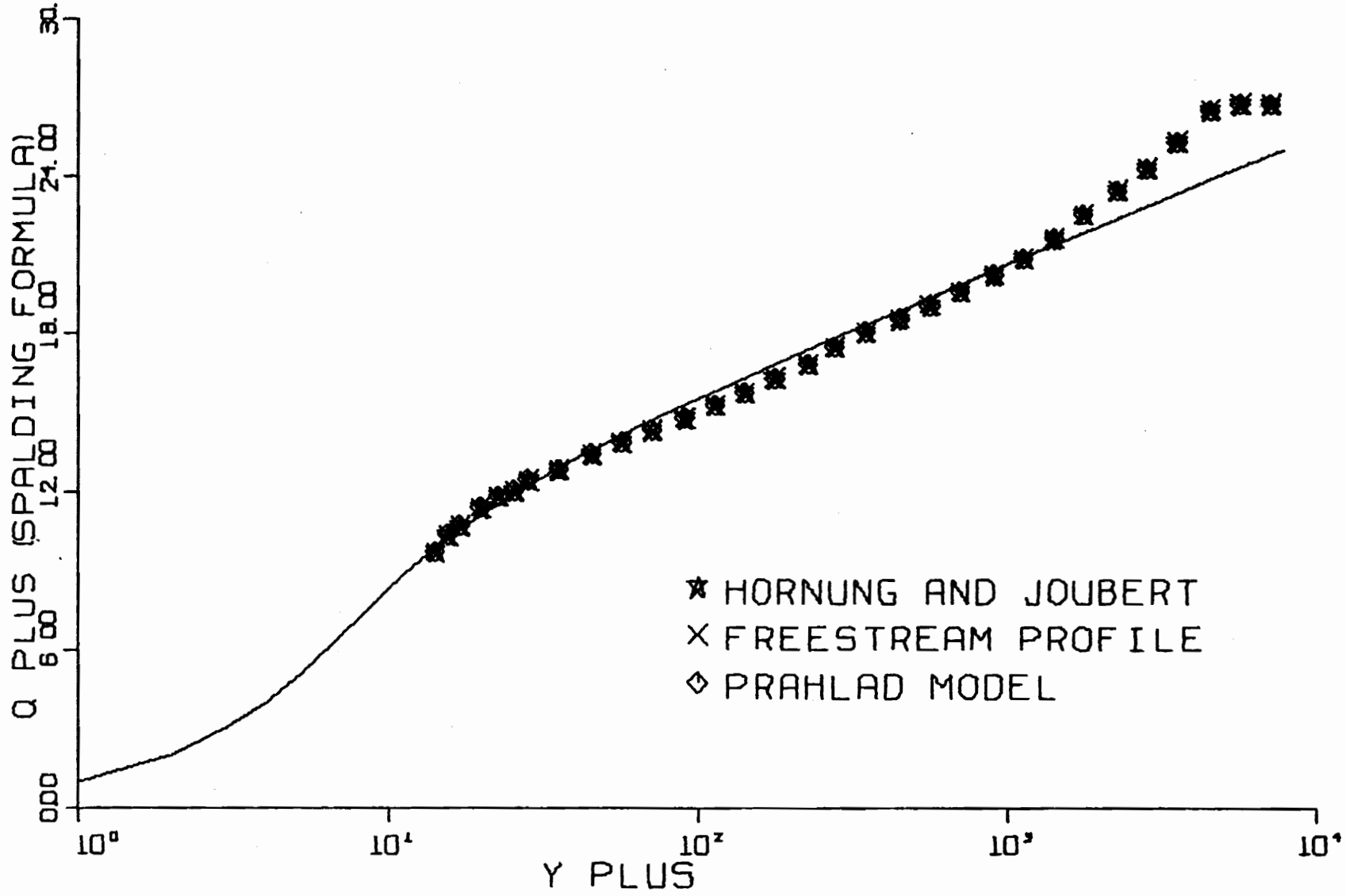

FIG. B24-2. THREE-DIMENSIONAL SIMILARITY PLOT-RUN I7-01.

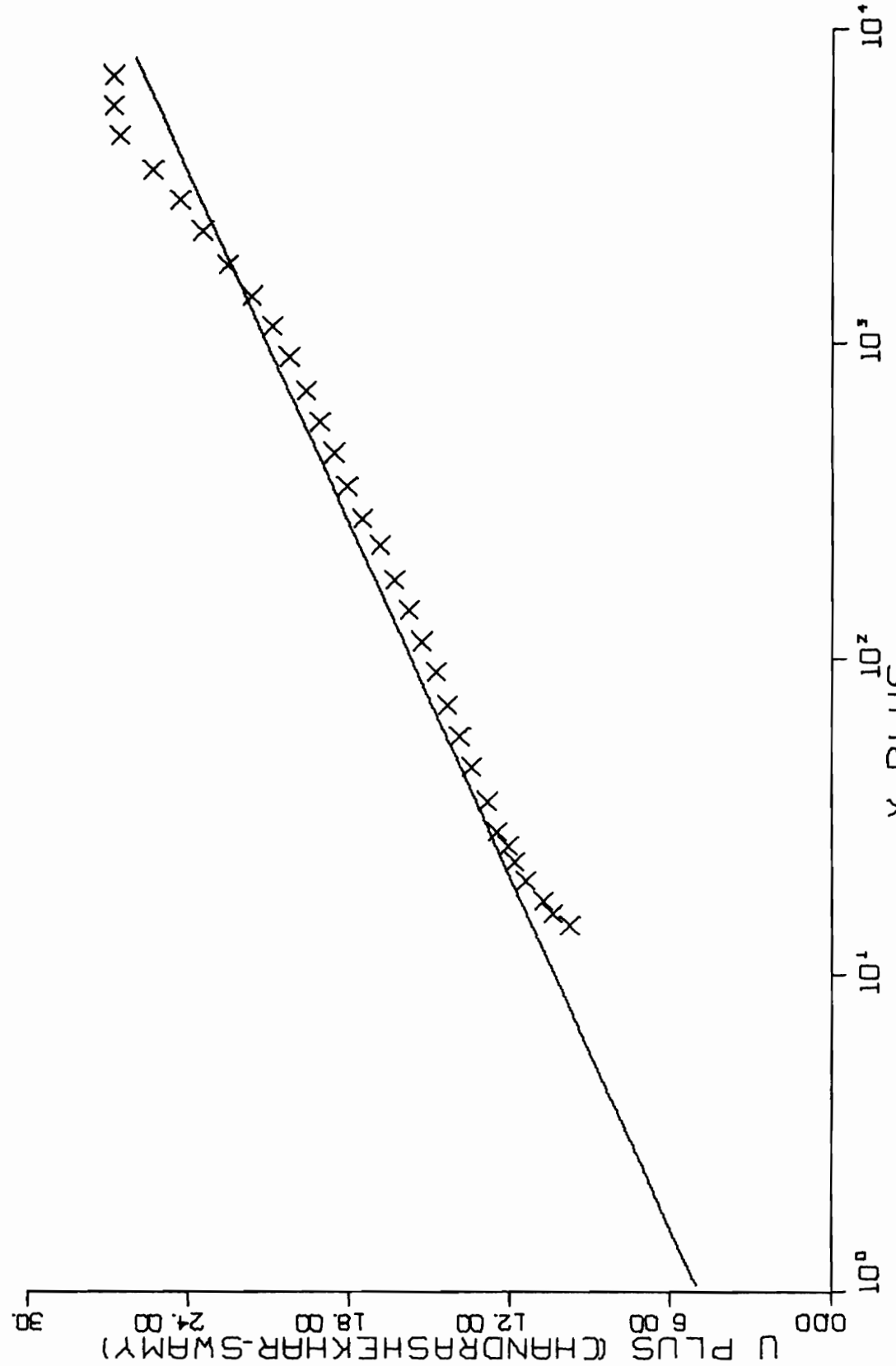

FIG. B24.4. THREE-DIMENSIONAL SIMILARITY PLOT-RUN I7-01.

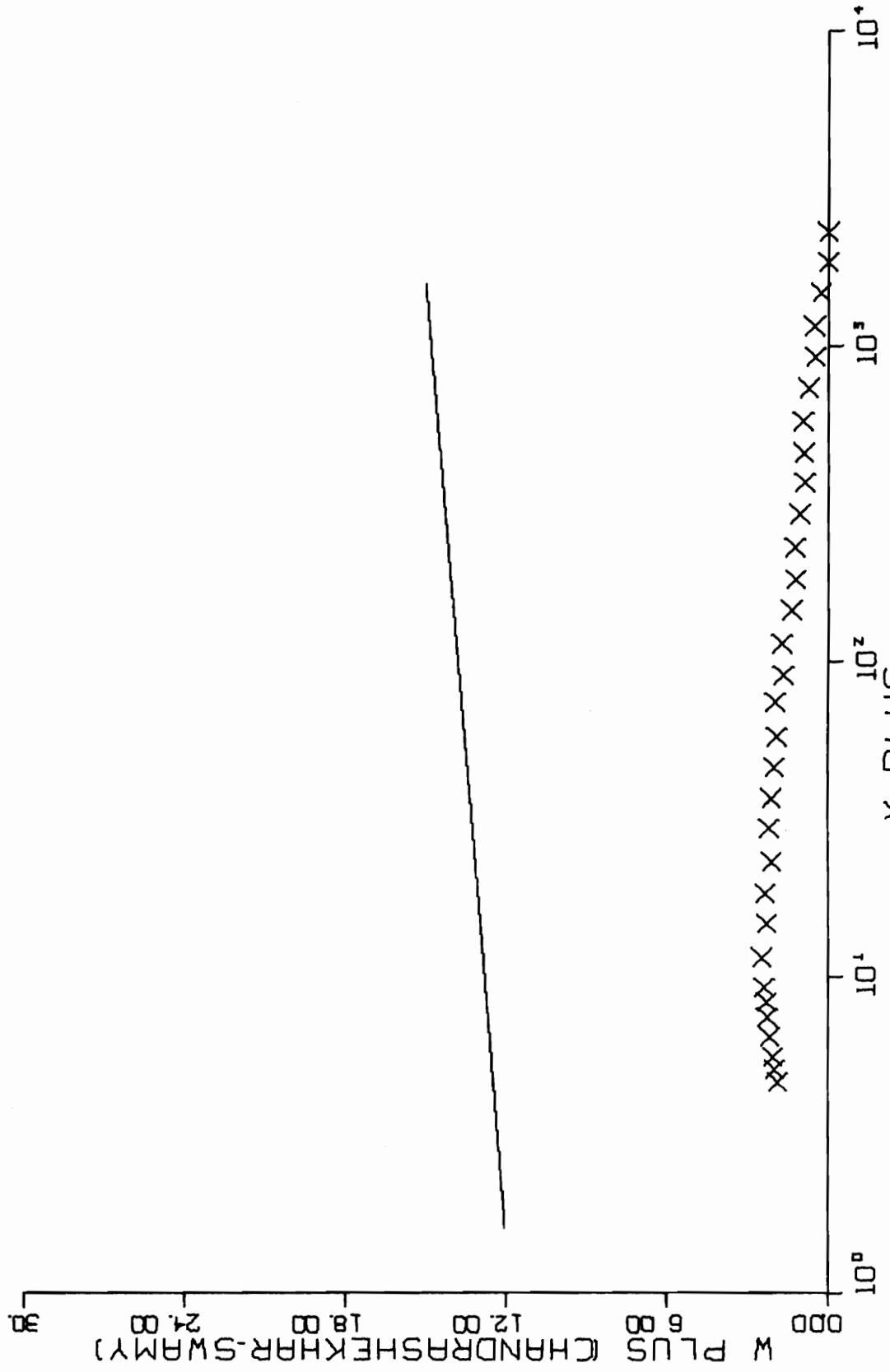

FIG. B24-4. CONTINUED FOR RUN I7-01.

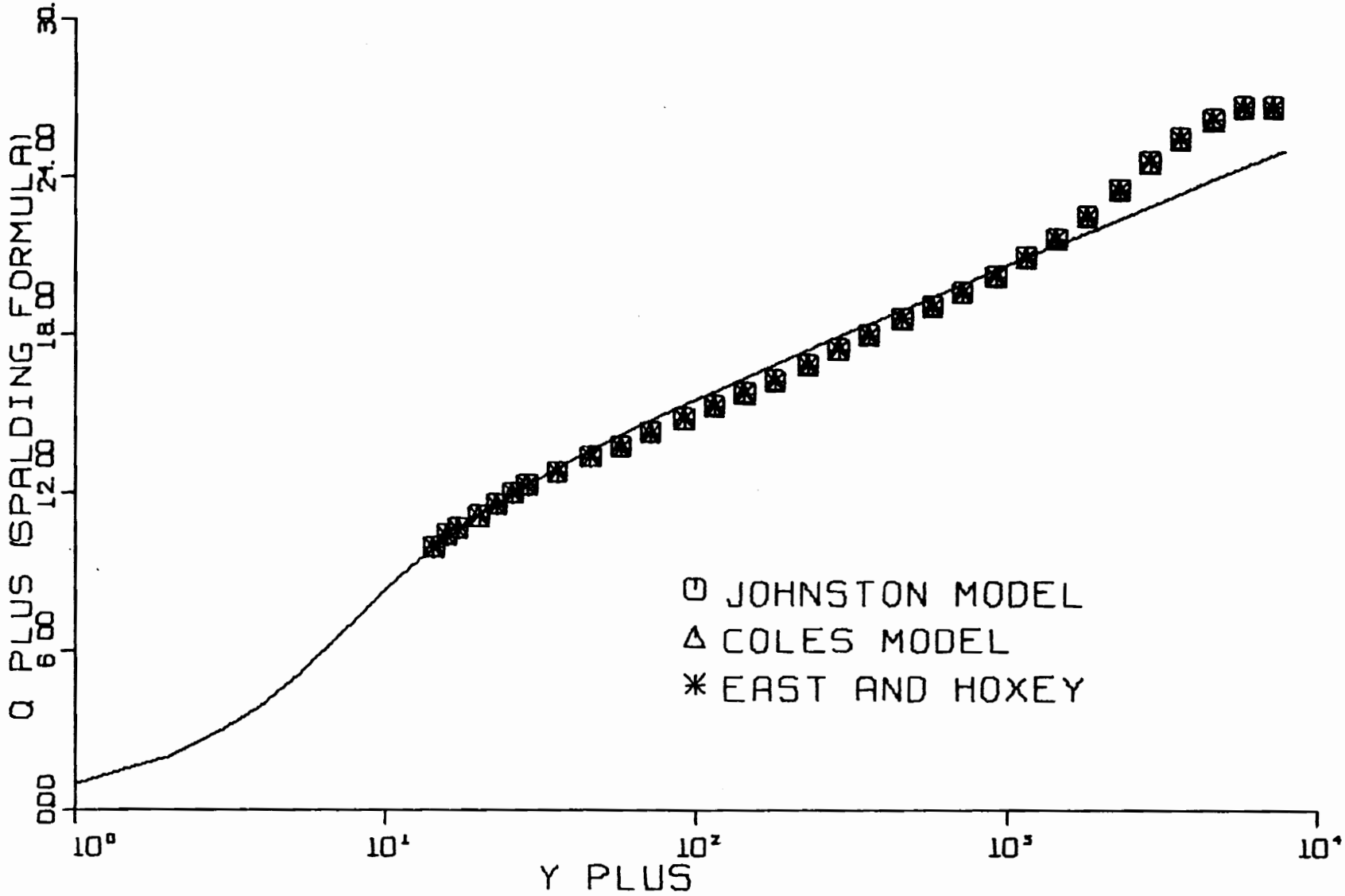

FIG. B25-1. THREE-DIMENSIONAL SIMILARITY PLOT-RUN I7-02.

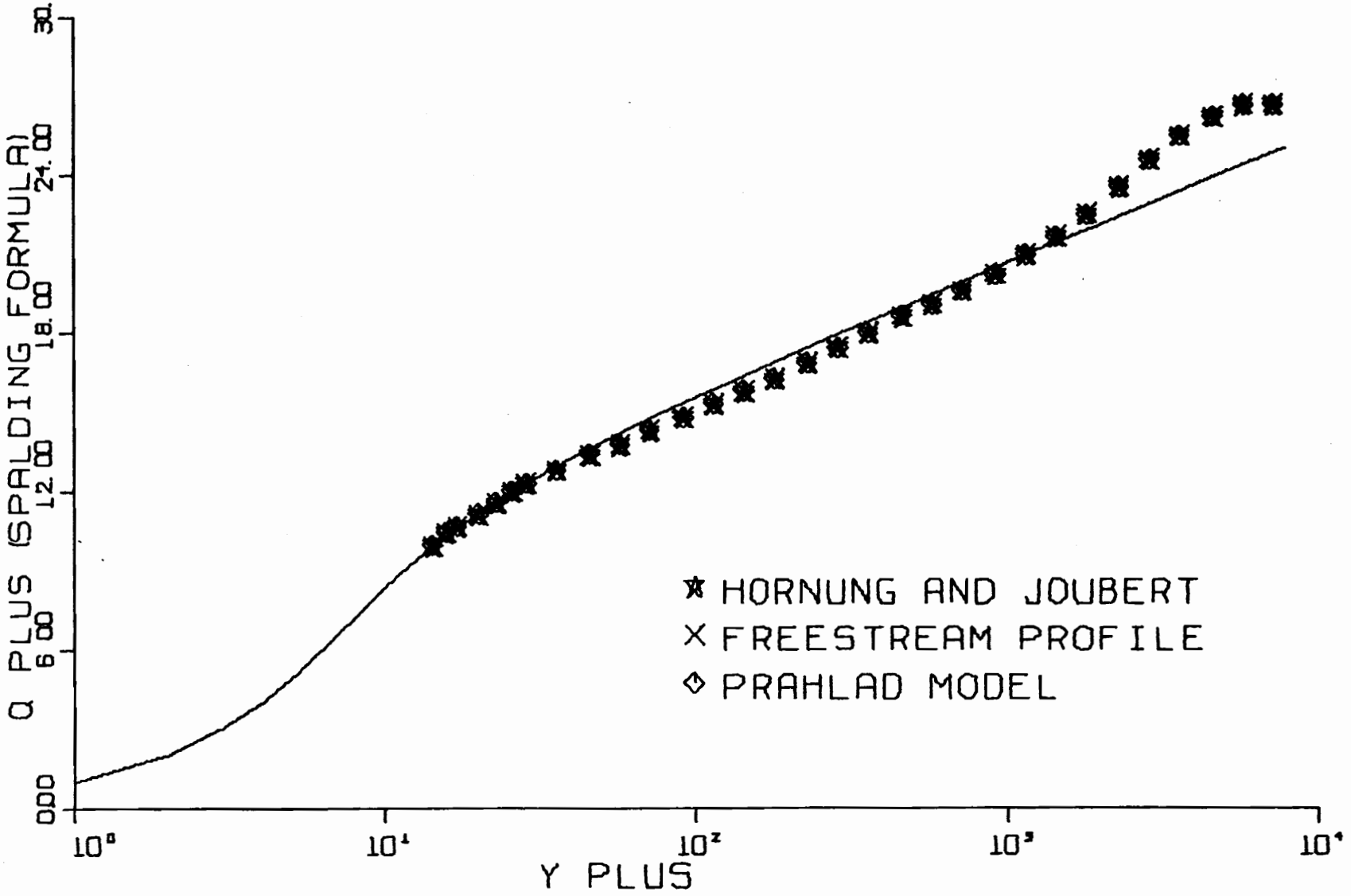

FIG. B25-2. THREE-DIMENSIONAL SIMILARITY PLOT-RUN I7-02.

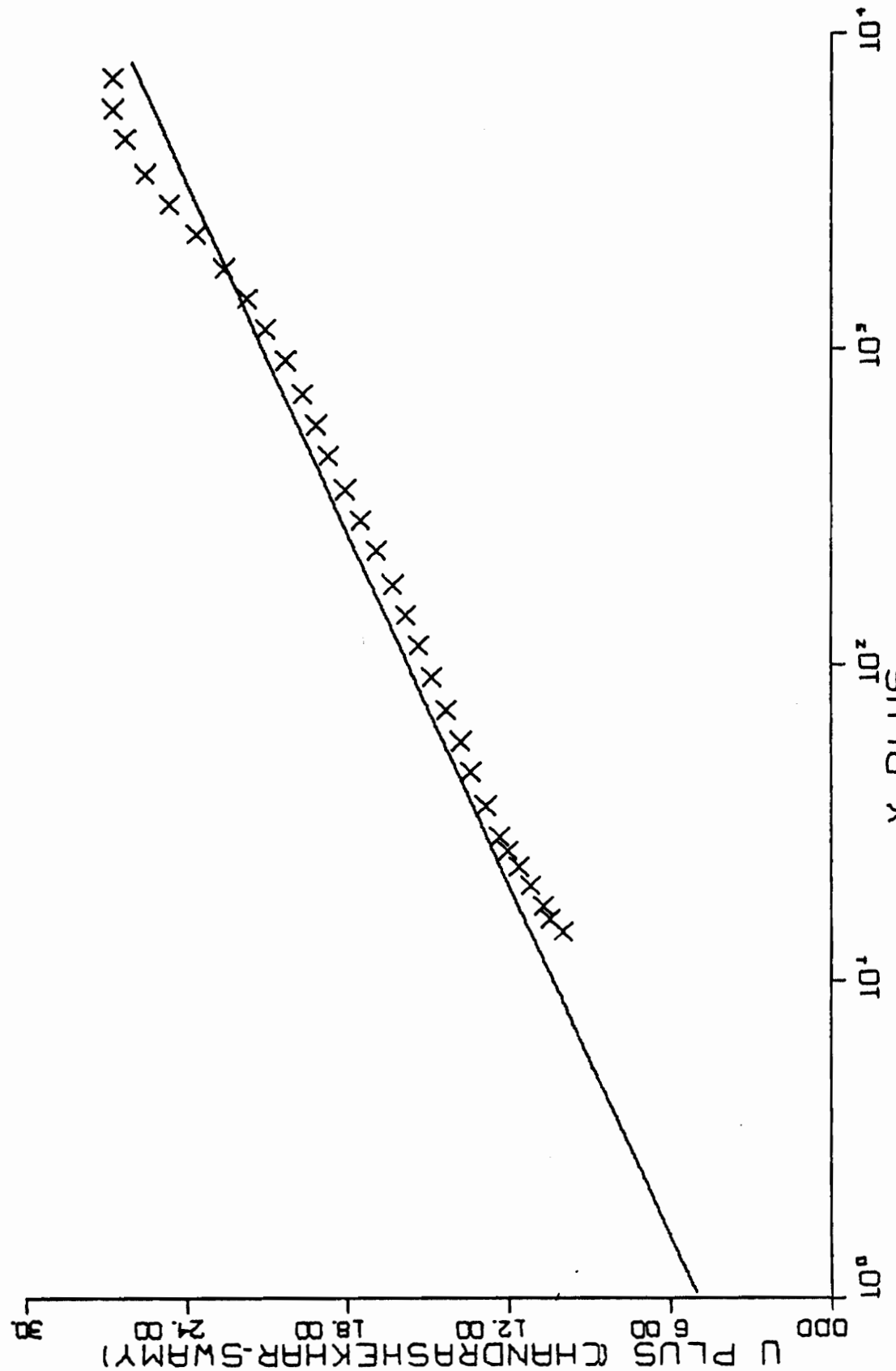

FIG. B25-4. THREE-DIMENSIONAL SIMILARITY PLOT-RUN I7-02.

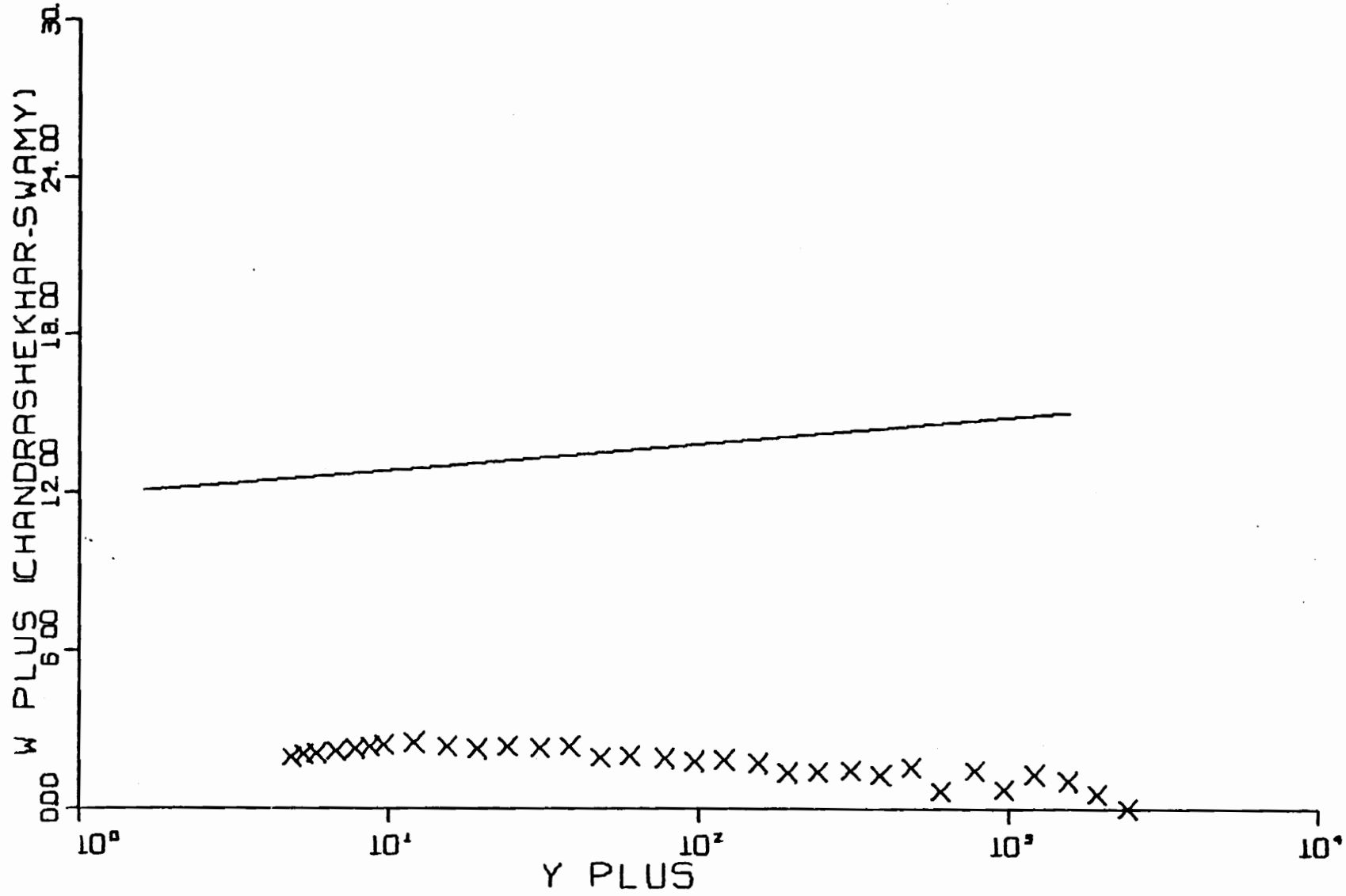

FIG. B25-4. CONTINUED FOR RUN I7-02.

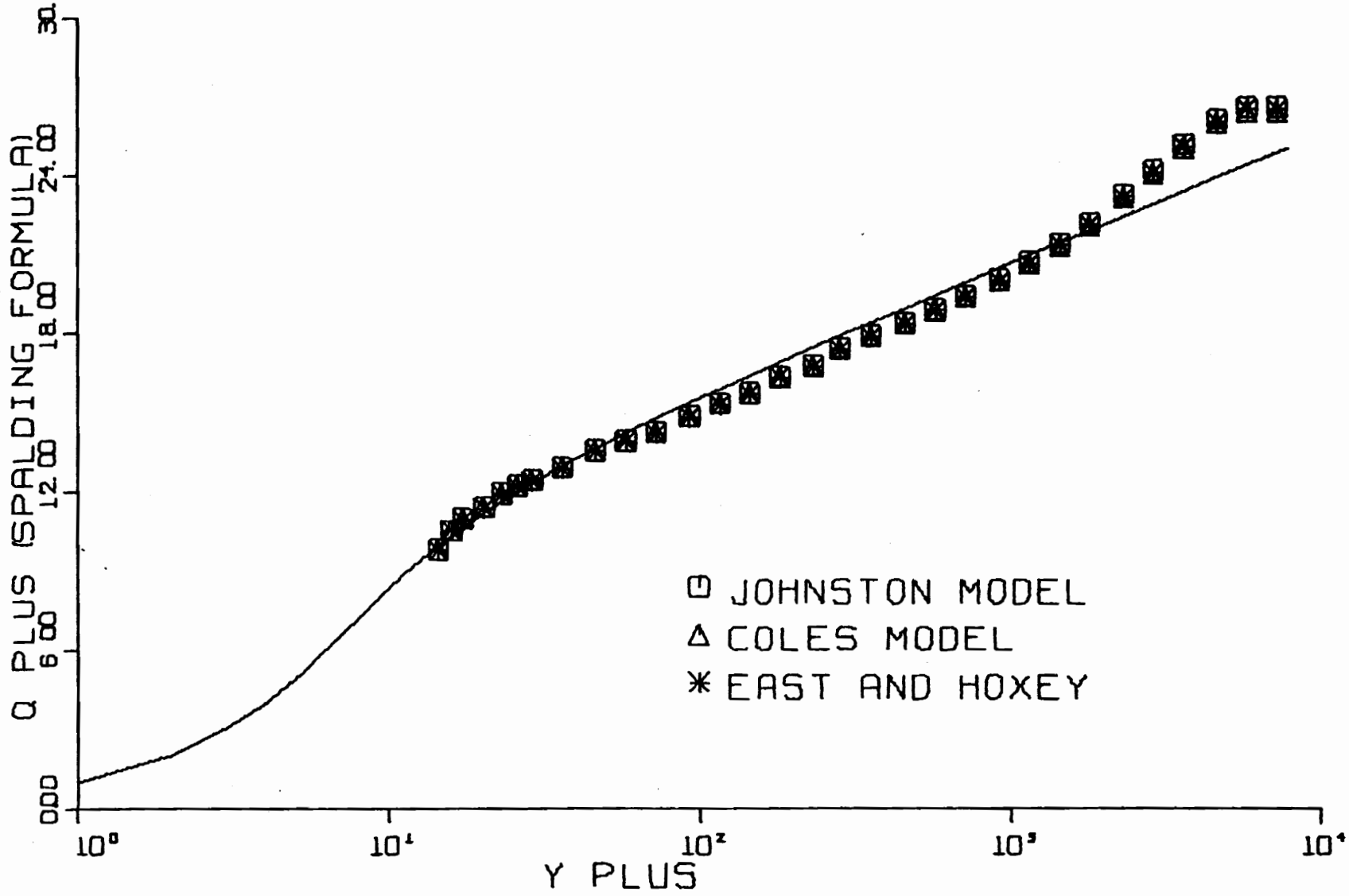

FIG. B26-1. THREE-DIMENSIONAL SIMILARITY PLOT-RUN I5-01.

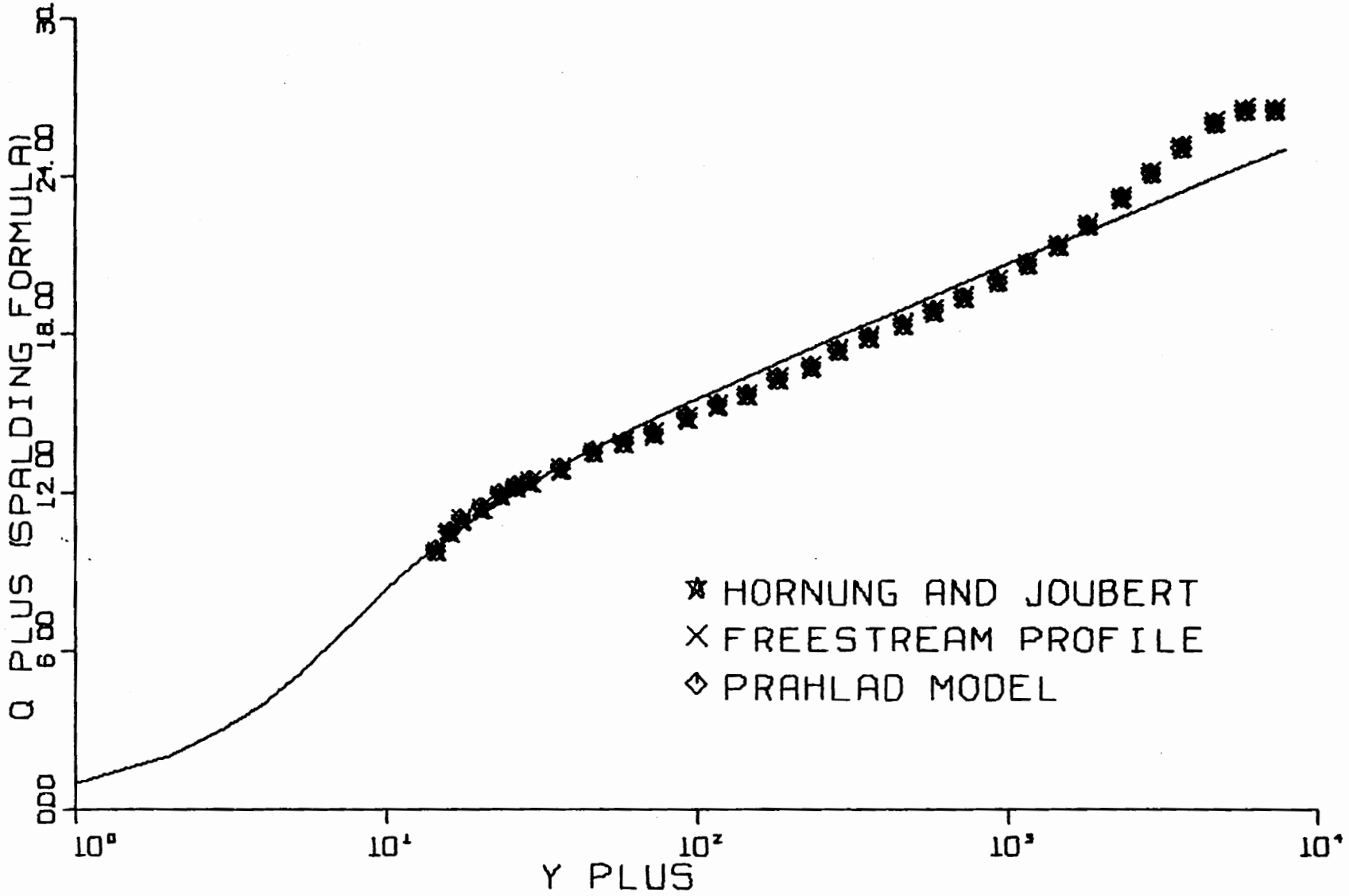

FIG. B26-2. THREE-DIMENSIONAL SIMILARITY PLOT-RUN I5-01.

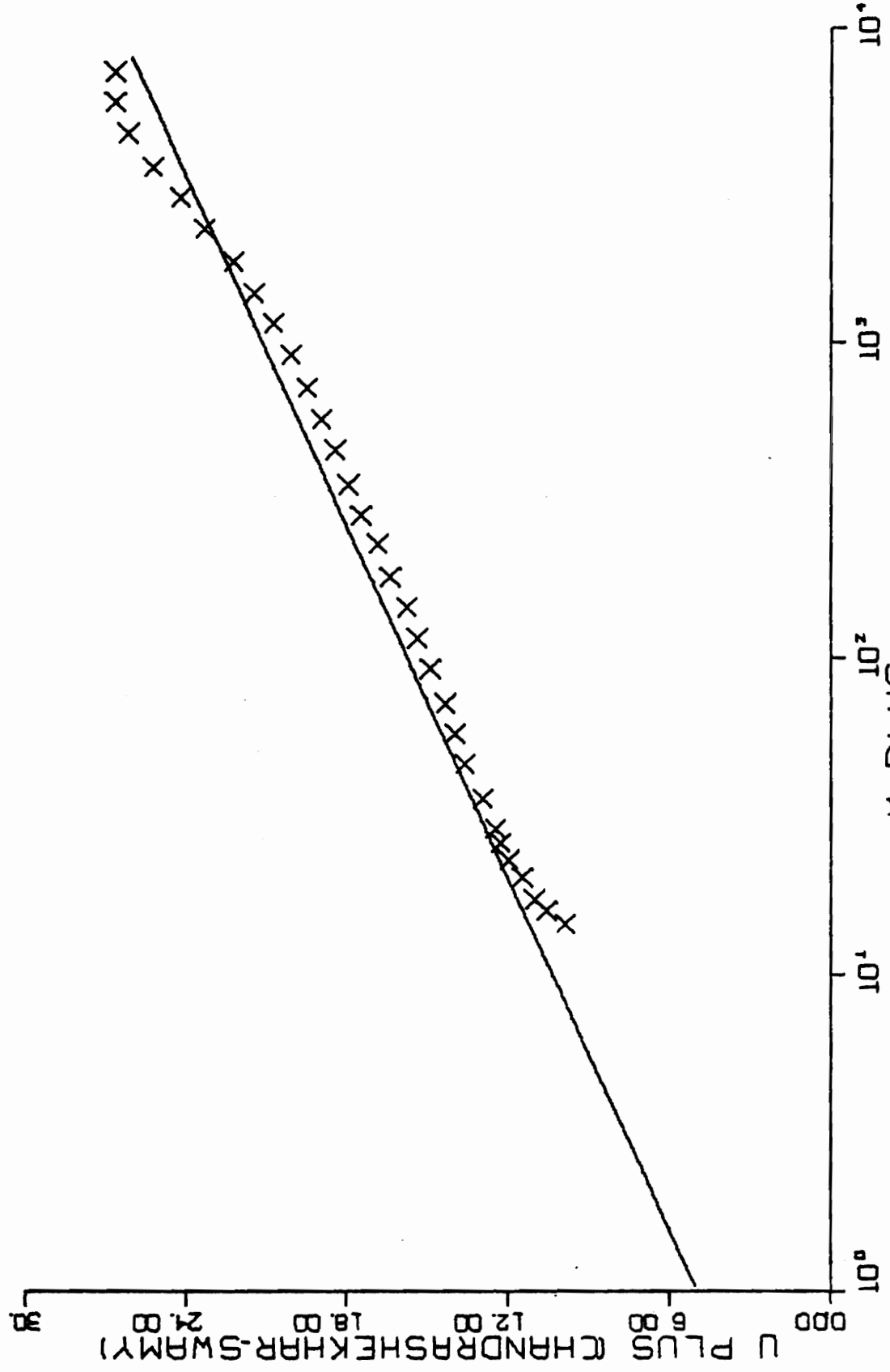

FIG. B26-4. THREE-DIMENSIONAL SIMILARITY PLOT.RUN 15-01.

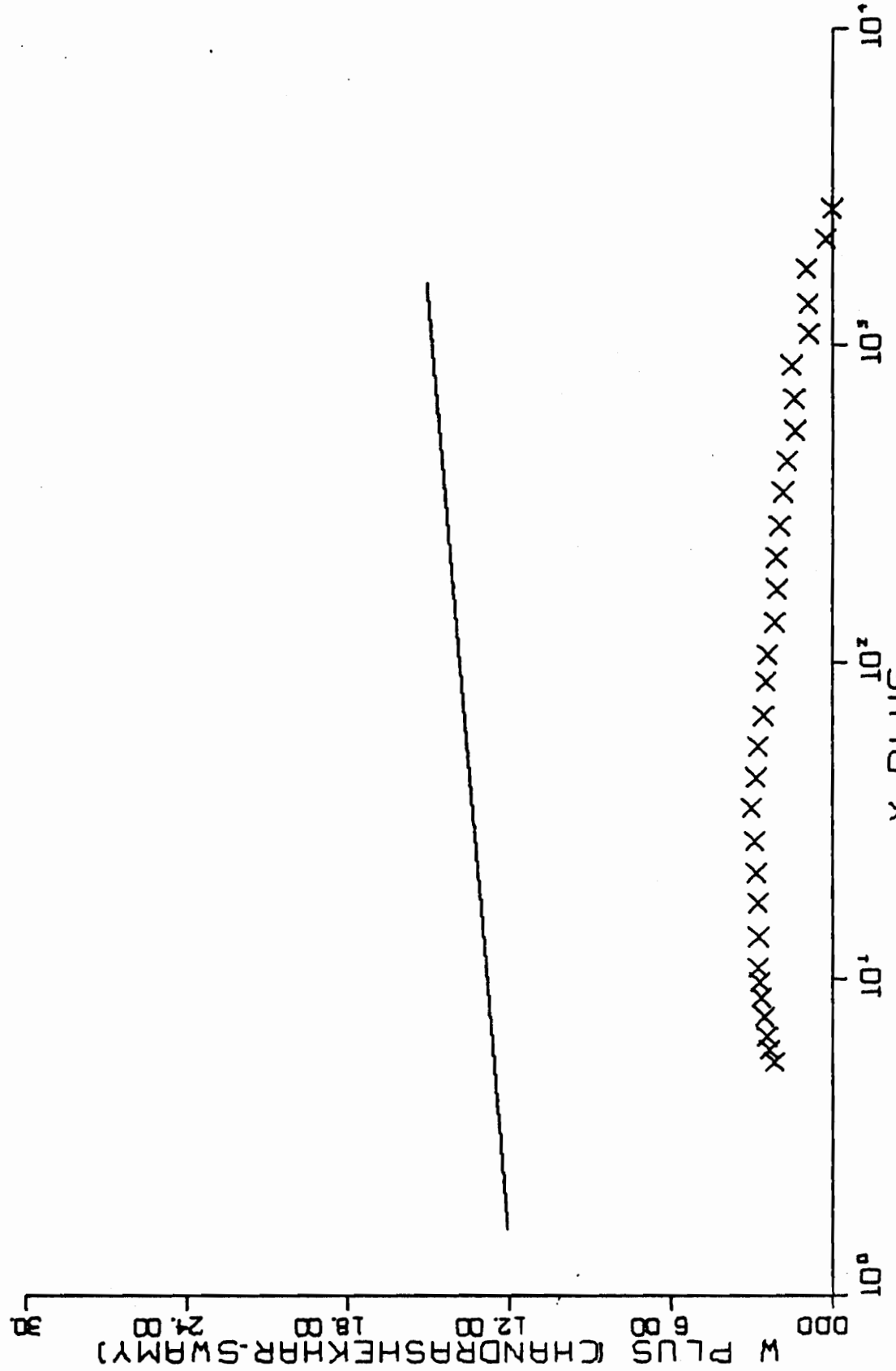

FIG. B26-4. CONTINUED FOR RUN 15-01.

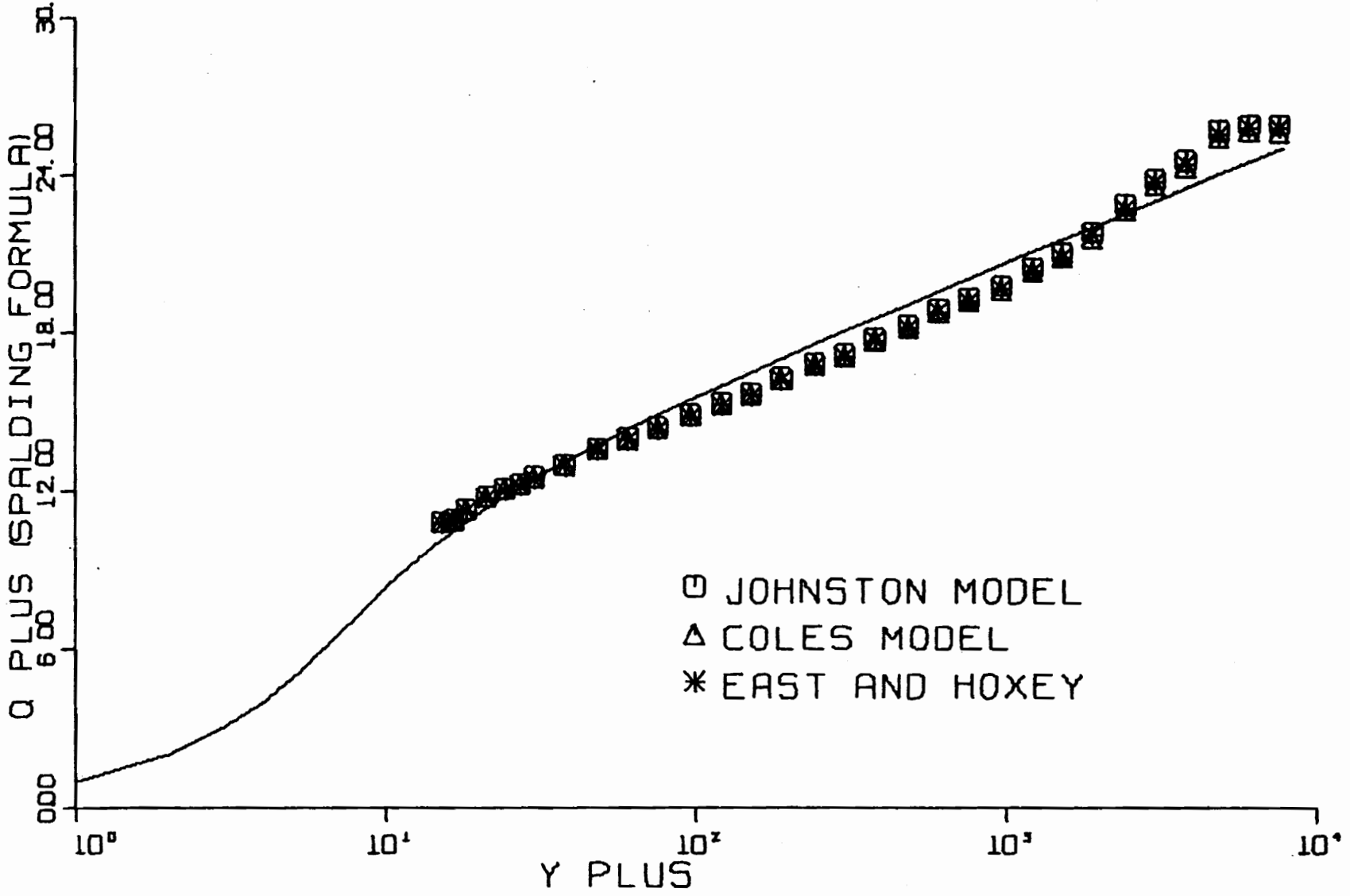

FIG. B27-1. THREE-DIMENSIONAL SIMILARITY PLOT-RUN I3-01.

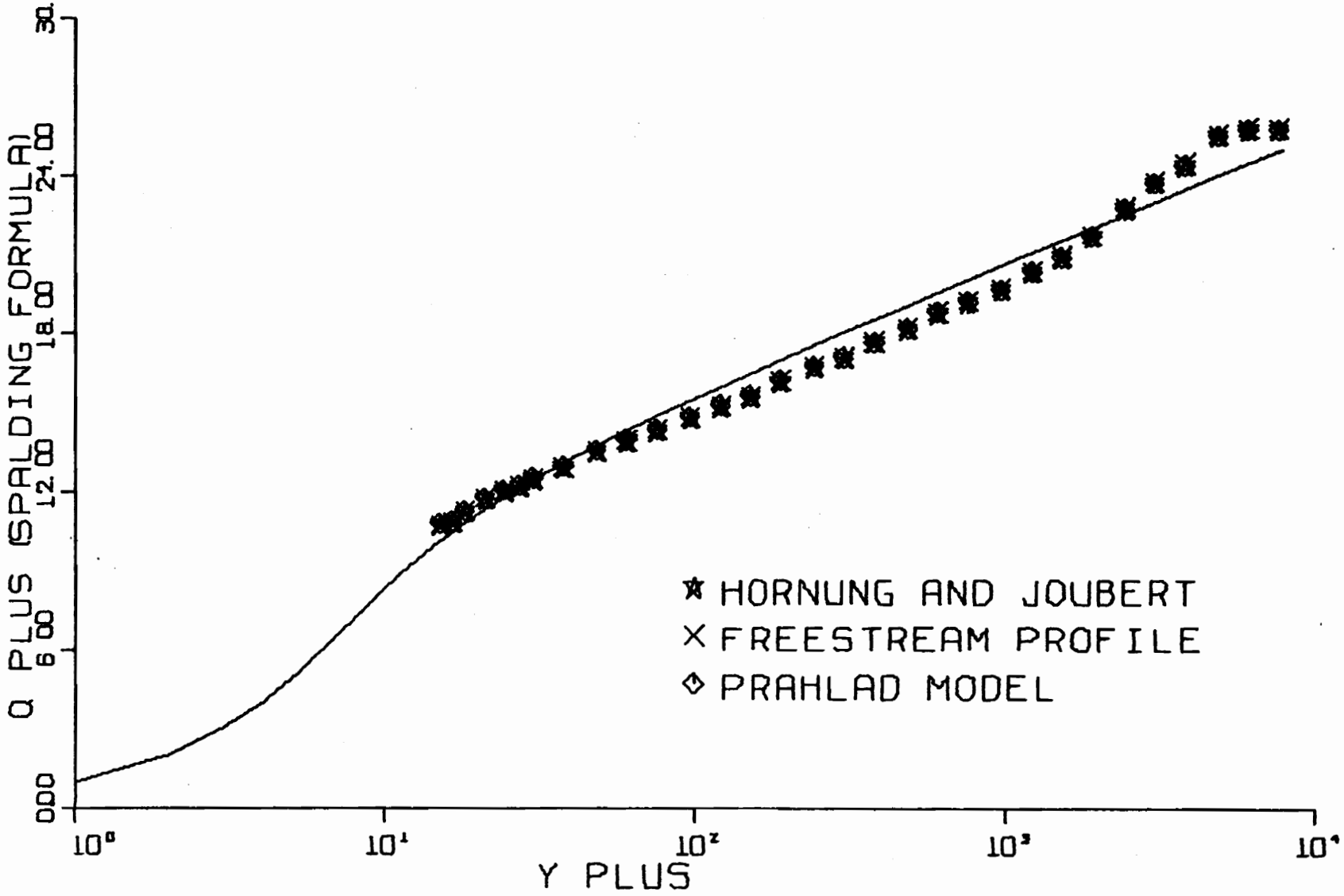

FIG. B27-2. THREE-DIMENSIONAL SIMILARITY PLOT-RUN I3-01.

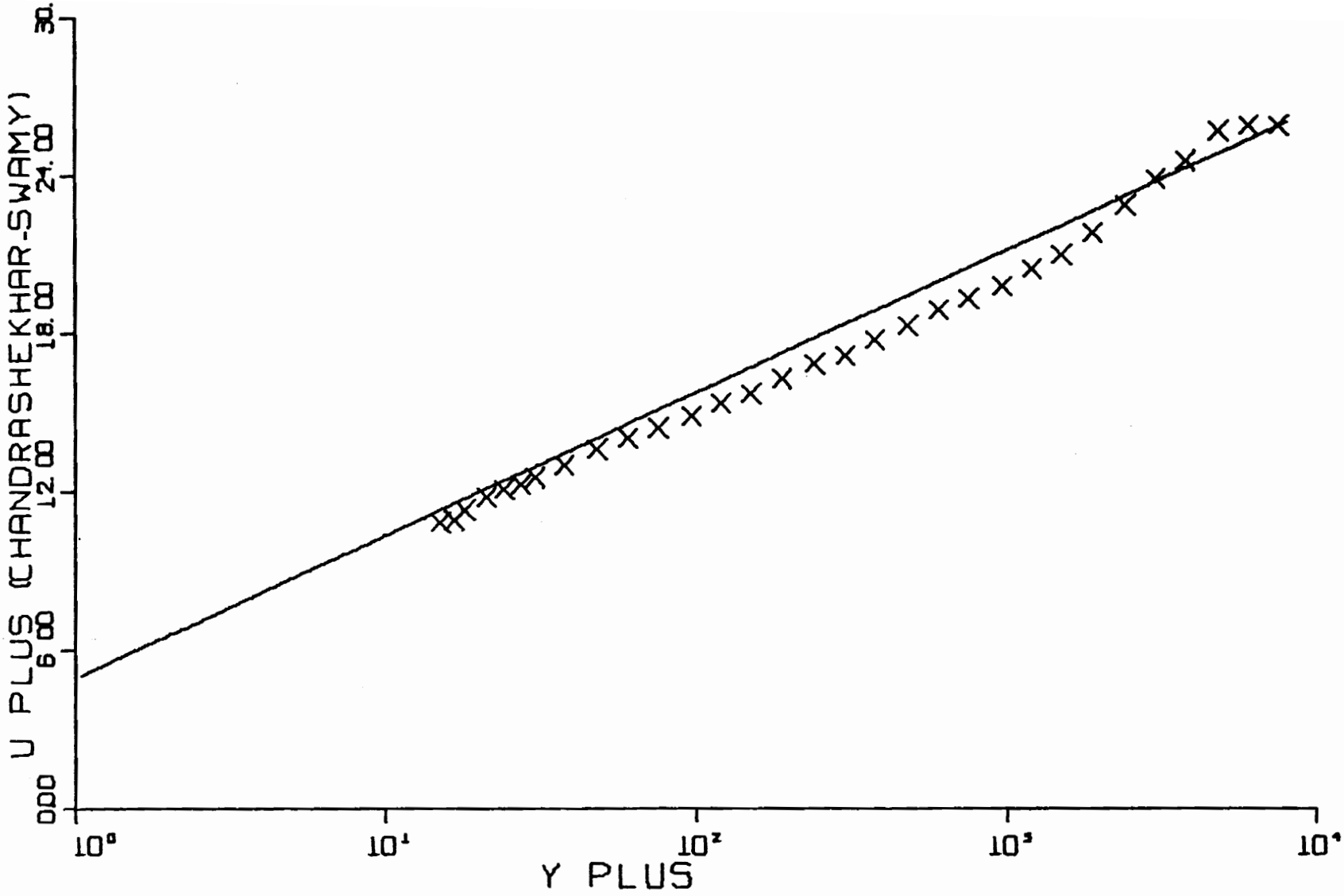

FIG. B27-4. THREE-DIMENSIONAL SIMILARITY PLOT-RUN I3-01.

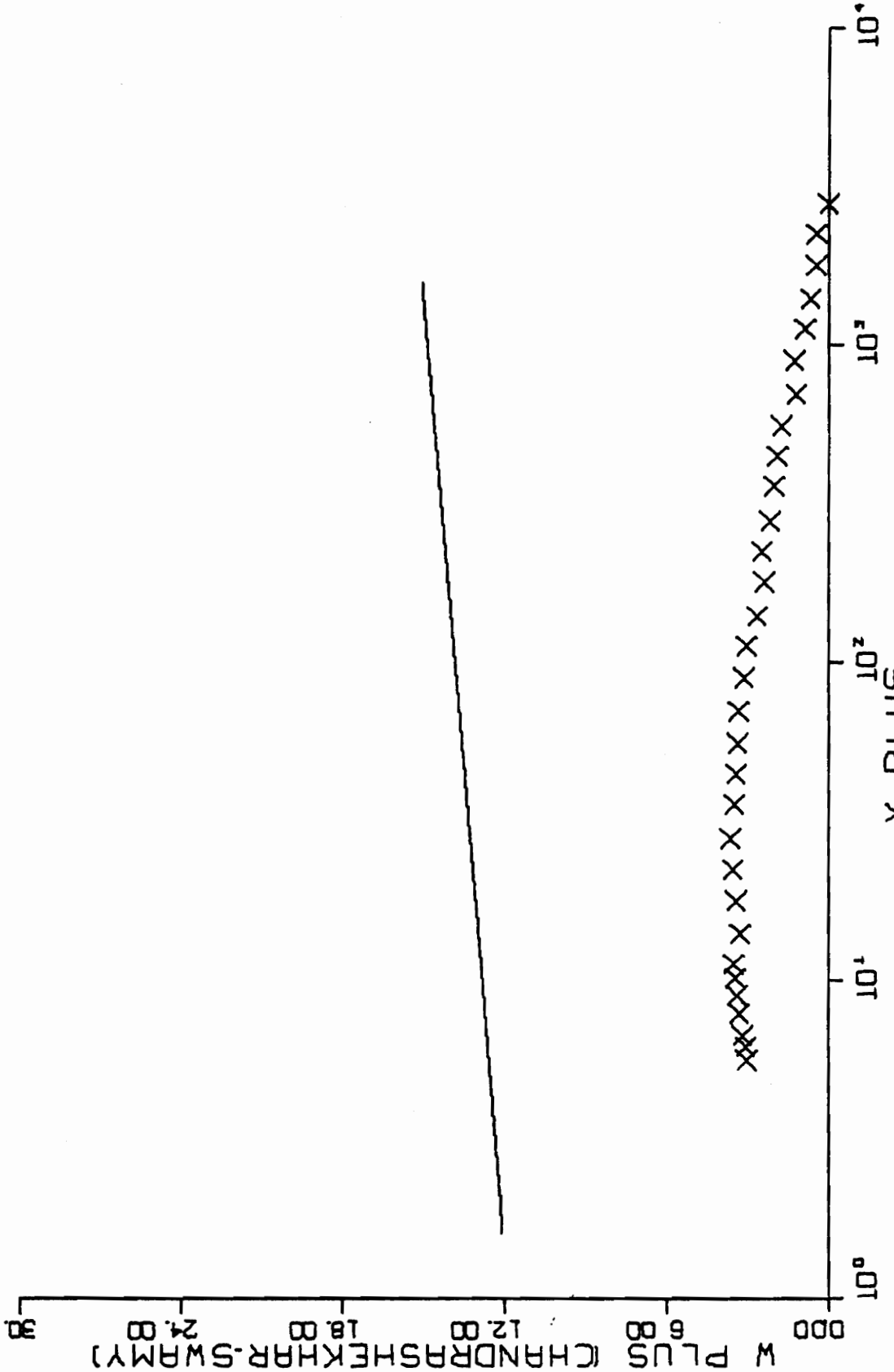

FIG. B27-4. CONTINUED FOR RUN I3-01.

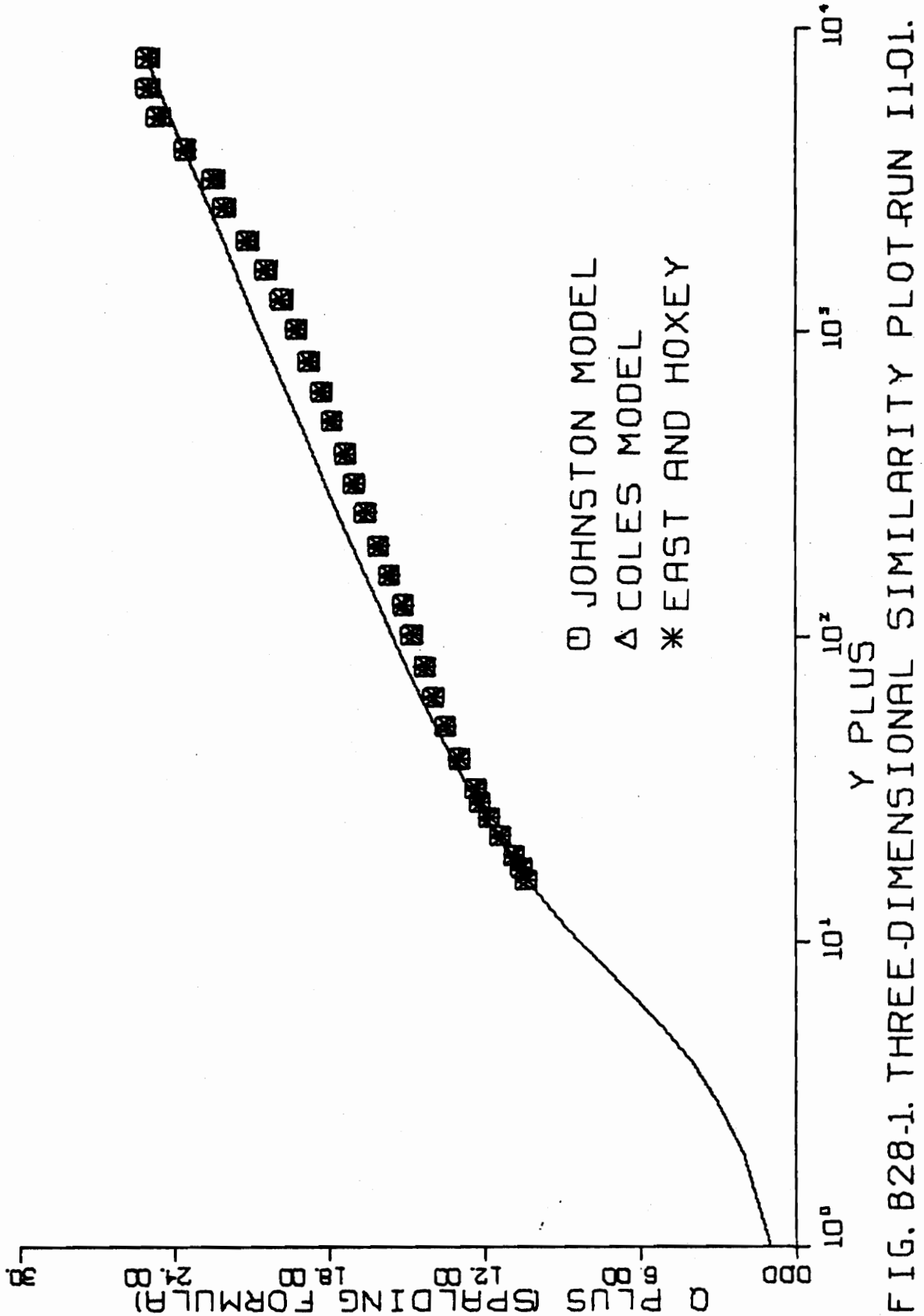

FIG. B28-1. THREE-DIMENSIONAL SIMILARITY PLOT-RUN I1-01.

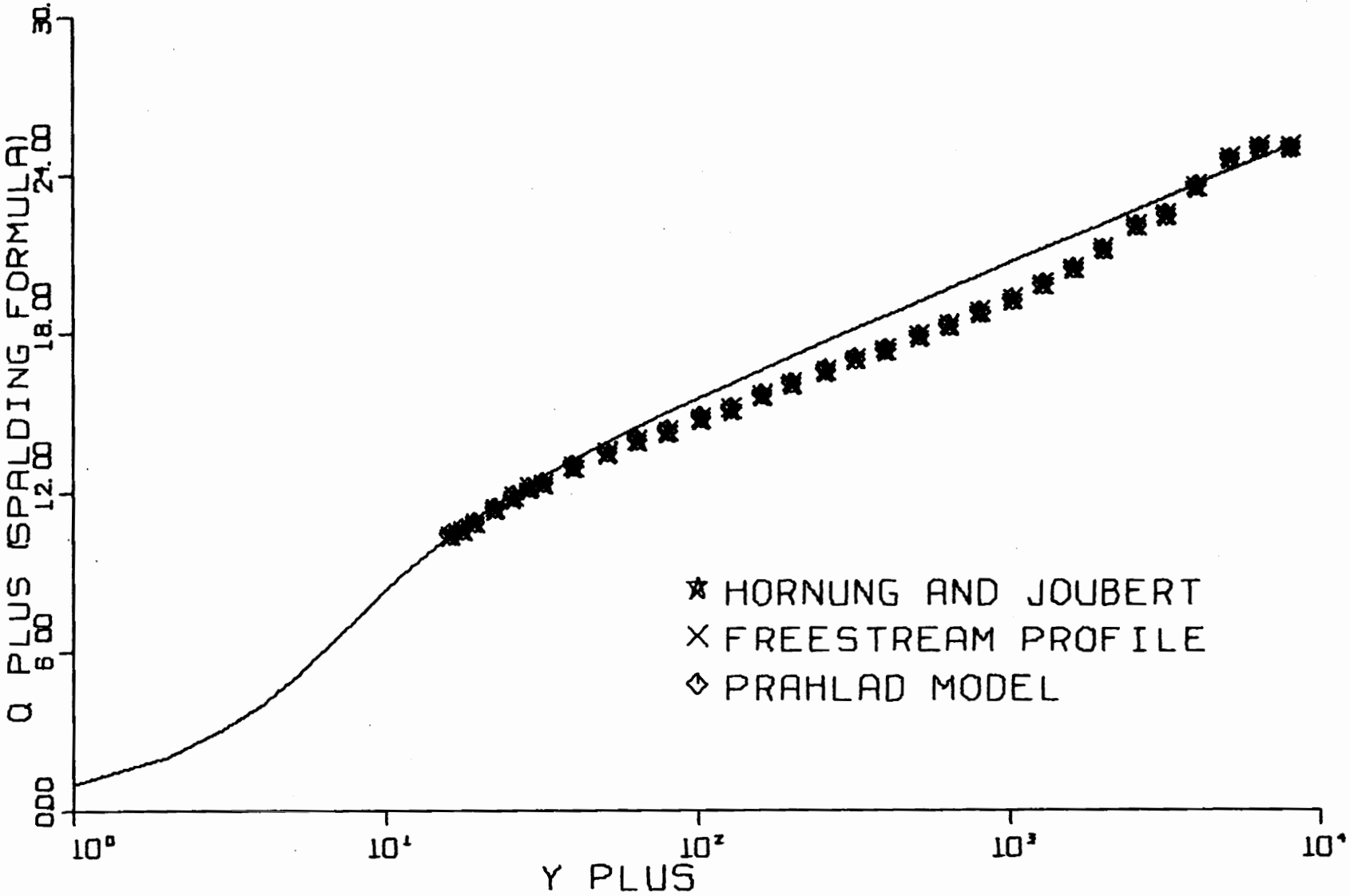

FIG. B28-2. THREE-DIMENSIONAL SIMILARITY PLOT-RUN I1-01.

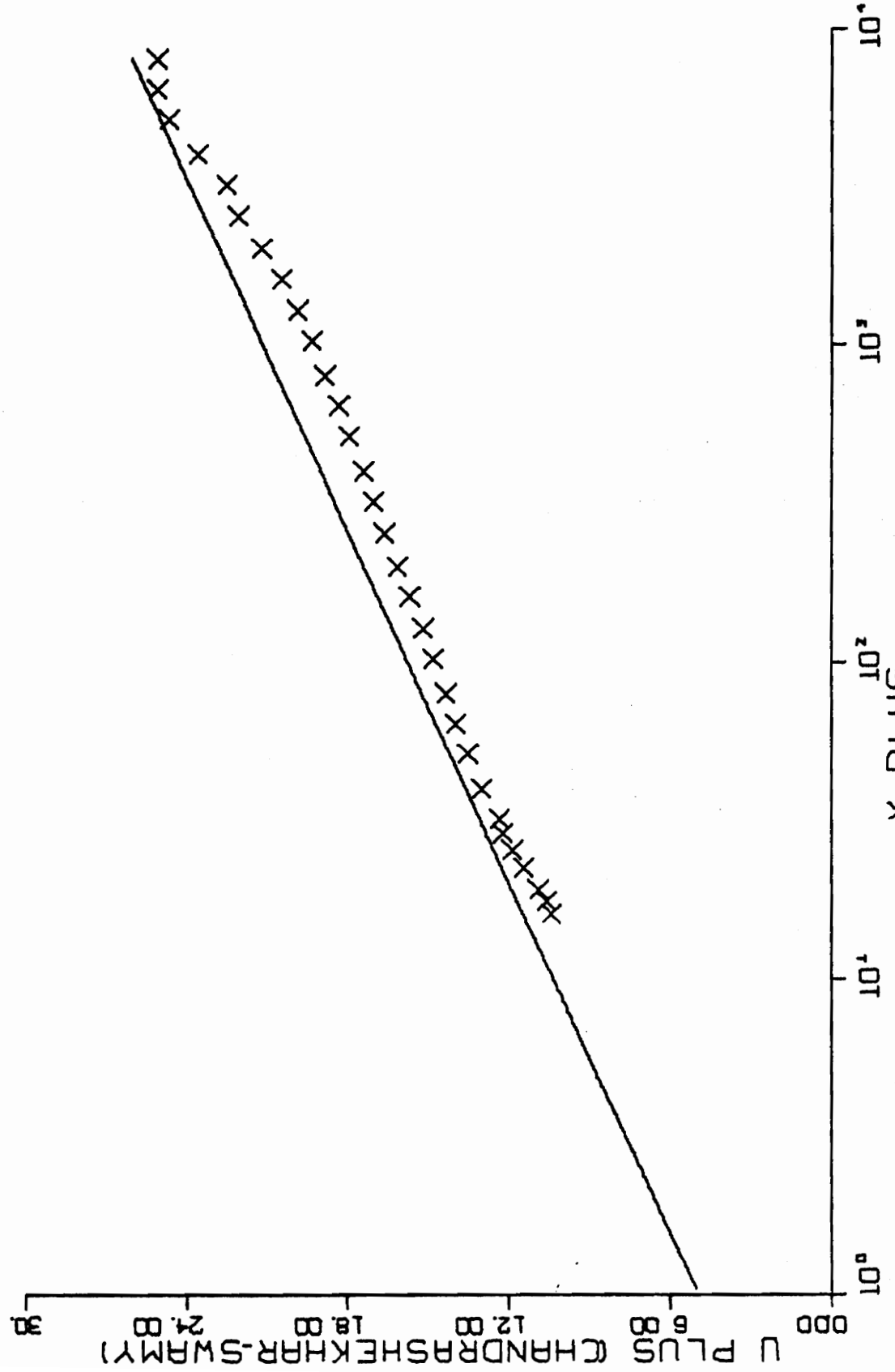

FIG. B28-4. THREE-DIMENSIONAL SIMILARITY PLOT-RUN I1-01.

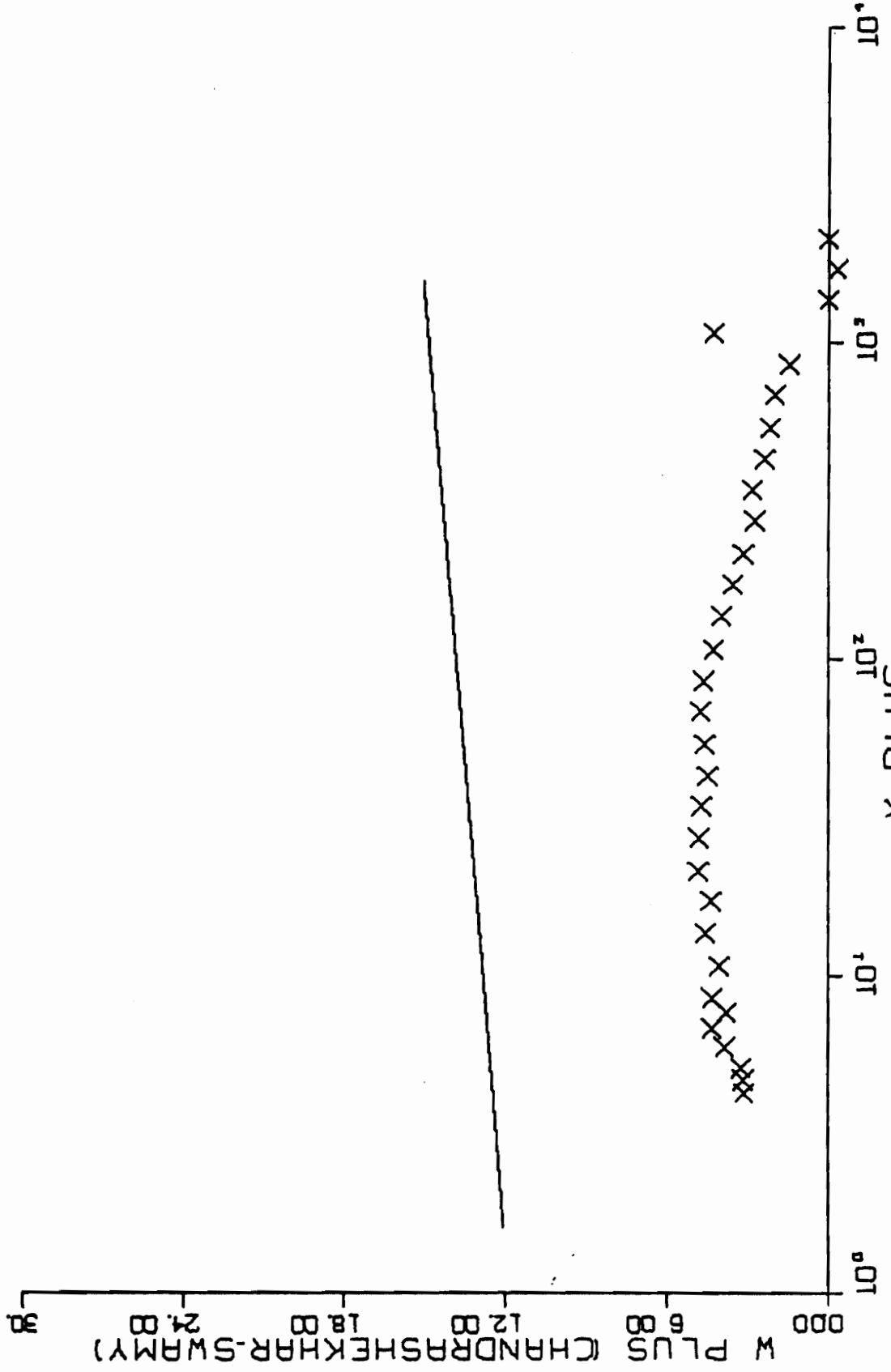

FIG. B28-4. CONTINUED FOR RUN 11-01.

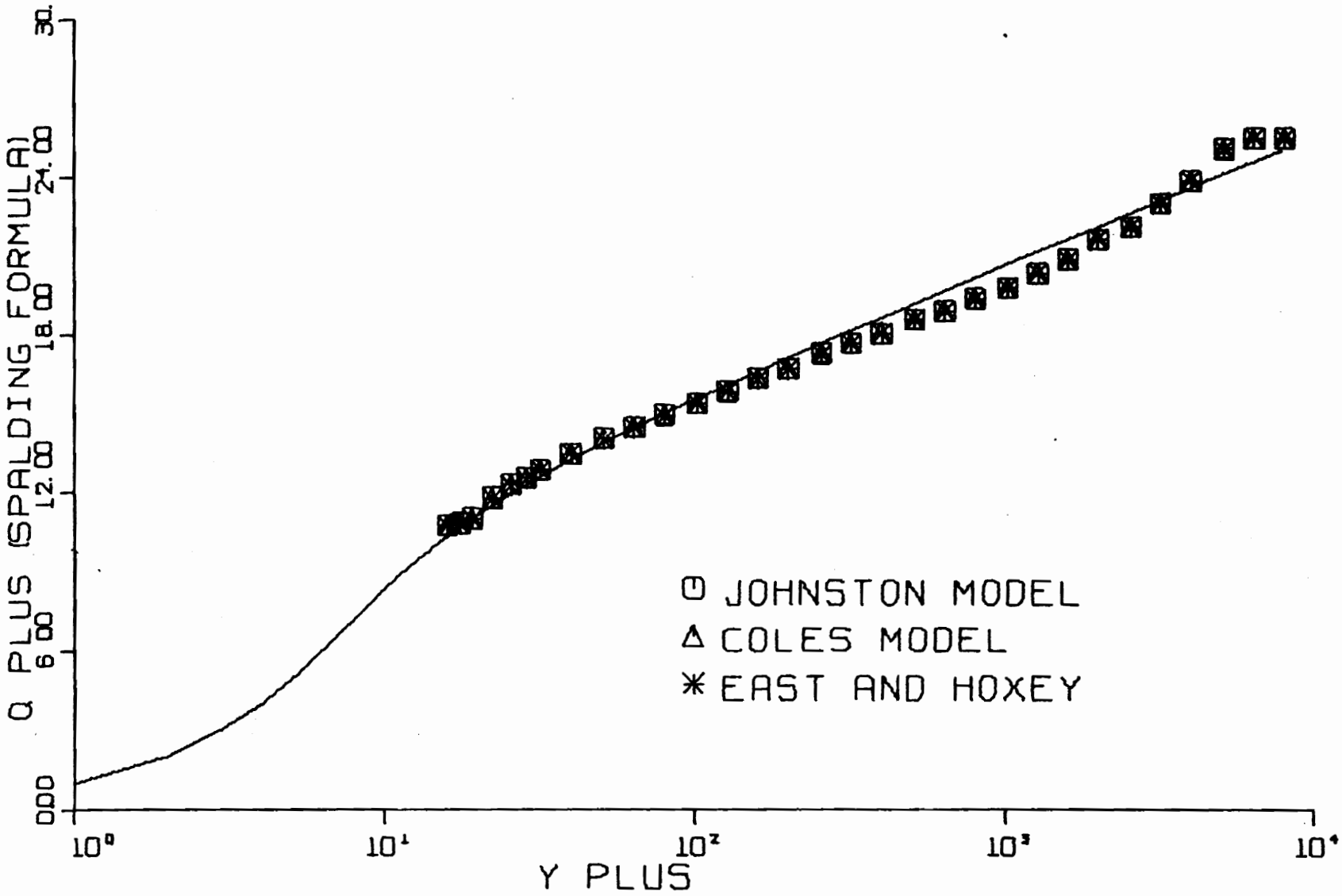

FIG. B29-1. THREE-DIMENSIONAL SIMILARITY PLOT-RUN I-1-01.

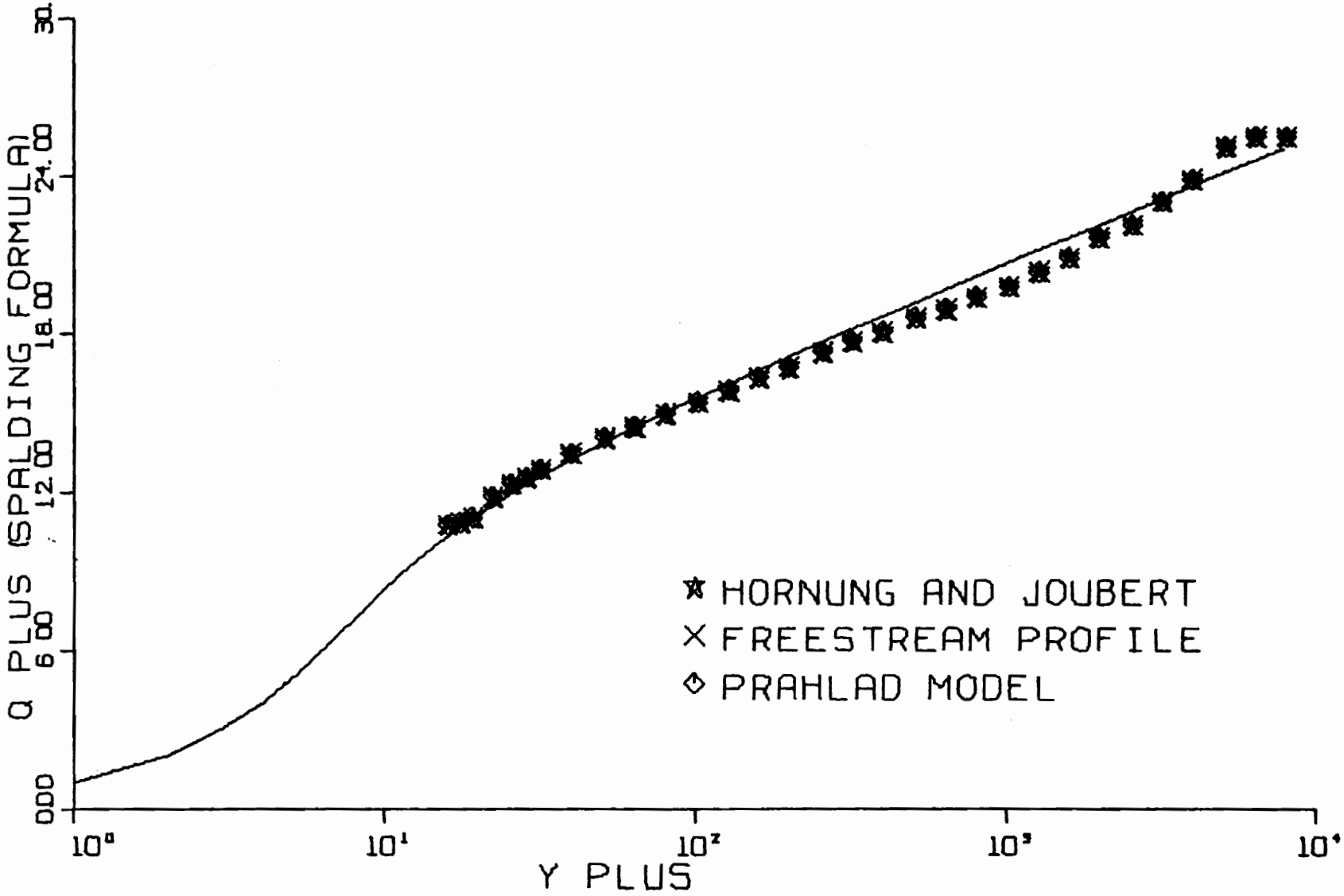

FIG. B29-2. THREE-DIMENSIONAL SIMILARITY PLOT-RUN I-1-01.

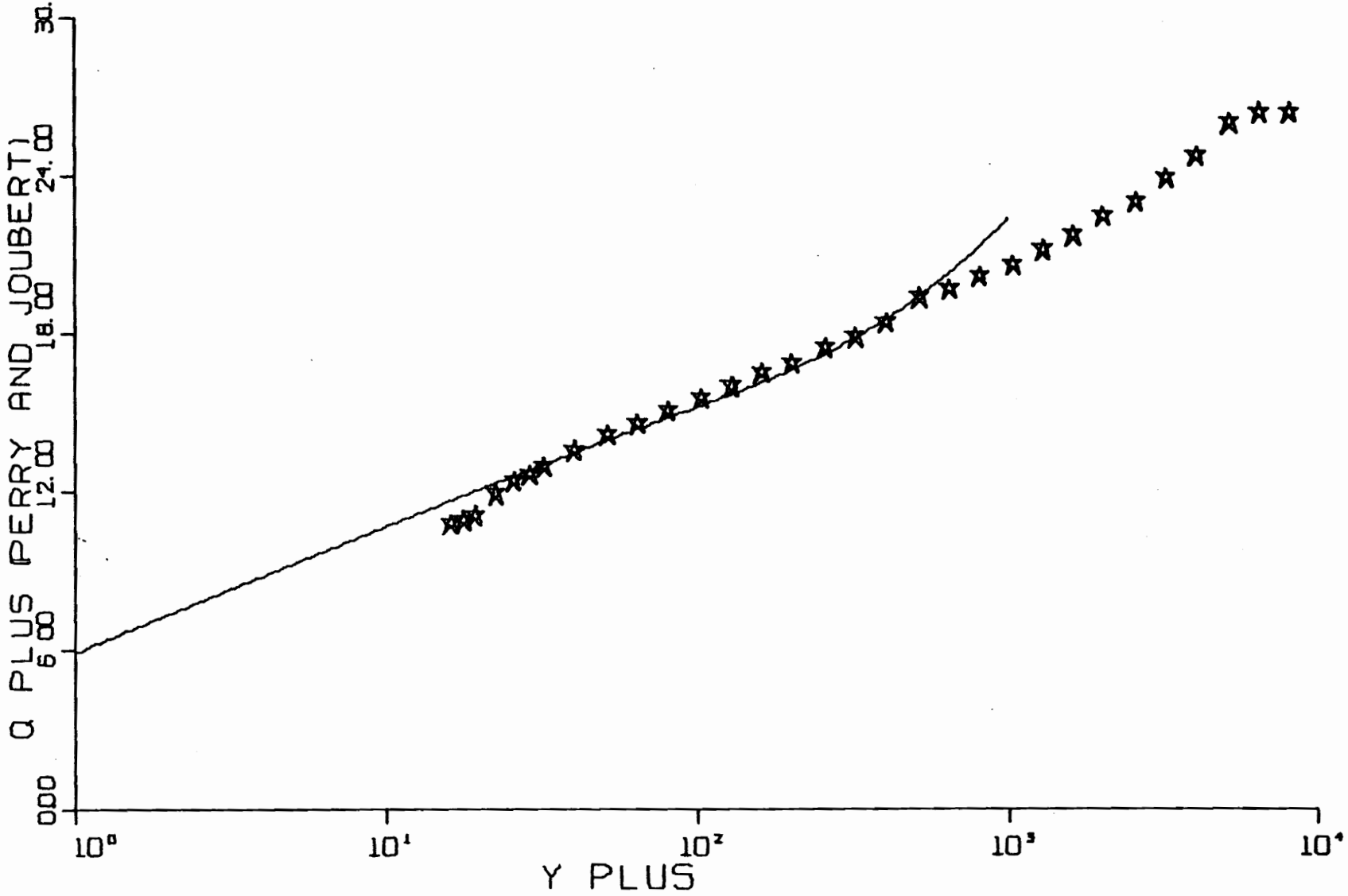

FIG. B29-3. THREE-DIMENSIONAL SIMILARITY PLOT-RUN I-1-01.

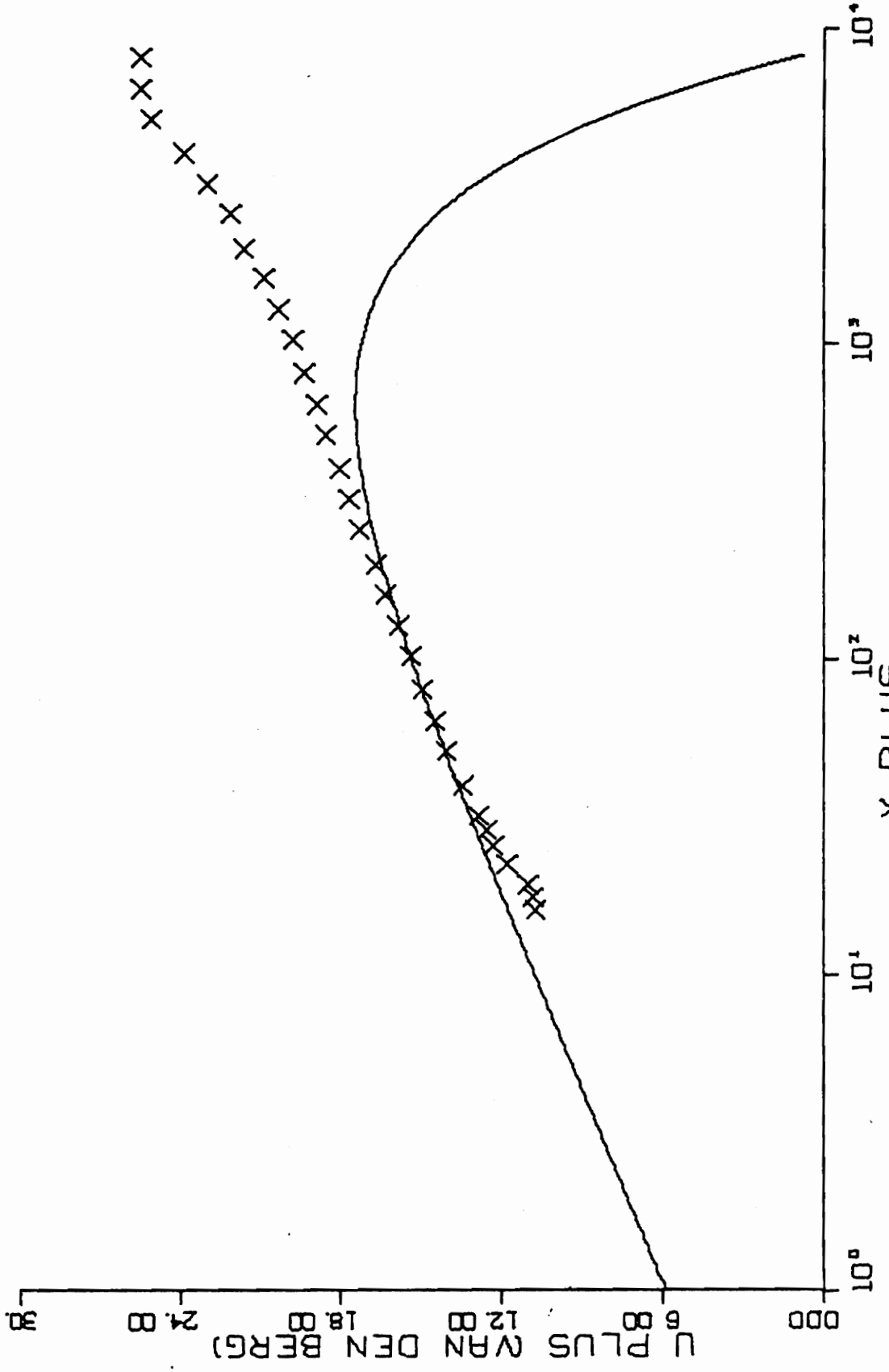

FIG. B29-4. THREE-DIMENSIONAL SIMILARITY PLOT-RUN I-1-01.

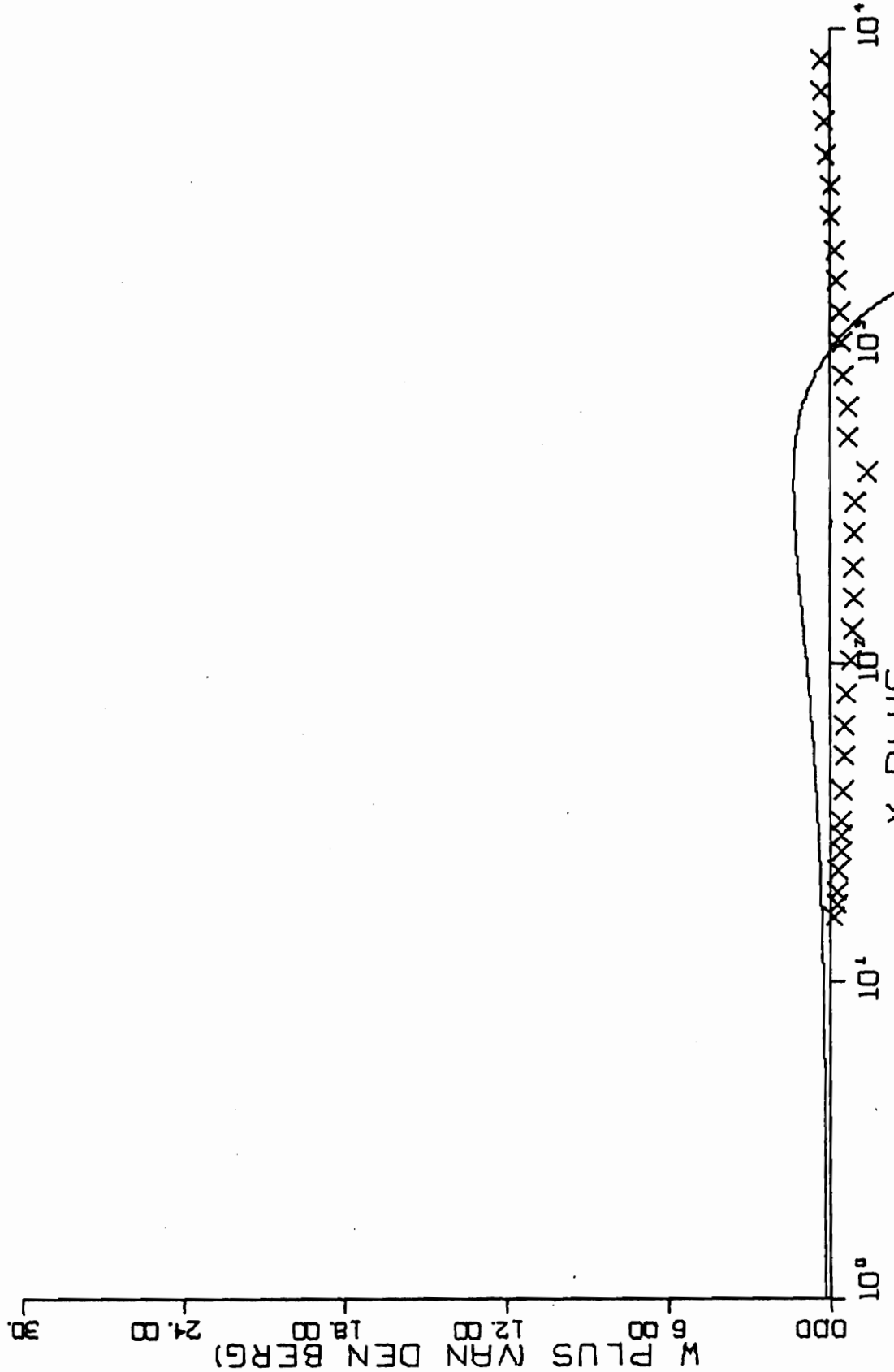

FIG. B29-4. CONTINUED FOR RUN I-1-01.

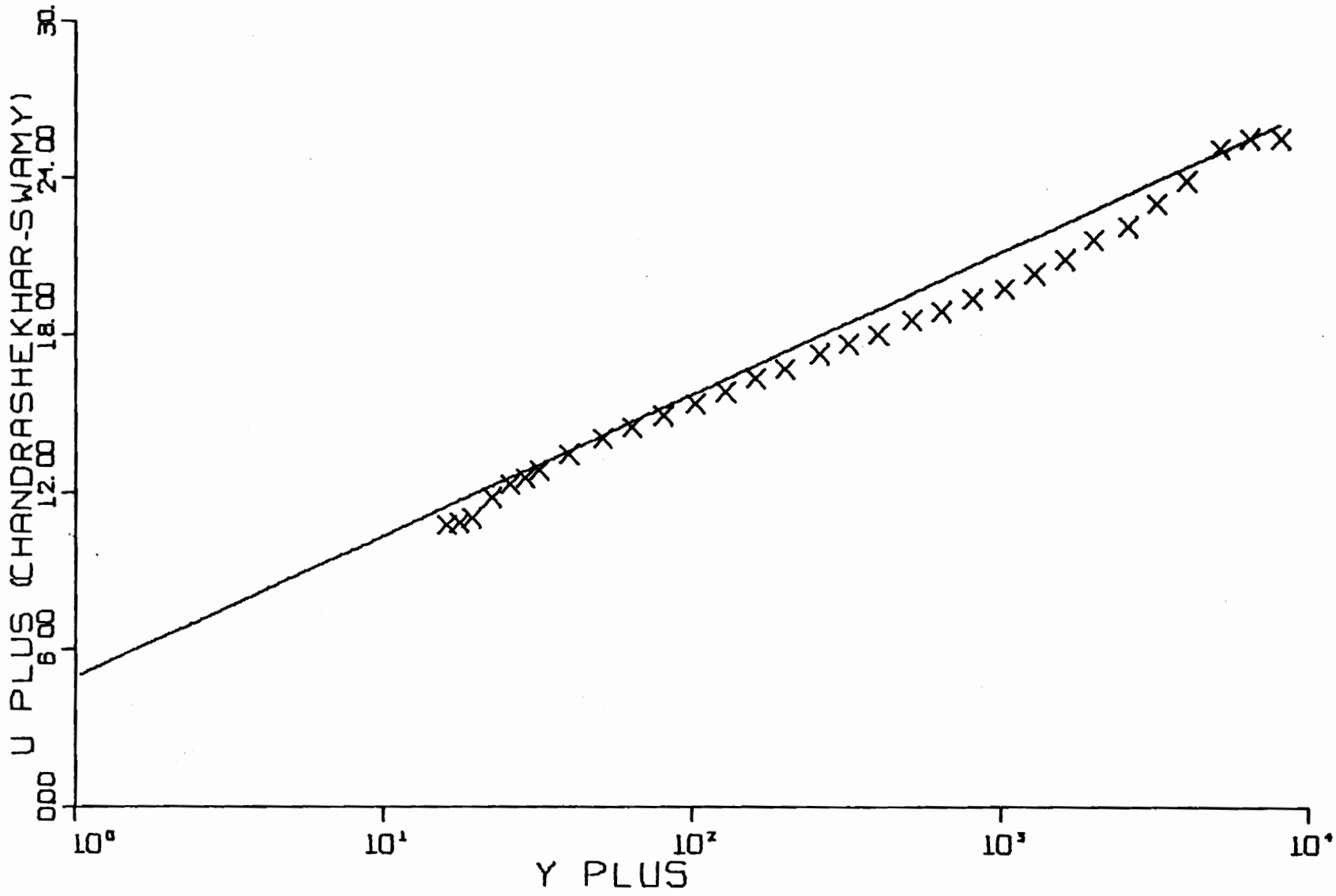

FIG. B29-5. THREE-DIMENSIONAL SIMILARITY PLOT-RUN I-1-01.

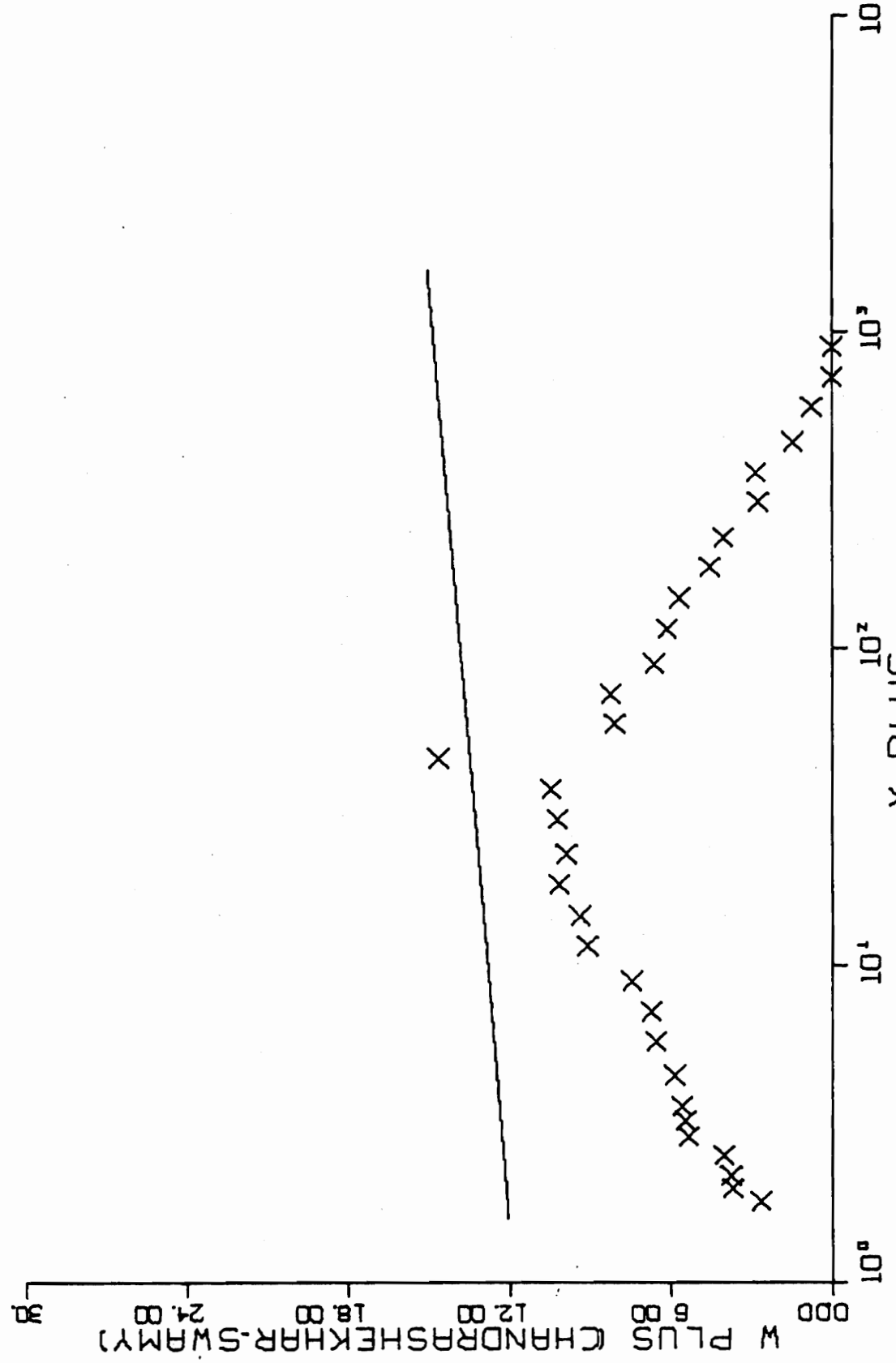

FIG. B29-5. CONTINUED FOR RUN I-1-01.

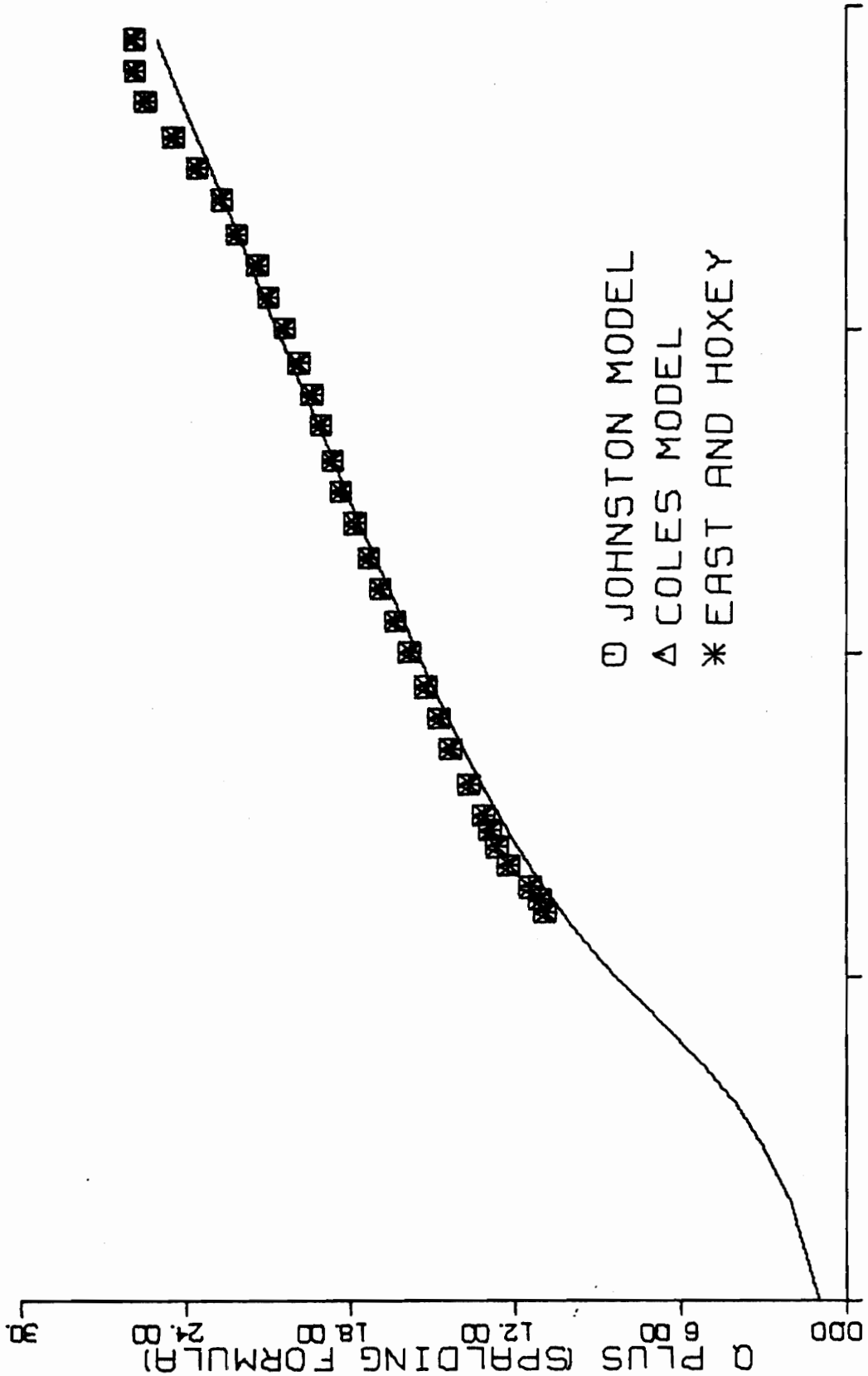

FIG. B30-1. THREE-DIMENSIONAL SIMILARITY PLOT-RUN I-3-01.

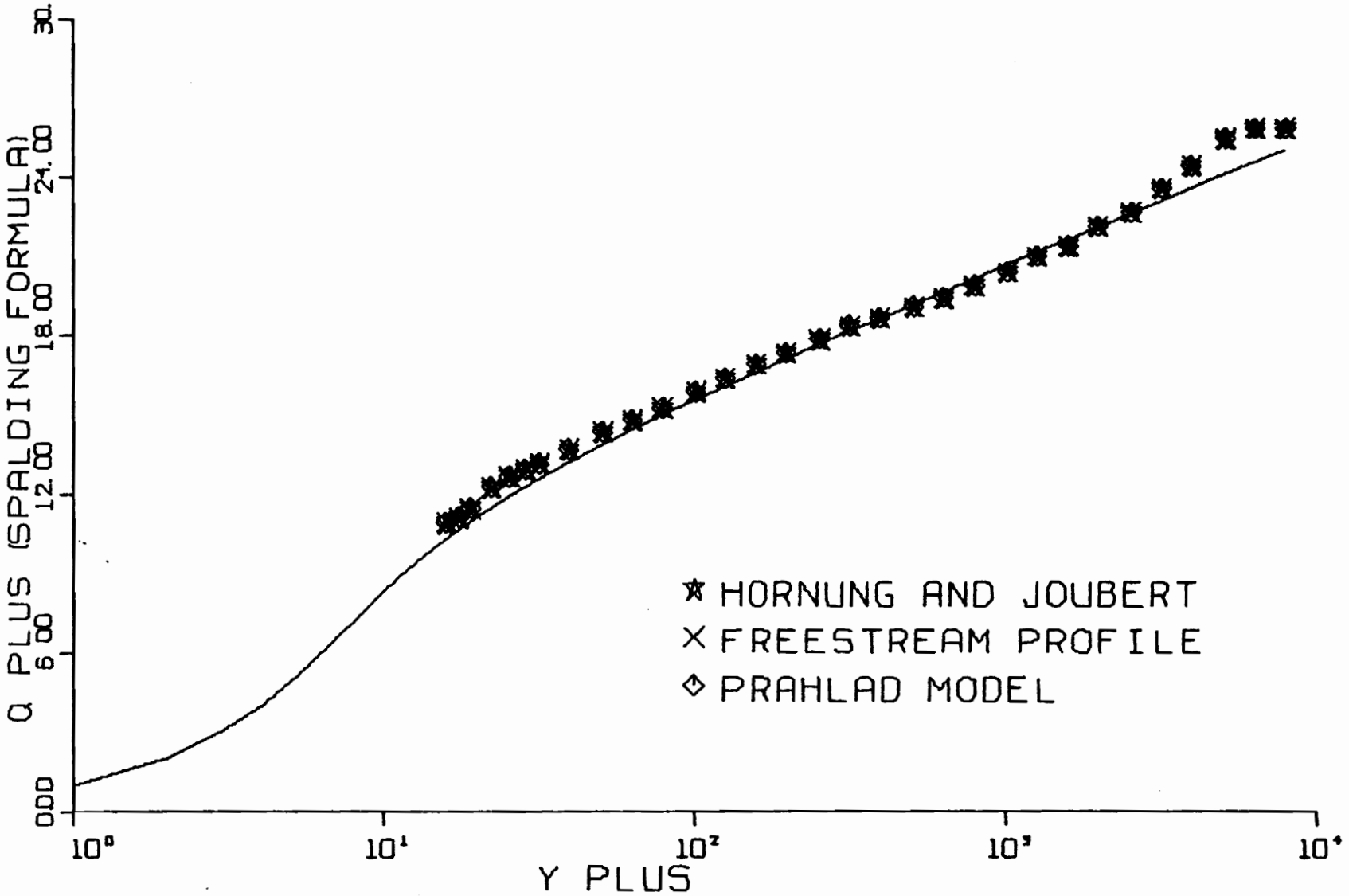

FIG. B30-2. THREE-DIMENSIONAL SIMILARITY PLOT-RUN I-3-01.

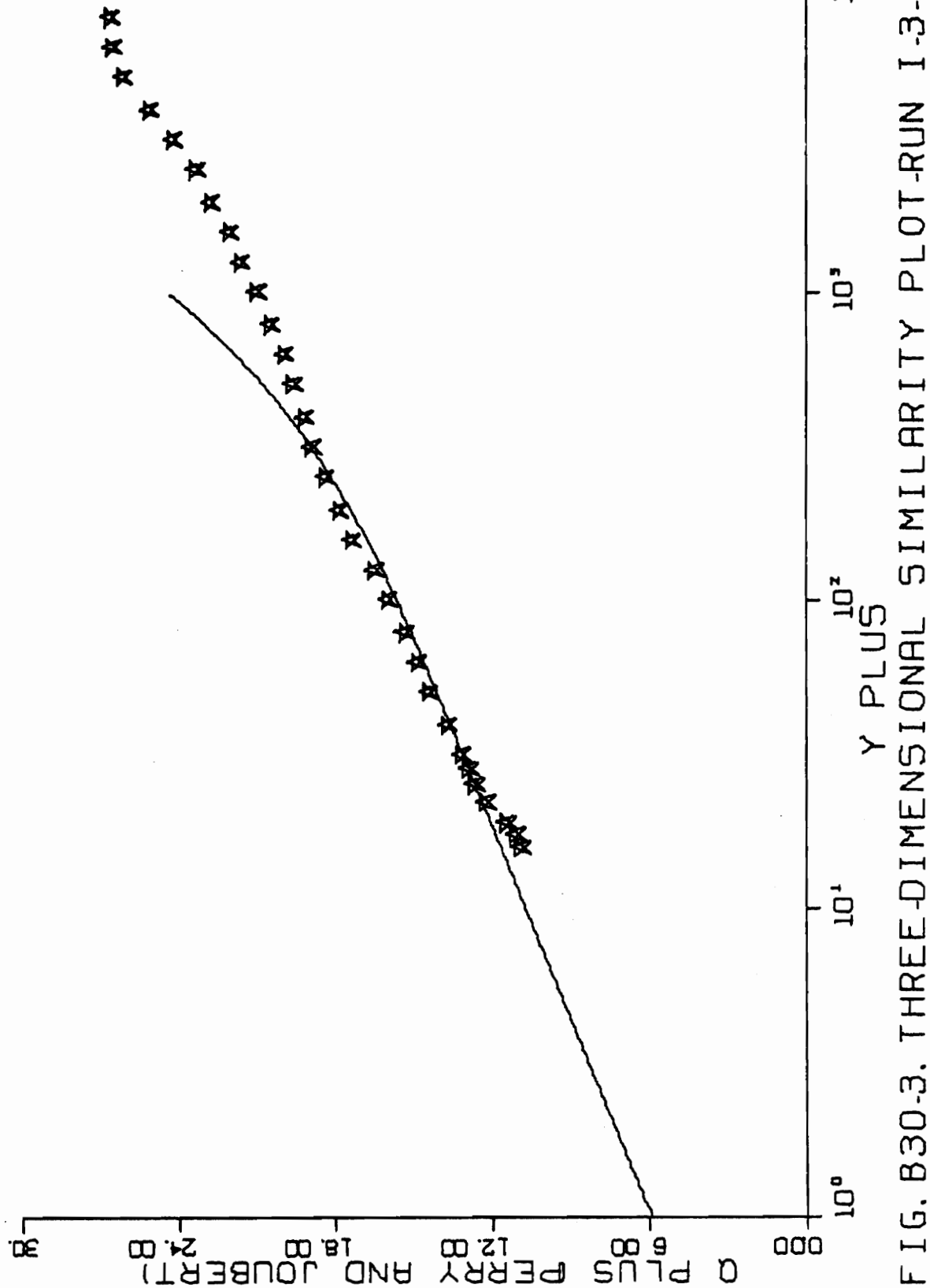

FIG. B30-3. THREE-DIMENSIONAL SIMILARITY PLOT-RUN I-3-01.

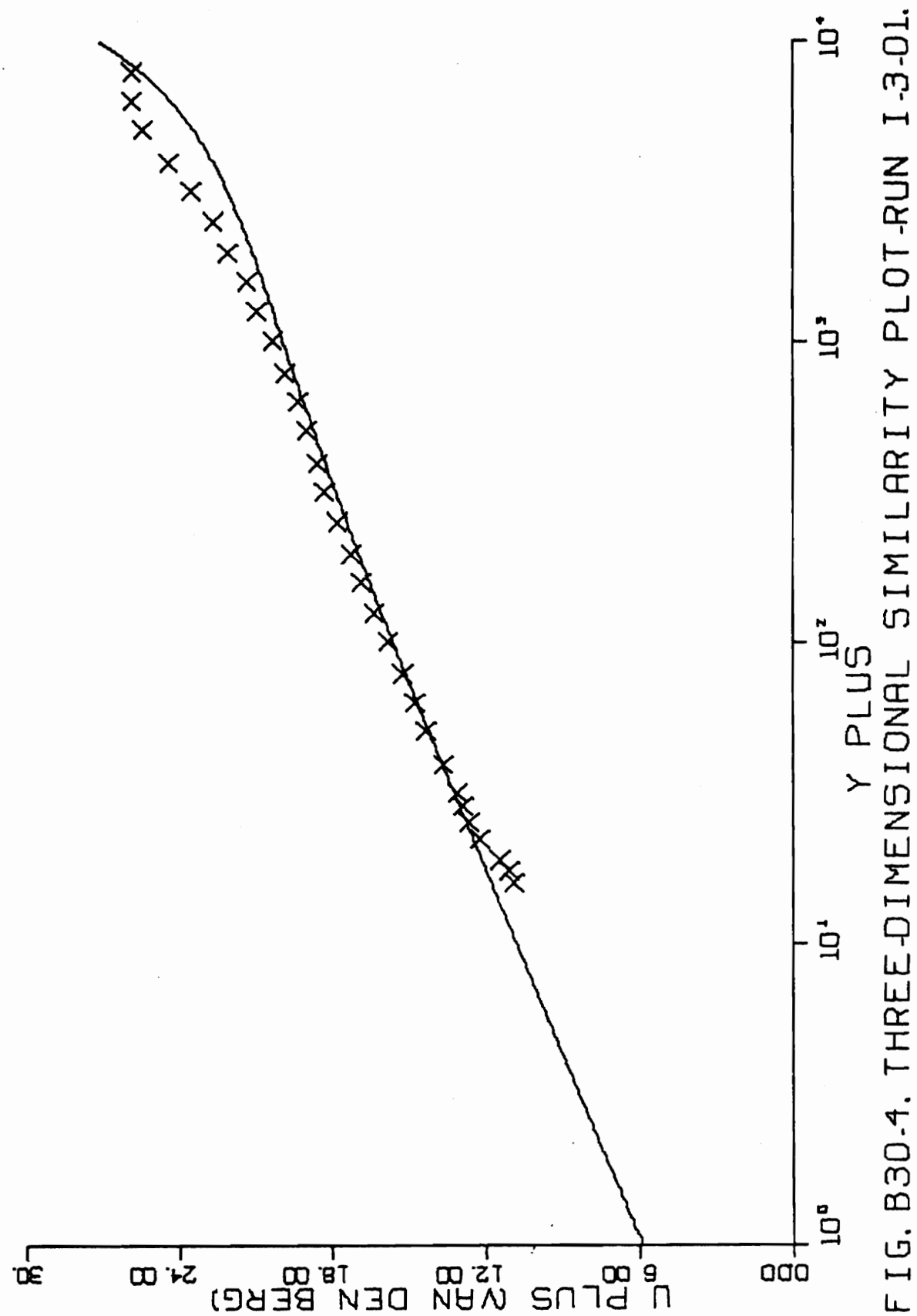

FIG. B30-4. THREE-DIMENSIONAL SIMILARITY PLOT-RUN I-3-01.

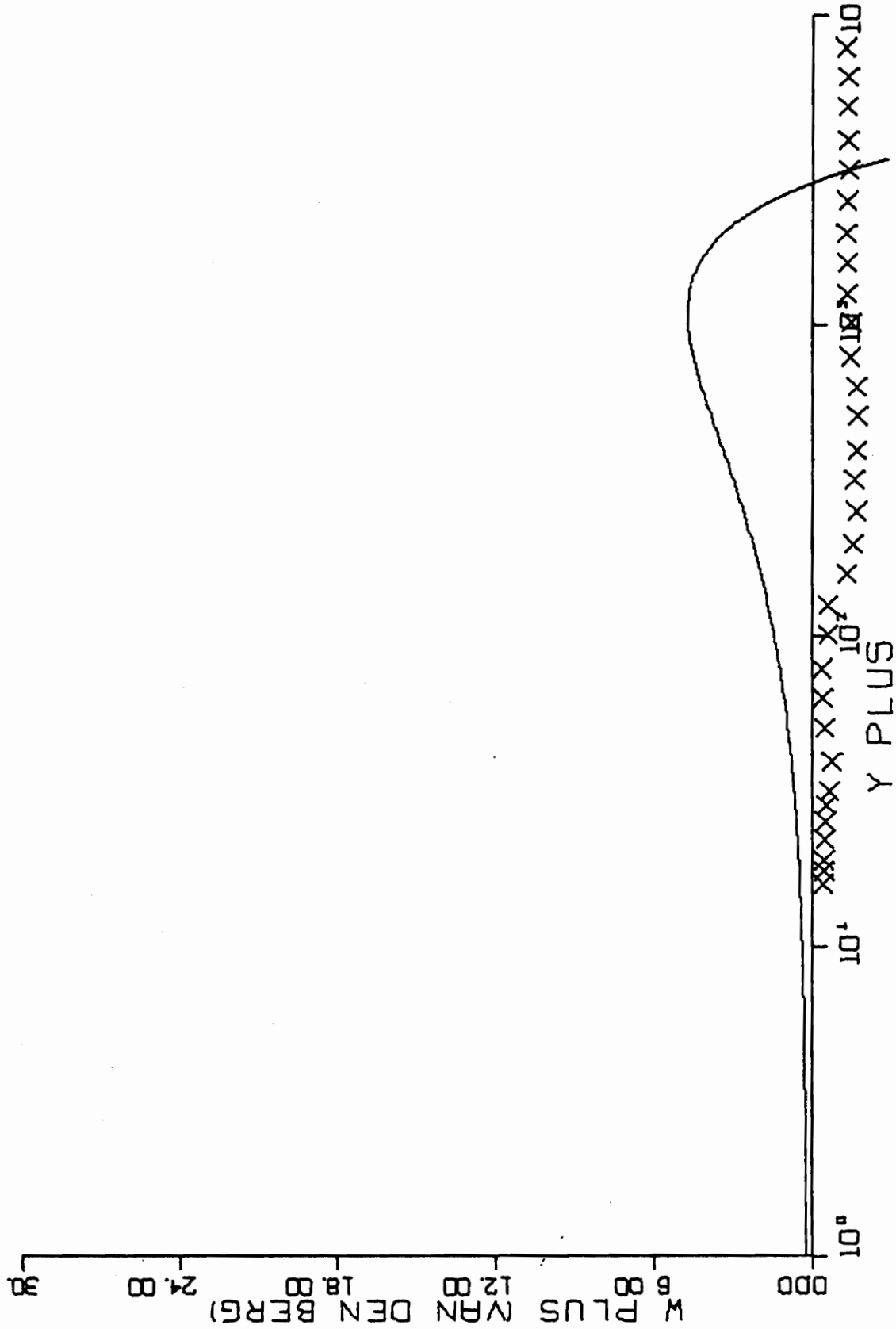

FIG. B30-4. CONTINUED FOR RUN I-3-01.

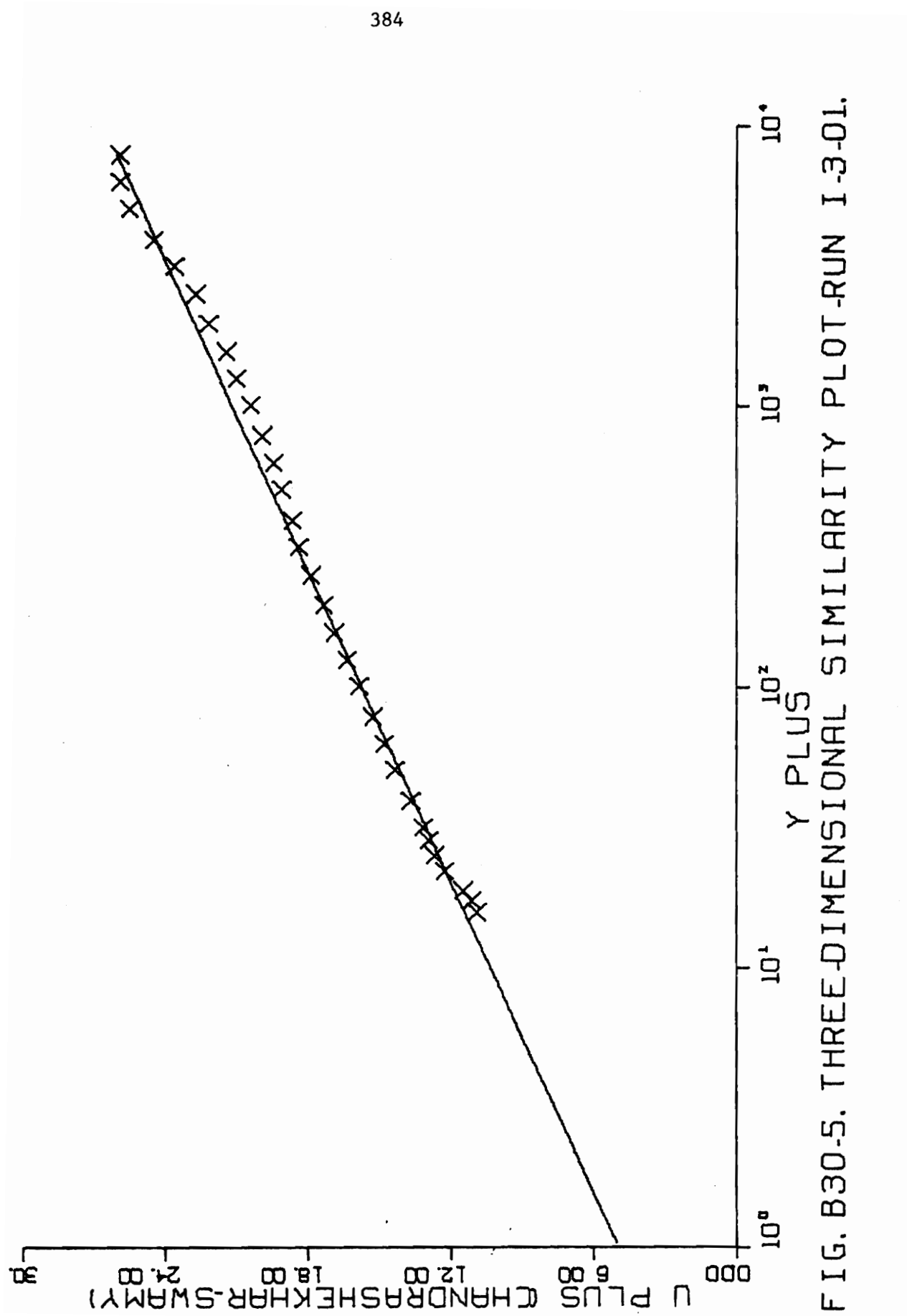

FIG. B30-5. THREE-DIMENSIONAL SIMILARITY PLOT-RUN I-3-01.

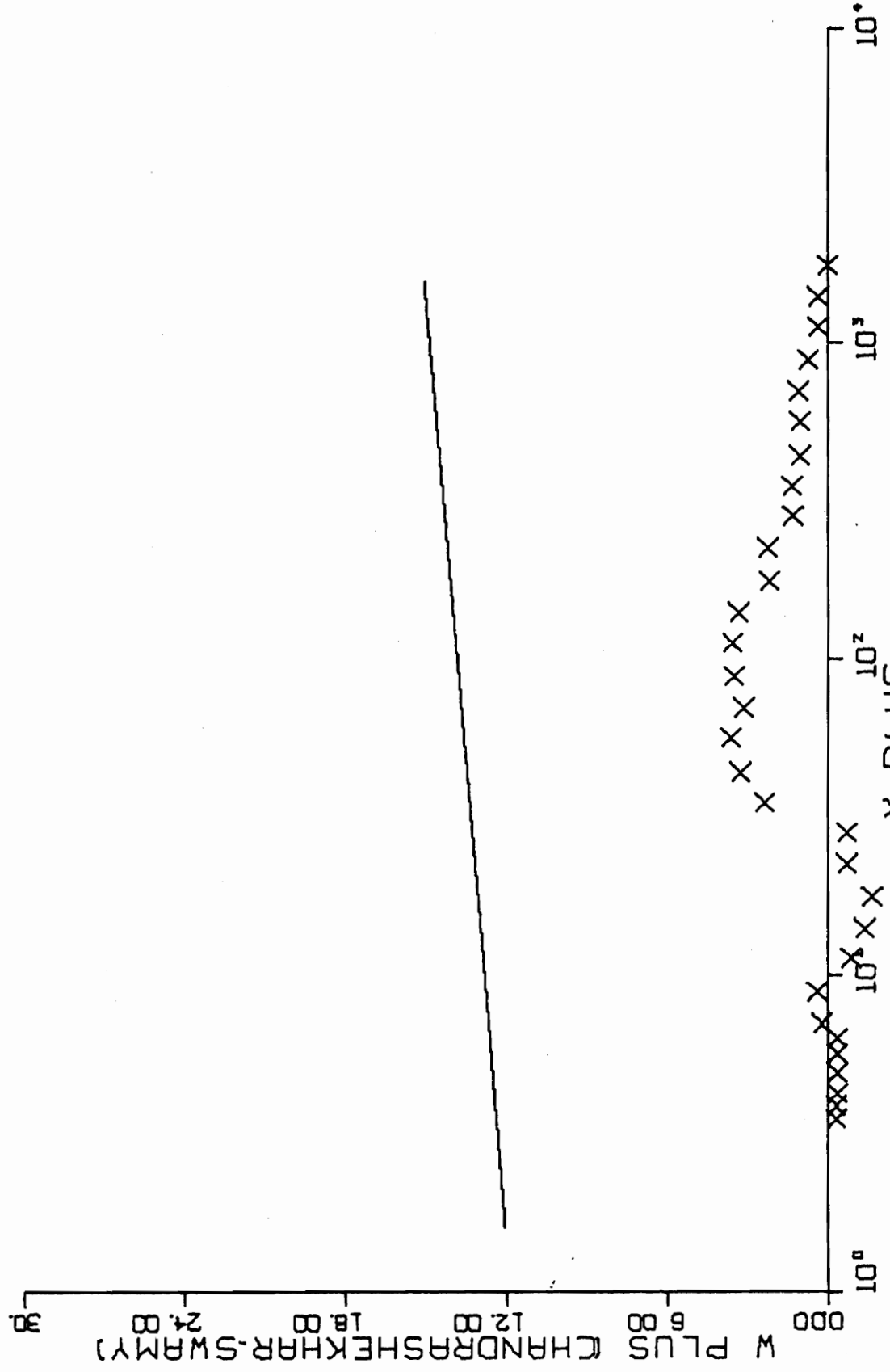

FIG. B30-5. CONTINUED FOR RUN I-3-01.

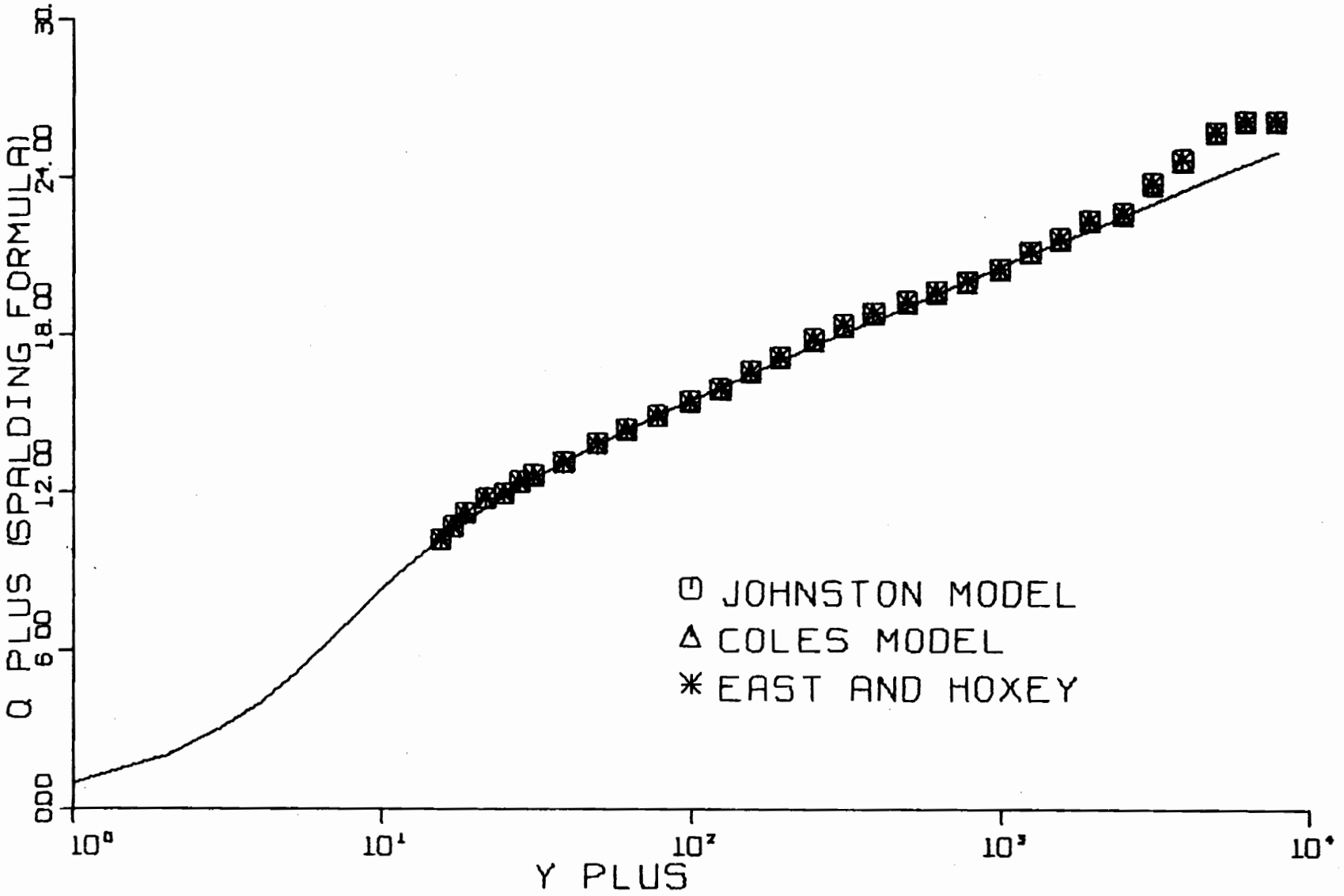

FIG. B31-1. THREE-DIMENSIONAL SIMILARITY PLOT-RUN I-5-01.

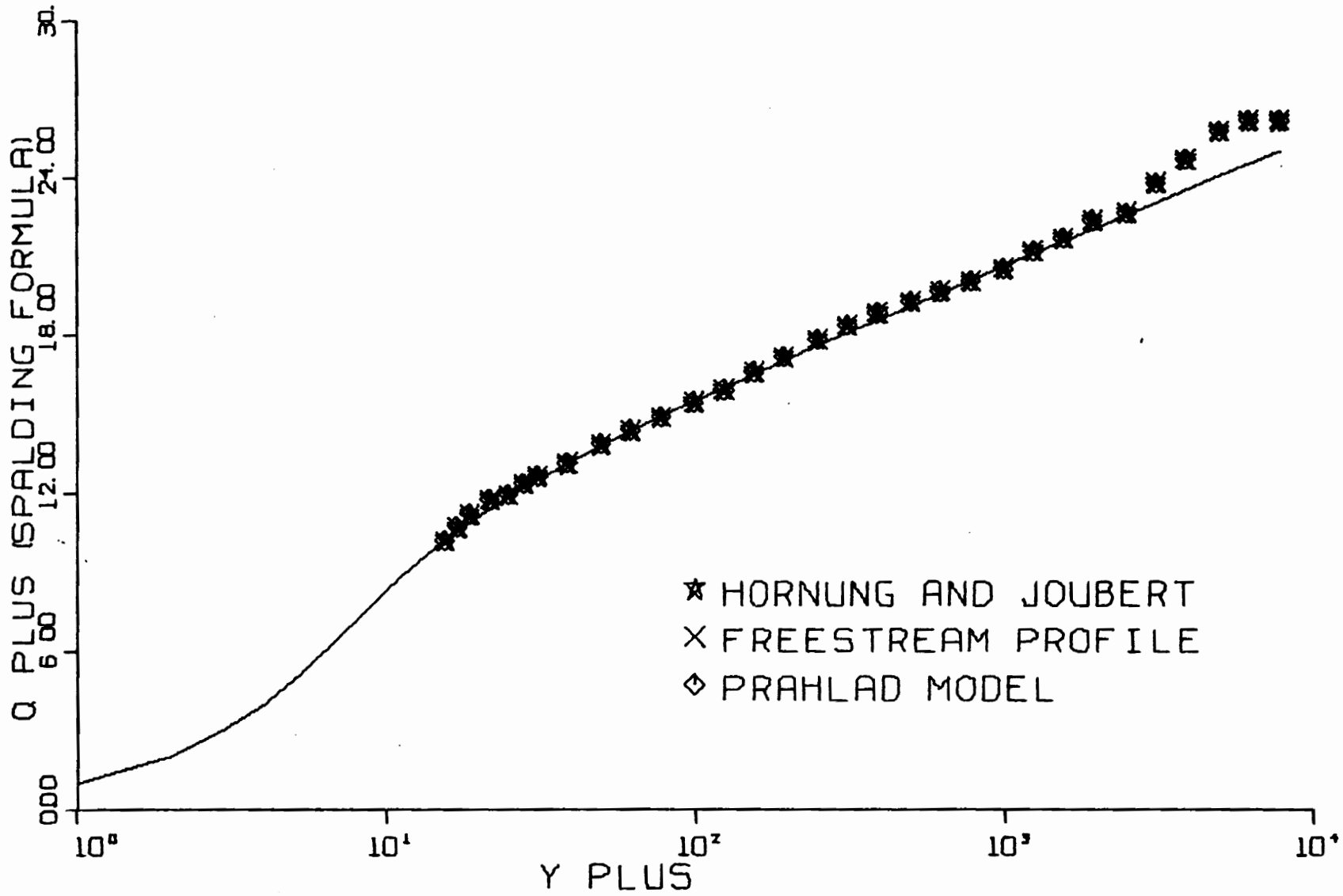

FIG. B31-2. THREE-DIMENSIONAL SIMILARITY PLOT-RUN I-5-01.

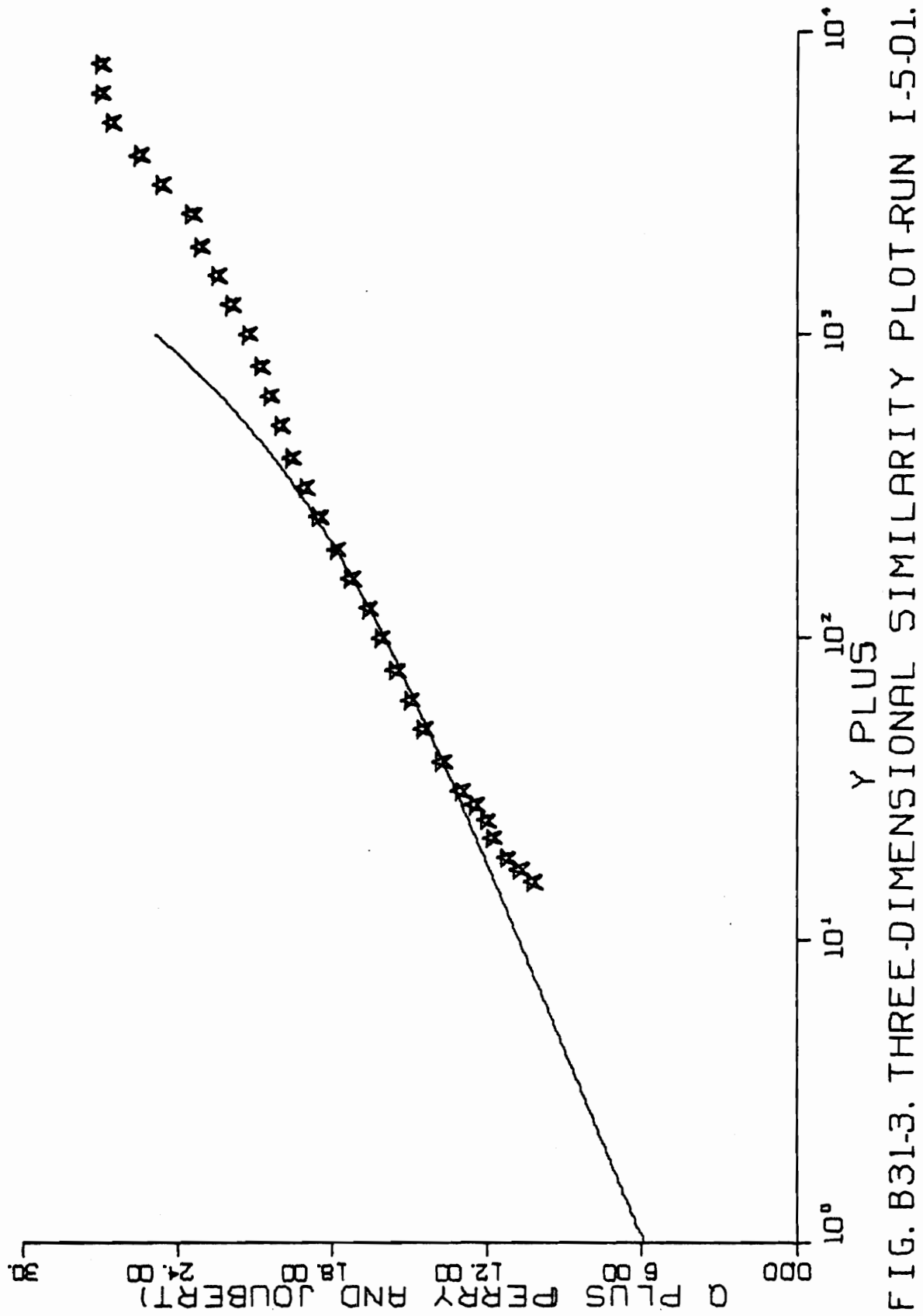

FIG. B31-3. THREE-DIMENSIONAL SIMILARITY PLOT-RUN I-5-01.

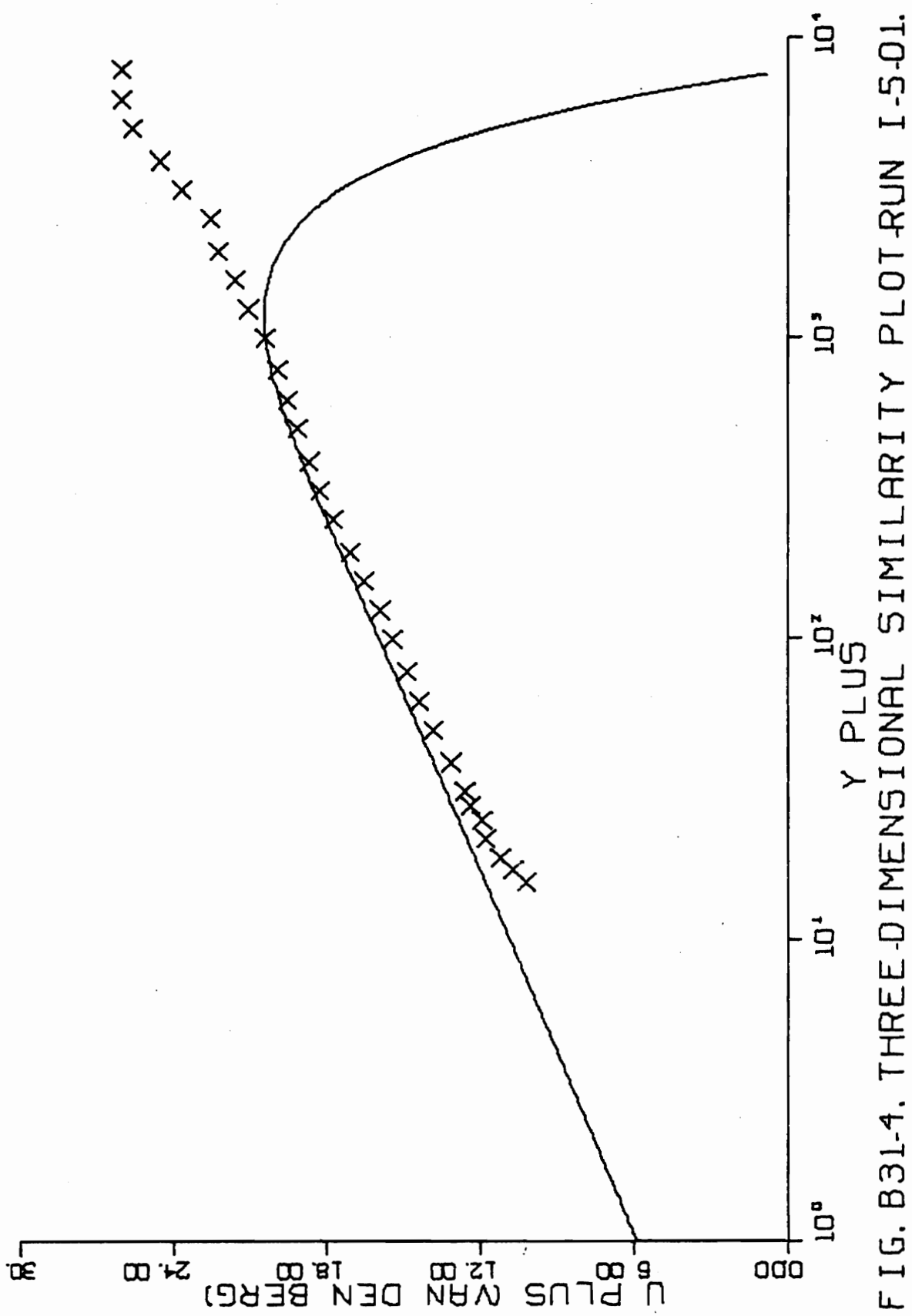

FIG. B31-4. THREE-DIMENSIONAL SIMILARITY PLOT-RUN I-S-01.

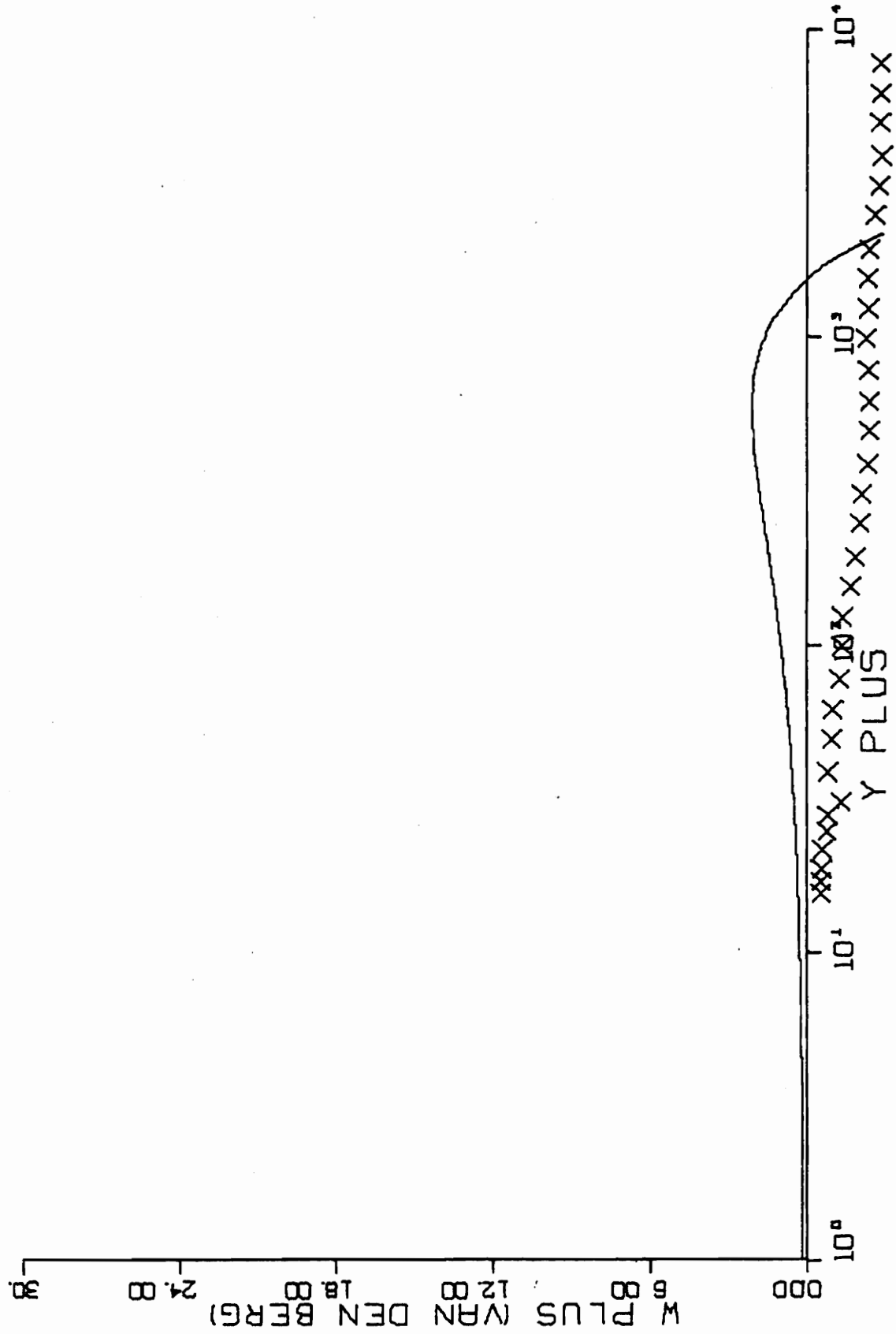

FIG. B31-4. CONTINUED FOR RUN I-5-01.

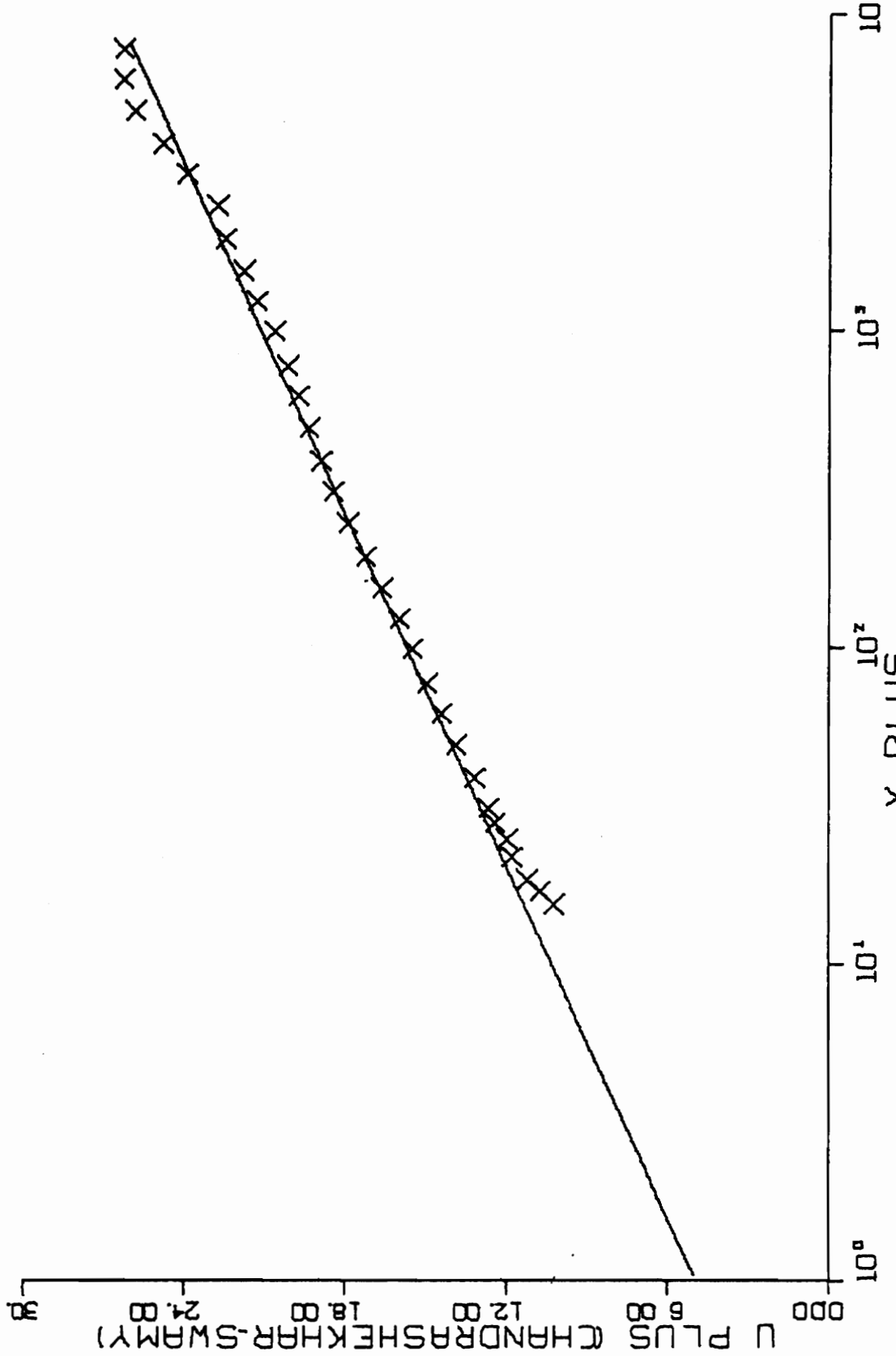

FIG. B31-5. THREE-DIMENSIONAL SIMILARITY PLOT-RUN I-5-01.

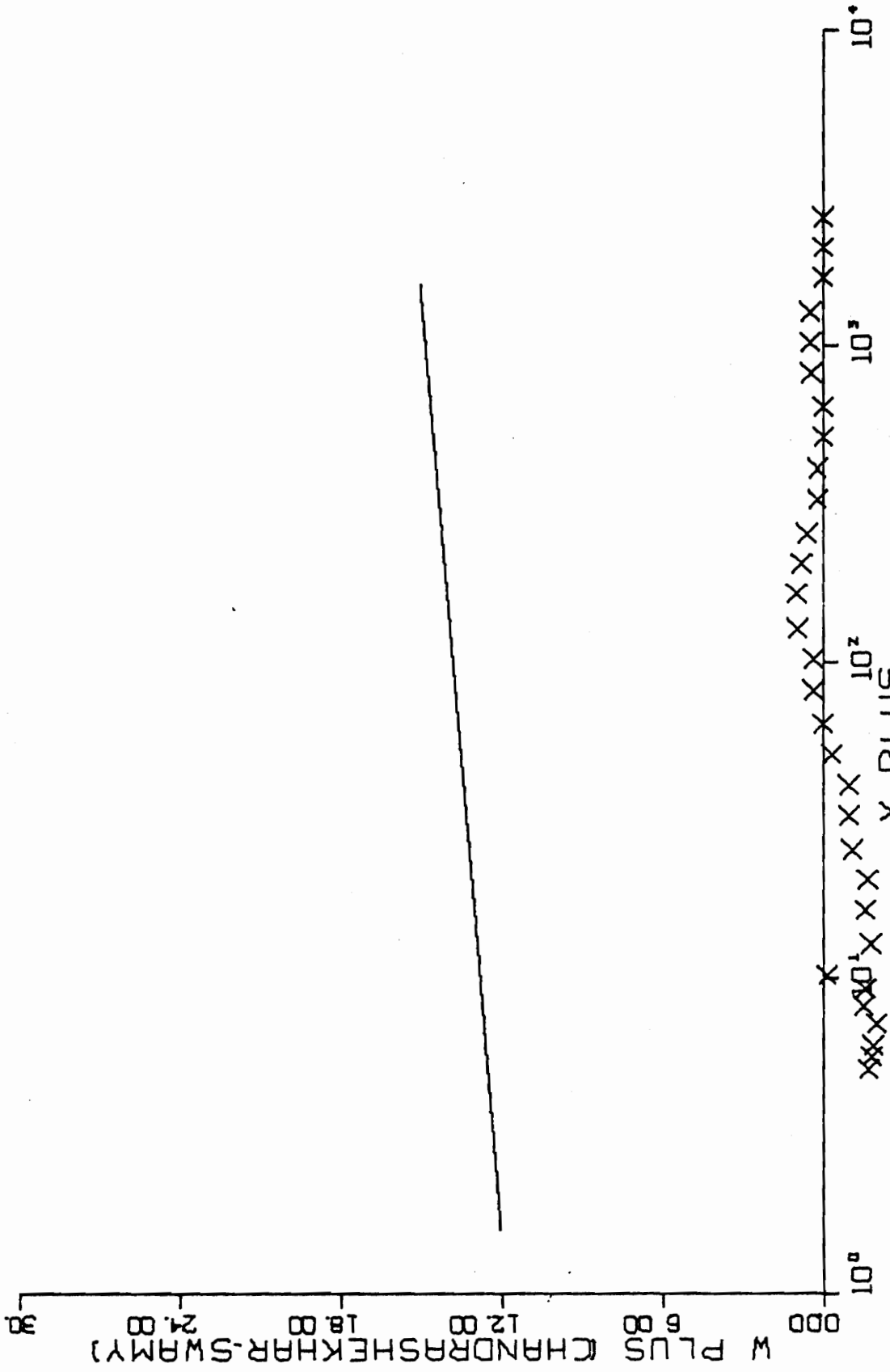

FIG. B31-5. CONTINUED FOR RUN I-5-01.

VITA

Mark Harris Tennant was born in Phillipi, W. Va. on January 10, 1948. He is the son of Evelyn H. and the late Paul S. Tennant. His childhood was spent in North Augusta, S.C., where he graduated from North Augusta High School in 1966 with honors. As an undergraduate at Clemson University, Clemson, S.C., he was elected to Tau Beta Pi and Phi Kappa Phi, and received a ROTC Superior Cadet Award as well as a Biomedical Engineering Award presented by the Department of Surgery, Medical College of South Carolina. There he began his continued membership in AIAA and ASME. Graduating with honor, he received a Bachelor of Science degree in Mechanical Engineering in 1970. Two years later, he received a Master of Science degree in Mechanical Engineering, also from Clemson University. Joining Westinghouse Electric Corporation as an Engineer in 1972, he performed thermal-hydraulic analysis for the development and testing of the A4W nuclear reactor core at Bettis Atomic Power Laboratory, West Mifflin, Penn. In 1973, he joined the faculty of the Department of Mechanical Engineering at Virginia Polytechnic Institute and State University as an Instructor, and has since worked toward a Doctor of Philosophy degree. Upon completion of that degree, he will be employed as a Research Engineer with E. I. DuPont at the Savannah River Laboratory in Aiken, S.C. Mr. Tennant is a Captain in the Army Reserves and a registered Professional Engineer.

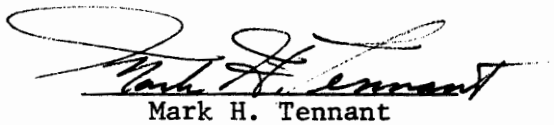

Mark H. Tennant

NEAR-WALL SIMILARITY IN THREE-DIMENSIONAL TURBULENT BOUNDARY LAYERS

by

Mark H. Tennant

(ABSTRACT)

A comprehensive set of data was measured for the three-dimensional case of plane, incompressible, turbulent boundary layer flow around a vertical cylinder with a trailing edge. Included were over one hundred direct measurements of wall shear stress using a specially designed, omnidirectional, floating element device, over thirty corresponding velocity profiles, and the neighboring static pressure field.

Using these data, comparisons were made among nine near-wall similarity models. Evidence from these comparisons tends to support the hypothesis of three-dimensional near-wall similarity, at least for regions moderately remote from separation. The form of the three-dimensional near-wall similarity law apparently must at least consider pressure gradient effects, and appears to be approximated by the model suggested in 1965 by Perry and Joubert.